UQAC
Université du Québec
à Chicoutimi

Les roles de Te, As, Bi, Sb et Sn (TABS) lors de la formation des gisements d'elements du groupe du platine

par Eduardo Mansur

Thèse présentée à l'Université du Québec à Chicoutimi en vue de l'obtention du grade de Doctorat (Ph.D.) en Sciences de la Terre et de l'atmosphère

Québec, Canada

RÉSUMÉ

Les processus requis pour former une gisement magmatique à sulfures de Ni-Cu et éléments du groupe du platine (EGP) comprennent: la saturation d'un magma mafique ou ultramafique avec un liquide sulfure de métal de base; interaction du liquide sulfuré avec le magma mafique; cristallisation d'une solution solide de monosulfure (*MSS*), d'une solution solide intermédiaire (*ISS*) et éventuellement de minéraux du groupe du platine (MGP) à partir du liquide sulfuré; exsolution de *MSS* et *ISS* pour former des sulfures de métaux de base (SMB) et MGP; et modification des SMB par des fluides magmatiques tardifs ou métamorphiques. Indépendamment des processus impliqués au cours de la genèse, dans la plupart des dépôts de sulfures magmatiques, les EGP sont trouvés généralement dans la structure des SMB, ou sous la forme de MGP. Ces MGP consistent principalement en la combination des EGP avec au moins un des éléments suivants: Te, As, Bi, Sb et Sn (TABS). Par conséquent, l'association fréquente des EGP avec les TABS amène à la question principale de ce projet: quel est le rôle de TABS lors de la formation des gisements de EGP?

Les rôles suggérés pour TABS lors de la formation de dépôts de sulfures magmatiques sont:

i) La présence des concentrations élevées de TABS provoque la cristallisation directe des MGP à partir d'un magma silicaté;

ii) Le liquide sulfuré pourrait devenir saturé dans un liquide immiscible riche en TABS, qui collecte des EGP, et les MGP pourrait cristalliser à partir de ce liquide;

iii) Des concentrations progressivement plus élevées de TABS dans le liquide sulfuré pourraient amener à la cristallisation directe des MGP.

iv) Pendant le refroidissement, les EGP peuvent se combiner avec les TABS et se exsolvé sous la forme des MGP à partir des SMB.

v) Les TABS peuvent soit être remobilisés avec le EGP pendant l'altération post-magmatique, ou soit agir comme des agents de fixation des EGP pendant la remobilisation tardive.

Une partie du problème dans l'étude des TABS est que ces éléments ne sont pas systématiquement déterminés dans les analyses de roche en totale ou dans les minéraux. La très faible concentration de TABS, combinée à leur volatilité, a conduit à les négliger au cours des dernières décennies. Par conséquent, la première étape du projet a été de mettre en place une routine analytique pour déterminer les TABS dans le roche totale à de faibles concentrations, en utilisant la spectroscopie de fluorescence atomique couplée à un générateur d'hydrure (*HG-AFS*).

À la suite du développement analytique, les concentrations de TABS dans les roche totale, les SMB et les minéraux silicatés ont été mesurées dans des échantillons provenant: i) du district minier de Noril'sk-Talnakh; i) les gisements de type *PGE-reef* des complexes du Bushveld et Stillwater (*Merensky Reef, J-M Reef et Picket Pin*); iii) des horizons stériles en EGP localisé à l'extérieur des intervalles minéralisé des complexes du Bushveld et Stillwater et; iv) la *Marginal Zone* du complexe du Bushveld. Les échantillons du district minier de Noril'sk-Talnakh comprennent des sulfures massifs riches en Ni-Cu-EGP, ce qui a permis d'étudier le comportement des TABS lors de la cristallisation fractionnée du liquide sulfuré. Par contre, les échantillons des *Reefs* de EGP des complexes du Bushveld et Stillwater contiennent des sulfures disséminés, ce qui a permis d'étudier la distribution de TABS dans les minerais qui ont subi une cristallisation à l'équilibre. Les échantillons de la *Marginal Zone* du complexe du Bushveld ont permis de déterminer la concentration de TABS dans les

liquides initiaux qui ont cristallisé cette intrusion, ainsi que les processus qui ont affecté la distribution de TABS dans ces liquides.

Pendant la cristallisation fractionnée du liquide sulfuré, les TABS (avec Pt et Pd) sont incompatibles dans le *MSS* et *ISS,* et restent dans le dernier liquide sulfuré, plus fractionné. Bien que les concentrations de TABS n'atteignent pas des niveaux suffisamment élevés pour qu'un liquide imiscible riche en TABS se forme, elles se combinent avec Pd et Pt et cristallisent sous la forme des MGP, directement à partir du liquide sulfuré fractionné. D'un autre côté, les minerais formés par cristallisation à l'équilibre, tels que les *Reefs* à EGP des complexes du Bushveld et Stillwater, enregistrent l'effet de l'exsolution des MGP à partir des SMB. Dans ces cas, des concentrations élevées des EGP dans les SMB ont créé un potentiel chimique pour l'exsolution des MGP. Par conséquent, les EGP ont combiné avec les TABS et ont exsolvé sous la forme des MGP. Par conséquent, le SMB trouvé dans les *Reefs* sont épuisé dans TABS par rapport au SMB trouvé dans des échantillons provenant de l'extérieur des *Reefs*.

Les résultats obtenus pour les TABS dans les liquides initiaux qui ont cristallisé le complexe du Bushveld (*Marginal Zone*) ont montré que leur distribution dépend en grande partie de leur comportement chalcophile. Le Te et le Se sont des éléments fortement chalcophiles, et leur distribution est principalement contrôlée par les sulfures. Par contre, As et Sb ne sont que des éléments légèrement chalcophiles, et leur distribution est principalement contrôlée par le degré de cristallisation fractionnée et l'assimilation crustale des magmas. Le Bi est modérément chalcophile et sa distribution résulte d'une combinaison des processus susmentionnés.

ABSTRACT

Processes required to form magmatic sulfide Ni-Cu and platinum-group element (PGE) deposits include: saturation of a mafic or ultramafic magma with a base metal sulfide liquid; interaction of the sulfide liquid with the mafic magma; crystallization of monosulfide solid solution (MSS), intermediate solid solution (ISS) and possibly platinum-group minerals (PGM) from the sulfide liquid; exsolution of MSS and ISS to form base metal sulfides and PGM; and modification of the magmatic BMS by late magmatic or metamorphic fluids. However, regardless of the processes involved during the genesis, in most magmatic sulfide deposits the PGE generally occur within BMS structure, or as discrete PGM. These PGM mainly consist of the binding of PGE with at least one of the elements Te, As, Bi, Sb and Sn (TABS). Therefore, the frequent association of PGE with TABS leads to the main question of this project: what is the role of TABS during the formation of PGE deposits?

Suggested roles for TABS during the formation of magmatic sulfide deposits are:

i) The presence of high concentrations of TABS leads to direct crystallization of PGM from silicate magma;

ii) The sulfide liquid could become saturated in an immiscible TABS-rich liquid, which collects PGE, and PGM could further crystallize from this liquid;

iii) Progressively higher concentrations of TABS in the sulfide liquid could lead to the direct crystallization of PGM.

iv) Upon cooling PGE may combine with TABS and exsolve as PGM from BMS.

v) TABS may either be remobilized together with PGE during post-magmatic alteration, or alternatively, act as fixing agents for PGE during late remobilization.

Part of the problem of studying TABS is that these elements are not routinely determined in whole rock or mineral analyses. The very low concentration of TABS, combined with their volatility, has resulted in them being neglected by researchers over the past decades. Therefore,

the first step of the project was to implement an analytical routine to determine TABS in whole-rock at low concentrations, using hydride generation-atomic fluorescence spectrometry (HG-AFS).

Following the analytical development, concentrations of TABS in whole-rock, BMS and silicate minerals were measured in samples from: i) the Noril'sk-Talnakh mining district; i) the PGE-reef type deposits of the Bushveld and Stillwater Complexes (Merensky Reef, J-M Reef and Picket Pin deposit); iii) PGE-barren horizons from outside the reef intervals of the Bushveld and Stillwater Complexes and; iv) the Marginal Zone of the Bushveld Complex. The samples from the Noril'sk-Talnakh mining district comprise massive sulfide ores, which allowed investigating the behaviour of TABS during fractional crystallization of the sulfide liquid. In contrast, samples from the PGE-reefs of the Bushveld and Stillwater Complexes contain disseminated sulfide minerals, which allowed investigating the distribution of TABS in ores than underwent predominantly equilibrium crystallization. Finally, the samples from the Marginal Zone of the Bushveld Complex allowed constraining the concentration of TABS in the initial liquids that crystallized this intrusion, and also which processes affected the distribution of TABS in initial liquids.

During fractional crystallization of the sulfide liquid, TABS (together with Pt and Pd) are incompatible into the crystallizing MSS and ISS, and remain in the lattermost fractionated sulfide liquid. Although concentrations of TABS do not reach sufficiently high levels for an immiscible TABS-rich liquid to segregate, they combine with Pd and Pt and crystallize as composite PGM, directly from the fractionated sulfide liquid which is enriched in TABS. On the other hand, ores formed by equilibrium crystallization, such as the PGE reefs of the Bushveld and Stillwater Complexes, record the effect of PGM exsolution from BMS. In these cases, high PGE concentrations in BMS created a chemical potential for the exsolution of PGM. Therefore, PGE combined with TABS and exsolved as PGM. Consequently, the BMS found within the PGE reefs are depleted in TABS relative to the BMS found in samples from outside the reef intervals.

The results for TABS in the initial liquids that crystallized the Bushveld Complex (Marginal Zone) revealed that their distribution largely relies on their chalcophile behaviour. Tellurium and Selenium are strongly to highly chalcophile elements, and their distribution is mainly controlled by sulfide minerals. In contrast, As and Sb are only slightly chalcophile elements, and their distribution is mainly controlled by the degree of fractional crystallization, and crustal assimilation of the magmas. Bismuth is moderately chalcophile, and its distribution results from a combination of the aforementioned processes.

TABLE DES MATIÈRES

LISTE DES FIGURES

CHAPITRE 1

CHAPTER 2

CHAPTER 3

CHAPTER 4

CHAPTER 5

CHAPTER 6

LISTE DES TABLEAUX

CHAPITRE 1

CHAPTER 2

CHAPTER 3

CHAPTER 5

LISTE DES ANNEXES

Chapitre 1 - Introduction, problème et méthodologie

1.1 - Introduction

Les éléments critiques et les matières premières critiques sont définis comme des ressources d'importance économique qui présentent un risque lié à leur approvisionnement (European Commission, 2014). Ces ressources sont généralement utilisées dans le développement de technologies durables. Des études récentes ont présenté une liste de matières premières (Fig. 1.1) qui sont essentielles pour de nombreuses technologies émergentes (European Commission, 2010 et 2014). Parmi ces matériaux critiques figurent les éléments du groupe du platine (EGP) et les éléments appelés TABS (Te, As, Bi, Sb et Sn; Barnes, 2016). Bien que certains ne soient pas indiqués comme étant une matière première critique dans ces études, ils ont une importance économique significative (Fig. 1.1). D'autres études soulignent également que certains des TABS sont essentiels au développement de technologies énergétiques à faible émission de carbone (Zweibel, 2010; Moss et al., 2013). La production de ces éléments et matériaux est souvent limitée à la production de sous-produits de l'extraction des métaux de base (USGS, 2020). Étant donné que le développement récent de sources d'énergie durables accroît la demande pour ces éléments essentiels, il est très intéressant de comprendre leur distribution dans les différents réservoirs terrestres.

Les TABS sont aussi étudiés en raison du risque qu'ils présentent pour l'environnement (notamment As et Sb). Diverses études ont mis en évidence plusieurs zones sensibles à la contamination par l'antimoine et l'arsenic (par exemple, le sol, les eaux de surface et souterraines; Singh et al., 2015; Jamieson, 2016). Par conséquent, l'intérêt pour la surveillance de ces éléments pendant les opérations minières et la récupération des zones contaminées a considérablement augmenté au cours des dernières années (Jamieson, 2016 et références y contenues). Ce problème a également conduit les agences gouvernementales à développer des routines analytiques pour contrôler la concentration de ces éléments dans les aliments (U.S Food and Drug Administration, 2015).

Les EGP sont essentiels dans les industries de l'énergie durable, des catalyseurs automatiques et des bijoux (revue annuelle Johnson Matthey 2019). De nombreuses études ont révélé que les EGP sont généralement trouvés dans la structure des SMB (Barnes et Ripley, 2016 et références), ou sous forme de MGP. Ces MGP consistent principalement en la combinaison des EGP avec au moins un des TABS. Compte tenu de l'association fréquente dee EGP avec TABS, une question majeure se pose: quel est le rôle des TABS lors de la formation des gisements de EGP?

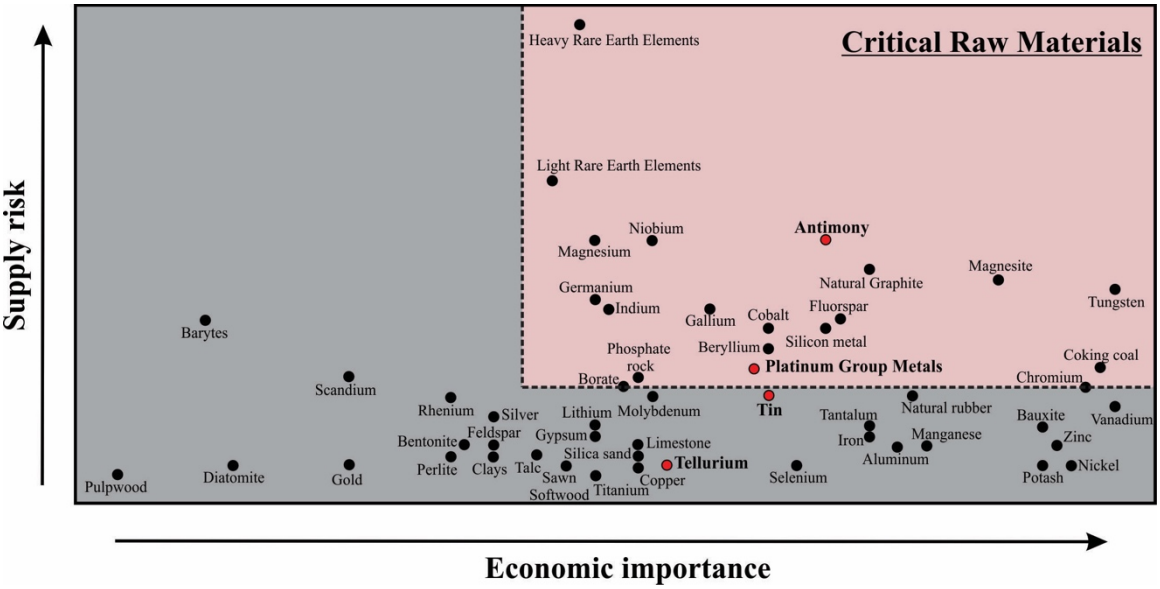

Figure 1.1 - Matières premières critiques indiquées par la Commission européenne en 2013. Les matières premières critiques sont indiquées comme celles ayant une importance économique élevée, associées à un risque d'approvisionnement élevé. Au total, 54 matériaux ont été étudiés et un groupe de 20 est indiqué comme critique. L'antimoine, l'étain, le tellure et des EGP sont mis en évidence. Données de la Commission européenne, 2014.

Différents processus ont été proposés. Certaines études indiquent que les MGP cristallisent directement à partir du magma silicaté (Park et al., 2013; Maier et al., 2015; Barnes et al., 2016). D'autres que les MGP cristallisent à partir d'un liquide sulfuré immiscible (Barnes et al., 2006; Hutchinson et McDonald, 2008; Dare et al., 2010a, 2010b et 2014). Le liquide sulfuré pourrait devenir saturé dans une liquide immiscible riche en TABS, et les MGP pourraient cristalliser à partir de cette liquide (Hanley, 2007; Helmy et al. 2007, 2013; Holwell et McDonald 2007; Cafagna et Jugo, 2016; Sinyakova et al., 2017). Alternativement, les EGP

peuvent se combiner avec les TABS et exsolver comme MGP à partir des SMB (Prichard et al., 2004; Godel et al., 2007; Barnes et al., 2008).

D'autres auteurs préfèrent une origine hydrothermale pour les gisements des EGP (Boudreau et Meurer, 1999; Tuba et al., 2014). La mobilité des EGP et des TABS dans les fluides magmatiques / hydrothermaux a été abordée dans des expériences récentes (Guo et Audétat, 2017; Sullivan et al., 2018) et des études empiriques (Zelenski et al., 2013 et 2014; Edmonds et al., 2018; Cox et al., 2019; Wiesener et al., 2020). Par contre, à des températures plus basses, les TABS se sont révélés avoir une faible solubilité, et ils pourraient donc agir comme agents de fixation pendant le transport hydrothermal des EGP (Wood, 2002). Le rôle précis des TABS lors de la remobilisation des EGP est encore mal contraint.

Un problème majeur dans l'étude du rôle des TABS est leurs niveaux intrinsèquement faibles dans les roches silicatées des gisements de EGP (Barnes et Ripley, 2016). Cependant, la forte volatilité des TABS entrave les procédures analytiques courantes (Lodders, 2003). Par conséquent, les concentrations de TABS dans les gisements de EGP sont limitées. Par conséquent, le développement d'une routine analytique pour TABS dans les roches silicatées est une partie essentielle de ce projet.

Afin d'explorer le rôle que jouent les TABS dans la minéralisation de EGP, des échantillons des gisements des EGP dans des différents milieux géologiques ont été étudiés. Les gisements sélectionnés sont: i) le district minier de Noril'sk-Talnakh ii) le Complexe du Bushveld – *Merensky Reef*; iii) le Complexe du Stillwater - *John Manville Reef*. De plus, des échantillons de la *Marginal Zone* du Complexe du Bushveld ont également été étudiés. Ces derniers échantillons sont interprétés pour enregistrer la composition des magmas initiaux qui ont cristallisé le Complexe du Bushveld. Par conséquent, ils permettent d'évaluer la distribution de TABS dans les liquides qui ont cristallisé certains des gisements de EGP le plus bien étudiés dans le monde. Dans l'ensemble, les caractéristiques générales des échantillons sélectionnés ont

fait l'objet d'études antérieures, qui fournissent une solide base géologique à la présente enquête. Une brève revue de la littérature des concepts pertinents pour le projet est présentée comme suit.

1.2 – Problème

1.2.1 – Cycle géochimique des TABS

Étant donné le comportement similaire et également l'association avec des EGP, se sera considéré avec des TABS dans cette section.

Selon la classification séculaire de Goldschmidt, les TABS sont considérés comme des éléments chalcophiles (aimant le soufre) (Goldschmidt, 1923). Cependant, des concentrations plus élevées de TABS dans le noyau de la Terre par rapport au manteau primitif soutiennent que les TABS se sont comportés comme des éléments sidérophiles pendant la ségrégation du noyau (Tableau 1.1). Les concentrations de As, de Se et de Te dans le noyau sont 100 fois plus élevées, tandis que les concentrations de Sn, Sb et Bi sont 5 à 20 fois plus élevées que celles du manteau primitif (Fig. 1.2). Cela reflète probablement des conditions de faible fugacité en oxygène au cours des premiers stades de différenciation de la terre (Lodders, 2003).

Une fois que la fugacité en oxygène dans le manteau primitif ne permet pas la formation extensive d'alloys, les TABS se comportent comme des éléments chalcophiles lors de la fusion du manteau (Harvey et Day, 2016 et références). Par conséquent, leur distribution dépend fortement de la présence des sulfures résiduels dans le manteau. Cependant, les sulfures n'exercent pas un contrôle uniforme sur tous les TABS. Sur la base des coefficients de partage entre les liquides sulfurés et silicatés, Sn, As et Sb peuvent être classés comme éléments légèrement chalcophiles, Bi et Se comme éléments modérément chalcophiles et Te comme élément fortement chalcophile (Tableau 1.1; Li et Audétat, 2015; Liu et Brenan, 2015; Barnes, 2016). Le résultat du comportement chalcophile distinct de TABS pendant la fusion du manteau devient évident lorsque l'on compare différents magmas (Fig. 1.3).

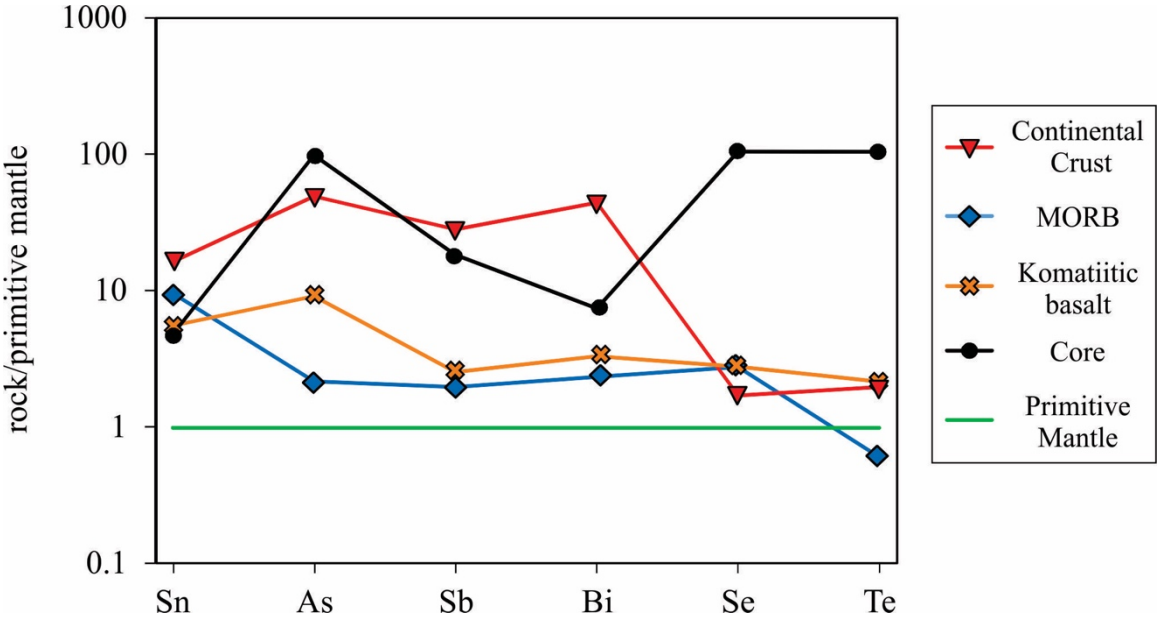

Figure 1.2 - Concentrations TABS + Se normalisées au manteau primitif dans le noyau (McDonough, 2003), les basaltes komatiitiques (Barnes, 2016), les MORB moyenne (Arevalo et McDonough, 2010) et la croûte continentale moyenne (Rudnick et Gao, 2003). Les éléments sont mis par ordre d'incompatibilité avec un basalte komatiitique, d'après Barnes (2016). Valeurs du manteau primitif de Lyubetskaya et Korenaga (2007).

Tableau 1.1 - Concentration moyenne de TABS + Se (ppm) dans le noyau, le manteau primitif, les basaltes komatiitiques, le MORB et la croûte continentale, leurs coefficients de partage entre les liquides sulfurés et les liquides silicatés, et les températures de condensation. Sources: 1- McDonough (2003); 2- Lubetskaya and Korenaga (2007); 3- Arevalo and McDonough (2010); 4- Barnes (2016); 5- Rudnick and Gao (2003); 6- Barnes and Ripley (2016); 7- Lodders (2003).

	Noyau[1]	Manteau primitif[2]	Basalte komatiitique[4]	MORB[3]	Croûte continentale[5]	coefficients de partage entre les liquides sulfurés et les liquides silicatés ($K_D^{sulf/sil}$)[6]	Températures de condensation (K)[7]
Te	0.85	0.008	0.017	0.005	0.016	1005 - 8789	709
As	5	0.05	0.46	0.11	2.5	0.3 - 15	1065
Bi	0.03	0.004	0.013	0.01	0.18	130 - 1130	746
Sn	0.5	0.103	0.58	1	1.7	2.7-8.6	704
Sb	0.13	0.007	0.018	0.014	0.2	1.4 - 67	979
Se	8	0.075	0.211	0.21	0.13	226 - 2339	697

Les concentrations de Te dans les MORB sont légèrement inférieures à celles du manteau primitif, tandis que les concentrations de Se, Bi, Sb, As et Sn dans les MORB sont de 2

à 100 fois plus élevées que celles du manteau primitif. Par contre, les concentrations de tous les TABS dans les basaltes komatiitiques sont de 2 à 10 fois plus élevées par rapport à celles trouvées dans le manteau primitif (Fig. 1.2). En effet, les sulfures résiduels garderaient une fraction d'éléments fortement chalcophiles (par exemple Se et Te) dans le manteau pendant la ségrégation des MORB. Cependant, une fusion plus étendue du manteau, et donc une consommation totale de sulfures, permettrait des concentrations plus élevées de TABS dans les basaltes komatiitiques (Fig. 1.2).

Il est à noter que bien que de nombreuses contributions aient étudié le rôle des sulfures contrôlant la distribution de Te et Se pendant la fusion du manteau (Rose-Weston et al., 2009; Lorand et Alard, 2010; König, et al., 2012; Wang et Becker , 2013; Lissner et al., 2014; Luguet et al., 2015; Yierpan et al., 2019), il n'en va pas de même pour Bi, Sb, Sn et As. Par exemple, Hattori et al. (2002) ont étudié la distribution d'As et de Sb dans les sulfures du manteau. Cependant, des études plus récentes montrent que des minéraux tels que l'apatite ou les micas peuvent également héberger des quantités variables d'As et de Sb (Maciag et Brenan, 2020). De plus, les résultats de Kamenetsky et Eggins (2012), Jenner et O'Neill (2012), Jenner (2017) et Maciag et Brenan (2020) soutiennent le comportement incompatible d'As et de Sb même à des petites degrées de fusion partielle du manteau, où les sulfures resteraient encore comme phase réfractaire. Le besoin de plus d'études sur l'influence de phases autres que les minéraux sulfurés sur la distribution de As, Sb, Sn et Bi pendant la fusion du manteau est soulignée.

La croûte continentale moyenne a des concentrations de Se et de Te proches des valeurs du manteau primitif, tandis que les concentrations de As, Sb, Sn et Bi sont 10 à 50 fois supérieures aux valeurs du manteau primitif (Fig. 1.2). Par conséquent, l'interaction des magmas ultramafiques et mafiques avec les roches crustales est susceptible d'augmenter leurs concentrations en As, Sb, Sn et Bi, mais peu susceptible de modifier les teneurs en Se et Te. Cela devient encore plus critique lorsque on considère l'assimilation de roches sédimentaires telles que les schistes noirs, qui sont considérablement enrichis en éléments chalcophiles (Ketris et Yudovich, 2009). En effet, plusieurs études ont démontré l'augmentation des concentrations

en As, Sb, Sn et Bi dans les magmas ultramafiques et mafiques en raison de l'assimilation des roches crustales (Godel et al., 2012; Piña et al., 2013, 2015; Duran et al. , 2017; Samalens et al., 2017; LeVaillant et al., 2018).

À des pressions plus faibles, les magmas peuvent devenir saturés dans une phase de vapeur, ce qui pourrait affecter la distribution des TABS. En effet, les TABS sont classés comme éléments volatils en raison de leurs températures de condensation relativement faibles lors de la formation du système solaire (Tableau 1.1; Lodders, 2003). Les études expérimentales portant sur la concentration des éléments dans les inclusions fluides par rapport à leurs magmas mafiques hôtes soutiennent également que le TABS se partage à une phase vapeur (Guo et Audétat, 2017). De plus, les TABS sont enrichis en gaz volcaniques (Mather et al., 2012; Zelensky et al., 2013, 2014; Edmonds et al., 2018; Cox et al., 2019; Wiesener et al., 2020) et en fluides provenant de systèmes hydrothermaux (Aguilera et al., 2016; Patten et al., 2017, 2019; Stucker et al., 2017; Shevko et al 2018; Genna et Gaboury, 2019). Récemment, Forrest et al. (2017) ont montré que les basaltes progressivement moins profonds de la crête de Reykjanes vers l'Islande ont des concentrations plus faibles de Se et Te par rapport à leurs équivalents de la dorsale médio-atlantique, ce qui soutient leur perte par dégazage. Cox et al. (2019) ont également trouvé des résultats similaires soutenant le dégazage du Se à basse pression lors de l'enquête sur les laves d'Antuco, au Chili.

1.2.2 – La formation des gisements de sulfures magmatiques

Afin de mieux comprendre la relation entre TABS et EGP dans les gisements de sulfures magmatiques, les principaux processus impliqués dans la formation de ces gisements seront brièvement décrits. Les processus affectant la formation des gisements de sulfure magmatique sont: i) a saturation d'un magma mafique ou ultramafique avec un liquide sulfuré des métaux de base; ii) Interaction du liquide sulfuré avec le magma mafique (*R-factor)*; iii)

Cristallisation d'une solution solide de monosulfure (MSS), d'une solution solide intermédiaire (ISS) et éventuellement des MGP à partir du liquide sulfuré; iv) Exsolution du MSS et de l'ISS pour former de la pyrrhotite (Po), de la pentlandite (Pn), de la chalcopyrite (Ccp) et des MGP; et v) Modification des SMB magmatiques par des fluides magmatiques tardifs ou métamorphiques (Fig.1.3; Campbell et Naldrett 1979; Brügmann et al.1993; Li et al.1996; Naldrett 2004; Prichard et al.2004; Barnes et Lightfoot 2005; Godel et al.2007; Barnes et al.2008; Godel et Barnes 2008; Dare et al.2010b, 2011, 2014; Djon et Barnes 2012; Wirth et al.2013; Duran et al.2015, 2017; Junge et al. 2015; Mota-e-Silva et al.2015; Holwell et al.2017).

Les magmas dérivés directement du manteau ne sont pas saturés dans un liquide sulfuré (Mavrogenes et O'Neill 1999). Par conséquent, pour qu'un magma devienne saturé dans un liquide sulfuré, il est généralement proposé que l'assimilation des sédiments riches en S soit la première étape de la formation d'un gisement (Grinenko 1985; Lesher et Burnham 2001; Ripley et Li 2003; Ripley et al.2003, 2010; Keays et Lightfoot 2010; Fiorentini et al.2012; Robertson et al.2015). Lors de leur mise en place, les magmas mafiques incorporent des xénolithes avec des sulfures des roches hôtes, qui sont progressivement fondus, séparant ainsi les gouttelettes de sulfure dans le magma (Fig.1.3; Queffurus et Barnes 2014; Robertson et al.2015; Samalens et al.2017; Barnes et Robertson 2019). Par conséquent, le liquide sulfuré qui se sépare initialement est enrichi en éléments qui ont des concentrations élevées dans la croûte (Sn, Mo, As, Sb, Pb, Tl, Bi) et pauvres en éléments concentrés dans le magma mafique (PGE, Se, Te, Ni, Co). Les détails concernant le transfert du liquide sulfuré des xénolithes crustaux vers au magmas mafiques, et les effets sur les concentrations d'éléments chalcophiles dans le liquide sulfuré, ont été expliqués en détail par Samalens et al. (2017).

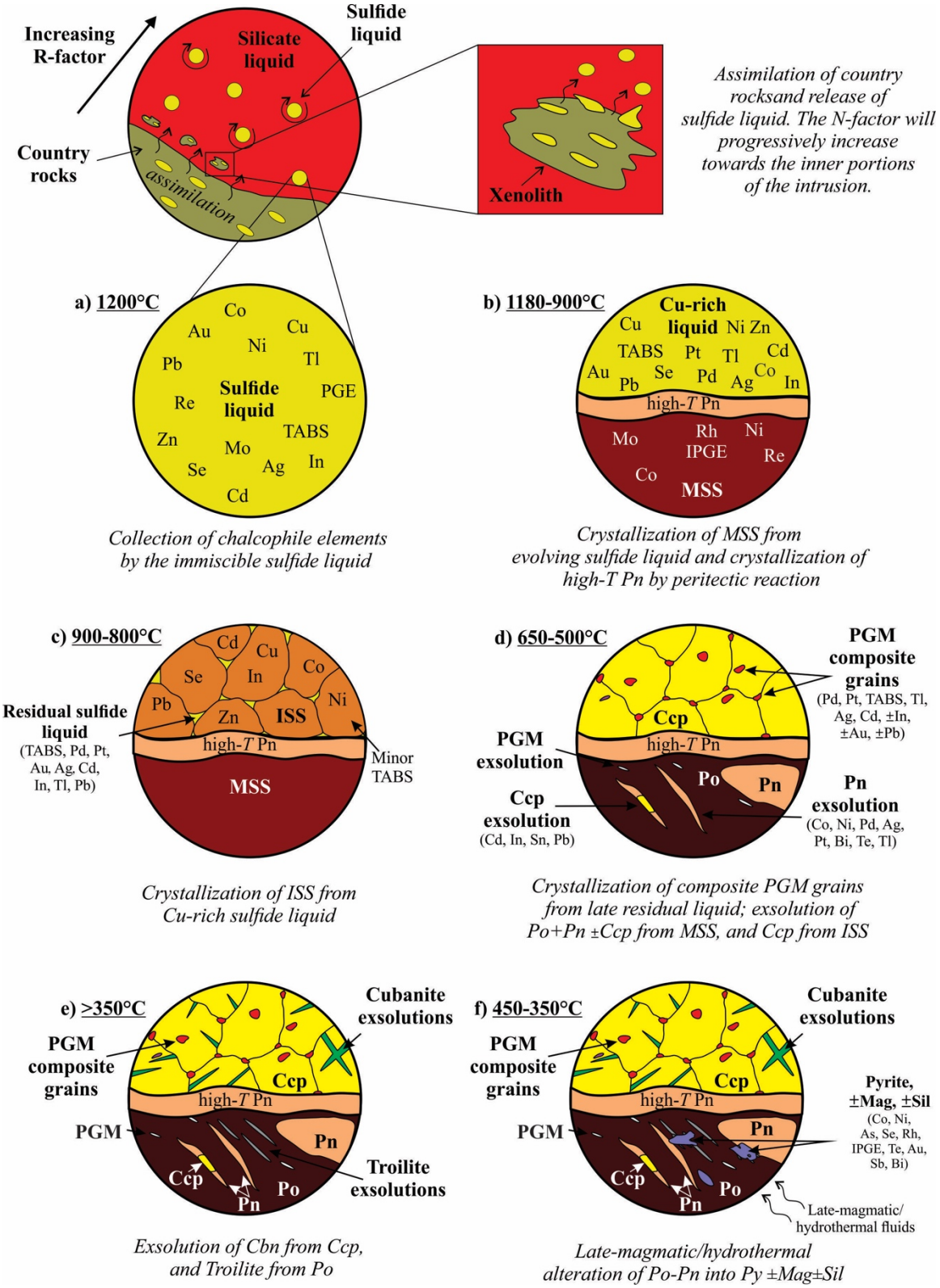

Figure 1.3 - Modèles schématiques illustrant l'histoire de la formation et de la cristallisation d'un gisement de sulfure magmatique et la distribution des éléments chalcophiles. Voir le texte pour plus d'explications. Notez que le modèle présenté comprend une partie des contributions de cette thèse. MSS, solution solide de monosulfure; ISS, solution solide intermédiaire, PGM, minéraux du groupe du platine; Po, pyrrhotite; Pn, pentlandite; Ccp, chalcopyrite; Py, pyrite; Mag, magnétite; Sil, silicates.

Une fois que le liquide sulfuré a été incorporé des roches assimilées, il commence à s'équilibrer avec le magma silicaté (Fig. 1.3a). Les concentrations d'éléments chalcophiles dans le liquide sulfuré équilibré dépendent de leur concentration dans le magma silicaté, du coefficient de partage de l'élément entre le liquide silicaté et le liquide sulfuré et du rapport du liquide sulfuré en relation au liquide silicaté présent (Campbell et Naldrett 1979; Brügmann et al. 1993). La plupart des éléments apportés par la croûte (As, Sb, Bi) ne sont que légèrement à modérément chalcophiles ($D^{sulf\ liq\ /\ sil\ liq}$ = 1-100), tandis que la plupart des éléments chalcophiles dérivés du magma mafique sont fortement ($D^{sulf\ liq\ /\ sil\ liq}$ = 100-1000) à très chalcophile ($D^{sulf\ liq\ /\ sil\ liq}$> 1000) (Fig.1.4; Barnes 2016). Plus le liquide sulfuré réagit avec le magma mafique (c.-à-d. Facteur R plus élevé; Campbell et Naldrett 1979; Brügmann et al. 1993), plus le degré d'enrichissement se rapprochera de son coefficient de partage (Campbell et Barnes 1984). Ainsi, les éléments fortement chalcophiles (par exemple Se et Te) s'enrichissent dans le liquide sulfuré en réagissant avec plus de magma, tandis que les éléments légèrement à modérément chalcophiles (par exemple Sn, As, Sb et Bi) ne sont pas aussi fortement enrichis (Lesher et Burnham 2001; Queffurus et Barnes 2014; Samalens et al. 2017).

Lors du refroidissement (en dessous de 1190ºC), le MSS commence à cristalliser. Le Re, l'IPGE (Ru, Ir, Os), le Rh et le Mo sont compatibles avec le MSS, et le Ni, le Co et le Se sont compatibles a légèrement incompatibles (selon la température: Li et al.1996; Barnes et al.1997; Mungall et al.2005). La plupart des autres éléments chalcophiles sont incompatibles: TABS, Cu, Pt, Pd, Au, Zn, Ag, Pb, Cd, In, Tl (Fig.1.3b; Li et al.1996; Mungall et al.2005; Mungall 2007; Li et Audétat 2015; Liu et Brenan 2015, Sinyakova et al. 2016, 2019). En dessous de 950°C, le liquide riche en Cu commence à cristalliser sous forme d'ISS (Cabri 1973; Dutrizac 1976; Kosyakov et al. 2012), qui incorpore Cu, Cd, In, Se, Sn, Pb et Zn. Le Pd, le Pt, le TABS, l'Ag et le Tl sont incompatibles avec l'ISS et le MSS, et leurs concentrations dans le liquide sulfure riche en Cu augmentent (Fig.1.3c; Dare et al. 2014; Li et Audétat 2015; Liu et Brenan 2015). À environ 900°C, une réaction péritectique entre le liquide fractionné et le MSS

est possible, ce qui conduit à la formation de Pn (figure 1.3b; Kosyakov et Sinyakova 2012; Kitakaze et al. 2016). Aux stades avancés de la cristallisation, le liquide sulfuré piégé peut devenir suffisamment enrichi en éléments incompatibles (en particulier Pt, Pd et TABS) pour cristalliser sous forme de grains de MGP (Dare et al. 2014; Liu et Brenan 2015; Duran et al. 2017) .

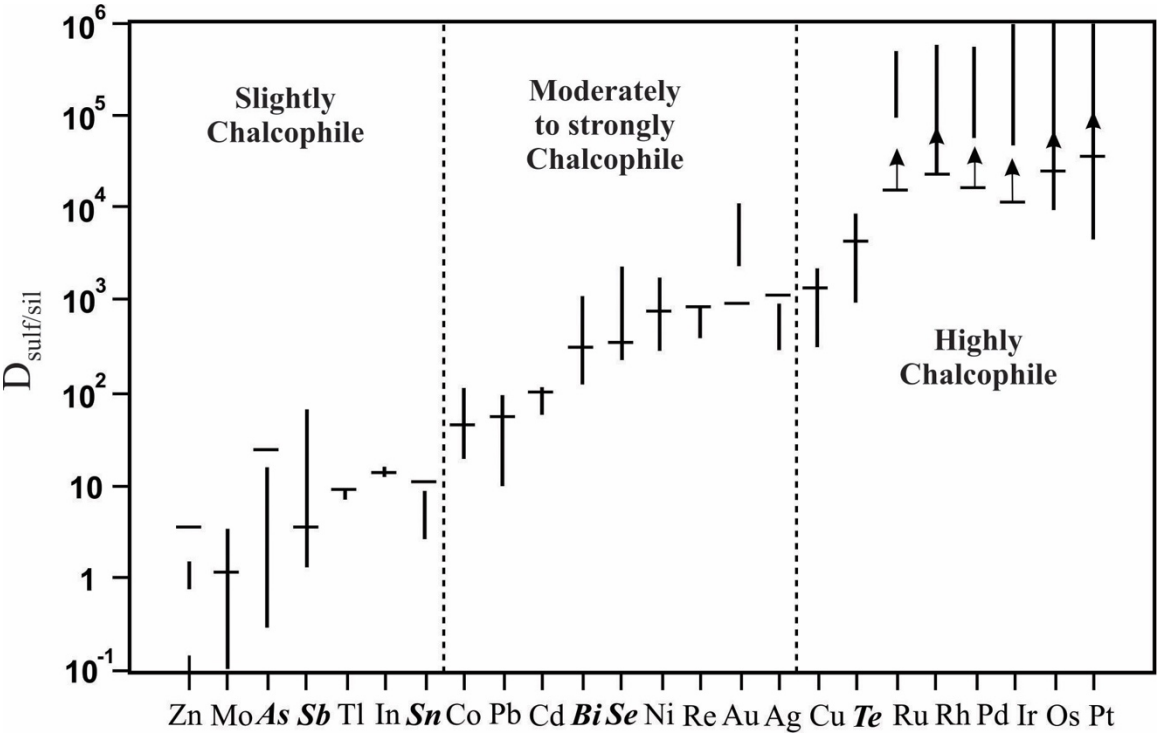

Figure 1.4 - Coefficients de partage entre un magma mafique et une liquide sulfuré. Les lignes verticales indiquent la plage de valeurs des essais menées à fO_2 entre -2 FMQ +2; Les traces horizontales indiquent des coefficients de partage entre le MORB et les gouttelettes de sulfure. Les TABS et Se sont mis en évidence pour référence. Données compilées par Barnes et Ripley (2016), ainsi que Li et Audétat (2015). Figure modifiée de Barnes (2016).

Vers 650ºC, le MSS s'exsolve en Po + Pn ± Ccp (Kelly et Vaughan 1983), et les éléments présents dans le MSS (Mo, Re, Rh et IPGE) se partagent entre Pn et Po. En dessous de 500°C, l'ISS s'exsolve principalement en Ccp et Py. À fS_2 intermédiaire, l'ISS est présent à 335°C, et en dessous il s'exsolve en Ccp et Po (Fig. 1.3d et 1.3e). À faible fS_2, l'ISS est stable à 210°C, et en dessous de cette température, il s'exsolve en cubanite et Po (Lusk et Bray 2002).

Enfin, la troilite peut exsoudre à partir de Po en dessous de 145°C (Fig. 1.3e; Kissin et Scott 1982; Naldrett 2011). Au fur et à mesure que la température baisse, le MSS et l'ISS peuvent devenir saturés en EGP et en TABS, et les MGP peut s'exsolver du MSS et de l'ISS (Fig.1.3e; Makovicky et al. 1990; Prichard et al. 2004; Godel et al. 2007; Godel et Barnes 2008; Dare et al. 2011; Wirth et al. 2013; Junge et al. 2015; Duran et al. 2017).

Bien que la formation de dépôts de sulfures magmatiques puisse être considérée comme un continuum de processus ignés, le produit final peut avoir subi des modifications telles que l'interaction avec des fluides magmatiques tardifs, la déformation et le métamorphisme. La pyrite est couramment trouvée en remplacement des assemblages des SMB préexistants (principalement Po) en raison de la rééquilibration post-cumulus avec des fluides magmatiques tardifs qui entraînent la stabilisation de Py sur Po (Fig.1.3f; Dare et al. 2011; Djon et al. 2012; Kanitpanyacharoen et Boudreau 2013; Piña et al. 2013, 2016; Boudreau et al. 2014; Duran et al. 2015; Holwell et al. 2017; Knight et al. 2017). Dans ce cas, la pyrite forme des grains anédriques et l'assemblage des SMB est généralement entouré de minéraux silicatés hydratés secondaires tels que la chlorite et l'actinolite, et occasionnellement par la magnétite. Le développement de la pyrite peut être le résultat d'une perte de Fe, d'un gain de S ou d'une oxydation, comme indiqué par les réactions:

1) Perte de Fe: $FeS + \text{silicate} + H_2O \rightleftharpoons FeS_2 + \text{silicate riche en Fe}$

$Po + \text{silicate magmatique} + H_2O = \text{pyrite} + \text{silicate hydraté riche en Fe}$

2) Gain de S (sulfuration): $FeS + H_2S \rightleftharpoons FeS_2 + H_2$

$Po + \text{fluide} = \text{pyrite} + \text{gaz}$

3) Oxydation: $FeS + O_2 \rightleftharpoons FeS_2 + Fe_3O_4 + S_2$

$Po + \text{fluide} = \text{pyrite} + \text{magnétite} + \text{soufre}$

Dans certains cas, une forte altération peut entraîner le remplacement total de Po et le remplacement de Pn et Ccp par la millérite et la cubanite (Djon et Barnes 2012), respectivement. L'évaluation quantitative par Holwell et al. (2017) a montré que l'altération continue des SMB est associée à une perte de masse se produisant couramment avec des pertes combinées de Fe et de S, conduisant finalement à une remobilisation des métaux communs et précieux lors d'une altération complète de l'assemblage primaire.

1.2.3 – Hypothèses

L'association fréquente des EGP avec des TABS soit dans la structure des SMB, soit sous forme des MGP conduit à la question principale de cette étude: Quel est le rôle des TABS lors de la formation des gisements de EGP? Cinq hypothèses principales peuvent être mises en évidence pour tenter de répondre à cette question.

1.2.3.1 – Cristallisation directe des MGP à partir du liquide silicaté

La première possibilité est la cristallisation directe des MGP à partir du magma silicaté, en réponse à l'augmentation des concentrations de TABS et des EGP avec l'assimilation des roches crustales. Ici, la présence des TABS dans un magma déclencherait la cristallisation des MGP. Arguin et al. (2016) montrent des preuves texturales de la cristallisation des MGP (principalement des alliages) aux marges des cristaux de chromite (Fig. 1.5) dans les picrites en Chine. Des descriptions détaillées des horizons minéralisés d'EGP dans le complexe des Monts de Cristal (Gabon) suggèrent également une cristallisation directe des arséniures de Pt à partir d'un magma basaltique (Maier et al., 2015; Barnes et al., 2016).

La cristallisation directe des arséniures de Pt n'est pas appuyée par les données expérimentales actuelles. Canali et al. (2017) ont effectué une série d'expériences pour limiter la solubilité du Pt et des arséniures de Pt dans les magmas silicatés. Les résultats de cette étude indiquent que la saturation de Pt peut être atteinte, dans des conditions réductrices, avec seulement quelques ppb en concentration (Fig. 1.6). Ces concentrations sont similaires aux

concentrations dans un magma basaltique typique, et soutiennent la cristallisation directe des phases de Pt, induite par la formation de chromite (Finnigan et al., 2008; Arguin et al., 2016). Cependant, les niveaux d'As requis pour la saturation en Pt-arséniure sont d'environ 50 à 500 ppm, beaucoup plus élevés que ceux observés dans le magma mafique (<1ppm) et nécessitant un énorme enrichissement en arsenic pour que la saturation en Pt-arséniure se produise (Canali et al., 2017), peu probable dans les cas naturels.

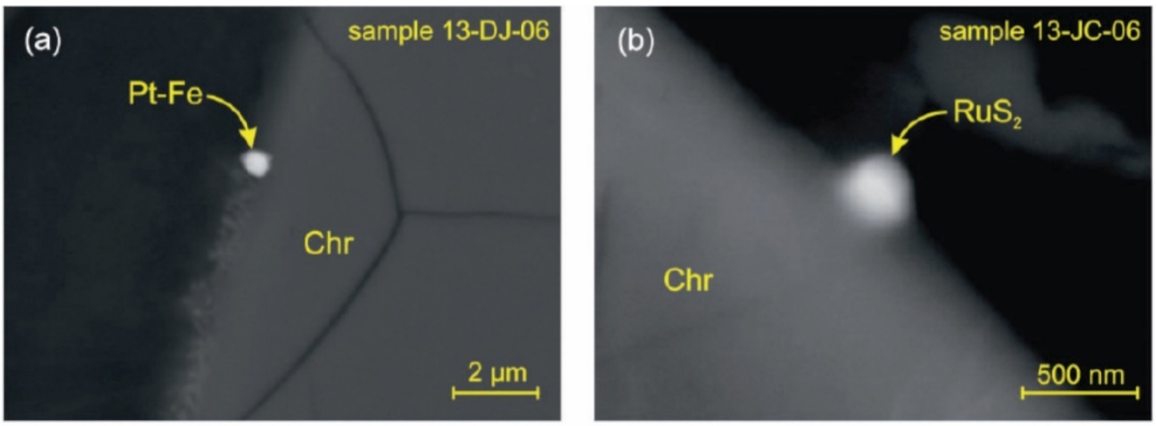

Figure 1.5 - Images d'électrons rétrodiffusées des MGP aux marges des cristaux de chromite: (a) un grain d'alliage à Pt – Fe à la marge d'un cristal de chromite; (b) une laurite euhédrique (RuS_2) à la marge d'un cristal de chromite. Figures d'Arguin et al. (2016).

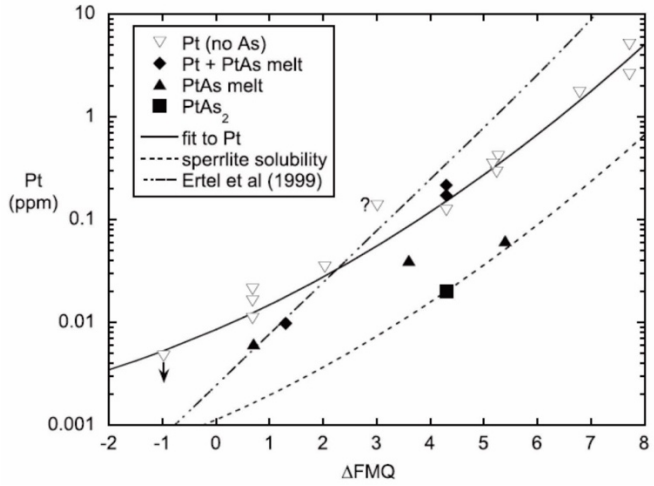

Figure 1.6 - Variation de la concentration de platine dans le magma silicaté en fonction de la fugacité en oxygène pour les expériences saturées en alliage à Pt-Fe (± As dans le magma silicaté), Pt-As fondu et sperrylite ($PtAs_2$). La figure de Canali et al. (2017).

Pour les autres TABS, il n'y a pas de données expérimentales pour évaluer leur effet sur la saturation en MGP dans les magmas silicatés.

1.2.3.2 – Ségrégation d'un liquide immiscible riche en TABS

La deuxième hypothèse est que le liquide sulfuré pourrait devenir saturé dans un liquide immiscible riche en TABS (Fig. 1.7), qui recueille des EGP, et des MGP pourrait cristalliser à partir de ce liquide (Hanley 2007; Holwell et McDonald 2007). En effet, des études expérimentales montrent que des liquides immiscible riche en TABS peuvent se former à partir d'un liquide sulfuré (Helmy et al. 2007, 2013; Cafagna et Jugo 2016; Sinyakova et al. 2017) et des exemples naturels de ce processus ont été proposés. Par exemple, Piña et al. (2015) ont fait valoir que l'assimilation de roches riches en As lors de la mise en place d'un magma pourrait conduire à la ségrégation d'une liquide riche en As, pour lequelle les EGP ont un coefficient de partage élevé. Les auteurs ont documenté la présence de ces liquides immiscibles riches en As et EGP dans les dépôts magmatiques de la Serranía de Ronda, en Espagne.

Cependant, le modèle de ségrégation d'un liquide immiscible riche en TABS présente une limitation majeure. Les concentrations de TABS nécessaires pour atteindre la saturation sont très élevées (200 à 1000 ppm), et la plupart des liquides sulfurés naturels ne semblent pas atteindre ces niveaux. Par conséquent, bien que des expériences aient démontré qu'un liquide immiscible riche en TABS peut se former (Fig. 1.7), les matériaux de départ ne sont pas compatibles avec la plupart des concentrations naturelles dans les matériaux géologiques. Cela signifie que bien qu'applicable, le modèle nécessiterait des processus conduisant à un enrichissement extrême des concentrations de TABS dans le liquide sulfuré (Piña et al., 2015), qui ne

semblent pas s'être produits dans la plupart des gisements magmatiques. Par exemple, Liu et Brenan (2015) ont appliqué leurs résultats expérimentaux aux minerais de McCreedy East (Sudbury) et ont conclu que le liquide sulfuré ne contenait pas suffisamment de TABS pour avoir séparé un liquide immiscible riche en TABS. Des conclusions similaires ont également été tirées par Duran et al. (2017) pour les minerais sulfurés massifs du district de Noril'sk-Talnakh.

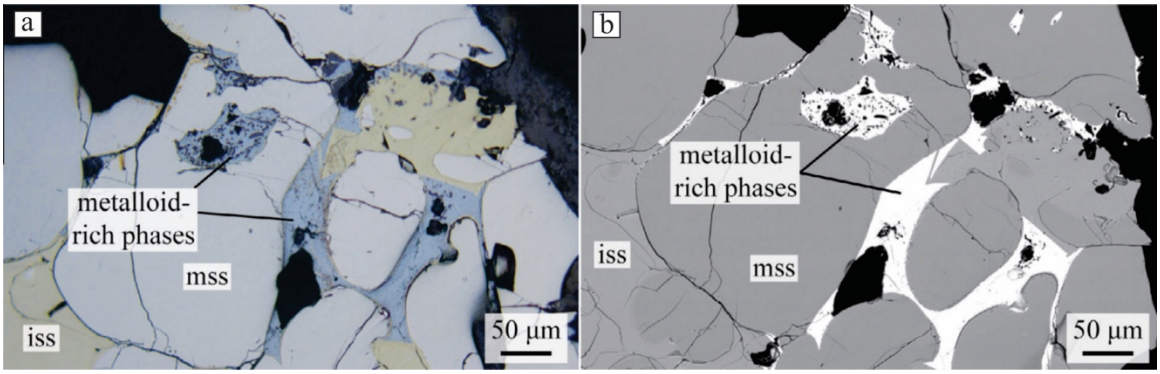

Figure 1.7 - Lumière réfléchie (a) et images d'électrons rétrodiffusées (b) de produits expérimentaux de Cafagna et Jugo (2016) illustrant la présence d'un liquide immiscible riche en métalloïdes (TABS). Notez que le liquide immiscible riche en TABS est interstitiel à le MSS et l'ISS de forme ronde. Figure de Cafagna et Jugo (2016).

1.2.3.3 – Cristallisation des MGP à partir du liquide sulfuré

La troisième hypothèse est une variation du modèle d'un liquide immiscible riche en TABS, et soutient que des concentrations progressivement plus élevées de TABS dans le liquide sulfuré pourraient conduire à la cristallisation directe de PGM, avant la formation d'un liquide immiscible. Les concentrations plus élevées pourraient être obtenues soit par addition externe de TABS pendant la contamination crustale, soit par cristallisation fractionnée du liquide sulfuré. Plusieurs études au complexe de Sudbury montrent les effets de l'ajout de TABS sur l'évolution de différents gisements

de Ni-Cu-EGP (Ames et Farrow 2007; Dare et al. 2010a et 2011). Les dépôts hébergés sur la chaîne sud contiennent des concentrations d'As plus élevées que celles de la chaîne nord. Cette anomalie régionale dans As sur la chaîne sud est attribuée à l'assimilation des roches volcano-sédimentaires (Ames et Farrow 2007). Dare et al (2010a) soutiennent que l'activité plus élevée d'As dans le gisement Creighton (c.-à-d. la chaîne sud) a mené à la cristallisation précoce des MGP contenant de l'As à haute température (c.-à-d. jusqu'à 1200 ° C).

Alternativement, les MGP peut ne pas cristalliser à des températures élevées en raison d'une augmentation de TABS dans le liquide sulfuré par assimilation crustale, mais aux derniers stades de la cristallisation fractionnée du liquide sulfuré. Comme indiqué ci-dessus, le Pd, le Pt et le TABS sont incompatibles avec le MSS et l'ISS, et leurs concentrations dans le liquide sulfuré riche en Cu progressivement plus fractionné augmentent. Par conséquent, au cours des derniers stades de la cristallisation, le liquide sulfuré piégé peut devenir saturé en Pd, Pt et TABS, et les grains composites des MGP peuvent cristalliser (Dare et al. 2014; Liu et Brenan 2015; Duran et al. 2017). Des exemples de grains de PGM composites interstitiels au SMB dans des minerais riches en Cu ont été décrits par Dare et al. (2014) et Duran et al. (2017) dans les districts de Sudbury et de Noril’sk-Talnakh, respectivement (Fig. 1.8). Les auteurs ont interprété les grains composites des MGP comme le résultat d'une cristallisation directe à partir du liquide sulfuré fractionné, sans formation d'un liquide immiscible riche en TABS.

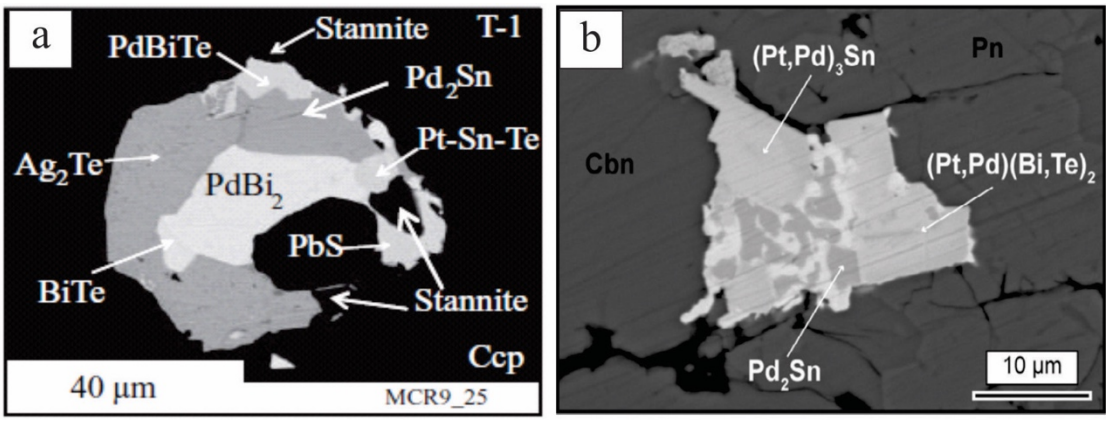

Figure 1.8 - Images électroniques rétrodiffusées de grains composites de MGP provenant des gisements McCreedy East, Sudbury (Dare et al. 2014) et Talnakh, district de Noril'sk (Duran et al. 2017). Les deux échantillons comprennent des sulfures massifs fractionnés riches en Cu. Notez que les grains de MGP se produisent interstitiels dans des SMB. Abréviations: Cbn - cubanite; Ccp - chalcopyrite; Pn - pentlandite.

1.2.3.4 – Combinaison des EGP et TABS et exsolution des MGP

La quatrième hypothèse est que lors du refroidissement, les EGP peuvent se combiner avec les TABS et s'exsolver sous forme de MGP à partir des SMB. Bien que Pt, Pd et TABS soient incompatibles avec le MSS et l'ISS, leurs coefficients de partage ne sont pas 0 (Mungall et al. 2005; Mungall et Brenan 2014; Liu et Brenan 2015), et donc une petite fraction de ces éléments sont inclus dans l'ISS et le MSS. Lors du refroidissement, ou pendant la perte de S, Pd, Pt et TABS pourraient s'exsolver de l'ISS et du MSS. En effet, des travaux expérimentaux ont montré que les SMB contient moins d'EGP lors du refroidissement (Makovicky et al. 1990; Makovicky 2002), ainsi que la forme allongée des MGP inclus dans les SMB (Prichard et al. 2004; Godel et al. 2007 ; Holwell et McDonald 2007; Godel et Barnes 2008; Dare et al. 2011 ; Duran et al. 2017) soutiennent le modèle d'exsolution (Fig. 1.9).

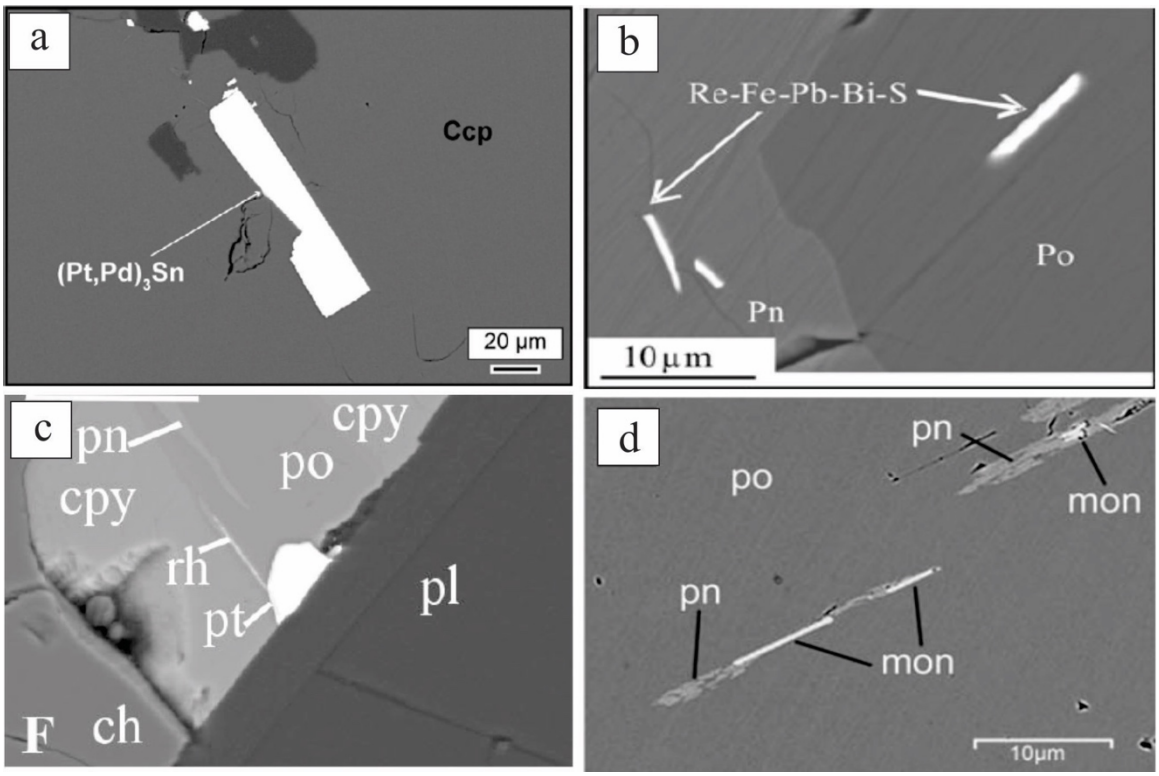

Figure 1.9 - Images électroniques rétrodiffusées des grains de MGP allongés et inclus dans les SMB du (a) district de Noril'sk-Talnakh (Duran et al. 2017), (b) gisement Creighton, Sudbury (Dare et al. 2010), (c) Merensky Reef et (d) Platreef, Complex du Bushveld (Prichard et al. 2004; Holwell et McDonald 2007). Il a été interprété que les MGP de ces diverses localités se sont formées par exsolution des SMB en raison de leur forme allongée. Abréviations: Ccp / Cpy - chalcopyrite; Po - pyrrhotite; Pn - pentlandite; Pl - plagioclase; Mon - moncheite.

Récemment, Wirth et al. (2013) et Junge et al. (2015) ont étudié la distributition minéralogique des EGP dans des échantillons de chromitite du *UG-2* et du *Merensky Reef*, en utilisant la microscopie électronique à transmission. Les auteurs ont découvert que les EGP se produisent en solution solide dans les SMB (en particulier Pn), et également sous forme de lamelles de MGP alignées dans la structure des SMB, qu'ils ont interprétées comme des lamelles d'exsolution. De plus, Junge et al. (2015) ont suggéré que la concentration initiale des TABS dans les SMB pourrait contrôler l'étendue de l'exsolution de MGP. En effet, les EGP nécessiterait des partenaires de réaction nécessaires pour former les MGP, qui serait les TABS. Bien que les preuves actuelles soutiennent la formation des MGP par exsolution, il n'est pas clair si le

contenu de TABS peut limiter le processus d'exsolution, d'autant plus que les EGP peuvent s'exsolver non seulement sous la forme des MGP porteur des TABS, mais également sous la forme des sulfures et des alloys (Prichard et al., 2004; Godel et al., 2007; Godel et Barnes, 2008). Ceci est important car si les TABS limitent le processus d'exsolution, la concentration de TABS dans les SMB affectera probablement la distribution minéralogique des EGP.

1.2.3.5 – Redistribution post-magmatique des EGP

La cinquième hypothèse est que les TABS peuvent soit être remobilisés avec les EGP pendant l'altération post-magmatique, ou soit agir comme agents de fixation des EGP pendant les processus de remobilisation tardive. En effet, la formation de gisements de sulfures magmatiques par des processus hydrothermaux a également été argumentée par plusieurs auteurs (Boudreau et Meurer, 1999; Péntek et al., 2008; Tuba et al., 2014). Dans ces modèles, un fluide magmatique tardif (généralement très salin et acide) dissout les SMB magmatique et le redépose lorsque les conditions physico-chimiques changent. La migration de ces fluides contenant des métaux pourrait conduire à la formation de zones à faible S-haut-Pd-Pt entourant les intrusions. Par exemple, Péntek et al. (2008) et Tuba et al. (2014) soutiennent que les fluides riches en Cl ont lessivé les métaux des gisements de Ni-Cu-PGE de type contact de Sudbury pour former des dépôts à faible S-haut-Pd-Pt. Cependant, bien que des études expérimentales récentes soutiennent le transport des TABS par les fluides hydrothermaux (Fig.1.10; Guo et Audétat 2017), il n'en va pas de même pour les EGP, qui sont immobiles (Sullivan et al. 2018).

Bien que les EGP ne semblent pas être remobilisés par les fluides hydrothermaux, les TABS peuvent toujours être importants lors de l'altération des gisements de sulfures magmatiques et peuvent agir comme agents de fixation des EGP. Wood (2002) soutient que les TABS forment des composés insolubles avec les EGP. Par exemple, certains gisements de EGP sont considérés comme ayant subi une perte de soufre en raison de processus post-magmatiques

(Godel et Barnes 2008; Polovina et al. 2004; Kawohl et Frimmel 2016). Par conséquent, le TABS peut agir comme des éléments de fixation et éviter, dans une certaine mesure, la perte des EGP avec le S et d'autres métaux de base. Si cette hypothèse est valide, la caractérisation des TABS dans les roches métamorphisées et altérées est fondamentale pour mieux contraindre la mobilité des EGP lors de la recristallisation.

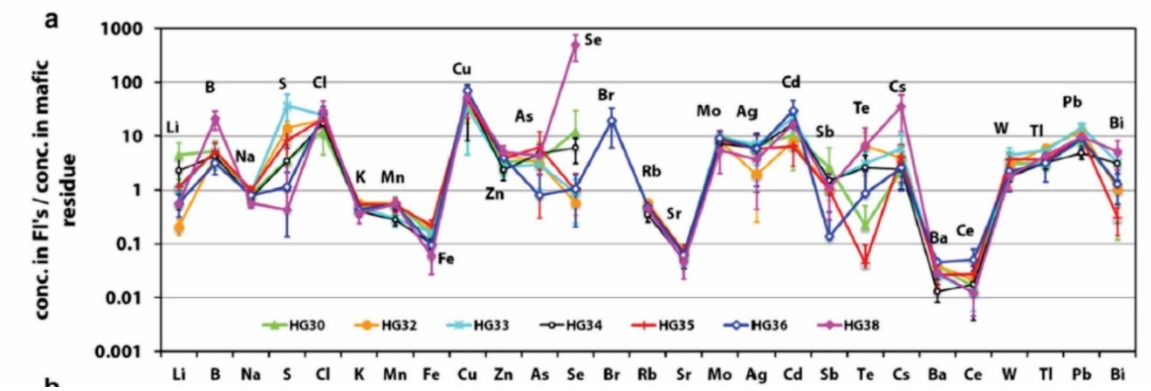

Figure 1.10 - Coefficients de partage fluide / roche calculés en divisant les concentrations d'éléments dans les inclusions fluides (FI) par leur concentration dans les résidus mafiques dans les expériences de Guo et Audétat (2017). Notez que As, Sb, Te et Bi affichent un coefficient de partage dans la phase fluide supérieur à 1 pour la plupart des produits de test expérimental. Les éléments sont classés par masse ascendante.

1.3 – Objectifs

Cette thèse se concentrera sur le test des hypothèses de i) la ségrégation d'un liquide immiscible riche en TABS, ii) la cristallisation des MGP à partir du liquide sulfuré et iii) l'exsolution des EGP et TABS à partir des SMB sous la forme des MGP. Les principaux objectifs sont les suivants:

- **Développer une routine analytique pour déterminer les TABS dans des échantillons de roche totale à des concentrations faibles à ultra faibles, au LabMaTer (UQAC)**
  - Mettre en œuvre l'utilisation de la spectroscopie de fluorescence atomique couplée à un générateur d'hydrure (*HG-AFS*) dans les échantillons géologiques.

- Analyser différents matériaux de référence, avec des concentrations variables en TABS, afin de vérifier l'exactitude et la précision de la méthode.

➢ **Comprendre si la concentration des TABS peut permettre la ségrégation d'un liquide immmiscible riche en TABS, ou la cristallisation directe de PGM à partir du liquide sulfuré**

- Mesurer la concentration des TABS dans des échantillons de roche total à degré de fractionnement variable du district minier de Noril'sk-Talnakh.
- Examiner la distribution des TABS dans le SMB des sulfures massifs du district minier de Noril'sk-Talnakh.
- Combiner les compositions de roche totale et des SMB pour calculer un bilan de masse pour des TABS dans différents types de minerai et comprendre les variations possibles.

➢ **Etudier la formation des MGP par exsolution des EGP et TABS à partir des SMB**

- Déterminer les concentrations de TABS en roches totale dans les échantillons des gisements *Merensky Reef*, *J-M Reef* et *Picket Pin* et comparer les résultats avec ceux des échantillons stériles en EGP.
- Étudier la distribution des TABS dans les SMB provenant des intervalles des *PGE Reef* et d'échantillons en dehors des *PGE Reef*.
- Comparer le bilan de masse des TABS dans des échantillons de minéralisés en EGP et stériles.

➢ **Vérifier si la distribution des TABS peut être utilisée pour comprendre les processus conduisant à la formation des gisements de sulfures magmatiques**

- Étudier la distribution des TABS dans les échantillons de la *Marginal Zone* du complexe du Bushveld, qui enregistrent la composition des magmas initiaux qui ont cristallisé l'intrusion.

- Comprendre quels sont les principaux processus affectant la distribution des TABS dans les magmas initiaux qui ont cristallisé les gisements de EGP du complexe du Bushveld.
- Utiliser la concentration de TABS dans les roches de la *Marginal Zone* pour essayer de modéliser les concentrations observées dans le *Merensky Reef.*
- Comprendre comment les SMB affectent la distribution des TABS dans le *Merensky Reef.*

1.4 – Zones d'étude

Afin d'étudier les hypothèses proposées, trois zones d'étude ont été sélectionnés. Les zones comprennent le district minier de Noril'sk-Talnakh (riche en S), le complexe du Bushveld et le complexe de Stillwater (pauvre en S). Seulement un bref contexte est fourni ici, tandis qu'une description plus détaillée des zones d'étude et des échantillons peut être trouvée dans les chapitres suivants.

1.4.1 – Le district minier de Noril'sk-Talnakh

La plate-forme sibérienne, située à travers la Sibérie occidentale et orientale (Fig. 1.11), comprend un très grand magmatisme mafique et felsique qui a été mis en place à la limite permo-triasique. Les études géochronologiques soutiennent que la mise en place du *Large Igneous Province (LIP)* sibérien a duré moins de 1 Ma (entre 252,3 et 251,3 Ma; Milanovskiy, 1976; Reichow et al., 2009; Burgess et al., 2014). Les magmas ont interagi avec les roches sédimentaires riches en volatiles et les gaz associés libérés pendant l'événement LIP sibérien seraient responsables de l'extinction de masse du Permien final (Polozov et al., 2016, et les références qui s'y trouvent).

Le district minier de Noril'sk-Talnakh est situé à la limite nord-ouest de la plate-forme sibérienne (Fig. 1.11). Dans la région, la séquence volcanique complète a été forée et 11 formations ont été identifiées sur la base des caractéristiques pétrographiques et géochimiques

(Fedorenko, 1994). Les formations les plus basses sont dérivées de magmas modérément riches en Ti, tandis que les formations les plus hautes sont dérivées de magmas pauvres en Ti. Le degré de contamination a progressivement diminué la séquence ascendante et la formation la plus contaminée (la formation Nadezhdinsky) est épuisée en Ni, Cu et EGP (Naldrett et al., 1992; Brügmann et al., 1993). Cet épuisement des métaux a été interprété comme le résultat d'un piégeage des métaux par des sulfures magmatiques avant l'extrusion des magmas basaltiques.

Des intrusions hypabyssales traversent les roches sédimentaires sous-jacentes à la séquence volcanique et certaines sont considérées comme synchrones avec les différentes roches basaltiques (Fedorenko et Czamanske, 1997). Les sulfures magmatiques se trouvent exclusivement dans des intrusions différenciées mafiques-ultramafiques au sein desquelles les roches varient de l'olivinegabbronorite à la gabbronorite. Les trois principales intrusions minéralisées, Noril'sk I, Kharaelakh et Talnakh, se trouvent dans les jonctions de Noril'sk et de Talnakh (Fig. 1.11). L'assimilation des roches sédimentaires riches en S a conduit à la saturation en S et à la ségrégation des liquides sulfurés (Gorbachev et Grinenko, 1973; Grinenko, 1985; Ripley et al., 2003, 2010). Les liquides sulfurés s'équilibraient avec un grand volume de magmas, collectant ainsi de grandes quantités de métaux de base et précieux avant de s'accumuler dans les parties inférieures des intrusions hypabyssales (Naldrett et al., 1992).

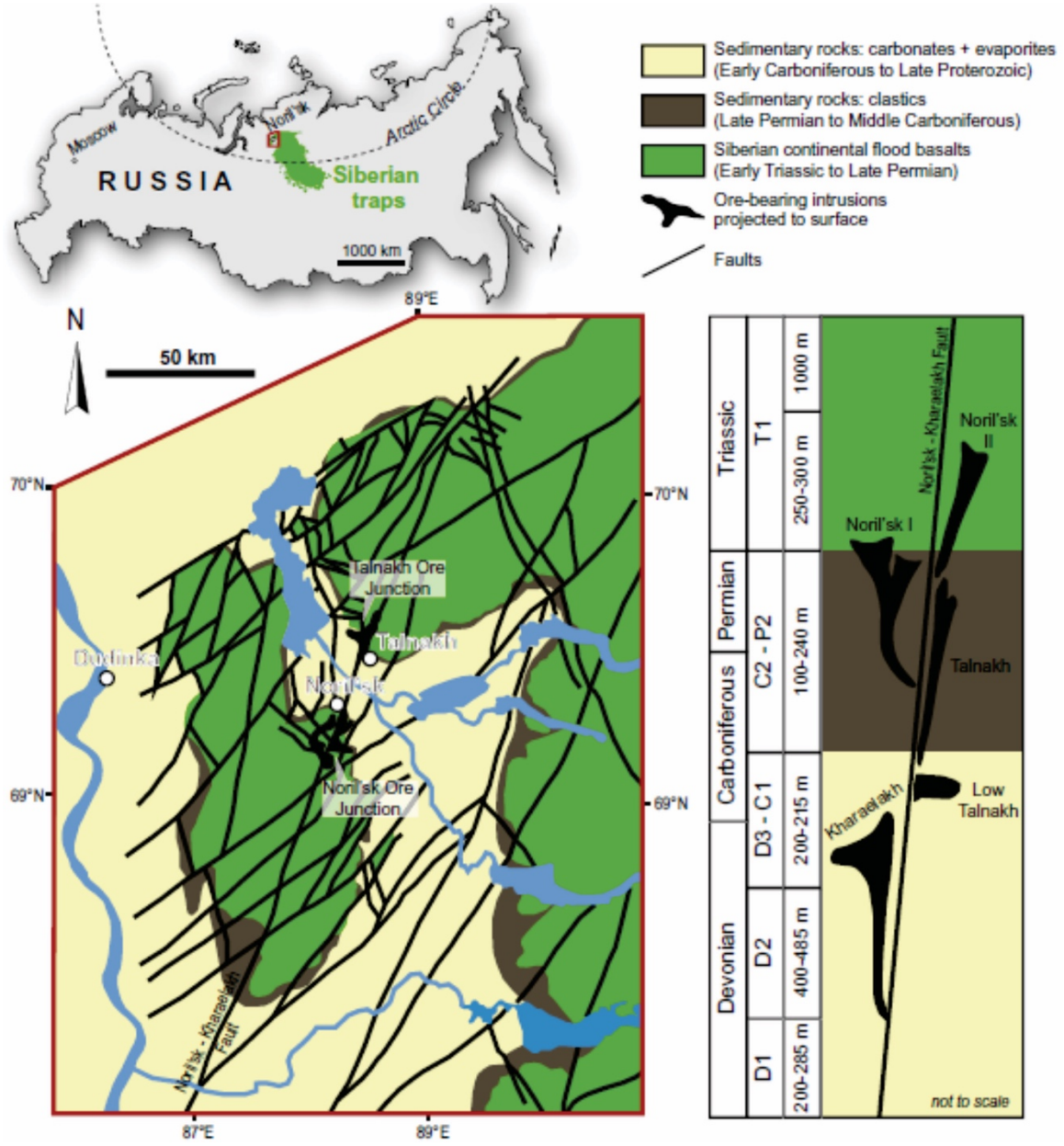

Figure 1.11 - Carte géologique simplifiée (modifiée après Zientek et al., 1994) de la région de Noril'sk montrant les projections de surface des intrusions minéralisées et la section stratigraphique idéalisée (modifiée après Likhachev, 1994) montrant les emplacements des intrusions minéralisées dans la séquence de la tratigraphie. La figure de Duran et al. (2017).

1.4.2 – Le complexe du Bushveld

Le complexe du Bushveld (Fig. 1.12), situé près du milieu du craton de Kaapvaal, en Afrique du Sud, est le plus grand complexe intrusif au monde (240 km sur 350 km). Le complexe a été mis en place dans des roches sédimentaires du Supergroupe Transvaal à 2054

+/- 1,3 Ma (Scoates et Friedman, 2008), et se compose de trois unités stratigraphiques (*South African Committee for Stratigraphy, 1980*): i) les roches stratifiées ultramafiques à mafiques de la *Rustenburg Layered Suite*, ii) les granophyres et granites recouvrant la *Rustenburg Layered Suite*, et iii) une suite de filons-couches ultramafiques à mafiques injectés dans les sédiments rocheux sous-jacents à la *Rustenburg Layered Suite*. La *Rustenburg Layered Suite* (Fig. 1.12) est divisée, de la base au sommet, en cinq zones (Hall, 1932): la *Marginal Zone* (gabbro-norites), la *Lower Zone* (péridotites et pyroxénites), la *Critical Zone* (pyroxénites et chromitites) , *Main Zone* (gabbro-norites) et *Upper Zone* (anorthosites, diorites et magnétitites). La *Critical Zone* abrite plusieurs *Reefs* riches en EGP, dont le *Merensky Reef* étudié dans le cadre du projet.

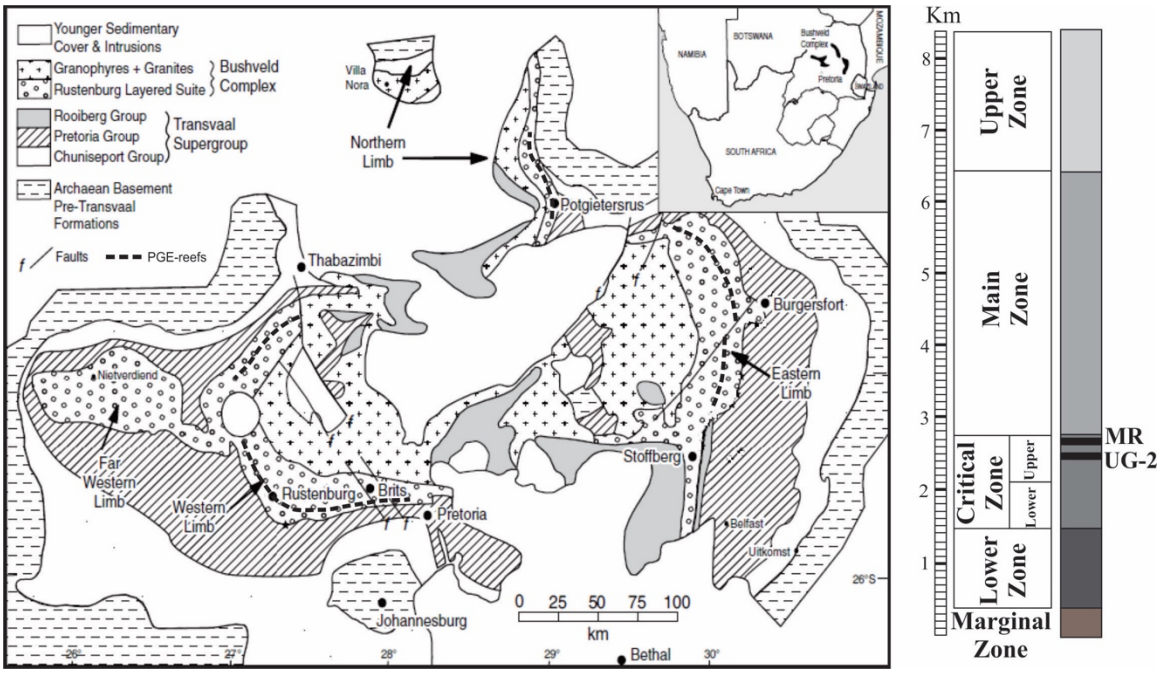

Figure 1.12 - Carte géologique simplifiée du complexe du Bushveld (à gauche) et carte stratigraphique de la Rustenburg Layered Suite (à droite). MR – Merensky Reef; UG2- Upper Group 2 Chromitite. Carte modifiée de Barnes et al. (2010) et carte stratigraphique de Godel et al. (2007).

Le *Merensky Reef* est situé dans la partie supérieure de la *Upper Critical Zone* (fig. 1.13) et s'étend latéralement sur plus de 280 km (Cawthorn, 2002). En moyenne, le *Reef* a une épaisseur de 1 m, avec 1 à 3% de SMB disséminé et environ 6-8 ppm de Pt et Pd (Barnes et

Maier, 2002; Godel et al., 2007). Le *Reef* présente des variations lithologiques régionales et locales considérables (Leeb-du Toit, 1986). En dehors des variations lithologiques, la stratigraphie du *Reef* normal peut être largement divisée, de la base au sommet, sous forme d'anorthosite basale, de chromitite inférieure, de mélanorite à gros grains, de chromitite supérieure et de mélanorite (Fig.1.13; Barnes et Maier, 2002; Godel et al., 2007). Différents processus ont été proposés pour expliquer l'origine du *Merensky Reef*, tels que: i) la collecte de l'EGP du magma silicaté par un liquide sulfuré (Campbell et al., 1983; Naldrett et al., 1986; Barnes et Maier , 2002; Godel et al., 2007), ii) la cristallisation des EGP directement à partir du magma silicaté sous la forme des MGP (Hiemstra, 1979; Cawthorn, 1999), et iii) la collecte des EGP par le dessous du *Reef* par un fluide riche en Cl ascendant (Boudreau et Meurer, 1999).

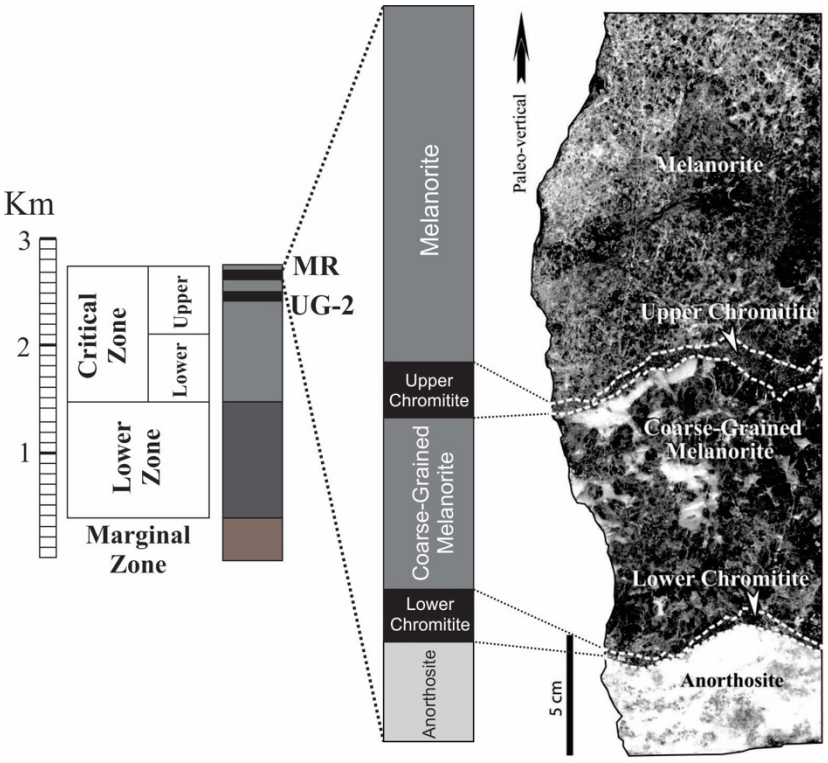

Figure 1.13 - Échantillon macroscopique du Merensky Reef et diagramme stratigraphique schématique illustrant les variations lithologiques à travers le Reef. L'échantillon provient de Rustenburg Platinum Mine. Modifié à partir de Godel et al. (2007).

1.4.3 – Le complexe de Stillwater

Le complexe de Stillwater (Fig. 1.14) est une intrusion litée ultramafique à mafique située dans le centre-sud du Montana. Le complexe est daté de 2709 +/- 1 Ma et a été mis en place dans les roches métasédimentaires Archéenes (Wall et al., 2010). Le complexe a subi un métamorphisme au faciès schiste vert inférieur à environ 1700 Ma (Page, 1977). La taille d'origine de l'intrusion n'est pas connue car ses parties supérieures ont été érodées et une faille limité aux deux extrémités. À partir de la section exposée, le complexe a une structure alignée NW-SE et mesure environ 42 km de long et 5-6 km d'épaisseur (Zientek et al., 2002).

Les roches du complexe sont divisées en cinq séries (Fig. 1.14), de bas en haut: la *Basal Series* se compose de norites et de bronzitites avec des SMB mineurs; la *Ultramafic Series* est formée essentiellement de harzburgite et de bronzitite, avec des lits mineures de chromitites; les *Lower, Middle* et *Upper Banded Series* contiennent principalement de la norite, de la gabbronorite, de la gabbronorite olivine et de l'anorthosite (Zientek et al., 2002; Boudreau, 2016). Le complexe Stillwater abrite plusieurs *Reefs* enrichies en EGP, dont le *John Manville Reef* (*JM Reef*) et le gisement *Picket Pin* dans les *Lower Banded* et *Upper Banded Series*, respectivement (figure 1.14; McCallum et al., 1980; Zientek et al., 2002; Godel et Barnes, 2008). Ce projet se concentre principalement sur le *J-M Reef*.

Le *JM Reef* est un lit situé à la base de la *Olivine-bearing I zone* avec des sulfures disséminés riches en EGP (c.-à-d. 0,5-3% vol.) (Bow et al., 1982; Zientek et al., 2002) . Le *Reef* a généralement une épaisseur de 1 à 3 m et présente la teneur moyenne la plus élevée en Pt + Pd (c'est-à-dire environ 18 ppm) de tous les gisements de EGP connus (Zientek et al., 2002). Trois modèles principaux ont été proposés pour expliquer l'enrichissement en EGP de cette *Reef*: i) la collecte des EGP par un liquide sulfuré (Campbell et al., 1983), ii) la collecte des EGP par des fluides magmatiques (Boudreau et McCallum, 1992; Boudreau, 2016), ou iii) une combinaison des deux processus (Godel et Barnes, 2008).

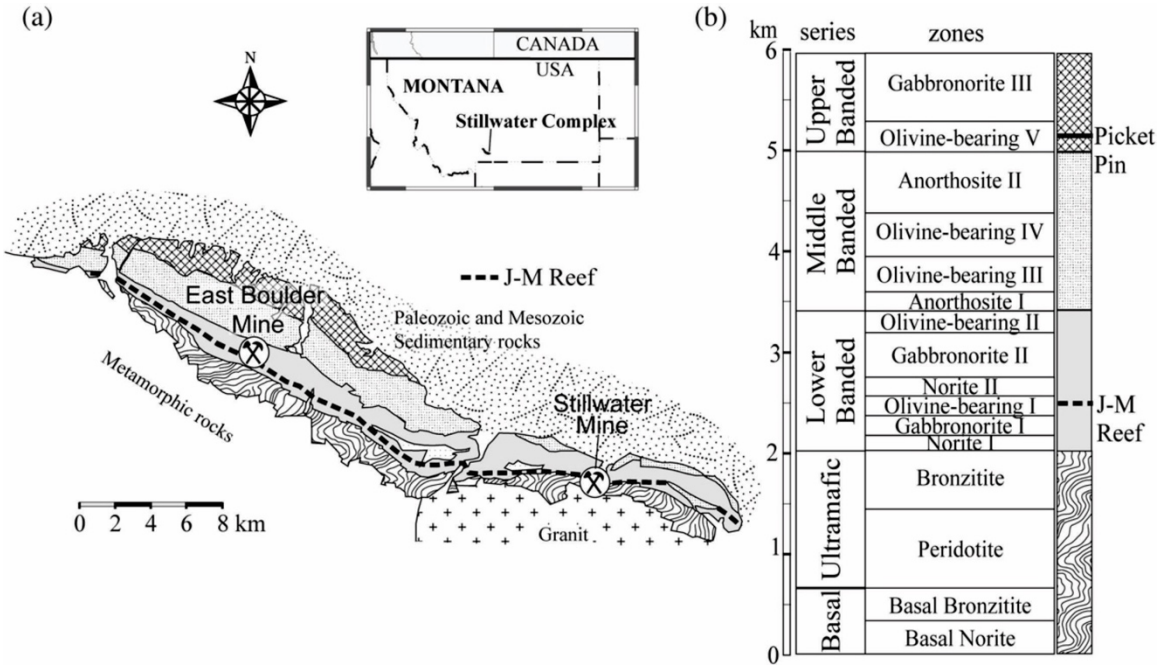

Figure 1.14 - Échantillon macroscopique du Merensky Reef et diagramme stratigraphique schématique illustrant les variations lithologiques à travers le Reef. L'échantillon provient de Rustenburg Platinum Mine. Modifié à partir de Godel et al. (2007).

Dans le modèle magmatique, la ségrégation d'un liquide sulfuré et son interaction avec un volume élevé de magma silicaté conduisent à la collecte des EGP. Par contre, le modèle hydrothermal suppose que les fluides magmatiques interstitiels tardifs sous-saturés en S lessivent les EGP et d'autres métaux des roches des parties inférieures de l'intrusion et les redéposent à l'horizon du *Reef*. Godel et Barnes (2008) soutiennent qu'aucun des deux processus ne peut expliquer uniquement les caractéristiques observées du *J-M Reef*. Les auteurs soutiennent que la formation du *J-M Reef* a nécessité une ségrégation initiale du liquide sulfuré pour collecter les EGP et une addition postérieure de Pd et de Pt par les fluides hydrothermaux tardifs (Godel et Barnes, 2008).

1.5 – Méthodologie

Cette section présente une synthèse des méthodes utilisées pour enquêter sur les hypothèses susmentionnées et ainsi atteindre les objectifs fixés. Plus de détails sur les méthodes analytiques sont fournis dans les chapitres individuels.

1.5.1 – Fluorescence atomique couplée à un générateur d'hydrure (*HG-AFS*)

Afin de déterminer les concentrations de Te, As, Bi, Sb et Se à de faibles niveaux (<10 ppb), la technique de fluorescence atomique couplée à un générateur d'hydrure (*HG-AFS*) a été mise en place au LabMaTer (UQAC). La description détaillée de la méthode est fournie au chapitre 2 et seul un résumé est présenté ici.

Environ 0.4 g d'échantillon ont été digérés avec 5 ml d'aqua regia (1: 3 HNO_3: HCl) dans un bécher à capuchon fermé à 70 °C pendant 24 heures. L'aliquote a été laissée à refroidir et diluée à 25 ml avant d'être mélangée avec une solution réductrice (0.7% $NaBH_4$ et 0.4% NaOH). La solution mélangée a été analysée par *HG-AFS*, en utilisant un PSA Millenium Excalibur 10.055 à flux continu de PS Analytical. Six solutions d'étalonnage avec des concentrations de 0.1, 0.25, 0.5, 1, 2.5 et 5 ppb ont été préparées en utilisant des solutions standard de chaque élément (PlasmaCAL, SCP Science, Québec, Canada). Les solutions d'étalonnage ont été mélangées avec le blanc réactif avant la mesure, dans la même proportion que les aliquotes d'échantillon. Des matériaux de référence internationaux et un blanc ont été déterminés en même temps que les échantillons pour contrôler la qualité des résultats. Dans l'ensemble, les limites de détection 3σ sont de 0.005, 0.003, 0.005, 0.005 et 0.002 ppm pour Te, As, Bi, Sb et Se, respectivement.

1.5.2 - Microscope électronique à balayage

Un microscope électronique à balayage a été utilisé pour mesurer les concentrations des principaux éléments dans les sulfures, et également pour rechercher la présence des MGP. Ceux-ci ont été acquis à l'aide d'un microscope électronique à balayage Zeiss Sigma 300 VP, équipé d'un système EDS d'Oxford Instruments Ultim Max chez IOS Services Géocientifiques, Chicoutimi, Québec. L'instrument a été étalonné en utilisant des matériaux de référence de puremetal et la dérive instrumentale a été surveillée en utilisant les matériaux de référence des étalons Astimex. Le détail des résultats se trouve au chapitre 3.

1.5.3 – Ablation laser et spectroscopie de masse (*LA-ICP-MS*)

La concentration et la distribution des éléments mineurs et traces dans les sulfures et silicates ont été déterminées par Ablation laser et spectroscopie de masse (*LA-ICP-MS*) chez LabMaTer (UQAC), à l'aide d'un laser Excimer 193 nm RESOlution M-50 laser ablation system (*Australian Scientific Instrument*) équipé d'une cellule double volume S-155 (*Laurin Technic*) et couplé à un spectromètre de masse Agilent 7900. Les paramètres de réglage de *LA-ICP-MS* pour chaque section analytique, les mesures des isotopes, les corrections d'interférence et les résultats pour les matériaux de référence sont rapportés dans les chapitres 3, 4 et 6. La réduction des données a été effectuée en utilisant le package Iolite pour le logiciel Igor Pro (Paton et al. 2011).

Des cartes de distribution des éléments ont été faites sur différents assemblages de sulfure en utilisant une fréquence laser de 15 Hz et une puissance de 5 mJ / pulse. La taille du faisceau (15 à 58 μm) et la vitesse de déplacement (10 à 15 μm / s) ont été adaptées pour optimiser la résolution spatiale et le temps d'analyse pour des grains de tailles différentes. Les cartes ont été générées à l'aide du logiciel Iolite sur la base de la composition résolue en temps

de chaque élément. Les cartes indiquent la concentration relative des éléments et sont semi-quantitatives.

1.6 – Format de la thèse

Cette thèse est organisée sous forme d'articles de recherche qui sont publiés au moment de la soumission finale. Chaque article est inséré sous la forme d'un chapitre distinct, qui n'est pas organisé dans l'ordre chronologique de publication.

Le premier article a été publié dans la revue « Geostandards and Geoanalytical Research » en juillet 2019 et s'intitule « Determination of Te, As, Bi, Sb and Se (TABS) in Geological Reference Materials and GeoPT Proficiency Test Materials by Hydride Generation-Atomic Spectrométrie de fluorescence (HG-AFS) ». Cet article constitue le chapitre 2 de la thèse. Le manuscrit présente une description détaillée de la méthode *HG-AFS* qui a été développée pour mesurer la concentration de TABS dans les matériaux géologiques. Afin de valider la méthode, plusieurs matériaux de référence internationaux d'échantillons géologiques ont été analysés. L'étude fournit le support analytique pour les autres études présentées dans la thèse.

Le deuxième article a été publié dans la revue «Mineralium Deposita» en novembre 2019 et s'intitule «Distribution of chalcophile and platinum-group elements among pyrrhotite, pentlandite, chalcopyrite and cubanite from the Noril'sk-Talnakh ores: implications for the formation of platinum-group minerals». Cet article constitue le chapitre 3 de la thèse. Le manuscrit étudie la variation cryptique des SMB lors de la cristallisation fractionnée d'un liquide sulfuré, en utilisant des minerais sulfurés massifs du district minier de Noril'sk Talnakh. Les résultats permettent d'évaluer si un liquide immiscible riche en TABS peut se former dans des cas naturels, et également si les MGP peuvent cristalliser directement à partir du liquide sulfuré.

Le troisième article est intitulé «Textural and compositional evidence for the formation of pentlandite via peritectic reaction: Implications for the distribution of highly siderophile elements» et a été publié en février 2019 dans la revue «Geology». Cet article constitue le chapitre 4 de la thèse. L'article traite de la formation de pentlandite par réaction péritectique entre le MSS et le liquide sulfuré à des températures élevées (~ 900 ° C), qui est une alternative à la formation de pentlandite exclusivement à partir de l'exsolution du MSS à des températures plus basses (~ 650 ° C). Les résultats fournissent des informations importantes sur les étapes conduisant à la formation de gisements de sulfure magmatique, ainsi que l'incorporation d'éléments chalcophiles dans le réseau des SMB. Par conséquent, étant donné que l'hypothèse à étudier est l'exsolution des EGP et TABS à partir du réseau des SMB, il faut d'abord bien comprendre comment différents éléments sont incorporés dans des SMB.

Le quatrième article est intitulé «Concentrations of Te, As, Bi, Sb and Se in the Marginal Zone of the Bushveld Complex: Evidence for crustal contamination and the nature of the magma that formed the Merensky Reef», et a été publié en avril 2020, dans la revue "Lithos". Cet article constitue le chapitre 5 de la thèse. Le manuscrit explore la distribution de TABS dans des échantillons de la *Marginal Zone* du complexe du Bushveld. Cette étude permet de comprendre les principaux processus affectant la distribution des TABS dans les magmas initiaux qui ont cristallisé certains des gisements de EGP les plus importants au monde (*Merensky Reef* et *UG-2 chromitite*). De plus, les résultats permettent de modéliser la distribution attendue des TABS dans le *Merensky Reef*, et ainsi de comprendre comment l'accumulation de sulfure dans le *Reef* affecte la distribution des TABS.

Le cinquième article a été publié dans la revue "Geochimica et Cosmochimica Acta" en mars 2020 et s'intitule " The role of Te, As, Bi, Sn and Sb during the formation of platinum-group-element reef deposits: Examples from the Bushveld and Stillwater Complexes». Cet article constitue le chapitre 6 de la thèse. Le manuscrit présente la distribution des TABS dans des échantillons de roches totale et des SMB du *Merensky Reef*, du *J-M Reef*, du gisement *Picket Pin* et également des échantillons stériles en EGP provenant de l'extérieur des *Reefs*.

L'étude permet de comprendre le rôle de TABS lors de l'exsolution des MGP à partir du réseau des SMB. De plus, les résultats obtenus fournissent également des moyens de tester si les compositions d'échantillons de la *Marginal Zone* (chapitre 5) conviennent comme liquides initiaux pour cristalliser le *Merensky Reef*.

Le chapitre 7 donne un aperçu des principales conclusions de la thèse. Cela permet de comprendre quelles hypothèses sont plus appropriées pour le rôle des TABS lors de la formation des gisements de EGP.

1.7 - Références

Aguilera, F., Layana, S., Rodríguez-Díaz, A., González, C., Cortés, J., Inostroza, M. (2016) Hydrothermal alteration, fumarolic deposits and fluids from Lastarria Volcanic Complex: A multidisciplinary study. Andean Geology, 43(2): 166-196.

Ames, D.E., Farrow, C.E.G. (2007) Metallogeny of the Sudbury mining camp, Ontario. In: Goodfellow WD (ed) Mineral deposits of Canada: a synthesis of major deposit-types, district metallogeny, the evolution of geological provinces, and exploration methods. Geological Association of Canada, Special Publication No. 5, Mineral Deposits Division, 329–350.

Arevalo, R., McDonough, W. F. (2010) Chemical variations and regional diversity observed in MORB. Chemical Geology, 271(1-2): 70-85.

Arguin, J.P., Pagé, P., Barnes, S.-J., Yu, Y., Song, X.Y., (2016) The Effect of Chromite Crystallization on the Distribution of Osmium, Iridium, Ruthenium and Rhodium in Picritic Magmas: an Example from the Emeishan Large Igneous Province, Southwestern China. Journal of Petrology, 57(5): 1019-1048.

Barnes, S.J., Fisher, L.A., Godel, B., Maier, W.D., Paterson, D., Howard, D.L., Ran, C.G., Laird, J.S., Pearce, M.A. (2016) Primary cumulus platinum minerals in the Monts de Cristal Complex, Gabon: magmatic microenvironments inferred from high-resolution X-ray fluorescence microscopy. Contributions to Mineralogu and Petrology, 171: 23.

Barnes, S.J., Robertson, J.C. (2019) Time scales and length scales in magma flow pathways and the origin of magmatic Ni–Cu–PGE ore deposits. Geoscience Frontiers, 10(1): 77-87.

Barnes, S-J. (2016) Chalcophile Elements. In Encyclopedia of Geochemistry: A Comprehensive Reference Source on the Chemistry of the Earth (ed. W.M. White), pp. 1-5.

Barnes, S-J., Makovicky, E., Makovicky, M., Rose-Hansen, J., Karup-Moller, S. (1997) Partition coefficients for Ni, Cu, Pd, Pt, Rh, and Ir between monosulfide solid solution and sulfide liquid and the formation of compositionally zoned Ni–Cu sulfide bodies by fractional crystallization of sulfide liquid. Canadian Journal of Earth Sciences, 34: 366-374.

Barnes, S-J., Cox, R.A., Zientek, M.L. (2006) Platinum-group element, Gold, Silver and Base Metal distribution in compositionally zoned sulfide droplets from the Medvezky

CreekMine, Noril'sk, Russia. Contributions to Mineralogy and Petrology, 152: 187–200.

Barnes, S-J., Prichard, H.M., Cox, R.A., Fisher, P.C., Godel, B. (2008) The location of the chalcophile and siderophile elements in platinum-group element ore deposits (a textural, microbeam and whole rock geochemical study): Implications for the formation of the deposits. Chemical Geology, 248: 295–317.

Barnes, S-J., Maier,W.D., Curl, E. (2010) Composition of the marginal rocks and sills of the Rustenburg layered suite, Bushveld Complex, South Africa: implications for the formation of the PGE deposits. Economic Geology, 105: 1491–1511.

Barnes S-J., Maier W.D. (2002) Platinum-group elements and microstructures of Normal Merensky Reef from Impala Platinum Mines, Bushveld Complex. Journal of Petrology, 43(1): 103-128.

Barnes, S.-J., Ripley, E.M. (2016) Highly siderophile and strongly chalcophile elements in magmatic ore deposits. Reviews in Mineralogy and Geochemistry, 81: 725–774.

Boudreau, A.E. (2016) The Stillwater Complex, Montana – Overview and the significance of volatiles. Mineralogical Magazine, 80(4): 585-637.

Boudreau, A.E., Mc Callum, I.S. (1992) Infiltration metasomatism in layered intrusions - an example from the Stillwater Complex, Montana. Journal of Volcanology and Geothermal Research, 52 (1–3): 171–183.

Boudreau, A.E., Meurer, W.P. (1999) Concentration of platinum-group elements by magmatic fluids in layered intrusions. Economic Geology, 87: 1830–1848.

Boudreau, A., Djon, L., Tchalikian, A., Corkery, J. (2014) The Lac Des Iles Palladium deposit, Ontario, Canada part I. The effect of variable alteration on the offset zone. Mineralim Deposita, 49(5): 625-654.

Bow, C., Wolfgram, D., Turner, A., Barnes, S., Evans, J., Zdepski, M., Boudreau, A.E. (1982) Investigations of the Howland reef of the Stillwater Complex, Minneapolis Adit area: Stratigraphy, structure and mineralization. Economic Geology, 77: 1481-1492.

Brügmann, G.E., Naldrett, A.J., Asif, M., Lightfoot, P.C., Gorbachev, N.S., Fedorenko, V.A. (1993) Siderophile and chalcophile metals as tracers of the evolution of the Siberian

Trap in the Noril'sk region, Russia. Geochimica et Cosmochimica Acta, 57(9): 2001-2018.

Burgess, S.D., Bowring, S., Shen, S.Z. (2014) High-precision timeline for Earth's most severe extinction. Proceedings of the National Academy of Sciences, 111: 3316–3321.

Cabri, L.J. (1973) New data on phase relations in the Cu-Fe-S system. Economic Geology, 68: 443–454.

Cafagna, F., Jugo, P.J. (2016) An experimental study on the geochemical behavior of highly siderophile elements (HSE) and metalloids (As, Se, Sb, Te, Bi) in a mss-iss-pyrite system at 650° c: A possible magmatic origin for Co-HSE-bearing pyrite and the role of metalloid-rich phases in the fractionation of HSE. Geochimica et Cosmochimica Acta, 178: 233-258.

Campbell, I.H., Naldrett, A.J. (1979) The influence of silicate: sulfide ratios on the geochemistry of magmatic sulfides. Economic Geology, 74(6): 1503-1506.

Campbell, I.H., Barnes, S.J. (1984) A model for the geochemistry of the platinum-group elements in magmatic sulfide deposits. The Canadian Mineralogist, 22(1): 151-160.

Campbell, I.H., Naldrett, A.J., Barnes, S.J. (1983) A model for the origin of the platinum-rich sulfide horizons in the Bushveld and Stillwater Complexes. Journal of Petrology, 24(2): 133-165.

Canali, A.C., Brenan, J.M., Sullivan, N.A. (2017) Solubility of platinum-arsenide melt and sperrylite in synthetic basalt at 0.1 MPa and 1200ºC with implications for arsenic speciation and platinum sequestration in mafic igneous systems. Geochimica et Cosmochimica Acta, 216: 153-168.

Cawthorn, R.G. (1999) The platinum and palladium resources of the Bushveld Complex. South African Journal of Science, 95(11-12): 481.

Cawthorn, R.G. (2002) Platinum-Group Element deposits of the Bushveld Complex in South Africa. In Geology, Geochemistry, Mineralogy and Mineral Benefication of Platinum Group Element (ed. L.J. Cabri). Canadian Institute of Mining, Metallurgy and Petroleum, Special volume 54: 389-429.

Cox, D., Watt, S.F.L., Jenner, F.E., Hastie, A.R., Hammond, S.J. (2019) Chalcophile element processing beneath a continental arc stratovolcano. Earth and Planetary Science Letters, 522: 1-11.

Dare, S.A.S., Barnes, S.-J., Prichard, H.M., Fisher, P.C. (2010a) The timing and formation of platinum-group minerals from the Creighton Ni-Cu-platinum-group element sulfide deposit, Sudbury, Canada: Early crystallization of PGE-rich sulfarsenides. Economic Geology, 105: 1071-1096.

Dare, S.A.S., Barnes, S.-J., Prichard, H.M. (2010b) The distribution of platinum group elements (PGE) and other chalcophile elements among sulfides from the Creighton Ni–Cu–PGE sulfide deposit, Sudbury, Canada, and the origin of palladium in pentlandite. Mineralium Deposita 45: 765-793.

Dare, S., Barnes, S.-J., Prichard, H., Fisher, P. (2011) Chalcophile and platinum-group element (PGE) concentrations in the sulfide minerals from the McCreedy East deposit, Sudbury, Canada, and the origin of PGE in pyrite. Mineralium Deposita, 46: 381-407.

Dare, S.A.S., Barnes, S-J., Prichard, H.M., Fisher, P.C. (2014) Mineralogy and geochemistry of Cu-rich ores from the McCreedy East Ni-Cu-PGE deposit (Sudbury, Canada): Implications for the behavior of platinum group and chalcophile elements at the end of crystallization of a sulfide liquid. Economic Geology, 109: 343-366.

Djon, M.L.N., Barnes, S-J. (2012) Changes in sulfides and platinum-group minerals with the degree of alteration in the Roby, Twilight, and High Grade Zones of the Lac des Iles Complex, Ontario, Canada. Mineralium Deposita, 47: 875-896.

Duran, C.J., Barnes, S.-J., Corkery, J.T. (2015) Chalcophile and platinum-group element distribution in pyrites from the sulfide-rich pods of the Lac des Iles Pd deposits, Western Ontario, Canada: implications for post-cumulus reequilibration of the ore and the use of pyrite compositions in exploration. Journal of Geochemical Exploration, 158: 223-242.

Duran, C.J., Barnes, S-J., Pleše, P., Prašek, M.K., Zientek, M.L., Pagé, P. (2017) Fractional crystallization-induced variations in sulfides from the Noril'sk-Talnakh mining district (polar Siberia, Russia). Ore Geology Reviews, 90: 326-351.

Dutrizac, J.E. (1976) Reactions in cubanite and chalcopyrite. The Canadian Mineralogist, 14(2): 172-181.

Edmonds, M., Mather, T.A., Liu, E.J. (2018) A distinct metal fingerprint in arc volcanic emissions. Nature Geoscience, 11(10): 790-794.

European Commission, (2010) Critical Raw Materials for the EU. Report of the Ad-hoc Working Group on Defining Critical Raw Materials. European Commission, Enterprise and Industry.

European Commission, (2014) Report on critical raw materials for the EU. Report of the Ad-hoc Working Group on Defining Critical Raw Materials. European Commission, Enterprise and Industry.

Fedorenko, V.A. (1994) Evolution of magmatism as reflected in the volcanic sequence of the Noril'sk region. In: Lightfoot, P.C., Naldrett, A.J. (Eds), Proceedings of the Sudbury-Noril'sk Symposium, Ontario Geological Survey, special publication issue 5. Ontario Geological Survey, Greater Sudbury: 171–184.

Fedorenko, V.A., Czamanske, G.K. (1997) Results of new field and geochemical studies of the volcanic and intrusive rocks of the Maymecha-Kotuy area, Siberian Flood-Basalt Province, Russia. International Geology Review, 39: 479-531.

Fiorentini, M.L., Bekker, A., Rouxel, O., Wing, B.A., Maier, W., Rumble, D. (2012) Multiple sulfur and iron isotope composition of magmatic Ni-Cu-(PGE) sulfide mineralization from eastern Botswana. Economic Geology, 107(1): 105-116.

Finnigan, C.S., Brenan, J.M., Mungall, J.E., McDonough, W.F. (2008) Experiments and model bearing on the role of chromite as a collector of platinum group minerals by local reduction. Journal of Petrology, 49: 1647–1665.

Forrest, A., Keller, K.A., Schilling, J.G. (2017) Selenium, tellurium and sulfur variations in basalts along the Reykjanes Ridge and extension over Iceland, from 50ºN to 65ºN. Interdisciplinary Earth Data Alliance (IEDA), Palisades, NY.

Genna, D., Gaboury, D. (2019) Use of semi-volatile metals as a new vectoring tool for VMS exploration: Example from the Zn-rich McLeod deposit, Abitibi, Canada. Journal of Geochemical Exploration, 207: 106358.

Godel, B., Barnes, S-J., Maier, W.D. (2007) Platinum-group elements in sulphide minerals, platinum-group minerals, and whole-rocks of the Merensky Reef (Bushveld Complex, South Africa): Implications for the formation of the reef. Journal of Petrology, 48: 1569-1604.

Godel, B., González-Álvarez, I., Barnes, S.J., Barnes, S-J., Parker, P., Day, J. (2012) Sulfides and sulfarsenides from the Rosie nickel prospect, Duketon greenstone belt, Western Australia. Economic Geology, 107: 275-294.

Goldschmidt, V. M. (1923) Geochemische Verteilungsgesetze der Elemente. Skrifter utg. av det Norske Visenskaps-Akademii i Oslo I. Mat.-Naturv. Klasse, 2, p. 1–17.

Gorbachev, N.S., Grinenko, L.N. (1973) The sulfur-isotope ratios of the sulfides and sulfates of the Oktyabr'sky sulfide deposit, Noril'sk region, and the problem of its origin. Geokhimiya, 8: 1127–1136.

Grinenko, L.I. (1985) Sources of sulfur of the nickeliferous and barren gabbro-dolerite intrusions of the northwest Siberian platform. International Geology Review, 27(6): 695-708.

Guo, H., Audetat, A. (2017) Transfer of volatiles and metals from mafic to felsic magmas in composite magma chambers: An experimental study. Geochimica et Cosmochimica Acta, 198: 360-378.

Hall, A.L. (1932) The Bushveld Igneous Complex in the central Transvaal. Geological Society, South Africa, Memoir 28, 544 p.

Hanley, J.J. (2007) The role of arsenic-rich melts and mineral phases in the development of high-grade Pt-Pd mineralization within komatiite-associated magmatic Ni-Cu sulfide horizons at Dundonald Beach South, Abitibi subprovince, Ontario, Canada. Economic Geology, 102: 305-317.

Harvey, J., Day, J.M. (2016) Highly Siderophile and Strongly Chalcophile Elements in High-Temperature Geochemistry and Cosmochemistry. Reviews in Mineralogy and Geochemistry, 81: 774 p.

Hattori, K.H., Arai, S., Clarke, D.B. (2002) Selenium, tellurium, arsenic and antimony contents of primary mantle sulfides. The Canadian Mineralogist, 40(2): 637-650.

Helmy, H.M., Ballhaus, C., Berndt, J., Bockrath, C. (2007) Wohlgemuth-Ueberwasser, C. Formation of Pt, Pd and Ni tellurides: Experiments in sulfide–telluride systems. Contributions to Mineralogy and Petrology, 153: 577-591.

Helmy, H.M., Ballhaus, C., Fonseca, R., Nagel, T. (2013) Fractionation of platinum, palladium, nickel, and copper in sulfide–arsenide systems at magmatic temperature. Contributions to Mineralogy and Petrology, 166: 1725-1737.

Hiemstra, S. A. (1979) The role of collectors in the formation of the platinum deposits in the Bushveld Complex. The Canadian Mineralogist, 17: 469-482.

Holwell, D., McDonald, I. (2007) Distribution of platinum-group elements in the Platreef at Overysel, northern Bushveld Complex: A combined PGM and LA-ICP-MS study. Contributions to Mineralogy and Petrology, 154: 171-190.

Holwell, D., Adeyemi, Z., Ward, L.A., Smith, D.J., Graham, S.D., McDonald, I., Smith, J.W. (2017) Low temperature alteration of magmatic Ni-Cu-PGE sulfides as a source for hydrothermal Ni and PGE ores: A quantitative approach using automated mineralogy. Ore Geology Reviews, 91: 718-740.

Hutchinson, D., McDonald, I. (2008) Laser ablation ICP-MS study of platinum-group elements in sulphides from the Platreef at Turfspruit, northern limb of the Bushveld Complex, South Africa. Mineralium Deposita, 43: 695–711.

Jamieson, H.E. (2016) The Legacy of Arsenic Contamination from Mining and Processing Refractory Gold Ore at Giant Mine, Yellowknife, Northwest Territories, Canada. Reviews in Mineralogy and Geochemistry, 79: 533-551.

Jenner, F.E. (2017) Cumulate causes for the low contents of sulfide-loving elements in the continental crust. Nature Geoscience, 10(7): 524-529.

Jenner, F.E., O'Neill, H.S.C. (2012) Analysis of 60 elements in 616 ocean floor basaltic glasses. Geochemistry, Geophysics, Geosystems, 13(2).

Junge, M., Wirth, R., Oberthür, T., Melcher, F., Schreiber, A. (2015) Mineralogical siting of platinum-group elements in pentlandite from the Bushveld Complex, South Africa. Mineralium Deposita, 50: 41-54.

Kamenetsky, V.S., Eggins, S.M. (2012) Systematics of metals, metalloids, and volatiles in MORB melts: effects of partial melting, crystal fractionation and degassing (a case study of Macquarie Island glasses). Chemical Geology, 302: 76-86.

Kanitpanyacharoen, W., Boudreau, A.E. (2013) Sulfide-associated mineral assemblages in the Bushveld Complex, South Africa: platinum-group element enrichment by vapor refining by chloride–carbonate fluids. Mineralium Deposita, 48(2): 193-210.

Kawohl, A., Frimmel, H.E. (2016) Isoferroplatinum-pyrrhotite-troilite intergrowth as evidence of desulfurization in the Merensky Reef at Rustenburg (western Bushveld Complex, South Africa). Mineralogical Magazine, 80: 1041-1053.

Keays, R.R., Lightfoot, P.C. (2010) Crustal sulfur is required to form magmatic Ni-Cu sulfide deposits: Evidence form chalcophile element signatures of Siberian and Deccan Trap basalts: Mineralium Deposita, 45: 241-257.

Kelly, D.P., Vaughan, D.J. (1983) Pyrrhotine-pentlandite ore textures: a mechanistic approach. Mineralogical Magazine, 47: 453–463.

Ketris, M.P., Yudovich, Y.E. (2009) Estimations of Clarkes for Carbonaceous biolithes: World averages for trace element contents in black shales and coals. International Journal of Coal Geology, 78(2): 135-148.

Kissin, S.A., Scott, S.D. (1982) Phase relations involving pyrrhotite below 350 degrees C. Economic Geology, 77(7): 1739-1754.

Kitakaze, A., Machida, T., Komatsu, R. (2016) Phase relations in the Fe-Ni-S system from 875 to 650°C. The Canadian Mineralogist, 54: 1175-1186.

Knight, R.D., Prichard, H.M., Ferreira Filho, C.F. (2017) Evidence for As Contamination and the Partitioning of Pd into Pentlandite and Co+ Platinum Group Elements into Pyrite in the Fazenda Mirabela Intrusion, Brazil. Economic Geology, 112(8): 1889-1912.

König, S., Luguet, A., Lorand, J-P., Wombacher, F., Lissner, M. (2012) Selenium and tellurium systematics of the Earth's mantle from high precision analyses of ultra-depleted orogenic peridotites. Geochimica et Cosmochimica Acta, 86: 354-366.

Kosyakov, V.I., Sinyakova, E.F. (2012) Physicochemical prerequisites for the formation of primary orebody zoning at copper-nickel sulfide deposits (by the example of the systems Fe–Ni–S and Cu–Fe–S). Russian Geology and Geophysics, 53(9): 861-882.

Le Vaillant, M., Barnes, S.J., Fiorentini, M.L., Barnes, S-J., Bath, A., Miller, J. (2018) Platinum-group element and gold contents of arsenide and sulfarsenide minerals associated with Ni and Au deposits in Archean greenstone belts. Mineralogical Magazine, 82(3): 625-647.

Leeb-du Toit, A. (1986) The Impala Platinum Mines. In: Anhaeusser CR, Maske S (ed) Mineral deposits of Southern Africa. Geol Soc S Afr Johannesburg, 1091–1106.

Lesher, C.M., Burnham, O.M. (2001) Multicomponent elemental and isotopic mixing in Ni–Cu–(PGE) ores at Kambalda, Western Australia. The Canadian Mineralogist, 39(2): 421-446.

Li, C., Barnes, S.J., Makovicky, E., Karup-Moller, S., Makovicky, M., Rose-Hansen, J. (1996) Partitioning of Ni, Cu, Ir, Rh, Pt and Pd between monosulfide solid solution and sulfide liquid: effects of composition and temperature. Geochimica et Cosmochimica Acta, 60: 1231–1238.

Li Y., Audétat, A. (2015) Effects of temperature, silicate melt composition, and oxygen fugacity on the partitioning of V, Mn, Co, Ni, Cu, Zn, As, Mo, Ag, Sn, Sb, W, Au, Pb, and Bi between sulfide phases and silicate melt. Geochimica et Cosmochimica Acta 162, 25-45.

Likhachev, A.P. (1994) Ore-bearing intrusions of the Noril'sk region. In: Lightfoot, P. C., Naldrett, A.J. (Eds.), Proceedings of the Sudbury-Noril'sk Symposium, Ontario Geological Survey, special publication issue 5. Ontario Geological Survey, Greater Sudbury: 185–201.

Liu, Y., Brenan, J. (2015) Partitioning of platinum-group elements (PGE) and chalcogens (Se, Te, As, Sb, Bi) between monosulfide-solid solution (MSS), intermediate solid solution (ISS) and sulfide liquid at controlled fO2–fS2 conditions. Geochimica et Cosmochimica Acta, 159: 139-161.

Lissner, M., König, S., Luguet, A., Le Roux, P., Schuth, S., Heuser, A., le Roex, A.P. (2014) Selenium and tellurium systematics in MORBs from the southern Mid-Atlantic Ridge (47–50 S). Geochimica et Cosmochimica Acta, 144: 379-402.

Lodders, K. (2003) Solar system abundances and condensation temperatures of the elements. The Astrophysical Journal, 591: 1220-1247.

Lorand, J-P., Alard, O. (2010) Determination of selenium and tellurium concentrations in Pyrenean peridotites (Ariege, France): new insight into S/Se/Te systematics of the upper in mantle samples. Chemical Geology, 278(1-2): 120-130.

Luguet, A., Behrens, M., Pearson, D.G., König S., Herwartz, D. (2015) Significance of the whole rock Re–Os ages in cryptically and modally metasomatised cratonic peridotites: constraints from HSE–Se–Te systematics. Geochimica et Cosmochimica Acta, 164: 441–463.

Lusk, J., Bray, D.M. (2002) Phase relations and the electrochemical determination of sulfur fugacity for selected reactions in the Cu–Fe–S and Fe–S systems at 1 bar and temperatures between 185 and 460ºC. Chemical Geology, 192(3-4): 227-248.

Lyubetskaya, T., Korenaga, J. (2007) Chemical composition of Earth's primitive mantle and its variance: 1. Method and results. Journal of Geophysical Research ,112: B03211.

Maciag, B.J., Brenan, J.M. (2020) Speciation of Arsenic and Antimony in Basaltic Magmas. Geochimica et Cosmochimica Acta, 276: 198-218.

Maier, W.D., Rasmussen, B., Fletcher, I., Godel, B., Barnes, S.J., Fisher, L., Yang, S.H., Huhma, H., Lahaye, Y. (2015) Petrogenesis of the ~2.77 Ga Monts de Cristal Complex, Gabon: evidence for direct precipitation of Pt-arsenides from basaltic magma. Journal of Petrology, 56: 1285-1308.

Makovicky, E., Karup-Møller, S., Makovicky, M., Rose-Hansen, J. (1990) Experimental studies on the phase systems Fe-Ni-Pd-S and Fe-Pt-Pd-As-S applied to PGE deposits. Mineralog and Petrology, 42(1-4): 307-319.

Makovicky, E. (2002) Ternary and quaternary phase systems in PGE: Canadian Institute of Mining, Metallurgy and Petroleum, Special Volume 54: 131–175.

Mather, T.A., Witt, M.L.I., Pyle, D.M., Quayle, B.M., Aiuppa, A., Bagnato, E., Ilyinskaya, E. (2012) Halogens and trace metal emissions from the ongoing 2008 summit eruption of Kīlauea volcano, Hawaii. Geochimica et Cosmochimica Acta, 83: 292-323.

Mavrogenes, J.A., O'Neill, H.S.C. (1999) The relative effects of pressure, temperature and oxygen fugacity on the solubility of sulfide in mafic magmas. Geochimica et Cosmochimica Acta, 63(7-8): 1173-1180.

McCallum, I.S., Raedeke, L.D., Mathez, E.D. (1980) Investigations of the Stillwater Complex: Part I. Stratigraphy and structure of the Banded zone. American Journal of Science, 280: 59–87.

McDonough, W.F. (2003) 2.15 - Compositional model for the earth's core. Treatise on geochemistry, 547-568.

Milanovskiy, Y.Y. (1976) Rift zones of the geological past and their associated formations, report 2. International Geology Review, 18, 619–639.

Moss, R.L., Tzimas, E., Kara, H., Willis, P., Kooroshy, J. (2013) The potential risks from metals bottlenecks to the deployment of strategic energy technologies. Energy Policy, 55: 556-564.

Mota-e-Silva, J., Prichard, H.M., Ferreira Filho, C.F.,Fisher, P.C., McDonald, I. (2015) Platinum-group minerals in the Limoeiro Ni–Cu–(PGE) sulfide deposit, Brazil: the effect of magmatic and upper amphibolite to granulite metamorphic processes on PGM formation. Mineralium Deposita, 50(8): 1007–1029.

Mungall, J.E. (2007) Crystallization of magmatic sulfides: An empirical model and application to Sudbury ores. Geochimica et Cosmochimica Acta, 71(11): 2809-2819.

Mungall, J.E., Andrews, D.R., Cabri, L.J., Sylvester, P.J., Tubrett, M. (2005) Partitioning of Cu, Ni, Au, and platinum-group elements between monosulfide solid solution and sulfide melt under controlled oxygen and sulfur fugacities. Geochimica et Cosmochimica Acta, 69: 4349-4360.

Naldrett, A.J. (2004) Magmatic sulfide deposits: Geology, geochemistry and exploration: Berlin, Germany, Springer Verlag: 727 p.

Naldrett, A.J. (2011) Fundamentals ofmagmatic sulfide deposits. Reviews in Economic Geology, 17: 1-50.

Naldrett, A.J., Gasparrini, E.C., Barnes, S-J., Von Gruenewaldt, G., Sharpe, M.R. (1986) The upper critical zone of the Bushveld Complex and the origin of Merensky-type ores. Economic Geology, 81: 1105–1117.

Naldrett, A.J., Lightfoot, P.C., Fedorenko, V.A., Gorbachev, N.S., Doherty, W. (1992) Geology and geochemistry of intrusions and flood basalts of the Noril'sk region, USSR, with implications for the origin of the Ni-Cu Ores. Economic Geology, 87, 975– 1004.

Page, N.J. (1977) Stillwater Complex, Montana: rock succession, metamorphism and structure of the Complex and adjacent rocks. U.S. Geological Survey Professional Paper, 999. Reston, Virginia, USA.

Park, J-W., Campbell, I.H., Arculus, R.J. (2013) Platinum alloy and sulfur saturation in an arc-related basalt to rhyolite suite; evidence from the Pual Ridge lavas, the eastern Manus Basin. Geochimica et Cosmochimica Acta, 101: 76-95.

Paton, C., Hellstrom, J., Paul, B., Woodhead, J., Hergt, J. (2011) Iolite: Freeware for the visualisation and processing of mass spectrometric data. The Journal of Analytical Atomic Spectrometry, 26: 2508-2518.

Patten, C.G., Pitcairn, I.K., Teagle, D.A.H. (2017) Hydrothermal mobilisation of Au and other metals in supra-subduction oceanic crust: Insights from the Troodos ophiolite. Ore Geology Reviews, 86: 487-508.

Patten, C.G.C., Pitcairn, I.K., Alt, J.C., Zack, T., Lahaye, Y., Teagle, D.A.H., Markdahl, K. (2019) Metal fluxes during magmatic degassing in the oceanic crust: sulfide mineralisation at ODP site 786B, Izu-Bonin forearc. Mineralium Deposita: 1-21.

Péntek, A., Molnár, F., Watkinson, D.H., Jones, P.C. (2008) Footwall-type Cu-Ni-PGE Mineralization in the Broken Hammer Area, Wisner Township, North Range, Sudbury Structure. Economic Geology, 103: 1005-1028.

Piña, R., Gervilla, F., Barnes, S-J., Ortega, L., Lunar, R. (2013) Partition coefficients of platinum group and chalcophile elements between arsenide and sulfide phases as determined in the Beni Bousera Cr-Ni mineralization (North Morocco). Economic Geology, 108(5): 935-951.

Piña, R., Gervilla, F., Barnes, S-J., Ortega, L., Lunar, R. (2015) Liquid immiscibility between arsenide and sulfide melts: evidence from a LA-ICP-MS study in magmatic deposits at Serranía de Ronda (Spain). Mineralium Deposita, 50(3): 265-279.

Piña, R., Gervilla, F., Barnes, S-J., Oberthür, T., Lunar, R. (2016) Platinum-group element concentrations in pyrite from the Main Sulfide Zone of the Great Dyke of Zimbabwe. Mineralium Deposita, 51(7): 853-872.

Polovina, J.S., Hudson, D.M., Jones, R.E. (2004) Petrographic and geochemical characteristics of postmagmatic hydrothermal alteration and mineralization in the J-M Reef, Stillwater Complex, Montana. The Canadian Mineralogist, 42: 261-278.

Polozov, A.G., Svensen, H.H., Planke, S., Grishina, S.N., Fristad, K.E., Jerram, D.A. (2016) The basalt pipes of the Tunguska Basin (Siberia, Russia): High temperature processes and volatile degassing into the end-Permian atmosphere. Palaeogeography, Palaeoclimatology, Palaeoecology, 441: 51–64.

Prichard, H., Hutchinson, D., Fisher, P. (2004) Petrology and crystallization history of multiphase sulfide droplets in a mafic dike from Uruguay: Implications for the origin of Cu-Ni-PGE sulfide deposits. Economic Geology, 99: 365-376.

Queffurus, M., Barnes, S-J. (2014) Selenium and sulfur concentrations in country rocks from the Duluth Complex, Minnesota, USA: Implications for formation of the Cu-Ni-PGE sulfides. Economic Geology, 109(3): 785-794.

Reichow, M.K., Pringle, M.S., Al'Mukhamedov, A.I., Allen, M.B., Andreichev, V.L., Buslov, M.M., Davies, C.E., Fedoseev, G.S., Fitton, J.G., Inger, S., Medvedev, A.Y., Mitchell, C., Puchkov, V.N., Safonova, I.Y., Scott, R.A., Saunders, A.D. (2009) The timing and extent of the eruption of the Siberian traps large igneous province: implications for the end-Permian environmental crisis. Earth and Planetary Science Letters, 277: 9–20.

Ripley, E.M., Li, C. (2003) Sulfur isotope exchange and metal enrichment in the formation of magmatic Cu-Ni-(PGE) deposits. Economic Geology, 98: 635-641.

Ripley, E.M., Lightfoot, P.C., Li, C., Elswick, E.R. (2003) Sulfur isotopic studies of continental flood basalts in the Noril'sk region: Implications for the association between lavas and ore-bearing intrusions. Geochimica et Cosmochimica Acta, 67(15): 2805-2817.

Ripley, E.M., Li, C., Moore, C.H., Schmitt, A.K. (2010) Micro-scale S isotope studies of the Kharaelakh intrusion, Noril'sk region, Siberia: constraints on the genesis of coexisting anhydrite and sulfide minerals. Geochimica et Cosmochimica Acta, 74(2): 634-644.

Robertson, J., Ripley, E.M., Barnes, S.J., Li, C. (2015) Sulfur liberation from country rocks and incorporation in mafic magmas. Economic Geology, 110(4): 1111-1123.

Rose-Weston, L., Brenan, J.M., Fei, Y.W., Secco, R.A., Frost, D.J. (2009) Effect of pressure, temperature, and oxygen fugacity on the metal-silicate partitioning of Te, Se, and S: Implications for earth differentiation. Geochimica et Cosmochimica Acta, 73(15): 4598-4615.

Rudnick, R. L., Gao, S. (2003) Composition of the continental crust. The crust, 3: 1-64.

Samalens, N., Barnes, S-J., Sawyer, E.W. (2017) The role of black shales as a source of sulfur and semimetals in magmatic nickel-copper deposits: Example from the Partridge River Intrusion, Duluth Complex, Minnesota, USA. Ore Geology Reviews, 81(1): 173-187.

Scoats, J.S., Friedman, R.M. (2008) Precise age of the platiniferous Merensky reef, Bushveld Complex, South Africa, by U-Pb zircon chemical abrasion ID-TIMS technique. Economic Geology, 103: 465–471.

Shevko, E.P., Bortnikova, S.B., Abrosimova, N.A., Kamenetsky, V.S., Bortnikova, S.P., Panin, G.L., Zelenski, M. (2018) Trace elements and minerals in fumarolic sulfur: the case of Ebeko volcano, Kuriles. Geofluids: 16.

Singh, R., Singh, S., Parihar, P., Singh, V.P., Prasad, S.M. (2015) Arsenic contamination, consequences and remediation techniques: a review. Ecotoxicology and Environmental Safety, 112: 247–270.

Sinyakova, E., Kosyakov, V., Distler, V., Karmanov, N. (2016) Behavior of Pt, Pd, and Au during crystallization of Cu-rich magmatic sulfide minerals. The Canadian Mineralogist, 54(2): 491-509.

Sinyakova, E. F., Kosyakov, V. I., Borisenko, A. S. (2017). Effect of the presence of As, Bi, and Te on the behavior of Pt metals during fractionation crystallization of sulfide magma. Doklady Earth Sciences, 477: 1422-1425.

Sinyakova, E., Kosyakov, V., Palyanova, G., Karmanov, N. (2019) Experimental Modeling of Noble and Chalcophile Elements Fractionation during Solidification of Cu-Fe-Ni-S Melt. Minerals, 9(9): 531.

South African Committee for Stratigraphy (1980) Stratigraphy of Southern Africa. Part I. Lithostratigraphy of South Africa, South West Africa/Namibia, and the Republics of Boputhatswana, Transkei and Venda. Geological Survey of South Africa Handbook 8: 690pp.

Stucker, V.K., Walker, S.L., de Ronde, C.E., Caratori Tontini, F., Tsuchida, S. (2017) Hydrothermal Venting at Hinepuia Submarine Volcano, Kermadec Arc: Understanding Magmatic-Hydrothermal Fluid Chemistry. Geochemistry, Geophysics, Geosystems, 18(10): 3646-3661.

Sullivan, N.A., Zajacz, Z., Brenan, J.M. (2018) The solubility of Pd and Au in hydrous intermediate silicate melts: The effect of oxygen fugacity and the addition of Cl and S. Geochimica et Cosmochimica Acta, 231: 15-29.

Tuba, G., Molnár, F., Ames, D.E., Péntek, A., Watkinson, D.H., Jones, P.C. (2014) Multi-stage hydrothermal processes involved in ―low-sulfide‖ Cu (-Ni)-PGE mineralization in the footwall of the Sudbury Igneous Complex (Canada): Amy Lake PGE zone, East Range. Mineralium Deposita, 49: 7-47.

U.S Food and Drug Administration, (2015) Inductively Coupled Plasma-Mass Spectrometric Determination of Arsenic, Cadmium, Chromium, Lead, Mercury, and Other Elements in Food Using Microwave Assisted Digestion. Accessed at << https://www.fda.gov/food/laboratory-methods-food/elemental-analysis-manual-eam-food-and-related-products >>

U.S. Geological Survey, (2020) MineralCommodity Summaries. Accessed at <<https://www.usgs.gov/media/images/mineral-commodities-february-2020>>

Wall, C.J., Scoates, J.S., Friedman, R.M., Meurer,W.P. (2010) Refining the precise age and duration of magmatism related to the Stillwater Complex. In: 11th International Platinum Symposium, Sudbury, Ontario, June 20–24, 2010.

Wang, Z., Becker, H. (2013) Ratios of S, Se and Te in the silicate Earth require a volatile-rich late veneer. Nature, 499: 328-331.

Wieser, P., Jenner, F., Edmonds, M., Maclennan, J., Kunz, B. (2020) Chalcophile elements track the fate of sulfur at Kīlauea Volcano, Hawai'i. Geochimica et Cosmochimica Acta.

Wirth, R., Reid, D., Schreiber, A. (2013) Nanometer-sized platinum-group minerals (PGM) in base metal sulfides: new evidence for an orthomagmatic origin of the Merensky Reef PGE ore deposit, Bushveld Complex, South Africa. The Canadian Mineralogist, 51: 143-155.

Wood, S.A. (2002) The aqueous geochemistry of the platinum-group elements with applications to the ore deposits. In Geology, Geochemistry, Mineralogy and Mineral Benefication of Platinum Group Element (ed. L.J. Cabri). Canadian Institute of Mining, Metallurgy and Petroleum, Special volume 54: 211−249.

Yierpan, A., König, S., Labidi, J., Schoenberg, R. (2019) Selenium isotope and S-Se-Te elemental systematics along the Pacific-Antarctic ridge: Role of mantle processes. Geochimica et Cosmochimica Acta, 249: 199-224.

Zelenski, M.E., Fischer, T.P., de Moor, J.M., Marty, B., Zimmermann, L., Ayalew, D., Nekrasov, AN., Karandashev, V.K. (2013) Trace elements in the gas emissions from the Erta Ale volcano, Afar, Ethiopia. Chemical Geology, 357: 95-116.

Zelenski, M., Malik, N., Taran, Y. (2014) Emissions of trace elements during the 2012–2013 effusive eruption of Tolbachik volcano, Kamchatka-enrichment factors, partition coefficients and aerosol contribution. Journal of Volcanology and Geothermal Research, 285: 136–149.

Zientek, M.L., Likhachev, A.P., Kunilov, V.E., Barnes, S-J., Meier, A.L., Carlson, R.R., Briggs, P.H., Fries, T.L., Adrian, B.M. (1994) Cumulus processes and the composition of magmatic ore deposits: examples from the Talnakh District, Russia. In: Lightfoot, P.C., Naldrett, A.J. (Eds.), Proceedings of the Sudbury-Noril'sk Symposium, Ontario Geological Survey, special publication issue 5. Ontario Geological Survey, Greater Sudbury: 373–392.

Zientek, M.L., Cooper, R.W., Corson, S.R., Geraghty, E.P. (2002) Platinum-group element mineralization in the Stillwater Complex, Montana. In Geology, Geochemistry, Mineralogy and Mineral Benefication of Platinum Group Element (ed. L.J. Cabri). Canadian Institute of Mining, Metallurgy and Petroleum, Special volume 54: 459 –481.

Zweibel, K. (2010) The Impact of Tellurium Supply on Cadmium Telluride Photovoltaics. Science, 328: 699-701.

Chapter 2 - Determination of Te, As, Bi, Sb and Se (TABS) in Geological Reference Materials and GeoPT Proficiency Test Materials by Hydride Generation-Atomic Fluorescence Spectrometry (HG-AFS)

Eduardo Teixeira **Mansur (1)**, Sarah-Jane **Barnes (1),** Dany **Savard (1)** and Peter **Webb (2)**

(1) Sciences de la Terre, Université du Québec à Chicoutimi, Québec, G7H 2B1, Canada

(2) Formerly of the Department of Environment, Earth and Ecosystems, The Open University, Walton Hall, Milton Keynes, MK7 6AA, United Kingdom

Author contributions:

Mansur wrote the manuscript, collected and analyzed the data and created the figures. **Barnes** edited the manuscript and analyzed the data. **Savard** and **Webb** helped implementing the analytical protocol presented in the manuscript as well as contributed to the interpretation of the analyzed and literature data.

Geostandards and Geoanalytical Research (2019)

DOI: 10.1111/ggr.12289

2.1 - Abstract

The study of Te, As, Bi, Sb and Se (TABS) has increased over the past years due to their use in the development of low-carbon energy technologies. However, there is a scarcity of concentrations of TABS in geological reference materials. This underlines the difficulty in undertaking routine analysis of these elements. The concentrations of TABS were determined in geological reference materials using hydride generation-atomic fluorescence spectrometry (HG-AFS), calibrated with standard solutions. Comparisons with literature values were used to validate the method. Samples from the Geo*PT* proficiency test were also analyzed. For most elements there are no assigned or even provisional values for many of the Geo*PT* and reference materials because of the wide range of results reported. For concentrations above the quantification limit of the method our results are in good agreement with the median of Geo*PT* results. Thus, we propose Geo*PT* median values as informational values for these elements. In contrast, at concentrations < 0.5 μg/g median values of Se from Geo*PT* are systematically higher than our results. Our Se results are in agreement with the reference materials down to 0.02 μg/g, which suggest that many of the results for Se reported in Geo*PT* testing are too high.

Keywords: Te, As, Bi, Sb, Se; HG-AFS; geological reference materials; Geo*PT*.

2.2 – Introduction

The determination of Te, As, Bi, Sb and Se (TABS; Barnes 2016) is critical for both environmental and economic reasons. These elements pose risks to the environment (especially As and Sb), such as through the contamination of soils, surface drainage and groundwater (*e.g.* Jamieson 2014; Singh *et al.* 2015). Consequently, most TABS are routinely monitored in various materials as elevated concentrations can be highly toxic (Wu 2004; Duker *et al.* 2005; Sundar and Chakravarty 2010). On the other hand, TABS are also classified as critical raw materials for the development of low-carbon energy technologies (Zweibel 2010; Moss *et al.* 2013). Thus, the demand for analytical methods capable of quantifying these elements down to low levels is continually increasing.

Although most studies have focused on the importance of TABS in environmental and health issues over the past decades, there is a growing demand to understand their geochemical cycles (Hattori *et al.* 2002; Wang and Becker 2013; Brenan 2015). For example, TABS may be particularly important during the formation of platinum-group elements and gold deposits (Pitcairn *et al.* 2015; Barnes and Ripley 2016). However, there are very few values for TABS concentrations in geological reference materials (especially of Bi, Se and Te), and consequently analytical protocols are difficult to validate. Therefore, the geological interpretations of the data are weakened by the uncertainty in the analytical results.

Atomic fluorescence spectrometry (AFS), coupled to hydride generation (HG), is an effective method for determining elements such as TABS that form covalent hydrides (Corns *et al.* 1993). Consequently, HG-AFS has been applied for monitoring

trace amounts of TABS in materials such as food (Reyes *et al.* 2008; Zhang *et al.* 2011; Cava-Montesinos *et al.* 2013; Lai *et al.* 2016) and water (He *et al.* 1998; Yan *et al.* 2002). This technique has also been used by geologists to assess the behaviour of TABS during various geological processes (Pitcairn 2004; Pitcairn *et al.* 2015; Patten *et al.* 2016). The concentrations of TABS in geological materials are variable (Hattori *et al.* 2002; Ketris and Yudovich 2009; Samalens *et al.* 2017; Henrique-Pinto *et al.* 2015), and in some cases (especially for Se and Te), very low (Wang and Becker 2014; König *et al.* 2012, 2014; Lissner *et al.* 2014). The method appears suitable for studying the distribution of TABS in geological materials. However, to date HG-AFS has not been comprehensively tested using geological reference materials.

In this work we first establish the effectiveness of HG-AFS by determining the concentrations of TABS in a series of geological reference materials and comparing the results with literature values. In addition, we report results for TABS in Geo*PT* proficiency test materials, and compare the results with Geo*PT* assigned and provisional values where available, and where not, with ranges of values reported by participating laboratories. We will show that our results mostly agree with the median values of results reported by Geo*PT* participating laboratories for Te, As, Bi and Sb and propose that these values could be used as informational values. However, the median values for the generally rather small Se datasets reported in Geo*PT* proficiency tests are elevated in comparison to our results. Because the values that we determined for Se in the reference materials are in agreement with certified or provisional values we suggest that many of the results contributed to the Geo*PT* tests are probably overestimations.

2.3 – Experimental

The analytical protocol is a slightly modified version of the method implemented by Pitcairn (2004).

2.3.1 - Digestion of the rock samples

Around 0.2 g of rock powder was mixed with 5 ml of aqua regia (1:3 HNO_3:HCl; PlasmaPURE – SPC Science) in a 50 ml-disposable beaker (Digi TUBES – SCP Science). The closed-cap beaker was swirled and then placed in a digestion block for 2 hours at room temperature, and further heated up to 80ºC for 22 hours. The solution was then allowed to cool and diluted to 25 ml with distilled water (Fig. 2.1). A different sample digest was prepared for each individual measurement.

The digestion of rock samples has to take into account the volatile behaviour of TABS (Corns *et al.* 1993; König *et al.* 2012; Wang and Becker 2014), and thus avoid a loss by volatilization. The use of closed-cap beakers and low temperature are fundamental (Wang and Becker 2014). Previous studies indicate that heating the sample up to 80ºC in a closed system results in digestion without any analyte loss. In fact, heating the analytes to temperatures below 100ºC is a common step adopted in several analytical routines to ensure the reduction of TABS prior to analysis without any loss (Pitcairn 2004; He *et al.* 1998; Savard *et al.* 2006, 2009; König *et al.* 2012; Wang and Becker 2014).

2.3.2 - Preparation of analytical solutions

The hydride generation method makes use of the ability of TABS to form covalent gaseous hydrides (*e.g.,* AsH_3, SbH_3). However, the formation of hydrides by

these elements depends on them being in the reduced oxidation state (Corns *et al*. 1993). Consequently, the preparation of solutions for analysis requires a pre-reduction step, which varies for each element. Hence, As and Sb were measured in a different aliquot from Te, Se and Bi.

The aliquots were prepared by adding 10 ml of the digested rock solution to 30 ml of a reagent blank (Fig. 2.1) in a 50 ml disposable beaker. For the As and Sb aliquot, the reagent blank was a solution of 6 mol l^{-1} HCl, 13 g l^{-1} potassium iodide (KI; VWR Chemicals), and 3.5 g l^{-1} ascorbic acid (VWR Chemicals; Fig. 2.1). The KI and the ascorbic acid are used to reduce the oxidation state of Sb^{V} and As^{V} to Sb^{III} and As^{III}, respectively (Nielsen and Hansen 1997; Potin-Gautier *et al.* 2005). For the Te, Se and Bi aliquot the reagent blank does not need any KI or ascorbic acid, and consists only of a 6 mol l^{-1} HCl solution (Fig. 2.1). The pre-reduction of Se and Te was achieved by heating the aliquot to 80ºC for 40 minutes in a water bath, in a closed-cap beaker (Cava-Montesinos *et al.* 2003; Savard *et al.* 2006). During this step, the Se^{VI} and the Te^{VI} are converted to Se^{IV} and Te^{IV}, respectively, which is necessary to ensure the formation of hydrides (Corns *et al*. 1993).

2.3.3 - Instrumentation

Analyses were performed at LabMaTer, Université du Québec à Chicoutimi (UQAC), using a continuous flow hydride generation-atomic fluorescence spectrometer, the PSA Millenium Excalibur 10.055 from PS Analytical. The instrument was equipped with boosted hollow cathode discharge (BHCD) lamps for As, Sb, Se, Te and Bi, and the primary currents were 27.5, 17.5, 20, 15 and 20 mA, respectively. The analytical solution was mixed with a reductant solution (Fig. 2.1), at flow rates of 9 ml min^{-1} and

4.5 ml min^{-1}, respectively. The reductant solution was prepared by mixing 14 g of $NaBH_4$ and 8 g of NaOH with 2 l of distilled water. Hence, the gaseous hydrides were formed after the reaction between HCl and $NaBH_4$, and further atomised using a hydrogen flame fed by excess H_2 gas created during the reaction. The BHCD lamp focussed on the flame provided the excitation source for the fluorescence of the element analysed, which was then measured by an AFS detector. Atomic fluorescence signals were recorded and measured on the basis of the peak height of the signal.

2.3.4 - Calibration

Six calibration solutions with concentrations of 0.1, 0.25, 0.5, 1, 2.5 and 5 ng ml^{-1} were prepared for each element of interest. These solutions were prepared from 1000 µg ml^{-1} standard solutions of each element (PlasmaCAL, SPC Science). All the calibration solutions were mixed with the reagent blank prior to measurement, in the same proportion as sample aliquots (i.e. 10 ml of calibration solution and 30 ml of reagent blank). Calibration solutions were measured at the beginning and the end of each sequence of analysis to monitor fluctuations of the fluorescence signal. The calibration curves obtained were all linear.

2.3.5 - Detection limits of the method

As the detection limit (LoD) for each element we used three times the standard deviation (3σ) of corresponding measurements on the blank solutions (Long and Winefordner 1983; Potts 1987). These values were calculated using the results for thirty blank solutions prepared in the same manner as the samples (total procedure). The detection limits obtained were 0.01, 0.019, 0.016, 0.026 and 0.002 µg g^{-1} for Te, As, Bi,

Sb and Se, respectively (Table 2.1). We chose to use ten times the standard deviation (10σ) of the blank solutions to estimate limits of quantification for each element (LoQ; Potts 1987).

2.4 – Results and Discussion

2.4.1 – Precision and accuracy based on geological reference materials

The average HG-AFS measurements, the standard deviations (1σ) and the relative standard deviations (% RSD) obtained for ten geological reference materials (CH-4, TDB-1, OKUM, WPR-1, WMG-1, AN-G, BE-N, BIR-1, W-2 and WGB-1) and one in-house reference material (KPT-1) are presented in Table 2.1. The full dataset is available in the *ANNEXES* (*ANNEXE 1*). Three reference materials (CH-4, TDB-1 and KPT-1) were measured in every round to monitor the reproducibility of the method. Only reference materials CH-4 and TDB-1 have been previously analyzed using HG-AFS (Pitcairn *et al.* 2015; Patten *et al.* 2016), and the reported values for Te, Se, As and Sb are in the same range of our results (*ANNEXE 1*).

The Horwitz function (Horwitz *et al.* 1980) was used to evaluate the acceptable variability of the measurements, which will vary following the concentration in the material. For example, according to the Horwitz function a relative uncertainty of 32% is acceptable at a concentration of 0.01 μg g^{-1}, whereas the uncertainty should fall to 11.3% at a concentration of 10 μg g^{-1}. The HG-AFS measurement results have % RSD values below the acceptable limits as derived from the Horwitz function (%RSD (Hz); Table 2.1) for most samples. A characteristic of the Horwitz function is for greater variations in the %RSD to be obtained for lower concentrations of an element. Moreover, individual measurements of the same sample digest for reference materials

CH-4, TDB-1 and KPT-1 were carried out (Table 2.1), and were characterised by lower %RSD than those from different sample digests (Table 2.1). This suggests that the general variations in %RSD mostly reflect different concentrations of TABS in the reference materials.

The only two HG-AFS measurements with %RSD greater than the acceptable variability were the Bi and Sb determinations for reference material TDB-1 (Table 2.1). High uncertainties reported for Bi and Sb in the certificate of analysis for TDB-1 suggest that high % RSD may reflect sample heterogeneity. In order to evaluate the problem, different sample masses were used in digestion of materials CH-4, TDB-1 and KPT-1 (i.e. 0.1, 0.2 and 0.4g). The HG-AFS results are recorded in Table 2.2. The %RSD are similar to slightly lower for sample digests of 0.4 g. However, for Bi and Sb determinations in TDB-1 the %RSD are significantly lower for sample digests of 0.4 g (Table 2.2). This supports the belief that %RSD values greater than the acceptable variability are likely reflect minor heterogeneities of some elements. Therefore, for most reference materials 0.2 g is suitable, whereas measurements with high %RSD may be improved by preparing a sample of a greater sample mass.

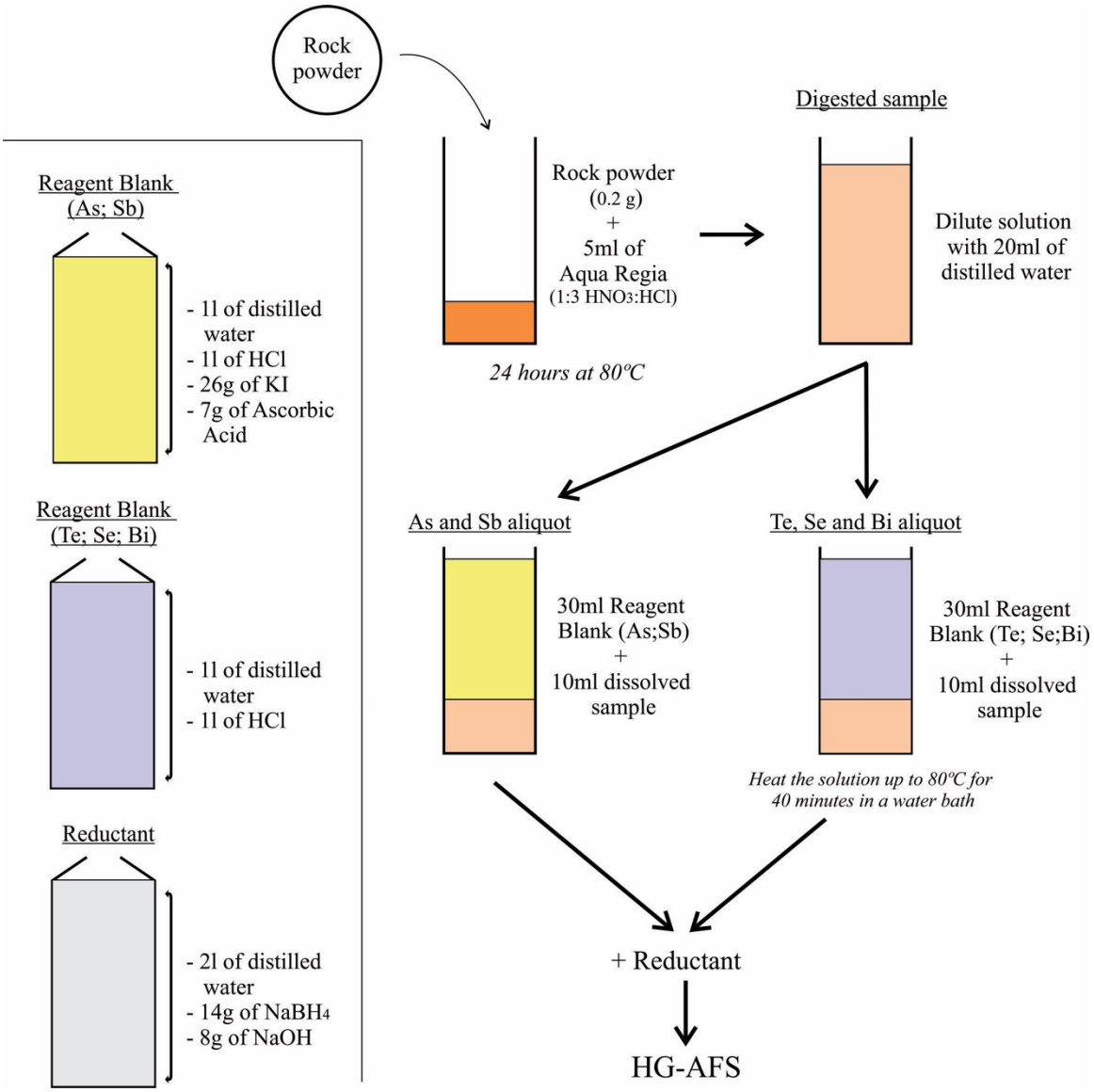

Figure 2.1 - Schematic flow diagram showing the main preparation steps for reagents and aliquots. See text for further explanation. HG-AFS – hydride generation-atomic fluorescence spectrometry.

Table 2.1 - Te, As, Bi, Sb and Se results for geological reference materials by HG-AFS.

Sample ID	n*	Rock type		Te	As	Bi	Sb	Se
LoD		Blank	3σ (μg g^{-1})	0.010	0.019	0.016	0.026	0.002
LoQ		Blank	10σ (μg g^{-1})	0.032	0.064	0.055	0.088	0.0081
CH-4	7	Anorthosite	Ave (μg g^{-1})	0.414	8.534	0.676	0.844	1.942
			SD (1σ)	0.073	0.355	0.094	0.062	0.044
			% RSD	17.712	4.163	13.900	7.334	2.272
			% RSD (Hz)	18.266	11.585	16.968	16.409	14.476
TDB-1	7	Diabase	Ave (μg g^{-1})	0.043	2.127	0.064	1.034	0.344
			SD (1σ)	0.006	0.207	0.024	0.176	0.029
			% RSD	12.961	9.717	37.609	16.984	8.494
			% RSD (Hz)	25.656	14.279	24.186	15.916	18.785
KPT-1	7	Quartz diorite	Ave (μg g^{-1})	0.498	2.151	0.907	11.077	2.959
			SD (1σ)	0.060	0.280	0.085	0.247	0.113
			% RSD	11.959	13.041	9.361	2.232	3.832
			% RSD (Hz)	17.768	14.255	16.234	11.139	13.587
OKUM	3	Komatiite	Ave (μg g^{-1})	0.053	0.241	0.072	0.111	0.101
			SD (1σ)	0.006	0.039	0.011	0.014	0.011
			% RSD	10.340	16.128	15.799	12.234	10.950
			% RSD (Hz)	24.862	19.819	23.785	22.271	22.588
WPR-1	3	Peridotite	Ave (μg g^{-1})	0.474	1.070	0.194	0.876	3.859
			SD (1σ)	0.027	0.130	0.015	0.108	0.083
			% RSD	5.606	12.111	7.568	12.326	2.143
			% RSD (Hz)	17.900	15.834	20.471	16.319	13.055
WMG-1	3	Gabbro	Ave (μg g^{-1})	1.419	7.087	0.489	1.920	13.635
			SD (1σ)	0.081	0.207	0.050	0.081	0.536
			% RSD	5.716	2.915	10.277	4.216	3.930
			% RSD (Hz)	15.176	11.913	17.817	14.501	10.796
AN-G	3	Anorthosite	Ave (μg g^{-1})	<0.01	0.024	0.070	0.117	0.028
			SD (1σ)	n.a.	0.003	0.014	0.007	0.005
			% RSD	n.a.	12.633	20.204	6.278	17.726
			% RSD (Hz)	n.a.	28.069	23.893	22.096	27.430
BEN	3	Basalt	Ave (μg g^{-1})	<0.01	1.808	<0.016	0.294	0.070
			SD (1σ)	n.a.	0.045	n.a.	0.006	0.006
			% RSD	n.a.	2.473	n.a.	1.894	8.975
			% RSD (Hz)	n.a.	14.633	n.a.	19.238	23.895
BIR-1	3	Basalt	Ave (μg g^{-1})	<0.01	0.054	0.017	0.543	0.016
			SD (1σ)	n.a.	0.005	0.002	0.024	0.002
			% RSD	n.a.	8.968	14.280	4.428	14.863
			% RSD (Hz)	n.a.	24.801	29.449	17.539	29.689
W-2	3	Diabase	Ave (μg g^{-1})	0.011	0.767	0.073	0.786	0.087
			SD (1σ)	0.001	0.048	0.016	0.037	0.004
			% RSD	4.660	6.259	21.623	4.659	4.981
			% RSD (Hz)	31.379	16.650	23.731	16.588	23.121
WGB-1	3	Gabbro	Ave (μg g^{-1})	0.013	1.595	0.052	1.810	0.092
			SD (1σ)	0.002	0.047	0.009	0.040	0.008
			% RSD	18.085	2.946	17.925	2.184	8.549
			% RSD (Hz)	30.674	14.911	24.934	14.630	22.903

LoD = limit of dection; LoQ = limit of quantification; Ave= Average value; % RSD (Hz)= Target % RSD calculated using the Horwitz function; n.a= non applicable; * Number of individual determinations

Table 2.2 - Te, As, Bi, Sb and Se results for geological reference materials by HG-AFS using different samples weights.

			CH-4				TDB-1				KPT-1			
			Anorthosite				Diabase				Quartz diorite			
	Sample weight (grams)	N	Ave (µg g^{-1})	SD (1σ)	% RSD	% RSD (Hz)	Ave (µg g^{-1})	SD (1σ)	% RSD	% RSD (Hz)	Ave (µg g^{-1})	SD (1σ)	% RSD	% RSD (Hz)
Te	0.1 (n=4)	4	0.369	0.094	25.4	18.6	0.047	0.006	13.6	25.3	0.533	0.070	13.2	17.6
	0.2 (n=7)	7	0.414	0.073	17.7	18.3	0.043	0.006	13.0	25.7	0.498	0.060	12.0	17.8
	0.4 (n=4)	4	0.43	0.04	8.1	18.2	0.030	0.004	14.6	27.1	0.49	0.04	8.2	17.8
	0.2 (n=3)	1	0.469	0.035	7.4	17.9	0.047	0.004	8.5	25.4	0.533	0.048	9.1	17.6
As	0.1 (n=4)	4	8.773	0.245	2.8	11.5	2.210	0.270	12.2	14.2	1.878	0.131	7.0	14.5
	0.2 (n=7)	7	8.534	0.355	4.2	11.6	2.127	0.207	9.7	14.3	2.151	0.280	13.0	14.3
	0.4 (n=4)	4	8.400	0.219	2.6	11.6	2.041	0.213	10.4	14.4	2.246	0.111	4.9	14.2
	0.2 (n=3)	1	8.455	0.320	3.8	11.6	2.210	0.196	8.9	14.2	1.878	0.100	5.3	14.5
Bi	0.1 (n=4)	4	0.610	0.092	15.1	17.2	0.062	0.030	48.9	24.3	0.847	0.068	8.1	16.4
	0.2 (n=7)	7	0.676	0.094	13.9	17.0	0.064	0.024	37.6	24.2	0.907	0.085	9.4	16.2
	0.4 (n=4)	4	0.800	0.074	9.2	16.5	0.084	0.005	6.0	23.2	0.943	0.075	7.9	16.1
	0.2 (n=3)	1	0.748	0.063	8.4	16.7	0.046	0.002	5.1	25.4	0.847	0.048	5.6	16.4

Table 2.2 – *Continuation*

Sb	0.1 (n=4)	4	0.876	0.068	7.8	16.3	0.857	0.136	15.8	16.4	11.113	0.240	2.2	11.1
	0.2 (n=7)	7	0.844	0.062	7.3	16.4	1.034	0.176	17.0	15.9	11.077	0.247	2.2	11.1
	0.4 (n=4)	4	0.877	0.082	9.4	16.3	0.931	0.064	6.9	16.2	11.031	0.153	1.4	11.1
	0.2 (n=3)	1	0.790	0.019	2.4	16.6	0.857	0.018	2.1	16.4	11.113	0.173	1.6	11.1
Se	0.1 (n=4)	4	1.944	0.057	3.0	14.5	0.343	0.026	7.5	18.8	3.029	0.134	4.4	13.5
	0.2 (n=7)	7	1.942	0.044	2.3	14.5	0.344	0.029	8.5	18.8	2.959	0.113	3.8	13.6
	0.4 (n=4)	4	1.928	0.039	2.0	14.5	0.394	0.071	13.1	18.4	2.934	0.054	1.8	13.6
	0.2 (n=3)	1	1.936	0.044	2.3	14.5	0.343	0.020	5.8	18.8	3.029	0.102	3.4	13.5

Abbreviations: Ave= Average value; % RSD (Hz)= Target % RSD calculated using the Horwitz function; n = number of individual determinations; N= number of sample digests.

The accuracy of the method was evaluated by comparing measured quantities for reference materials with literature values. The literature values of TABS for all the reference materials were compiled from the GeoReM database (Jochum et al. 2005). Comparisons are shown in Fig. 2.2., where measures values mostly fall within the range of literature values.

All determinations of Sb and Se are above their respective limits of quantification, i.e. 0.088 μg g^{-1} and 0.008 μg g^{-1} (Table 2.1), and are within uncertainties with literature values for all the reference materials (Fig. 2.2a and 2.2b). For five reference materials (TDB-1, OKUM, AN-G, BIR and BEN), Se measurements by the isotopic dilution method are available (König *et al.* 2012, 2014; Wang and Becker 2013). Our results are within uncertainties of the results for TDB-1, BIR and BEN, but are slightly lower compared to OKUM and AN-G. However, results obtained by other methods for these materials are within uncertainties of our results. Thus, the method is validated for Sb and Se down to 0.09 μg g^{-1} and 0.008 μg g^{-1}, respectively (the limits of quantification).

Arsenic and Bi concentrations in most of the reference materials are above the limits of quantification (0.064 and 0.055 μg g^{-1} respectively). Measured quantities of As are within the range of literature values except for the two samples (AN-G and BIR-1), which are below the limit of quantification, but above the limit of detection (Fig. 2.2c). For these samples, the results are lower than literature values but still within range of literature results when the uncertainties of the literature values are considered. Therefore, we consider the method validated for As down to the limit of quantification. For Bi there is a more limited range of reference materials available and the results are variable. The results are in the same range as the literature values down to 0.2 μg g^{-1} (Fig. 2.2d), and we consider the method validated down to this level. There are a number of reference materials with concentrations close to the limit of quantification, for three of these the

obtained values are higher than the literature values and for two they are lower than literature values. The source of the differences is not clear, but a weakness of the literature values is that all were determined by the same method (ICP-MS).

For Te, literature values are very sparse and variable making comparison problematic. For the six reference materials above the limits of quantification of 0.032 μg g^{-1} the values fall within the range of literature values except for OKUM, where the value is slightly higher (Fig. 2.2e). For the reference materials TDB-1, OKUM, AN-G, BIR and BEN, Te measurements by the isotopic dilution method are also available (König *et al.* 2012, 2014; Wang and Becker 2013). Obtained results are below the quantification limits for materials AN-G, BIR and BEN, which is in accord with isotopic dilution results lower than 0.004 μg g^{-1} for these materials. For TDB-1 and OKUM our Te measurements (0.043 μg g^{-1} and 0.053 μg g^{-1}, respectively) are higher than those obtained by isotopic dilution (0.006 μg g^{-1} and 0.025 μg g^{-1}, respectively). However, our results are within uncertainties of literature values of TDB-1, including results by HG-AFS by Patten *et al.* (2016), obtained at a different laboratory. For the reference material OKUM, only a Te measurement by isotopic dilution data is available, not allowing a comparison with results from various studies, ideally using different analytical methods. The discrepancies of Te results for these two reference materials suggest that either the HG-AFS measurements (Patten *et al.* 2016 and this study) are slightly overestimated, or isotopic dilution results are slightly underestimated (Wang and Becker 2013; König *et al.* 2012, 2014).

In summary, the HG-AFS method is considered sufficiently accurate for measuring concentrations of Te, As, Bi, Sb and Se above their respective limits of quantification (Table 2.1). The % RSD values are below the acceptable limits calculated

from the Horwitz function in almost all of the reference materials, which demonstrates that the method is sufficiently precise to satisfy the analytical requirements.

2.4.2 – IAG Geo*PT* Proficiency Test Samples

The International Association of Geoanalysts (IAG) conducts a proficiency testing program, named Geo*PT*, designed to enable geoanalytical laboratories to routinely assess their analytical performance. In each round of Geo*PT*, participating laboratories analyze powders of the same test material (Geo*PT* samples), and report quantity values of major and trace element constituents to the Geo*PT* organisers. A detailed account of the proficiency testing programme and how proficiency testing values are obtained may be found in the Geo*PT* protocol (IAG 2018). To increase the dataset of measurement results for TABS in geological materials, 34 test samples from previous Geo*PT* rounds were analyzed by HG-AFS (Table 2.3), and the results compared with values derived from the proficiency tests (Table 2.4).

The Horwitz function was calculated for the HG-AFS measurement results on each sample, and 85% of the results had %RSD values lower than those acceptable limits (Table 2.3), validating the precision of the method. For most results with % RSD values higher than the tolerance provided by the Horwitz function, the measurements are close to the LoD of the method, which may explain the discrepancy.

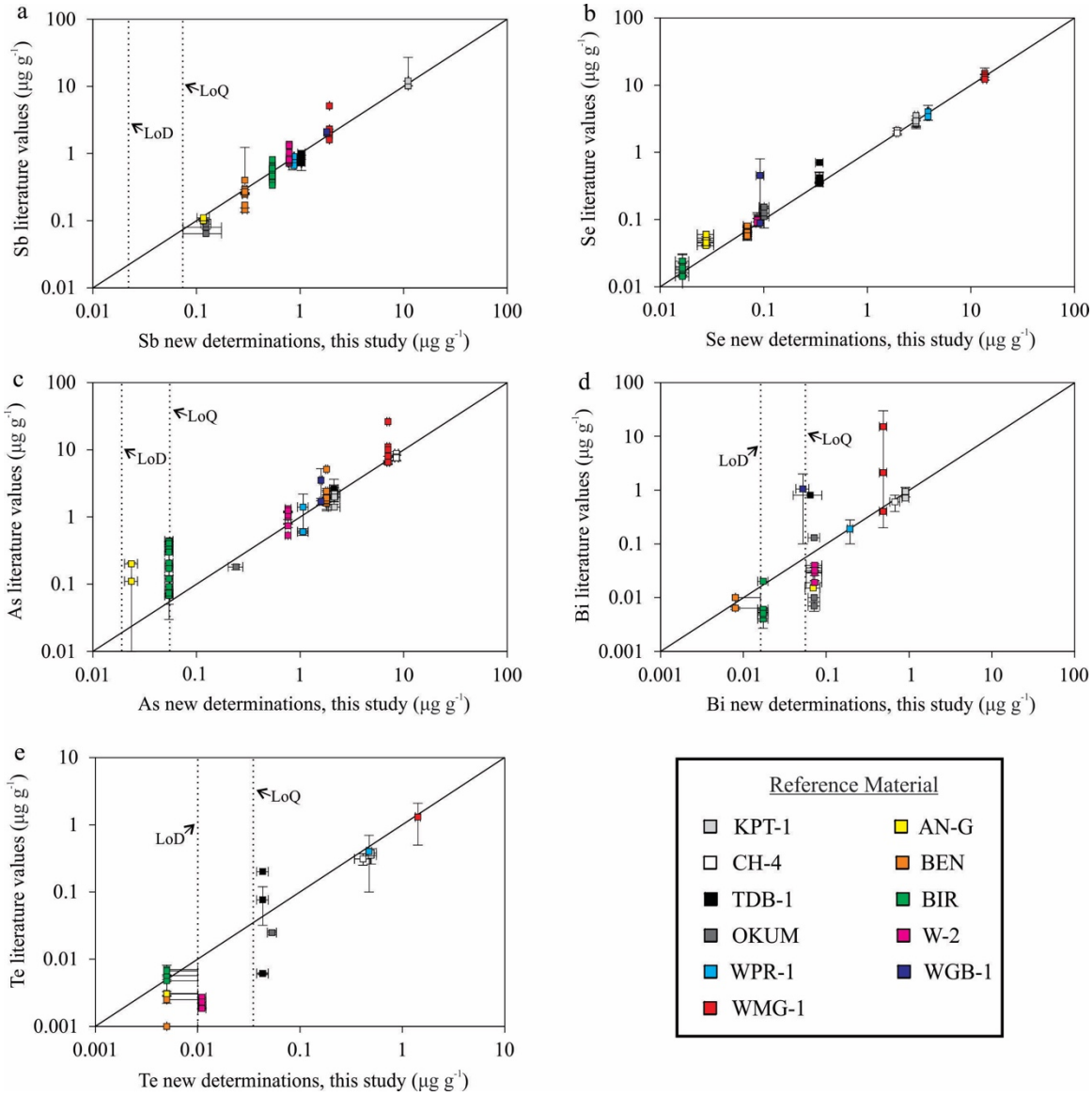

Figure 2.2 - Comparison of new HG-AFS determinations and literature values for (a) Sb, (b) Se, (c) As, (d) Bi and (e) Te. Uncertainties are shown by error bars at the 1r level. For materials with a compositional range, instead of a result, the range is plotted using an error bar. Dashed lines indicate the limit of detection (LoD) and limit of quantification (LoQ) for HG-AFS.

Table 2.3 - Te, As, Bi, Sb and Se results for GeoPT proficiency test samples by HG-AFS.

Sample ID	n*	Rock type		Te	As	Bi	Sb	Se
LoD		blank	3σ (μg g^{-1})	0.010	0.019	0.016	0.026	0.002
LoQ		blank	10σ (μg g^{-1})	0.032	0.064	0.055	0.088	0.0081
Geo*PT*-06 (OU-3)	4	Nanhoron microgranite	Ave (μg g^{-1})	0.020	0.917	0.227	0.221	0.028
			SD (1σ)	0.007	0.052	0.085	0.018	0.011
			% RSD	31.9	5.6	37.7	8.1	39.6
			% RSD (Hz)	28.7	16.2	20.0	20.1	27.4
Geo*PT*-08 (OU-4)	4	Penmaenmawr microdiorite	Ave (μg g^{-1})	0.019	1.317	0.090	0.289	0.019
			SD (1σ)	0.010	0.071	0.017	0.038	0.004
			% RSD	53.7	5.4	18.7	13.2	20.3
			% RSD (Hz)	29.1	15.3	23.0	19.3	29.1
Geo*PT*-10 (CH-1)	4	Marine sediment	Ave (μg g^{-1})	0.080	3.648	0.309	0.960	0.543
			SD (1σ)	0.009	0.184	0.033	0.022	0.019
			% RSD	11.3	5.1	10.6	2.3	3.6
			% RSD (Hz)	23.4	13.2	19.1	16.1	17.5
Geo*PT*-11 (OU-5)	4	Leiton dolerite	Ave (μg g^{-1})	0.028	2.413	0.073	0.470	0.021
			SD (1σ)	0.017	0.046	0.023	0.031	0.001
			% RSD	58.8	1.9	31.1	6.6	6.3
			% RSD (Hz)	27.4	14.0	23.7	17.9	28.7
Geo*PT*-12 (GAS)	4	Serpentine	Ave (μg g^{-1})	0.027	115.628	0.141	12.304	0.029
			SD (1σ)	0.008	3.514	0.046	0.340	0.003
			% RSD	30.9	3.0	32.8	2.8	11.4
			% RSD (Hz)	27.6	7.8	21.5	11.0	27.2
Geo*PT*-13 (UoK Loess)	4	Köln loess	Ave (μg g^{-1})	0.016	6.470	0.159	0.350	0.029
			SD (1σ)	0.008	0.230	0.020	0.056	0.001
			% RSD	51.9	3.6	12.7	16.0	3.7
			% RSD (Hz)	29.7	12.1	21.1	18.7	27.3
Geo*PT*-15 (MSAN)	4	Ocean Floor sediment	Ave (μg g^{-1})	0.078	7.161	0.112	0.457	0.533
			SD (1σ)	0.006	0.301	0.041	0.066	0.049
			% RSD	7.3	4.2	36.6	14.5	9.1
			% RSD (Hz)	23.5	11.9	22.2	18.0	17.6
Geo*PT*-16 (BNV-1)	4	Nevada basalt	Ave (μg g^{-1})	0.023	2.358	0.063	0.164	0.025
			SD (1σ)	0.013	0.112	0.002	0.019	0.004
			% RSD	58.9	4.7	3.0	11.5	15.5
			% RSD (Hz)	28.3	14.1	24.3	21.0	27.9
Geo*PT*-17 (OU-8)	4	Calcareous sandstone	Ave (μg g^{-1})	<0.01	0.963	0.058	0.165	0.007
			SD (1σ)	n.a.	0.076	0.016	0.022	0.002
			% RSD	n.a.	7.9	27.7	13.2	28.4
			% RSD (Hz)	n.a.	16.1	24.5	21.0	34.0
Geo*PT*-18 (KPT-1)	4	Quartz diorite	Ave (μg g^{-1})	0.500	2.199	0.854	10.720	2.988
			SD (1σ)	0.021	0.158	0.078	0.353	0.085
			% RSD	4.1	7.2	9.1	3.3	2.9
			% RSD (Hz)	17.8	14.2	16.4	11.2	13.6
Geo*PT*-19 (MGR-N)	4	Gabbro	Ave (μg g^{-1})	0.082	1.764	0.162	0.151	0.500
			SD (1σ)	0.009	0.070	0.013	0.008	0.055
			% RSD	11.4	4.0	7.9	5.1	11.0
			% RSD (Hz)	23.3	14.7	21.0	21.3	17.8
Geo*PT*-20 (OPY-1)	4	Ultramafic rock	Ave (μg g^{-1})	0.037	0.324	<0.016	0.188	0.105
			SD (1σ)	0.005	0.047	n.a.	0.028	0.009
			% RSD	13.1	14.4	n.a.	14.8	8.3
			% RSD (Hz)	26.3	19.0	n.a.	20.6	22.4

Table 2.3 - *Continuation*

Geo*PT*-21 (MGT-1)	4	Granite	Ave (µg g^{-1})	0.043	2.080	1.102	0.244	0.009
			SD (1σ)	0.020	0.115	0.041	0.033	0.005
			% RSD	46.0	5.5	3.7	13.6	54.5
			% RSD (Hz)	25.7	14.3	15.8	19.8	32.6
Geo*PT*-22 (MBL-1)	4	Basalt	Ave (µg g^{-1})	0.208	1.624	0.092	0.224	0.028
			SD (1σ)	0.036	0.089	0.010	0.022	0.008
			% RSD	17.3	5.5	10.3	9.9	30.3
			% RSD (Hz)	20.3	14.9	22.9	20.0	27.4
Geo*PT*-23 (OU-9)	4	Separation Lake pegmatite	Ave (µg g^{-1})	0.211	2.670	0.064	6.443	0.006
			SD (1σ)	0.017	0.073	0.028	0.437	0.000
			% RSD	8.1	2.7	43.8	6.8	6.7
			% RSD (Hz)	20.2	13.8	24.2	12.1	34.5
Geo*PT*-24 (OU-10)	4	Longmyndian greywacke	Ave (µg g^{-1})	0.186	1.769	0.143	0.242	0.010
			SD (1σ)	0.036	0.015	0.016	0.027	0.002
			% RSD	19.1	0.9	11.0	11.2	20.3
			% RSD (Hz)	20.6	14.7	21.4	19.8	32.0
Geo*PT*-25 (HTB-1)	4	Basalt	Ave (µg g^{-1})	0.226	0.203	0.054	0.233	0.173
			SD (1σ)	0.040	0.014	0.027	0.021	0.031
			% RSD	17.9	6.8	50.2	9.2	18.1
			% RSD (Hz)	20.0	20.3	24.8	19.9	20.8
Geo*PT*-27 (MGL-AND)	4	Andesite	Ave (µg g^{-1})	0.198	2.004	0.074	0.230	0.003
			SD (1σ)	0.025	0.084	0.018	0.012	0.001
			% RSD	12.8	4.2	24.2	5.0	17.1
			% RSD (Hz)	20.4	14.4	23.7	20.0	38.0
Geo*PT*-29 (NKT-1)	4	Nephelinite	Ave (µg g^{-1})	<0.01	1.836	0.052	0.358	0.035
			SD (1σ)	n.a.	0.064	0.016	0.019	0.002
			% RSD	n.a.	3.5	31.1	5.4	5.0
			% RSD (Hz)	n.a.	14.6	24.9	18.7	26.6
Geo*PT*-30 (CG-2)	4	Syenite	Ave (µg g^{-1})	<0.01	4.244	0.169	0.819	0.011
			SD (1σ)	n.a.	0.138	0.021	0.046	0.001
			% RSD	n.a.	3.2	12.5	5.7	9.9
			% RSD (Hz)	n.a.	12.9	20.9	16.5	31.4
Geo*PT*-31 (SdAR-1)	4	Modified River Sediment	Ave (µg g^{-1})	0.399	35.139	1.775	5.923	0.300
			SD (1σ)	0.031	0.538	0.066	0.384	0.020
			% RSD	7.9	1.5	3.7	6.5	6.6
			% RSD (Hz)	18.4	9.4	14.7	12.2	19.2
Geo*PT*-32 (WG-1)	4	Woodstock basalt	Ave (µg g^{-1})	0.016	0.575	0.052	0.071	0.021
			SD (1σ)	0.009	0.065	0.018	0.014	0.001
			% RSD	60.2	11.3	35.2	19.6	4.4
			% RSD (Hz)	29.9	17.4	24.9	23.8	28.6
Geo*PT*-33 (DBC-1)	4	Ball Clay	Ave (µg g^{-1})	0.259	3.285	1.683	1.587	2.442
			SD (1σ)	0.037	0.093	0.150	0.054	0.091
			% RSD	14.3	2.8	8.9	3.4	3.7
			% RSD (Hz)	19.6	13.4	14.8	14.9	14.0
Geo*PT*-34 (GRI-1)	4	Granite	Ave (µg g^{-1})	<0.01	1.044	0.057	0.204	0.049
			SD (1σ)	n.a.	0.088	0.010	0.015	0.003
			% RSD	n.a.	8.5	17.1	7.4	6.7
			% RSD (Hz)	n.a.	15.9	24.6	20.3	25.2

Table 2.3 - *Continuation*

Geo*PT*-35 (TLM-1)	4	Tonalite	Ave (µg g^{-1})	<0.01	2.295	0.092	1.556	0.010
			SD (1σ)	n.a.	0.100	0.025	0.062	0.001
			% RSD	n.a.	4.4	27.4	4.0	5.7
			% RSD (Hz)	n.a.	14.1	22.9	15.0	31.9
Geo*PT*-36 (GSM-1)	4	Gabbro	Ave (µg g^{-1})	0.032	2.470	0.116	1.934	0.213
			SD (1σ)	0.007	0.214	0.015	0.038	0.015
			% RSD	23.3	8.6	12.9	2.0	6.9
			% RSD (Hz)	26.8	14.0	22.1	14.5	20.2
Geo*PT*-36A (SdAR-M2)	4	Metal-rich sediment	Ave (µg g^{-1})	1.096	72.972	1.051	111.793	3.321
			SD (1σ)	0.084	2.455	0.108	2.520	0.268
			% RSD	7.7	3.4	10.3	2.3	8.1
			% RSD (Hz)	15.8	8.4	15.9	7.9	13.4
Geo*PT*-37 (ORPT-1)	4	Rhyolite	Ave (µg g^{-1})	<0.01	0.423	0.063	0.253	0.005
			SD (1σ)	n.a.	0.025	0.021	0.042	0.003
			% RSD	n.a.	5.9	33.1	16.7	53.8
			% RSD (Hz)	n.a.	18.2	24.2	19.7	35.3
Geo*PT*-38 (OU-7)	4	Ardnamurchan gabbro	Ave (µg g^{-1})	<0.01	0.152	0.032	0.059	0.082
			SD (1σ)	n.a.	0.008	0.008	0.014	0.003
			% RSD	n.a.	5.3	24.8	24.5	3.2
			% RSD (Hz)	n.a.	21.2	26.8	24.5	23.3
Geo*PT*-38A (HARZ01)	4	Modified harzgurgite	Ave (µg g^{-1})	0.014	0.282	0.077	1.175	0.031
			SD (1σ)	0.004	0.029	0.018	0.050	0.005
			% RSD	26.4	10.4	23.1	4.3	14.9
			% RSD (Hz)	30.5	19.4	23.5	15.6	26.9
Geo*PT*-39 (SyMP-1)	4	Syenite	Ave (µg g^{-1})	0.138	3.666	0.800	0.231	0.182
			SD (1σ)	0.011	0.117	0.028	0.012	0.004
			% RSD	7.6	3.2	3.5	5.2	2.1
			% RSD (Hz)	21.6	13.2	16.5	19.9	20.7
Geo*PT*-39A (MNS-1)	4	Nepheline syenite	Ave (µg g^{-1})	0.020	22.144	1.062	3.176	0.035
			SD (1σ)	0.004	0.971	0.081	0.196	0.003
			% RSD	18.6	4.4	7.6	6.2	9.9
			% RSD (Hz)	28.8	10.0	15.9	13.4	26.5
Geo*PT*-40 (ShWYO-1)	4	Silty marine shale	Ave (µg g^{-1})	0.071	10.275	0.334	0.907	0.565
			SD (1σ)	0.010	0.722	0.008	0.056	0.022
			% RSD	14.3	7.0	2.3	6.2	3.9
			% RSD (Hz)	23.8	11.3	18.9	16.2	17.4
Geo*PT*-41 (ORA-1)	4	Andesite	Ave (µg g^{-1})	<0.01	0.258	0.050	0.975	0.004
			SD (1σ)	n.a.	0.020	0.011	0.050	0.001
			% RSD	n.a.	7.8	21.8	5.1	34.9
			% RSD (Hz)	n.a.	19.6	25.1	16.1	37.3

LoD = limit of dection; LoQ = limit of quantification; Ave= Average value; % RSD (Hz)= Target % RSD calculated using the Horwitz function; n.a= non applicable; * Number of individual determinations

Whenever possible, assigned and provisional values from Geo*PT* reports were taken for comparison with measured values of each element (Table 2.4). For the materials for which neither assigned nor provisional values were available from Geo*PT* reports, median values of all concentration values reported by participants were used as a reference (Table 2.4). Figure 2.3 shows the comparison of our measurement results with Geo*PT* assigned, provisional and median values. Our results are also compared with all individual concentrations reported by the participating laboratories, for each element in Fig. 2.4.

2.4.2.1 - Antimony and Bismuth

Our Sb and Bi measurement results are in close agreement with assigned and provisional values for most of the test materials (Fig. 2.3a and 2.3b; Tables 2.3 and 2.4). Exceptions are Geo*PT* samples 13, 29 and 33 for Sb, and Geo*PT* sample 36 for Bi. Although these four results do not agree with the assigned or provisional values, they fall well within the range of reported values (Fig. 2.4a and 2.4b). For those samples which have neither assigned nor provisional values, and which are above the respective limits of quantification, the Sb and Bi HG-AFS results are similar to the median values of the Geo*PT* contributed data (Fig. 2.3a and 2.3b; Tables 2.3 and 2.4). Therefore, for most samples without assigned or provisional values, and for which HG-AFS results are above our quantification limits, we suggest that the median values for Bi and Sb could be used as informational values. Exceptions to this are for Bi in Geo*PT* samples 12, 16, 19, 23 and 29, and Sb for Geo*PT* sample 25, where our results fall within the range of reported results (Fig. 2.4a and 2.4b), but differ from the median value. All of these samples contain less than 0.2 μg g^{-1} Bi according to the HG-AFS determination. Below 0.3 μg g^{-1}

Bi, the range of values reported in some cases by Geo*PT* participants increases from one order of magnitude to over three, and in some cases too few data were reported, thus the median Geo*PT* values may not always be adequate, especially at low levels. Therefore, there appears to be considerable room for improvement in determination of Bi at low levels by the geoanalytical community.

2.4.2.2 – Arsenic

Arsenic results are in good agreement with most of the assigned and provisional values (Fig. 2.3c; Tables 2.3 and 2.4). The exceptions are results on Geo*PT* test samples 06 and 33. Our results are lower than assigned and provisional values for these two samples, and at the lower end of reported values (Fig. 2.4c). The reasons for these discrepancies are not clear.

For samples with no assigned or provisional values, the medians of the Geo*PT* rounds are in agreement with our results for concentrations above 1 μg g^{-1} (Fig. 2.3c, and Table 2.4). However, for samples with As concentrations below 1 μg g^{-1}, our results are lower than Geo*PT* median values (Fig. 2.3c), although still within the range of reported values (Fig. 2.4c). However, as discussed above we consider our method valid down to the limit of quantification (0.064 μg g^{-1}), and all of these samples appear to contain more than 0.1 μg g^{-1} As. Therefore, we suggest that the Geo*PT* median values for samples with As concentrations below 1 μg g^{-1} overestimate the As concentrations. As in the case of Bi, the ranges of the results reported from the Geo*PT* tests are much wider for samples with less than 1 μg g^{-1} As (2 to 3 orders of magnitude), than for samples above 1 μg g^{-1} (generally 1 order of magnitude, Fig. 2.4c). We suggest that median values for samples with As concentrations greater than 1 μg g^{-1} could be used as informational values.

Table 2.4 - Assigned, provisional and median values for GeoPT proficiency test samples.

Sample ID	**Assigned**, *provisional* and median values (μg g^{-1})					Reference
	Te	As	Bi	Sb	Se	
Geo*PT*-06	0.17	**3.379**	0.2	**0.305**	8	Potts *et al.* 2000
Geo*PT*-08	0.32	1.85	0.098	**0.302**	4	Potts *et al.* 2000b
Geo*PT*-10	n.r.	4.465	**0.31**	**1.05**	0.9	Potts *et al.* 2001
Geo*PT*-11	0.30	*2.45*	0.067	**0.42**	1.5	Potts *et al.* 2002
Geo*PT*-12	n.r.	**121.1**	0.07	**12.29**	1.8	Potts *et al.* 2003
Geo*PT*-13	n.r.	**6.746**	0.13	**0.58**	1.1	Potts *et al.* 2003b
Geo*PT*-15	0.22	**7.32**	0.11	*0.49*	1.05	Potts *et al.* 2004
Geo*PT*-16	13.5	*2.328*	0.4	*0.13*	2	Potts *et al.* 2005
Geo*PT*-17	0.04	1.214	*0.043*	*0.215*	0.414	Potts *et al.* 2005b
Geo*PT*-18	0.35	2.21	**0.945**	**10.005**	**2.93**	Webb *et al.* 2006
Geo*PT*-19	0.072	*1.75*	0.068	*0.124*	1	Webb *et al.* 2006b
Geo*PT*-20	0.03	0.8	0.1	0.145	0.31	Webb *et al.* 2007
Geo*PT*-21	0.036	*2.315*	**1.06**	0.2	n.r.	Webb *et al.* 2007b
Geo*PT*-22	0.502	1.8	0.069	*0.29*	0.07	Webb *et al.* 2008
Geo*PT*-23	0.24	2.82	0.19	**7.669**	0.25	Webb *et al.* 2008b
Geo*PT*-24	0.05	2.02	0.1	0.287	0.238	Webb *et al.* 2009
Geo*PT*-25	0.09	1.915	0.053	0.1	0.329	Webb *et al.* 2009b
Geo*PT*-27	1	*2.346*	**0.106**	*0.237*	0.31	Webb *et al.* 2010
Geo*PT*-29	0.03	2.2	0.023	*0.12*	0.2	Webb *et al.* 2011
Geo*PT*-30	0.041	5.85	*0.17*	**1.054**	1.5	Webb *et al.* 2012
Geo*PT*-31	0.825	*36.43*	*1.77*	**6.667**	1.48	Webb *et al.* 2012b
Geo*PT*-32	0.1	1.486	0.07	0.12	0.556	Webb *et al.* 2013
Geo*PT*-33	0.101	*9*	*2.04*	*2.809*	*3.006*	Webb *et al.* 2013b
Geo*PT*-34	0.07	0.99	*0.057*	0.205	0.158	Webb *et al.* 2014
Geo*PT*-35	0.023	3.255	*0.083*	*1.49*	1	Webb *et al.* 2014b
Geo*PT*-36	0.836	2.86	*0.079*	*1.83*	0.41	Webb *et al.* 2015
Geo*PT*-36A	2.12	*75.82*	**1.05**	*106.6*	2.5	Webb *et al.* 2015b
Geo*PT*-37	0.19	1	**0.09**	0.27	1.8	Webb *et al.* 2015c
Geo*PT*-38	0.424	0.7	0.013	0.079	0.153	Webb *et al.* 2016
Geo*PT*-38A	0.03	0.39	0.1	*1.473*	0.05	Webb *et al.* 2016b
Geo*PT*-39	0.439	7.1	**0.79**	*0.194*	0.8	Webb *et al.* 2016c
Geo*PT*-39A	0.4	**22.94**	**1.086**	**2.8**	1.02	Webb *et al.* 2016d
Geo*PT*-40	0.085	**11.75**	*0.3*	**0.9**	0.784	Webb *et al.* 2017
Geo*PT*-41	0.048	1.35	0.04	0.858	0.801	Webb *et al.* 2017b

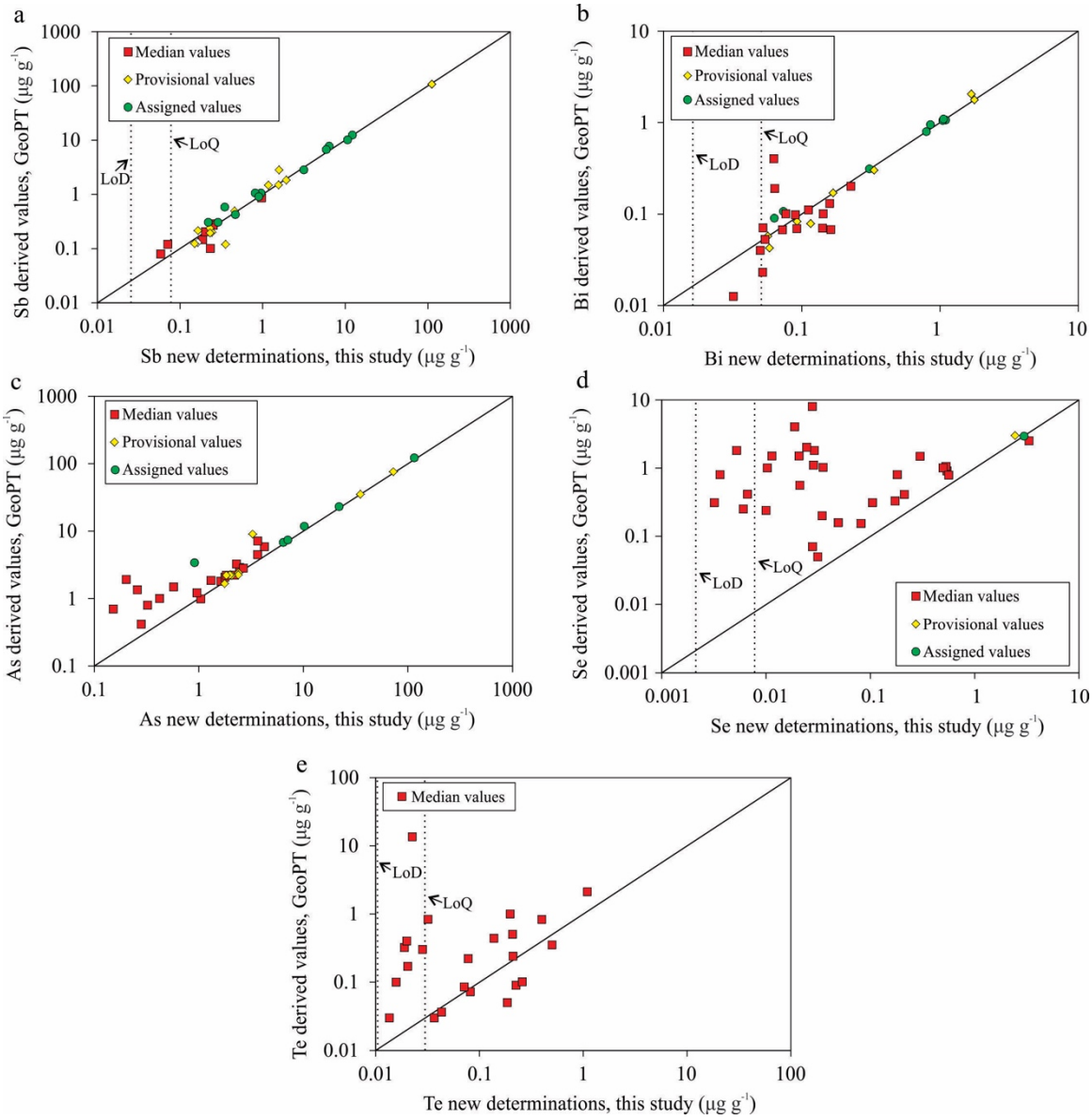

Figure 2.3 - Comparison of new HG-AFS determinations with assigned and provisional values from GeoPT reports and median values (this work, from Table 2.4) of GeoPT proficiency test materials for (a) Sb, (b) Bi, (c) As, (d) Se and (e) Te. Values with mass fractions below the detection limits (Table 2.3) are not plotted. Dashed lines indicate the limit of detection (LoD) and limit of quantification (LoQ) for HG-AFS.

2.4.2.3 - Selenium

Among the Geo*PT* samples only KPT-1 (Geo*PT*-18) and DBC-1 (Geo*PT*-33) have assigned and provisional values for Se, respectively (Table 2.4). The HG-AFS results for these samples are in excellent agreement with these assigned and provisional

values (Fig. 2.3d). In addition, the median values for samples 36A and 40 are close to our determinations (Tables 2.3 and 2.4). For the other samples, the values determined for Se by HG-AFS are lower than the Geo*PT* median values (Fig. 2.4d; Tables 2.3 and 2.4), and below 0.1 μg g^{-1} most of our results are less than Geo*PT* results by one to two orders of magnitude. All of the samples contain Se concentrations above the HG-AFS detection limit, and all but four are above the quantification limit (i.e. 0.008 μg g^{-1}). As discussed above, the method was demonstrated to be sufficiently accurate at these concentrations as evidenced by measurement of geological reference materials (Fig. 2.2b). Therefore, we must conclude that the majority of Se values reported in the Geo*PT* test (especially those below 0.1 μg g^{-1}) are significant overestimates (see especially Fig. 2.4d).

2.4.2.4 – Tellurium

The number of laboratories that have reported Te concentrations for Geo*PT* test materials is low, and thus no assigned or provisional values are available (Table 2.4). Moreover, the median values are unlikely to be reliable unless a sufficient number of measurements have been reported. For samples above the limit of quantification (0.032 μg g^{-1}) there is broadly a positive correlation (0.86) between the HG-AFS Te results and the median values of the Geo*PT* contributed values (Fig. 2.3e). This observation suggests that the median results for the samples with Te concentrations greater than 0.032 μg g^{-1} approximate to the correct order of magnitude. However, the range of Geo*PT* test values reported by participants is very large (0.01 to 10 μg g^{-1}; Fig. 2.4e). Unlike the observations for As and Bi the variability did not change regardless of the median concentration. Based on the validation of the HG-AFS with reference materials (Fig. 2.2e), we propose that our HG-AFS Te results, above the limit of quantification (0.032 μg

g^{-1}), could be used as informational values. Once again, this illustrates the lack of well-characterised reference materials for Te at sub μg g^{-1} levels, and reinforces the need of further studies.

2.4.3 - Variability of TABS values in Geo*PT* Proficiency Test Results

The datasets of measurement results for TABS in Geo*PT* samples are, in some cases, extremely variable. The variability of results is greater for samples with low concentrations of a given element. Such variability may be due to some participating laboratories reporting measurements close to their detection limits. These measurements may have consequently been overestimated, resulting in a wide range of measurements and in some cases overestimated median values. For less commonly analyzed elements such as Se and Te, precise and accurate measurements normally require a highly specialized analytical procedure (Savard *et al.* 2006, 2009; Wang and Becker 2014; König *et al.* 2012, 2014; Lissner *et al.* 2014). Therefore, the wide range of measurements may reflect analyses performed in routine analytical procedures, which may not properly account for properties such as the oxidation state, and volatile behaviour of these elements.

A final consideration is the "nugget" effect. All of these elements are chalcophile and could be present in the samples only as minute sulfide grains, thus at low concentrations nugget effects maybe in part the source of the variation (Bédard *et al.* 2016). Tellurium, Bi and Se are strongly to highly chalcophile elements with partition coefficients into sulfides greater than 400 (Barnes and Ripley 2016), and their concentrations are very low, thus they are particularly vulnerable to the nugget effect.

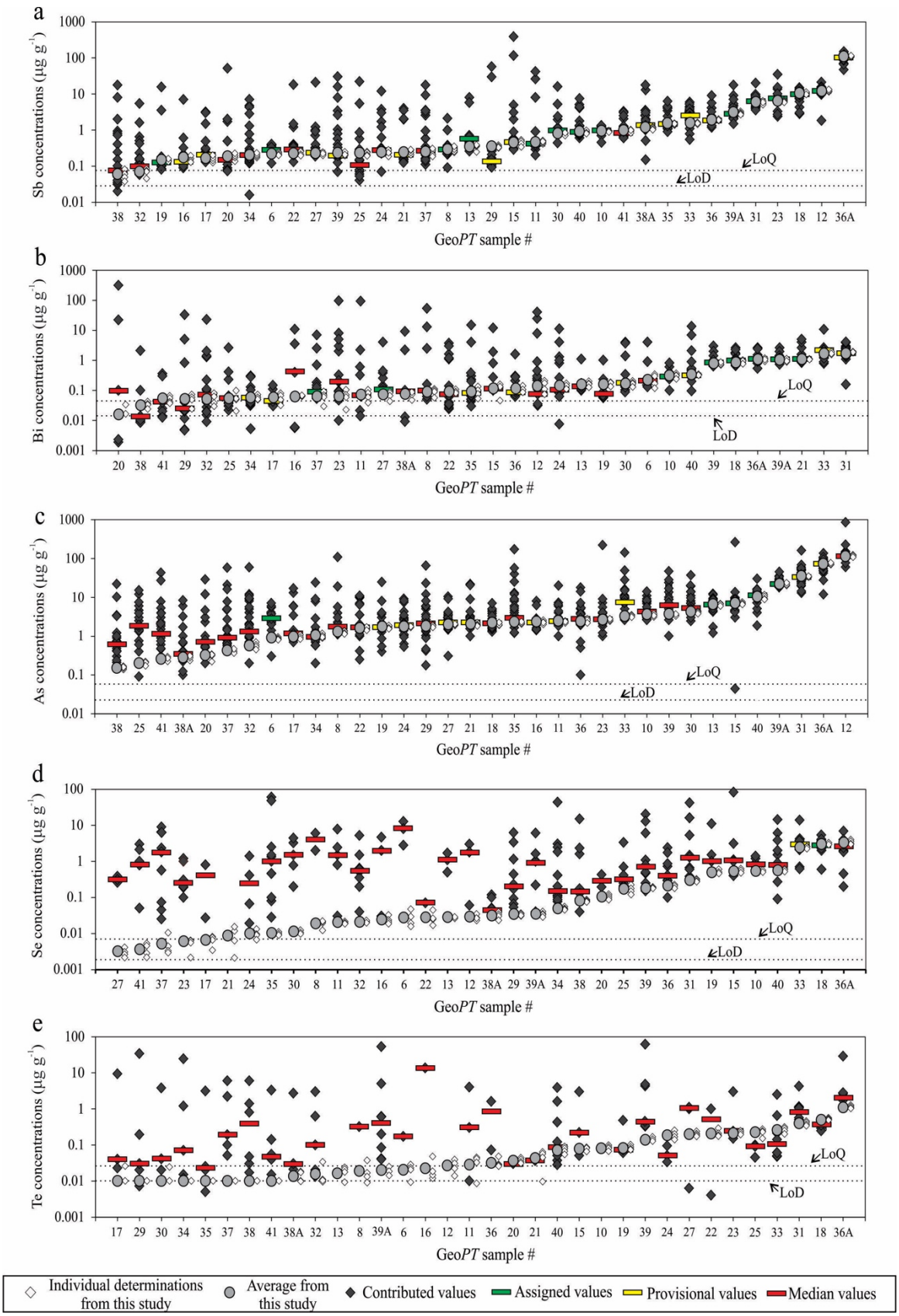

Figure 2.4 - Comparison of new determinations and all previously reported results by other laboratories for GeoPT proficiency test materials for (a) Sb, (b) Bi, (c) As, (d) Se and (e) Te. Dashed lines indicate the limit of detection (LoD) and limit of quantification (LoQ) for HG-AFS.

2.5 – Conclusion

The characterisation of TABS in geological reference materials is a subject that needs more attention, as illustrated by the paucity of information and wide variation of literature values. This work demonstrates that aqua regia digestion followed by HG-AFS is an appropriate method for determination of TABS in geological materials to sub μg g^{-1} level. The study provides results for TABS in 10 international geological reference materials (CH-4, TDB-1, OKUM, WPR-1, WMG-1, AN-G, BE-N, BIR-1, W-2 and WGB-1) and 34 test materials from the Geo*PT* programme. The comparison between HG-AFS results and geological reference materials results validates the method for measuring Te, As, Bi, Sb and Se above their respective limits of quantification. Our results agree with Geo*PT* results for Sb, and we suggest that for those samples with no assigned or provisional values the Geo*PT* median values could be used as informational values. Above 0.3 μg g^{-1} Bi, and 1 μg g^{-1} As, our results agree with the Geo*PT* results, and for those samples with no assigned or provisional values the Geo*PT* median values could potentially be used as informational values. Below 1 μg g^{-1} As the median Geo*PT* values are systematically higher than ours. For Se the median Geo*PT* values are systematically higher than our values. Considering that for these two elements the HG-AFS method was successful in determining the concentrations in a range of geological reference materials, we consider that the median results from the Geo*PT* test overestimate As concentrations below 1 μg g^{-1} and Se in most samples. This overestimation is probably related with the fact that fewer and less reliable results are reported for materials with low concentrations, and the medians may not be an appropriate estimate. The Geo*PT* dataset for Te is limited, but above the limit of quantification the median Geo*PT* test results correlate with the HG-AFS results. We suggest that the HG-AFS results could be used as informational values for As in Geo*PT* test samples with less than 1 μg g^{-1}. The

HG-AFS results could also be used as informational values for Se and Te in Geo*PT* materials with concentrations above the quantification limits.

2.6 - Acknowledgements

This work was supported by a Canada Research Chair program grant to Sarah-Jane Barnes (215503). This manuscript benefited from insightful comments from two anonymous reviewers, and careful editorial handling by the editor Mary Horan.

2.7 - References

Amereih S., Meisel T., Scholger R. and Wegscheider W. (2005) Antimony speciation in soil samples along two Austrian motorways by HPLC-ID-ICP-MS. Journal of Environmental Monitoring, 7, 1200-1206.

Babechuk M.G., Kamber B.S., Greig A., Canil D. and Kodolányi J. (2010) The behaviour of tungsten during mantle melting revisited with implications for planetary differentiation time scales. Geochimica et Cosmochimica Acta, 74, 1448-1470.

Baranov B.V., Werner R., Hoernle K.A., Tsoy I.B., van den Bogaard P. and Tararin I.A. (2002) Evidence for compressionally induced high subsidence rates in the Kurile Basin (Okhotsk Sea). Tectonophysics, 350, 63-97.

Barnes S.-J. (2016) Chalcophile elements. Encyclopedia of Geochemistry. Springer, pp. 1-5.

Barnes S.-J., Prichard H.M., Cox R.A., Fisher P.C. and Godel B. (2008) The location of the chalcophile and siderophile elements in platinum-group element ore deposits (a textural, microbeam and whole rock geochemical study): Implications for the formation of the deposits. Chemical Geology, 248, 295-317.

Barnes S.-J. and Gomwe T.S. (2011) The Pd deposits of the Lac des Iles complex, northwestern Ontario. Reviews in Economic Geology, 17, 351–370.

Barnes S-J. and Ripley E.M. (2016) Highly siderophile and strongly chalcophile elements in magmatic ore deposits. Reviews in Mineralogy and Geochemistry, 81, 725-774.

Bédard L.P. and Barnes S.-J. (2002) A comparison of N-type semi-planar and coaxial INAA detectors for 33 geochemical reference samples. Journal of radioanalytical and nuclear chemistry, 254, 485-497.

Bédard L.P., Esbensen, K.H. and Barnes, S.-J. (2016) Empirical Approach for Estimating Reference Material Heterogeneity and Sample Minimum Test Portion Mass for “Nuggety” Precious Metals (Au, Pd, Ir, Pt, Ru). Analytical chemistry, 88(7), 3504-3511.

Bossy A., Grosbois C., Beauchemin S., Courtin-Nomade A., Hendershot W. and Bril H. (2010) Alteration of As-bearing phases in a small watershed located on a high grade arsenic-geochemical anomaly (French Massif Central). Applied Geochemistry 25, 1889-1901.

Branch S., Ebdon L., Ford M., Foulkes M. and O'Neill P. (1991) Determination of arsenic in samples with high chloride content by inductively coupled plasma mass spectrometry. Journal of Analytical Atomic Spectrometry, 6(2), 151-154.

Brenan J.M. (2015) Se–Te fractionation by sulfide–silicate melt partitioning: Implications for the composition of mantle-derived magmas and their melting residues. Earth and Planetary Science Letters, 422, 45-57.

Carignan J., Hild P., Mevelle G., Morel J. and Yeghicheyan D. (2001) Routine analyses of trace elements in geological samples using flow injection and low pressure on-line liquid

chromatography coupled to ICP-MS: A study of geochemical reference materials BR, DR-N, UB-N, AN-G and GH. Geostandards Newsletter, 25, 187-198.

Cava-Montesinos P., Cervera M.L., Pastor A. and de la Guardia M. (2003) Hydride generation atomic fluorescence spectrometric determination of ultratraces of selenium and tellurium in cow milk. Analytica Chimica Acta, 481, 291-300.

Chauvel C., Maury R.C., Blais S., Lewin E., Guillou H., Guille G., Rossi P. and Gutscher M.A. (2012) The size of plume heterogeneities constrained by Marquesas isotopic stripes. Geochemistry, Geophysics, Geosystems, 13, 1-23.

Constantin M. (2006) Determination of Au, Ir and thirty-two other elements in twelve geochemical reference materials by instrumental neutron activation analysis. Journal of Radioanalytical and Nuclear Chemistry, 267, 407-414.

Corns W.T., Stockwell P.B., Ebdon L.C. and Hill S.J. (1993) Development of an atomic fluorescence spectrometer for the hydride forming elements. Journal of Analytical Spectrometry, 8, 71–76.

Cotta A.J. and Enzweiler J. (2012) Classical and new procedures of whole rock dissolution for trace element determination by ICP-MS. Geostandards and Geoanalytical Research, 36, 27-50.

Dampare S., Shibata T., Asiedu D., Osae S. and Banoeng-Yakubo B. (2008) Geochemistry of Paleoproterozoic metavolcanic rocks from the southern Ashanti volcanic belt, Ghana: Petrogenetic and tectonic setting implications. Precambrian Research, 162, 403-423.

Dare S.A., Barnes S.-J., Prichard H.M. and Fisher P.C. (2011) Chalcophile and platinum-group element (PGE) concentrations in the sulfide minerals from the McCreedy East deposit, Sudbury, Canada, and the origin of PGE in pyrite. Mineralium Deposita, 46, 381-407.

Debret B., Andreani M., Godard M., Nicollet C., Schwartz S. and Lafay R. (2013) Trace element behavior during serpentinization/de-serpentinization of an eclogitized oceanic lithosphere: A LA-ICPMS study of the Lanzo ultramafic massif (Western Alps). Chemical Geology, 357, 117-133.

Duker A.A., Carranza E.J.M. and Hale M. (2005) Arsenic geochemistry and health. Environment International, 31, 631-641.

Eggins S., Woodhead J., Kinsley L., Mortimer G., Sylvester P., McCulloch M., Hergt J. and Handler M. (1997) A simple method for the precise determination of≥ 40 trace elements in geological samples by ICPMS using enriched isotope internal standardisation. Chemical Geology, 134, 311-326.

Elmaleh A., Galy A., Allard T., Dairon R., Day J., Michel F., Marriner N., Morhange C. and Couffignal F. (2012) Anthropogenic accumulation of metals and metalloids in carbonate-rich sediments: Insights from the ancient harbor setting of Tyre (Lebanon). Geochimica et Cosmochimica Acta, 82, 23-38.

Falloon T.J., Danyushevsky L.V., Crawford T.J., Maas R., Woodhead J.D., Eggins S.M., Bloomer S.H., Wright D.J., Zlobin S.K. and Stacey A.R. (2007) Multiple mantle plume components involved in the petrogenesis of subduction-related lavas from the northern termination of the Tonga Arc and northern Lau Basin: Evidence from the geochemistry of arc and backarc submarine volcanics. Geochemistry, Geophysics, Geosystems, 8, 1-45.

Fávaro D., Damatto S., Moreira E., Mazzilli B., Campagnoli F. (2007) Chemical characterization and recent sedimentation rates in sediment cores from Rio Grande reservoir, SP, Brazil. Journal of Radioanalytical and Nuclear Chemistry, 273, 451-463.

Fourny A., Weis D. and Scoates J.S. (2016) Comprehensive Pb-Sr-Nd-Hf isotopic, trace element, and mineralogical characterization of mafic to ultramafic rock reference materials. Geochemistry, Geophysics, Geosystems, 17, 739-773.

Freymuth H., Ivko B., Gill J.B., Tamura Y. and Elliott T. (2016) Thorium isotope evidence for melting of the mafic oceanic crust beneath the Izu arc. Geochimica et Cosmochimica Acta, 186, 49-70.

Gaeta M., Giuliani A., Perilla S. and Misiti V. (2013) Reddish metagranites from the Gennargentu Igneous Complex (Sardinia, Italy): insight into metasomatism induced by magma mingling. Journal of petrology, 54, 839-859.

Garbe-Schönberg C.D. (1993) Simultaneous determination of thirty-seven trace elements in twenty-eight international rock standards by ICP-MS. Geostandards Newsletter, 17, 81-97.

Garçon M., Chauvel C., France-Lanord C., Huyghe P. and Lavé J. (2013) Continental sedimentary processes decouple Nd and Hf isotopes. Geochimica et Cosmochimica Acta, 121, 177-195.

Gaschnig R.M., Rudnick R.L. and McDonough W.F. (2015) Determination of Ga, Ge, Mo, Ag, Cd, In, Sn, Sb, W, Tl and Bi in USGS Whole-Rock Reference Materials by Standard Addition ICP-MS. Geostandards and Geoanalytical Research, 39, 371-379.

Gladney E. and Knab D. (1981) Determination of selenium in twenty geological reference materials by neutron activation and inorganic ion exchange. Geostandards Newsletter, 5, 67-69.

Godel B. and Barnes S.-J. (2008) Platinum-group elements in sulfide minerals and the whole rocks of the JM Reef (Stillwater Complex): Implication for the formation of the reef. Chemical Geology, 248, 272-294.

Govindaraju K. (1994) 1994 compilation of working values and sample description for 383 geostandards. Geostandards Newsletter, 18, 1-158.

Gurenko A., Hoernle K., Hauff F., Schmincke H.-U., Han D., Miura Y. and Kaneoka I. (2006) Major, trace element and Nd–Sr–Pb–O–He–Ar isotope signatures of shield stage lavas from the central and western Canary Islands: insights into mantle and crustal processes. Chemical Geology, 233, 75-112.

Haase K.M., Lima S., Krumm S. and Garbe-Schönberg D. (2014) The magmatic evolution of young island arc crust observed in gabbroic to tonalitic xenoliths from Raoul Island, Kermadec Island Arc. Lithos, 210, 199-208.

Hattori K.H., Arai S. and Clarke D.B. (2002) Selenium, tellurium, arsenic and antimony contents of primary mantle sulfides. The Canadian Mineralogist, 40, 637-650.

He Y., Moreda-Pineiro J., Cervera M.L. and de la Guardia M. (1998) Direct determination of dissolved selenium (vi) and selenium (vi) in sea-water by continuous flow hydride generation atomic fluorescence spectrometry. Journal of Analytical Atomic Spectrometry, 13, 289-293.

Henrique-Pinto R., Barnes S.J., Savard D. and Mehdi S. (2017) Quantification of Metals and Semimetals in Carbon-Rich Rocks: A New Sequential Protocol Including Extraction from Humic Substances. Geostandards and Geoanalytical Research, 41(1), 41-62.

Horwitz W., Kamps L.R. and Boyer, K.W. (1980) Quality assurance in the analysis of foods and trace constituents. Journal-Association of Official Analytical Chemists, 63(6), 1344-1354.

Hu Z., Gao S., Hu S., Yuan H., Liu X. and Liu Y. (2005) Suppression of interferences for direct determination of arsenic in geological samples by inductively coupled plasma mass spectrometry. Journal of Analytical Atomic Spectrometry, 20, 1263-1269.

Hu Z. and Gao S. (2008) Upper crustal abundances of trace elements: a revision and update. Chemical Geology, 253, 205-221.

IAG (2018) Protocol for the Operation of the GeoPT Proficiency Testing Scheme. International Association of Geoanalysts, Keyworth, England (http://www.geoanalyst.org/wp-content/uploads/2018/06/GeoPT-revised-protocol-2018.pdf).

Jamieson H.E. (2014) The legacy of arsenic contamination from mining and processing refractory gold ore at Giant Mine, Yellowknife, Northwest Territories, Canada. Reviews in Mineralogy & Geochemistry, 79, 533-551.

Jochum K. and Hofmann A.W. (1997) Constraints on earth evolution from antimony in mantle-derived rocks. Chemical Geology, 139, 39-49.

Jochum K.P., Nohl U., Herwig K., Lammel E., Stoll B. and Hofmann A.W. (2005) GeoReM: a new geochemical database for reference materials and isotopic standards. Geostandards and Geoanalytical Research, 29, 333-338

Jochum K., Seufert H., Midinet-Best S., Rettmann E., Schönberger K. and Zimmer M. (1988) Multi-element analysis by isotope dilution-spark source mass spectrometry (ID-SSMS) Multielement-Analyse mit Isotopenverdünnung-Funkenmassenspektrometrie (ID-SSMS). Fresenius' Zeitschrift für Analytische Chemie, 331, 104-110.

Jochum K.P., Weis U., Schwager B., Stoll B., Wilson S.A., Haug G.H., Andreae M.O. and Enzweiler J. (2016) Reference values following ISO guidelines for frequently requested rock reference materials. Geostandards and Geoanalytical Research, 40, 333-350.

Ketris M.P. and Yudovich Y. E. (2009) Estimations of Clarkes for Carbonaceous biolithes: World averages for trace element contents in black shales and coals. International Journal of Coal Geology, 78(2), 135-148.

Kodolányi J., Pettke T., Spandler C., Kamber B.S. and Gméling K. (2011) Geochemistry of ocean floor and fore-arc serpentinites: constraints on the ultramafic input to subduction zones. Journal of Petrology, 53, 235-270.

Kokfelt T.F., Hoernle K., Lundstrom C., Hauff F. and van den Bogaard C. (2009) Time-scales for magmatic differentiation at the Snaefellsjökull central volcano, western Iceland: constraints from U–Th–Pa–Ra disequilibria in post-glacial lavas. Geochimica et Cosmochimica Acta, 73, 1120-1144.

Komorowicz I. and Barałkiewicz D. (2011) Arsenic and its speciation in water samples by high performance liquid chromatography inductively coupled plasma mass spectrometry—last decade review. Talanta, 84(2), 247-261.

König S., Luguet A., Lorand J.-P., Wombacher F. and Lissner M. (2012) Selenium and tellurium systematics of the Earth's mantle from high precision analyses of ultra-depleted orogenic peridotites. Geochimica et Cosmochimica Acta, 86, 354-366.

König S., Lorand J.-P., Luguet A., Pearson D.G. (2014) A non-primitive origin of near-chondritic S–Se–Te ratios in mantle peridotites; implications for the Earth's late accretionary history. Earth and Planetary Science Letters, 385, 110-121.

Konter J.G., Staudigel H., Blichert-Toft J., Hanan B., Polvé M., Davies G., Shimizu N. and Schiffman P. (2009) Geochemical stages at Jasper Seamount and the origin of intraplate volcanoes. Geochemistry, Geophysics, Geosystems, 10, 1-24.

Korotev R.L. (1996) A self-consistent compilation of elemental concentration data for 93 geochemical reference samples. Geostandards Newsletter, 20, 217-245.

Lai G., Chen G. and Chen T. (2016) Speciation of AsIII and AsV in fruit juices by dispersive liquid–liquid microextraction and hydride generation-atomic fluorescence spectrometry. Food Chemistry, 190, 158-163.

Lissner M., König S., Luguet A., Le Roux P., Schuth S., Heuser A. and le Roex A.P. (2014) Selenium and tellurium systematics in MORBs from the southern Mid-Atlantic Ridge (47–50 S). Geochimica et Cosmochimica Acta, 144, 379-402.

Locmelis M., Fiorentini M.L., Rushmer T., Arevalo Jr R., Adam J. and Denyszyn S.W. (2016) Sulfur and metal fertilization of the lower continental crust. Lithos 244, 74-93.

Long G.L. and Winefordner J.D. (1983) Limit of detection: a closer look at the IUPAC definition. Analytical Chemistry, 55, 712A–724A.

Maghraoui M.E., Joron J.L., Etoubleau J., Cambon P. and Treuil M. (1999) Determination of forty four major and trace elements in GPMA magmatic rock reference materials using X-ray Fluorescence Spectrometry (XRF) and Instrumental Neutron Activation Analysis (INAA). Geostandards Newsletter 23, 59-68.

Mariano D.B., Figueiredo A.M. and Semmler R. (2014) Implementation of the k0-standardization method for analysis of geological samples at the Neutron Activation Analysis Laboratory, São Paulo, Brazil. Journal of Radioanalytical and Nuclear Chemistry, 299, 725-731.

Marin L., Lhomme J. and Carignan J. (2001) Determination of selenium concentration in sixty five reference materials for geochemical analysis by GFAAS after separation with thiol cotton. Geostandards Newsletter, 25, 317-324.

Martin A.P., Price R.C., Cooper A.F. and McCammon C.A. (2015) Petrogenesis of the rifted southern Victoria Land lithospheric mantle, Antarctica, inferred from petrography, geochemistry, thermobarometry and oxybarometry of peridotite and pyroxenite xenoliths from the Mount Morning eruptive centre. Journal of Petrology, 56, 193-226.

Melluso L., Morra V., Riziky H., Veloson J., Lustrino M., Del Gatto L. and Modeste V. (2007) Petrogenesis of a basanite–tephrite–phonolite volcanic suite in the Bobaomby (Cap d'Ambre) peninsula, northern Madagascar. Journal of African Earth Sciences, 49, 29-42.

Mizera J. and Řanda Z. (2010) Instrumental neutron and photon activation analyses of selected geochemical reference materials. Journal of radioanalytical and nuclear chemistry, 284, 157-163.

Mohan M.R., Kamber B.S., Piercey S.J. (2008) Boron and arsenic in highly evolved Archean felsic rocks: implications for Archean subduction processes. Earth and Planetary Science Letters, 274, 479-488.

Moss R.L., Tzimas E., Kara H., Willis P. and Kooroshy J. (2013) The potential risks from metals bottlenecks to the deployment of Strategic Energy Technologies. Energy Policy, 55, 556-564.

Nielsen S. and Hansen E.H. (1997) Determination of As (III) and As (V) by flow injection-hydride generation-atomic absorption spectrometry via on-line reduction of As (V) by KI. Analytica Chimica Acta 343, 5-17.

Norman M., Duncan R.A. and Huard J.J. (2010) Imbrium provenance for the Apollo 16 Descartes terrain: Argon ages and geochemistry of lunar breccias 67016 and 67455. Geochimica et Cosmochimica Acta, 74, 763-783.

Norman M., Taylor L.A., Shih C.-Y. and Nyquist L. (2016) Crystal accumulation in a 4.2 Ga lunar impact melt. Geochimica et Cosmochimica Acta, 172, 410-429.

Parks J., Lin S., Davis D.W., Yang X.-M., Creaser R.A. and Corkery M.T. (2014) Meso-and Neoarchean evolution of the Island Lake greenstone belt and the northwestern Superior Province: Evidence from lithogeochemistry, Nd isotope data, and U–Pb zircon geochronology. Precambrian Research, 246, 160-179.

Patten C.G., Pitcairn I.K., Teagle D.A. and Harris M. (2016) Mobility of Au and related elements during the hydrothermal alteration of the oceanic crust: implications for the sources of metals in VMS deposits. Mineralium Deposita, 51, 179-200.

Paul D.K. (2005) Petrology and geochemistry of the Salma dike, Raniganj coalfield (Lower Gondwana), eastern India: linkage with Rajmahal or Deccan volcanic activity?. Journal of Asian Earth Sciences, 25, 903-913.

Peters D. and Pettke T. (2017) Evaluation of Major to Ultra Trace Element Bulk Rock Chemical Analysis of Nanoparticulate Pressed Powder Pellets by LA-ICP-MS. Geostandards and Geoanalytical Research 41, 5-28.

Pitcairn I.K. (2004) Sources of fluids and metals in orogenic gold deposits: the Otago Schists, New Zealand. University of Southampton.

Pitcairn I.K., Craw D. and Teagle D.A.H. (2015) Metabasalts as sources of metals in orogenic gold deposits. Mineralium Deposita, 50, 373-390.

Potin-Gautier M., Pannier F., Quiroz W., Pinochet H. and De Gregori I. (2005) Antimony speciation analysis in sediment reference materials using high-performance liquid

chromatography coupled to hydride generation atomic fluorescence spectrometry. Analytica Chimica Acta, 553, 214-222.

Potra A., Dodd J.W. and Ruhl L.S. (2017) Distribution of trace elements and Pb isotopes in stream sediments of the Tri-State mining district (Oklahoma, Kansas, and Missouri), USA. Applied Geochemistry, 82, 25-3.

Potts P.J. (1987) A handbook of silicate rock analysis. Blackie (London), 622pp.

Potts P.J., Thompson M., Kane J.S., Webb P.C. and Carignan J. (2000) GeoPT6 - an international proficiency test for analytical geochemistry laboratories - report on round 6 (OU-3: Nanhoron microgranite) and 6A (CAL-S: CRPG limestone). International Association of Geoanalysts report.

Potts P.J., Thompson M., Kane J.S., Webb, P.C. and Watson J.S. (2000) GeoPT8 - an international proficiency test for analytical geochemistry laboratories - report on round 8 / February 2001 (OU-4 Penmaenmawr microdiorite). International Association of Geoanalysts report.

Potts P.J., Thompson M., Webb, P.C., Watson J.S. and Wang Yimin (2001) GeoPT10 - an international proficiency test for analytical geochemistry laboratories - report on round 10 / December 2001 (CH1 Marine sediment). International Association of Geoanalysts report.

Potts P.J., Thompson M., Chenery S.R., Webb, P.C. and Watson J.S. (2002) GeoPT11 - an international proficiency test for analytical geochemistry laboratories - report on round 11 / July 2002 (OU-5 Leaton dolerite). International Association of Geoanalysts report.

Potts P.J., Thompson M., Chenery S.R., Webb, P.C. and Batjargal B. (2003) GeoPT12 - an international proficiency test for analytical geochemistry laboratories - report on round 12 / January 2003 (GAS Serpentinite). International Association of Geoanalysts report.

Potts P.J., Thompson M., Chenery S.R., Webb, P.C. and Kaspar H.U. (2003) GeoPT13 - an international proficiency test for analytical geochemistry laboratories - report on round 13 / July 2003 (Köln Loess). International Association of Geoanalysts report.

Potts P.J., Thompson M., Chenery S.R., Webb, P.C. and Wang Yimin (2004) GeoPT15 - an international proficiency test for analytical geochemistry laboratories - report on round 15 / June 2004 (Ocean floor sediment MSAN). International Association of Geoanalysts report.

Potts P.J., Thompson M., Webb, P.C. and S.Wilson (2005) GeoPT16 - an international proficiency test for analytical geochemistry laboratories - report on round 16 / February 2005 (Nevada basalt, BNV-1). International Association of Geoanalysts report.

Potts P.J., Thompson M., Webb, P.C. and J. Nicholas Walsh (2005) GeoPT17 - an international proficiency test for analytical geochemistry laboratories - report on round 17 / July 2005 (Calcareous sandstone, OU-8). International Association of Geoanalysts report.

Reyes M.N.M., Cervera M.L., Campos R.C. and de la Guardia M. (2008) Non-chromatographic speciation of toxic arsenic in vegetables by hydride generation-atomic fluorescence spectrometry after ultrasound-assisted extraction. Talanta, 75, 811-816.

Riley T., Curtis M., Flowerdew M. and Whitehouse M.J. (2016) Evolution of the Antarctic Peninsula lithosphere: Evidence from Mesozoic mafic rocks. Lithos, 244, 59-73.

Robin-Popieul C.C., Arndt N.T., Chauvel C., Byerly G.R., Sobolev A.V. and Wilson A. (2012) A new model for Barberton komatiites: deep critical melting with high melt retention. Journal of Petrology, 53, 2191-2229.

Rukhlov A.S., Blinova A.I. and Pawlowicz J.G. (2013) Geochemistry, mineralogy and petrology of the Eocene potassic magmatism from the Milk River area, southern Alberta, and Sweet Grass Hills, northern Montana. Chemical Geology, 353, 280-302.

Samalens N., Barnes S.J. and Sawyer E.W. (2017) The role of black shales as a source of sulfur and semimetals in magmatic nickel-copper deposits: Example from the Partridge River Intrusion, Duluth Complex, Minnesota, USA. Ore Geology Reviews, 81, 173-187.

Savard D., Bédard L.P. and Barnes S.-J. (2006) TCF selenium preconcentration in geological materials for determination at sub-μg g− 1 with INAA (Se/TCF-INAA). Talanta, 70, 566-571.

Savard D., Bédard L.P., Barnes S.-J. (2009) Selenium concentrations in twenty-six geological reference materials: New determinations and proposed values. Geostandards and Geoanalytical Research, 33, 249-259.

Sheppard B.S., Shen W.L., Caruso J.A., Heitkemper D.T. and Fricke F.L. (1990) Elimination of the argon chloride interference on arsenic speciation in inductively coupled plasma mass spectrometry using ion chromatography. Journal of Analytical Atomic Spectrometry, 5(6), 431-435.

Singer B.S., Smith K.E., Jicha B.R., Beard B.L., Johnson C.M. and Rogers N.W. (2011) Tracking open-system differentiation during growth of Santa María volcano, Guatemala. Journal of Petrology, 52, 2335-2363.

Singh R., Singh S., Parihar P., Singh V.P. and Prasad S.M.J.E. (2015) Arsenic contamination, consequences and remediation techniques: a review. Ecotoxicology and Environmental Safety, 112, 247-270.

Søager N., Portnyagin M., Hoernle K., Holm P.M., Hauff F. and Garbe-Schönberg D. (2015) Olivine major and trace element compositions in southern Payenia basalts, Argentina: evidence for pyroxenite–peridotite melt mixing in a back-arc setting. Journal of Petrology, 56, 1495-1518.

Sundar S. and Chakravarty J. (2010) Antimony toxicity. International Journal of Environmental Research and Public Health, 7, 4267-4277.

Terashima S. and Imai N. (2000) Determination of selenium in fifty two geochemical reference materials by hydride generation atomic absorption spectrometry. Geostandards Newsletter, 24, 83-86.

Terashima S. (2001) Determination of indium and tellurium in fifty nine geological reference materials by solvent extraction and graphite furnace atomic absorption spectrometry. Geostandards Newsletter, 25, 127-132.

Van der Sloot H., Hoede D., Klinkers T.J. and Das H. (1982) The determination of arsenic, selenium and antimony in rocks, sediments, fly ash and slag. Journal of Radioanalytical Chemistry, 71, 463-478.

Volkert R.A., Feigenson M.D., Mana S. and Bolge L. (2015) Geochemical and Sr–Nd isotopic constraints on the mantle source of Neoproterozoic mafic dikes of the rifted eastern Laurentian margin, north-central Appalachians, USA. Lithos, 212, 202-213.

Wang Z. and Becker H. (2013) Ratios of S, Se and Te in the silicate Earth require a volatile-rich late veneer. Nature, 499, 328-331.

Wang Z. and Becker H. (2014) Abundances of sulfur, selenium, tellurium, rhenium and platinum-group elements in eighteen reference materials by isotope dilution sector-field ICP-MS and negative TIMS. Geostandards and Geoanalytical Research, 38, 189-209.

Webb, P.C., Thompson M., Potts P.J. and L. Paul Bedard (2006) GeoPT18 - an international proficiency test for analytical geochemistry laboratories - report on round 18 / Jan 2006 (Quartz Diorite, KPT-1). International Association of Geoanalysts report.

Webb, P.C., Thompson M., Potts P.J. and B. Batjargal (2006) GeoPT19 - an international proficiency test for analytical geochemistry laboratories - report on round 19 / July 2006 (Gabbro, MGR-N). International Association of Geoanalysts report.

Webb, P.C., Thompson M., Potts P.J. and M. Burnham (2007) GeoPT20 - an international proficiency test for analytical geochemistry laboratories - report on round 20 / Jan 2007 (Ultramafic rock, OPY-1). International Association of Geoanalysts report.

Webb, P.C., Thompson M., Potts P.J. and B. Batjargal (2007) GeoPT21 - an international proficiency test for analytical geochemistry laboratories - report on round 21 / July 2007 (Granite, MGT-1). International Association of Geoanalysts report.

Webb, P.C., Thompson, M., Potts, P.J. and Batjargal, B. (2008) GeoPT22 - an international proficiency test for analytical geochemistry laboratories - report on round 22 / January 2008 (Basalt, MBL-1). International Association of Geoanalysts report.

Webb, P.C., Thompson, M., Potts, P.J., Watson, J.S. and Kriete, C. (2008) GeoPT23 - an international proficiency test for analytical geochemistry laboratories - report on round 23 / September 2008 (Separation Lake pegmatite, OU-9) and 23A (Manganese nodule, FeMn-1). International Association of Geoanalysts report.

Webb, P.C., Thompson, M., Potts, P.J. and Watson, J.S. (2009) GeoPT24 - an international proficiency test for analytical geochemistry laboratories - report on round 24 / January 2009 (Longmyndian greywacke, OU-10). International Association of Geoanalysts report.

Webb, P.C., Thompson, M., Potts, P.J. and Enzweiler, J. (2009) GeoPT25 - an international proficiency test for analytical geochemistry laboratories - report on round 25 / July 2009 (Basalt, HTP-1). International Association of Geoanalysts report.

Webb, P.C., Thompson, M., Potts, P.J. and Batjargal, B. (2010) GeoPT27 - an international proficiency test for analytical geochemistry laboratories - report on round 27 / July 2010 (Andesite, MGL-AND). International Association of Geoanalysts report.

Webb, P.C., Thompson, M., Potts, P.J. and Wilson, S. (2011) GeoPT29 - an international proficiency test for analytical geochemistry laboratories - report on round 29 / July 2011 (Nephelinite, NKT-1). International Association of Geoanalysts report.

Webb, P.C., Thompson, M., Potts, P.J., Long, D. and Batjargal, B. (2012) GeoPT30 - an international proficiency test for analytical geochemistry laboratories - report on round 30 / January 2012 (Silty marine shale, CG-2) and 30A (Limestone, ML-2). International Association of Geoanalysts report.

Webb, P.C., Thompson, M., Potts, P.J and Wilson, S. (2012) GeoPT31 - an international proficiency test for analytical geochemistry laboratories - report on round 31 / July 2012 (Modified river sediment, SdAR-1). International Association of Geoanalysts report.

Webb, P.C., Thompson, M., Potts, P.J and Webber, E. (2013) GeoPT32 - an international proficiency test for analytical geochemistry laboratories - report on round 32 / January 2013 (Woodstock Basalt, WG-1). International Association of Geoanalysts report.

Webb, P.C., Thompson, M., Potts, P.J., Prusisz, B., and Young, K. (2013) GeoPT33 - an international proficiency test for analytical geochemistry laboratories - report on round 33 / July-August 2013 (Ball Clay, DBC1). International Association of Geoanalysts report.

Webb, P.C., Thompson, M., Potts, P.J and Wilson, S. (2014) GeoPT34 - an international proficiency test for analytical geochemistry laboratories - report on round 34 (Granite, GRI-1) / January 2014. International Association of Geoanalysts report.

Webb, P.C., Thompson, M., Potts, P.J and Wilson, S. (2014) GeoPT35 - an international proficiency test for analytical geochemistry laboratories - report on round 35 (Tonalite, TLM-1) / August 2014. International Association of Geoanalysts report.

Webb, P.C., Thompson, M., Potts, P.J and Wilson, S. (2015) GeoPT36 - an international proficiency test for analytical geochemistry laboratories - report on round 36 (Gabbro, GSM-1) / January 2015. International Association of Geoanalysts report.

Webb, P.C., Thompson, M., Potts, P.J and Wilson, S. (2015) GeoPT36A - an international proficiency test for analytical geochemistry laboratories - report on round 36A (Metal-rich sediment, SdAR-M2) / January 2015. International Association of Geoanalysts report.

Webb, P.C., Thompson, M., Potts, P.J, Gowing, C.J.B. and Burnham, M. (2015) GeoPT37 - an international proficiency test for analytical geochemistry laboratories - report on round 37 (Rhyolite, ORPT-1) / July 2015. International Association of Geoanalysts report

Webb, P.C., Thompson, M., Potts, P.J, Gowing, C.J.B. and Wilson, S.A. (2016) GeoPT38 - an international proficiency test for analytical geochemistry laboratories - report on round 38 (Gabbro, OU-7) / January 2016. International Association of Geoanalysts report.

Webb, P.C., Thompson, M., Potts, P.J, Gowing, C.J.B. and Meisel, T. (2016) GeoPT38A - an international proficiency test for analytical geochemistry laboratories – special report on round 38A (Modified harzburgite, HARZ01) / June 2016. International Association of Geoanalysts report.

Webb, P.C., Thompson, M., Potts, P.J, Gowing, C.J.B. and Wilson, S.A. (2016) GeoPT39 - an international proficiency test for analytical geochemistry laboratories - report on round 39 (Syenite, SyMP-1) / July 2016. International Association of Geoanalysts report.

Webb, P.C., Thompson, M., Potts, P.J, and Gowing, C.J.B. (2016) GeoPT39A - an international proficiency test for analytical geochemistry laboratories - report on round 39A (Nepheline syenite, MNS-1) / July 2016. International Association of Geoanalysts report.

Webb, P.C., Thompson, M., Potts, P.J, Gowing, C.J.B. and Wilson, S.A. (2017) GeoPT40 - an international proficiency test for analytical geochemistry laboratories - report on round 40 (Silty marine shale, ShWYO-1) / January 2017. International Association of Geoanalysts report.

Webb, P.C., Thompson, M., Potts, P.J, Gowing, C.J.B. and Wilson, S.A. (2017) GeoPT41 — an international proficiency test for analytical geochemistry laboratories - report on round 41 (Andesite, ORA-1) / July 2017. International Association of Geoanalysts report.

Wu L.J.E. (2004) Review of 15 years of research on ecotoxicology and remediation of land contaminated by agricultural drainage sediment rich in selenium. Ecotoxicology and Environmental Safety, 57(3), 257-269.

Yan X.-P., Yin X.-B., He X.-W. and Jiang Y. (2002) Flow injection on-line sorption preconcentration coupled with hydride generation atomic fluorescence spectrometry for determination of (ultra) trace amounts of arsenic (III) and arsenic (V) in natural water samples. Analytical Chemistry, 74, 2162-2166.

Yi W., Halliday A.N., Lee D.C. and Rehkämper M. (1998) Precise determination of cadmium, indium and tellurium using multiple collector ICP-MS. Geostandards Newsletter, 22, 173-179.

Yu Z., Robinson P., Townsend A.T., Mnker C. and Crawford A.J. (2000) Determination of high field strength elements, Rb, Sr, Mo, Sb, Cs, Tl and Bi at ng g− 1 levels in geological reference materials by magnetic sector ICP-MS after HF/HClO4 high pressure digestion. Geostandards Newsletter, 24, 39-50.

Zhang N., Fu N., Fang Z., Feng Y. and Ke L. (2011) Simultaneous multi-channel hydride generation atomic fluorescence spectrometry determination of arsenic, bismuth, tellurium and selenium in tea leaves. Food Chemistry, 124, 1185-1188.

Zweibel K.J.S. (2010) The impact of tellurium supply on cadmium telluride photovoltaics. Science, 328, 699-701.

Chapter 3 - Distribution of chalcophile and platinum-group elements among pyrrhotite, pentlandite, chalcopyrite and cubanite from the Noril'sk-Talnakh ores: implications for the formation of platinum-group minerals

*Eduardo T. Mansur[1], Sarah-Jane Barnes[1], Charley J. Duran[1] Sergey F. Sluzhenikin[2]

[1]Sciences de la Terre, Université du Québec à Chicoutimi, Québec, G7H 2B1, Canada

[2]Institute of Geology of Ore Deposits, Mineralogy, Petrography, and Geochemistry (IGEM RAS), Staromonetny 35, Moscow 119017 Russia

Author contributions:

Mansur wrote the manuscript, collected and analyzed the data and created the figures. **Barnes** edited the manuscript and analyzed the data. **Duran** collected part of the data and also analyzed the results. **Sluzhenikin** helped collecting the samples used in the preparation of the manuscript.

Mineralium Deposita

DOI: 10.1007/s00126-019-00926-z

3.1 - Abstract

In most magmatic sulfide deposits, platinum-group elements (PGE) are found both within the structure of the base metal sulfides (BMS), pyrrhotite (Po), pentlandite (Pn), chalcopyrite (Ccp) and cubanite (Cbn) and as platinum-group minerals (PGM). Tellurium, As, Bi, Sb, Sn (TABS) are essential elements in many of these PGM. The potential role of TABS in collecting PGE, and thus forming a PGE-dominated deposit has not been closely investigated. We have determined the concentrations of a full suite of chalcophile elements in Po, Pn, Ccp and Cbn using laser ablation-inductively coupled plasma-mass spectrometry on samples from the Noril'sk-Talnakh Ni-deposits. In these deposits the Po-rich ore is thought to represent monosulfide solid solution (MSS) cumulate of the initial sulfide liquid, and the Ccp-rich ore a mixture of the fractionated sulfide liquid and intermediate solid solution (ISS). The BMS from the Po-rich ore contain lower concentrations of TABS, Pd, Pt and Au, and higher concentrations of Mo, Ru, Rh, Re, Os and Ir than BMS from the Ccp-rich ores. This observation is consistent with the results from experimental results which show that TABS, Pd, Pt and Au are incompatible with MSS, whereas the other elements are compatible in MSS. Counter intuitively, in the Po-rich ore the bulk of the Pd and TABS are hosted by BMS. This is because during crystallization although only a small amount of the incompatible elements partitioned into the BMS, the fractionated liquid has migrated away, thus the Po-rich ores represent MSS adcumulates. Therefore, as the Po-rich ores contain very little trapped liquid fraction the BMS host the bulk of Pd and TABS. In contrast, in the Ccp-rich ore the bulk of Au, Pd, Pt and TABS are present as PGM or electrum grains. This is because more trapped liquid is present, and as TABS, Au, Pd and Pt are not compatible with ISS, they concentrated into the very last sulfide liquid, and crystallized as intergrowths of Pd-Pt-TABS PGM. The TABS then do not appear to collect Pd, Pt and Au but rather all elements are concentrated in the most fractionated sulfide liquid by crystal fractionation.

Keywords: LA-ICP-MS, pyrrhotite, pentlandite, chalcopyrite, cubanite, PGE, Te, As, Bi, Sb, chalcophile elements, Noril'sk-Talnakh.

3.2 - Introduction

Chalcophile elements are collected by magmatic sulfide liquid during the formation of Ni-Cu-platinum-group element (PGE) deposits. The concentration of these elements in the sulfide liquid is affected by: i) Partition coefficients between silicate and sulfide liquid; ii) The ratio of silicate to sulfide liquid present (R-factor); and iii) The composition of the silicate liquid, which may be contaminated by a variety of crustal sources (Naldrett 2004; Barnes and Ripley 2016). The distribution of these elements within the deposits is controlled by: i) the degree of fractional crystallization of the sulfide liquid; ii) subsolidus cooling history of the sulfides; and iii) metamorphic and hydrothermal history of the deposit (Li et al. 1996; Naldrett et al. 1996; Barnes et al. 1997; Frost et al. 2002; Mungall et al. 2005; Dare et al. 2010b, 2011, 2014; Cafagna 2015; Liu and Brenan 2015; Mota-e-Silva et al. 2015). Whereas the distributions of Ni, Cu, Co and PGE have been studied, both in whole rock and base-metal-sulfide minerals (BMS), the behaviour of most of the other chalcophile elements has not been closely examined at some localities.

Constraining the distribution of trace chalcophile elements in Ni-Cu-PGE deposits is important for a number of reasons. Firstly, many platinum-group minerals (PGM) contain the chalcophile elements Te, As, Bi, Sb and Sn (TABS) as essential elements (Barnes and Ripley 2016). However, the exact role these elements may play in forming PGE-dominated deposits has not been established. Secondly, some (e.g. Co, Te and Bi) are considered important for the development of the Green economy (Zweibel 2010; Moss et al. 2013), but are only produced as by-products. Therefore, establishing whether magmatic sulfides could be a source of these elements is of economic importance. Thirdly, some (As, Cd and Pb) are pollutants (Jamieson 2014; Singh et al. 2015), and tracking their distribution is important in controlling pollution when exploiting the deposits.

It has been shown that in most deposits investigated to date, Pt is present mainly as PGM associated with BMS, whereas the other PGE exhibit variable behaviour. In some deposits, the IPGE (Os, Ir, Ru, Rh) and Pd are largely accommodated in pyrrhotite (Po) and/or pentlandite (Pn), whereas in other deposits TABS-rich PGM are the main carriers (Barnes et al. 2006, 2008;

Godel et al. 2007, 2012; Holwell and McDonald 2007; Godel and Barnes 2008; Dare et al. 2010b, 2011, 2014; Piña et al. 2012; Osbahr et al. 2014; Smith et al. 2014; Chen et al. 2015; Duran et al. 2016). The distribution of the TABS is thus important as they may influence the timing of the formation of the PGM. Several processes have been proposed for the formation of PGM: i) During crystallization of a sulfide liquid, monosulfide solid solution (MSS) and intermediate solid solution (ISS) are the two main phases to crystallize. Palladium, Pt and TABS are incompatible with both MSS and ISS, and thus the concentration of these elements in the fractionated liquid could reach levels sufficiently elevated to permit PGM to crystallize (Barnes et al. 2006; Hutchinson and McDonald 2008; Dare et al. 2010a, 2010b, 2014; Duran et al. 2017); ii) In some cases the TABS concentrations in the sulfide liquid could reach the levels that are sufficiently elevated for an immiscible TABS-rich liquid to segregate and collect the PGE, from which the PGM could crystallize (Cafagna 2015; Hanley 2007; Helmy et al. 2007, 2013; Holwell and McDonald 2007; Liu and Brenan 2015); iii) The PGM could form by exsolution, when TABS and PGE are expelled from the BMS lattice during subsolidus cooling (Makovicky 2002; Prichard et al. 2004; Godel et al. 2007; Barnes et al. 2008; Godel and Barnes 2008; Hutchinson and McDonald 2008; Junge et al. 2015); iv) Hydrothermal fluids could concentrate TABS and PGE, and the PGM could further precipitate from these fluids (Pentek et al. 2008; Tuba et al. 2014); and v) Late magmatic or metamorphic fluids could dissolve most of the BMS, but the PGE are not mobilized and combine with TABS to form PGM (Wood 2002; Djon and Barnes 2012; Sullivan et al. 2018).

In this contribution we examine the distribution of chalcophile elements in BMS from samples of the Noril'sk-Talnalk Ni-deposits (Fig. 1.11; Distler et al. 1977; Fedorenko 1994; Lightfoot et al. 1994; Kosyakov et al. 2012; Ryabov et al. 2014; Sluzhenikin et al. 2014; Krivolutskaya 2016; Krivolutskaya et al. 2018). The wide range of textures and compositions of the ores have been attributed to fractional crystallization of a sulfide liquid. The absence of metamorphism, and limited deformation of the ores permitted us to examine the behaviour of

chalcophile elements during fractional crystallization of a sulfide liquid, as well as during sub-solidus cooling.

This work will show that the chalcophile elements collected by the immiscible sulfide liquid (with the exception of As, Au and Pt) are predominantly present in Po, Pn and Ccp in Po-rich ores, whereas in the Ccp-rich ores most of the Au, Pd, Pt and TABS are found in intergrowths of PGM among the BMS. It will also show that there is a systematic variation in the concentration of elements in BMS with the degree of fractionation of the sulfide liquid. Pyrrhotite and Pn contain higher concentrations of compatible elements, and lower concentrations of incompatible elements in the Po-rich ores compared to the Ccp-rich ores. Partition coefficients among Po, Pn, Ccp and Cbn will also be presented.

3.3 - Methodology

3.3.1 - Sample selection

Our samples were selected from 113 specimens described by Duran et al. (2017), who presented BMS textures, platinum-group mineralogy and whole-rock geochemistry for the full collection. Both massive and disseminated sulfides are present. The massive sulfides show a wide mineralogical variation from Po-rich samples to Ccp-rich samples. The Po-rich samples contain only Pt-PGM, interpreted to be exsolutions from the enclosing BMS, whereas the Ccp-rich samples contain a variety of Pd-Pt-TABS PGM that occur as intergrowths among the BMS (Duran et al. 2017). In terms of whole rock composition, the Po-rich samples are richer in IPGE, Rh and Mo, but have similar Ni, Co and Se concentrations to the Ccp-rich ores. On the other hand, the Ccp-rich ores are richer in Ag, As, Au, Bi, Cd, Cu, In, Pb, Pd, Pt, Sb, Sn, Te, Tl and Zn than the Po-rich ores (Duran et al. 2107). The disseminated sulfides occur as 1 to 5 cm globules (Czmanske et al., 1992; Barnes et al., 2006; Le Vaillant et al. 2017). These globules show a similar zonation to the massive ores with a Po-rich and a Ccp-Cbn-rich zone. The variations in

texture and composition are thought to reflect fractional crystallization of sulfide liquid (Distler 1994; Zientek et al. 1994; Ryabov et al. 2014; Duran et al. 2017).

Eighteen samples (16 massive sulfides and 2 disseminated globular sulfide ores) were chosen to reflect the range in texture, mineralogy and composition present in the ores, aiming to investigate the behaviour of the chalcophile elements during differentiation. The whole rock (Pd+Pt)/(Os+Ir+Ru+Rh) ratio, previously determined in Duran et al. (2017), was used to reflect the degree of fractionation of the liquid (*ANNEXE 2*). The samples were also selected to cover all 3 ore bearing intrusions, Noril'sk-I, Talnakh and Kharaelakh (Fig. 1.11).

3.3.2 - Scanning electron microscope and laser ablation-inductively coupled plasma-mass spectrometry

The concentrations of major elements in BMS were determined using a Zeiss Sigma 300 VP scanning electron microscope, equipped with an Oxford Instruments Ultim Max EDS system at IOS Services Géocientifiques, Chicoutimi - Québec. The instrument was calibrated using pure metal standards, and instrumental drift was monitored using the Astimex Standards reference materials.

The concentration and distribution of the minor and trace elements were determined by laser ablation-inductively coupled plasma-mass spectrometry (LA-ICP-MS) at LabMaTer, Université du Québec à Chicoutimi (UQAC), using an Excimer 193 nm RESOlution M-50 laser ablation system (Australian Scientific Instrument) equipped with a double volume cell S-155 (Laurin Technic) and coupled with an Agilent 7900 mass spectrometer. The LA-ICP-MS tuning parameters were a laser frequency of 10 Hz, a power of 3 to 5 mJ/pulse, a dwell time of 7.5 ms, a rastering speed of 5 to 10 μm/s, and a fluence of 3 J/cm^2. Line scans across the surface of sulfides grains were made with beam sizes of 44, 33, and 25 μm, depending on grain size. The gas blank was measured for 30s before switching on the laser for at least 60s. The ablated material was carried into the ICP-MS by an Ar–He gas mix at a rate of 0.8–1 L/min for Ar and 350 mL/min for

He, and 2mL/min of nitrogen was also added to the mixture. Data reduction was carried out using the Iolite package for Igor Pro software (Paton et al. 2011).

Maps of element distribution were made on different sulfide assemblages using a laser frequency of 15 Hz and a power of 5 mJ/pulse. The beam size (15 to 58 μm) and the stage movement speed (10 to 15 μm/s) were adapted to optimize spatial resolution and analysis time for grains of different sizes. The maps were generated using the Iolite software package on the basis of the time-resolved composition of each element. The maps indicate the relative concentration of the elements and are semi-quantitative.

The following isotopes were measured: ^{57}Fe, ^{59}Co, ^{61}Ni, ^{65}Cu, ^{66}Zn, ^{75}As, ^{82}Se, ^{95}Mo, ^{101}Ru, ^{103}Rh, ^{108}Pd, ^{109}Ag, ^{111}Cd, ^{115}In, ^{118}Sn, ^{121}Sb, ^{130}Te, ^{185}Re, ^{189}Os, ^{193}Ir, ^{195}Pt, ^{197}Au, ^{205}Tl, ^{208}Pb and ^{209}Bi. In addition, ^{28}Si, ^{34}S and ^{44}Ca were monitored to ensure no silicate or sulphate inclusions were present. Polyatomic interference of ^{63}Cu^{40}Ar on ^{103}Rh was corrected using ^{103}Rh measured in MASS-1, which contains 13.4% ^{63}Cu but no ^{103}Rh. One percent Cu produced ~ 1 ppm Rh interference. Thus, the ^{103}Rh values in Ccp and Cbn are not reported as the interference is too large to be corrected. Direct interferences of ^{108}Cd on ^{108}Pd and ^{115}Sn on ^{115}In were corrected manually by monitoring ^{111}Cd and ^{118}Sn, respectively. Interference of ^{68}Zn^{40}Ar on ^{108}Pd is negligible as Zn occurs as at trace element. Polyatomic interference of ^{61}Ni^{40}Ar on ^{101}Ru was corrected using ^{101}Ru measured in a NiS blank, which does not contain Ru. The Ni interference is only significant for Pn.

^{57}Fe was used for internal standardization. Three certified reference materials were used for external calibration: Laflamme Po727, which is a synthetic FeS doped with ~40 ppm PGE and Au supplied by Memorial University of Newfoundland, was used to calibrate for PGE and Au; MASS-1, which is a ZnCuFeS pressed powder pellet doped with 50–70 ppm of most chalcophile elements, supplied by the United States Geological Survey (USGS), was used to calibrate for Cu, Se, Te, Tl and Zn; GSE-1g, which is a natural basaltic glass fused and doped with most elements at 300-500 ppm, supplied by the USGS, was used to calibrate for Ag, As, Bi, Cd, Co, In, Mo, Ni, Pb, Re, Sb and Sn using preferred values from the GeoReM database (Jochum et al. 2005). MASS-1, GSE-1g and JB-MSS5 (an FeS sulfide containing 50-70 ppm of most chalcophile

elements, supplied by James Brenan) were used to monitor the results. The reference materials were analyzed at the beginning and the end of each analytical session to monitor a potential instrumental drift. The results obtained for the monitors were generally in good agreement with the working values (*ANNEXE 3*).

3.4 - Results

The samples are described in detail in Czamanske et al. (1992), Zientek et al. (1994) and Duran et al. (2017), and only a brief summary is provided here. In the disseminated ore, sulfides occur as millimetric to centimetric droplets within olivine-gabbronorite. Typical droplets are characterized by Po at the base and Ccp and Cbn at the top, with a thin Pn layer in between (Fig. 10 of Barnes and Ripley 2016; Duran et al. 2017; Le Vaillant et al. 2017).

The Po-poor massive sulfides are characterized by abundant Po (50 to 80 modal %), Pn (10 to 20 modal %), and minor Ccp (5 to 20 modal %; Fig. 1a). Pyrrhotite occurs as centimetric anhedral grains. Pentlandite is mostly observed as coarse grains (generally >1mm in apparent diameter), thin exsolution flames (<100 μm) within Po (Fig. 1a and 1b), and loops at the contact between Po and Ccp grains. The loop-textured Pn is described in detail in Mansur et al. (2019). Chalcopyrite occurs either as small anhedral grains dispersed among Po and Pn grains, or associated with Pn in exsolution lamellae within Po grains (Figs. 1a and b). Magnetite (Mag) is present in minor proportions and occurs as euhedral to anhedral grains (Fig. 1a). In some samples, Po hosts sub parallel exsolution lamellae of troilite (Tro; Fig. 1b).

The Ccp-rich massive sulfides are dominated by the presence of Ccp (60 to 90% vol.), together with Pn (5 to 20% vol.), and magnetite (Figs. 1c and d). Minor Po (<5% vol.) is present in a few samples. Chalcopyrite occurs as centimetric anhedral patches and in some cases contains Cbn exsolutions (<25% vol.; Fig. 1c). Pentlandite mainly occurs as large grains (i.e. up to several cm in apparent diameter), associated with Ccp (Fig. 1d). Pyrrhotite occurs mostly as anhedral patches, and in a few cases as exsolution lamellae in Ccp (Figs. 5b and 5d of Duran et al. 2017). Galena is present in minor amounts (<<0.01% vol.) as grains <0.05 mm. Magnetite occurs as

euhedral to anhedral grains, and in some cases as late veins crosscutting Ccp and/or Pn grains (Fig. 1d).

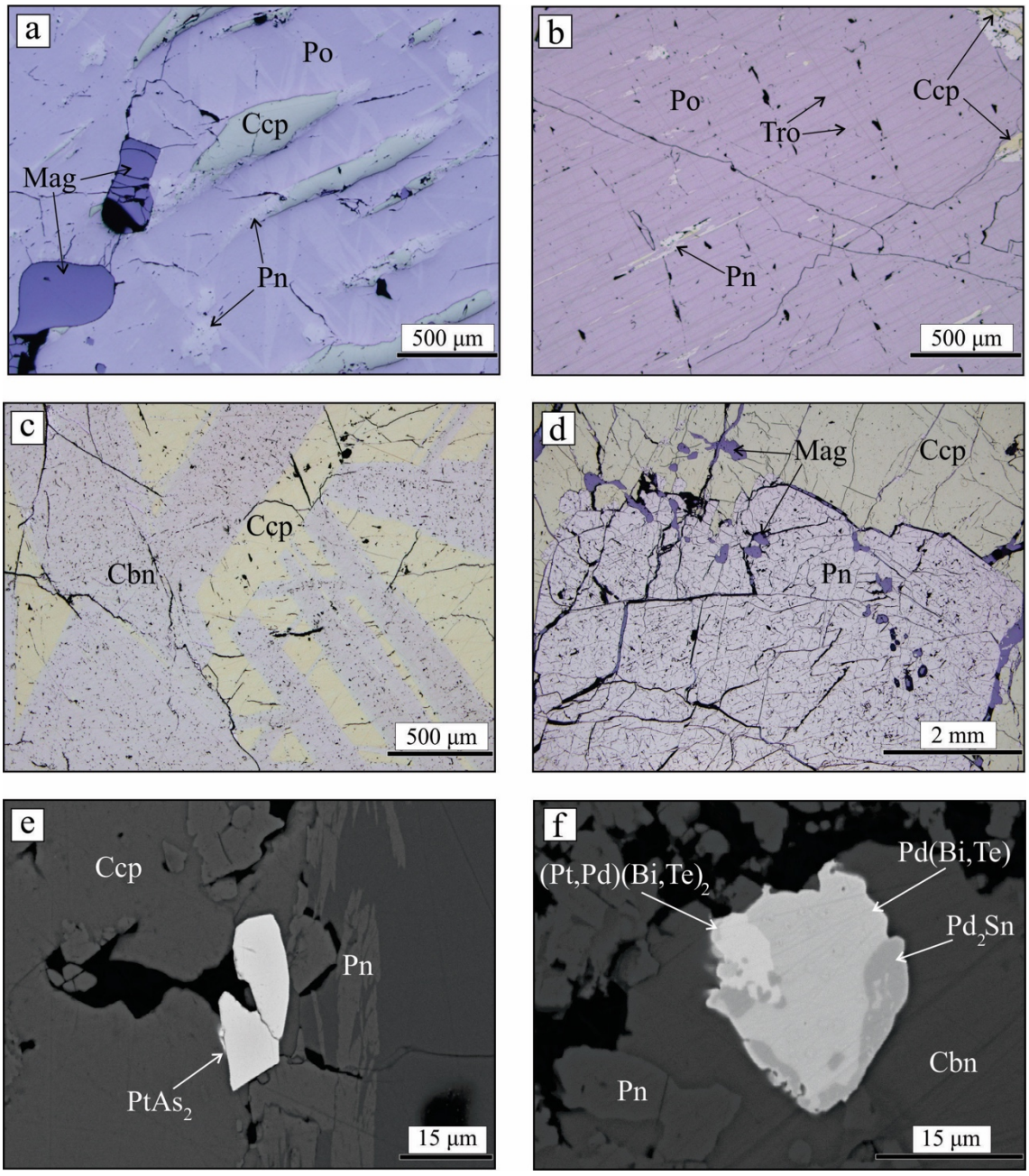

Figure 3.1 - Reflected light photomicrographs of representative textures of main massive sulfides from Noril'sk-Talnakh mining district, and backscattered electron images of platinum-group minerals in Cu-poor and Cu-rich ores. a) Exsolutions of pentlandite and chalcopyrite in pyrrhotite. b) Thin exsolution lamellae (<20µm) of troilite in pyrrhotite. c) Large (>100µm wide) exsolution lamellae of cubanite in chalcopyrite. d) Coarse-granular pentlandite in contact with chalcopyrite. Note inclusions of magnetite in pentlandite and chalcopyrite, and magnetite veinlets crosscutting both sulfides. e) Sperrylite ($PtAs_2$) grain enclosed in pentlandite and chalcopyrite in Cu-poor massive sulfide. f) Composite grain of maslovite ($(Pt,Pd)(Bi,Te)_2$) sobolevskite (Pd(Bi,Te)), and paolovite (Pd_2Sn) included in cubanite in a Cu-rich massive sulfide. Cbn- cubanite; Ccp- chalcopyrite; Mag- magnetite; Pn- pentlandite; Po- pyrrhotite; Tro- troilite.

The PGM and accessory phases of the samples are described in detail in Duran et al. (2017), and only a brief summary is provided here for the purpose of our study. In the disseminated sulfides and Cu-poor massive sulfides, Pt-bearing PGM (mainly sperrylite; Fig. 1e) and minor electrum are the main precious metal minerals. No Pd-, Rh- or IPGE-bearing PGM were observed in these ore types. In contrast, in the Cu-rich massive sulfides, Pt-only-PGM are rare, and most PGM consist of Pd-Pt-bismuthtellurides, arsenides and stanides. These minerals commonly form sub-spherical composite grains, showing intergrowth textures (Fig. 1f). The PGM of all ore types occur mainly enclosed by and/or in contact with BMS. No discrete phases that could potentially host significant levels of PGE other than PGM (e.g. Le Vaillant et al. 2018) were identified in previous studies (Duran et al. 2017).

3.4.1 - Distribution of chalcophile elements among the base-metal sulfides

The LA-ICP-MS compositional maps of samples containing Po, Pn and Ccp (Fig. 2) show that Mo, Re, Os and Ir are concentrated in Po. Cobalt, Ni, Pd, Ag, Pt, Tl, Pb and Bi are preferentially concentrated in Pn, and Cu, Zn, Cd, In, Sn and Te are concentrated in Ccp (Fig. 2). Ruthenium is evenly distributed between Po and Pn. In samples containing both Ccp and Cbn, Cu, In, Se, Te and Tl are more concentrated in Ccp, whereas Zn, Ag, Cd and Pb are more concentrated in Cbn (Fig. 3). The distribution of the trace elements in Cbn lamellae is not homogeneous. Higher concentrations of Zn, Ag and Cd are observed in the center of the Cbn lamellae relative to the edges (Fig. 3). Troilite lamellae are present in a few samples and compositional maps indicate similar trace-element concentrations between Po and Tro (Fig. 4). Compositional LA-ICP-MS maps of the rare galena grains (Fig. 5) indicate that they are enriched in Ag Cd, Te, Tl, Pb and Bi relative to the other base metal sulfides, but they do not contain PGE.

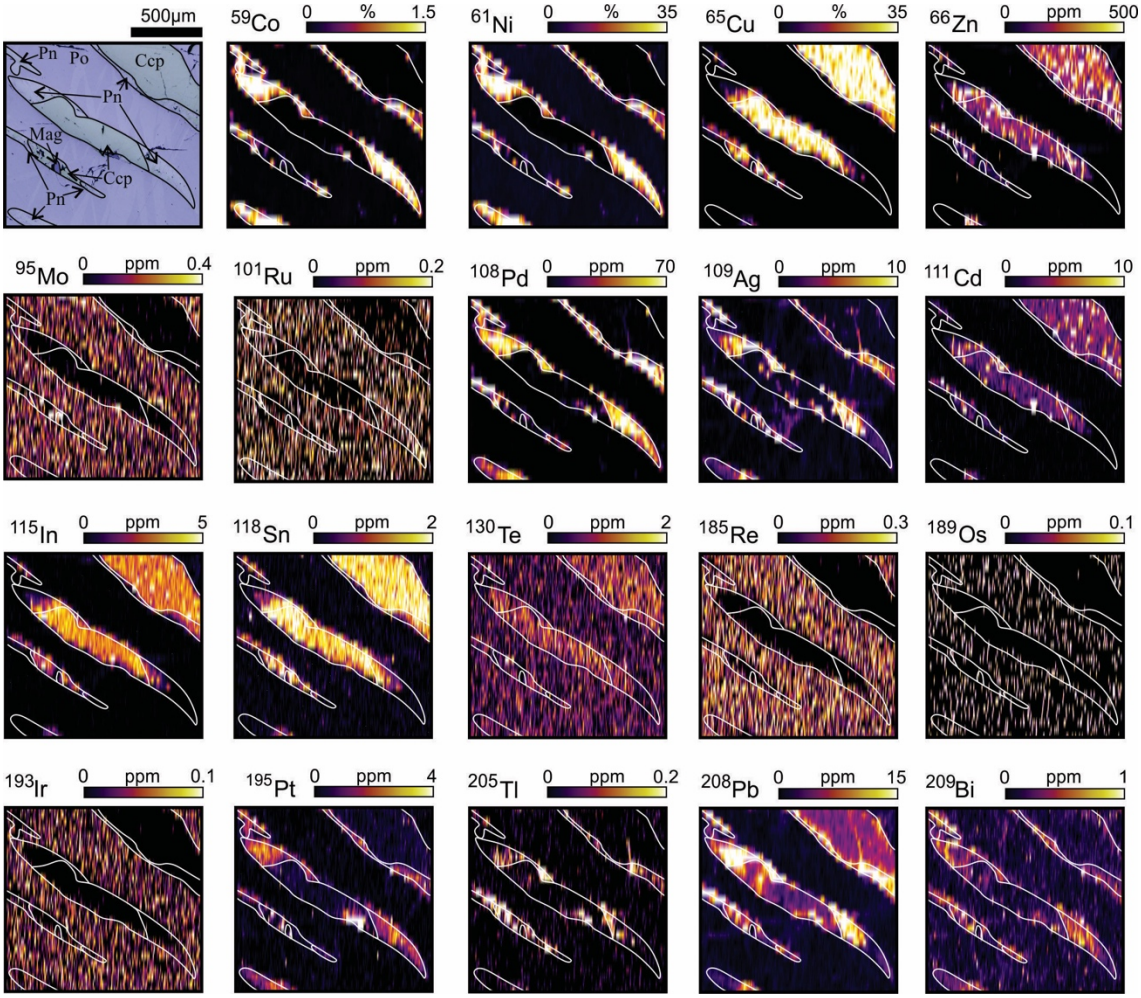

Figure 3.2 - LA–ICP-MS elemental maps showing the distribution of chalcophile elements in chalcopyrite and pentlandite exsolution lamellae in pyrrhotite from Cu-poor massive sulfides. White lines show the grain outlines. The concentrations of the elements are semi-quantitative. Ccp- chalcopyrite; Mag- magnetite; Pn- pentlandite; Po- pyrrhotite.

Median concentrations of Pn, Po, Ccp and Cbn from each sample, and the full LA-ICP-MS data set are reported in *ANNEXE 4 to 7*. Medians for each ore type and each locality are reported in Table 1.1. Typical time-signal diagrams show flat patterns for all of the elements, illustrating their homogeneous distribution within BMS. In some cases, the time-signal diagrams show peaks for some elements, indicating inclusions of PGM within BMS, these were not included in the integration that calculated the compositions.

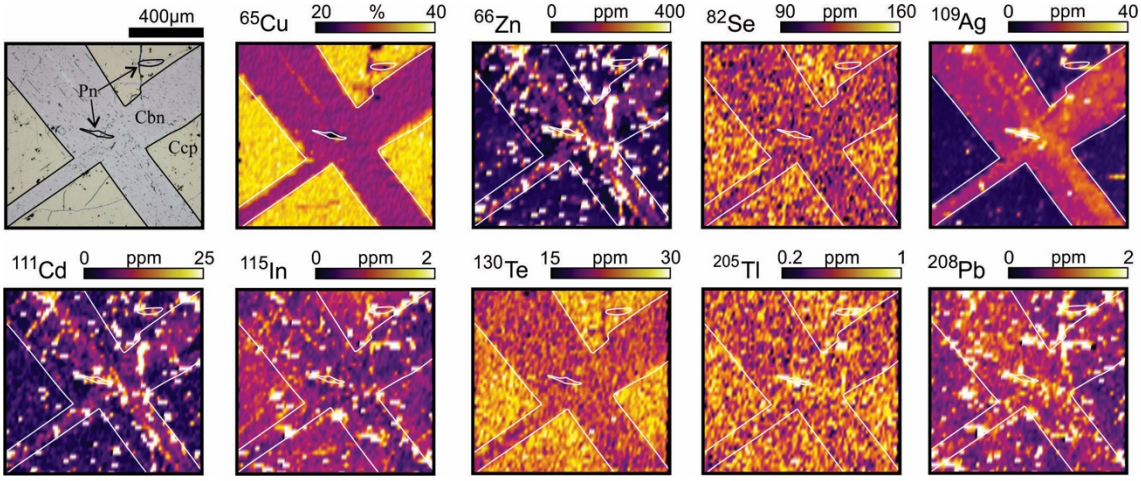

Figure 3.3 - LA–ICP-MS elemental maps showing the distribution of chalcophile elements in cubanite exsolution lamellae in chalcopyrite from Cu-rich massive sulfides. White lines show the grain outlines. The concentrations of the elements are semi-quantitative. Cbn- cubanite; Ccp- chalcopyrite; Pn- pentlandite.

As indicated by the maps of element distributions Co, Ni, As, Pd, Pt and Tl concentrations are highest in Pn (Table 1). Cobalt median concentrations in Pn are in the 0.4 to 1.5 weight percent range. Cobalt and Ni median concentrations in Po are in the 20 to 400 ppm, and 2000 to 25000 ppm range respectively, and are much higher than in Ccp or Cbn, which contain 0.1 to 10 ppm Co and 50 to 100 ppm Ni. Palladium is in the 50 to 1000 ppm range for Pn, whereas Po and Ccp contain only 0.01 to 7 ppm. Arsenic, Pt and Tl concentrations are in the 0.1 to 15 ppm range. In Po and Ccp the concentrations of As and Tl are close to detection limits and mostly <0.1 ppm.

Molybdenum, Ru, Rh, Re, Os and Ir are preferentially concentrated in Po, with Mo, Ru, Rh and Re in the 0.1 to 10 ppm range and Os and Ir in the 0.02 to 2 ppm range. Concentrations of these elements in Ccp and Cbn are close to detection limit. Pentlandite contains intermediate levels of the elements.

Zinc, Ag, Cd, In, Sn, Te and Pb are enriched in Ccp and Cbn (generally 100 to 1000 ppm for Zn, 1-50 ppm for Ag, Cd, Te and Pb and 0.1 to 10 ppm for In and Sn) relative to Pn and Po (Table 1). Overall, concentrations of these elements are higher in Pn than Po and concentrations covering the range of 0.05 to 10 ppm (Table 1). Copper concentrations in Pn and Po are similar in both minerals mostly in the 1 to 500 ppm range.

Selenium and Bi have similar concentrations in all sulfides in the 30 to 130 ppm and 0.1 to 1 ppm ranges, respectively. Gold concentrations are low in all sulfides at 0.01 to 0.1 ppm. Antimony concentrations are less than detection level for most of the sulfides (<0.05 ppm).

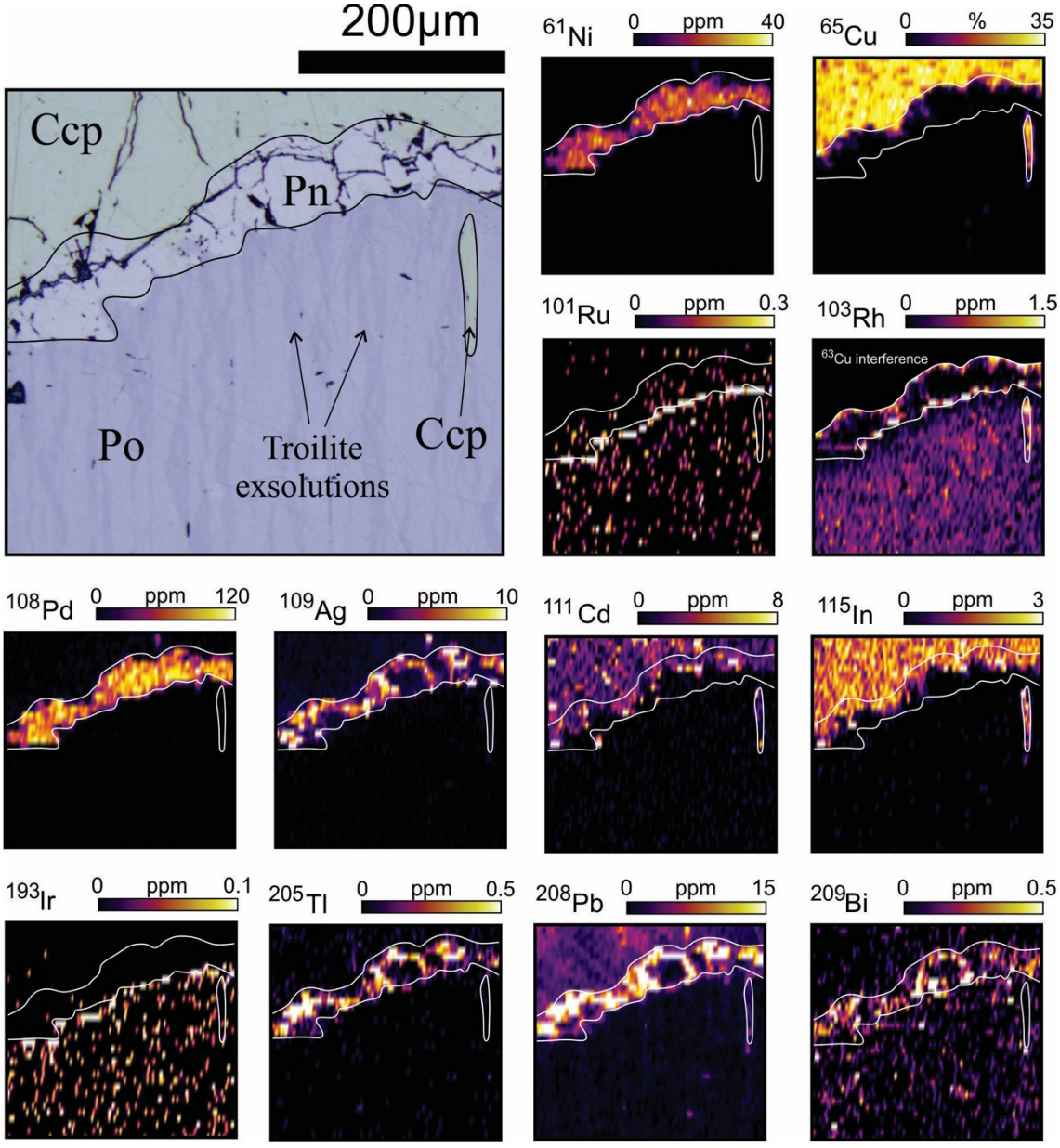

Figure 3.4 - LA–ICP-MS elemental maps showing the distribution of chalcophile elements among pyrrhotite (Po), pentlandite (Pn), chalcopyrite (Ccp) and troilite, in Cu-poor massive sulfide. White lines show the grain outlines. The concentrations of the elements are semi-quantitative.

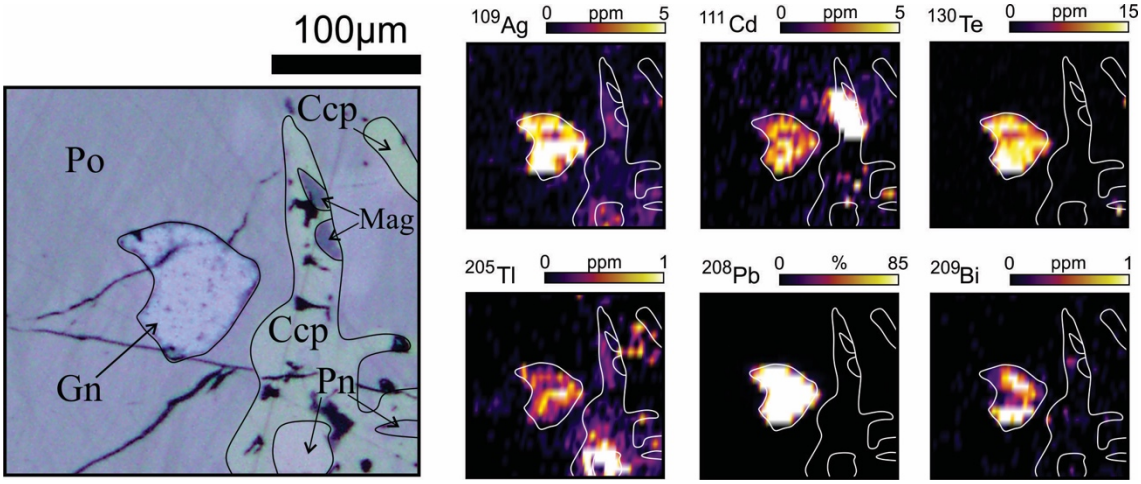

Figure 3.5 - LA–ICP-MS elemental maps showing the distribution of Ag, Bi, Cd, Pb, Te and Tl among galena (Gn), pyrrhotite (Po), pentlandite (Pn), chalcopyrite (Ccp) and magnetite (Mag), in Cu-rich massive sulfide. White lines show the grain outlines. The concentrations of the elements are semi-quantitative.

3.4.2 - Partition coefficients between base-metal sulfides

Partition coefficients were calculated for each sample using the median values of the minerals from the sample (*ANNEXE 8*). Figure 6 shows the median, minimum and maximum partition coefficients calculated between Pn and Po ($D_{Pn/Po}$), Pn and Ccp ($D_{Pn/Ccp}$), Ccp and Po ($D_{Ccp/Po}$), and Ccp and Cbn ($D_{Ccp/Cbn}$). The 25th and 75th percentile of the results are also shown for each element.

Estimates of the partitioning between Pn and Po (Fig. 6a) show that Pd and Co have the highest partition coefficients ($D_{Pn/Po}>10^2$), and Au, Tl, Pb, Pt and Ag have moderately high partition coefficients into Pn ($D_{Pn/Po}$= 1 to 10^2). Bismuth, Te, Sn, Se, As, Ru, Os, Ir, Rh, Re, Mo and Cd have partition coefficients around 1. Indium has a slightly preference for Po in comparison to Pn ($D_{Pn/Po}$ around 0.5). Copper and Zn have a median $D_{Pn/Po}$ of 1, but show wide variation according to the sample (Fig. 6a; *ANNEXE 8*).

The partition coefficients between Pn and Ccp (Fig. 6b) for Co, Ir, Pd, Pt Au and Tl are all high and vary from 10 to 10^3. Selenium, Pb, Ag, Bi, As, Te and Ru are evenly distributed between Pn and Ccp ($D_{Pn/Ccp}$ around 1), whereas Sn, Zn, Cd and In ($D_{Pn/Ccp}$= 10^{-2} to 10^{-1}) partition into Ccp. The partitioning between Ccp and Po (Fig. 6c) for Pt, Bi and Se is around 1. However,

Co, Ni, Mo ($D_{Ccp/Po}$ = 10^{-2} to 10^{-1}), Pd, Ru and Re ($D_{Ccp/Po}$ = 10^{-1} to 1) partition into Po and, Te, Tl, Au, Ag, Sn, Pb ($D_{Ccp/Po}$ = 1 to 10), Cd, In and Zn ($D_{Ccp/Po}$ = 10 to 10^{3}) partition into Ccp (Fig. 6c).

Estimates of the partitioning between Ccp and Cbn (Fig. 6d) reveal a more evenly distribution of elements in comparison to Pn and Po. The median partition coefficients between Ccp and Cbn ($D_{Ccp/Po}$) for Mo, Pd, Ru, Pt, Bi, Se, Te, Sn, Pb, As, In and Zn are around 1. Cobalt, Ni ($D_{Ccp/Cbn}$= 10^{-2} to 10^{-1}), Tl, Ag and Cd ($D_{Ccp/Cbn}$=10^{-1} to 1) partition into Cbn, whereas Au ($D_{Ccp/Cbn}$= 1 to 10) shows a preference for Ccp (Fig. 6d).

Table 3.1 - Median concentrations (in ppm) of chalcophile elements in base-metal sulfides from different intrusions and ores from the Noril'sk-Talnakh mining district.

	Pyrrhotite						Pentlandite			
Intrusion	Kharaelakh		Noril'sk I			Talnakh	Kharaelakh		Noril'sk I	
Ore type	Cu-poor	Cu-rich	Cu-poor	Cu-rich	Dissem.	Cu-poor	Cu-poor	Cu-rich	Cu-poor	Cu-rich
N (n)	4 (26)	4 (19)	2 (10)	1 (3)	1 (6)	1 (6)	4 (20)	5 (24)	2 (9)	3 (15)
Ag	0.35	3.22	1.63	0.90	2.85	1.34	4.55	4.20	2.98	33.5
As	bdl	bdl	0.45	0.60	0.18	bdl	0.22	0.17	0.23	0.57
Au	bdl	0.01	0.02	bdl	0.01	bdl	0.01	bdl	0.03	bdl
Bi	0.09	0.76	0.82	0.34	0.09	0.16	0.25	0.65	0.59	0.89
Cd	bdl	2.96	bdl	0.09	bdl	bdl	0.14	0.07	bdl	0.45
Co	50.9	48.6	368	99.7	534	399	13521	10256	10633	4370
Cu	3.14	269	1.39	22.44	0.97	1.10	195	71	13.4	11103
In	bdl	0.05	bdl	bdl	bdl	bdl	0.02	0.01	0.01	bdl
Ir	0.08	bdl	0.35	bdl	1.89	0.43	0.02	bdl	0.27	bdl
Mo	0.38	0.02	1.91	0.12	0.55	1.38	0.25	bdl	1.38	0.12
Ni	4151	2368	22367	8913	24433	17172	296052	354090	377696	308018
Os	0.06	bdl	0.17	bdl	0.89	0.21	bdl	bdl	0.12	bdl
Pb	1.12	36.2	9.70	2.72	0.06	0.17	15.7	25.6	45.9	8.35
Pd	bdl	1.50	1.37	0.37	0.61	1.83	54.9	180	390	1007
Pt	0.07	0.05	0.29	bdl	0.59	0.27	1.00	0.11	0.92	3.99
Re	0.16	0.14	0.15	bdl	0.16	0.34	0.09	bdl	0.11	0.16
Rh	0.91	bdl	3.55	bdl	16.7	3.78	0.11	bdl	3.90	1.80
Ru	0.20	bdl	0.69	bdl	4.73	0.53	0.21	0.13	0.68	0.21
Sb	bdl	bdl	bdl	bdl	bdl	bdl	bdl	bdl	bdl	bdl
Se	49.0	73.7	64.5	38.0	106	69.6	42.5	72.1	55.5	123
Sn	bdl	0.16	0.05	bdl	bdl	bdl	0.14	0.23	0.06	0.07
Te	0.89	3.66	2.11	0.39	11.70	1.60	1.00	5.18	1.88	35.88
Tl	bdl	0.04	0.01	bdl	bdl	bdl	0.15	0.89	1.00	0.37
Zn	0.28	111	0.19	1.43	0.21	bdl	17.3	1.27	63.7	1.81

Abbreviations: Dissem.= disseminated; N= number of samples; n= number of individual analysis; bdl= below etection limit; n.r.= not reported.

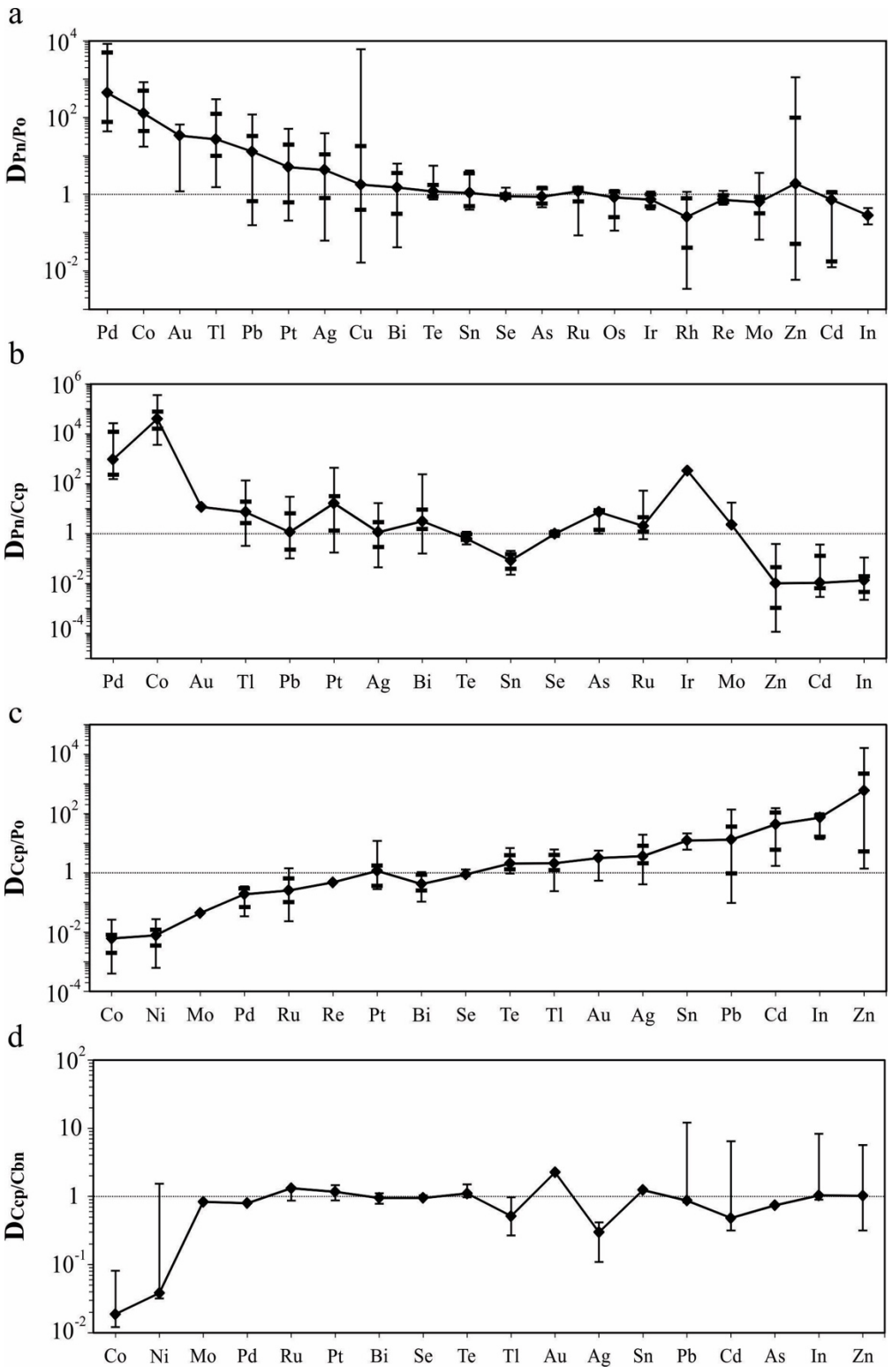

Figure 3.6 - Plots of median partition coefficients of each trace element between a) pentlandite and pyrrhotite (DPn/Po), b) pentlandite and chalcopyrite (DPn/Ccp), c) chalcopyrite and pyrrhotite (DCcp/Po), and d) chalcopyrite and cubanite (DCcp/Cub). The range indicates the minimun and maximun values obtained for each element in individual samples. The black dashes in the central part of the variation ranges indicate the 25th and 75th percentile of results. The results are reported in *ANNEXE 8*.

3.4.3 - Mass balance

The weight fraction of each element in each BMS was calculated to examine which mineral(s) host the bulk of each element for each ore type. The proportion of each element hosted in each BMS was calculated following the method used by Barnes et al. (2006). This calculation requires: i) the concentration of each element in the whole rock; ii) the median concentration of each element in each BMS (Table 1); and iii) the weight fraction of each BMS. The weight fraction of Ccp, Cbn, Po, and Pn were calculated using whole-rock Cu, Ni, and S and the concentrations of Cu and Ni in each mineral. The contribution of Ni present in Po was determined by LA-ICP-MS (*ANNEXE 4*) and subtracted from the Ni in the whole rock before the amount of Pn was calculated. In Cbn-free samples, all of the Cu was assigned to Ccp. In samples containing Cbn, Cu was assigned to Ccp and Cbn, using the Cbn/Ccp ratio obtained by petrographic observations (approximately 1:5). The remaining S was attributed to Po. The accumulated error of the different results used for the mass balance calculation is approximately 20% at one standard deviation (1σ). The mass balance of Re was not calculated as the whole-rock concentrations are too low (Duran et al. 2017). The mass balance for Rh, Ru, Ir and Os was also not calculated for the Cu-rich ores because of the low levels of these elements in the whole rock (*ANNEXE 9*).

The BMS from the Cu-poor ores host the bulk (>70%) of the Cd, Co, In, Mo, Pd, Te, Se, Zn, Rh, Ru, Ir and Os (Fig. 7a; *ANNEXE 9*). Given the various uncertainties in the calculation (e.g. sampling, precision of whole-rock and LA-ICP-MS analyses), we consider that all of these elements are essentially present in the BMS. The BMS assemblage also hosts significant amounts of the Bi, Pb, Ag, Sn and Tl (15-70%), but only minor amounts (<10%) of the As, Au and Pt.

In Cu-rich ores (Fig. 7b), the BMS host a significantly lower proportion of chalcophile elements in comparison to Cu-poor ores. The BMS host the bulk (>50%) of the Co, Cd, In, Se, Te and Zn, and significant amounts (20 to 50 %) of the Ag, Pb and Pd. Less than 10 % of the As, Au, Bi, Mo, Pt and Tl is present in BMS. Samples with Cbn were treated separately in order to consider the contribution of this mineral, which hosts less than 10% of bulk Ag, Cd, In, Mo, Pb, Te, Tl and Zn (Fig. 7c). The mass balance for samples with Cbn is similar to other Cu-rich

samples but with some minor differences for Ag, Cd, Co, Mo, Pb, Sn, Te, Tl and Zn (Fig. 7b and 7c).

Pyrrhotite hosts most of Os, Ir, Ru, Rh, and Mo. Chalcopyrite and cubanite host most of the Cd, In, Sn, Pb and Zn. Pentlandite hosts most of the Co and Pd. Selenium and Te are present in all BMS, and the main host is the most common mineral in each ore type. Thus, Po is the main host of Se and Te in the Cu-poor ore, whereas Ccp is the main host in the Cu-rich ore.

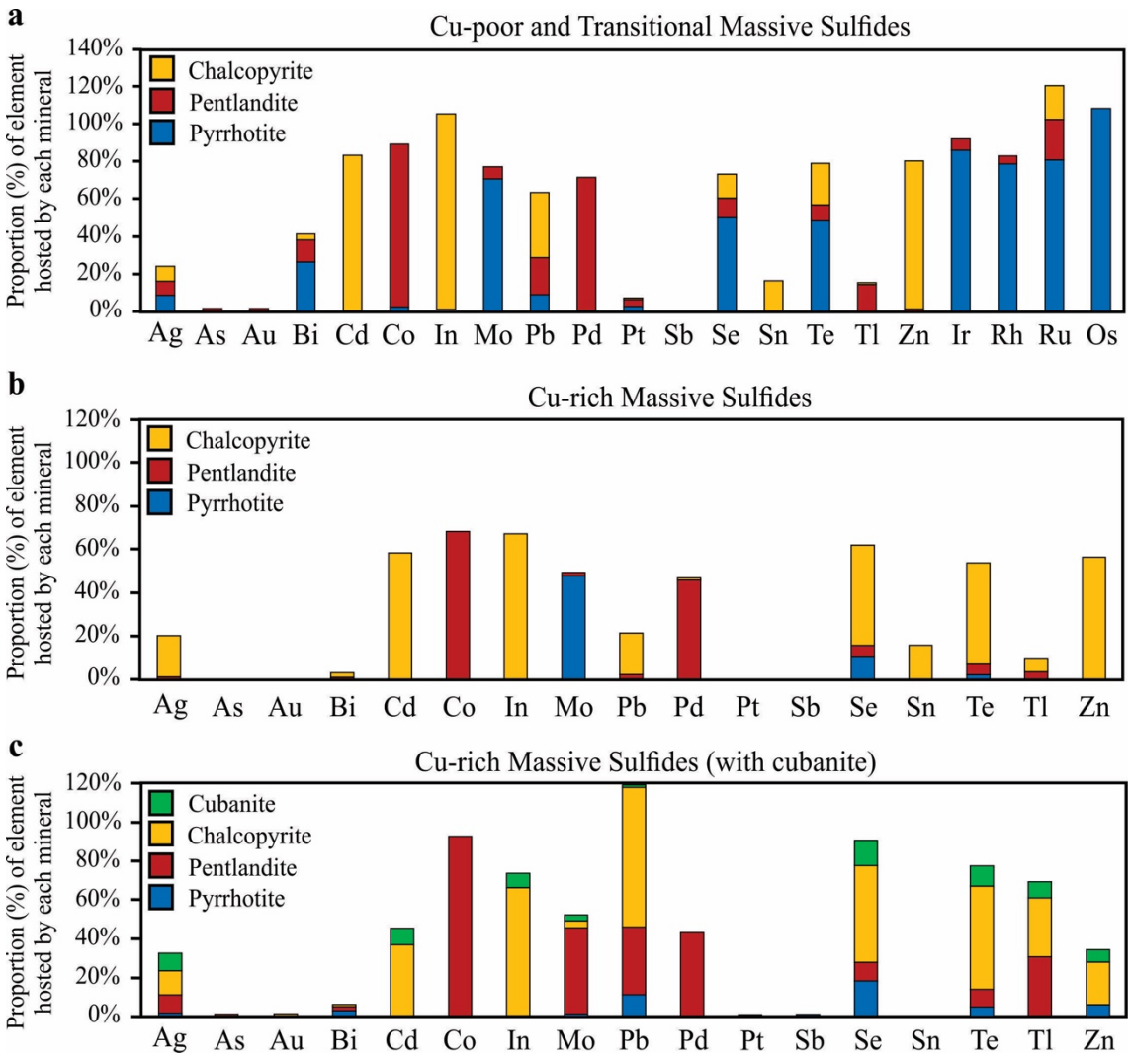

Figure 3.7 - Average proportion (%) of each element hosted in pyrrhotite (Po), pentlandite (Pn), chalcopyrite (Ccp), cubanite (Cbn) and sum, from the a) Cu-poor and Transitional, b) Cu-rich and c) Cu-rich (with cubanite) ores of the Noril'sk-Talnakh mining district. The whole-rock data used for the calculation is reported by Duran et al. (2017). Values above 100% are related to low whole-rock concentrations.

3.5 - Discussion

3.5.1 - Variations in chalcophile element content of the minerals with fractional crystallization

There is a systematic variation in the median trace element concentration in the BMS with (Pt+Pd)/(Ru+Rh+Ir+Os) of the whole rocks. The median concentrations of elements predominantly hosted by Po: Ru, Rh, Re, Os, Ir and Mo, decrease as the whole-rock (Pt+Pd)/(Ru+Rh+Ir+Os) increases (Fig. 8a-d). The median concentration of elements hosted by Ccp: Cd, In, Sn and Pb increases as the whole-rock (Pt+Pd)/(Ru+Rh+Ir+Os) increases (Fig. 8l-o). Zinc is the only element showing a different behaviour with respect to different BMS, with increasing concentrations in Po, and decreasing concentrations in Ccp as the whole-rock (Pt+Pd)/(Ru+Rh+Ir+Os) increases (Fig. 8e and m). Decreasing Zn concentrations in Ccp likely reflect a dilution caused by the larger amount of ISS (and consequently Ccp) crystallizing, with progressive fractionation of the sulfide liquid.

Our results support the model that progressive crystallization of the sulfide liquid fractionates PGE, and other chalcophile elements, at least partially in response to their different compatibility with MSS and ISS. As the sulfide liquid evolves, concentration of the elements compatible with MSS (Co, Mo, Re, Rh and IPGE; Barnes et al., 1997; Mungall, 2005; Liu and Brenan, 2015) decreases in the liquid. This is reflected in a decrease in their concentrations in BMS antithetical to whole-rock (Pt+Pd)/(Rh+Ru+Os+Ir) (Fig. 8a-d). In contrast, a striking outcome is that BMS crystallizing from the evolving liquid become richer in most incompatible elements (Pd, Ag, Bi, Cd, In, Pb, Sn, Se, Te, Tl and Zn; Patten et al. 2013; Dare et al. 2014; Liu and Brenan, 2015; Fig. 9e-o), but at the same time account for lesser amounts of their whole-rock budget (Fig. 7).

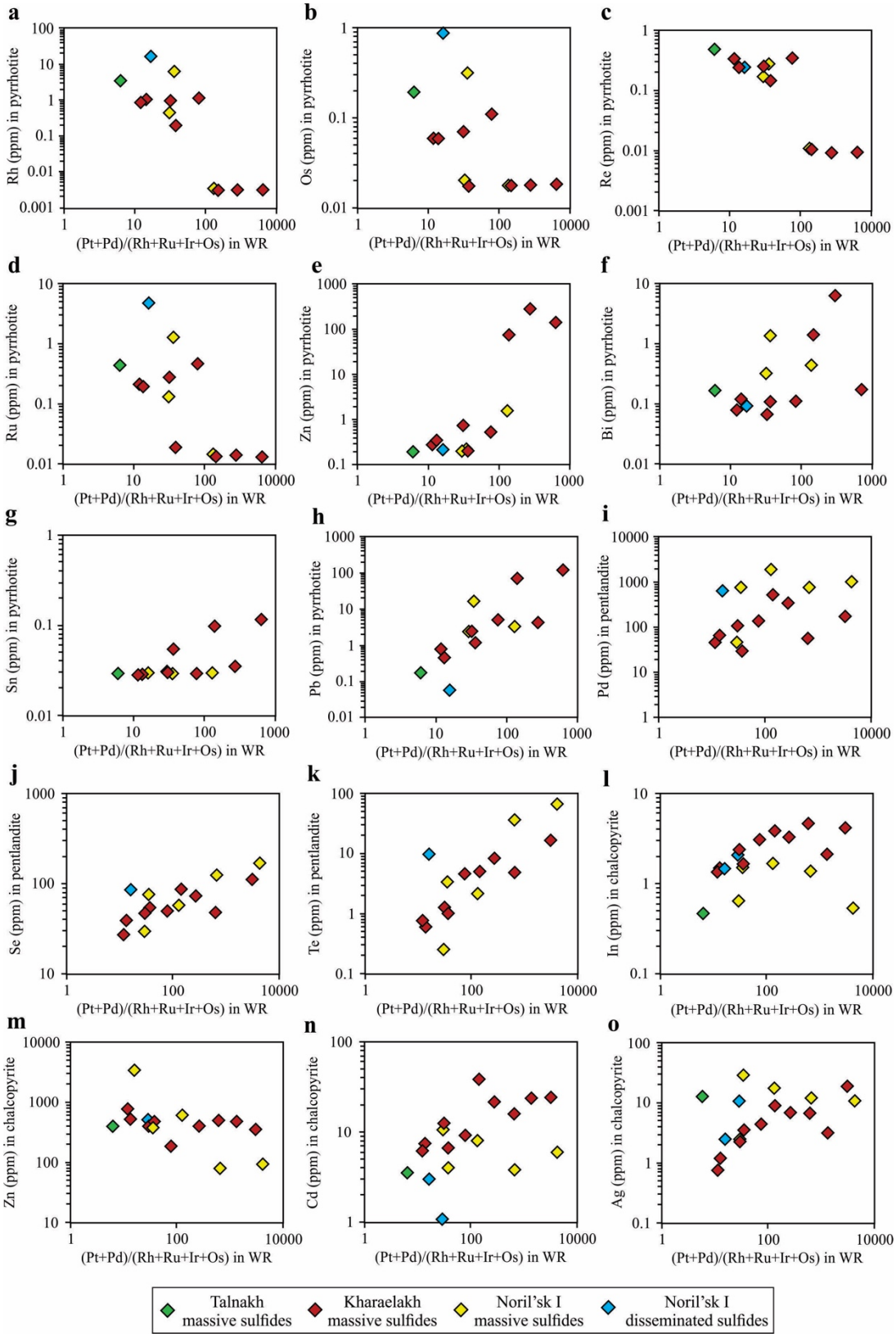

Figure 3.8 - Binary plots of Rh (a), Os (b), Re (c), Ru (d), Zn (e and m), Bi (f), Sn (g), Pb (h), Pd (i), Se (j), Te (k), In (l), Cd (n) and Ag (o) median concentrations (ppm) in pyrrhotite, chalcopyrite and pentlandite versus (Pt+Pd)/(Rh+Ru+Ir+Os) in whole-rock (WR), for massive sulfides from Noril'sk I, Kharaelakh and Talnakh intrusions, and disseminated sulfides from the Noril'sk I intrusion.

In the ore formed from the least fractionated liquid (Cu-poor), the BMS host the majority of trace chalcophile elements, but in the ore formed from the most fractionated liquid (Cu-rich), BMS host significantly less of these elements (Fig. 7). To further assess how fractional crystallization affects the distribution of chalcophile elements within a crystallizing sulfide liquid, especially in the latest stages, we discuss below the possible scenarios for the origin of PGM. Thereafter, we will summarize the fractional crystallization history of BMS in the Norils'k-Talnakh mining district, and reconstruct the partition of chalcophile elements during the evolution of the sulfide liquid.

It is noteworthy that although the concentration of trace elements in BMS is controlled by the fractional crystallization of the sulfide liquid, other processes may also affect their distribution. This may be particularly important considering that not all BMS crystallized at the same time. Mansur et al. (2019) showed that loop-textured Pn, located at the contact between Po and Ccp formed via peritectic reaction at higher temperatures (i.e. around 950ºC) relative to granular and flame Pn, which exsolved from the MSS at low temperatures (i.e. below 650ºC). The authors also indicate that some incompatible elements such as Pd could be incorporated from the fractionated sulfide liquid into this high-form of Pn. Thus, higher concentrations of Pd in Pn could be also found in Pn from Cu-poor massive sulfides, even though these crystallized from a less fractionated sulfide liquid. A possible illustration of this process is the distribution of Pd in Pn from massive sulfides of the Noril'sk I intrusion, which is not entirely controlled by the whole-rock fractionation (Fig. 3.8i). In this case, the Pn grains most likely formed during two different stages, and their composition is not exclusively controlled by the degree of fractionation of the sulfide liquid.

3.5.2 - Timing of PGM formation

In both the Cu-poor and Cu-rich ores, the bulk of trace elements that are not entirely hosted by BMS minerals must be accounted for by the presence of PGM and other discrete minerals. In Cu-poor ore, Pt, As, Au, Ag and Sb are hosted by Pt-arsenides (mostly sperrylite),

isoferroplatinum, and minor electrum (Duran et al. 2017). In contrast, a greater variety of PGM was observed by Duran et al. (2017) in the Cu-rich ores. The PGM assemblage consists of Pd-Pt-bismuthtellurides, arsenides and stanides, which occur either as single-phased grains, or sub-spherical composite grains (Fig. 1e and f). Laser profiles reveal the presence of Ag, Pb, Sb, and Tl within these composite PGM grains. In addition to their presence in the PGM some of the Ag, Cd, Te, Tl and Pb and Bi could be also hosted by galena as indicated by the LA-ICP-MS map (Fig. 5). Duran et al. (2017) interpreted these composite grains as the crystallization product of the lattermost fractionated sulfide liquid. A similar model was proposed for composite PGM grains in Cu-rich veins at Sudbury (Dare et al. 2014).

In contrast to this model of late crystallization of the PGM, it has been shown that the PGM may directly crystallize from the sulfide liquid prior to MSS crystallization at some localities e.g. the Creighton deposit, Sudbury (Dare et al. 2010a), and the Platreef (Bushveld. Power et al. 2004; Hutchinson and McDonald 2008). Assimilation of TABS (especially As) from the surrounding country rocks is thought to have favoured this direct crystallization (Hutchinson and McDonald 2008; Dare et al. 2010a). However, although the contamination of TABS from country rocks appears to be an important process in the Noril'sk-Talnakh mining district, there is no evidence for early crystallization of PGM from the sulfide liquid. On the contrary, high-resolution X-Ray computed tomography in Cu-poor ores indicated that the few PGM present in this ore type have an elongated shape, and likely formed by exsolution from the BMS (Duran et al. 2017).

The progressive concentration of TABS during fractionation could lead to the crystallization of PGM from a much fractionated sulfide liquid, or as suggested by a number of authors, to the segregation of an immiscible TABS-rich liquid (Hanley 2007; Helmy et al. 2007, 2013; Holwell and McDonald 2007; Mavrogenes et al. 2013). The form of PGM in the Cu-rich ores as intergrowths of Pd-Pt-Au-TABS minerals in small sub spherical patches (Fig. 1f and Duran et al. 2017) could be interpreted to support either model.

Experimental studies show that immiscible TABS-rich liquids can form from a BMS liquid (Helmy et al. 2007, 2010, 2013; Mavrogenes et al. 2013; Liu and Brenan 2015; Cafagna and Jugo 2016; Distler et al. 2016; Sinyakova et al. 2017; Bai et al. 2017) and natural examples of this process have been proposed (Piña et al. 2015). However, the concentrations of TABS required to achieve saturation are very high (200 to 1000 ppm), and most natural sulfide liquids do not appear to reach these levels. Liu and Brenan (2015) applied their experimental results to the Cu-rich ores of McCreedy East (Sudbury) and concluded that the liquid did not contain sufficient TABS to have segregated an immiscible TABS liquid. The Noril'sk and Kharaelakh Cu-rich samples are similar to McCreedy East, both in terms of textures of PGM and concentrations of TABS (Fig. 9). The Cu-rich samples with highest TABS concentrations only contain ~50 ppm (Duran et al. 2017), insufficient to form an immiscible TABS liquid. Duran et al. (2017) calculated that the sulfide liquid would have to have undergone more than 99.9% fractional crystallization for the liquid to be sufficiently rich in TABS to form an immiscible liquid. Therefore we propose that the PGM intergrowths in the Cu-rich ores crystallized from the sulfide liquid after extensive fractional crystallization of MSS and ISS.

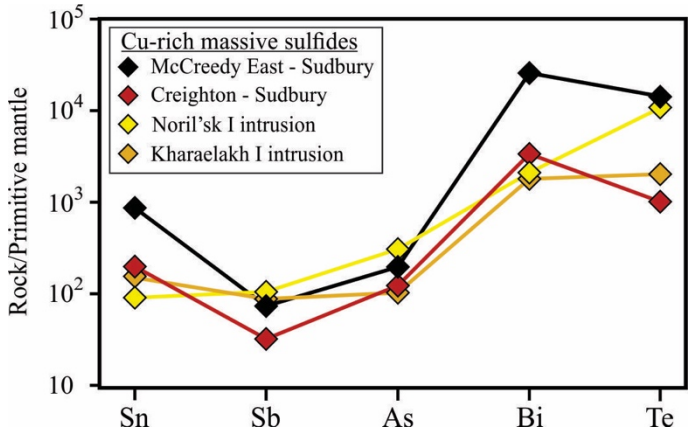

Figure 3.9 - Mantle-normalized Te, As, Bi, Sb and Sn (TABS) whole-rock concentrations of Cu-rich massive sulfides from McCreedy East (Dare et al. 2014) and Creighton (Dare et al. 2010a) deposits, and Noril'sk I and Kharaelakh intrusions (Duran et al. 2017). Concentrations have been recalculated to 100% sulfides following Barnes and Lightfoot (2005). Primitive mantle values from Lyubetskaya and Korenaga (2007).

3.5.3 - Fractional crystallization of massive sulfides and constraints for the formation of platinum-group minerals

We used the systematic variation of trace elements in BMS, and mass balance, to assess the behaviour of PGE and other chalcophile elements during fractional crystallization of sulfide liquid (Fig. 10a). Upon cooling (below 1190 ºC), MSS started to crystallize from the initial sulfide liquid and incorporated IPGE, Rh, Re, Mo and some Ni, Co, Se, whereas Cu, Pt, Pd, Au, TABS, Zn, Ag, Pb, Cd, In and Tl largely partitioned into the fractionated liquid (Fig. 10b; Li et al. 1996; Barnes et al. 1997; Mungall et al. 2005; Liu and Brenan 2015). We interpret the Cu-poor ores as being representative of MSS adcumulates.

Below 950ºC, the Cu-rich liquid started to crystallize as ISS, which incorporated Cu, Cd, Co, In, Se, Sn and Zn. Palladium, TABS, Ag, Pb, and Tl are moderately to strongly incompatible with ISS, and their concentrations in the remaining sulfide liquid increased (Fig. 10c). In the late stages of crystallization, the trapped sulfide liquid became sufficiently enriched in incompatible elements (i.e. especially TABS) to crystallize as composite PGM grains, electrum and galena (Duran et al., 2017; Fig. 10d). We interpret the Cu-rich ores as ISS cumulates with variable amounts of fractionated sulfide liquid trapped among the grains.

Not all Pn formed in the same way. Pentlandite found at the contact between Ccp and Po formed by peritectic reaction between MSS and Cu-rich liquid, below 900ºC (Mansur et al. 2019). The distribution of trace elements in Pn formed during this peritectic reaction is detailed by Mansur et al. (2019*)*. Some Pn formed during exsolutions of MSS. Below 650ºC, MSS exsolved into Po+Pn±Ccp (Fig. 10d). During this exsolution the elements compatible with MSS (Mo, Re, Rh and IPGE) distributed evenly between Pn and Po ($D_{Pn/Po}$ around 1; Fig. 7). The elements slightly to moderately incompatible with MSS partitioned either into Pn (Ni, Co, Pd and Tl), Ccp (Zn, Cd, In, Sn) and PGM (Pt, As) (Fig. 10d). Some incompatible elements (Ag, Te, Pb, Bi) partitioned into both Pn and Ccp, whereas Se shows no preference among the BMS (Fig. 6).

Thus, although concentrations of incompatible elements are expected to be low in BMS exsolved from the MSS, slightly higher concentrations can be locally found, such as Pd in exsolved Pn (Fig. 2). This is because the small fraction of incompatible elements incorporated by the MSS have partitioned into reduced volumes of exsolved Pn, leading to locally higher concentrations.

Intermediate solid solution exsolved into Ccp+Pn±Cbn (Fig. 10d and 10e). During the exsolution of the ISS, the elements distributed themselves between Ccp and Pn in a similar manner to that observed during the exsolutions of the MSS. However, some PGM that exsolved from BMS are more varied with some containing Pd-Te-Bi and many containing Pt-Pd-Sn (Fig. 10a to c of Duran et al. 2017). Cubanite only exsolves below 200ºC and the partition coefficients between Ccp and Cbn ($D_{Ccp/Cbn}$) are normally around 1 for most elements. Exceptions to this are Ni, Co, Tl and Ag which partition into Cbn (Fig. 6).

The partition coefficients between Pn and Po (Fig. 6a) for Pd and Co are much higher (with $D_{Pn/Po}$ up to 10^3) than the partition coefficients between Ccp and Cbn (with $D_{Ccp/Cbn}$ normally below 10; Fig. 6d). This may be due to relative similarity of the Ccp and Cbn structures as compared with to Pn and Po structures. Alternatively, this may be related to the temperatures at which these minerals formed. Pentlandite starts to form via peritectic reaction between the MSS and the sulfide liquid around 950ºC (Mungall 2007; Mansur et al. 2019). Furthermore, MSS begins to exsolve into Pn around 650 ºC, whereas Cbn only forms around 200 ºC (Cabri 1973; Dutrizac 1976; Kelly and Vaughan 1983;). In fact, Tro exsolutions in Po, which form at even lower temperatures (i.e. <145ºC; Kissin and Scott 1982; Naldrett 2011; Fig. 10e), do not affect the distribution of chalcophile elements (Fig. 4).

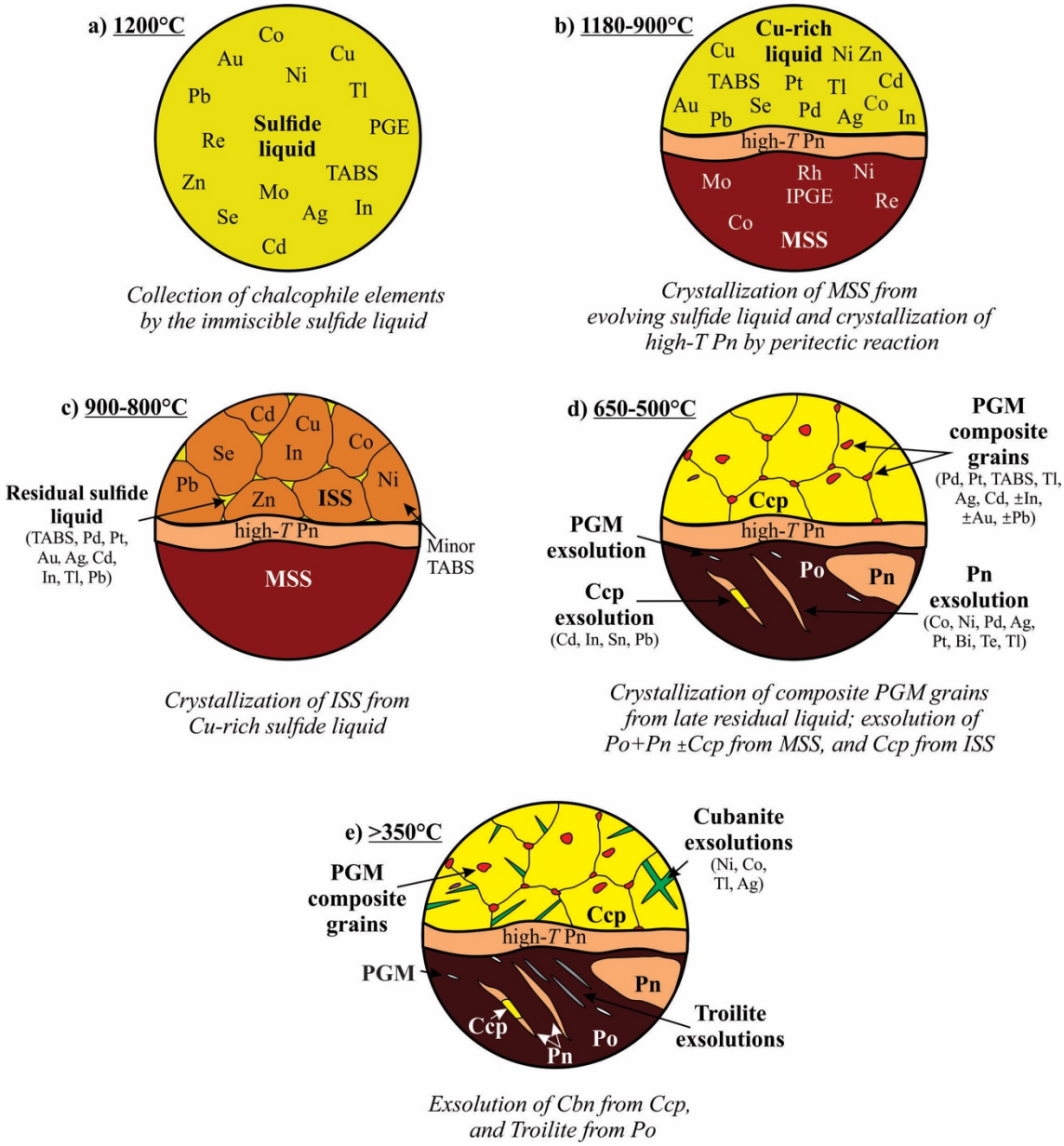

Figure 3.10 - Schematic models illustrating the crystallization history of massive sulfides from the Noril'sk-Talnakh mining district, and the processes controlling the distribution of PGE and other chalcophile elements. See text for further explanation. Abbreviations: MSS- monosulfide solid solution ; ISS- intermediate solid solution; Po- pyrrhotite; Pn- pentlandite; Ccp- chalcopyrite; Cbn- cubanite.

3.5.4 - Assessing the evolution of magmatic sulfide deposits via comparison of BMS compositions

Over the past few years, many authors have investigated the distribution of PGE among BMS in Ni-Cu-PGE deposits (Barnes et al. 2006, 2008; Godel et al. 2007, 2012; Holwell and McDonald 2007; Godel and Barnes 2008; Smith et al. 2014; Chen et al. 2015; Junge et al. 2015; Sessa et al. 2017; Yudovskaya et al. 2017). Recent studies have determined the concentrations of a wider range of chalcophile elements (e.g. Sudbury – Dare et al. 2010b, 2011, 2014; Aguablanca – Piña et al. 2012; Lac des Iles – Duran et al. 2016, 2019; Voisey's Bay – Amaral 2017). Comparisons of the deposits using a wide suite of trace element in BMS may now begin to be used as an attempt to access processes that took place during ore formation.

Compositions of the minerals are compared on mantle normalized diagrams with the elements in increasing order of incompatibility with picritic basalt mantle sources (Barnes 2016). We have plotted the compositions of Po, Pn, Ccp and Cbn from Cu-poor and Cu-rich ores from Sudbury (Creighton and McCreedy East deposits), Voisey's Bay (Ovoid body) and Noril'sk I, Talnakh and Kharaelakh intrusions (Fig. 11). Given that in the Aguablanca and Lac des Iles deposits massive sulfide bodies are relatively minor and poorly zoned in terms of Cu, we only compare the massive sulfide from the Noril'sk-Talnakh mining district, with those of Sudbury and Voisey's Bay.

In most magmatic sulfide deposits Pt, As, Sb and Au concentrations in BMS are very low, but Pt concentrations in BMS (especially in Pn and Po) from Noril'sk I, Talnakh and Kharaelakh intrusions are slightly higher (Fig. 11a to 11d). This observation supports the interpretation of Barnes et al. (2008), which related the higher concentrations of PGE in BMS to faster cooling rate at Noril'sk I. In addition, Pd concentrations are also higher in Pn from Noril'sk I and Kharaelakh intrusions in comparison to Voisey's Bay and Sudbury (Fig. 11c and d). The higher concentrations of Pd in BMS are thought to be the result of the higher concentration of Pd in the Noril'sk-Talnakh sulfide liquid.

The degree of fractional crystallization experienced by the sulfide liquid is also recorded by BMS. The concentrations of elements incompatible with MSS (Cd, Se, Ag and Te) are higher in Ccp and Cbn from Cu-rich ores from the Noril'sk I and McCreedy East deposits (Fig. 11f and g) relative to those from Kharaelakh and Voisey's Bay. This probably indicates that sulfides from Noril'sk I and McCreedy East have experienced more extensive fractionation. In fact, Cu-rich ores at Noril'sk I and McCreedy East show a physical separation (as veins) from the MSS (Mungall 2007; Dare et al. 2014; Duran et al. 2017). Mungall (2007) supports that these physically separated sulfides record an extensive degree of fractional crystallization, and may be regarded as ISS cumulates segregated from a fractionated sulfide liquid. This is not the case for the samples from the other localities that were analysed.

Another variable that affects the distribution of chalcophile elements in magmatic sulfide deposits is the nature of the co-crystallizing phases. Chalcopyrite and Cbn from McCreedy East and the Ovoid, respectively, host significant amounts of Sn, whereas Ccp and Cbn from Noril'sk I and Kharaelakh, are not main hosts of Sn (Fig 11f and g). Magnetite can be important for the Sn budget (Dare et al. 2012). At Noril'sk and Kharaelakh Sn is present in composite PGM grains and magnetite. It seems likely that the crystallization of these other phases affected the composition of co-crystallizing BMS, but this still need to be investigated.

The compositions of BMS from Voisey's Bay (Amaral 2017) also give some clues about the influence of BMS assemblage on the distribution of trace elements. Cubanite from Cu-rich ores at Voisey's Bay has high concentrations of incompatible elements (Ag, Bi, Cd, Pb, Sn, Te and Zn; Fig. 11g). These high contents are probably related to a greater proportion of Cbn in comparison to Ccp in the Cu-rich ores. Therefore, in the absence of Ccp, incompatible elements that were once incorporated by ISS partitioned into Cbn exsolutions.

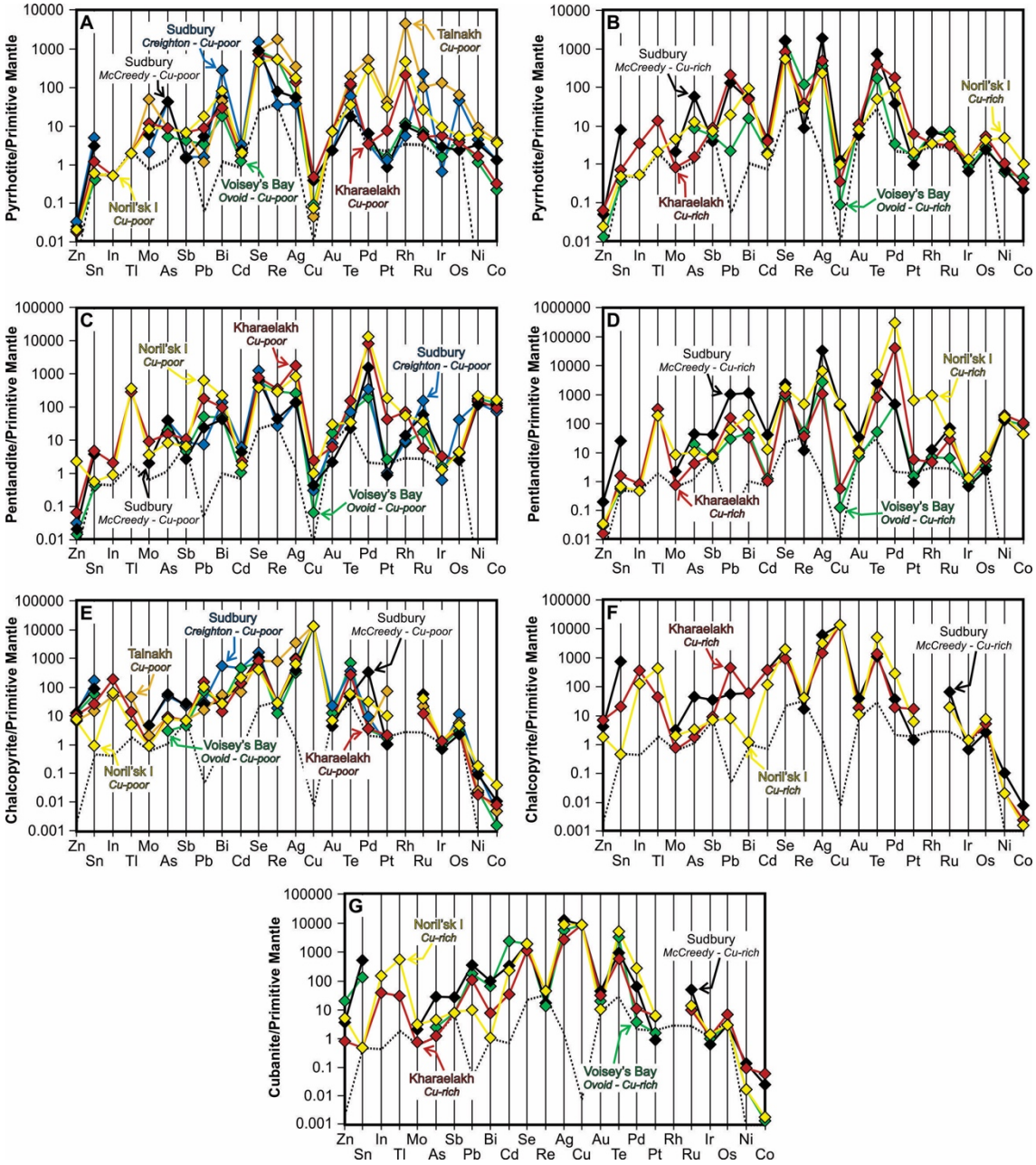

Figure 3.11 - Primitive mantle normalized multi-element diagrams of median compositions of pyrrhotite (a-b), pentlandite (c-d), chalcopyrite (e-f) and cubanite (g) in Cu-poor and Cu-rich ores from different deposits. Comparison of BMS from Noril'sk I, Kharaelakh and Talnakh intrusion (this study), with Creighton (Dare et al. 2010b), McCreedy East (Dare et al. 2014), and Voisey's Bay (Amaral 2017). Primitive mantle values from Lyubetskaya and Korenaga (2007). Elements are plotted from left to right in increasing order of incompatibility with picritic basalt mantle sources (Barnes 2016). Detection limits are plotted for reference (dashed line).

3.6 - Conclusions

This study provides insights into the behaviour of chalcophile elements during fractional crystallization of sulfide liquid, and whether Te, As, Bi, Sb and Sn (TABS) are important for controlling the timing for the formation of PGM. Our main findings are summarized as follows:

1 – Massive sulfides formed via fractional crystallization of a sulfide liquid. Cu-poor ores consist of early formed MSS adcumulates, and Cu-rich ores consist of ISS cumulates with various amounts of trapped fractionated sulfide liquid.

2- Mass balance reveals that in Cu-poor ores, BMS minerals contain the bulk of the PGE and other chalcophile elements. Platinum, Au, As and Sb are exceptions to this. Platinum, Au and As are present as PGM. In contrast, in the Cu-rich ores, the BMS minerals host a significantly lower proportion of the PGE and chalcophile elements. In the Cu-rich ores the balance of chalcophile elements are accounted by subspherical intergrowths of PGM and Au, and grains of galena.

3 – In the Cu-poor ores, TABS do not play a role in controlling the PGE, with most IPGE and Pd in Po and Pn. Platinum is an exception. Platinum and As appear to be exsolved to out of the MSS structure and to have formed discrete minerals, but these are still enclosed in Po or Pn. In the Cu-rich ore the Pd is partly present in Pn, and some Pt and Pd are present as exsolutions of Pd-Te-Bi and sperrylite and rustenburgite. However most of the Pd and Pt are present as intergrowths of Pd-Pt-TABS-rich minerals, representing the lattermost sulfide liquid.

4 – Cryptic variations in trace element contents of the BMS show variable co-variance with the degree of crystallization as indicated by whole rock (Pd+Pt)/(Rh+Ru+Ir+Os). Elements compatible with MSS (Co, Mo, Re, Rh and IPGE) are enriched in Po and Pn in rocks with low (Pd+Pt)/(Rh+Ru+Ir+Os), relative to rocks with high (Pd+Pt)/(Rh+Ru+Ir+Os). Similarily, Po, Pn and Ccp from early formed MSS are depleted in elements incompatible with MSS (Ag, Bi, Cd, Cu, In, Se, Sn, Te, Tl, Pb, Pd and Zn) relative to BMS that formed from the more fractionated sulfide liquid. These variations support that the composition of BMS is partially controlled by the degree of fractional crystallization underwent by the sulfide liquid.

5 – Comparison of a wide suite of trace element in BMS from different Ni-Cu-PGE deposits may allow for the assessment of different steps of the evolution of magmatic sulfide deposits including: i) the degree of fractionation of the sulfide liquid, and ii) the possible influences of co-crystallizing phases in the composition of BMS.

3.7 - Acknowledgments

This work was supported by a Canada Research Chair program grant to Sarah-Jane Barnes (215503). We would like to thank Dany Savard (LabMaTer, UQAC) for his assistance with LA-ICP-MS analyses, and Michael Zientek (USGS) for sharing his valuable samples. Organizers of the 12th International Platinum Symposium, field trip leaders (Nadezhda Krivolustskaya, Viktor Rad'ko, Kreshimir Malitch, Vadim Distler, and Valery Fedorenko), and Noril'sk Nickel geologists are gratefully acknowledged for providing rare access to the Noril'sk area. This manuscript benefited from insightful comments from Marco Fiorentini and Steve Barnes, and careful editorial handling by the editors Wolfgang Maier and Georges Beaudoin.

3.8 - References

Amaral LFS (2017) The distribution of platinum-group elements and other chalcophile elements among sulfide minerals from the ovoid ore body of the voisey's bay Ni-Cu sulfide deposit, canada. Unpubl MSc thesis, Université du Québec à Chicoutimi, 166 pp

Bai L, Barnes S-J, Baker DR (2017) Sperrylite saturation in magmatic sulfide melts: Implications for formation of PGE-bearing arsenides and sulfarsenides. Am Mineral 102(5): 966-974

Barnes S-J (2016) Chalcophile Elements. In: White,W.M. (Ed.) Encyclopedia of Geochemistry: A Comprehensive Reference Source on the Chemistry of the Earth, Part of the series Encylopedia of Earth Sciences Series pp 1–5

Barnes S-J, Lightfoot PC (2005) Formation of magmatic nickel sulfide ore deposits and processes affecting their copper and platinum group element contents. Economic Geology 100th Anniversary. pp 179–213

Barnes S-J, Makovicky E, Makovicky M, Rose-Hansen J, Karup-Moller S (1997) Partition coefficients for Ni, Cu, Pd, Pt, Rh, and Ir between monosulfide solid solution and sulfide liquid and the formation of compositionally zoned Ni–Cu sulfide bodies by fractional crystallization of sulfide liquid. Can J Earth Sci 34:366-374

Barnes S-J, Cox R, Zientek M (2006) Platinum-group element, gold, silver and base metal distribution in compositionally zoned sulfide droplets from the Medvezky Creek Mine, Noril'sk, Russia. Contrib Mineral Petrol 152:187-200

Barnes S-J, Prichard HM, Cox RA, Fisher PC, Godel B (2008) The location of the chalcophile and siderophile elements in platinum-group element ore deposits (a textural, microbeam and whole rock geochemical study): Implications for the formation of the deposits. Chem Geol 248:295-317

Barnes S-J, Ripley EM (2016) Highly siderophile and strongly chalcophile elements in magmatic ore deposits. Rev Mineral Geochem 81:725-774

Cabri LJ (1973) New data on phase relations in the Cu-Fe-S system. Econ Geol 68:443-454

Cafagna F (2015) The geochemical behavior of metalloids and their effect on the highly siderophile elements during the crystallization of a magmatic sulfide liquid in relation to the formation of Ni-Cu-PGE magmatic sulfide deposits. Unpubl PhD thesis, Laurentian University, 206 pp

Cafagna F, Jugo PJ (2016) An experimental study on the geochemical behavior of highly siderophile elements (HSE) and metalloids (As, Se, Sb, Te, Bi) in a mss-iss-pyrite system at 650° c: A possible magmatic origin for Co-HSE-bearing pyrite and the role of metalloid-rich phases in the fractionation of HSE. Geochim Cosmochim Acta 178:233-258

Chen L-M, Song XY, Danyushevsky LV, Wang Y-S, Tian Y-L, Xiao J-F (2015) A laser ablation ICP-MS study of platinum-group and chalcophile elements in base metal sulfide minerals of the jinchuan Ni–Cu sulfide deposit, NW China. Ore Geol Rev 65:955-967

Czamanske GK, Kunilov VE, Zientek ML, Cabri LJ, Likhachev AP, Calk LC, Oscarson RL (1992) A proton microprobe study of magmatic sulfide ores from the Noril'sk-Talnakh District, Siberia. Can Mineral 30:249-287

Dare SAS, Barnes S-J, Prichard HM, Fisher PC (2010a) The timing and formation of platinum-group minerals from the Creighton Ni-Cu-platinum-group element sulfide deposit, Sudbury, Canada: Early crystallization of PGE-rich sulfarsenides. Econ Geol 105:1071-1096

Dare SAS, Barnes S-J, Prichard HM (2010b) The distribution of platinum group elements (PGE) and other chalcophile elements among sulfides from the Creighton Ni–Cu–PGE sulfide deposit, Sudbury, Canada, and the origin of palladium in pentlandite. Miner Deposita 45:765-793

Dare SAS, Barnes S-J, Prichard HM, Fisher PC (2011) Chalcophile and platinum-group element (PGE) concentrations in the sulfide minerals from the McCreedy East deposit, Sudbury, Canada, and the origin of PGE in pyrite. Miner Deposita 46:381-407

Dare SAS, Barnes S-J, Beaudoin G (2012) Variation in trace element content of magnetite crystallized from a fractionating sulfide liquid, Sudbury, Canada: Implications for provenance discrimination. Geochim Cosmochim Acta 88:27-50

Dare SAS, Barnes S-J, Prichard HM, Fisher PC (2014) Mineralogy and geochemistry of Cu-rich ores from the McCreedy East Ni-Cu-PGE deposit (Sudbury, Canada): Implications for the behavior of platinum group and chalcophile elements at the end of crystallization of a sulfide liquid. Econ Geol 109:343-366

Distler VV (1994) Platinum mineralization of the Noril'sk deposits. In: Lightfoot PC, Naldrett AJ (eds) Proceedings of Sudbury- Noril'sk Symposium, Ontario Geological Survey Special Volume 5, pp 243–260

Distler VV, Malevsky AY, Laputina IP (1977) Distribution of platinoids between pyrrhotite and pentlandite in crystallization of a sulphide melt. Geochim Int 14:30-40

Distler V.V., Sinyakova E. F. and Kosyakov V. I. (2016) Behavior of noble metals upon fractional crystallization of copper-rich sulfide melts. Dokl Earth Sci 469:811-814.

Djon MLN, Barnes S-J (2012) Changes in sulfides and platinum-group minerals with the degree of alteration in the Roby, Twilight, and High Grade Zones of the Lac des Iles Complex, Ontario, Canada. Miner Deposita 47:875-896

Duran CJ, Barnes S-J, Corkery JT (2016) Trace element distribution in primary sulfides and Fe–Ti oxides from the sulfide-rich pods of the Lac des Iles Pd deposits, Western Ontario, Canada: Constraints on processes controlling the composition of the ore and the use of pentlandite compositions in exploration. J Geochem Explor 166:45-63

Duran CJ, Barnes S-J, Pleše P, Prašek MK, Zientek ML, Pagé P (2017) Fractional crystallization-induced variations in sulfides from the Noril'sk-Talnakh mining district (polar Siberia, Russia). Ore Geol Rev 90:326-351

Duran CJ, Dubé-Loubert H, Pagé P, Barnes S-J, Roy M, Savard D, Cave B, Arguin, JP, Mansur E (2019) Applications of trace element chemistry of pyrite and chalcopyrite in glacial sediments to mineral exploration targeting: Example from the Churchill Province, northern Quebec, Canada. J Geochem Explor 196: 105-130

Dutrizac J (1976) Reactions in cubanite and chalcopyrite. Can Mineral 14:172-181

Fedorenko V (1994) Evolution of magmatism as reflected in the volcanic sequence of the Noril'sk region. In: Lightfoot PC, Naldrett AJ (eds) Proceedings of Sudbury- Noril'sk Symposium, Ontario Geological Survey Special Volume 5, pp 171-184

Frost BR, Mavrogenes JA, Tomkins AG (2002) Partial melting of sulfide ore deposits during medium-and high-grade metamorphism. Can Mineral 40(1):1-18

Godel B, Barnes S-J (2008) Platinum-group elements in sulfide minerals and the whole rocks of the JM Reef (Stillwater Complex): Implication for the formation of the reef. Chem Geol 248:272-294

Godel B, Barnes S-J, Maier WD (2007) Platinum-group elements in sulphide minerals, platinum-group minerals, and whole-rocks of the Merensky Reef (Bushveld Complex, South Africa): Implications for the formation of the reef. J Petrol 48:1569-1604

Godel B, González-Álvarez I, Barnes SJ, Barnes S-J, Parker P, Day J (2012) Sulfides and sulfarsenides from the Rosie nickel prospect, Duketon greenstone belt, Western Australia. Econ Geol 107:275-294

Hanley JJ (2007) The role of arsenic-rich melts and mineral phases in the development of high-grade Pt-Pd mineralization within komatiite-associated magmatic Ni-Cu sulfide horizons at Dundonald Beach South, Abitibi subprovince, Ontario, Canada. Econ Geol 102:305-317

Helmy HM, Ballhaus C, Berndt J, Bockrath C (2007) Wohlgemuth-Ueberwasser, C. Formation of Pt, Pd and Ni tellurides: Experiments in sulfide–telluride systems. Contrib Mineral Petrol 153:577-591

Helmy HM, Ballhaus C, Wohlgemuth-Ueberwasser C, Fonseca RO, Laurenz V (2010) Partitioning of Se, As, Sb, Te and Bi between monosulfide solid solution and sulfide melt–application to magmatic sulfide deposits. Geochim Cosmochim Acta 74:6174-6179

Helmy HM, Ballhaus C, Fonseca R, Nagel T (2013) Fractionation of platinum, palladium, nickel, and copper in sulfide–arsenide systems at magmatic temperature. Contrib Mineral Petrol 166:1725-1737

Holwell D, McDonald I (2007) Distribution of platinum-group elements in the Platreef at Overysel, northern Bushveld Complex: A combined PGM and LA-ICP-MS study. Contrib Mineral Petrol 154:171-190

Hutchinson D McDonald I (2008) Laser ablation ICP-MS study of platinum-group elements in sulphides from the Platreef at Turfspruit, northern limb of the Bushveld Complex, South Africa. Miner Deposita 43:695-711

Jamieson HE (2014) The Legacy of Arsenic Contamination from Mining and Processing Refractory Gold Ore at Giant Mine, Yellowknife, Northwest Territories, Canada. Rev Mineral Geochem 79:533-551

Jochum KP, Nohl U, Herwig K, Lammel E, Stoll B, Hofmann AW (2005) GeoReM: a new geochemical database for reference materials and isotopic standards. Geostand Geoanal Res 29:333-338

Junge M, Wirth R, Oberthür T, Melcher F, Schreiber A (2015) Mineralogical siting of platinum-group elements in pentlandite from the Bushveld Complex, South Africa. Miner Deposita 50(1):41-54

Kelly D, Vaughan D (1983) Pyrrhotine-pentlandite ore textures: A mechanistic approach. Mineral Mag 47:453-463.

Kissin S, Scott S (1982) Phase relations involving pyrrhotite below 350 degrees C. Econ Geol **77**:1739-1754

Kosyakov F, Sinyakova E, Distler V (2012) Experimental simulation of phase relationships and zoning of magmatic nickel-copper sulfide Ores, Russia. Geol Ore Deposits 54:179-208

Krivolutskaya NA (2016) Siberian traps and Pt-Cu-Ni deposits in the Noril'sk area. Springer, Amsterdam, 377 pp

Krivolutskaya NA, Gongalsky BI, Kedrovskaya TB, Kubrakova IV, Tyutyunnik OA, Chikatueva VY, Bychkova YV, Magazina L, Kovalchuk EN, Yakushev AI, Kononkova NN (2018) Geology of the western flanks of the Oktyabr'skoe deposit, Noril'sk district, Russia: evidence of a closed magmatic system. Miner Deposita 1-20

Le Vaillant M, Barnes SJ, Mungall JE, Mungall EL (2017) Role of degassing of the Noril'sk nickel deposits in the Permian-Triassic mass extinction event. PNAS 114:2485-2490

Le Vaillant M, Barnes SJ, Fiorentini ML, Barnes SJ, Bath AB, Miller JM (2018) Platinum group element and gold contents of arsenide and sulfarsenide minerals associated with Ni and Au deposits in Archean greenstone belts. Mineral Mag 82: 625-47

Li C, Barnes S-J, Makovicky E, Rose-Hansen J, Makovicky M (1996) Partitioning of Ni, Cu, Ir, Rh, Pt and Pd between monosulfide solid solution and sulfide liquid: Effects of composition and temperature. Geochim Cosmochim Acta 60:1231-1238

Lightfoot PC, Naldrett AJ, Gorbachev NS, Fedorenko VA, Howkesworth CJ, Hergt J, Doherty W (1994) Chemistratigraphy of Siberian trap lavas, Noril'sk district: implication for the source of flood basalts magmas and their associated Ni-Cu mineralization. In: Lightfoot PC, Naldrett AJ (eds) Proceedings of Sudbury- Noril'sk Symposium, Ontario Geological Survey Special Volume 5, pp 185–201

Likhachev AP (1994) Ore-bearing intrusions of the Noril'sk region. In: Proceeding of the Noril'sk-Sudbury symposium, vol 5. Geol Surv Spec, Ontario, pp 185–201

Liu Y, Brenan J (2015) Partitioning of platinum-group elements (PGE) and chalcogens (Se, Te, As, Sb, Bi) between monosulfide-solid solution (MSS), intermediate solid solution (ISS) and sulfide liquid at controlled fO2–fS2 conditions. Geochim Cosmochim Acta 159:139-161

Lyubetskaya T. Korenaga J (2007) Chemical composition of Earth's primitive mantle and its variance: 1. Method and results. J Geophys Res 112:B03211

Makovicky E (2002) Ternary and quaternary phase systems in PGE. In: Cabri LJ (ed) The geology, geochemistry, mineralogy and mineral benefication of the platinum-group elements. Canadian Institute of Mining, Metallurgy and Petroleum, vol 54, pp 131-175

Mansur ET, Barnes S-J, Duran CJ (2019) Textural and compositional evidence for the formation of pentlandite via peritectic reaction: Implications for the distribution of highly siderophile elements. Geology 47 (4): 351-354.

Mavrogenes JA, Frost R, Sparks HA (2013) Experimental evidence of sulfide melt evolution via immiscibility and fractional crystallization. Can Mineral 51:841–850

Moss RL, Tzimas E, Kara H, Willis P, Kooroshy J (2013) The potential risks from metals bottlenecks to the deployment of strategic energy technologies. Energy Policy 55:556-564

Mota-e-Silva J, Prichard H, Ferreira Filho C, Fisher PC, McDonald I (2015) Platinum-group minerals in the Limoeiro Ni–Cu–(PGE) sulfide deposit, brazil: The effect of magmatic and upper amphibolite to granulite metamorphic processes on PGM formation. Miner Deposita 50:1007-1029

Mungall JE (2007) Crystallization of magmatic sulfides: an empirical model and application to Sudbury ores. Geochim Cosmochim Acta 71: 2809-2819

Mungall JE, Andrews DR, Cabri LJ, Sylvester PJ, Tubrett M (2005) Partitioning of Cu, Ni, Au, and platinum-group elements between monosulfide solid solution and sulfide melt under controlled oxygen and sulfur fugacities. Geochim Cosmochim Acta 69:4349-4360

Naldrett AJ (2004) Magmatic sulfide deposits: geology, geochemistry and exploration. Springer, Berlin, 727 pp

Naldrett AJ (2011) Fundamentals of magmatic sulfide deposits. Rev Econ Geol 17:1-50

Naldrett AJ, Fedorenko V, Asif M, Lin S, Kunilov V, Stekhin A, Lightfoot PC, Gorbachev N (1996) Controls on the composition of Ni-Cu sulfide deposits as illustrated by those at Noril'sk, Siberia. Econ Geol 91:751-773

O'Driscoll B, González-Jiménez JM (2016) Petrogenesis of the platinum-group minerals. Rev Mineral Geochem 81:489-578

Osbahr I, Oberthür T, Klemd R, Josties A (2014) Platinum-group element distribution in base-metal sulfides of the UG2 chromitite, Bushveld Complex, South Africa - a reconnaissance study. Miner Deposita 49(6):655-665

Paton C, Hellstrom J, Paul B, Woodhead J, Hergt J (2011) Iolite: Freeware for the visualisation and processing of mass spectrometric data. J Anal Atom Spec 26:2508-2518

Patten C, Barnes S-J, Mathez EA, Jenner FE (2013) Partition coefficients of chalcophile elements between sulfide and silicate melts and the early crystallization history of sulfide liquid: LA-ICP-MS analysis of MORB sulfide droplets. Chem Geol 358:170-188

Péntek A, Molnár F, Watkinson DH, Jones PC (2008) Footwall-type Cu-Ni-PGE Mineralization in the Broken Hammer Area, Wisner Township, North Range, Sudbury Structure. Econ Geol 103:1005-1028

Piña R, Gervilla F, Barnes S-J, Ortega L, Lunar R (2012) Distribution of platinum-group and chalcophile elements in the aguablanca Ni-Cu sulfide deposit (SW spain): Evidence from a LA-ICP-MS study. Chem Geol 302**:**61-75

Piña R. Gervilla F, Barnes S-J, Ortega L, Lunar R (2015) Liquid immiscibility between arsenide and sulfide melts: Evidence from a LA-ICP-MS study in magmatic deposits at Serranía de Ronda (Spain). Mineral Depos 50:265–279

Power M, Pirrie D, Jedwab J, Stanley C (2004) Platinum-group element mineralization in an As-rich magmatic sulphide system, Talnotry, southwest Scotland. Mineral Mag 68:395-411

Prichard H, Hutchinson D, Fisher P (2004) Petrology and crystallization history of multiphase sulfide droplets in a mafic dike from Uruguay: Implications for the origin of Cu-Ni-PGE sulfide deposits. Econ Geol 99:365-376

Ryabov VV, Shevko AY, Gora MP (2014) Trap magmatism and ore formation in the Siberian Noril'sk region. v. 1, 2. Springer

Samalens N, Barnes S-J, Sawyer EW (2017) The role of black shales as a source of sulfur and semimetals in magmatic nickel-copper deposits: Example from the Partridge River Intrusion, Duluth Complex, Minnesota, USA. Ore Geol Rev 81(1):173-187

Sessa G, Moroni M, Tumiati S, Caruso S, Fiorentini ML (2017) Ni-Fe-Cu-PGE ore deposition driven by metasomatic fluids and melt-rock reactions in the deep crust: The ultramafic pipe of Valmaggia, Ivrea-Verbano, Italy. Ore Geol Rev 90: 485-509

Singh R, Singh S, Parihar P, Singh VP, Prasad SM (2015) Arsenic contamination, consequences and remediation techniques: a review. *Ecotoxicol Environ Saf* 112:247-270

Sinyakova E, Kosyakov V, Borisenko A (2017) Effect of the presence of As, Bi, and Te on the behavior of Pt metals during fractionation crystallization of sulfide magma. Dokl Earth Sci 477:1422-1425

Sluzhenikin SF, Krivolutskaya NA, Rad'ko VA, Malitch KN, Distler VV, Fedorenko VA (2014) Ultramafic-mafic intrusions, volcanic rocks and PGE-cu-Ni sulfide ores of the Noril'sk province. IGM, Yekaterinburg

Smith J, Holwell DA, McDonald I (2014) Precious and base metal geochemistry and mineralogy of the Grasvally Norite–Pyroxenite–Anorthosite (GNPA) member, northern Bushveld Complex, SouthAfrica: Implications for a multistage emplacement. Miner Deposita 49:667-692

Sullivan NA, Zajacz Z, Brenan JM (2018) The solubility of Pd and Au in hydrous intermediate silicate melts: the effect of oxygen fugacity and the addition of Cl and S. Geochim Cosmochim Acta 231:15-29

Tuba G, Molnár F, Ames DE, Péntek A, Watkinson DH, Jones PC (2014) Multi-stage hydrothermal processes involved in "low-sulfide" Cu (–Ni)–PGE mineralization in the footwall of the Sudbury Igneous Complex (Canada): Amy Lake PGE zone, East Range. Miner Deposita 49:7-47

Wilson SA, Ridley WI, Koenig AE (2002) Development of sulfide calibration standards for the laser ablation inductively-coupled plasma mass spectrometry technique. J Anal At Spectrom 17:406-409

Wood SA (2002) The aqueous geochemistry of the platinum group elements with applications to ore deposits. Can Inst Min Metall 54:211-249

Yudovskaya MA, Kinnaird JA, Grobler DF, Costin G, Abramova VD, Dunnett T, Barnes S-J (2017) Zonation of Merensky-Style Platinum-Group Element Mineralization in Turfspruit Thick Reef Facies (Northern Limb of the Bushveld Complex). Econ Geol 112:1333-1365

Zientek M, Likhachev A, Kunilov V, Barnes S-J, Meier AL, Carlson R, Briggs PH, Fries T, Adrian B, Lightfoot PC (1994) Cumulus processes and the composition of magmatic ore deposits: Examples from the Talnakh district, Russia. In: Lightfoot PC, Naldrett AJ (eds) Proceedings of Sudbury- Noril'sk Symposium, Ontario Geological Survey Special Volume 5, pp 373-392

Zweibel K (2010) The Impact of Tellurium Supply on Cadmium Telluride Photovoltaics. Science 328:699-701

Chapter 4 - Textural and compositional evidence for the formation of pentlandite via peritectic reaction: Implications for the distribution of highly siderophile elements

Eduardo T. Mansur[1], Sarah-Jane Barnes[1], Charley J. Duran[1]

[1]*Sciences de la Terre, Université du Québec à Chicoutimi, Québec, G7H 2B1, Canada*

Author contributions:

Mansur wrote the manuscript, collected and analyzed the data and created the figures. **Barnes** edited the manuscript and analyzed the data. **Duran** collected part of the data and also analyzed the results.

Geology, 2019, 47 (4): 351–354
DOI : 10.1130/G45779.1

4.1 - Abstract

The distribution of the highly siderophile elements is used in a wide variety of geological studies, from planet formation and evolution to the formation of ore deposits. Under mantle and crustal conditions, these elements behave as highly chalcophile elements and pentlandite (Pn) is an important host for most of these elements. Therefore, understanding how Pn forms is important to understanding the processes that control these elements. The classic model for the formation of Pn is that below 650^{o} C the high temperature sulfides: monosulfide solid solution (MSS) and intermediate solid solution (ISS), are no longer stable and exsolve into pyrrhotite (Po), Pn and chalcopyrite (Ccp). However, Pn has been shown to be the main host of Pd in many ore deposits and given that Pd is incompatible with both MSS and ISS this observation is inconsistent with the exsolution model. Furthermore, experimental work has shown that Pn can form by peritectic reaction between MSS and fractionated sulfide liquid. To date this type of Pn has not been reported in natural samples. In our study of chalcophile element concentrations in Pn from iconic magmatic Ni-Cu-PGE deposits we observed three textures of Pn: contact-Pn in between Po and Ccp, granular Pn included within Ccp or Po, and flame-Pn included within Po. The contact-Pn shows zonation in Mo, Rh, Ru, Re, Os and Ir with these elements being enriched towards the Po contact, and depleted towards the Ccp contact. In some cases, Pd displays a zonation antithetical to these elements. In this contribution we propose that the contact-Pn formed via this peritectic reaction and inherited Mo, Ru, Rh, Re, Os and Ir from the MSS, whereas Pd was contributed from the fractionated sulfide liquid. We predict that this type of Pn should be present wherever MSS and fractionated sulfide liquid remained in contact.

Keywords: Pentlandite; Peritectic reaction; Highly siderophile elements; Magmatic sulfide deposits; Merensky reef; Noril'sk; LA-ICP-MS.

4.2 – Introduction

The distribution of highly siderophile elements (Ru, Rh, Pd, Re, Os Ir, Pt and Au) is studied in numerous branches of geology such as the planetary evolution, timing of segregation of the Earth's core, the late planetary bombardment, evolution of the Earth's mantle and basalts (Harvey and Day, 2016 and references therein). Furthermore, many of these elements are of economic importance and hence their behaviour during ore formation is of interest. In the Earth's crust and mantle, most of these elements behave as highly chalcophile elements and are found either in base metal sulfides or as platinum-group minerals associated with base metal sulfides (Barnes and Ripley, 2016; O'Driscoll and González-Jiménez, 2016). Pentlandite is a major host of many of the HSE. Therefore, understanding when and how Pn forms is important to many branches of geology.

Magmatic Ni-Cu-Platinum-group elements (PGE) sulfide deposits offer an opportunity to study the formation of Pn. These deposits are formed when a sulfide liquid segregates from mafic/ultramafic magmas and collects Ni, Cu, PGE and other chalcophile elements (Naldrett, 2004). Upon cooling of this sulfide liquid, chalcophile elements partition between the fractionating liquid and the crystallizing phases: initially monosulfide solid solution (MSS), followed by intermediate solid solution (ISS), and finally discrete precious metal minerals that accommodate the elements incompatible with MSS and ISS (e.g. bismuthtellurides, arsenides, stanides). Experimental work has shown that MSS and ISS subsequently exsolve essentially into pyrrhotite (Po), pentlandite (Pn), chalcopyrite (Ccp) and cubantite (Kelly and Vaughvan, 1983; Etschmann et al., 2004; Peregoedova and Ohnenstetter, 2002). Furthermore, the texture of Pn depends on the temperature at which it started to exsolve (Kelly and Vaughan, 1983). Exsolutions that start at relatively high temperature (650ºC) have more time to form and result in coarse granular Pn. Exsolution that commence at intermediate

temperature (400ºC) form veins, and exsolutions that form at lower temperature (200ºC) form flames. Most studies of magmatic sulfides attribute different textures observed for Pn to this exsolution history (Dare et al., 2010; Piña et al., 2012). However, experimental studies also reveal that a Ni-rich phase (referred to as high-temperature Pn) can form via peritectic reaction between MSS and the fractionated sulfide liquid at temperatures around 870ºC (Waldner and Pelton, 2004; Kosyakov and Sinyakova, 2012; Kitakaze et al., 2016). Pentlandite formed by peritectic reaction has the potential to explain some observations in natural samples that exsolution cannot. Although this problem has been addressed experimentally, studies of natural samples have not considered this alternative Pn origin.

The exsolutions model does not explain some aspects of texture and composition of some Pn. Pentlandite is the main host for Pd in many magmatic Ni-Cu-PGE sulfide deposits (Barnes et al. 2006; Dare et al., 2010; Osbar et al., 2014), but Pd is incompatible with both MSS and ISS (Li et al., 1996; Liu and Brenan, 2015; Cafagna and Jugo, 2016). Therefore, Pn formed by exsolutions from these phases would not be expected to contain significant amounts of Pd. Furthermore, rims of a Ni-rich phase are found between Po and Ccp in sulfide droplets from Mid-Ocean-Ridge Basalt (MORB; Patten et al., 2012). These droplets have cooled too quickly for the rims to have formed by exsolution.

To address this problem, we have combined petrographic examination and trace-element chemistry of Pn from the disseminated and massive sulfides of the Noril'sk-Talnakh mining district, and the disseminated sulfides from the Impala Mine of the Merensky Reef of the Bushveld Complex. The effects of metamorphism, deformation, and alteration on sulfide minerals in these deposits are limited, and their textures and chemical compositions record the original ore-forming processes (Barnes and Maier, 2002; Duran et al., 2017). On the basis of our textural and geochemical investigation, this

contribution supports the formation of Pn via peritectic reaction between MSS and the fractionated sulfide liquid in natural cases, thus supporting previous experimental work.

4.3 - Textural occurrences of pentlandite

The investigated samples are described in detail in Duran et al. (2017) for the Noril'sk-Talnakh mining district and in Barnes and Maier (2002) for the Merensky Reef. All samples contain the typical Po-Pn-Ccp assemblage, and Pn displays three distinct textures, referred as contact-, granular and flame-Pn. Contact-Pn occurs as μm- to mm-thick layers at the contact between Ccp and Po grains (Fig. 4.1a and 4.1b). Granular Pn occurs as coarse grains (mm to cm in apparent diameter) associated with either Po or Ccp, but not both (Fig. 4.1c), whereas Pn flames occur as thin (μm thick) lamellas within Po (Fig. 4.1d). In disseminated sulfide samples from the Noril'sk I intrusion and the Merensky Reef (Fig. 4.1a) the main Pn texture is contact-Pn, whereas in massive sulfide samples from the Kharaelakh intrusion of the Noril'sk-Talnakh mining district (Fig. 4.1b, 4.1c and 4.1d) all three Pn textures occur.

4.4 - Composition and distribution of trace elements in pentlandite

Pentlandite was analyzed using laser ablation-inductively coupled plasma-mass spectrometry (LA-ICP-MS). Details of the methodology are presented in *ANNEXE 10*.

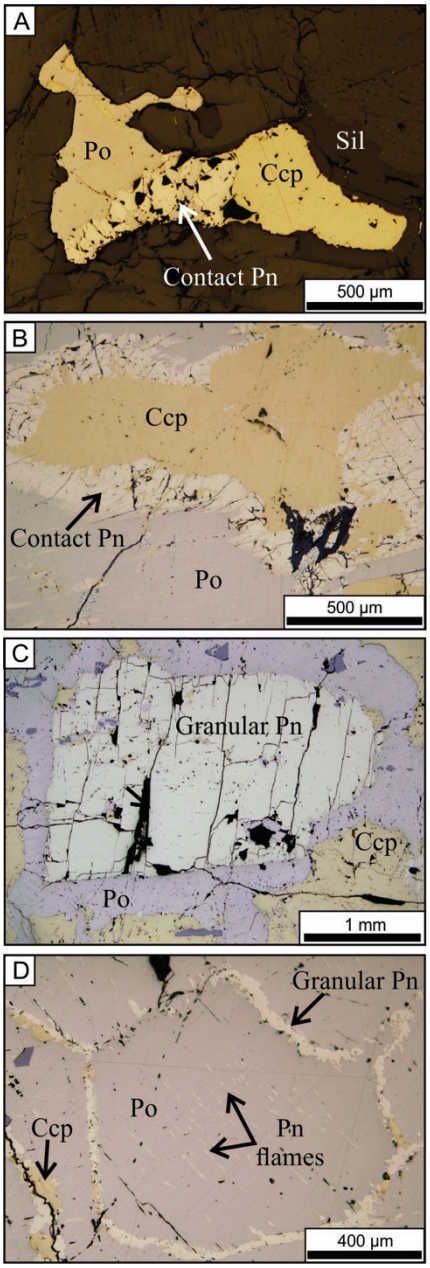

Figure 4.1 - Reflected light images of pentlandite textures from the disseminated sulfides of the Merensky Reef of the Bushveld Complex (A), and massive sulfides of the Noril'sk-Talnakh mining district (B, C and D). A) Typical disseminated sulfide bleb with contact-pentlandite between pyrrhotite and chalcopyrite. B) Contact-pentlandite surrounding a chalcopyrite grain, at the contact with pyrrhotite. C) Typical coarse granular pentlandite enclosed within pyrrhotite. D) Exsolution flames of pentlandite in pyrrhotite, and veinlets of granular pentlandite grains in between or included within pyrrhotite grains. Ccp- chalcopyrite; Pn- pentlandite; Po- pyrrhotite; Sil- silicates.

Granular Pn from massive sulfides of the Kharaelakh intrusion displays homogenous distribution of trace elements. In contrast, contact-Pn from disseminated sulfides of the Noril'sk I intrusion (Fig. 4.2a), massive sulfides of the Kharaelakh intrusion (Fig. 4.2b and 4.2c), and disseminated sulfides of the Merensky Reef (Fig. 4.2d and 4.2e) show a trace element zonation. The trace elements compatible with MSS (Os, Ir, Ru, Rh, Re and Mo) have higher concentrations where Pn is in contact with Po, whereas Pd (Fig. 4.2b) and to a lesser extent Te, Bi and Pb (Fig. 4.2c and Fig. 1 of *ANNEXE 10*) (which are incompatible with MSS) have higher concentrations where Pn is in contact with Ccp. These zonation patterns are not an analytical artefact. As shown in Figure 4.3, the time-resolved analysis for two LA-ICP-MS lines (red lines indicated in Fig. 4.2b and 4.2c) indicate no mixing between the different sulfide phases. The Pd is clearly concentrated in Pn, with higher concentration at the contact close to the Ccp (Fig. 4.3a). In contrast, Mo, Ru, Rh, Re, Os and Ir are present in Po and constrained to the Pn contact close to the Po (Fig. 4.3b).

The LA-ICP-MS compositional maps also reveal that in some grains the distribution of trace elements is homogeneous in contact-Pn from Merensky Reef, but is heterogeneous in associated Po (Fig. 4.2e). Elements compatible with MSS have lower concentrations where Po is in contact with Pn, and this distribution seems to form a depletion halo in Po close to the contact with Pn (Fig. 4.2e). This texture suggests that Ru, Os and Ir were inherited from Po.

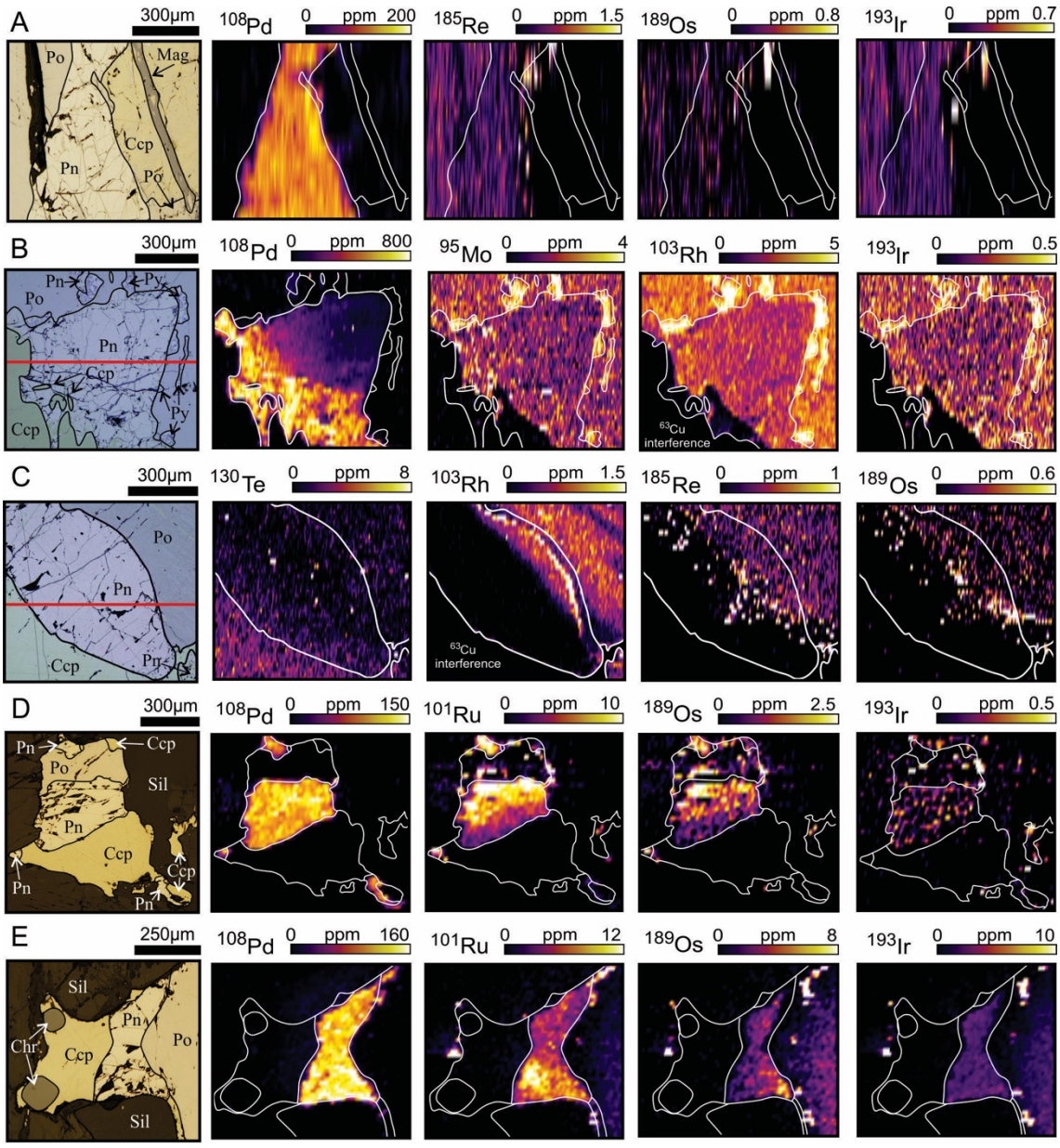

Figure 4.2 - LA–ICP-MS elemental maps showing the distribution of chalcophile elements in pentlandite and associated pyrrhotite and chalcopyrite. A) Contact-pentlandite from disseminated sulfide droplets of the Noril'sk I intrusion. B) and C) Contact-pentlandite from massive sulfides of the Kharaelakh intrusion. D) and E) Contact-pentlandite from disseminated sulfides of the Merensky Reef. Ccp- chalcopyrite; Pn- pentlandite; Po- pyrrhotite; Py – Pyrite; Sil- silicates.

4.5 - Formation of pentlandite via peritectic reaction

In their studies of Pn from the Creighton ores of the Sudbury Complex and Aquablanca ores, Dare et al. (2010) and Piña et al. (2012) noted that coarse grained Pn is richer in Pd than flame-Pn. These authors attributed this to the diffusion of Pd into the

granular Pn from the MSS at high temperature, leaving the remaining MSS depleted in Pd at the time of flame-Pn formation. In addition, they noted that coarse grained Pn associated with Ccp is richer in Pd relative to coarse grained Pn associated with Po. They interpreted this difference as the result of ISS being richer in Pd than MSS, and that Pd diffused from ISS into Pn. Given that the partition coefficient for Pd into ISS is higher (~0.5) than for Pd into MSS (~0.1) (Liu and Brenan, 2015), and considering that Ccp exsolved from ISS, Pn grains associated with Ccp would be enriched in Pd relative to Pn grains associated with Po. Whereas these processes could explain some of the variations in the Pn composition, they do not explain why Pn contains most of the Pd in the Noril'sk-Talnakh and Merensky Reef sulfides (Barnes and Ripley 2016) despite Pd incompatibility with MSS and ISS. Additionally, they do not explain the zonation in the concentrations of Mo, Ru, Rh, Re, Os and Ir observed in contact-Pn (Fig. 4.2). Therefore, we suggest that contact-Pn formed by peritectic reaction.

Experimental work shows that Pn can form by reaction between MSS and the fractionated sulfide liquid (Waldner and Pelton, 2004; Kosyakov and Sinyakova, 2012; Kitakaze et al., 2016) between 870 and 800 ºC. Therefore, when cumulus MSS is not separated from the fractionating sulfide liquid, Pn could form by reaction prior to Pn exsolution from MSS or ISS below 650 ºC. We interpret the different textures and distribution of trace elements in Pn as reflecting these two stages of Pn formation during the crystallization of sulfide liquid (Fig. 4.4a). Homogeneous distribution of trace elements in granular Pn is consistent with MSS and ISS exsolving into Po+Pn, and Ccp+Pn, respectively. In contrast, heterogeneous distribution of trace elements in contact-Pn is consistent with reaction between MSS and fractionated sulfide liquid.

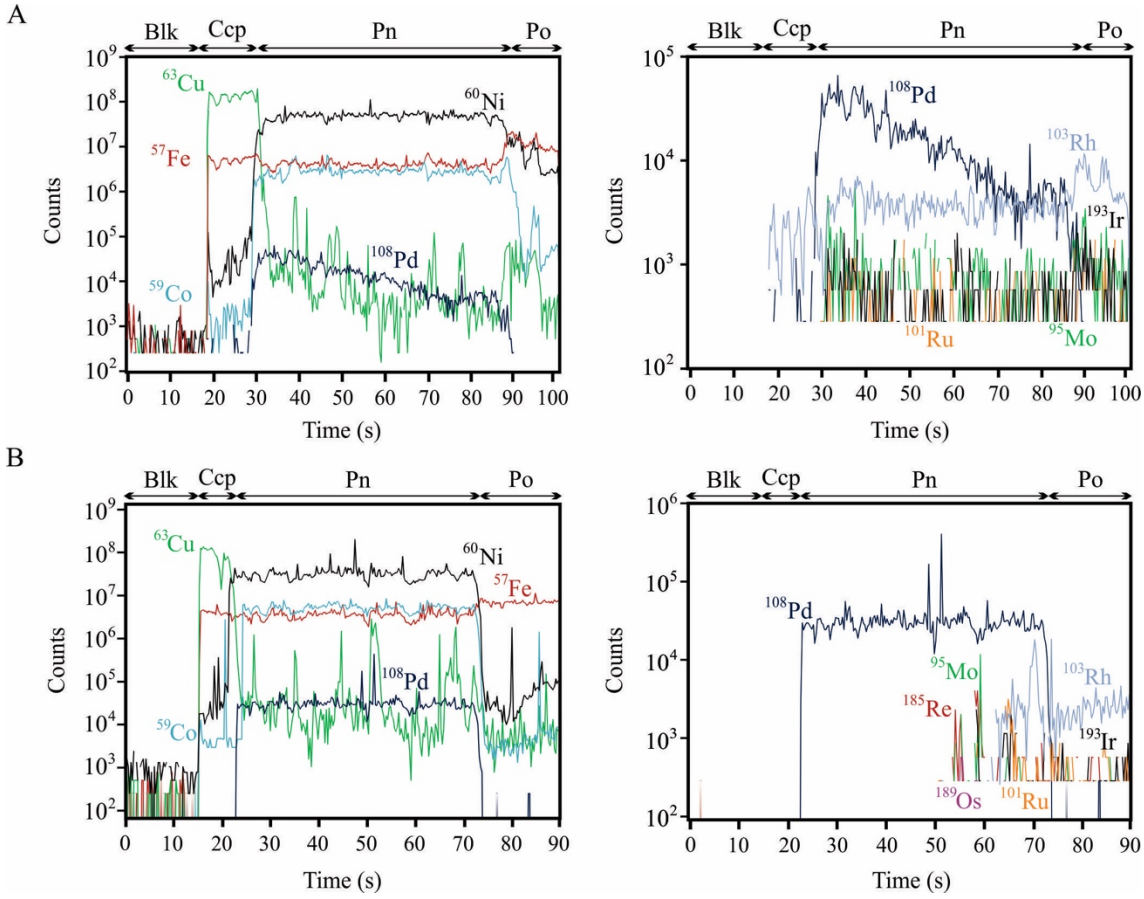

Figure 4.3 - Time-resolved analysis for the LA-ICP-MS lines indicated in Fig. 2B (A) and 2C (B). Note that the zonation patterns are not caused by mixing between different sulfides. A) The Pd signal is uniform across Pn, whereas Mo, Ru, Rh, Re, Os and Ir are present in Po and constrained to the Pn contact close to the Po. B) The Mo, Ru, Rh and Ir signals are uniform across Pn, whereas Pd is higher at the contact close to Ccp, decreasing towards Po. Blk- blank; Ccp- chalcopyrite; Pn- pentlandite; Po- pyrrhotite.

In contact-Pn, concentrations of elements compatible with MSS (Ru, Rh, Ir, Os, Re, Mo; Fig. 4.4b) are higher at the Po-Pn boundary and decrease towards Ccp. These elements were inherited from the MSS as it reacted with the fractionated sulfide liquid to form Pn (Fig. 4.4c). The abrupt decrease in the concentration of elements compatible with MSS (Fig. 4.2a, 4.2b and 4.2c) could represent the original grain boundary between the MSS and the fractionated liquid. Experimental work (Kitakaze et al., 2016) indicates that the high-T Pn keeps growing from the sulfide liquid below the peritectic temperature (i.e. 850ºC). Therefore, the further growth beyond the initial contact between MSS and

sulfide liquid could result in Pn being depleted in these compatible elements. On the other hand, Pd, Te, Pb and Bi concentrations (incompatible with MSS; Liu and Brenan, 2015; Cafagna and Jugo, 2016) decrease from the Ccp-Pn boundary towards the Po-Pn boundary, and record the incorporation of these elements from the fractionated sulfide liquid towards Pn (Fig. 4.4c and Fig. 1 of *ANNEXE 10*).

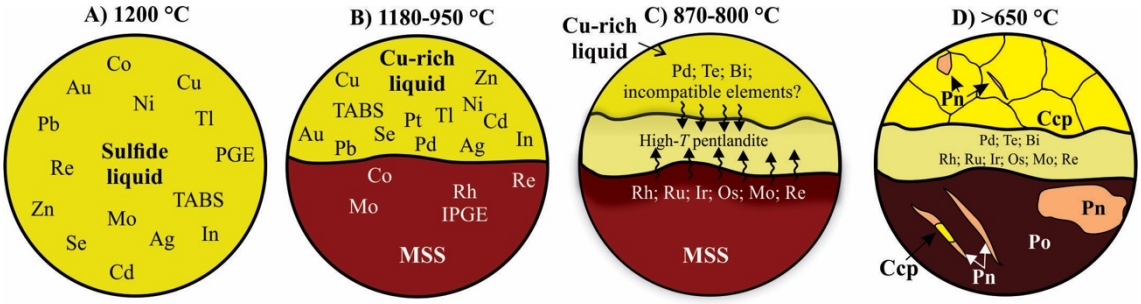

Figure 4.4 - Schematic model illustrating the crystallization history of a sulfide liquid, and the formation of pentlandite via peritectic reaction. See text for further explanation. MSS- monosulfide solid solution; ISS- intermediate solid solution; Ccp- chalcopyrite; Po- pyrrhotite; Pn- pentlandite.

The formation of Pn via peritectic reaction may be expected to occur wherever MSS remains in contact with the fractionated liquid. In sulfide blebs or droplets that formed via equilibrium crystallization, such as those from the Merensky Reef (Barnes and Maier, 2002) and the Noril'sk I intrusion (Barnes et al., 2006; Barnes et al., 2017), the MSS and the fractionated liquid were not separated and reacted at high temperature to form Pn. A similar interpretation can be inferred for Pn at the MSS-ISS interface in sulfide droplets of MORB glasses described in Patten et al. (2012).

In MSS cumulates, where the fractionated liquid has largely been expelled, contact-Pn is less common. However, if the separation is not complete, some liquid remains trapped among the MSS grains. This liquid has the potential to react with the MSS and form peritectic Pn. In the case of the massive sulfide samples of the Kharaelakh

intrusion, some samples have compositions similar to the initial sulfide liquid (Duran et al., 2017), implying that the MSS component remained associated with the fractionated liquid.

4.6 - Implications for the incorporation of palladium into pentlandite

In many magmatic sulfide deposits, Pn hosts significant amounts of Pd (Holwell and McDonald, 2007; Dare et al., 2010; Piña et al., 2012; Barnes and Ripley, 2016). If Pn only formed by exsolutions from MSS and ISS, and given that Pd is incompatible with both MSS and ISS, the majority of Pd should not be present in pentlandite. However, if Pn formed via peritectic reaction between MSS and the fractionated sulfide liquid, then the Pd concentrated in the fractionated liquid could have partitioned into Pn during the peritectic reaction (Fig. 4.2b and 4.4c). We suggest that not all Pn described in previous studies are formed by MSS and ISS exsolution, but also via peritectic reaction at higher temperature. For example, some Pn in the Creighton ores from Sudbury are located at the contact between Po and Ccp (Fig. 3a of Dare et al., 2010), and could have formed via peritectic reaction. The partitioning of Pd from the fractionated sulfide liquid into peritectic Pn provides an elegant explanation for the mass balance of Pd.

4.7 - Conclusions

Our study provides textural and compositional evidence for the formation of Pn by two distinct processes at two distinct stages of sulfide liquid evolution: i) at a higher temperature (870 to 800ºC) via peritectic reaction between MSS and fractionated sulfide liquid, and ii) at a lower temperature (<650ºC) via exsolution of MSS and ISS. Pentlandite formed via peritectic reaction is enriched in Ru, Rh, Ir, Os, Re and Mo close

to the contact with Po, and in Pd, Te, Bi and Pb close to the contact with Ccp. The formation of Pn via peritectic reaction also explains the presence of almost 100% of the whole-rock Pd in the Pn of some deposits, even though Pd is neither compatible with MSS nor ISS. Our study confirms previous experiments in that Pn can form via peritectic reaction in natural cases, and suggest that this process occurred in the main Ni-Cu-PGE deposits worldwide and magmatic sulfides in general.

4.7 - Acknowledgements

This work was supported by a Canada Research Chair program grant to Sarah-Jane Barnes (215503). We would like to thank Dany Savard (LabMaTer, UQAC) for his assistance with LA-ICP-MS analyses. This manuscript benefited from insightful comments from David Holwell, Rubén Piña and one anonymous reviewer and careful editorial handling by the editor Chris Clark.

4.8 – References

Barnes, S.-J., and Maier, W.D., 2002, Platinum-group elements and microstructures of normal Merensky Reef from Impala Platinum Mine, Bushveld Complex: Journal of Petrology, v. 43, p. 103–128.

Barnes, S.-J., Cox, R., and Zientek, M., 2006, Platinum-group element, gold, silver and base metal distribution in compositionally zoned sulfide droplets from the Medvezky Creek Mine, Noril'sk, Russia: Contributions to Mineralogy and Petrology, v. 152, no. 2, p. 187-200.

Barnes, S.-J., and Ripley, E. M., 2016, Highly siderophile and strongly chalcophile elements in magmatic ore deposits: Reviews in Mineralogy and Geochemistry, v. 81, no. 1, p. 725-774.

Barnes, S. J., Holwell, D. A., and Le Vaillant, M., 2017, Magmatic sulfide ore deposits: Elements, v. 13, no. 2, p. 89-95.

Cafagna, F., and Jugo, P. J., 2016, An experimental study on the geochemical behavior of highly siderophile elements (HSE) and metalloids (As, Se, Sb, Te, Bi) in a mss-iss-pyrite system at 650° C: a possible magmatic origin for Co-HSE-bearing pyrite and the role of metalloid-rich phases in the fractionation of HSE: Geochimica et Cosmochimica Acta, v. 178, p. 233-258.

Dare, S. A., Barnes, S.-J., and Prichard, H. M., 2010, The distribution of platinum group elements (PGE) and other chalcophile elements among sulfides from the Creighton Ni–Cu–PGE sulfide deposit, Sudbury, Canada, and the origin of palladium in pentlandite: Mineralium Deposita, v. 45, no. 8, p. 765-793.

Duran, C.J., Barnes, S-J., Pleše, P., Prašek, M. K., Zientek, M. L., and Pagé, P., 2017, Fractional crystallization-induced variations in sulfides from the Noril'sk-Talnakh mining district (polar Siberia, Russia): Ore Geology Reviews, v. 90, p. 326-351.

Etschmann, B., Pring, A., Putnis, A., Grguric, B. A., and Studer, A., 2004, A kinetic study of the exsolution of pentlandite (Ni, Fe)9S8 from the monosulfide solid solution (Fe,Ni)S: American Mineralogist, v. 89, p. 39-50.

Harvey, J., and Day, J. M., 2016, Highly siderophile and strongly chalcophile elements in high temperature geochemistry and cosmochemistry: Reviews in Mineralogy and Geochemistry, v. 81, no. 1, p. 1-774.

Holwell, D., and McDonald, I., 2007, Distribution of platinum-group elements in the Platreef at Overysel, northern Bushveld Complex: a combined PGM and LA-ICP-MS study: Contributions to Mineralogy and Petrology, v. 154, no. 2, p. 171-190.

Jochum, K. P., Nohl, U., Herwig, K., Lammel, E., Stoll, B., and Hofmann, A.W., 2005, GeoReM: a new geochemical database for reference materials and isotopic standards: Geostandards and Geoanalytical Research, v. 29, p. 333-338.

Kelly, D., and Vaughan, D., 1983, Pyrrhotine-pentlandite ore textures: a mechanistic approach: Mineralogical Magazine, v. 47, no. 4, p. 453-463.

Kitakaze, A., Machida, T., and Komatsu, R., 2016, Phase Relations in the Fe–Ni–S System from 875 To 650° C: The Canadian Mineralogist, v. 54, no. 5, p. 1175-1186.

Kosyakov, V. I., and Sinyakova, E. F., 2012, Physicochemical prerequisites for the formation of primary orebody zoning at copper-nickel sulfide deposits (by the example of the systems Fe–Ni–S and Cu–Fe–S): Russian Geology and Geophysics, v. 53, no. 9, p. 861-882.

Li, C., Barnes, S.-J., Makovicky, E., Rose-Hansen, J., and Makovicky, M., 1996, Partitioning of Ni, Cu, Ir, Rh, Pt and Pd between monosulfide solid solution and sulfide liquid: effects of composition and temperature: Geochim Cosmochim Acta, v. 60, p. 1231-1238.

Liu, Y., and Brenan, J., 2015, Partitioning of platinum-group elements (PGE) and chalcogens (Se, Te, As, Sb, Bi) between monosulfide-solid solution (MSS), intermediate solid solution (ISS) and sulfide liquid at controlled fO2–fS2 conditions: Geochimica et Cosmochimica Acta, v. 159, p. 139-161.

Naldrett, A. J., 2004, Magmatic sulfide deposits: geology, geochemistry and exploration: Berlin, Springer, 727 p.

O'Driscoll, B. and González-Jiménez J. M., 2016, Petrogenesis of the platinum-group minerals: Reviews in Mineralogy and Geochemistry, v. 81, p. 489-578.Osbahr, I., Oberthür, T., Klemd, R., and Josties, A., 2014, Platinum-group element distribution in base-metal sulfides of the UG2 chromitite, Bushveld Complex, South Africa - a reconnaissance study: Mineralium Deposita, v. 49, p. 655–665.

Paton, C., Hellstrom, J., Paul, B., Woodhead, J., and Hergt, J., 2011, Iolite: Freeware for the visualisation and processing of mass spectrometric data: Journal of Analytical Atomic Spectrometry, v. 26, no. 12, p. 2508-2518.

Patten C., Barnes S.-J., and Mathez E. A., 2012, Textural variations in MORB sulfide droplets due to differences in crystallization history: The Canadian Mineralogist, v. 50, p. 675–692.

Peregoedova, A., and Ohnenstetter, M., 2002, Collectors of Pt, Pd and Rh in a S-poor Fe–Ni–Cu sulfide system at 760 C: experimental data and application to ore deposits: The Canadian Mineralogist, v. 40, no. 2, p. 527-561.

Piña, R., Gervilla, F., Barnes, S.-J., Ortega, L., and Lunar, R., 2012, Distribution of platinum-group and chalcophile elements in the Aguablanca Ni–Cu sulfide deposit (SW Spain): evidence from a LA-ICP-MS study: Chemical Geology, v. 302, p. 61-75.

Waldner, P., and Pelton, A. D., 2004, Critical thermodynamic assessment and modeling of the Fe-Ni-S system: Metallurgical and Materials Transactions B, v. 35, no. 5, p. 897-907.

Wilson, S. A., Ridley, W. I., and Koenig, A. E., 2002, Development of sulfide calibration standards for the laser ablation inductively-coupled plasma mass spectrometry technique: Journal of Analytical Atomic Spectrometry, v. 17, p. 406-409.

Chapter 5 - Concentrations of Te, As, Bi, Sb and Se in the Marginal Zone of the Bushveld Complex: Evidence for crustal contamination and the nature of the magma that formed the Merensky Reef

Eduardo T. Mansur[1], Sarah-Jane Barnes[1]

[1]Sciences de la Terre, Université du Québec à Chicoutimi, Québec, G7H 2B1, Canada

Author contributions:

Mansur wrote the manuscript, collected and analyzed the data and created the figures. **Barnes** edited the manuscript and analyzed the data.

Lithos, 2020, 358-359: 105407

DOI : 10.1016/j.lithos.2020.105407

5.1 - Abstract

The association of platinum-group elements (PGE) and the chalcophile elements Te, As, Bi, Sb and Sn (TABS) has been extensively documented in several magmatic sulfide deposits over the past years. However, understanding the roles of TABS during the formation of magmatic sulfide deposits partially depends on constraining the concentration of TABS on the liquids from which they crystallized. This study presents the distribution of TABS (apart from Sn) in rocks of the Marginal Zone of the Bushveld Complex. These rocks record the composition of the parental magmas from which the Bushveld Complex have crystallized. The major and trace elements of the marginal rocks have been modelled as mixtures of komatiite, continental crust and a plagioclase-rich residuum. Similar mixtures are required to model the TABS in the marginal rocks, with the continental crust component contributing a large part of the As, Sb and Bi budgets in these melts. The concentrations of the TABS in the Merensky Reef can be modelled as a mixture of two of the magma types present in the Marginal Zone (the B-1 and B-2). The modelling also reveals that the distributions of Se, Te and Bi in the reef are essentially controlled by the presence of sulfide minerals, whereas As and Sb distributions are controlled by both sulfide minerals and melt component. This is because Se, Te and Bi are moderately to strongly chalcophile elements, but As and Sb are only slightly chalcophile elements. Thus, whole-rock As and Sb concentrations are not upgraded by the formation of the sulfide minerals, and may still be used to trace crustal contamination.

Keywords: Te, As, Bi, Sb, Se; platinum-group elements; magmatic sulfide deposits; Bushveld Complex; Marginal Zone.

5.2 – Introduction

The number of studies investigating the roles of the chalcophile elements Te, As, Bi, Sb and Sn (TABS) and Se during the formation of magmatic sulfide deposits has significantly increased over the past years (Hattori et al., 2002; Queffurus and Barnes, 2015; Duran et al., 2017; Samalens et al., 2017; Keith et al., 2018; LeVaillant et al., 2018; Liang et al., 2019; Mansur et al., 2019a; Mansur and Barnes, 2020). The main motivation for studying the TABS is to understand the frequent association of platinum-group elements (PGE) and TABS in the form of platinum-group minerals (PGM; O'Driscoll and González-Jiménez, 2016 and references therein). It has been suggested: i) that TABS stabilize PGE nanoclusters in silicate liquids leading to the inclusion of clusters in magmatic sulfide liquids (Tredoux et al., 1995; Helmy et al., 2013; González-Jiménez et al., 2018, 2019; Liang et al., 2019); ii) that high TABS concentrations lead to the saturation of PGM in magmatic sulfide liquid (Dare et al., 2010a; Hutchinson et al., 2015; Duran et al., 2017); iii) that TABS control the formation of PGM during exsolutions of sulfide minerals (Hutchinson and McDonald, 2008; Wirth et al., 2013; Junge et al., 2015; Mansur and Barnes, 2020); and iv) that TABS affect the post-magmatic remobilization of PGE (Péntek et al., 2008; Djon and Barnes, 2012; Tuba et al., 2014; Scholten et al., 2018; Sullivan et al., 2018). However, these studies are hampered by the lack of data on the concentrations of TABS in the parental magmas from which magmatic sulfide liquid segregated.

There are several reasons for the limited information on the concentration of TABS in parental liquids. First, the concentration of TABS in mafic magmas is low (generally <1 ppm, Hattori et al., 2002; Wang and Becker, 2013; Lissner et al., 2014; Mansur et al., 2019b; Yierpan et al., 2019) and the elements suffer from a number of interferences using the common method of analysis (ICP-MS). Secondly, due to their volatility (Lodders, 2003) TABS are not reliably determined during routine analysis and specific protocols must be used to obtain accurate results (Pitcairn, 2004; König et al., 2012, 2014; Patten et al., 2016; Mansur et al., 2019b). Consequently, most studies have concentrated on the distribution of TABS in sulfide ore deposits, where concentrations are high and simple aqua regia digest will dissolve the sample (e.g., Dare et al.,

2010b, 2014; Piña et al., 2012, 2013; Godel et al., 2012; Duran et al., 2016, 2017; Yudovskaya et al., 2017; LeVaillant et al., 2018; Liang et al., 2019; Mansur et al., 2019a).

In this contribution, we report the concentrations of TABS (apart from Sn) and Se in samples from the Marginal Zone of the Bushveld Complex, measured by hydride generation-atomic fluorescence spectrometry, which allows precise and accurate measurements at low levels. These rocks have been proposed as representative of the liquids from which the Bushveld Complex crystallized (Sharpe and Hulbert, 1985; Barnes et al., 2009, 2010; Godel et al., 2011; Wilson, 2012; Maier et al., 2016; Yang et al., 2018), thus allowing us to assess the concentration of Se and TABS in the liquids from which some of the largest PGE deposits in the world have formed.

This work will show that the concentrations of As and Sb in the initial Bushveld liquid (B-1) are significantly higher than in primary magmas, whereas the Se and TABS of later magmas (B-2 and B-3) are similar to primary magmas. We attribute the difference due to upper crustal contamination of the B-1 magma, whereas the B-2 and B-3 magmas were most likely contaminated with a plagioclase-rich residuum from the partial melting of the upper crust. We show that the distributions of the Se, Te and Bi across the Merensky Reef are controlled by the sulfide liquid component. In contrast, As and Sb distributions are influenced by the amount of silicate melt component in the cumulates. As suggested by Lesher and Burnham (2001) the effect of crustal contamination for elements with high partition coefficients between sulfide and silicate liquid (Te, Bi and Se) is obscured by the interaction of sulfides with a large volume of silicate magma. In contrast, for elements with lower partition coefficients (As and Sb) the effect of contamination is more evident. The implications for the formation of PGE deposits are also discussed.

5.3 – Geological Setting

The Bushveld Complex (Fig. 5.1) occurs in the northeastern portion of South Africa, covering an area of approximately 450 km x 350 km, with a total areal extent greater than 65,000 km^2 (Cawthorn, 2015 and references therein). The mafic-ultramafic rocks of the Bushveld Complex were emplaced discordantly into Neoarchean to Paleoproterozoic sedimentary rocks of the Transvaal Supergroup and Archean basement granites and gneisses at approximately 2,055 Ma (Scoates and Wall, 2015; Zeh et al., 2015; Mungall et al., 2016). The stratigraphic succession of the Bushveld Complex, which attains a maximum thickness of 8 km, is divided into five main zones (Hall, 1932). From the base to the top these are the noritic Marginal Zone at the bottom, followed by the ultramafic Lower Zone, the ultramafic to mafic Critical Zone, the gabbronoritic Main Zone, and the ferrogabbroic Upper Zone at the top. The major PGE-rich layers of the intrusion, Merensky Reef and UG-2 chromitite, are found in the upper part of the Critical Zone. A detailed description of these zones is provided by Maier et al. (2013) and references therein, and a summary of the features given here for the purpose of the study.

The Marginal Zone consists of fine-grained rocks at the margins of the intrusion and sills in the adjacent country rocks. Harmer and Sharpe (1985) and Sharpe and Hulbert (1985) divided the rocks into three groups based on their stratigraphic position and geochemistry. The *Bushveld 1* (B-1) rocks have textures ranging from quench (consisting of a skeletal orthopyroxene with a matrix of plagioclase laths) to fine-grained equigranular norite. These rocks occur mainly in contact or adjacent to the Lower Zone and lower Critical Zone. The *Bushveld 2* and *3* (B-2 and B-3) are in contact with or adjacent to the upper Critical Zone, and the Main Zone, respectively. Both consist mainly of gabbronorite with grain size varying from very fine (i.e. below 0.1 mm) at contact zones, and fine to medium (i.e. up to 2mm) within sills.

In terms of major element compositions, B-1 magmas are Mg-rich basaltic andesites, and the B-2 and B-3 are tholeiitic basalts (Barnes et al., 2010). The trace elements and Sr, Nd and O isotopes show evidence that all of the magmas have been contaminated with 30-50% continental crust (Harmer and Sharpe, 1985; Harris et al., 2005; Barnes et al., 2010). Barnes et al. (2010)

argued that the B-1 requires upper continental crust as a contaminant. However, Maier et al. (2000) argued against the model of simple crustal contamination for B-2 and B-3 rocks based on high Sr_i in these rocks. Instead, the authors propose that B-2 and B-3 magmas were contaminated with the residuum of the partial melt which was added to the B-1 magma. This residuum would have been rich in radiogenic plagioclase. The modelling of lithophile elements also supports the assimilation of a plagioclase-rich residuum by B-2 and B-3 magmas (Barnes et al. 2010). Furthermore, Barnes et al. (2010) and Godel et al. (2011) modeled the Lower Zone and lower Critical Zone as having crystallized from the B-1 magma. Barnes et al. (2010) found that to model the upper Critical Zone a 60:40 mixture of the B-1:B-2 magmas is required. Barnes et al. (2010) and Yang et al. (2018) also model the crystallization of the Main Zone using the B-3 magma composition.

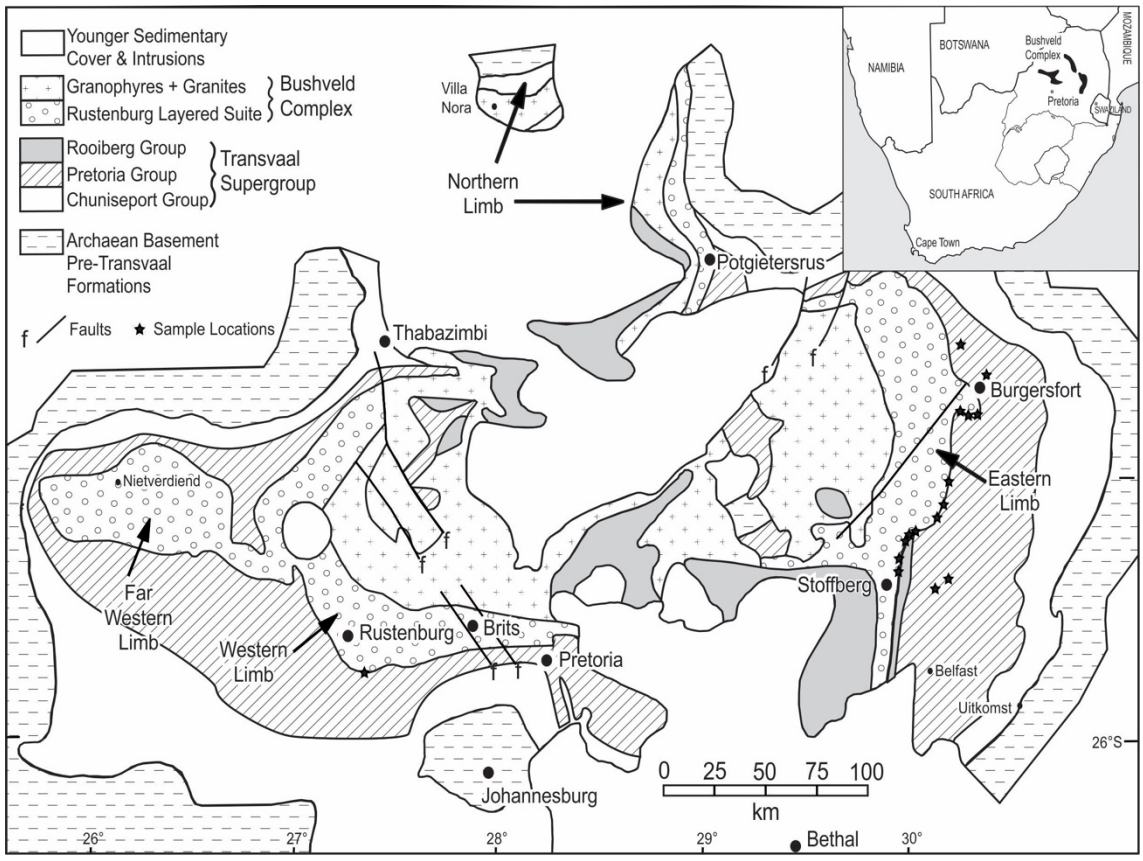

Figure 5.1 - Simplified geology of the Bushveld Complex and surrounding rocks, and location of samples utilized in this study. Modified from Reczko et al. (1995), Eales and Cawthorn (1996), and Barnes et al. (2010).

5.4 – Sample description

A suite of 23 samples, including 11 samples from B-1, 8 samples from B-2, and 4 samples from B-3 rocks, have been used in this study. Our samples were previously studied by Barnes et al. (2009), which investigated the distributions of S and Se, and also by Barnes et al. (2010), who documented their petrography and microstructures, as well as investigated their major and trace-element concentrations. All but one (ECBV111) of the selected samples are from the Eastern Limb of the Bushveld Complex, where the contact rocks are better exposed (Fig. 5.1). A detailed description on the petrography of the rocks from the Marginal Zone can be found in Harmer and Sharpe (1985) and Sharpe and Hulbert (1985), and a description of our samples is provided here.

The B-1 rocks show textures varying from quenched to granular. The quench-textured B-1 rocks show elongated skeletal crystals of orthopyroxene (up to 1cm) in a fine-grained matrix of devitrified glass. Plagioclase laths are also present in the matrix, and in some cases present a flow texture with plan parallel aligned crystals (Fig. 5.2a). Biotite, chromite and sulfide minerals are observed in trace abundances (< 1%) in almost all samples. The granular B-1 rocks consist of fine-grained (1–4 mm) orthopyroxene and plagioclase, with minor clinopyroxene (Fig. 5.2b). Biotite, chromite and sulfide minerals are also present as accessory phases. In both quench and granular B-1 rocks the sulfide assemblage is composed of fine intergrowths of pyrrhotite, pentlandite and chalcopyrite. The sulfides form mostly rounded droplets, which do not show any reaction features with the enclosing silicates (Fig. 5.2c). The quench-textured samples occur mainly as 10 to 100 meter thick sills, whereas the granular rocks occur both as contact rocks and sills (Barnes et al., 2010).

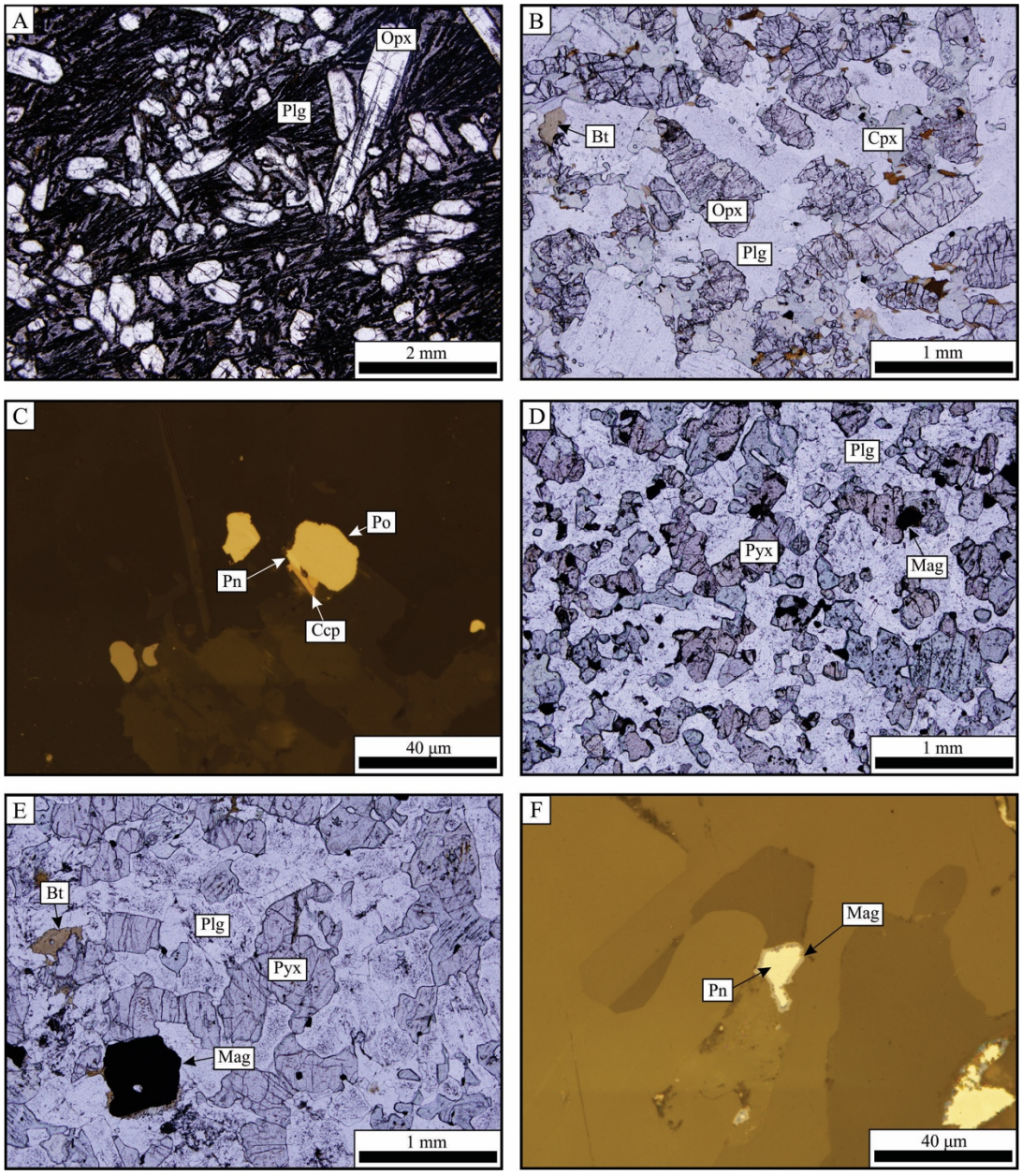

Figure 5.2 - Photomicrographs of the marginal rocks: (a) B-1 quenched textured sample with medium-grained orthopyroxene crystals in a fine matrix of plan parallel aligned plagioclase laths, and devitrified glass; (b) Fine-grained gabbronorite with orthopyroxene, clinopyroxene and plagioclase crystals. Biotite occurs as an accessory phase; (c) Sulfide intergrowth in a B-1 sample comprising pyrrhotite (Po), pentlandite (Pn), and chalcopyrite (Ccp). The sulfides have curved, regular boundaries and appear to be in equilibrium with surrounding silicates; (d) Fine-grained B-2 gabbronorite with plagioclase, orthopyroxene and clinopyroxene, and accessory magnetite crystals; (e) Medium-grained B-3 gabbronorite with plagioclase, orthopyroxene and clinopyroxene, and accessory magnetite, and biotite crystals; (f) Very fine-grained pentlandite (Pn) crystal with thin magnetite rim at the contact with surrounding silicates. The texture suggests that the sulfide minerals have reacted with the surrounding silicates. Abbreviations: Bt – biotite ; Cpx – clinopyroxene; Mag – magnetite; Opx – orthopyroxene; Plg – plagioclase; Pyx – pyroxene.

Both the B-2 (Fig. 5.2d) and B-3 (Fig. 5.2e) rocks show very similar mineralogy and texture. The samples consist of equigranular, fine-grained plagioclase, orthopyroxene and clinopyroxene. Biotite, magnetite, ilmenite and sulfide minerals also occur as accessory minerals. In some of the B-2 samples the sulfide minerals have thin magnetite rims (Fig. 5.2f). The texture suggests that in these samples the sulfide minerals have reacted with the surrounding silicates, and thus developed the magnetite rims. The B-2 and B-3 rocks are found at both the contact of the Marginal Zone and within sills. The samples found at the contact of the Marginal Zone tend to be slightly more finely grained relative to those found at the interior of sills (Barnes et al., 2010).

5.5 – Analytical techniques

Tellurium, As, Bi, Sb and Se analyses have been carried out following the technique described by Mansur et al. (2019b) at LabMaTer, Université du Québec à Chicoutimi (UQAC). Approximately 0.4 g of sample were digested with 5 ml of aqua regia (1:3 HNO_3:HCl) in close-caped beaker at 70ºC for 24 hours. The aliquot was allowed to cool and diluted to 25 ml prior to mixing with a reductant solution (0.7% $NaBH_4$ and 0.4%NaOH). The mixed solution was analysed by Hydride Generation-Atomic Fluorescence Spectrometry (HG-AFS), using a continuous flow PSA Millenium Excalibur 10.055 from PS Analytical. Six calibration solutions with concentrations of 0.1, 0.25, 0.5, 1, 2.5 and 5 ppb were prepared using standard solutions of each element (PlasmaCAL, SCP Science, Quebec, Canada). The calibration solutions were mixed with the reagent blank prior to measurement, in the same proportion as sample aliquots. Calibration solutions were measured at the beginning and the end of each sequence of analysis to monitor fluctuations of the fluorescence signal, which were not observed. International reference materials (CH-4 and TDB-1; Natural Resources Canada), GeoPt18 (KPT-1), and a blank were determined at the same time as the samples, and the results agree with working values (*ANNEXE*

11). The 3σ detection limits are 0.006, 0.003, 0.005, 0.005 and 0.002 ppm for Te, As, Bi, Sb and Se, respectively.

5.6 – Results

The concentrations of the TABS, Se and S for each sample and average concentrations of B-1, B-2 and B-3 rocks are listed in Table 5.1. The B-1 and B-3 rocks have S/Se ratios close to mantle (~3000 McDonough and Sun, 1995; Hattori et al., 2002; Lorand et al., 2003), with B-1 rocks having higher S and Se than then B-3 rocks (Fig. 5.3a). The S/Se ratios close to mantle most likely reflect no S-loss in these samples (Queffurus and Barnes, 2015). Most B-2 rocks have lower S/Se ratios of ~ 1000, although 2 are similar to mantle (Fig. 5.3a). Given the presence of magnetite rims on the sulfides in some B-2 samples (Fig. 5.2f) the low ratios are interpreted as the product of S-loss from some samples (Peck and Keays, 1990; Ripley, 1990; Queffurus and Barnes, 2015). Barnes et al. (2009), have determined the S and Se contents through a complete stratigraphic section of the Bushveld Complex, and also found S/Se ratios lower than mantle values for some B-2 samples. Nevertheless, although some S may have been loss, the relation observed between S and TABS is the same as that between Se and TABS. Because of the possibility of S loss, and because the precision of the Se analyses is higher than that of S analyses, Se is used as a proxy for S in the following section.

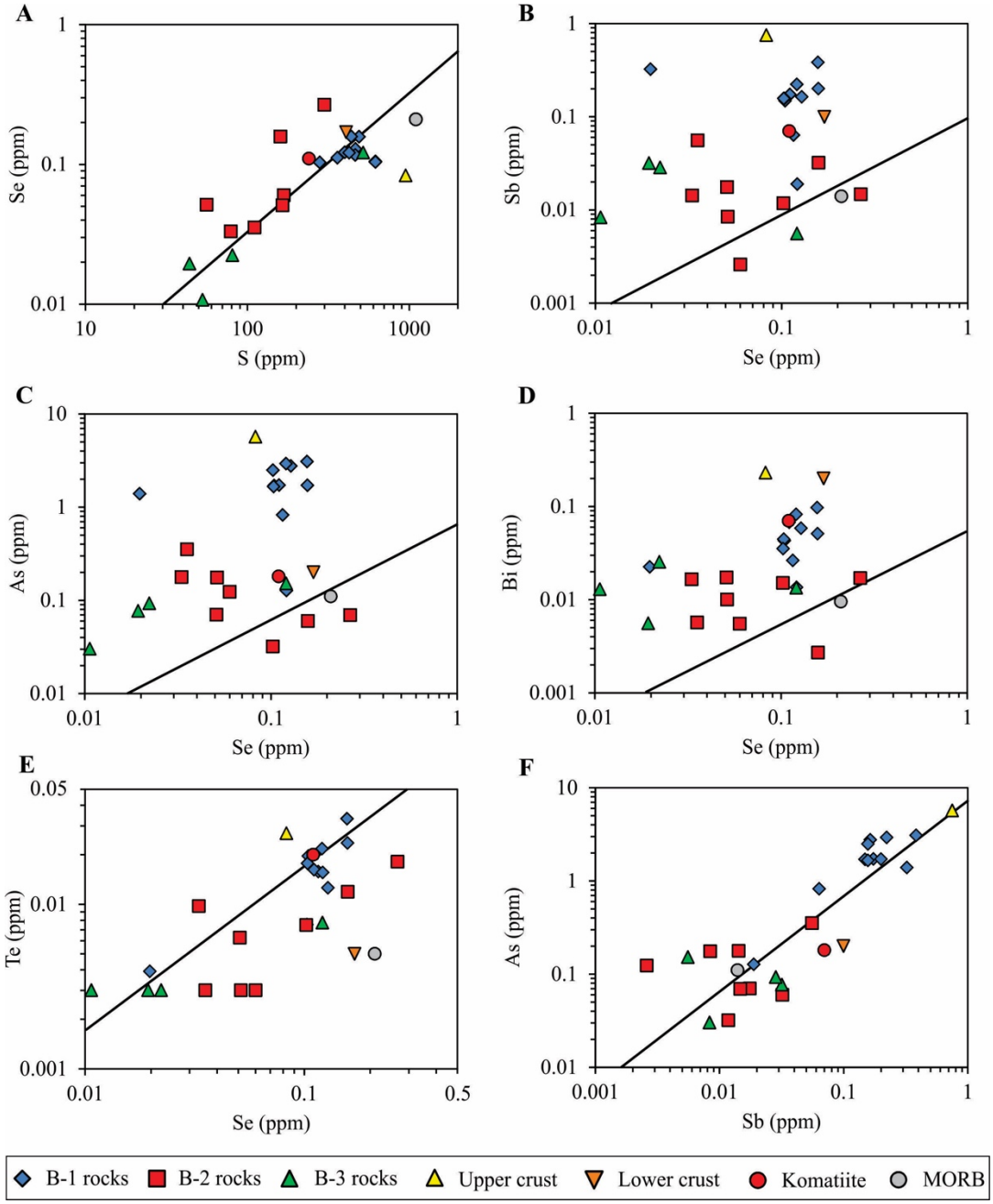

Figure 5.3 - Binary plots of Se vs S (a), Sb (b), As (c), Bi (d), and Te (e) vs Se, and As vs Sb (f) in samples from the Marginal Zone of the Bushveld Complex. Average concentrations in upper continental crust (Hu and Gao, 2008), lower continental crust (Rudnick and Gao, 2003), MORB (Arevalo and McDonough, 2010) and komatiite (OKUM reference material - IAG) are shown for reference. The black lines indicate the mantle ratios (Lyubetskaya and Korenaga, 2007).

Table 5.1 - Concentrations of As, Bi, S, Sb, Se and Te, and Se/Te and S/Se rations in the Marginal Zone rocks of the Bushveld Complex.

Sample	Unit	Texture	As ppm	Bi ppm	S ppm	Sb ppm	Se ppm	Te ppm	Se/Te	S/Se
DL			*0.003*	*0.005*		*0.005*	*0.002*	*0.006*		
DI-225	B-1	Quenched	1.702	0.043	619	0.148	0.104	0.020	5.3	5926
CD-001		Quenched	2.765	0.058	466	0.164	0.128	0.013	10.2	3634
CD-017		Quenched	3.079	0.097	491	0.383	0.157	0.033	4.7	3130
DI-204		Quenched	0.824	0.026	465	0.064	0.116	0.016	7.4	4008
ECBV-018		Granular	1.720	0.068	360	0.174	0.111	0.016	6.8	3247
ECBV-019		Quenched	1.716	0.051	439	0.200	0.157	0.024	6.7	2788
ECBV-021		Quenched	1.663	0.044	619	0.157	0.104	0.018	5.9	5970
ECBV-049A		Granular	0.127	0.014	400	0.019	0.122	0.016	7.8	3292
ECBV-105		Granular	2.927	0.082	426	0.222	0.121	0.022	5.5	3527
ECBV-106		Quenched	2.490	0.035	280	0.157	0.103	0.008	13.7	2722
ECBV-111		Granular	1.395	0.022	n.r.	0.322	0.020	0.004	5.1	n.r.
Average B-1			1.855	0.049	457	0.183	0.113	0.017	6.6	4042
Bc-6	B-2	Fine-grained	0.124	0.006	168	**0.003**	0.060	**0.003**	19.0	2798
Bc-25		Fine-grained	0.176	0.010	56	0.008	0.051	**0.003**	16.2	1089
CO-066		Granular	0.070	0.017	165	0.018	0.051	0.006	8.1	3240
CO-253		Granular	0.069	0.017	299	0.015	0.267	0.018	14.7	1122
ECBV-025		Granular	0.032	0.015	n.r.	0.012	0.102	0.007	13.7	n.r.
ECBV-026		Granular	0.060	**0.003**	160	0.032	0.158	0.012	13.3	1013
ECBV-058		Granular	0.178	0.017	79	0.014	0.033	0.010	3.4	2387
ECBV-064		Granular	0.354	0.006	111	0.056	0.035	**0.003**	11.2	3135
Average B-2			0.133	0.011	148	0.020	0.095	0.008	12.0	1566
CO-048	B-3	Fine-grained	0.077	0.006	44	0.032	0.019	**0.003**	6.1	2264
CO-252		Fine-grained	0.030	0.013	53	0.008	0.011	**0.003**	3.4	4959
ECBV-013		Fine-grained	0.093	**0.003**	81	0.028	0.022	**0.003**	7.0	3635
ECBV-063		Fine-grained	0.152	0.013	520	0.006	0.121	0.008	15.7	4291
Average B-3			0.088	0.009	175	0.019	0.043	0.004	10.1	4021

Abbreviations: n.r. - not reported; DL - Detection limit. Sulfur values are reported by Barnes et al. (2009, 2010). Values in bold are below the detection limit and were replaced by half of the detection limit values.

The B-1 samples are enriched in all of the TABS relative to the B-2 and B-3 samples (Table 5.1), with the B-1 samples having values between upper crust and komatiite, whereas the B-2 and B-3 samples have very low concentrations, close to MORB or lower crust (Figs. 5.3b to

5.3f; Rudnick and Gao, 2003; Arevalo and McDonough, 2010). There are no significant correlations between Se and As, Bi or Sb (Figs. 5.3b to 5.3d). The lack of correlation with Se implies that sulfide liquid was not the controlling phase for these elements during the formation of these rocks. Most samples have higher Sb/Se, As/Se and Bi/Se ratios than mantle (solid lines on Fig. 5.3b to 5.3d). In all of the samples, As shows a strong positive correlation with Sb (Fig. 5.3f), and both show a slightly positive correlation with Bi (not shown). In contrast to the other TABS, Te shows a positive correlation with Se for the B-1 samples (Fig. 5.3e) with Se/Te ratios close to mantle values (~7; Lyubetskaya and Korenaga, 2007; Wang and Becker, 2013). Where detectable, the B-2 samples have Se/Te ratios higher than mantle (Fig. 5.3e). The concentrations of Te in the B-3 rocks are mainly less than detection limit of 0.006 ppm.

Mantle-normalized TABS plots for B-1, B-2 and B-3 rocks are shown in Fig. 5.4. The elements are plotted in order of incompatibility with a pictric/komatiitic basalt mantle source (Barnes, 2016). The TABS mantle-normalized patterns for the B-1 rocks are enriched in As, Sb and Bi, and decrease from approximately 10 to 80 times mantle at As, Sb and Bi to 1 to 5 times mantle at Se and Te (Fig. 5.4a). In contrast, the TABS mantle-normalized patterns for the B-2 (Fig. 5.4b) and B-3 (Fig. 5.4c) rocks are much flatter at 0.1 to 10 times mantle. Most B-2 and some B-3 rocks show a slightly positive Bi anomaly.

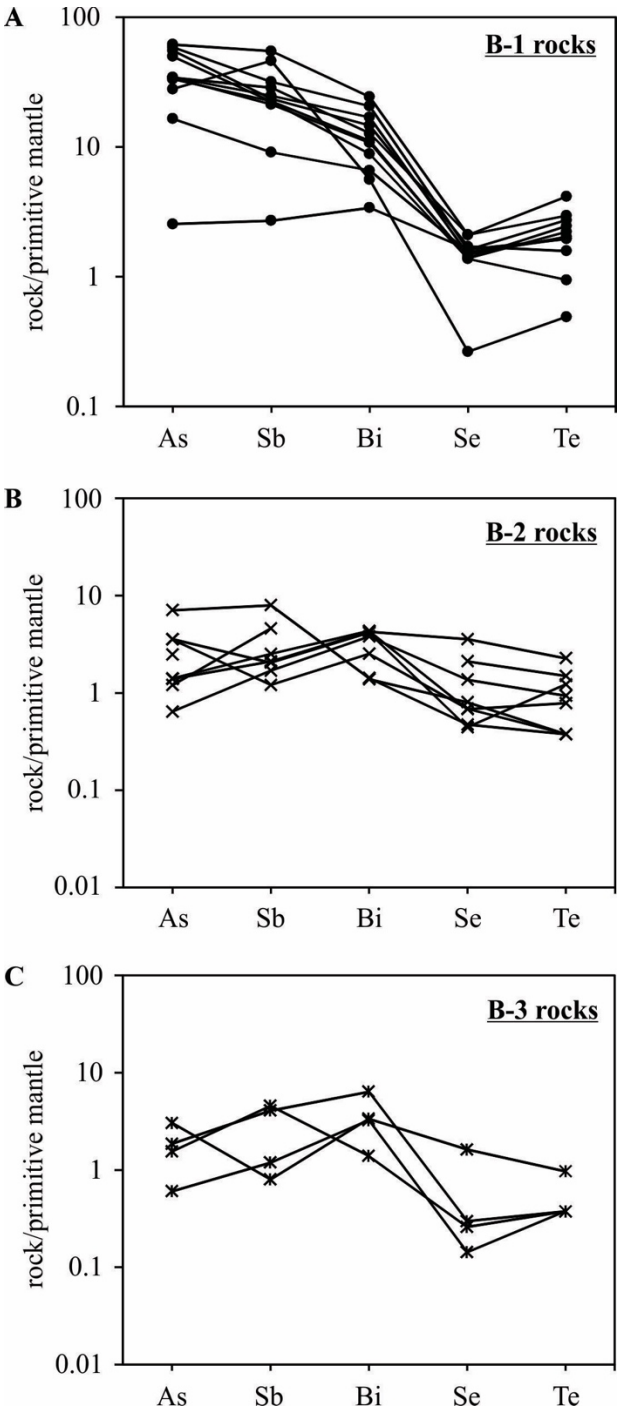

Figure 5.4 - Mantle-normalized TABS diagrams for (a) B-1 rocks, (b) B-2 rocks and (c) B-3 rocks. The elements are plotted in order of incompatibility with a pictric/komatiitic basalt mantle source (Barnes, 2016). Primitive mantle values from Lyubetskaya and Korenaga (2007).

Table 5.2 – Modelling of distribution of TABS, Se and Pd in the Merensky Reef at Impala and Rustenburg sections.

						N	As	Bi	Sb	Te	Se	Pd
Comp. cumulate sulfide inside reef (Csul)						20000	2.3	17.3	0.6	43.5	126.8	164.9
Comp. cumulate sulfide outside reef (Csul)						350	2.3	8.7	0.6	4.8	32.2	3.7
Ci = 60:40 mixture B1+B2							1.16	0.03	0.12	0.01	0.11	0.01
D sul/sil							2*	500*	5*	3000**	1200**	40000***
Locality	Impala mine							Rustenburg mine				
Sample	IM-3	IM-13	IM-21	IM-24	IM-25	IM-26		M4	M1	UC	CGM-2	AN
Rock	M	M	M	LC	AN	L		M	M	UC	CGM	AN
wt frac melt	0.19	0.51	0.24	0.10	0.10	0.07		0.12	0.13	0.13	0.11	0.11
wt frac cum sul	0.00	0.00	0.06	0.01	0.01	0.05		0.03	0.09	0.01	0.04	0.01
wt frac sil and oxide	0.80	0.49	0.71	0.89	0.89	0.88		0.85	0.78	0.85	0.85	0.88
As melt	0.22	0.59	0.27	0.12	0.12	0.08		0.14	0.15	0.15	0.13	0.13
As sul	0.01	0.00	0.13	0.03	0.03	0.12		0.06	0.21	0.03	0.09	0.02
As total	0.24	0.59	0.41	0.15	0.14	0.20		0.21	0.37	0.19	0.22	0.16
As observed	0.09	0.44	0.12	0.07	0.08	0.10		0.12	0.14	0.07	0.20	0.07
Bi melt	0.01	0.02	0.01	0.00	0.00	0.00		0.00	0.00	0.00	0.00	0.00
Bi sul	0.04	0.00	1.00	0.20	0.20	0.90		0.48	1.58	0.25	0.68	0.18
Bi total	0.05	0.02	1.01	0.20	0.20	0.90		0.48	1.58	0.26	0.68	0.18
Bi observed	0.02	0.01	0.94	0.17	0.16	0.73		0.38	1.40	0.33	0.61	0.22
Sb melt	0.02	0.06	0.03	0.01	0.01	0.01		0.01	0.02	0.02	0.01	0.01
Sb sul	0.00	0.00	0.03	0.01	0.01	0.03		0.02	0.05	0.01	0.02	0.01
Sb total	0.03	0.06	0.06	0.02	0.02	0.04		0.03	0.07	0.02	0.04	0.02
Sb observed	0.02	0.03	0.04	0.02	0.06	0.05		0.03	0.06	0.04	0.03	0.01
Te melt	0.00	0.01	0.00	0.00	0.00	0.00		0.00	0.00	0.00	0.00	0.00
Te sul	0.02	0.00	2.51	0.49	0.49	2.27		1.20	3.97	0.64	1.71	0.45
Te total	0.03	0.01	2.52	0.50	0.50	2.27		1.20	3.97	0.64	1.71	0.45
Te observed	0.12	0.02	2.39	0.40	0.51	2.60		0.86	4.45	0.75	1.76	0.67
Se melt	0.02	0.05	0.02	0.01	0.01	0.01		0.01	0.01	0.01	0.01	0.01
Se sul	0.15	0.02	7.33	1.44	1.44	6.61		3.51	11.58	1.87	4.99	1.30
Se total	0.18	0.07	7.36	1.45	1.45	6.62		3.52	11.59	1.89	5.01	1.31
Se observed	0.56	0.23	7.10	1.36	1.63	5.92		4.14	14.65	1.99	5.66	1.57
Pd melt	0.00	0.01	0.00	0.00	0.00	0.00		0.00	0.00	0.00	0.00	0.00
Pd sul	0.02	0.00	9.54	1.87	1.88	8.60		4.56	15.06	2.43	6.50	1.69
Pd total	0.02	0.01	9.54	1.87	1.88	8.60		4.56	15.06	2.44	6.50	1.69
Pd observed	0.02	0.01	6.33	4.17	3.03	9.87		2.16	11.90	4.27	5.94	4.03

All values in ppm. * Li and Audétat (2015) ** Liu and Brenan (2015) *** Mungall and Brenan (2014). AN - anorthosite; L - leuconorite; LC - lower chromitite; CGM - coarse-grained melanorite; UC - upper chromitite; M - melanorite. Observed values are from Mansur and Barnes (2020) for Se and TABS, and from Barnes and Maier (2002) and Godel et al. (2007) for Pd.

5.7 – Discussion

5.7.1 - Crustal contamination and the external addition of TABS

It has been shown that the Bushveld magmas were contaminated with continental crust, which affected the major and trace elements concentrations in these liquids (Maier et al., 2000; Harris et al., 2005; Barnes et al., 2010; Eales and Costin, 2012; Roelofse and Ashwal, 2012; Wilson, 2012; Roelofse et al., 2015; Maier et al., 2016). Many of these authors argue that B-1 magma represents a komatiitic magma contaminated with upper continental crust. Indeed, B-1 TABS patterns most closely resemble the average upper continental crust, with higher concentrations of As, Sb and Bi relative to komatiite pattern (Fig. 5.5a). Maier et al. (2016) modelled the B-1 magma and associated cumulates as the product of approximately 35% assimilation of upper crust accompanied by 27 % crystal fraction (AFC) of komatiite liquid. The product of AFC modelling of a komatiite with continental crust has a TABS-pattern that closely resembles that of B-1 rocks, supporting the addition of upper continental crustal material (Fig. 5.5a).

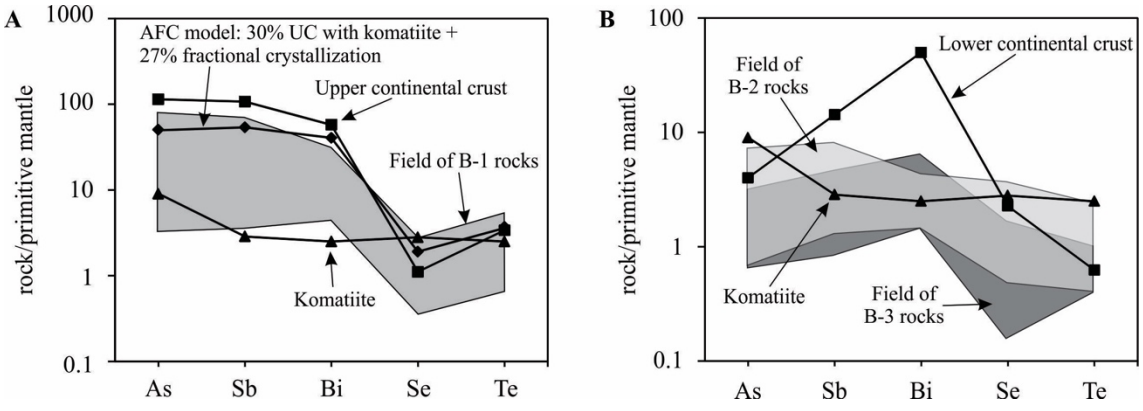

Figure 5.5 - Mantle-normalized TABS diagrams for (a) B-1 rocks compositional field relative to komatiite (Barnes, 2016), upper continental crust (Hu and Gao, 2008), and a AFC model of a mixture of a komatiite with 30% upper crust (UC) and 27% fractional crystallization; (b) B-2 and B-3 rocks compositional fields compared to komatiitic basalt (Barnes, 2016) and lower continental crust (Rudnick and Gao, 2003). Primitive mantle values from Lyubetskaya and Korenaga (2007).

Thorium is also strongly concentrated in the upper crust (10.5 ppm; Hu and Gao, 2008) relative to primitive mantle (0.06ppm; Lyubetskaya and Korenaga, 2007), and can also be used as a proxy for crustal contamination. Plots of As, Sb and Bi versus Th show that the B-1 magmas can be indeed modelled as the product of AFC of komatiite contaminated with average upper crust (Fig. 5.6a to 5.6c). However, the Se and Te concentrations of upper crust (0.083 and 0.027ppm, respectively) and komatiite (0.21 and 0.02ppm, respectively) are similar, thus contamination is not readily apparent for these two elements (Fig. 5.6d and 5.6e).

The origin of the B-2 and B-3 magmas is less well established. Possibly they are also product of AFC of komatiite, but in this case the contaminant is argued to have been plagioclase-rich residuum formed during partial melting of the upper crust during the formation of the B-1 magma (Maier et al., 2000; Barnes et al., 2010). Isotopic work support that the rocks have a large crustal component (Maier et al., 2000; Harris et al., 2005; Karykowski et al., 2017), but the low incompatible lithophile element content indicates that the contaminant is not average upper continental crust (Barnes et al., 2010). The low TABS content is in agreement with this. Neither is average lower continental crust suitable as it contains too much Sb (0.1ppm) and Bi (0.2ppm) to be a contaminant (Fig. 5.3d and 5.3f; Rudnick and Gao, 2003), and also the whole-rock Sr isotopic signature does not match lower crust (Maier et al., 2000).

Overall the B-2 and B-3 patterns are similar to komatiite and presumably the crustal contaminant contained very little TABS and thus did not affect the patterns (Fig. 5.5b). Therefore, our results support that a plagioclase-rich residuum is a suitable contaminant for these melts (Maier et al., 2010; Barnes et al., 2010). The partial melting of upper crust by B-1 magmas, and incorporation of As, Sb and Bi (Fig. 5.5a) possibly led to the formation of a residuum depleted in these elements. Consequently, during further assimilation by B-2 and B-3 magmas, the As, Sb, and Bi content of the melts remained mostly unaffected, and most likely resemble that of the parental komatiitic magmas. This suggestion is also in agreement with the previous modelling of lithophile elements (Barnes et al., 2010), and isotopic studies (Maier et al., 2000; Harris et al., 2005; Karykowski et al., 2017).

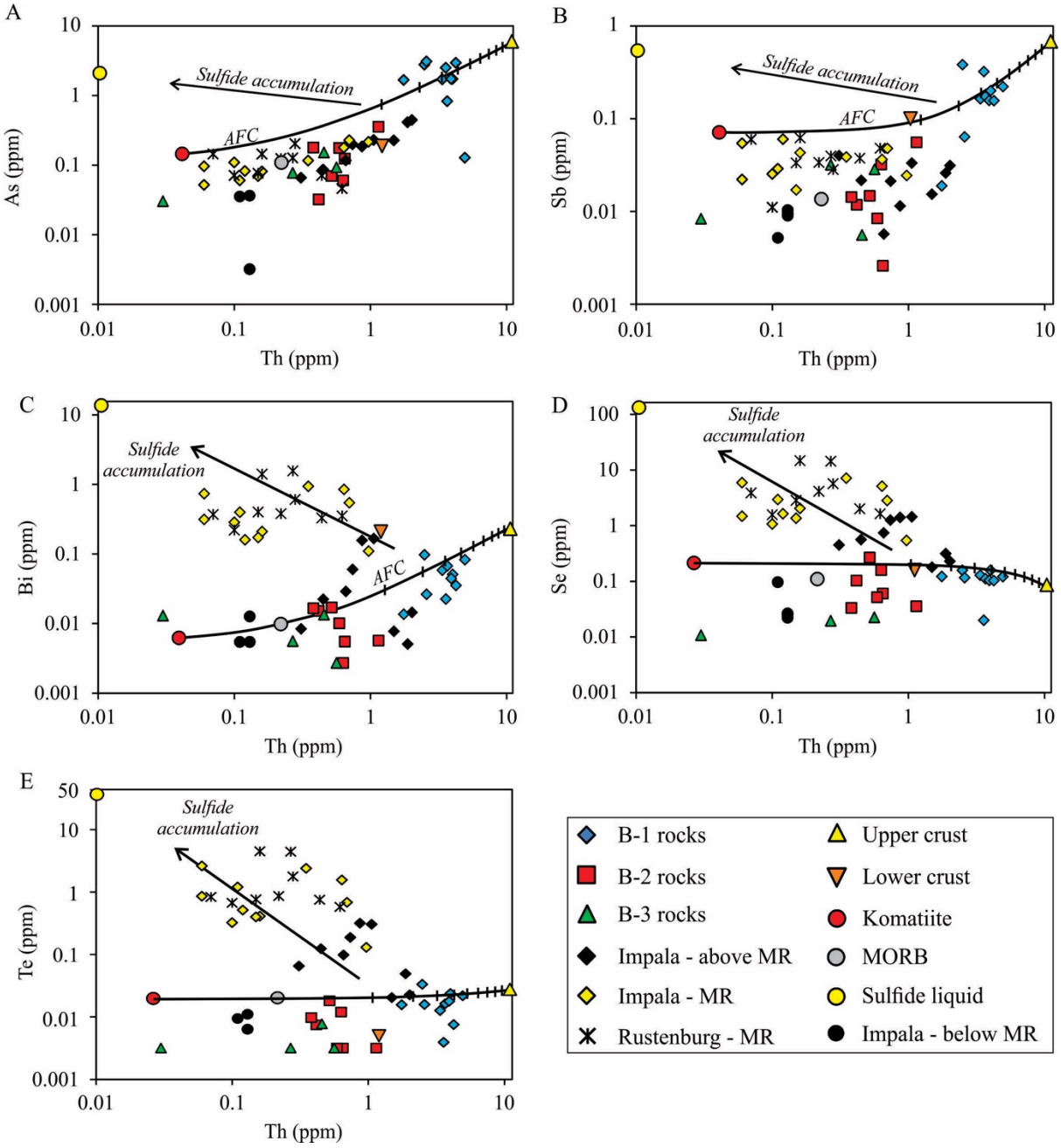

Figure 5.6 - Binary plots of As (a), Sb (b),Bi (c), Se and Te vs Hf in samples from the Marginal Zone, and Merensky Reef (MR) at the Impala and Rustenburg mines (Barnes and Maier 2002; Godel et al. 2007; Mansur and Barnes, 2020). Average concentrations in upper continental crust (Hu and Gao, 2008), lower continental crust (Rudnick and Gao, 2003), MORB (Arevalo and McDonough, 2010) and komatiite (OKUM reference material; IAG) are shown for reference. The black lines represent the AFC model of a mixture of a komatiite with 30% upper crust and 27% fractional crystallization, and the dash lines represent 10% increments. Individual analyses for the Merensky Reef samples are reported in the *ANNEXE 16*, whereas modelled composition of sulfide liquid is given in Table 5.2.

5.7.2 – Modelling the distribution of TABS in the Merensky Reef

The Merensky Reef is thought to have formed from a mixture of the B-1 and B-2 magmas (Naldrett and von Gruenewaldt, 1989; Li et al., 2001; Godel et al., 2007; Naldrett et al., 2009; Barnes et al., 2002, 2010; Maier et al., 2016). A 60:40 mixture of these magmas was shown as suitable for modelling the concentrations of a wide range of major, minor and trace elements in the reef (Barnes et al., 2009, 2010; Maier et al., 2016). The concentrations of TABS and Se across two sections of Merensky Reef (one from Impala Mine and one from Rustenburg Mine) have been determined (Mansur and Barnes, 2020*;* Fig. 5.7 and 5.8; *ANNEXE 16*). Below we model the TABS concentrations across the two reef locations assuming that the magma that formed the reefs was a 60:40 mixture of the B-1 and B-2 magmas (following Barnes et al., 2010).

The components of the reef have been modelled as cumulate sulfide liquid, silicate liquid and cumulate (silicate minerals and oxides). A summary of the modelling parameters and the results for selected samples are given in Table 5.2, and the complete modelling results are reported in the *ANNEXE 13*. The composition of the sulfide liquid was modelled using the zone refining equation of Brugmann et al. (1993)

$$(1) \qquad C_{Sul} = C_{Sil} \{D^{Sul/Sil} - (D^{Sul/Sil}-1) \exp^{[-(1/DSul/Sil*N)]}\}$$

where C_{Sul} is the concentration of an element in the sulfide liquid, C_{Sil} is the concentration of an element in the silicate liquid, $D^{Sul/Sil}$ is the partition coefficient for the element between sulfide and silicate liquid, and N is the ratio of silicate to sulfide liquid. The silicate liquid fraction in each sample was estimated based on the concentration of the incompatible elements (Hf, La and Sm) in the rocks divided by the composition of the magma (Table 5.2). The cumulate sulfide liquid fraction in each rock was estimated by

$$(2) \quad \text{Wt \%. sulf} = (\text{S rock} - 1000* \text{ wt. fraction silicate liquid})/350000$$

assuming that sulfide saturation occurred at ~1000 ppm (Li and Ripley, 2005) and that the sulfide liquid contained 35 weight percent S. The cumulate silicate and oxide minerals were assumed to

not contribute to mass balance of TABS, although experiments on this subject are still lacking. More details of the modelling can be found in *ANNEXE 13*.

Plots of modelling results versus depth across the Impala (Fig. 5.7) and Rustenburg (Fig. 5.8) sections show that the distributions of Se, Te and Bi closely follow each other and the PGE (here represented by Pd). These distributions can be modelled by variations in the fraction of cumulate sulfide liquid of the rocks, and thus their contribution to the whole rock budget (Fig. 5.7 and 5.8). In contrast, the As and Sb in large part follow the incompatible elements (Fig. 5.6), and are better modelled by the silicate liquid fraction, which represents the trapped melt component in the rocks (Fig. 5.7 and 5.8). The difference in behaviour between the two groups of elements reflects the differences in partition coefficients. Arsenic and Sb are only slightly chalcophile with partition coefficients between sulfide and silicate liquid of 1-10 (Table 5.2; Li and Audétat, 2015). In contrast, Bi and Se are strongly chalcophile with partition coefficients in the 100 to 1000 range, and Te and Pd are highly chalcophile with partition coefficients greater than 1000 (Table 5.2; Mungall and Brenan, 2014; Liu and Brenan, 2015; Barnes, 2016 and references therein).

If we regard the results for individual samples, we can see that the melt component in samples below and in the lower parts (below 6 cm height) of the Merensky Reef is low (i.e. 5 to 15%; *ANNEXE 16*). However, greater amounts of melt component are observed in the upper parts (above 8 cm height) and above the Merensky Reef (i.e. 15 to 55%; *ANNEXE 16*). This variation suggests that the reef interval has experienced compaction during crystallization (Godel et al., 2006), and the interstitial melt component was squeezed out from the reef interval into the upper portions. The compaction is also supported by petrographic studies (Barnes and Maier, 2002; Godel et al., 2007; Vukmanovic et al., 2013; Holness et al., 2017).

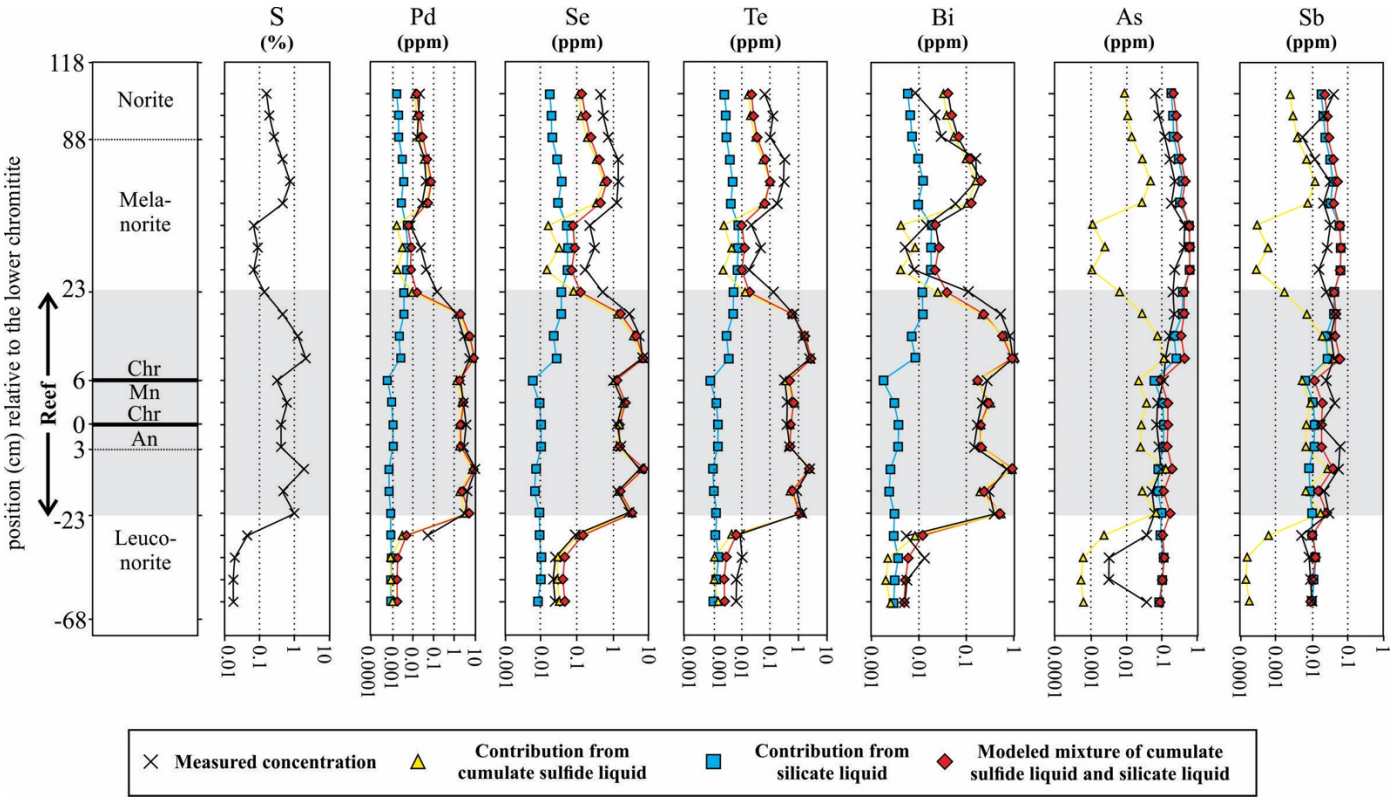

Figure 5.7 - Variations of Pd, Se, Te, Bi, As and Sb measured concentrations, and modeled contributions from cumulate sulfide liquid, trapped silicate liquid, and a mixture of both, with height across the Impala section. Note that the vertical scale is not linear and the samples are spaced out evenly. The reef interval (shade gray) is defined by rocks containing more than 1.5 ppm Pt+Pd in whole-rock analysis, and starts 23cm below the lower chromitite and ends 23cm above it (Barnes and Maier, 2002). Individual analyses and complete modelling results are reported in the *ANNEXE 13*. Abbreviations: An: anorthosite; Chr: chromitite; Mn: melanorite.

Although the modeled and measured distributions of PGE, Se and TABS across the Merensky Reef are correlated spatially, some divergences are observed. Modelled concentrations of As are higher (1 to 2 times) relative to measured concentrations across the entire section (Fig. 5.7 and 5.8; Table 5.2). Given its volatile behaviour (Lodders, 2003), this could suggest that some of the As was lost during the formation of the reef. However, all the other TABS and Se also show a volatile behaviour (Lodders, 2003), but their measured concentrations are not lower than modelled values.

The differences between modelled and measured As concentrations may also reflect regional heterogeneities in the compositions of rocks that contaminated the magmas. Most of the samples of the marginal rocks were collected at the eastern limb of the Bushveld Complex,

whereas the Impala and Rustenburg sections are located at the western limb of the intrusion (Fig. 5.1). Possibly the contaminant on the eastern limb was slightly richer in As than the contaminant on the western limb. Moreover, Willie et al. (2007) also reported variable As concentrations in sediments from the Transvaal Supergroup that support their regional heterogeneity.

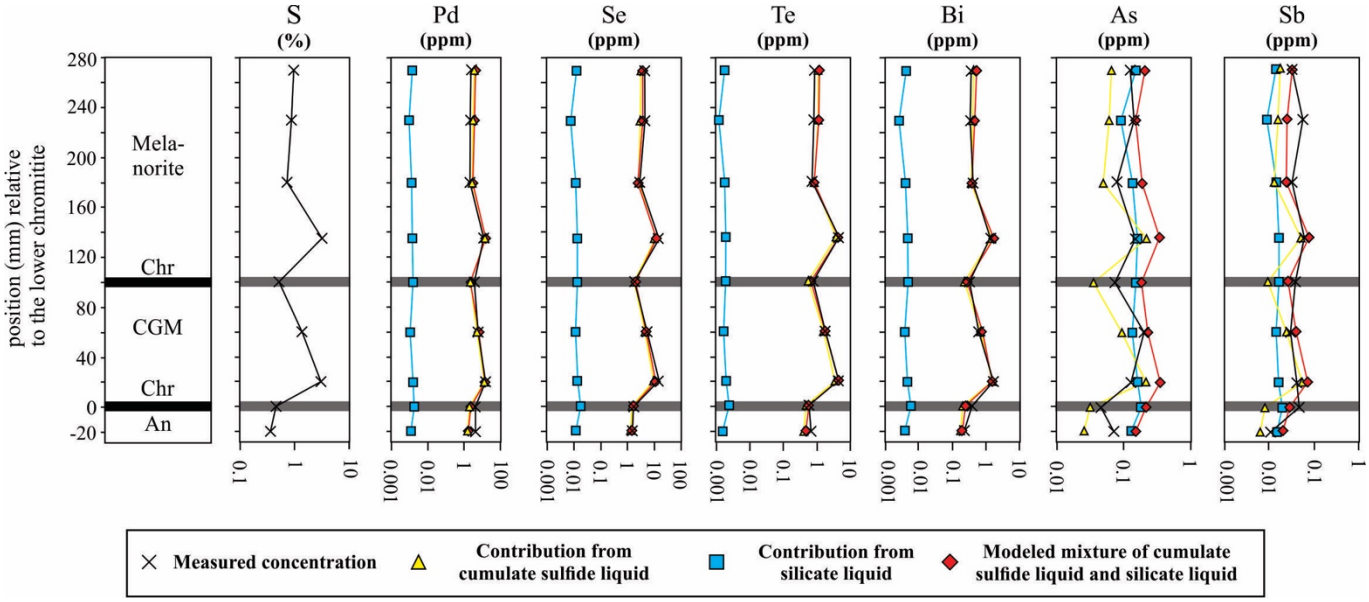

Figure 5.8 - Variations of Pd, Se, Te, Bi, As and Sb measured concentrations, and modeled contributions from cumulate sulfide liquid, trapped silicate liquid, and a mixture of both, with height across the Rustenburg section. Individual analyses and complete modelling results are reported in the *ANNEXE 13*. Abbreviations: An: anorthosite; Chr: chromitite; CGM: coarse-grained melanorite.

Another minor divergence between modelled and measured values is observed for Se and Te results (Table 5.2). Although the measured and modelled results are similar within the reef, the Se and Te modelled concentrations are lower (1 to 2 times) relative to measured values in samples above the reef interval (Fig. 5.7; *ANNEXE 13*). These differences most likely reflect the depletion of Te and Se in the silicate liquid as sulfide liquid segregated upon the formation of the Merensky Reef. This is because Te and Se behave as strongly chalcophile elements (Liu and Brenan, 2015; Barnes, 2016) and would have partitioned into the sulfide liquid upon the formation of the reef. Moreover, the differences may also originate from various uncertainties during the calculations. These are important to be considered given the strong control of Te and

Se by the cumulate sulfide fraction (Fig. 5.7 and 5.8), combined with very low values of S found in rocks above the reef interval (Fig. 5.7). Therefore, it is possible that the calculation of the sulfide liquid fraction (Wt %. Sulf in equation 2) is not completely accurate for samples above the reef.

Overall, the modelled and measured concentrations of PGE, Se and TABS in samples from the Merensky Reef are similar. This supports that a B-1:B-2 mixture (60:40) is appropriate as initial liquid for the formation of the upper Critical Zone, and crystallization of the Merensky Reef (Barnes et al., 2010; Maier et al., 2016). Moreover, the modelling results support that the distributions of PGE, Se, Te and Bi in the reef are essentially controlled by the fraction of cumulate sulfides. In contrast, As and Sb are strongly influenced by the amount of silicate liquid trapped in the cumulates, as well as the presence of sulfides.

5.7.3 – Constraints for the evolution of Bushveld magmas and formation of the Merensky Reef

Precisely determining the composition of the parental magma of the upper Critical Zone is crucial for understanding the formation of the PGE deposits of the Bushveld Complex. Our results show that the concentrations of TABS in the Bushveld parental magmas have been upgraded in response to the assimilation of crustal material (Fig. 5.9a). Furthermore, the upper Critical Zone of the Bushveld Complex, and thus its main PGE deposits, formed upon the mixing of B-1 and B-2 magmas. The new magma pulses would explain the higher N-factors (20000; Table 5.2) of sulfides from the reef interval (Barnes and Maier, 2002; Robertson et al., 2015; Fig. 5.8b).

The Se and Te concentrations in mantle rocks and derived magmas are used to assess the control of sulfide minerals on the distribution of chalcophile elements (Hattori et al., 2002; Rose-Weston et al., 2009; Lorand and Alard, 2010; Wang and Becker, 2013; Konig et al., 2012; Lissner et al., 2014; Luguet et al., 2015). The partition coefficient of Te between silicate and sulfide

liquid is much higher than that of Se (Patten et al., 2013; Wang and Becker, 2013; Brenan, 2015; Konig et al., 2015). Therefore, upon the segregation of an immiscible sulfide liquid, Te is preferentially collected relative to Se. Consequently, liquids that have experienced sulfide segregation may have higher Se/Te ratios relative to sulfide-undersaturated liquids. The high Se/Te ratio in B-2 rocks (average of 12) relative to other marginal rocks (averages of 6.6 and 10.1 for B-1 and B-3 rocks, respectively) suggests that B-2 rocks crystallized from a liquid that has segregated a sulfide liquid. This is in agreement with results reported by Barnes et al. (2010) which showed that B-2 liquids are also depleted in PGE, and have higher Cu/Pd ratios (above 8000) relative to other marginal rocks (below 4500). The authors have also interpreted the differences as the results of the segregation of an immiscible sulfide liquid, and subsequent collection of PGE from the silicate liquid.

Although the importance of crustal contamination for the addition of TABS is recorded in the B-1 rocks from the Marginal Zone, it is not equally recorded by all the TABS in samples from the reef interval. The interaction of sulfides with large volumes of silicate magma (i.e. high N factor; Fig. 5.9b) obscures the effect of crustal contamination for elements with high partition coefficients between sulfide and silicate liquids (Lesher and Burnham, 2001). Therefore, concentrations of Bi, Se and Te are higher in the reef samples relative to marginal rocks (Fig. 5.6c to 5.6e), whereas concentrations of As and Sb are similar in reef samples and marginal rocks (Fig. 5.6a and 5.6b). Thus, the presence of sulfide minerals do not markedly increase the whole-rock concentrations of As and Sb (Fig. 5.6a and 5.6b). Consequently, their concentrations in the reef samples still reflect those from the parental magmas, and can be used to assess the effects of crustal contamination.

The upward melt migration through the Merensky Reef cumulate pile in response to compaction is also recorded by the distribution of TABS. Slightly chalcophile elements such as As and Sb behave incompatibly during the formation of the reef, and remained in the more fractionated silicate liquid. Thus, upon compaction of the cumulate pile, the lattermost fractionated silicate liquid was squeezed up in the stratigraphy into cumulates directly above the

reef interval (Fig. 5.9c and 5.9d). Consequently, these rocks became richer in As and Sb relative to rocks from within and below the reef interval (Fig. 5.7). This difference in compatibility with a sulfide liquid led to a decoupling of TABS. Selenium, Te and Bi are richer in sulfide-bearing samples from the reef interval, whereas As and Sb are richer in cumulates with greater amounts of trapped silicate liquid (Fig. 5.7; Table 5.2).

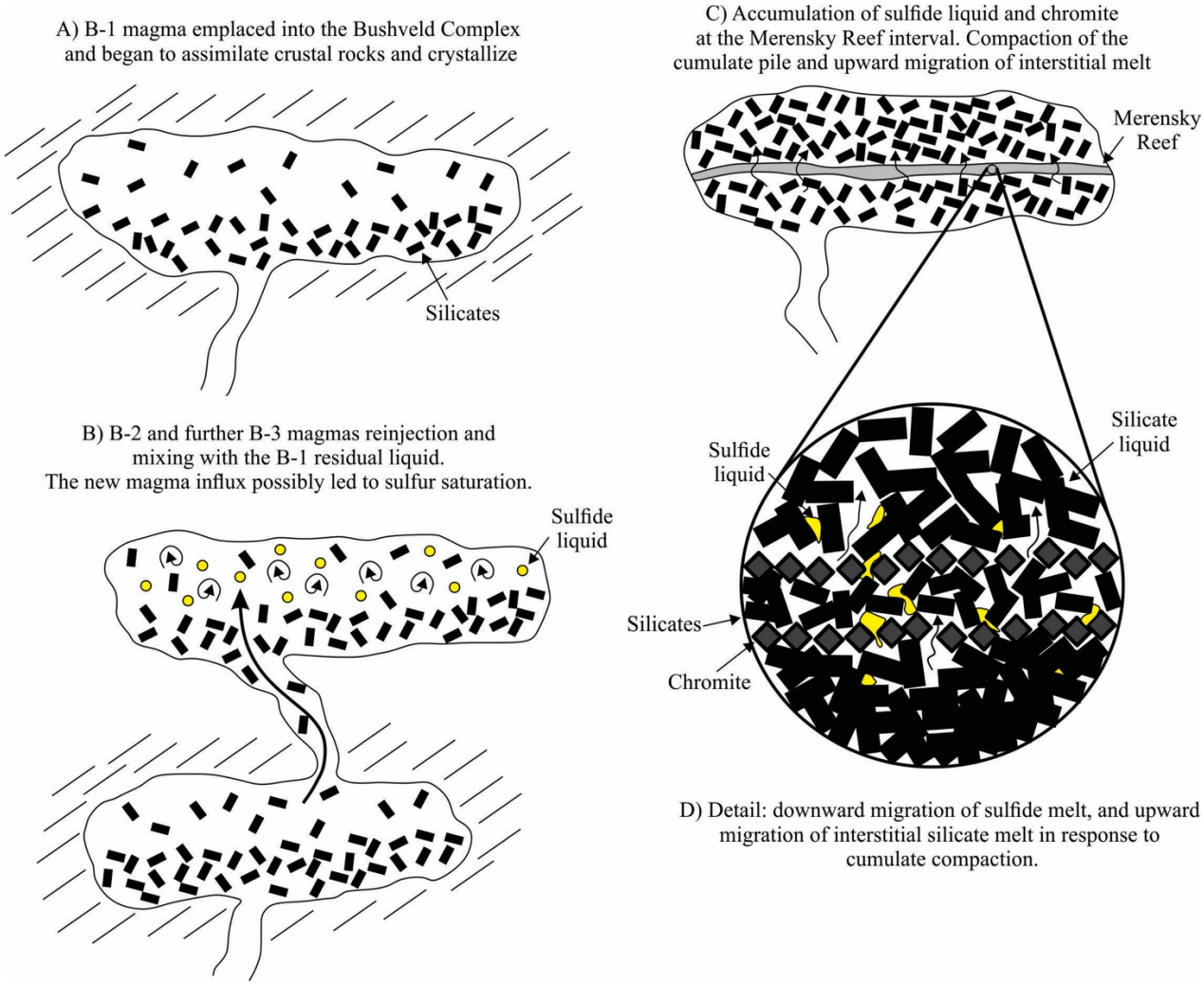

Figure 5.9 - Schematic models illustrating the evolution of Bushveld magmas and crystallization of the Merensky Reef interval. See text for further explanation.

5.7.4 – Implications for the formation of PGE deposits

There is an increasing interest in studying the distribution of TABS in magmatic sulfide deposits (Godel et al., 2012; Piña et al., 2013, 2015; Canali et al., 2017; Duran et al., 2017; Samalens et al., 2017; LeVaillant et al., 2018; Wang et al. 2018; Liang et al., 2019; Mansur et al. 2019a; Mansur and Barnes, 2020). This is mainly because the presence of TABS has been suggested to affect the distribution of PGE. However, assessing the concentration of TABS in parental magmas from which the PGE deposits formed is still a missing step for understanding the ore forming processes. Therefore, our study contributes by determining TABS concentrations in rocks interpreted to represent the parental liquids of some of the largest PGE deposits in the world (Harmer and Sharpe, 1985; Sharpe and Hulbert, 1985; Barnes et al., 2009, 2010; Wilson, 2012; Maier et al., 2016). Below, we use these results to evaluate some of the recently proposed models for the collection of PGE, and formation of the deposits, as follows.

It has been long argued that PGE have very high partition coefficients between sulfide and silicate liquids (Mungall and Brenan, 2014; Liu and Brenan, 2015 and references therein), and are collected by an immiscible sulfide liquid (Barnes and Ripley, 2016, and references therein). Moreover, experimental studies have also demonstrated that TABS also behave as chalcophile elements, and would also be collected by an immiscible sulfide liquid (Li and Audétat, 2015; Liu and Brenan, 2015 and references therein). Alternatively, some authors propose that PGE atoms self-organize as nanometer size clusters in the silicate liquid, which would be stabilized the by the surface adsorption of S, Fe and TABS atoms (Tredoux et al., 1995; Ballhaus et al., 2006; Helmy et al., 2013; Gonzalez-Jimenez et al., 2018, 2019).

In the cluster model, the distribution of PGE would be physically controlled by the surface properties of nanometer-sized particles (Tredoux et al., 1995; Ballhaus et al., 2006). Therefore, the main implication of this model is that the partition coefficients of PGE, and other cluster-forming elements, would not control their distribution. Once the clusters are physically

captured by the sulfide liquid, they are incorporated into the crystallizing base metal sulfides (Wirth et al., 2013; Junge et al., 2015; González-Jiménez et al., 2018, 2019; Liang et al., 2019). Indeed, recent studies in material science support that pre-nucleation clusters can be the precursors for nano-particles prior to their nucleation (Chakraborty and Pradeep, 2017, and references therein).

Some authors have also found nanometer-sized PGM in natural cases (Wirth et al., 2013; Junge et al., 2015; González-Jiménez et al., 2018, 2019; Liang et al., 2019). However, these particles are mainly Pt-arsenides (Kamenetsky et al., 2015; Maier et al., 2015; Arguin et al., 2016; Barnes et al., 2016; González-Jiménez and Reich, 2017; González-Jiménez et al., 2018, 2019). Experimental studies show that Pt and As are able to self-organize into nanometer-sized particles (Helmy et al., 2013; Helmy and Bragagni, 2017). Helmy et al. (2013) argue for the nanocluster model for the collection of PGE based on Pt-As clusters found in their high-temperature experiments, supporting the formation of PGE nanoclusters.

Although experimental and empirical studies provide substantial evidence for the existence of Pt-As nanometer-sized particles, our results do not support that PGE distribution can be exclusively physically controlled by cluster properties. Our modelling results were calculated taking into account the different partition coefficients of PGE (Mungall and Brenan, 2014), and TABS (Li and Audétat, 2015; Liu and Brenan, 2015) between silicate and sulfide liquids, and closely reproduce natural concentrations measured in PGE deposits (Fig. 5.7 and 5.8). Moreover, the results also support that sulfide minerals have a different control on the distribution of PGE and TABS, based on their different chalcophile behaviours. For instance, the distribution of As, which is the most frequently related element to the formation of PGE clusters (Helmy et al., 2013; Helmy and Bragagni, 2017), does not follow that of PGE (Fig. 5.7). This is because As is only slightly chalcophile, whereas PGE are strongly chalcophile elements.

Overall, although we do acknowledge for the presence of nanometer-sized PGE particles in natural cases (Wirth et al., 2013; Junge et al., 2015; Kamenetsky et al., 2015; Maier et al., 2015; Barnes et al., 2016; González-Jiménez et al., 2018, 2019; Liang et al., 2019), our findings do not support the hypothesis that PGE distribution is mainly controlled by the physical

properties of nanoclusters. Also, the whole-rock PGE/TABS ratios do not support the PGE collection by nanoclusters (Mansur and Barnes, 2020). Another restriction of the nanocluster model is the limitation of experimental work demonstrating the formation of PGE nanoclusters other than Pt-arsenides, and using realistic starting materials. Given that future studies will surely expand and support this discussion, our results on the concentrations of TABS in parental liquids may likely be used as an additional tool for evaluating the processes controlling the formation of PGE deposits.

5.8 – Conclusions

We have measured the concentrations of TABS in rocks from the Marginal Zone of the Bushveld Complex. Our main findings are summarized as follows:

1 – The B-1 samples are enriched in As, Sb and Bi relative to primary magmas and can be modelled by contamination of komatiite with upper crust. In contrast, the B-2 and B-3 magmas are not enriched and can be modelled by contamination of komatiitic magmas with a plagioclase-rich residuum.

2 - The distribution of TABS, Se and PGE below, above, and within the Merensky Reef can be modelled by a mixture of magmatic sulfide formed in equilibrium with a mixture of B-1 and B-2 melts, and trapped silicate liquid.

3 – In the Merensky Reef section the distributions of Te, Se, Bi and PGE are controlled by the presence of sulfide minerals, whereas the distributions of As and Sb are controlled by both sulfide minerals and trapped silicate liquid.

4 – The effect of crustal contamination in samples from the Merensky Reef is not equally recorded by all TABS. This is because the interaction of sulfides with large volumes of silicate

magma obscures the effect of crustal contamination for more chalcophile elements. Therefore, As and Sb concentrations are more likely to record crustal contamination.

5 – The distribution of PGE, TABS and Se within the Merensky Reef does not require the presence of nanoclusters and can be modelled using the partition coefficients of each element.

5.9 - Acknowledgements

This work was supported by a Canada Research Chair program grant to Sarah-Jane Barnes (215503) and Discovery Grant 1884-2013. We would like to thank Dany Savard and Audrey Lavoie (LabMaTer, UQAC) for their assistance with HG-AFS analyses. This manuscript benefited from insightful comments from Dr. Hannah Hughes and one anonymous reviewer, and careful editorial handling by Dr. Greg Shellnutt.

5.10 - References

Arevalo, R., McDonough, W.F., 2010. Chemical variations and regional diversity observed in MORB. Chemical Geology 271(1-2), 70-85.

Arguin, J.P., Pagé, P., Barnes, S-J., Yu, S.Y., Song, X.Y., 2016. The effect of chromite crystallization on the distribution of osmium, iridium, ruthenium and rhodium in picritic magmas: an example from the Emeishan Large Igneous Province, Southwestern China. Journal of Petrology 57(5), 1019-1048.

Ballhaus, C., Bockrath, C., Wohlgemuth-Ueberwasser, C., Laurenz, V., Berndt, J., 2006. Fractionation of the noble metals by physical processes. Contributions to Mineralogy and Petrology 152(6), 667-684.

Barnes, S.J., Fisher, L.A., Godel, B., Pearce, M.A., Maier, W.D., Paterson, D., Howard D.L., Ryan C.G., Laird, J.S. (2016) Primary cumulus platinum minerals in the Monts de Cristal Complex, Gabon: magmatic microenvironments inferred from high-definition X-ray fluorescence microscopy. Contributions to Mineralogy and Petrology 171(3), 23.

Barnes, S-J., Ripley, E.M., 2016. Highly siderophile and strongly chalcophile elements in magmatic ore deposits. Reviews in Mineralogy and Geochemistry 81(1), 725-774.

Barnes, S-J., 2016. Chalcophile Elements. In: White WM (Ed.) Encyclopedia of Geochemistry: A Comprehensive Reference Source on the Chemistry of the Earth, Part of the series Encylopedia of Earth Sciences Series, pp 1-5.

Barnes, S-J., Savard, D., Bédard, L.P., Maier, W.D., 2009. Selenium and sulfur concentrations in the Bushveld Complex of South Africa and implications for formation of the platinum-group element deposits. Mineralium Deposita 44(6), 647.

Barnes, S-J., Maier, W.D., Curl, E.A., 2010. Composition of the marginal rocks and sills of the Rustenburg Layered Suite, Bushveld Complex, South Africa: implications for the formation of the platinum-group element deposits. Economic Geology 105(8), 1491-1511.

Barnes, S-J., Maier, W.D., 2002. Platinum-group elements and microstructures of Normal Merensky Reef from Impala Platinum Mines, Bushveld Complex. Journal of Petrology 43(1), 103-128.

Brenan, J.M., 2015. Se–Te fractionation by sulfide–silicate melt partitioning: Implications for the composition of mantle-derived magmas and their melting residues. Earth and Planetary Science Letters 422, 45-57.

Brügmann, G.E., Naldrett, A.J., Asif, M., Lightfoot, P.C., Gorbachev, N.S., Fedorenko, V.A., 1993. Siderophile and chalcophile metals as tracers of the evolution of the Siberian Trap in the Noril'sk region, Russia. Geochimica et Cosmochimica Acta 57(9), 2001-2018.

Canali, A.C., Brenan, J.M., Sullivan, N.A., 2017. Solubility of platinum-arsenide melt and sperrylite in synthetic basalt at 0.1 MPa and 1200° C with implications for arsenic speciation and platinum sequestration in mafic igneous systems. Geochimica et Cosmochimica Acta 216, 153-168.

Cawthorn, R.G., 2015. The Bushveld Complex, South Africa. In: Layered Intrusions, Springer, Dordrecht, pp. 517-587.

Chakraborty, I., Pradeep, T., 2017. Atomically precise clusters of noble metals: emerging link between atoms and nanoparticles. Chemical Reviews 117(12), 8208-8271.

Dare, S.A.S., Barnes, S-J., Prichard, H.M., Fisher, P.C., 2010a. The timing and formation of platinum-group minerals from the Creighton Ni-Cu-platinum-group element sulfide deposit, Sudbury, Canada: Early crystallization of PGE-rich sulfarsenides. Economic Geology 105, 1071-1096.

Dare, S.A.S., Barnes, S-J., Prichard, H.M., 2010b. The distribution of platinum group elements (PGE) and other chalcophile elements among sulfides from the Creighton Ni–Cu–PGE sulfide deposit, Sudbury, Canada, and the origin of palladium in pentlandite. Mineralium Deposita 45, 765-793.

Dare, S.A.S., Barnes, S-J., Prichard, H.M., Fisher, P.C., 2014. Mineralogy and geochemistry of Cu-rich ores from the McCreedy East Ni-Cu-PGE deposit (Sudbury, Canada): Implications for the behavior of platinum group and chalcophile elements at the end of crystallization of a sulfide liquid. Economic Geology 109, 343-366.

Djon, M.L.N., Barnes, S-J., 2012. Changes in sulfides and platinum-group minerals with the degree of alteration in the Roby, Twilight, and High Grade Zones of the Lac des Iles Complex, Ontario, Canada. Mineralium Deposita 47, 875-896.

Duran, C.J., Barnes, S-J., Corkery, J.T., 2016. Trace element distribution in primary sulfides and Fe–Ti oxides from the sulfide-rich pods of the Lac des Iles Pd deposits, Western Ontario, Canada: Constraints on processes controlling the composition of the ore and the use of pentlandite compositions in exploration. Journal of Geochemical Exploration 166, 45-63.

Duran, C.J., Barnes, S-J., Pleše, P., Prašek, M.K., Zientek, M.L., Pagé, P., 2017. Fractional crystallization-induced variations in sulfides from the Noril'sk-Talnakh mining district (polar Siberia, Russia). Ore Geology Reviews 90, 326-351.

Eales, H.V., Cawthorn, R.G., 1996. The Bushveld Complex. In: Cawthorn RG (Ed.) Layered intrusions. Amsterdam, Elsevier, pp. 181–229.

Eales, H.V., Costin, G., 2012. Crustally contaminated komatiite: primary source of the chromitites and Marginal, Lower, and Critical Zone magmas in a staging chamber beneath the Bushveld Complex. Economic Geology 107(4), 645-665.

Godel, B., Barnes, S-J., Maier, W.D., 2006. 3-D distribution of sulphide minerals in the Merensky Reef (Bushveld Complex, South Africa) and the JM Reef (Stillwater Complex, USA) and their relationship to microstructures using X-ray computed tomography. Journal of Petrology 47(9), 1853-1872.

Godel, B., Barnes, S-J., Maier, W.D., 2007. Platinum-group elements in sulphide minerals, platinum-group minerals, and whole-rocks of the Merensky Reef (Bushveld Complex, South Africa): Implications for the formation of the reef. Journal of Petrology 48, 1569-1604.

Godel, B., Barnes, S-J., Maier, W.D., 2011. Parental magma composition inferred from in situ trace elements in cumulus and intercumulus silicate minerals: example from the lower and lower critical zones of the Bushveld Complex (South-Africa). Lithos 125, 537-552.

Godel, B., González-Álvarez, I., Barnes, S.J., Barnes, S-J., Parker, P., Day, J., 2012. Sulfides and sulfarsenides from the Rosie nickel prospect, Duketon greenstone belt, Western Australia. Economic Geology 107, 275-294.

González-Jiménez, J.M., Reich, M., 2017. An overview of the platinum-group element nanoparticles in mantle-hosted chromite deposits. Ore Geology Reviews 81, 1236-1248.

González-Jiménez, J.M., Deditius, A., Gervilla, F., Reich, M., Suvorova, A., Roberts, M.P., Proenza, J.A., 2018. Nanoscale partitioning of Ru, Ir, and Pt in base-metal sulfides from the Caridad chromite deposit, Cuba. American Mineralogist 103(8), 1208-1220.

González-Jiménez, J.M., Roqué-Rosell, J., Jiménez-Franco, A., Tassara, S., Nieto, F., Gervilla, F., Schilling, M., 2019. Magmatic platinum nanoparticles in metasomatic silicate glasses and sulfides from Patagonian mantle xenoliths. Contributions to Mineralogy and Petrology 174(5), 47.

Hall, A.L., 1932. The Bushveld Igneous Complex in the central Transvaal. Geological Society, South Africa, Memoir 28: pp. 544.

Harmer, R.E., Sharpe, M.R., 1985. Field relations and strontium isotope systematics of the Eastern Bushveld Complex. Economic Geology 80, 813–837.

Harris, E.R., Kinnaird, J.A., Harris, C., Horstmann, U.E., 2005. A new look at sulphide mineralisation of the northern limb, Bushveld Complex: a stable isotope study. Applied Earth Science 114(4), 252-263.

Hattori, K.H., Arai, S., Clarke, D.B., 2002. Selenium, tellurium, arsenic and antimony contents of primary mantle sulfides. Canadian Mineralogy 40(2), 637-650.

Helmy, H.M., Ballhaus, C., Fonseca, R., Nagel, T., 2013. Fractionation of platinum, palladium, nickel, and copper in sulfide–arsenide systems at magmatic temperature. Contributions to Mineralogy and Petrology 166, 1725-1737.

Helmy, H.M., Bragagni, A., 2017. Platinum-group elements fractionation by selective complexing, the Os, Ir, Ru, Rh-arsenide-sulfide systems above 1020°C. Geochimica et Cosmochimica Acta 216, 169-183.

Holness, M.B., Vukmanovic, Z., Mariani, E., 2017. Assessing the role of compaction in the formation of adcumulates: a microstructural perspective. Journal of Petrology 58(4), 643-673.

Hu, Z., Gao, S., 2008. Upper crustal abundances of trace elements: a revision and update. Chemical Geology 253(3-4), 205-221.

Hutchinson, D., McDonald, I., 2008. Laser ablation ICP-MS study of platinum-group elements in sulphides from the Platreef at Turfspruit, northern limb of the Bushveld Complex, South Africa. Mineralium Deposita 43, 695-711.

Hutchinson, D., Foster, J., Pritchard, H., Gilbert, S., 2015. Concentration of particulate platinum-group minerals during magma emplacement; a case study from theMerensky Reef, Bushveld Complex. Journal of Petrology 56, 113-159.

Junge, M., Wirth, R., Oberthür, T., Melcher, F., Schreiber, A., 2015. Mineralogical siting of platinum-group elements in pentlandite from the Bushveld Complex, South Africa. Mineralium Deposita 50, 41-54.

Kamenetsky, V.S., Park, J.W., Mungall, J.E., Pushkarev, E.V., Ivanov, A.V., Kamenetsky, M.B., Yaxley, G.M., 2015. Crystallization of platinum-group minerals from silicate melts: Evidence from Cr-spinel–hosted inclusions in volcanic rocks. Geology 43(10), 903-906.

Karykowski, B.T., Yang, S.H., Maier, W.D., Lahaye, Y., Lissenberg, C.J., O'Brien, H., 2017. In situ Sr isotope compositions of plagioclase from a complete stratigraphic profile of the Bushveld Complex, South Africa: Evidence for extensive magma mixing and percolation. Journal of Petrology 58(11), 2285-2308.

Keith, M., Smith, D.J., Jenkin, G.R.T., Holwell, D.A., Dye, M.D., 2018. A review of Te and Se systematics in hydrothermal pyrite from precious metal deposits: Insights into ore-forming processes. Ore Geology Reviews 96, 269-282.

König, S., Luguet, A., Lorand, J-P., Wombacher, F., Lissner, M., 2012. Selenium and tellurium systematics of the Earth's mantle from high precision analyses of ultra-depleted orogenic peridotites. Geochimica et Cosmochimica Acta 86, 354-366.

König, S., Lorand, J-P., Luguet, A., Pearson, D.G., 2014. A non-primitive origin of near-chondritic S–Se–Te ratios in mantle peridotites: implications for the Earth's late accretionary history. Earth Planetary Science Letters 385, 110-121.

König, S., Lissner, M., Lorand, J-P., Bragagni, A., Luguet, A., 2015. Mineralogical control of selenium, tellurium and highly siderophile elements in the Earth's mantle: Evidence from mineral separates of ultra-depleted mantle residues. Chemical Geology 396, 16-24.

Le Vaillant, M., Barnes, S.J., Fiorentini, M.L., Barnes, S-J., Bath, A., Miller, J., 2018. Platinum-group element and gold contents of arsenide and sulfarsenide minerals associated with Ni and Au deposits in Archean greenstone belts. Mineralogical Magazine 82(3), 625-647.

Lesher, C.M., Burnham, O.M., 2001. Multicomponent elemental and isotopic mixing in Ni–Cu–(PGE) ores at Kambalda, Western Australia. Canadian Mineralogist 39(2), 421-446.

Li, Y., Audétat, A., 2015. Effects of temperature, silicate melt composition, and oxygen fugacity on the partitioning of V, Mn, Co, Ni, Cu, Zn, As, Mo, Ag, Sn, Sb, W, Au, Pb, and Bi between sulfide phases and silicate melt. Geochimica et Cosmochimica Acta 162, 25-45.

Li, C., Ripley, E.M., 2005. Empirical equations to predict the sulfur content of mafic magmas at sulfide saturation and applications to magmatic sulfide deposits. Mineralium Deposita 40(2), 218-230.

Li, C., Maier, W.D., de Waal, S.A., 2001. The role of magma mixing in the genesis of PGE mineralization in the Bushveld Complex: Thermodynamic calculations and new interpretations. Economic Geology 96(3), 653-662.

Liang, Q.L., Song, X.Y., Wirth, R., Chen, L.M., Dai, Z.H., 2019. Implications of nano-and micrometer-size platinum-group element minerals in base metal sulfides of the Yangliuping Ni-Cu-PGE sulfide deposit, SW China. Chemical Geology 517, 7-21.

Lissner, M., König, S., Luguet, A., Le Roux, P., Schuth, S., Heuser, A., le Roex, A.P., 2014. Selenium and tellurium systematics in MORBs from the southern Mid-Atlantic Ridge (47–50 S). Geochimica et Cosmochimica Acta 144, 379-402.

Liu, Y., Brenan, J., 2015. Partitioning of platinum-group elements (PGE) and chalcogens (Se, Te, As, Sb, Bi) between monosulfide-solid solution (MSS), intermediate solid solution (ISS) and sulfide liquid at controlled fO2–fS2 conditions. Geochimica et Cosmochimica Acta 159, 139-161.

Lyubetskaya, T., Korenaga, J., 2007. Chemical composition of Earth's primitive mantle and its variance: 1. Method and results. Journal f Geophysical Research 112, B03211.

Lodders, K., 2003. Solar system abundances and condensation temperatures of the elements. The Astrohphysical Journal 591, 1220-1247.

Lorand, J-P., Alard, O., Luguet, A., Keays, R.R., 2003. Sulfur and selenium systematics of the subcontinental lithospheric mantle: inferences from the Massif Central xenolith suite (France). Geochimica et Cosmochimica Acta 67(21), 4137-4151.

Lorand, J-P., Alard, O., 2010. Determination of selenium and tellurium concentrations in Pyrenean peridotites (Ariege, France): new insight into S/Se/Te systematics of the upper in mantle samples. Chemical Geology 278(1-2), 120-130.

Luguet, A., Behrens, M., Pearson, D.G., König, S., Herwartz, D., 2015. Significance of the whole rock Re–Os ages in cryptically and modally metasomatised cratonic peridotites: Constraints from HSE–Se–Te systematics. Geochimica et Cosmochimica Acta 164, 441-463.

Maier, W.D., Arndt, N.T., Curl, E.A., 2000. Progressive crustal contamination of the Bushveld Complex: evidence from Nd isotopic analyses of the cumulate rocks. Contributions to Mineralogy and Petrology 140(3), 316-327.

Maier, W.D., Barnes, S-J., Groves, D.I., 2013. The Bushveld Complex, South Africa: formation of platinum–palladium, chrome-and vanadium-rich layers via hydrodynamic sorting of a mobilized cumulate slurry in a large, relatively slowly cooling, subsiding magma chamber. Mineralium Deposita 48(1), 1-56.

Maier, W.D., Rasmussen, B., Fletcher, I., Godel, B., Barnes, S.J., Fisher, L., Yang, S., Huhma, H., Lahaye, Y., 2015. Petrogenesis of the ~2.77 Ga Monts de Cristal Complex, Gabon: evidence for direct precipitation of Pt- arsenides from basaltic magma. Journal of Petrology 56, 1285-308.

Maier, W.D., Barnes, S-J., Karykowski, B.T., 2016. A chilled margin of komatiite and Mg-rich basaltic andesite in the western Bushveld Complex, South Africa. Contributions to Mineralogy and Petrology 171(6), 57.

Mansur, E.T., Barnes, S-J., Duran, C.J., Sluzhenikin, S.F., 2019a,.Distribution of chalcophile and platinum-group elements among pyrrhotite, pentlandite, chalcopyrite and cubanite from the Noril'sk-Talnakh ores: implications for the formation of platinum-group minerals. Mineralium Deposita, 1-18.

Mansur, E.T., Barnes, S-J., Savard, D., Webb, P.C., 2019b. Determination of Te, As, Bi, Sb and Se (TABS) in Geological Reference Materials and GeoPT Proficiency Test Materials by Hydride Generation-Atomic Fluorescence Spectrometry (HG-AFS). Geostandards and Geoanalytical Research.

Mansur, E.T., Barnes, S-J., 2020. The roles of Te, As, Bi, Sn and Sb during the formation of platinum-group-element reef deposits: examples from the Bushveld and Stillwater Complexes. Geochimica et Cosmochimica Acta. doi.org/10.1016/j.gca.2020.01.008

McDonough, W.F., Sun, S.S., 1995. The composition of the Earth. Chemical Geology 120(3-4), 223-253.

Mungall, J.E., Brenan, J.M., 2014. Partitioning of platinum-group elements and Au between sulfide liquid and basalt and the origins of mantle-crust fractionation of the chalcophile elements. Geochimica et Cosmochimica Acta 125: 265-289.

Mungall, J.E., Kamo, S.L., McQuade, S., 2016. U–Pb geochronology documents out-of-sequence emplacement of ultramafic layers in the Bushveld Igneous Complex of South Africa. Nature Communications 7, 13385.

Naldrett, A.J., Von Gruenewaldt, G., 1989. Association of platinum-group elements with chromitite in layered intrusions and ophiolite complexes. Economic Geology 84(1), 180-187.

Naldrett, A.J., Wilson, A., Kinnaird, J., Chunnett, G., 2009. PGE tenor and metal ratios within and below the Merensky Reef, Bushveld Complex: implications for its genesis. Journal of Petrology 50(4), 625-659.

O'Driscoll, B., González-Jiménez, J.M., 2016. Petrogenesis of the platinum-group minerals. Reviews in Mineralogy and Geochemistry 81, 489-578.

Patten, C., Barnes, S-J., Mathez, E.A., Jenner, F.E., 2013. Partition coefficients of chalcophile elements between sulfide and silicate melts and the early crystallization history of sulfide liquid: LA-ICP-MS analysis of MORB sulfide droplets. Chemical Geology 358, 170-188.

Patten, C.G., Pitcairn, I.K., Teagle, D.A., Harris, M., 2016. Mobility of Au and related elements during the hydrothermal alteration of the oceanic crust: implications for the sources of metals in VMS deposits. Mineralium Deposita 51, 179-200.

Peck, D.C., Keays, R.R., 1990. Insights into the behavior of precious metals in primitive, S-undersaturated magmas; evidence from the Heazlewood River Complex, Tasmania. Canadian Mineralogist 28, 553-577.

Péntek, A., Molnár, F., Watkinson, D.H., Jones, P.C., 2008. Footwall-type Cu-Ni-PGE Mineralization in the Broken Hammer Area, Wisner Township, North Range, Sudbury Structure. Economic Geology 103, 1005-1028.

Piña, R., Gervilla, F., Barnes, S-J., Ortega, L., Lunar, R., 2012. Distribution of platinum-group and chalcophile elements in the aguablanca Ni-Cu sulfide deposit (SW spain): Evidence from a LA-ICP-MS study. Chemical Geology 302, 61-75.

Piña, R., Gervilla, F., Barnes, S-J., Ortega, L., Lunar, R., 2013. Partition coefficients of platinum group and chalcophile elements between arsenide and sulfide phases as determined in the Beni Bousera Cr-Ni mineralization (North Morocco). Economic Geology 108(5), 935-951.

Piña, R., Gervilla, F., Barnes, S-J., Ortega, L., Lunar, R., 2015. Liquid immiscibility between arsenide and sulfide melts: Evidence from a LA-ICP-MS study in magmatic deposits at Serranía de Ronda (Spain). Mineralium Deposita 50, 265-279.

Pitcairn, I.K., 2004. Sources of fluids and metals in orogenic gold deposits: the Otago Schists, New Zealand. Dissertation, University of Southampton

Queffurus, M., Barnes, S-J., 2015. A review of sulfur to selenium ratios in magmatic nickel–copper and platinum-group element deposits. Ore Geology Reviews 69, 301-324.

Reczko, B.F.F., Oberholzer, J.D., Res, M., Erikson, P.G., Schriber, U.M., 1995. A re-evaluation of the volcanism of the Palaeoproterozoic Pretoria Group (Kaapvaal craton) and a hypothesis on basin development. Journal of African Earth Sciences 21, 505–519.

Ripley, E.M., 1990. Se/S ratios of the Virginia Formation and Cu–Ni mineralization in the Babbitt area, Duluth Complex, Minnesota. Economic Geology 85, 1935-1940.

Robertson, J.C., Barnes, S.J., Le Vaillant, M., 2015. Dynamics of magmatic sulphide droplets during transport in silicate melts and implications for magmatic sulphide ore formation. Journal of Petrology 56(12), 2445-2472.

Roelofse, F., Ashwal, L.D., 2012. The Lower Main Zone in the Northern Limb of the Bushveld Complex – a >1.3 km thick sequence of intruded and variably contaminated crystal mushes. Journal of Petrology 53(7), 1449-1476.

Roelofse, F., Ashwal, L.D., Romer, R.L., 2015. Multiple, isotopically heterogeneous plagioclase populations in the Bushveld Complex suggest mush intrusion. Geochemistry 75(3), 357-364.

Rose-Weston L, Brenan JM, Fei Y, Secco RA, Frost DJ (2009) Effect of pressure, temperature, and oxygen fugacity on the metal-silicate partitioning of Te, Se, and S: Implications for earth differentiation. Geochim Cosmochim Acta 73(15): 4598-4615.

Rudnick, R.L., Gao, S., 2003. Composition of the continental crust. In: Rudnick, R. L. (Ed.) The Crust. Amsterdam: Elsevier, pp. 1-70.

Samalens, N., Barnes, S-J., Sawyer, E.W., 2017. The role of black shales as a source of sulfur and semimetals in magmatic nickel-copper deposits: Example from the Partridge River Intrusion, Duluth Complex, Minnesota, USA. Ore Geology Reviews 81(1), 173-187.

Scholten, L., Watenphul, A., Beermann, O., Testemale, D., Ames, D., Schmidt, C., 2018. Nickel and platinum in high-temperature H2O+ HCl fluids: Implications for hydrothermal mobilization. Geochimica et Cosmochimica Acta 224, 187-199.

Scoates, J.S., Wall, C.J., 2015. Geochronology of layered intrusions. In: Layered intrusions, Springer, Dordrecht, pp. 3-74.

Sharpe, M.R., Hulbert, L.J., 1985. Ultramafic sills beneath the eastern Bushveld Complex: Mobilized suspensions of early lower zone cumulates in a parental magma with boninitic affinities. Economic Geology 80, 849-871.

Sullivan, N.A., Zajacz, Z., Brenan, J.M., 2018. The solubility of Pd and Au in hydrous intermediate silicate melts: the effect of oxygen fugacity and the addition of Cl and S. Geochimica et Cosmochimica Acta 231, 15-29.

Tredoux, M., Lindsay, N.M., Davies, G., McDonald, I., 1995. The fractionation of platinum-group elements in magmatic systems, with the suggestion of a novel causal mechanism. South African Journal of Geology 98, 157-167.

Tuba, G., Molnár, F., Ames, D.E., Péntek, A., Watkinson, D.H., Jones, P.C., 2014. Multi-stage hydrothermal processes involved in “low-sulfide” Cu (–Ni)–PGE mineralization in the footwall of the Sudbury Igneous Complex (Canada): Amy Lake PGE zone, East Range. Mineralium Deposita 49, 7-47.

Vukmanovic, Z., Barnes, S.J., Reddy, S.M., Godel, B., Fiorentini, M.L., 2013. Morphology and microstructure of chromite crystals in chromitites from the Merensky Reef (Bushveld Complex, South Africa). Contributions to Mineralogy and Petrology 165(6), 1031-1050.

Wang, C.Y., Wei, B., Zhou, M.F., Minh, D.H., Qi, L., 2018. A synthesis of magmatic Ni-Cu-(PGE) sulfide deposits in the ~260 Ma Emeishan large igneous province, SW China and northern Vietnam. Journal of Asian Earth Sciences 154, 162-186.

Wang, Z., Becker, H., 2013. Ratios of S, Se and Te in the silicate Earth require a volatile-rich late veneer. Nature 499, 328-331.

Wille, M., Kramers, J.D., Nägler, T.F., Beukes, N.J., Schröder, S., Meisel, T., Voegelin, A.R., 2007. Evidence for a gradual rise of oxygen between 2.6 and 2.5 Ga from Mo isotopes and Re-PGE signatures in shales. Geochimica et Cosmochimica Acta 71(10), 2417-2435.

Wilson, A.H., 2012. A chill sequence to the Bushveld Complex: insight into the first stage of emplacement and implications for the parental magmas. Journal of Petrology 53(6), 1123-1168.

Wirth, R., Reid, D., Schreiber, A., 2013. Nanometer-sized platinum-group minerals (PGM) in base metal sulfides: new evidence for an orthomagmatic origin of the Merensky Reef PGE ore deposit, Bushveld Complex, South Africa. Canadian Mineralogist 51, 143-155.

Yang, S.H., Maier, W.D., Godel, B., Barnes, S-J., Hanski, E., O’brien, H., 2018. Parental magma composition of the Main Zone of the Bushveld Complex: Evidence from in situ LA-ICP-MS trace element analysis of silicate minerals in the cumulate rocks. Journal of Petrology 60(2), 359-392.

Yierpan, A., König, S., Labidi, J., Schoenberg, R., 2019. Selenium isotope and S-Se-Te elemental systematics along the Pacific-Antarctic ridge: Role of mantle processes. Geochimica et Cosmochimica Acta, 249, 199-224.

Yudovskaya, M.A., Kinnaird, J.A., Grobler, D.F., Costin, G., Abramova, V.D., Dunnett, T., Barnes, S-J., 2017. Zonation of Merensky-Style Platinum-Group Element Mineralization in Turfspruit Thick Reef Facies (Northern Limb of the Bushveld Complex). Economic Geology 112, 1333-1365.

Zeh, A., Ovtcharova, M., Wilson, A.H., Schaltegger, U., 2015. The Bushveld Complex was emplaced and cooled in less than one million years–results of zirconology, and geotectonic implications. Earth Planetary Science Letters 418, 103-114.

Chapter 6 - The role of Te, As, Bi, Sn and Sb during the formation of platinum-group-element reef deposits: Examples from the Bushveld and Stillwater Complexes

Eduardo T. Mansur[1], Sarah-Jane Barnes[1]

[1]Sciences de la Terre, Université du Québec à Chicoutimi, Québec, G7H 2B1, Canada

Author contributions:

Mansur wrote the manuscript, collected and analyzed the data and created the figures. **Barnes** edited the manuscript and analyzed the data.

Geochimica et Cosmochimica Acta, 2020, 272 : 235-258

DOI : 10.1016/j.gca.2020.01.008

6.1 - Abstract

The distribution of platinum-group element (PGE) and Te, As, Bi, Sb and Sn (TABS) in whole-rock samples, and in disseminated base metal sulfides (BMS) pentlandite, pyrrhotite and chalcopyrite from the Bushveld and Stillwater Complexes are reported. The samples are from: the Merensky Reef (Bushveld), the J-M Reef (Stillwater), Picket Pin deposit (Stillwater), and also barren sulfide-bearing samples, from outside the reef intervals from both intrusions. The objective of the study was to document the distribution of PGE and TABS in PGE-reef deposits, and to investigate whether TABS play a significant role during the formation of PGE-reef deposits.

The whole-rock concentrations of PGE and TABS (except for As) correlate with S and PGE, and thus their distribution appear to be controlled by BMS. The distribution of As, and to a lesser extent Sb, correlate with incompatible elements and with changes in K-phlogopite compositions, suggesting that these elements are controlled both by the amount of trapped liquid in cumulate rocks, and the amount of sulfides. The possible role of TABS in forming pre-nucleation clusters (nanonuggets) to enrich the reefs in PGE is considered and discarded, because the ratio of TABS/PGE <0.3 is too low for TABS to form pre-nucleation clusters with PGE. A model where both the PGE and TABS are initially collected by a base metal sulfide liquid is favoured. During equilibrium crystallization of the sulfide liquid, Pd, Pt and the TABS were incompatible with the crystallizing BMS, and concentrated in the fractionated liquid eventually crystallizing as TABS-rich PGM. However, a portion of Pd, Pt and TABS also partitioned into the crystallizing BMS. During cooling and S-loss they exsolved from the BMS as PGM included in the BMS. In the reefs, the ratio of PGE/TABS is very high, and thus during exsolution all of the TABS could be accommodated in PGM, and consequently the BMS of the reefs have very low TABS concentrations. In contrast, outside the reefs the PGE/TABS ratios are low, and thus some TABS remained in the BMS, resulting in the BMS outside the reefs having higher TABS concentrations than those from within the reefs.

Keywords: Te, As, Bi, Sb, Sn; platinum-group elements; magmatic sulfide deposits; Bushveld Complex; Stillwater Complex; platinum-group minerals.

6.2 – Introduction

It has been demonstrated that in magmatic Ni-Cu-PGE sulfide deposits the platinum-group elements are bimodally distributed (Godel et al., 2007; Holwell and McDonald, 2007; Dare et al., 2010b; 2014; Piña et al., 2012; Osbahr et al., 2013, 2014; Junge et al., 2015; Duran et al., 2016). The PGE are present at the ppm level in the base metal sulfides (BMS) pyrrhotite, pentlandite, and to a lesser extent chalcopyrite, and these host much of the PGE budget (Barnes and Ripley, 2016, and references therein). The balance of the PGE is hosted by platinum-group minerals (PGM). These PGM commonly consist of PGE plus one or more of the elements Te, As, Bi, Sb and Sn (TABS; Barnes, 2016), or S (O'Driscoll and González-Jiménez, 2016 and references therein). Understanding the influence of TABS on the distribution of PGE in magmatic systems is critical given the importance of PGE in the study of various fields of geology (Harvey and Day, 2016 and references therein). Moreover, there is an increasing interest in understanding the geochemical cycle of volatile elements such as TABS, and in these studies BMS are frequently proposed as controlling the TABS (Hattori et al., 2002; Lodders, 2003; Lorand and Alard, 2010; Wang and Becker, 2013; Konig et al., 2012, 2014; Lissner et al., 2014; Patten et al., 2016, 2017; Canali et al., 2017; D'Souza and Canil, 2018).

To date, the concentrations of TABS in Ni-Cu-PGE deposits has mainly been addressed in relatively sulfide-rich deposits, for example those from Sudbury (Canada), Noril'sk-Talnakh (Russia), the Platreef (South Africa) and Aguablanca (Spain) (Holwell and McDonald, 2007; Dare et al., 2010a, 2010b, 2014; Piña et al., 2012; Yudovskaya et al., 2017; Mansur et al., 2019c). In these deposits, the whole-rock concentrations of TABS, Pd and Pt are found to increase from the Cu-poor parts of the deposits, thought to represent monosulfide solid solution (MSS) cumulates, to the Cu-rich parts of the deposits, thought to represent the products of the fractionated sulfide liquid (Dare et al., 2010b, 2014; Chen et al., 2013, 2015; Duran et al., 2017). The TABS, Pd and Pt concentrations of the BMS show positive covariance with the whole-rock values (Mansur et al., 2019c). However, the bulk of the TABS and Pt are not hosted by the BMS.

In the MSS cumulates, the PGM occur within BMS grains and appear to have formed predominantly by exsolutions (Dare et al., 2010b; Piña et al., 2012; Duran et al., 2017; Mansur et al., 2019c). In the Cu-rich portions of the deposits, some of the PGM occur as exsolutions, but predominately they occur among the sulfide grains, and are thought to have crystallized from the fractionated sulfide liquid (Dare et al., 2014; Duran et al., 2017; Mansur et al., 2019c). Alternatively, they could have crystallized from an immiscible TABS-rich liquid which segregated from the fractionated Cu-rich sulfide liquid (Helmy et al., 2007; 2010; Holwell and McDonald, 2010; Piña et al., 2015; Cafagna and Jugo, 2016).

In the case of PGE-reef deposits, which contain disseminated sulfides, the distribution of TABS has not been well documented, although a number of roles listed below have been proposed for TABS. i) In order to explain the very high PGE content of the PGE-dominated deposits, it has been proposed that TABS and PGE form pre-nucleation clusters (referred to as nanoparticles or nanoclusters). The clusters are incorporated in a magmatic sulfide liquid, and subsequently in the MSS and intermediate sulfide solid solutions (ISS) that crystalize from the sulfide liquid. These clusters could remain in the BMS, or coalesce to form PGM (Tredoux et al., 1995; Helmy et al., 2013; Wirth et al., 2013; Junge et al., 2015; Ling et al., 2019). ii) Alternatively, the TABS and PGE could behave as in sulfide-rich deposits, but with the difference that the disseminated sulfides in reefs are generally assumed to represent sulfide liquid compositions, as the sulfides represent the product of equilibrium crystallization. In this case, a small portion of these elements would have partitioned into MSS and ISS as they crystallized, and PGM exsolved from the sulfides during cooling (Prichard et al., 2004; Godel et al., 2007; Godel and Barnes, 2008a). However, given the incompatible nature of Pd, Pt and TABS (Helmy et al., 2010; Patten et al., 2013; Liu and Brenan, 2015) the bulk of these elements would have partitioned into the fractionated sulfide liquid, and crystallized as PGM among the sulfide grains. iii) A variation of this model is that the trapped fractionated sulfide liquid became saturated in a TABS-PGE rich liquid (Helmy et al., 2007, 2010; Piña et al., 2015; Cafagna and Jugo, 2016). This liquid could migrate away from the sulfides, or crystallize among the sulfide grains (Holwell

and McDonald, 2010). iv) The TABS could have a role in fixing the PGE during dissolution of the sulfides by late magmatic or metamorphic fluids. Loss of S from sulfides leads to the exsolutions of PGM (Ballhaus et al., 1994; Peregoedova et al., 2004; Li and Ripley, 2006; Godel and Barnes, 2008a; Djon and Barnes, 2012). If most of the BMS are dissolved leaving TABS and PGE, the TABS serve to fix the PGE, as TABS-rich PGM (Wood, 2002; Scholten et al., 2018; Sullivan et al., 2018).

In the current work we examine the distribution of PGE and TABS in whole-rock samples, and in disseminated BMS from the Bushveld and Stillwater Complexes. The samples comprise the main sulfide-related PGE reefs of the intrusions, the Merensky Reef (Bushveld), and the J-M Reef and Picket Pin deposit (Stillwater), and also barren sulfide-bearing samples, from outside the reef intervals from both intrusions. This allows assessment of the distribution of PGE and TABS in PGE reef type deposits, and investigation whether TABS play a significant role during the formation of PGE-dominated deposits.

This contribution will show that the whole-rock concentrations of Se and TABS (except for As) correlate with S and PGE, and thus their distribution is controlled by BMS. The distribution of As, and to a lesser extent Sb, are controlled by both the amount of liquid fraction in cumulate rocks, and the amount of sulfides. The study will also show that the concentrations of PGE are the highest in BMS from the reef samples, in contrast the concentrations of TABS are the lowest in BMS from the same samples. The highest concentrations of TABS in BMS were found in samples with the lowest whole-rock PGE contents. The formation of the PGM by pre-nucleation clusters is considered, and discarded. The hypotheses that PGM are formed by exsolutions, and by crystallization from the fractionated sulfide liquid is favoured. To explain the contrast in the behaviour of TABS and PGE in BMS of the reefs, it is proposed that the high concentration of PGE in BMS from the reef leads to the diffusion of the TABS from the BMS into the PGM. Therefore, the BMS from the reefs are depleted in TABS, although the whole-rock concentrations of TABS in the reefs are high.

6.3 – Description of studied samples

The samples of the Merensky Reef (Bushveld Complex, South Africa) are from the Rustenburg and Impala mines (Fig. 6.1a). The samples from the JM-Reef (Stillwater Complex, USA) are from the East Boulder and Stillwater mines (Fig. 6.1b). These rocks have been previously studied documenting petrography, microstructures, PGM distribution, whole-rock major and trace element, PGE and S contents of the reefs and surrounding rocks (Barnes and Maier, 2002 and Prichard et al., 2004 - Impala section; Godel et al., 2007, 2010 - Rustenburg section; Godel et al., 2008a, 2008b and Barnes et al., 2020 - J-M Reef package). Only a brief description of the samples is provided here. The reader is directed to Barnes and Maier (2002), Godel et al. (2006, 2007 and 2010), Godel and Barnes (2008a and 2008b) and Barnes et al. (2020) for a more detailed description.

6.3.1 – Bushveld Complex

The Merensky Reef sections from both mines consist of a basal anorthosite followed by a lower chromitite, a coarse-grained melanorite, an upper chromitite, and an overlying melanorite. All lithologies contain disseminated BMS (from 0.5 to 8 vol.%), composed of pyrrhotite (Po), pentlandite (Pn) and chalcopyrite (Ccp). These sulfides occur interstitial to silicate minerals. The samples from the Rustenburg mine only cover the reef interval (Godel et al., 2006; 2007). Sampling from the Impala section extends for around one meter below and above the Merensky Reef interval into an anorthosite and a melanorite, respectively. The samples from above the reef contain higher incompatible element concentrations, which were interpreted to indicate that the samples have a higher amount of trapped liquid (Barnes and Maier, 2002). This section of the reef also contains ~3% K-phlogoptite. Based on the concentrations of major and minor elements in K-

phlogopite from other localities Li et al. (2005) interpreted the K-phlogopite to have crystallized from the late silicate liquid, thus recording the presence of the fractionated liquid.

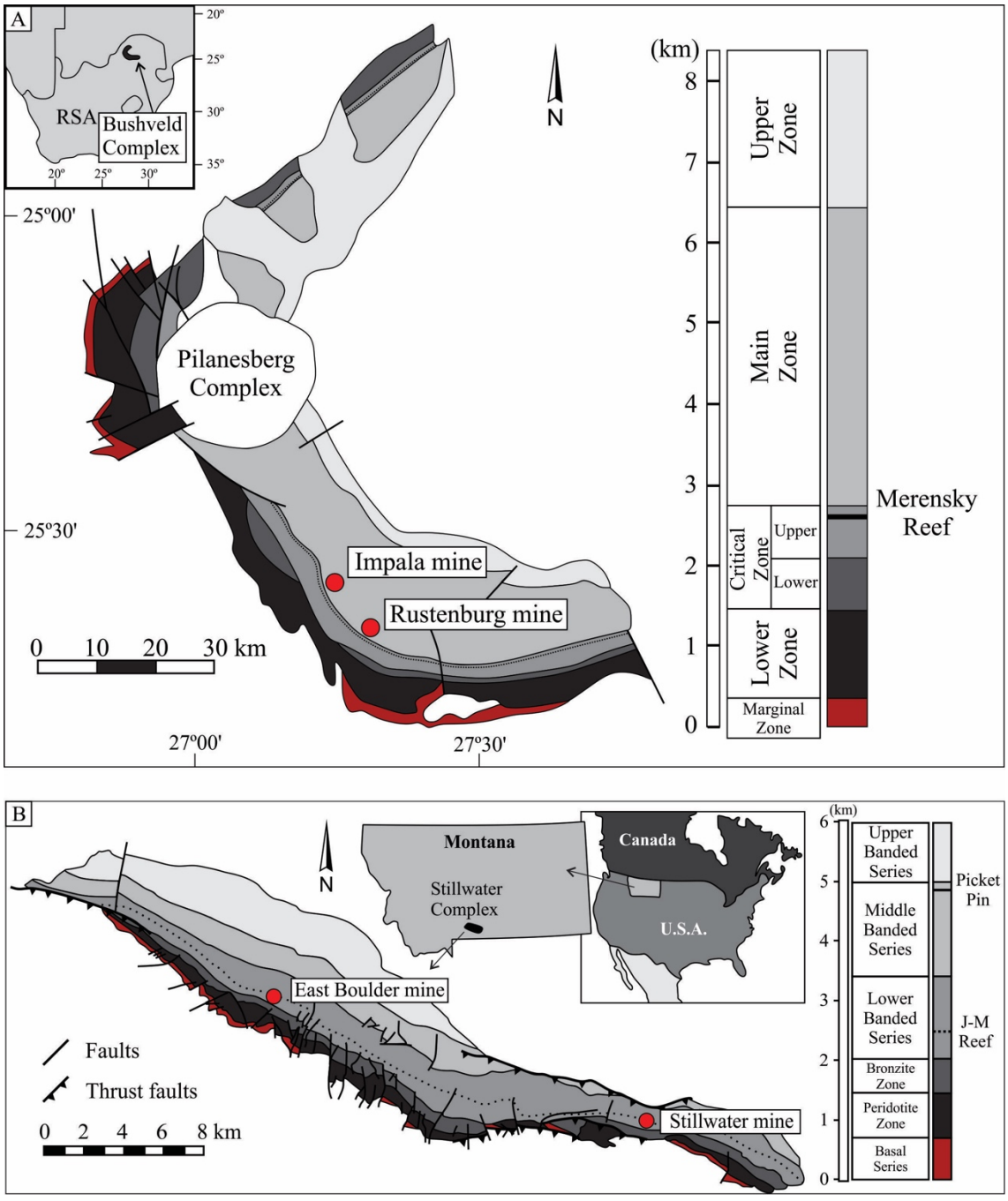

Figure 6.1 - a) Geology of the western lobe and generalized stratigraphy of the Bushveld Complex, Republic of South Africa (RSA; modified after Eales and Cawthorn, 1996; Von Gruenewaldt, 1986, 1989; Godel et al., 2006). Dashed line indicates the surficial projection of the Merensky Reef. The study localities are the Rustenburg and Impala mines. b) Geology and generalized stratigraphy of the Stillwater Complex (modified after McCallum et al., 1980; Zientek et al., 2002; Godel et al., 2006). Dashed line indicates the surficial projection of the J-M Reef. The study localities are the Stillwater and East Boulder mines.

Considering the Bushveld as a whole, the Merensky Reef displays significant regional and local lithological variations, which are beyond the scope of this study. Details on the reef variations are given by Naldrett et al. (2009) and Maier et al. (2013) and references therein. Barnes and Maier (2002) and Godel et al. (2007) attributed the formation of the reef to the collection of PGE by an immiscible sulfide liquid. Moreover, X-ray computed tomography results show that the sulfide minerals form a vertical network on a scale of 30 centimeters. This was interpreted to be the result of a sulfide liquid percolating downwards into the cumulate pile (Godel et al., 2006). The higher concentrations of Os, Ir, Ru, Rh and Pt, and lower Pd/Ir ratios in the chromite seams require and additional concentration step. Either laurite, $(Ru,Os,Ir)S_2$, and Pt-Fe alloy crystallized together with chromite before BMS saturation (Prichard et al., 2004; Godel et al., 2007), or the chromite layers originally contained more sulfide than currently observed. As consequence of Fe loss to chromite during cooling, S and Pd were mobilized from BMS partially dissolving the BMS, and enriching the remaining BMS in Os, Ir, Ru, Rh and Pt (Barnes and Maier, 2002; Prichard et al., 2004).

Godel et al. (2007) showed that 30 to 70 % of the Os, Ir, Ru, Rh and Pd are present in the BMS at the Rustenburg mine. Our current study for Rustenburg and Impala (to be presented below) yields similar results. The balance of the PGE is found as PGM. The PGM assemblages found in Impala and Rustenburg samples consist mainly of Pt-Pd sulfides, and Pd-Pt bismuth-tellurides (Prichard et al., 2004; Godel et al., 2008b), with sulfides being more common at Impala and bismuth-tellurides at Rustenburg (Fig. 6.2a). Arsenide, stanides, and antinomide PGM are rare. The other PGM present in minor amounts are laurite (RuS_2), and Pt-alloys. These observations are in broad agreement with PGM studies carried out on larger sample sets at both mines (Kinloch, 1982; McLaren and de Villiers, 1982).

At both the Impala and Rustenburg mines the PGM are mainly found associated with BMS, although some PGM are found included within silicate minerals (Fig. 6.2b). In both cases, the majority were found in association with Ccp. Prichard et al. (2004) found that most of the PGM were found at grain boundaries, or at the contact between BMS grains (Fig 6.2b). Godel et

al. (2010) found at Rustenburg that most of the PGM occur at the edges of the BMS grains. Based on experimental work showing that BMS accommodate less PGE on cooling (Makovicky et al., 1986; Makovicky, 2002), and the shape of the PGM, Prichard et al. (2004) and Godel et al. (2007) interpreted the PGM included within sulfides to have formed by exsolution during cooling. In addition, the reason that the PGM are more common at the edges of the sulfide grains was attributed to S loss from the BMS, which results in the sulfide minerals being less able to accommodate the PGE (Ballhaus et al., 1994; Peregoedova et al., 2004; Li and Ripley, 2006). Based on our observations of PGM at Sudbury and Noril'sk-Talnakh (Dare et al., 2010b, 2014; Duran et al., 2017; Mansur et al., 2019c), and the incompatible nature of Pd, Pt and TABS (Mungall et al., 2005; Patten et al., 2013; Liu and Brenan, 2015), we would now suggest that Pd-Pt PGM in contact with Ccp crystallized from the fractionated Cu-rich sulfide liquid.

6.3.2 – Stillwater Complex

The Stillwater Complex (Fig. 6.1b) hosts the John Manville Reef (J-M Reef) and the Picket Pin deposit (Boudreau, 2016 and references there in). Most of our samples come from the J-M Reef, with one samples from the Picket Pin (Godel and Barnes, 2008a; Barnes et al., 2020). In addition, a PGE-poor sample from the Banded series was also investigated. Samples from the J-M Reef were collected from the East Boulder and Stillwater mines, and consist of anorthosite, gabbronorite and troctolite. The sample from the Picket Pin deposit consists of an anorthosite, whereas the sample from the lower Banded series is a leucogabbronorite of Gabbronorite II (Barnes et al., 2020). All the samples contain disseminated BMS (from 2 to 7 vol.%), composed of Po, Pn and Ccp.

Several processes are proposed to explain the enrichment of PGE in the J-M Reef. Some authors propose that the BMS from the lower parts of the cumulate pile were dissolved by Cl-rich fluids and PGE were collected by the fluid. When this fluid encountered a fluid-undersaturated layer, the BMS and PGE precipitated (Boudreau, 2016 and references therein). In contrast, many

authors argue for an orthomagmatic model, where sulfide liquid collected the PGE from magma, and the sulfides collect on the cumulate pile (Campbell et al., 1983; Barnes and Naldrett, 1985; Irvine et al., 1983; Keays et al., 2012).

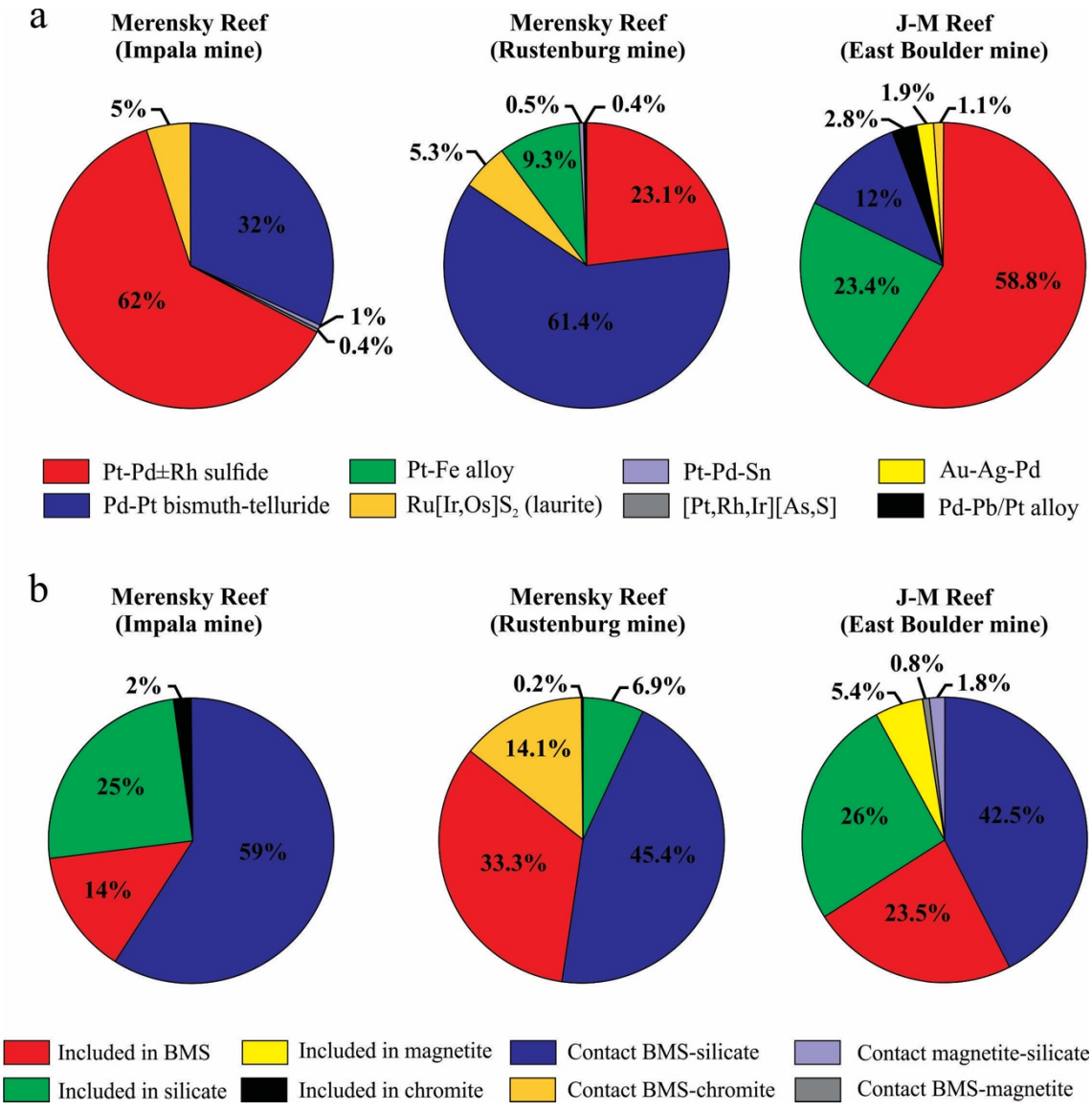

Figure 6.2 - Types (a) and textural association (b) of platinum-group minerals found in the Merensky Reef at the Impala and Rustenburg platinum mines, and the J-M Reef at the East Boulder Mine. The proportion of each mineral is given in area. Values from the Merensky Reef are from Prichard et al. (2004) for the Impala Mine, and Godel et al. (2007) for the Rustenburg Mine, and values for the J-M Reef are from Godel and Barnes (2008b).

In their study of the distribution of trace elements in BMS from the J-M Reef, Godel and Barnes (2008a) found that Rh, Ru, Ir and Os are predominantly hosted by Pn and Po. Approximately sixty percent of the Pd is hosted by Pn, with the remainder being present in PGM. As in the case of the Merensky Reef samples, the PGM from the J-M Reef are predominantly Pt-Pd sulfides, Pd-Pt tellurides and Pt-Fe alloy (Fig. 6.2a). In contrast to the Merensky Reef samples, the Pt-Fe alloy grains are more common than the bismuth-tellurides. Minor amounts of alloys (Au-Ag-Pd, Pd-Pb and Pt) and laurite are also present (Fig. 6.2a). Arsenides and antimonides were not observed. Interpretation of the textures of the PGM and BMS are complicated by greenschist metamorphic overprint. Most of the PGM occur included BMS, or at the contact between BMS and surrounding silicates or magnetite (Fig. 6.2b). Godel et al. (2008b) interpreted the PGM to have formed by two mechanisms. The PGM included in the BMS exsolved from the BMS during cooling, and S-loss. In addition, a late magmatic fluid migrated into the reef and partially dissolved the BMS and precipitated Pd and Pt in the form of alloys (Godel and Barnes 2008a).

6.4 – Analytical Methods

Tellurium, As, Bi, Sb and Se analyses were carried out at LabMaTer, Université du Québec à Chicoutimi (UQAC). A slightly modified version of the Hydride Generation-Atomic Fluorescence Spectrometry (HG-AFS) technique described by Mansur et al. (2019b) was used to determine these elements. The modification was that sample size was increased from 0.2 g to 0.4 g. This modification was introduced to lower the dilution factor, and consequently lower the limit of detection of the method. International reference materials (CH-4 and TDB-1; Natural Resources Canada), GeoPt18 (KPT-1), and a blank were determined at the same time as the samples. The obtained results agree with working values (*ANNEXE 14*).

The concentration and distribution of the minor and trace elements were determined by laser ablation-inductively coupled plasma-mass spectrometry (LA-ICP-MS) at LabMaTer, UQAC, using an Excimer 193 nm RESOlution M-50 laser ablation system (Australian Scientific Instrument) equipped with a double volume cell S-155 (Laurin Technic), and coupled with an Agilent 7900 mass spectrometer. The LA-ICP-MS tuning parameters were a laser frequency of 10 Hz, a power of 3 to 5 mJ/pulse, a dwell time of 7.5 ms, a rastering speed of 5 to 10 μm/s, and a fluence of 3 J/cm^2. Line scans across the surface of grains were made with beam sizes of 44, 33, and 25 μm, depending on grain size. The gas blank was measured for 30s before switching on the laser for at least 60s. The ablated material was carried into the ICP-MS by an Ar–He gas mix at a rate of 0.8–1 L/min for Ar and 350 mL/min for He, and 2mL/min of nitrogen was also added to the mixture. Data reduction was carried out using the Iolite package for Igor Pro software (Paton et al., 2011).

^{57}Fe was used for internal standardization of BMS. Three certified reference materials were used for external calibration of BMS: Laflamme Po727, which is a synthetic FeS doped with ~40 ppm PGE and Au supplied by Memorial University of Newfoundland, was used to calibrate for PGE, Au and S; MASS-1, which is a ZnCuFeS pressed powder pellet doped with 50–70 ppm of most chalcophile elements, supplied by the United States Geological Survey (USGS), was used to calibrate for Co, Cu, Zn, As, Se, Mo, Ag, Cd, Sn, Sb, Te, Tl, Pb and Bi; GSE-1g, which is a natural basaltic glass fused and doped with most elements at 300-500 ppm, supplied by the USGS, was used to calibrate for Ni, In, and Re using preferred values from the GeoReM database (Jochum et al., 2005). MASS-1, GSE-1g, JB-MSS5 (an FeS sulfide containing 50-70 ppm of most chalcophile elements, supplied by James Brenan) and UQAC-FeS1 (a synthetic sulfide developed at UQAC) were used to monitor the results.

Polyatomic interference of ^{63}Cu^{40}Ar on ^{103}Rh was corrected using ^{103}Rh measured in MASS-1, which contains 13.4% ^{63}Cu but no ^{103}Rh. One percent Cu produced ~0.1 ppm interference. Thus, the ^{103}Rh values in Ccp are not reported as the interference is too large to be corrected. Direct interferences of ^{108}Cd on ^{108}Pd and ^{115}Sn on ^{115}In were corrected by monitoring

^{111}Cd and ^{118}Sn, respectively. Interference of $^{68}Zn^{40}Ar$ on ^{108}Pd is negligible as Zn is present at <1000 ppm. Polyatomic interference of $^{61}Ni^{40}Ar$ on ^{101}Ru was corrected using ^{101}Ru measured in a NiS blank, which does not contain Ru. One percent Ni produced ~ 0.007 ppm interference and was not significant a significant part of the Ru signal.

For K-phlogopite analyses, ^{29}Si was used for internal standardization. GSE-1g was used for external calibration, and NIST-610 and NIST-612 (silicate glasses reference materials produced by National Institute of Standards and Technology), GSD-1g and Gprob-6 (USGS-certified artificial basalt glasses) were used to monitor the results. The reference materials were analyzed at the beginning and the end of each session to monitor a potential instrumental drift. The results obtained for the monitors were generally allowing for standard deviations on the working values (*ANNEXE 15*).

Maps of element distribution were made on different sulfide assemblages using a laser frequency of 15 Hz and a power of 5 mJ/pulse. The beam size (25 to 44 μm) and the stage movement speed (10 to 15 μm/s) were adapted to optimize spatial resolution and analysis time for grains of different sizes. The maps were generated using the Iolite software package on the basis of the time-resolved composition of each element. The maps indicate the relative concentration of the elements and are semi-quantitative.

6.5 – Results

6.5.1 – Whole-rock concentrations of TABS in the PGE reefs

The whole-rock concentrations of TABS plus the previously published S, Ni, Cu and PGE concentrations can be found in the *ANNEXE 16*.

The concentrations of S, PGE, Se, Te, Bi, As and Sb in the Impala (Fig. 6.3a) and Rustenburg (Fig. 6.3b) sections were plotted against the sample height to assess their distribution through the Merensky Reef. The distributions of TABS in the Merensky Reef at both the Impala and Rustenburg sections are similar. Selenium, Te and Bi correlate well with S and PGE. In the

reef interval, Se concentrations vary from 1 to 10 ppm, whereas Te and Bi concentrations vary from 0.1 to 1 ppm. In the chromitite layers the Se, Te and Bi values are slightly lower. Above the reef interval, Se ranges from 0.1 to 1 ppm, and below the reef interval the Se values are at their lowest, ranging from 0.01 to 0.1 ppm. Tellurium and Bi also have a similar distribution outside the reef interval, with values ranging from approximately 0.01 to 0.5 ppm above the reef, and lower than 0.01 ppm below the reef. The correlation between S and Se, Te and Bi supports the hypothesis that BMS are the main minerals controlling these elements. Moreover, the lowest values found in samples below the reef are in agreement with the absence of BMS in the samples (Fig. 6.3a).

The Se/Te ratio ranges from 2 to 5 within the reef interval, and increases up to 10 in samples above the reef (Fig. 6.3a and *ANNEXE 16*). This variation agrees with the distribution of these elements being controlled by BMS. Tellurium has a higher partition coefficient into a base metal sulfide liquid relative to Se (Liu and Brenan, 2015). Therefore, in samples with greater amounts of sulfide minerals (higher S concentrations), Te is expected to be more concentrated compared to Se (Brenan, 2015). Consequently, the Se/Te ratios are lower in samples from the reef interval, compared to samples above the reef (*ANNEXE 16*).

Arsenic and Sb do not show a clear correlation with S, Se, Te and Bi. Arsenic concentrations increase from 0.03ppm below the reef to 0.45ppm in samples slightly above the reef (Fig. 6.3a). In the upper part of the Impala section they decrease. The concentrations of Sb within and above the reef interval are similar, and range from 0.01 to 0.06 ppm, whereas Sb concentrations below the reef interval are lower than 0.01 ppm. Arsenic concentrations are slightly lower in the chromitite layers, and in contrast, the Sb values vary very little (Fig. 6.3a and 6.3b).

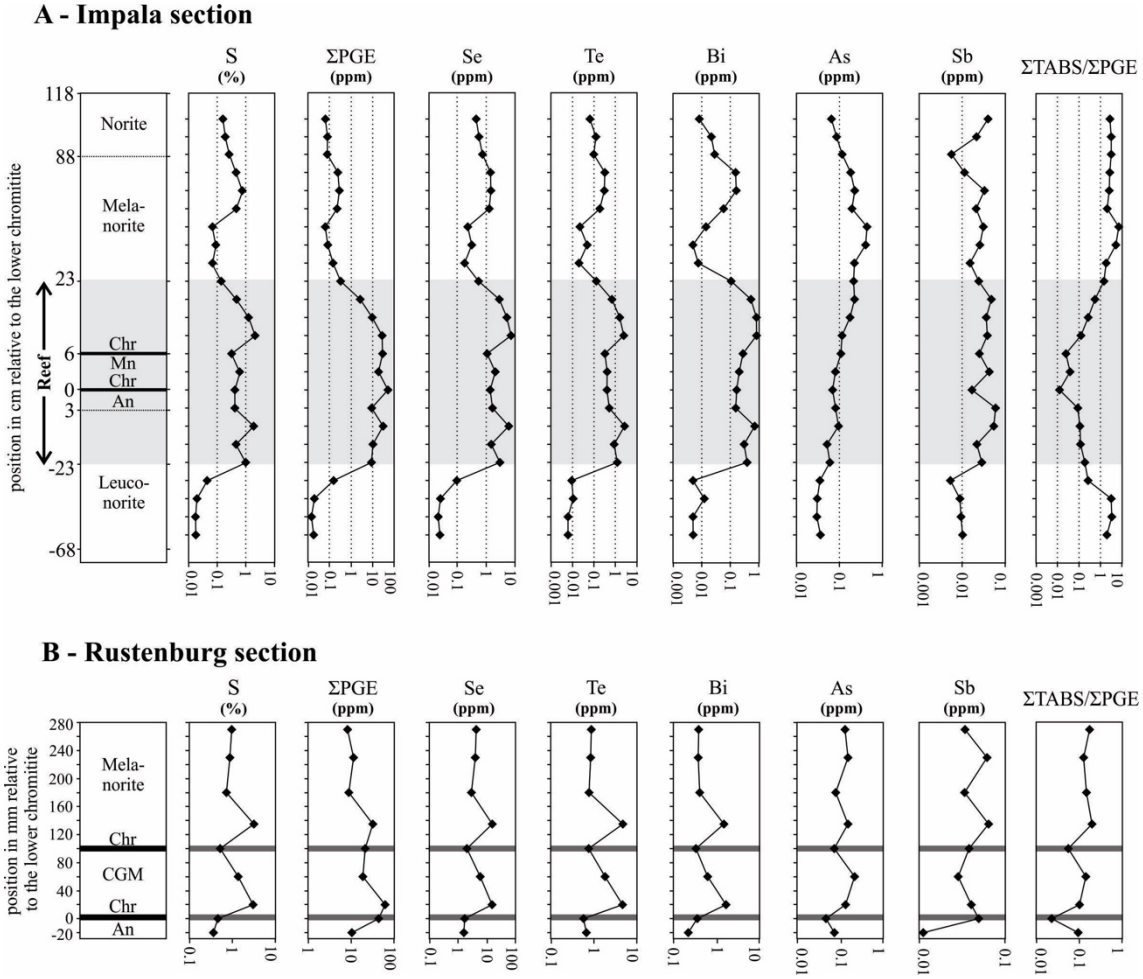

Figure 6.3 - Variations in whole-rock concentrations of chalcophile elements with height across the (a) Impala section and (b) Rustenburg section. Note that the vertical scales are not linear, the samples are spaced out evenly for clarity. At the Impala section the reef interval is defined by rocks containing more than 1.5 ppm Pt+Pd in whole-rock analyses, and starts 23cm below the lower chromitite and ends 23cm above it. Individual whole-rock are reported in the *ANNEXE 16*. Abbreviations: ΣPGE: Pt+Pd+Rh+Ru+Ir+Os; ΣTABS: Te+As+Bi+Se+Sb; An: anorthosite; Chr: chromitite; CGM: coarse-grained melanorite; Mn: melanorite.

The absolute concentration of TABS relative to PGE is lower in samples from the reef interval (Fig. 6.3a). Within the reef interval, the ratio of the sum of TABS over the sum PGE ranges from 0.01 to 1, whereas above and below the reef this ratio is mostly higher than 1 (Fig. 6.3a). Thus, although all these elements are concentrated in the reef samples, the PGE were more efficiently concentrated relative to TABS. This is in agreement with the observation that PGE have higher partition coefficients into a sulfide liquid than TABS (Mungall and Brenan, 2014; Barnes and Ripley, 2016 and references therein).

The concentrations of TABS are shown plotted against the concentrations of S in samples from the Stillwater and Bushveld complexes (Fig. 6.4). For both the Stillwater and Bushveld complexes, Se, Te and Bi concentrations correlate with S values (Fig. 6.4a, 6.4b and 6.4c). The concentrations of these elements in samples from the J-M Reef, Banded Series and Merensky Reef are in the same range (Fig. 6.4a, 6.4b and 6.4c). In the case of the Merensky Reef, Sb shows a weak correlation with S, with samples from inside the Merensky Reef having slightly higher values (0.1 to 0.6 ppm) than samples outside the reef (Fig. 6.3 and 6.4e). Some samples from the Stillwater follow the same trend, but most contain less than detection level of Sb. Arsenic does not show a clear correlation with S (Fig. 6.4d). In fact, As concentrations in samples from outside the Merensky Reef are slightly higher compared to those found in samples from within the reef (Fig. 6.3). The lack of clear correlation between As, and to a lesser extent Sb, with S shows that BMS are not the only minerals controlling these elements. This is in agreement with the low partition coefficients of As and Sb into the sulfide liquid (Li and Audétat, 2015), and thus their status as slightly chalcophile elements, in contrast with PGE, defined as highly chalcophile (Barnes, 2016).

Based on the incompatible element content of the rocks for the Impala section, Barnes and Maier (2002) concluded that samples directly above the Merensky Reef interval have a higher trapped liquid fraction. Given that both As and Sb are incompatible with the cumulate minerals present (orthopyroxene and plagioclase), these elements could also be present in the trapped liquid fraction. The positive correlation between the concentrations of As and Hf, with samples lying along a tie-line between the B1-B-2 melt mixture and cumulate silicate minerals (Barnes et al., 2002) support this hypothesis (Fig. 6.5a). Samples slightly displaced to the As-enriched side of the line reflect the presence of sulfides (Fig. 6.5a). For Sb, in samples containing less than 4000 ppm S the samples also lie along a tie-line between the melt and cumulate silicates. Samples with more than 4000 ppm S are displaced on the Sb-rich side of the tie-line, reflecting the presence of sulfides (Fig. 6.5b).

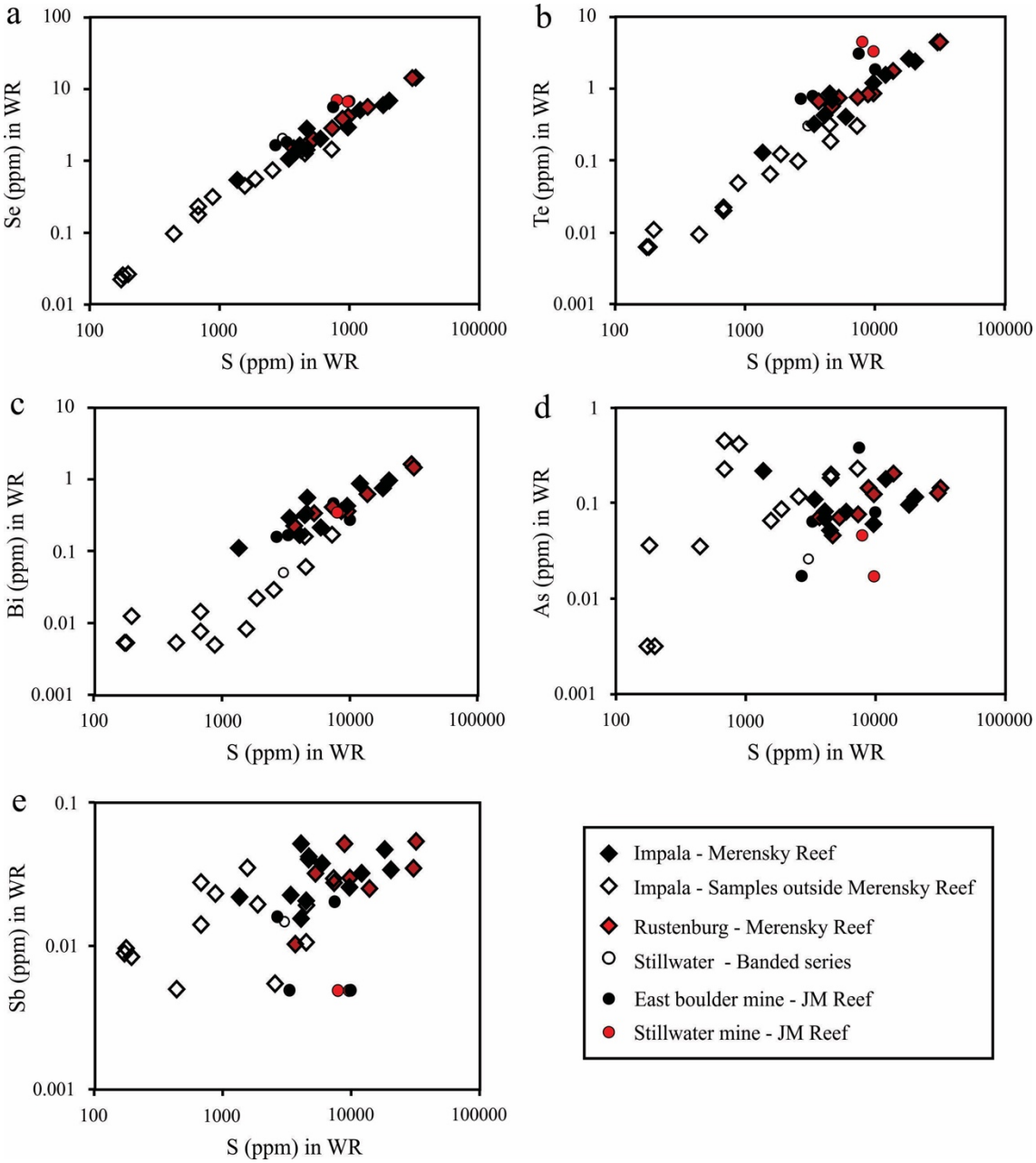

Figure 6.4 - Plots of (a) Se, (b) Te, (c) Bi, (d) As and (e) Sb vs S in whole rock (WR). Note that Se, Te and Bi correlate with S indicating sulfide control, whereas As and Sb do not. Individual whole-rock results are reported in the *ANNEXE 16*.

Li et al. (2005) proposed that the K-phlogopite present in the Merensky Reef crystallized from the trapped liquid. Therefore, we analyzed K-phlogopite by LA-ICP-MS to investigate whether it is host for As and Sb (*ANNEXE 17*). The concentrations of As and Sb in the K-phlogopite range from 0.1 to 4.2 ppm and 0.02 to 0.25 ppm, respectively, and show a positive correlation (Fig. 6.6a). Moreover, the concentration of As and Sb in K-phlogopite show positive

correlation with Hf concentrations (Fig. 6.6b and 6.6c), and negative correlations with Ba, Ti and Cr in K-phlogopite (Figs. 6.6d to 6.6f). The positive correlations among As, Sb and Hf can be attributed to all three elements being incompatible during the formation of the reef, and concentrating in the silicate liquid until the crystallization of K- phlogopite. In contrast, Ba, Cr and Ti behave as compatible elements with Ba partitioning into plagioclase and Cr and Ti partitioning into pyroxene and chromite (Dunn and Sen, 1994; Pagé et al., 2009). The distribution of As and Sb is partially controlled by the amount of trapped liquid fraction present, and not only by BMS.

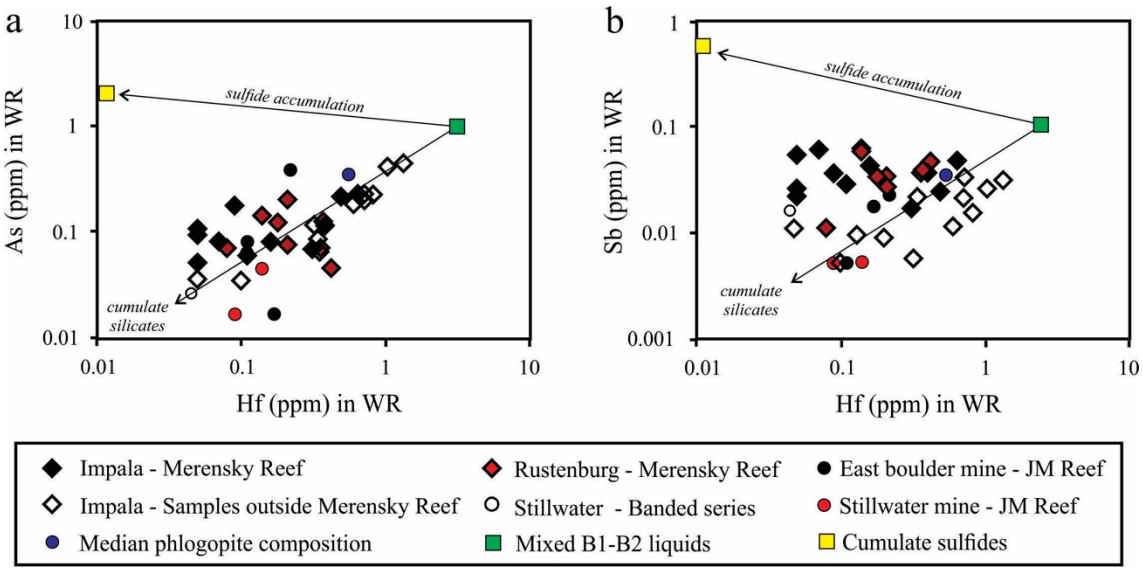

Figure 6.5 - Plots of (a) As and (b) Sb vs Hf in whole rock (WR). Note that samples plot along a tie-line between B1-B-2 melt mixture (Barnes and Maier, 2002) and silicate cumulates, indicating a melt control of As and Sb. However, some samples plot toward the cumulate sulfide composition (Barnes and Maier, 2002), suggesting a slight control by sulfide minerals. Individual whole-rock are reported in the *ANNEXE 16*.

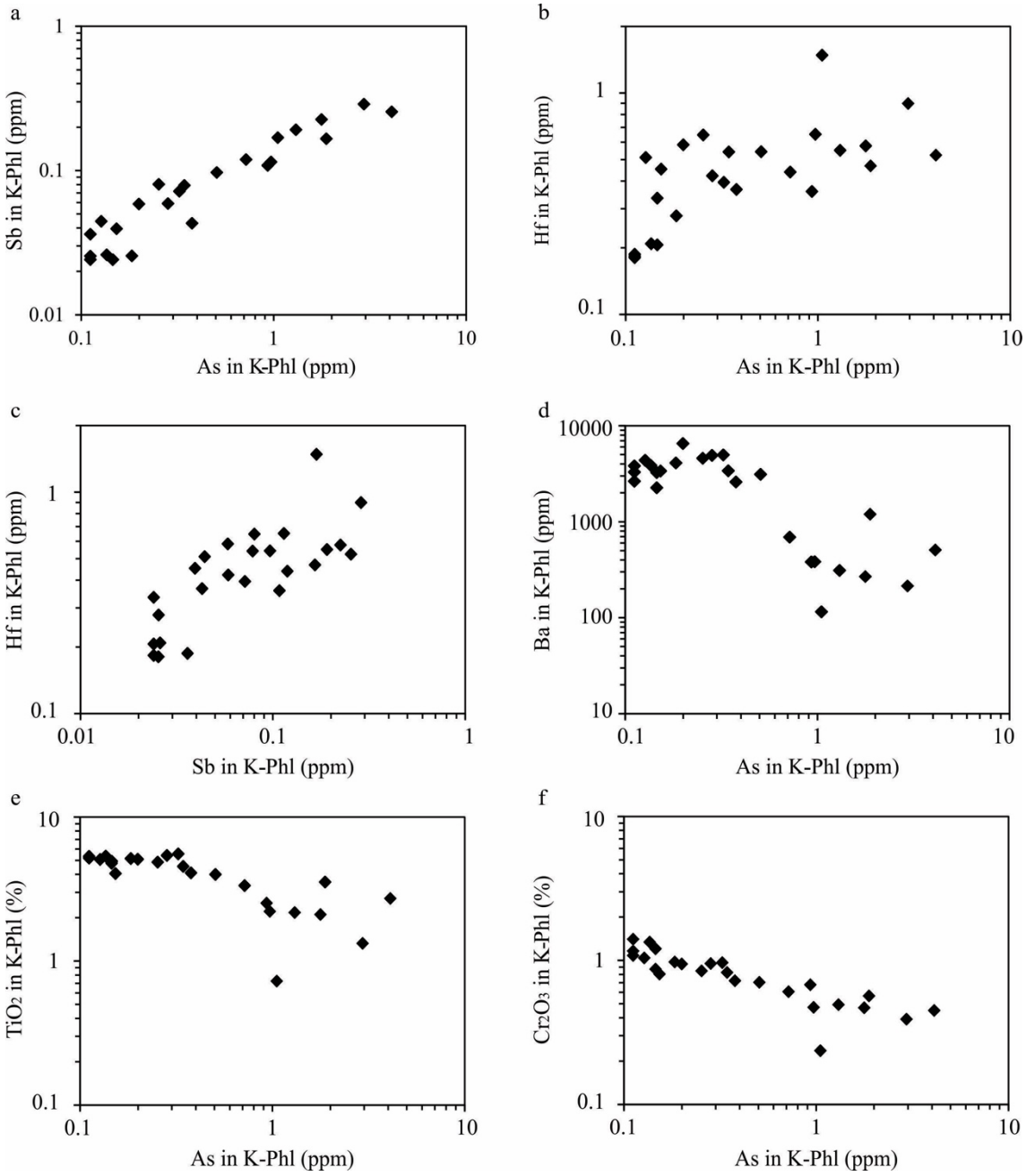

Figure 6.6 - Plots of (a) As vs Sb, (b) Hf vs As, (c) Hf vs Sb, and (d) Ba, (e) TiO2 and (f)Cr2O3 vs As in K-phlogopite (K-Phl). There is a positive correlation between As and Sb concentrations and Hf concentrations, supporting that As and Sb become progressively more concentrated in the fractionated silicate liquid. However, the negative correlation between Ba, Ti and Cr, and Hf support the compatible behaviour of these elements. Individual analyses of K-phlogopite are reported in the *ANNEXE 17*.

6.5.2 - Trace elements in BMS

Median concentrations of trace elements in Po, Pn and Ccp from each sample, and the full LA-ICP-MS data set are reported in *ANNEXE 18 to 20*. Time-resolved spectra were monitored to ensure that PGM inclusions were not included in the integrations when calculating the BMS compositions. Compositional LA-ICP-MS maps in typical BMS assemblages, composed of Po, Pn and Ccp are shown in Fig. 6.7 to 6.9. The distribution of trace elements among Po, Pn and Ccp is similar in all the different localities.

The LA-ICP-MS compositional maps show that the elements compatible with MSS (Ni, Co, Se, Mo, Ru, Rh, Re, Os) are more concentrated in Po and Pn (Fig. 6.7 to 6.9). Molybdenum is slightly more concentrated in Po than Pn, whereas Ru, Os, Ir and Re are distributed between Po and Pn, with a slight preference for Pn. The distribution of these elements in Pn is not always homogeneous, and in some cases they are more concentrated in the Pn next to the contact with Po (e.g. Ru and Os in Fig. 6.7 and 6.8). Selenium displays the same zonation pattern, and although present in all BMS, it is also more concentrated in the Pn next to the contact with Po (Fig. 6.7 to 6.9). Nickel and Co are preferentially concentrated in Pn.

Elements compatible, or only moderately incompatible with ISS (Cu, Zn, Cd, In and Sn), are concentrated in Ccp (Fig. 6.7 to 6.9). Silver is present in both Pn and Ccp, with a slight preference for Ccp (Fig. 6.7 and 6.9). Some elements incompatible with both MSS and ISS (As, Pd, Te and Pt) are enriched in Pn. The presence of these elements in Pn, and the zonation patterns in Pn for Se, Ru and Os are thought to be the product of peritectic reaction of MSS with fractionated sulfide liquid and are described in detail by Mansur et al. (2019a). Lead and Tl are found concentrated in the fractures of Pn grains (Fig. 6.8 and 6.9), which suggest that these elements have either been expelled from the BMS lattice, or precipitated from late fluids at grain boundaries. Antinomy and Bi (not shown) do not show a clear preference for any of the BMS.

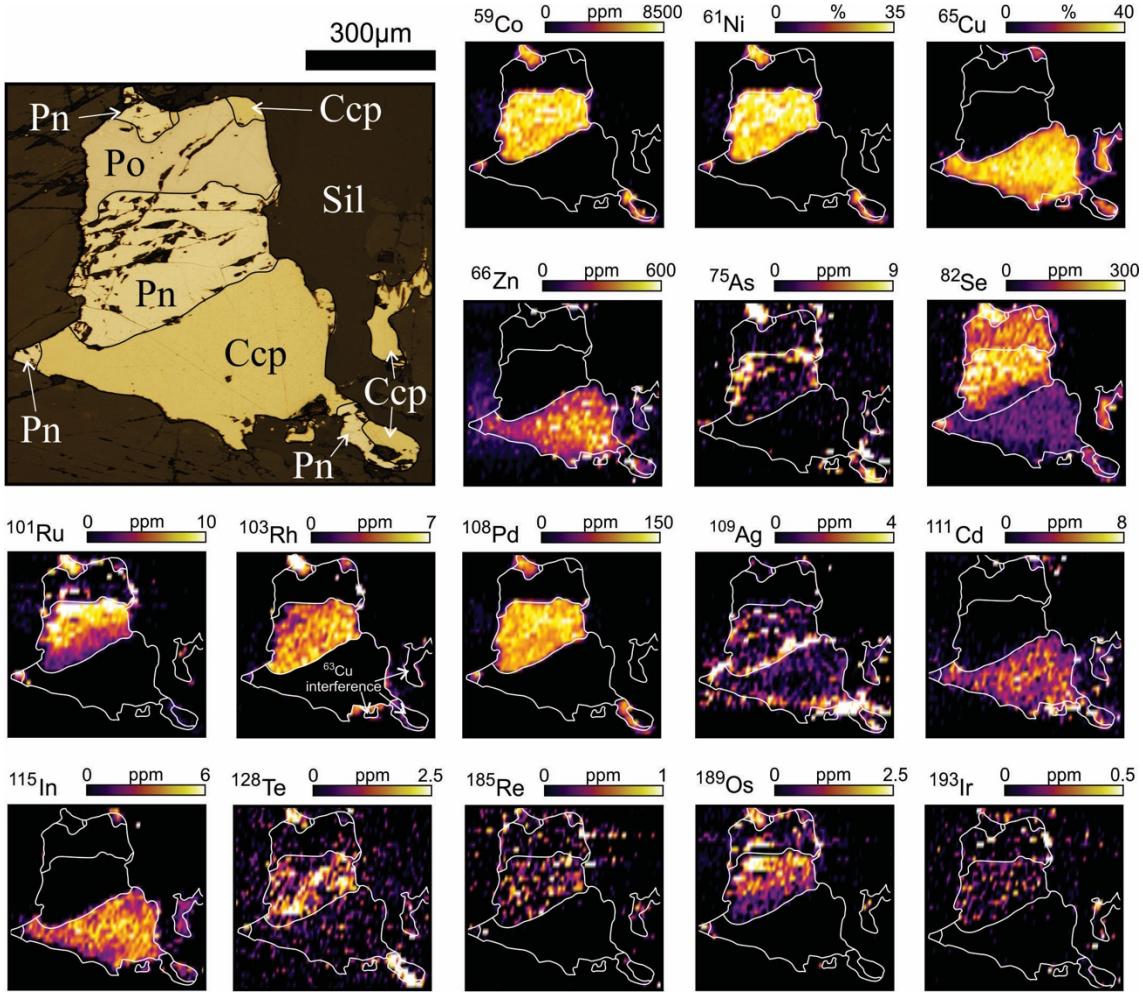

Figure 6.7 - LA–ICP-MS elemental maps showing the distribution of chalcophile elements among pyrrhotite (Po), pentlandite (Pn) and chalcopyrite (Ccp), in disseminated sulfide from the Merensky Reef at the Impala section. The zonation patterns for Ru and Os are thought to be the product of peritectic reaction of monosulfide solid solution (MSS) with fractionated sulfide liquid and are described in detail by Mansur et al. (2019a).White lines show the grain outlines. The relative concentrations of the elements are semi-quantitative.

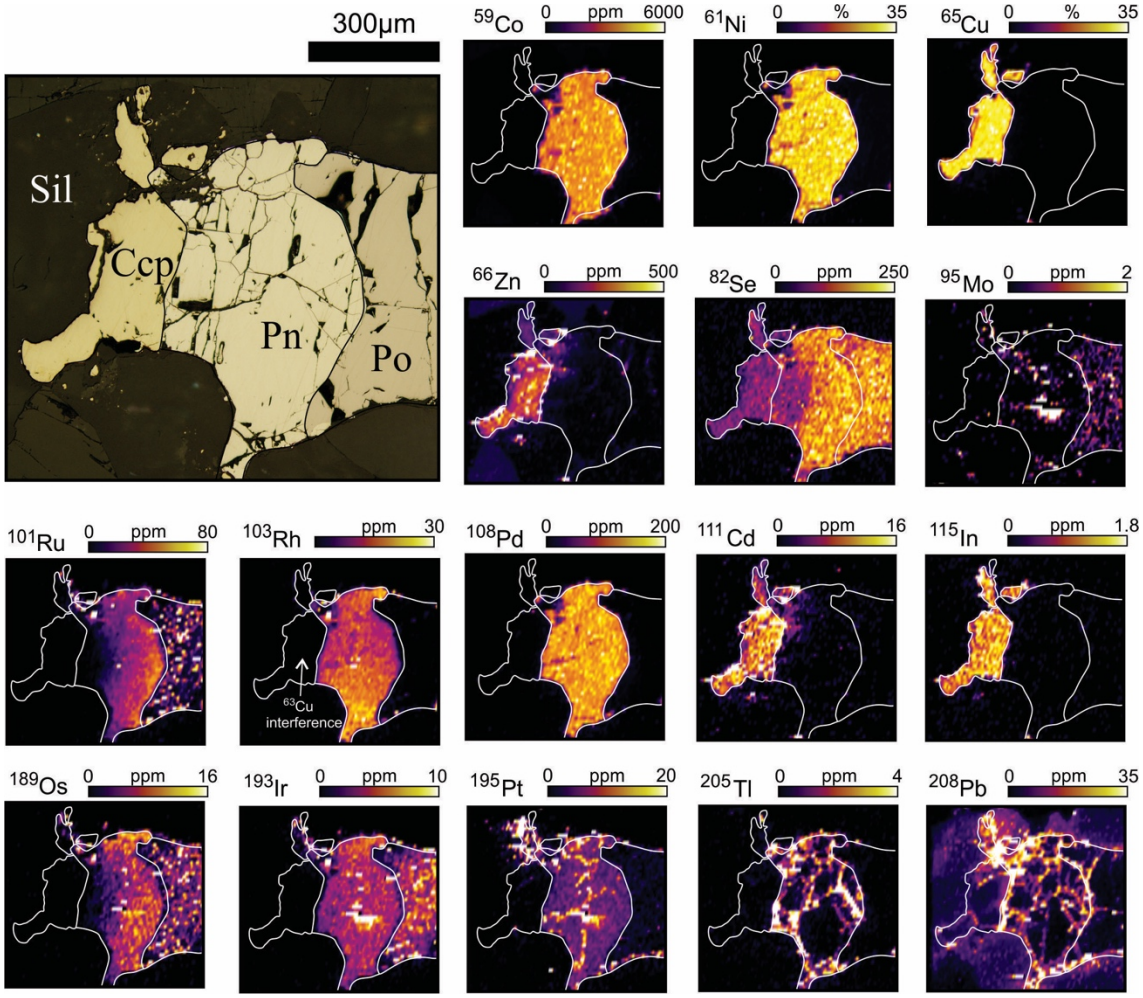

Figure 6.8 - LA–ICP-MS elemental maps showing the distribution of chalcophile elements among pyrrhotite (Po), pentlandite (Pn) and chalcopyrite (Ccp), in disseminated sulfide from the Merensky Reef at the Rustenburg section. White lines show the grain outlines. The relative concentrations of the elements are semi-quantitative.

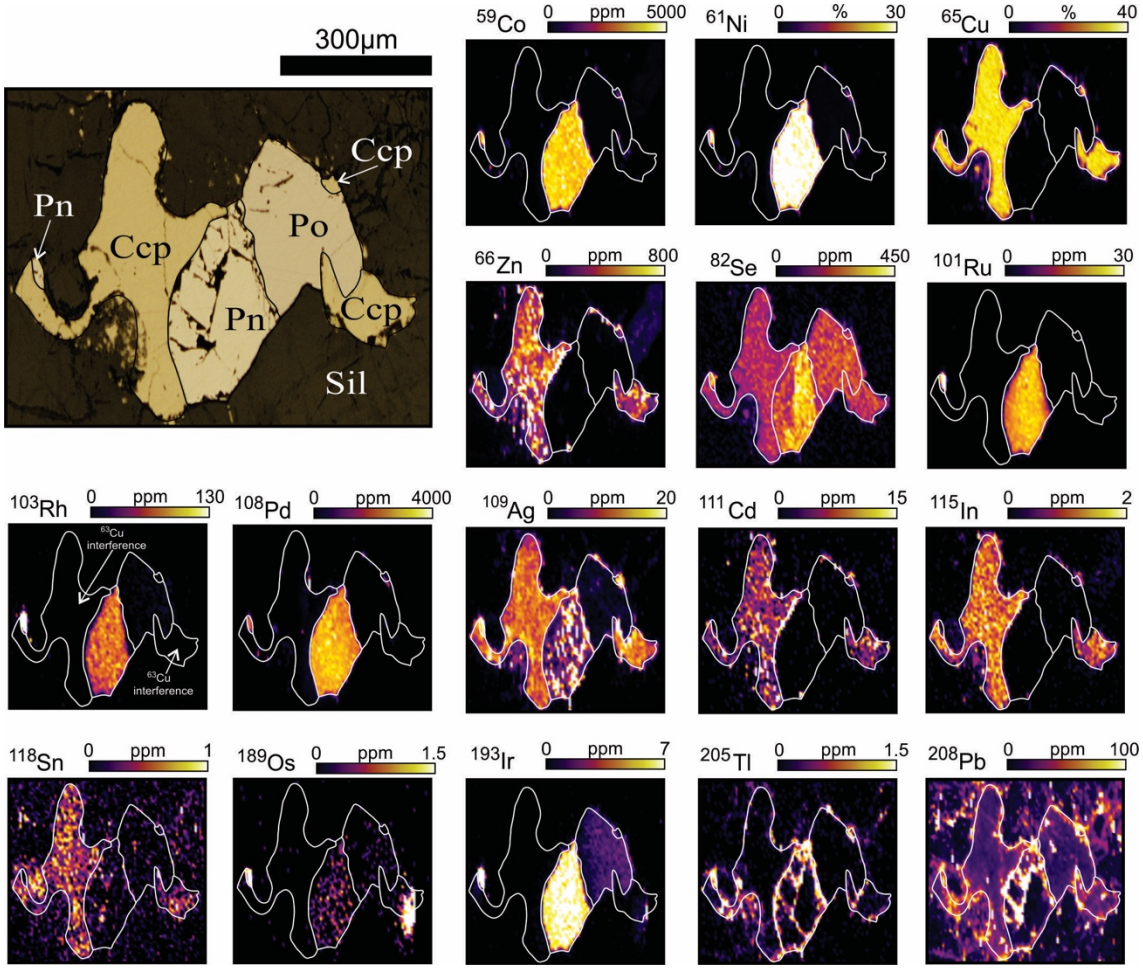

Figure 6.9 - LA–ICP-MS elemental maps showing the distribution of chalcophile elements among pyrrhotite (Po), pentlandite (Pn) and chalcopyrite (Ccp), in disseminated sulfide from the J-M Reef at the Stillwater mine. White lines show the grain outlines. The relative concentrations of the elements are semi-quantitative.

6.5.3 – Mass balance

The weight fraction of each element in each BMS was calculated to establish which mineral(s) host the bulk of each element at various localities. The proportion of each element hosted in each BMS was calculated following the method used by Barnes et al. (2006). This calculation requires: i) the concentration of each element in the whole rock (*ANNEXE 16*); ii) the median concentration of each element in each BMS (*ANNEXE 18 to 20*); and iii) the weight fraction of each BMS. The weight fraction of Ccp, Po, and Pn were calculated using whole-rock Cu, Ni, and S and the concentrations of Cu and Ni in each mineral. The Cu was assigned to Ccp,

whereas the Ni was assigned to Pn. The contributions of Ni from olivine and orthopyroxene were deducted prior to calculation the weight fraction of Pn. The concentrations of Ni in olivine and orthopyroxene used in the calculation were 3000 ppm and 800ppm, respectively. These concentrations correspond to average values found by Barnes and Naldrett (1985) in olivines from the J-M Reef, and by Cawthorn and Boerst (2006), and Godel et al. (2011) in orthopyroxenes from the Merensky Reef. The proportions of orthopyroxene and olivine in each sample are given in detail by Barnes and Maier (2002) for the Impala section, Godel et al. (2007) for the Rustenburg section, and Godel et al. (2008a) for the J-M Reef. The remaining S was attributed to Po. The fraction of K-phlogopite was obtained from petrographic observations and is around 3%. The K-phlogopite is restricted to samples above the Merensky Reef at the Impala section. The accumulated error of the different results used for the mass balance calculation is approximately 20% at one standard deviation (1σ). The results for mass balance calculations are summarized in *ANNEXE 21*.

The results for mass balance calculations are similar for samples from both the Rustenburg and Impala sections. The BMS from the silicate rocks account for a greater proportion of whole-rock PGE relative to the BMS from the chromitites (Fig. 6.10). In the silicate rocks, the BMS host most of Pd, Rh, Ir, Os (40 to 80 %), but only minor amounts of Ru (10 to 30%). However, in the chromitites the BMS host only 15 to 40% Pd, Rh and Os, and virtually no Ru and Ir (<10%). In all the samples, almost no Pt is present in the BMS minerals. The BMS from both silicate rocks and chromitites host all Se and variable amounts of Co and As (10 to 60%), but only account for minor Sb, Bi and Te (<5%). In contrast, BMS in samples above the Merensky Reef interval host significant amounts of the Te, Bi, Pd and Os (30-80%), but only minor Ir, Rh, Ru, Co and As (15 to 30%). The contribution of K-phlogopite to whole-rock budget of TABS was calculated and it only hosts minor amounts of As, Sb and Bi (<10%).

In samples from the J-M Reef the BMS host between 60 to 90% of whole-rock PGE (apart from Pt and Os) at the East Boulder mine, whereas only 10 to 50% at the Stillwater mine (Fig. 6.11). At both localities, the BMS host all the Se and significant amounts of Co (40-50%). In samples from the East Boulder mine the BMS do not host significant amounts of other

chalcophile elements (Fig. 6.11). However, BMS from the Stillwater mine also host virtually all of the Cd, and minor amounts of As, Sb and Zn (<30%). In the samples from the Banded Series the BMS host minor amounts of all PGE (<20%), whereas significant amounts of Te (>60%), and minor As and Bi (15-20%). As is observed in the J-M Reef samples, the BMS from the Banded Series (Fig. 6.11) also host virtually all Se, and variable amounts of Co, Cd and Zn (5-50%).

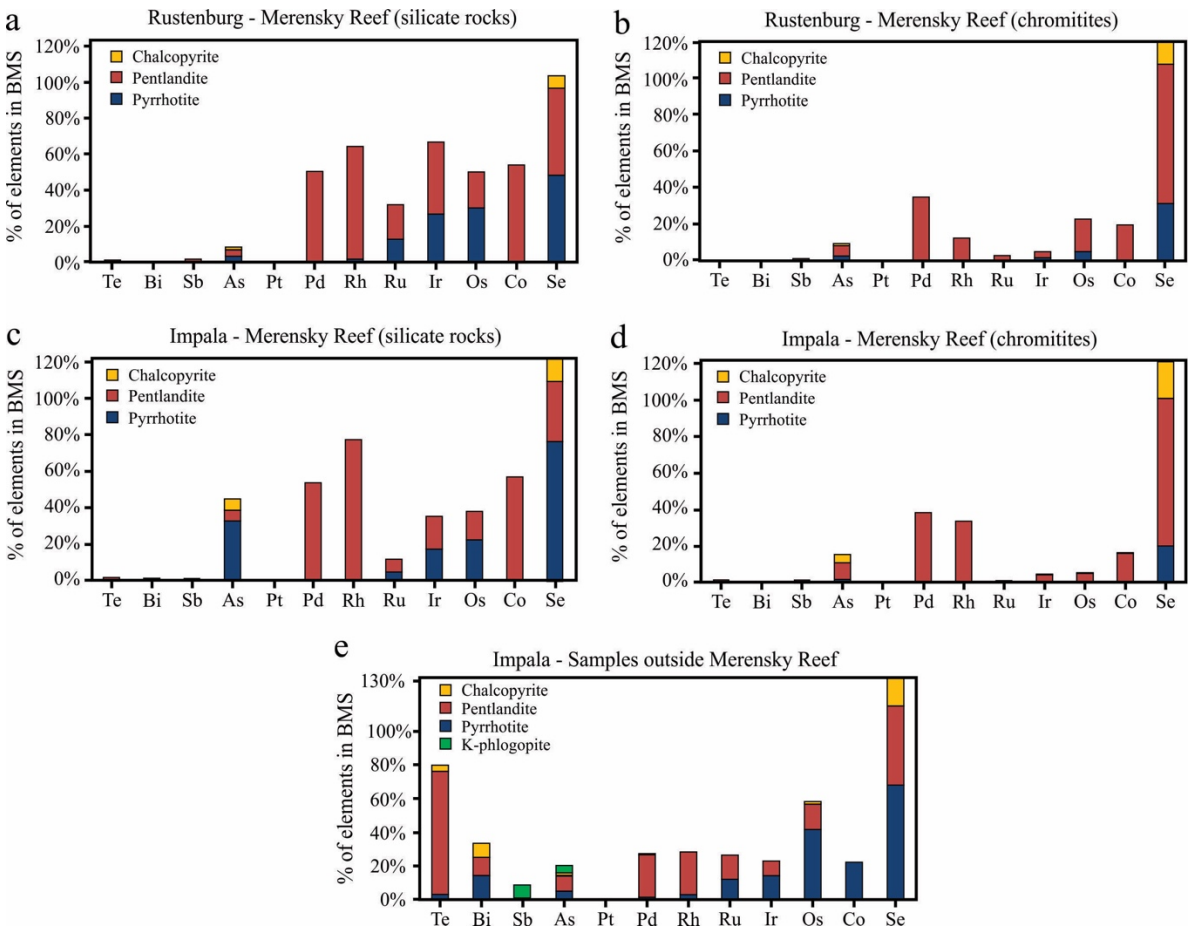

Figure 6.10 - Average proportion (%) of each element hosted in pyrrhotite, pentlandite, chalcopyrite and phlogopite from the Rustenburg (a and b), and Impala (c, d and e) sections of the Bushveld Complex. Samples from the reef interval were divide into silicate rocks (a and c) and chromites (b and d), and separated from samples from outside the reef interval (e).

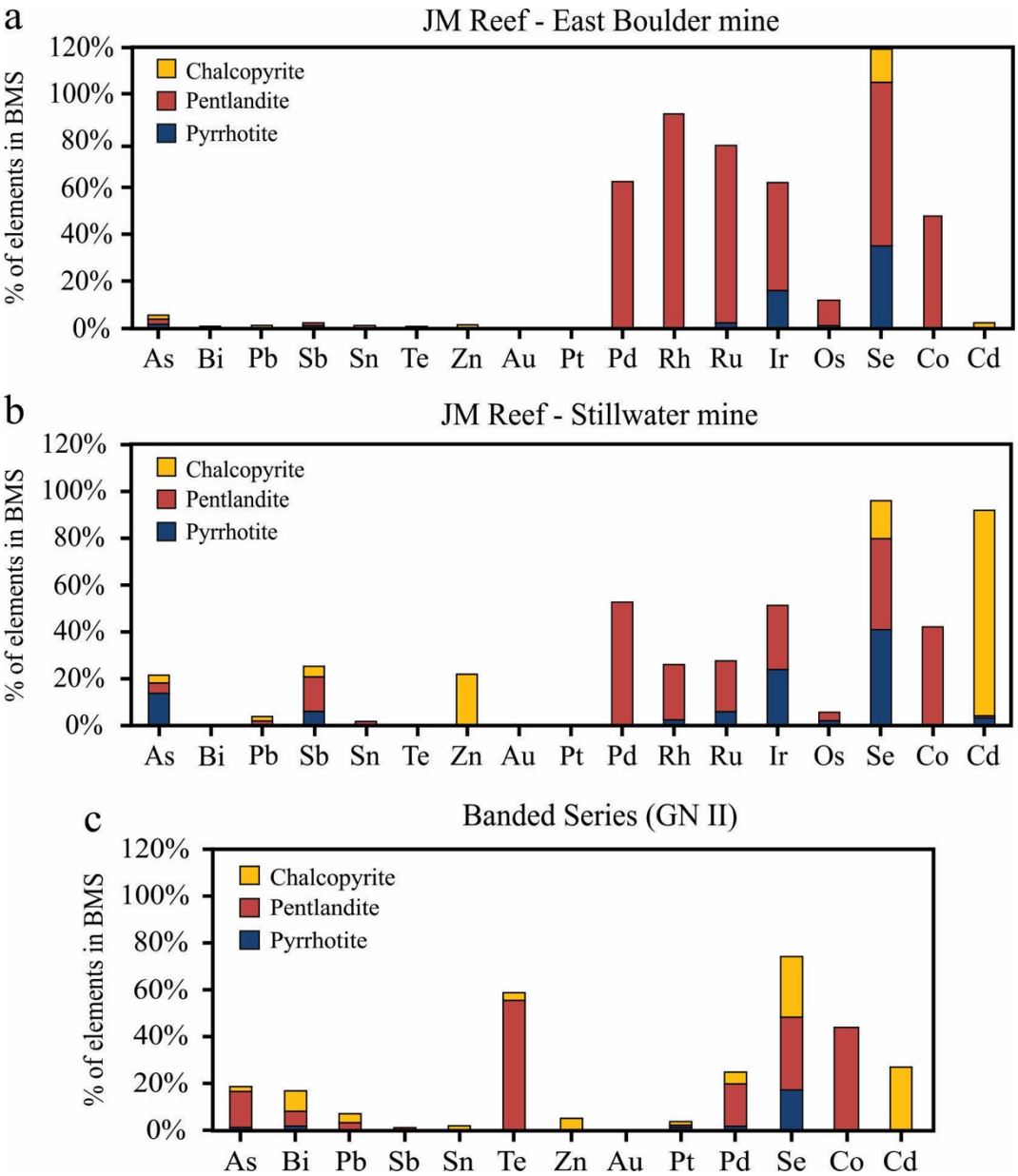

Figure 6.11 - Average proportion (%) of each element hosted in pyrrhotite, pentlandite and chalcopyrite from the J-M Reef at the East Boulder (a), and Stillwater (b) mines, and the Banded Series (c) of the Stillwater Complex.

In samples from both Bushveld (Fig. 6.10) and Stillwater (Fig. 6.11) complexes Pn hosts most of Co, Pd, Rh and Te, whereas Os, Ir and Ru are partitioned between Pn and Po. Chalcopyrite hosts most of the Cd and Zn. Selenium is evenly present in all BMS, and the main host is the most common mineral in each sample, normally Po and Pn. Arsenic, Bi, Pb, Sb are distributed among all the BMS, and no particular BMS seems to be the preferable host for these elements.

6.5.4 – Variations in PGE to TABS ratios in base metal sulfides

There appears to be a negative correlation between TABS contents of the BMS and PGE. At both the Bushveld (Fig. 6.12) and Stillwater (Fig. 6.13) complexes there is a negative correlation between the concentrations of Te, As and Bi, and the concentrations of PGE in Pn. Pentlandite from samples outside the reefs (i.e. Banded Series and above the Merensky Reef) has low concentrations of PGE, but high concentrations of Te, As and Bi. In contrast, Pn from the Merensky Reef, Picket Pin deposit and J-M Reef have the highest PGE contents, but the lowest concentrations of Te, As and Bi (Fig. 6.12 and 6.13).

The relationship between TABS and PGE content can be investigated more closely in the Impala mine section, where there is stratigraphic control. The median concentrations of PGE and TABS in BMS are plotted against the sample height (Fig. 6.14). Pentlandite was used to monitor median concentrations of Pt, Pd, Rh, Ir, Os, Te, As and Sb, whereas Po was used for Ru, and Ccp was used for Bi and Sn (Fig. 6.14). Median compositions of other BMS in each sample are also reported in *ANNEXE 18 to 20*. Median concentrations of PGE are higher in BMS from the reef than in BMS from above the reef (Fig. 6.14). One exception is a sample above the reef interval with higher PGE concentrations in BMS, which also correlates with slightly higher whole-rock PGE contents (i.e. sample IM-7; *ANNEXE 16*).

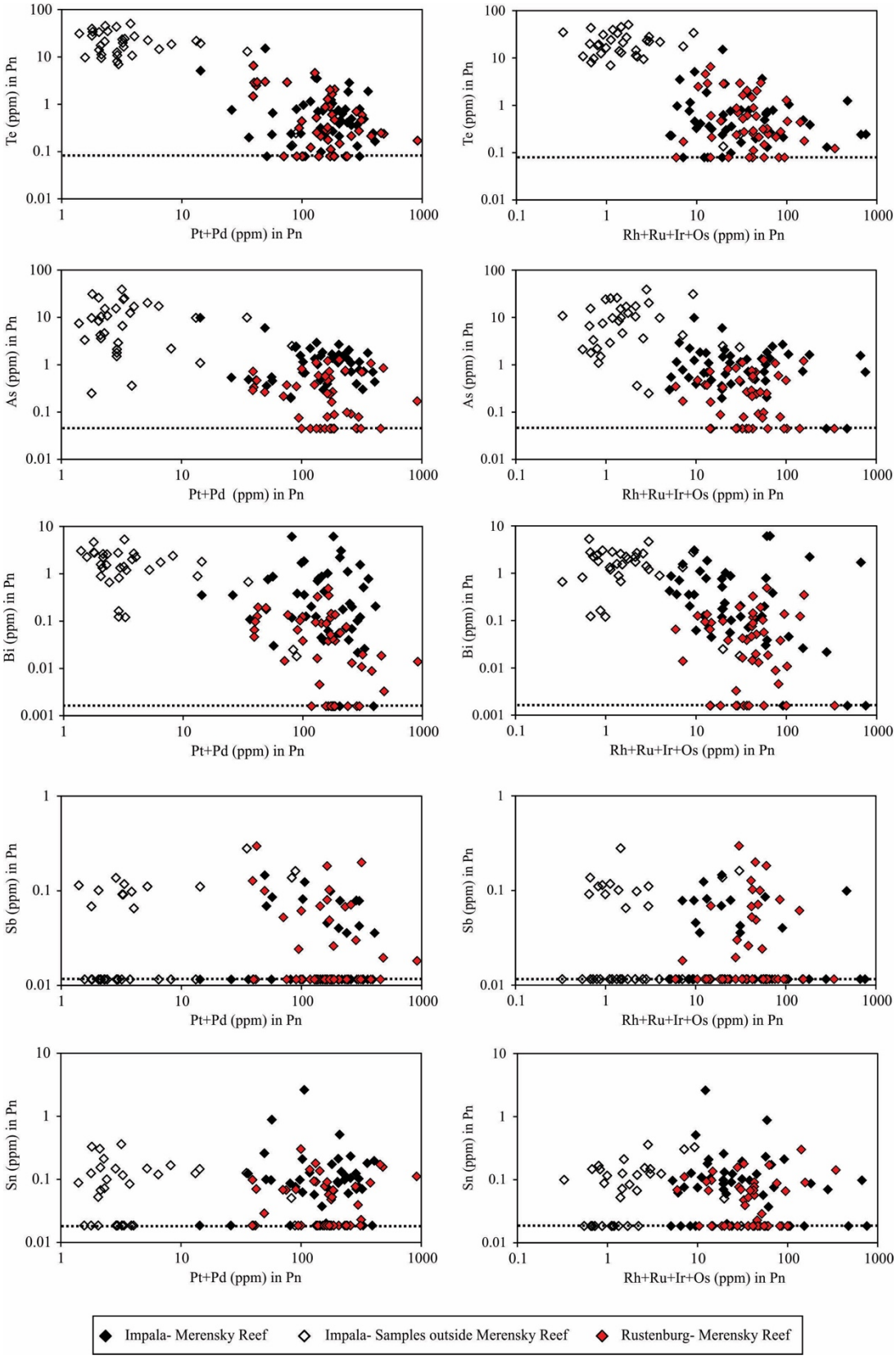

Figure 6.12 - Plots of Te, As, Bi, Sb and Sn vs Pt+Pd and Rh+Ru+Ir+Os in pentlandite (Pn) from samples of the Bushveld Complex. Note the negative correlation between Te, As and Bi concentrations and PGE concentrations in Pn. In contrast, there is no clear correlation between Sb and Sn concentrations and PGE contents in Pn. Dashed lines indicate the detection limits of LA-ICP-MS.

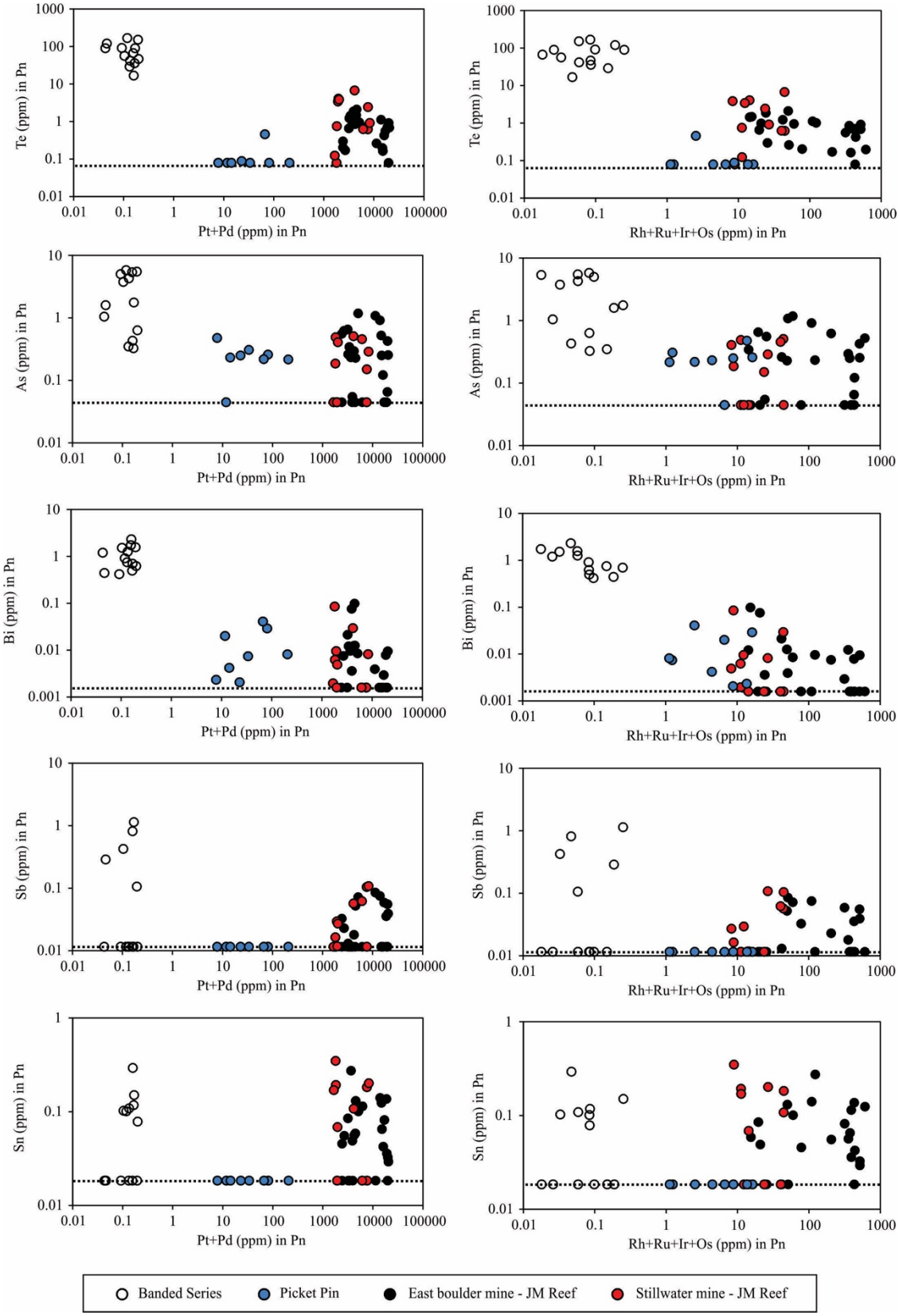

Figure 6.13 - Plots of Te, As, Bi, Sb and Sn vs Pt+Pd and Rh+Ru+Ir+Os in pentlandite (Pn) from samples of the Stillwater Complex. Note the negative correlation between Te, As and Bi concentrations and PGE concentrations in Pn. In contrast, there is no clear correlation between Sb and Sn concentrations and PGE contents in Pn. Dashed lines indicate the detection limits of LA-ICP-MS.

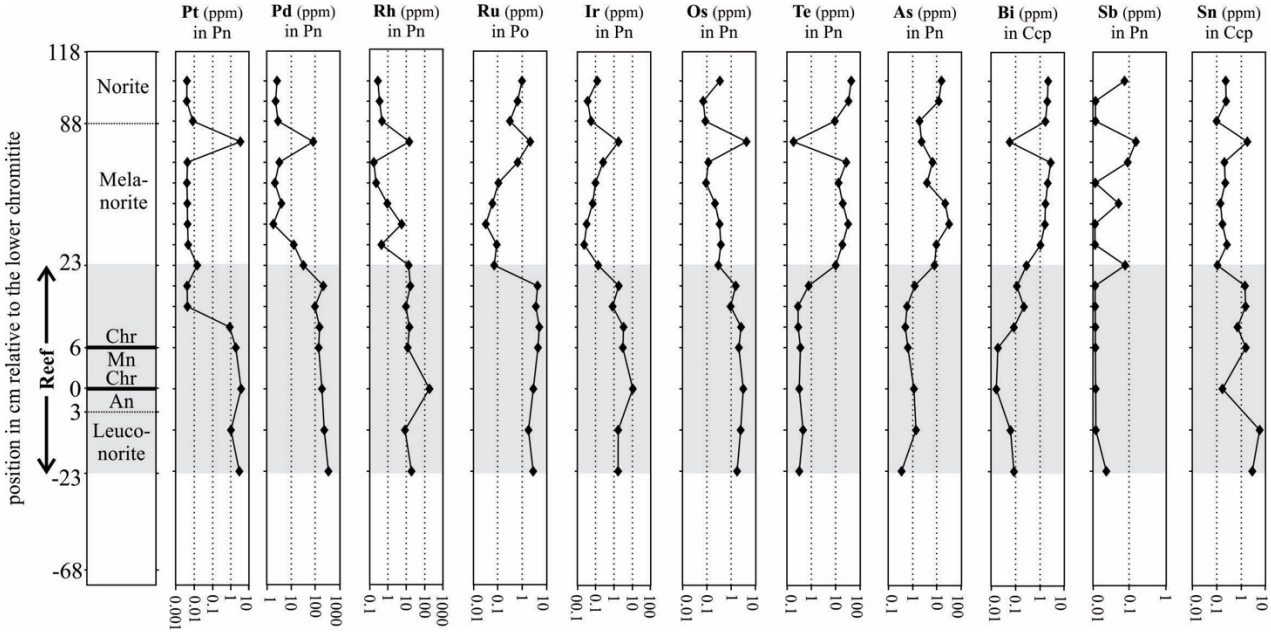

Figure 6.14 - Variations in median concentrations of Pt, Pd, Rh, Ru, Ir, Os, Te, As, Bi, Sb and Sn in pentlandite (Pn), pyrrhotite (Po) and chalcopyrite (Ccp) with height across the Impala section. Note that the vertical scale is not linear, the samples are spaced out evenly for clarity. Note that PGE concentrations are highest in BMS from the reef interval, whereas TABS concentrations in BMS from outside the reef, contrary to whole-rock results. Median concentrations and individual analyses of each BMS are reported in *ANNEXE 18 to 20*. Abbreviations: An: anorthosite; Chr: chromitite; Mn: melanorite.

Tellurium, As, Bi and Sb concentrations in BMS show a negative correlation with PGE. The BMS from above the reef are richer in Te, As, Bi and Sb in comparison to BMS from the reef interval (Fig. 6.14). Median concentrations of Te and As range from 10 to 50 ppm and 2 to 30 ppm above the reef interval, respectively, but fall below 1 ppm within the reef. Bismuth median concentrations range from 1 to 3 ppm above the reef, and from 0.01 to 0.3 ppm inside the reef interval. Median concentrations of Sb in BMS are below the detection limit of 0.01 ppm within the reef interval, whereas are scattered above the reef, ranging from 0.01 to 0.1 ppm (Fig. 6.14). The Sn median concentrations in BMS do not follow Te, As and Bi median concentrations. Median concentrations of Sn are in the 0.2 to 6 ppm range inside the reef interval, which is higher than the 0.1 to 0.3 ppm range above the reef (Fig. 6.14).

6.6 – Discussion

Our results show that BMS from PGE-rich samples (i.e. from the reef intervals) have high concentrations of PGE, however, they have low concentrations of TABS. In contrast, BMS from PGE-poor samples (i.e. from outside the reef intervals) have low concentrations of PGE, but the highest concentrations of TABS. Consequently, in samples from outside the reefs the BMS account for greater proportion of whole-rock budget of TABS compared to BMS from the reef intervals. These variations suggest that the presence of high concentrations of PGE in BMS leads to a depletion of TABS in the BMS.

To further assess how the presence of TABS may influence the distribution of PGE, we discuss below the possible scenarios for the collection of PGE. For this purpose, we will first discuss the possible role of TABS for the formation of PGE nanoparticles, and further explore the importance of TABS during the exsolution of PGM. Given the notable association between PGE and TABS, we discuss the importance of the external addition of TABS for the mineralogical sitting of PGE.

6.6.1 - Constrains for the formation of PGE pre-nucleation clusters

Platinum-group elements have very high partition coefficients between sulfide and silicate liquids (Fonseca et al., 2009; Mungall and Brenan, 2014; Liu and Brenan, 2015 and references therein), and are thus thought to be collected by a sulfide liquid to form PGE reefs (Barnes and Ripley, 2016 and references therein). However, some authors have also proposed that the distribution of PGE is more likely to be physically controlled by the surface properties of nanometer-sized particles (Tredoux et al., 1995; Ballhaus et al., 2006; Helmy et al., 2013; Gonzalez-Jimenez et al., 2018, 2019). In this model, PGE form clusters of 50-100 atoms. These clusters are stabilized by the surface adsorption of S, Fe and TABS atoms. The clusters are captured by the sulfide liquid (Fig. 6.15a), and incorporated into the crystallizing MSS, Pn and

ISS, which further exsolve into BMS (Fig. 6.15b and 6.15c) (Wirth et al., 2013; Junge et al., 2015; González-Jiménez et al., 2018, 2019; Liang et al., 2019). Recent studies in material science have shown nano-particles can exist prior to nucleation as pre-nucleation clusters (Chakraborty and Pradeep, 2017 and references therein). Junge et al. (2015) suggest that they could form the nucleation sites for PGM (Fig. 6.15d and 6.15e).

Although PGE and TABS are undersaturated in natural silicate liquids, experimental studies revealed that these elements, especially Pt and As, are able to self-organize into nanoparticles (Helmy et al., 2013; Helmy and Bragagni, 2017). Helmy et al. (2013) found Pt-As clusters in their high-temperature experiments, supporting the formation of PGE nanoclusters. Recent studies have also revealed natural occurrences of nanometer-sized PGE particles, which are mostly platinum arsenides (Kamenetsky et al., 2015; Maier et al., 2015; Arguin et al., 2016; Barnes et al., 2016; González-Jiménez and Reich, 2017; González-Jiménez et al., 2018, 2019). Moreover, Wirth et al. (2013) and Junge et al. (2015) found nanometer-sized PGM inclusions in Pn crystals from the Bushveld Complex. Liang et al. (2019) have also recently found similar particles included in various BMS from the Yangliuping deposit, China. These authors reported that the inclusions are not oriented relative to the crystal lattice, and may possibly represent pre-existing nanometer-sized clusters incorporated during sulfide growth.

However, the model of stabilization of nanocluster by TABS is not consistent with the observation that the whole-rock ratio of TABS/PGE in the reefs is much lower (0.01 to 0.3) than outside of the reefs (0.5 to 10)(Fig. 6.3). If PGE nanoclusters were critical to the formation of reefs, and TABS lead to the formation of nanoclusters, then the TABS/PGE ratio should be similar to that in TABS-PGM, because the nanocluster are pre-nucleation clusters. The low ratio of TABS to PGE in the reefs confirms that TABS-PGM are not the major hosts for the PGE, because most TABS-PGM have TABS to PGE ratios of 0.5 or higher (O'Driscoll and González-Jiménez, 2016 and references therein).

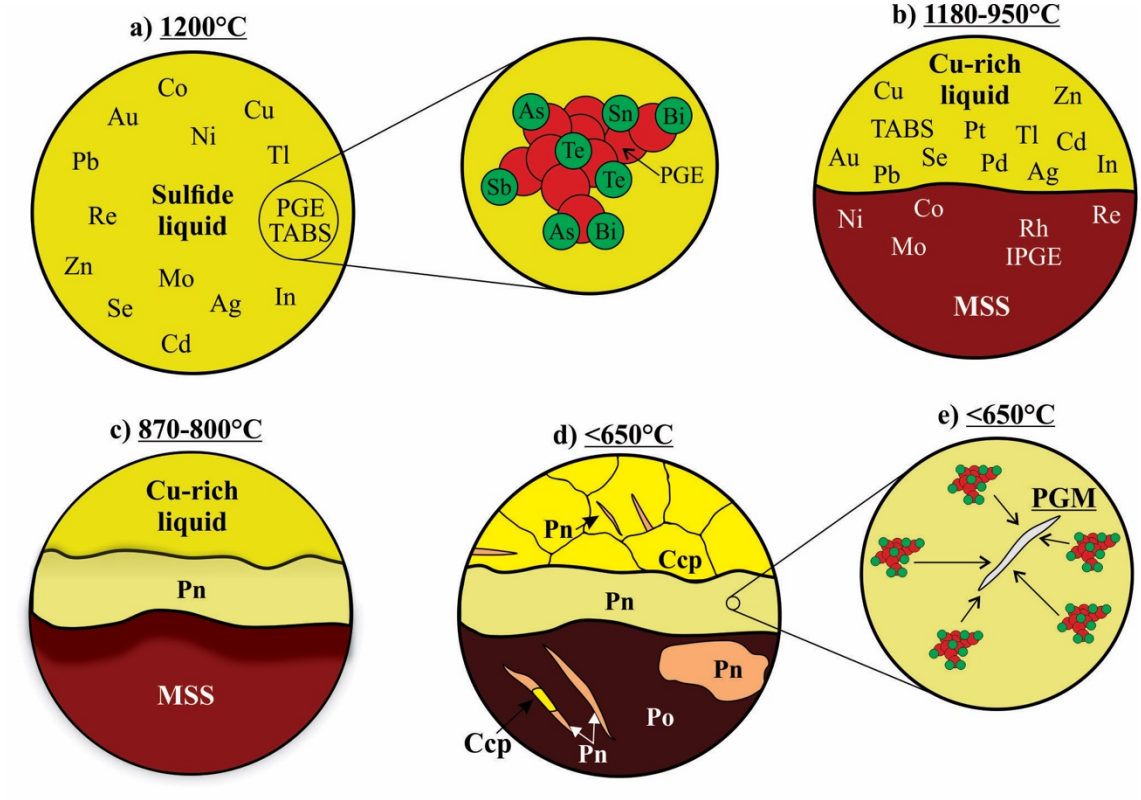

Figure 6.15 - Schematic models illustrating the crystallization history of sulfide liquid in the reef samples, and the potential importance of TABS for stabilizing PGE nanoclusters, and consequently form PGM. See text for further explanation. Abbreviations: MSS: monosulfide solid solution; Po: pyrrhotite; Pn: pentlandite; Ccp: chalcopyrite; IPGE: Ru, Ir and Os; TABS: Te, As, Bi, Sb and Sn; PGE: platinum-group elements; PGM: platinum-group minerals.

Another major limitation to interpret our data using the nanoclusters hypothesis is the lack of experimental work investigating the possible roles of Te, Bi, Sb and Sn in forming PGE clusters, especially Pd clusters. We do acknowledge for the presence of nanometer-sized PGE particles in natural cases (Wirth et al., 2013; Junge et al., 2015; González-Jiménez et al., 2018, 2019; Liang et al., 2019). However, most of the experimental and empirical studies have focused on the association of Pt and As to form nanoclusters (Helmy et al., 2013; Helmy and Bragagni, 2017). In fact, these elements are rarely hosted by BMS (Barnes and Ripley, 2016 and references therein). On the contrary, Pd-Pt bismuth-tellurides are more common in the samples than Pt-arsenides. Therefore, experimental studies demonstrating the formation of TABS and PGE nanoclusters (other than Pt-arsenides), using realistic starting materials, would be required prior to a more convincing evaluation of the model.

6.6.2 – The role of TABS during PGM exsolution

As outlined in the introduction, the disseminated sulfides could represent a sulfide liquid which has undergone equilibrium crystallization (Fig. 6.16a). Elements compatible, or only mildly incompatible with MSS (Ni, Co, Se, Mo, Rh, Ru, Re, Os and Ir; Mungall and Brenan, 2014; Liu and Brenan, 2015), would have partitioned into MSS, and subsequently been distributed between Po and Pn when these minerals exsolved. Platinum-group minerals rich in Rh, Ru, Os and Ir could also have exsolved during cooling. Elements compatible, or only mildly incompatible with ISS (Cu, Zn, Ag, Cd, In, Sn; Liu and Brenan, 2015), partitioned into ISS and subsequently into Ccp when it exsolved during cooling.

Palladium, Pt and TABS are incompatible with both MSS and ISS (Fig. 6.16b; Li et al., 1996; Barnes et al., 1997; Mungall et al., 2005; Helmy et al., 2010; Liu and Brenan, 2015). Therefore, very little Pt, Pd and TABS should be present in the BMS lattice, and thus Pt-Pd-TABS PGM formed by exsolutions would be expected to be very rare. Most of the Pt-Pd PGM would be expected to crystallize from the fractionated liquid, and be found among the BMS, rather than included in them. Indeed, most the Pt-Pd PGM both in the Merensky and J-M reefs are found at the margins of the BMS grains, and the majority are found in contact with Ccp as this model would predict (Fig. 6.2; Prichard et al., 2004; Godel et al., 2007; Godel and Barnes, 2008b).

However, there are some Pt-Pd PGM included in BMS, and Pn contains the bulk of the Pd in the reefs (Fig. 6.10 and 6.11). These two observations can be reconciled with the model as follows. Although these elements are incompatible with both MSS and ISS, their partition coefficients are not 0 (Liu and Brenan, 2015), and thus a small fraction of these elements are included in the ISS and MSS. On cooling, and during S-loss, Pd, Pt and TABS could exsolve from the ISS and MSS. Furthermore, Pn can form by peritectic reaction between the MSS and the sulfide liquid, around 870ºC (Fig. 6.16c; Mungall, 2007; Kosyakov and Sinyakova, 2012; Kitakaze et al., 2016). Mansur et al. (2019a) investigated the distribution of chalcophile elements

in Pn found between Po and Ccp, and argued that this Pn formed by peritectic reaction. Palladium, Te and Bi were incorporated into the peritectic Pn from the fractionated sulfide liquid. This provides another mechanism for the incorporation of incompatible metals into Pn.

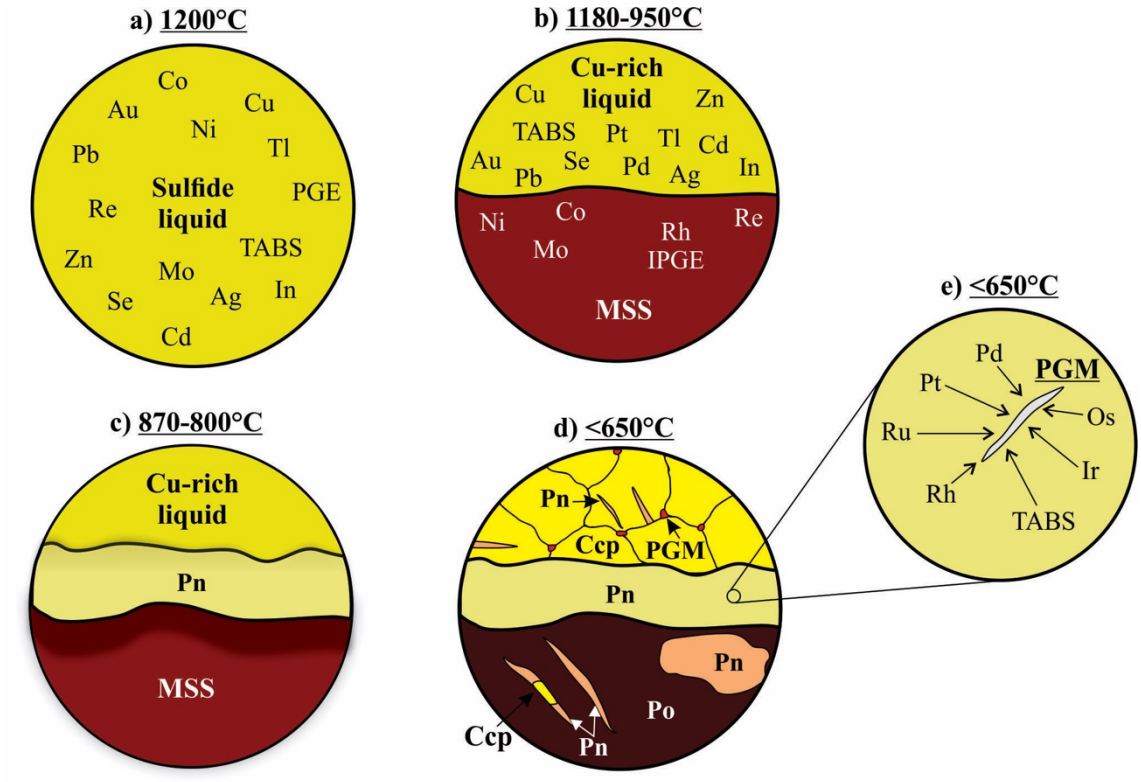

Figure 6.16 - Schematic models illustrating the crystallization history of sulfide liquid in the reef samples, and the formation of PGM by exsolution from the BMS upon cooling. See text for further explanation. Abbreviations: MSS: monosulfide solid solution; Po: pyrrhotite; Pn: pentlandite; Ccp: chalcopyrite; IPGE: Ru, Ir and Os; TABS: Te, As, Bi, Sb and Sn; PGE: platinum-group elements; PGM: platinum-group minerals.

In order to explain the difference in the TABS concentrations in BMS in rocks from the reefs and those outside the reefs we propose the following model. Upon cooling, the BMS in the reefs were not able to accommodate all of the PGE in their structure, resulting in the exsolution of TABS-PGM, and sulfide PGM (Fig. 6.16d and 6.16e). Given the excess of PGE relative to TABS in the reef BMS, most of the TABS were accommodated in PGM. In contrast, for samples outside the reefs, the lower proportion of PGE to TABS allows more TABS to remain in the BMS lattice.

Junge et al. (2015) suggested that the initial concentration of TABS in BMS may control the extent of PGM exsolution. In their transmission electron microscopy (TEM) studies of samples from the UG-2 chromitite, Merensky Reef and Platreef, Wirth et al. (2013) and Junge et al. (2015) investigated the mineralogical sitting of PGE. The authors found that PGE occur in solid solution in BMS (especially Pn), and also as aligned PGM lamellae within BMS structure, which they interpreted as exsolution lamellae. Junge et al. (2015) suggested that the absence of possible reaction partners necessary to form PGM (TABS) forced some PGE to remain in the BMS lattice. Our results support the observation that the PGM enclosed in sulfides combined with TABS and exsolved as PGM upon cooling. However, the fraction of PGE retained in BMS is similar in the BMS with low TABS concentrations, and those with high TABS concentrations (Fig. 6.10 and 6.11). Therefore, we do not think that the TABS concentrations in the BMS limit the PGM exsolution process. The PGE can exsolve not only as TABS PGM, but also as PGM sulfides, and PGM alloys.

6.6.3 - External addition of TABS and the implications for the PGM formation

A summary of the PGM assemblage from mines along the entire Merensky Reef shows that TABS-PGM make up 7 to 70% by volume of the PGM depending on the locality (Kinloch, 1982; McLaren and de Villiers, 1982), with the proportion of arsenides to tellurides varying from 0.4 to 22. The variability in PGM assemblage, combined with the observation that the concentrations of PGE along the reef from mine to mine do not vary greatly, led Cawthorn et al. (2002) to conclude that PGM assemblage is formed by secondary processes, and that they are not implicated in the initial collection of the PGE. In our sample set, both from the Merensky and J-M reefs, much of the PGE budget (except for Pt) is found in the BMS. The balance is found in PGM, some of which we postulate to have formed by exsolutions, and some of which appear to have crystallized among the PGM grains from fractionate sulfide liquid.

Although the TABS may not be essential to forming a reef, their concentrations in the reef, and elsewhere, provide important petrogenetic information. In order to bring about sulfide saturation, and collect the PGE, most primary magmas need to be contaminated with S-bearing rocks (Li and Ripley, 2005; Ripley and Li, 2013). The primary magma would contain only a few ppb of TABS, however, S-rich crustal rocks contain ppm levels of TABS (Barnes, 2016). Therefore, along with the S the crustal rocks would also add TABS (Samalens et al., 2017), which would then be collected by the sulfide liquid along with PGE, and eventually combine with PGE to form PGM.

Duran et al. (2017) showed the concentrations of TABS in the sulfide liquid formed from a primary magma would be much lower than the concentrations of TABS observed in the Ni-Cu-PGE ores from the Noril'sk-Talnakh district. Their modeling suggests an enrichment factor of 2 to 200, relative to a sulfide formed from an uncontaminated magma. Duran et al. (2017) also argued that the abundance of Sn-bearing PGM in massive sulfides of the Noril'sk-Talnakh mining district reflects the assimilation of granitic rocks by the mafic magmas. Therefore, if crustal contamination increases the concentration of TABS into the mafic magma, it could also affect the PGM assemblage and sitting of PGE.

Different assemblages of PGM have been interpreted to reflect contamination of the magma by different rock types. In the case of the Main Sulfide Zone of the Great Dyke, Oberthür (2011) found different PGM assemblages in the North and South Chambers. In the North chamber, PGM are predominantly bismuth-tellurides, whereas in the South Chamber these are predominantly arsenides and sulfarsenides. At Sudbury, the PGM assemblage in the North and South range deposits are different, with the North range containing more Sn-bearing PGE and the South range more As-bearing PGM (Ames and Farrow, 2007). This difference is attributed to the difference in the host rock with the North range being in contact with Archean gneiss and granites, and the South range being in contact with Proterozoic volcano-sedimentary rocks (Ames and Farrow, 2007).

The addition of TABS during crustal contamination may also influence the timing of PGM formation. Dare et al. (2010a) argued that the higher activity of As in the Creighton Deposit of the Sudbury South Range led to the early crystallization of As-bearing PGM at high temperature (i.e., up to 1200ºC). In the case of the Platreef of the Bushveld Complex, Hutchinson et al. (2015) also suggest that the external addition of TABS led to the early crystallization of PGM, and thus a lower proportion of PGE is hosted by the BMS. Thus, TABS concentrations can be used both to deducing what type of crustal contamination has occurred, and the timing of PGM formation.

6.7 – Conclusions

This contribution provides insights into the possible roles of Te, As, Bi, Sb and Sn (TABS) during the formation of PGE deposits. Our main findings are:

1. - The ratio of TABS to PGE in reef rocks (0.01 to 0.3) is too low for the TABS to have acted as stabilizers of pre-nucleation clusters (nanoclusters), and thus TABS nanoclusters are not essential to form reefs.

2 – Whole-rock analyses reveal that the concentrations of TABS (except As) correlate positively with S and PGE. This suggests that all the elements were initially collected by an immiscible sulfide liquid. The distributions of As, and to a lesser extent Sb, are also controlled by the melt fraction in the cumulate rocks, and this is also recorded by the presence and composition of K-phlogopite in the case of the Merensky Reef.

3- During crystallization of the sulfide liquid a small portion of the TABS, Pd and Pt partitioned into the MSS and ISS, but the bulk remained in the fractionated sulfide liquid. At below 870ºC there was a peritectic reaction between the fractionated liquid and MSS, which formed Pn, and

much of the Pd and some TABS partitioned into the Pn. The remainder of the TABS, Pd and Pt crystallized as PGM between the BMS grains.

4 –The whole-rock concentrations of PGE and TABS are highest in the reefs, and the PGE content of the BMS are highest in the reefs, but the TABS contents of the BMS from the reefs are lower than TABS contents of BMS from outside the reefs. This is thought to be a consequence of the PGE/TABS ratios of the whole rock. In the reefs, the PGE far exceed the TABS, thus during exsolutions of PGM all of the TABS can be accommodated by the PGM, and very little remains in the BMS. In contrast, in the rocks from outside of the reefs the TABS exceed the PGE. Thus, not all of the TABS can be accommodated in PGM and some remain in the BMS.

5 – Understanding the processes that potentially upgrade the concentrations of TABS during the formation of magmatic sulfide deposits is essential for understanding the distribution of PGE. Among the potential processes, the crustal contamination has been shown to significantly increase concentrations of TABS in mafic magmas. We suggest that the external addition of TABS needs to be closely considered whenever investigating the mineralogical sitting of PGE.

6.8 – Acknowledgements

This work was supported by a Canada Research Chair program grant to Sarah-Jane Barnes (215503). We would like to thank Dany Savard and Audrey Lavoie (LabMaTer, UQAC) for their assistance with LA-ICP-MS analyses. This manuscript benefited from insightful comments from Steve Barnes, Rubén Piña, and one anonymous reviewer, and careful editorial handling by the associate editor Edward Ripley.

6.9 - References

Ames D.E. and Farrow C.E.G. (2007) Metallogeny of the Sudbury mining camp, Ontario. In *Mineral deposits of Canada: a synthesis of major deposit-types, district metallogeny, the evolution of geological provinces, and exploration methods* (ed. W.D. Goodfellow). Geological Association of Canada, Special Publication no. 5. Mineral Deposits Division, Geological Association of Canada, St. John's, pp. 329-350.

Arguin, J.P., Pagé P., Barnes S-J., Yu S.Y. and Song X.Y. (2016) The effect of chromite crystallization on the distribution of osmium, iridium, ruthenium and rhodium in picritic magmas: an example from the Emeishan Large Igneous Province, Southwestern China. *J. Petrol.* **57(5)**, 1019-1048.

Ballhaus C., Ryan C.G., Mernagh T.P. and Green D.H. (1994) The partitioning of Fe, Ni, Cu, Pt, and Au between sulfide, metal, and fluid phases: A pilot study. *Geochim. Cosmochim. Acta* **58(2)**, 811-826.

Ballhaus C., Bockrath C., Wohlgemuth-Ueberwasser C., Laurenz V. and Berndt J. (2006) Fractionation of the noble metals by physical processes. *Contrib. Mineral. Petrol.* **152(6)**, 667-684.

Barnes S-J. (2016) Chalcophile Elements. In *Encyclopedia of Geochemistry: A Comprehensive Reference Source on the Chemistry of the Earth* (ed. W.M. White), pp. 1-5.

Barnes S.J. and Naldrett A.J. (1985) Geochemistry of the JM (Howland) Reef of the Stillwater Complex, Minneapolis Adit area; I, Sulfide chemistry and sulfide-olivine equilibrium. *Econ. Geol.* **80(3)**, 627-645.

Barnes S.J., Fisher L.A., Godel B., Pearce M.A., Maier W.D., Paterson D., Howard D.L., Ryan C.G. and Laird J.S. (2016) Primary cumulus platinum minerals in the Monts de Cristal Complex, Gabon: magmatic microenvironments inferred from high-definition X-ray fluorescence microscopy. *Contrib. Mineral. Petrol.* **171(3)**, 23.

Barnes S-J. and Maier W.D. (2002) Platinum-group elements and microstructures of Normal Merensky Reef from Impala Platinum Mines, Bushveld Complex. *J. Petrol.* **43(1),** 103-128.

Barnes S-J., Makovicky E., Makovicky M., Rose-Hansen J. and Karup-Moller S. (1997) Partition coefficients for Ni, Cu, Pd, Pt, Rh, and Ir between monosulfide solid solution and sulfide liquid and the formation of compositionally zoned Ni–Cu sulfide bodies by fractional crystallization of sulfide liquid. *Can. J. Earth Sci.* **34**, 366-374.

Barnes S-J. and Ripley E.M. (2016) Highly siderophile and strongly chalcophile elements in magmatic ore deposits. *Rev. Mineral. Geochem.* **81**, 725-774.

Barnes S-J., Pagé P. and Zientek M. (2020) The Lower Banded series of the Stillwater Complex, Montana: whole-rock lithophile, chalcophile, and platinum-group element distributions. *Miner. Deposita* **55**, 163-186.

Boudreau A. E. (2016) The Stillwater Complex, Montana–Overview and the significance of volatiles. *Mineral. Mag.* **80(4)**, 585-637.

Brenan J.M. (2015) Se–Te fractionation by sulfide–silicate melt partitioning: Implications for the composition of mantle-derived magmas and their melting residues. *Earth Planet. Sci. Lett.* **422**, 45-57.

Cafagna F. and Jugo P.J. (2016) An experimental study on the geochemical behavior of highly siderophile elements (HSE) and metalloids (As, Se, Sb, Te, Bi) in a mss-iss-pyrite system at 650° C: a possible magmatic origin for Co-HSE-bearing pyrite and the role of metalloid-rich phases in the fractionation of HSE. *Geochim. Cosmochim. Acta* **178**, 233-258.

Campbell I.H., Naldrett A.J. and Barnes S.J. (1983) A model for the origin of the platinum-rich sulfide horizons in the Bushveld and Stillwater Complexes. *J. Petrol*. **24**, 133-65.

Canali A.C., Brenan J.M. and Sullivan N.A. (2017) Solubility of platinum-arsenide melt and sperrylite in synthetic basalt at 0.1 MPa and 1200° C with implications for arsenic

speciation and platinum sequestration in mafic igneous systems. *Geochim. Cosmochim. Acta* **216**, 153-168.

Cawthorn R.G. (2002) Platinum-Group Element deposits of the Bushveld Complex in South Africa. In *Geology, Geochemistry, Mineralogy and Mineral Benefication of Platinum Group Element* (ed. L.J. Cabri). Canadian Institute of Mining, Metallurgy and Petroleum, Special volume 54, pp. 389-429.

Cawthorn R.G. and Boerst K. (2006) Origin of the pegmatitic pyroxenite in the Merensky unit, Bushveld Complex, South Africa. *J. Petrol.* **47(8)**, 1509-1530.

Chakraborty I. and Pradeep T. (2017) Atomically precise clusters of noble metals: emerging link between atoms and nanoparticles. *Chem. Rev.* **117(12),** 8208-8271.

Chen L.M., Song X.Y., Keays R.R., Tian Y.L., Wang Y.S., Deng Y.F. and Xiao J.F. (2013) Segregation and fractionation of magmatic Ni-Cu-PGE sulfides in the western Jinchuan intrusion, northwestern China: Insights from platinum group element geochemistry. *Econ. Geol.* **108(8),** 1793-1811.

Chen L.M., Song X.Y., Danyushevsky L.V., Wang Y.S., Tian Y.L. and Xiao J.F. (2015) A laser ablation ICP-MS study of platinum-group and chalcophile elements in base metal sulfide minerals of the Jinchuan Ni–Cu sulfide deposit, NW China. *Ore Geol. Rev.* **65**, 955-967.

Dare S.A.S., Barnes S-J., Prichard H.M. and Fisher P.C. (2010a) The timing and formation of platinum-group minerals from the Creighton Ni-Cu-platinum-group element sulfide deposit, Sudbury, Canada: Early crystallization of PGE-rich sulfarsenides. *Econ. Geol.* **105**, 1071-1096.

Dare S.A.S., Barnes S-J. and Prichard H.M. (2010b) The distribution of platinum group elements (PGE) and other chalcophile elements among sulfides from the Creighton Ni–Cu–PGE sulfide deposit, Sudbury, Canada, and the origin of palladium in pentlandite. *Miner. Deposita* **45**, 765-793.

Dare S.A.S., Barnes S-J., Prichard H.M. and Fisher P.C. (2014) Mineralogy and geochemistry of Cu-rich ores from the McCreedy East Ni-Cu-PGE deposit (Sudbury, Canada): Implications for the behavior of platinum group and chalcophile elements at the end of crystallization of a sulfide liquid. *Econ. Geol.* **109**, 343-366.

Djon M.L.N. and Barnes S-J. (2012) Changes in sulfides and platinum-group minerals with the degree of alteration in the Roby, Twilight, and High Grade Zones of the Lac des Iles Complex, Ontario, Canada. *Miner. Deposita* **47**, 875-896.

D'Souza R.J. and Canil D. (2018) The partitioning of chalcophile elements between sediment melts and fluids at 3 GPa, 950–1050° C with implications for slab fluids in subduction zones. *Earth Planet. Sci. Lett.* **498**, 215-225.

Dunn T. and Sen C. (1994) Mineral/matrix partition coefficients for orthopyroxene, plagioclase, and olivine in basaltic to andesitic systems: a combined analytical and experimental study. *Geochim. Cosmochim. Acta* **58(2),** 717-733.

Duran C.J., Barnes S-J. and Corkery J.T. (2016) Trace element distribution in primary sulfides and Fe–Ti oxides from the sulfide-rich pods of the Lac des Iles Pd deposits, Western Ontario, Canada: Constraints on processes controlling the composition of the ore and the use of pentlandite compositions in exploration. *J. Geochem. Explor.* **166**, 45-63.

Duran C.J., Barnes S-J., Pleše P., Prašek M.K., Zientek M.L. and Pagé P. (2017) Fractional crystallization-induced variations in sulfides from the Noril'sk-Talnakh mining district (polar Siberia, Russia). *Ore Geol. Rev.* **90**, 326-351.

Eales H.V. and Cawthorn R.G. (1996) The Bushveld Complex. In *Layered Intrusions* (ed. Cawthorn, R.G.). Elsevier, Amsterdam, pp. 181-230.

Fonseca R.O., Campbell I.H., O'Neill H.S.C. and Allen C.M. (2009) Solubility of Pt in sulphide mattes: Implications for the genesis of PGE-rich horizons in layered intrusions. *Geochim. Cosmochim. Acta* **73(19)**, 5764-5777.

Godel B. and Barnes S-J. (2008a) Platinum-group elements in sulfide minerals and the whole rocks of the JM Reef (Stillwater Complex): Implication for the formation of the reef. *Chem. Geol.* **248**, 272-294.

Godel B. and Barnes S.-J. (2008b) Image analysis and composition of platinum-group minerals in the JM Reef, Stillwater Complex. *Econ. Geol.* **103(3)**, 637-651.

Godel B., Barnes S-J. and Maier, W.D. (2006) 3-D distribution of sulphide minerals in the Merensky Reef (Bushveld Complex, South Africa) and the J-M Reef (Stillwater Complex, USA) and their relationship to microstructures using X-ray computed tomography. *J. Petrol.* **47**, 1853-1872.

Godel B., Barnes S-J. and Maier W.D. (2007) Platinum-group elements in sulphide minerals, platinum-group minerals, and whole-rocks of the Merensky Reef (Bushveld Complex, South Africa): Implications for the formation of the reef. *J. Petrol*. **48**, 1569-1604.

Godel B., Barnes S.J., Barnes S.J. and Maier W.D. (2010) Platinum ore in three dimensions: Insights from high-resolution X-ray computed tomography. *Geology* **38(12)**, 1127-1130.

Godel B., Barnes S-J. and Maier W. D. (2011) Parental magma composition inferred from trace element in cumulus and intercumulus silicate minerals: An example from the Lower and Lower Critical Zones of the Bushveld Complex, South-Africa. *Lithos* **125(1-2)**, 537-552.

González-Jiménez J.M. and Reich M. (2017) An overview of the platinum-group element nanoparticles in mantle-hosted chromite deposits. *Ore Geol. Rev.* **81**, 1236-1248.

González-Jiménez J.M., Deditius A., Gervilla F., Reich M., Suvorova A., Roberts M.P. and Proenza, J.A. (2018) Nanoscale partitioning of Ru, Ir, and Pt in base-metal sulfides from the Caridad chromite deposit, Cuba. *Am. Miner.* **103(8)**, 1208-1220.

González-Jiménez J.M., Roqué-Rosell J., Jiménez-Franco A., Tassara S., Nieto F., Gervilla F. and Schilling M. (2019) Magmatic platinum nanoparticles in metasomatic silicate glasses and sulfides from Patagonian mantle xenoliths. *Contrib. Mineral. Petrol.* **174(5)**, 47.

Harvey J. and Day J.M. (2016) Highly Siderophile and Strongly Chalcophile Elements in High-Temperature Geochemistry and Cosmochemistry. *Rev. Mineral. Geochem.* **81**, 774p.

Hattori K.H., Arai S. and Clarke D.B. (2002) Selenium, tellurium, arsenic and antimony contents of primary mantle sulfides. *Can. Mineral.* **40(2)**, 637-650.

Helmy H.M., Ballhaus C., Berndt J., Bockrath C. and Wohlgemuth-Ueberwasser C. (2007) Formation of Pt, Pd and Ni tellurides: experiments in sulfide–telluride systems. *Contrib. Mineral. Petrol.* **153(5),** 577-591.

Helmy H.M., Ballhaus C., Wohlgemuth-Ueberwasser C., Fonseca R.O. and Laurenz V. (2010) Partitioning of Se, As, Sb, Te and Bi between monosulfide solid solution and sulfide melt–application to magmatic sulfide deposits. *Geochim. Cosmochim. Acta* **74**, 6174-6179.

Helmy H.M., Ballhaus C. and Wirth R. (2013) Noble metal nanoclusters and nanoparticles precede mineral formation in magmatic sulphide melts. Nat. Commun. **4**, 2045.

Helmy H.M. and Bragagni A. (2017) Platinum-group elements fractionation by selective complexing, the Os, Ir, Ru, Rh-arsenide-sulfide systems above 1020° C. *Geochim. Cosmochim. Acta* **216**, 169-183.

Holwell D.A. and McDonald I. (2007) Distribution of platinum-group elements in the Platreef at Overysel, northern Bushveld Complex: A combined PGM and LA-ICP-MS study. *Contrib. Mineral. Petrol.* **154**, 171-190.

Holwell B. D. and McDonald I. (2010) A review of the behaviour of platinum group elements within natural magmatic sulfide ore systems. *Platinum Met. Rev.* **54(1)**, 26-36.

Hutchinson D., Foster J., Pritchard H. and Gilbert S. (2015) Concentration of particulate platinum-group minerals during magma emplacement; a case study from theMerensky Reef, Bushveld Complex. *J. Petrol.* **56**, 113-159.

Irvine T.N., Keith D.W. and Todd S.G. (1983) The J-M platinum-palladium reef of the Stillwater Complex, Montana: II. Origin by double diffusive convective magma mixing and implications for the Bushveld Complex. *Econ. Geol.* **78**, 1287-334.

Jochum K.P., Nohl U., Herwig K., Lammel E., Stoll B. and Hofmann A.W. (2005) GeoReM: a new geochemical database for reference materials and isotopic standards. *Geostand. Geoanal. Res.* **29**, 333-338.

Junge M., Wirth R., Oberthür T., Melcher F. and Schreiber A. (2015) Mineralogical siting of platinum-group elements in pentlandite from the Bushveld Complex, South Africa. *Miner. Deposita* **50**, 41-54.

Kamenetsky V.S., Park J.W., Mungall J.E., Pushkarev E.V., Ivanov A.V., Kamenetsky M.B. and Yaxley G.M. (2015) Crystallization of platinum-group minerals from silicate melts: Evidence from Cr-spinel–hosted inclusions in volcanic rocks. *Geology* **43(10)**, 903-906.

Keays R.R., Lightfoot P.C. and Hamlyn P.R. (2012) Sulfide saturation history of the Stillwater Complex, Montana: chemostratigraphic variation in platinum group elements. *Miner. Deposita* **47(1-2)**, 151-173.

Kinloch E.D. (1982) Regional trends in the platinum-group mineralogy of the critical zone of the Bushveld Complex, South Africa. *Econ. Geol.* **77(6)**, 1328-1347.

Kitakaze A., Machida T. and Komatsu R. (2016) Phase relations in the Fe-Ni-S system from 875 to 650 °C. *Can. Mineral.* **54**, 1175-1186.

König S., Luguet A., Lorand J-P., Wombacher F. and Lissner M. (2012) Selenium and tellurium systematics of the Earth's mantle from high precision analyses of ultra-depleted orogenic peridotites. *Geochim. Cosmochim. Acta* **86**, 354-366.

König S., Lorand J-P., Luguet A. and Pearson D.G. (2014) A non-primitive origin of near-chondritic S–Se–Te ratios in mantle peridotites: implications for the Earth's late accretionary history. *Earth Planet. Sci. Lett.* **385**, 110-121.

Kosyakov V.I. and Sinyakova E.F. (2012) Physicochemical prerequisites for the formation of primary orebody zoning at copper-nickel sulfide deposits (by the example of the systems Fe-Ni-S and Cu-Fe-S). *Russ. Geol. Geophys.* **53**, 861-882.

Li Y. and Audétat A. (2015) Effects of temperature, silicate melt composition, and oxygen fugacity on the partitioning of V, Mn, Co, Ni, Cu, Zn, As, Mo, Ag, Sn, Sb, W, Au, Pb, and Bi between sulfide phases and silicate melt. *Geochim. Cosmochim. Acta* **162**, 25-45.

Li C. and Ripley E.M. (2005) Empirical equations to predict the sulfur content of mafic magmas at sulfide saturation and applications to magmatic sulfide deposits. *Miner. Deposita* **40(2)**, 218-230.

Li C. and Ripley E.M. (2006) Formation of Pt–Fe alloy by desulfurization of Pt–Pd sulfide in the J–M reef of the Stillwater complex, Montana. *Can. Mineral.* **44(4),** 895-903.

Li C., Barnes S-J., Makovicky E., Rose-Hansen J. and Makovicky M. (1996) Partitioning of Ni, Cu, Ir, Rh, Pt and Pd between monosulfide solid solution and sulfide liquid: Effects of composition and temperature. *Geochim. Cosmochim. Acta* **60**, 1231-1238.

Li C., Ripley E.M., Sarkar A., Shin D. and Maier W.D. (2005) Origin of phlogopite-orthopyroxene inclusions in chromites from the Merensky Reef of the Bushveld Complex, South Africa. *Contrib. Mineral. Petrol.* **150(1)**, 119-130.

Liang Q.L., Song X.Y., Wirth R., Chen L.M. and Dai Z.H. (2019) Implications of nano-and micrometer-size platinum-group element minerals in base metal sulfides of the Yangliuping Ni-Cu-PGE sulfide deposit, SW China. *Chem. Geol.* **517**, 7-21.

Lissner M., König S., Luguet A., Le Roux P., Schuth S., Heuser A. and le Roex A.P. (2014) Selenium and tellurium systematics in MORBs from the southern Mid-Atlantic Ridge (47–50 S). *Geochim. Cosmochim. Acta* **144**, 379-402.

Liu Y. and Brenan J. (2015) Partitioning of platinum-group elements (PGE) and chalcogens (Se, Te, As, Sb, Bi) between monosulfide-solid solution (MSS), intermediate solid solution (ISS) and sulfide liquid at controlled fO2–fS2 conditions. *Geochim. Cosmochim. Acta* **159**, 139-161.

Lodders K. (2003) Solar system abundances and condensation temperatures of the elements. *Astrohphys. J.* **591**, 1220-1247.

Lorand J-P. and Alard O. (2010) Determination of selenium and tellurium concentrations in Pyrenean peridotites (Ariege, France): new insight into S/Se/Te systematics of the upper in mantle samples. *Chem. Geol.* **278(1-2)**, 120-130.

Maier W.D., Barnes S-J. and Groves D.I. (2013) The Bushveld Complex, South Africa: formation of platinum–palladium, chrome-and vanadium-rich layers via hydrodynamic sorting of a mobilized cumulate slurry in a large, relatively slowly cooling, subsiding magma chamber. *Miner. Deposita* **48(1)**, 1-56.

Maier W.D., Rasmussen B., Fletcher I., Godel B., Barnes S.J., Fisher L., Yang S., Huhma H. and Lahaye Y. (2015) Petrogenesis of the ~2.77 Ga Monts de Cristal Complex, Gabon: evidence for direct precipitation of Pt- arsenides from basaltic magma. *J. Petrol.* **56**, 1285-308.

Makovicky M., Makovicky E. and Rose-Hansen J. (1986)Experimental studies on the solubility and distribution ofplatinum group elements in base metal sulfides in platinumdeposits. In *Metallogeny of Basic and Ultrabasic Rocks* (ed. Gallagher M.J., Ixer R.A., Neary C.R. and Prichard H.M.). Institution of Mining and Metallurgy, pp. 415–425.

Makovicky E. (2002) Ternary and quaternary phase systems in PGE. In *Geology, Geochemistry, Mineralogy and Mineral Benefication of Platinum Group Element* (ed. L.J. Cabri). Canadian Institute of Mining, Metallurgy and Petroleum, Special volume 54, pp. 131-175.

Mansur E.T., Barnes S-J. and Duran C.J. (2019a) Textural and compositional evidence for the formation of pentlandite via peritectic reaction: Implications for the distribution of highly siderophile elements. *Geology* **47(4),** 351-354.

Mansur E.T., Barnes S-J., Savard D. and Webb P.C. (2019b) Determination of Te, As, Bi, Sb and Se (TABS) in Geological Reference Materials and GeoPT Proficiency Test Materials by Hydride Generation-Atomic Fluorescence Spectrometry (HG-AFS). *Geostand. Geoanal. Res*. doi.org/10.1111/ggr.12289

Mansur E.T., Barnes S.J., Duran C.J. and Sluzhenikin S.F. (2019c) Distribution of chalcophile and platinum-group elements among pyrrhotite, pentlandite, chalcopyrite and cubanite

from the Noril'sk-Talnakh ores: Implications for the formation of platinum-group minerals. *Miner. Deposita* 1-18.

Mc Callum I.S., Raedeke L.D. and Mathez E.A. (1980) Investigations of the Stillwater Complex: part I. Stratigraphy and structure of the banded zone. *Am. J. Sci.* **280**, 59-87.

McLaren C.H. and De Villiers J.P. (1982) The platinum-group chemistry and mineralogy of the UG-2 chromitite layer of the Bushveld Complex. *Econ. Geol.* **77(6)**, 1348-1366.

Mungall J.E. (2007) Crystallization of magmatic sulfides: An empirical model and application to Sudbury ores. *Geochim. Cosmochim. Acta* **71(11)**, 2809-2819.

Mungall J.E. and Brenan J.M. (2014) Partitioning of platinum-group elements and Au between sulfide liquid and basalt and the origins of mantle-crust fractionation of the chalcophile elements. *Geochim. Cosmichim. Acta* **125**, 265-89.

Mungall J.E., Andrews D.R., Cabri L.J., Sylvester P.J. and Tubrett M. (2005) Partitioning of Cu, Ni, Au, and platinum-group elements between monosulfide solid solution and sulfide melt under controlled oxygen and sulfur fugacities. *Geochim. Cosmochim. Acta* **69**, 4349-4360.

Naldrett A.J., Wilson A., Kinnaird J. and Chunnett G. (2009) PGE tenor and metal ratios within and below the Merensky Reef, Bushveld Complex: implications for its genesis. *J. Petrol*. **50(4)**, 625-659.

O'Driscoll B. and González-Jiménez J.M. (2016) Petrogenesis of the platinum-group minerals. *Rev. Mineral. Geochem.* **81**, 489-578.

Oberthür T. (2011) Platinum-group element mineralization of the Main Sulfide Zone, Great Dyke, Zimbabwe. *Rev. Econ. Geol.* **17**, 329-349.

Osbahr I., Klemd R., Oberthür T., Brätz H. and Schouwstra R. (2013) Platinum-group element distribution in base-metal sulfides of the Merensky Reef from the eastern and western Bushveld Complex, South Africa. *Miner. Deposita* **48(2)**, 211-232.

Osbahr I., Oberthür T., Klemd R. and Josties A. (2014) Platinum-group element distribution in base-metal sulfides of the UG2 chromitite, Bushveld Complex, South Africa - a reconnaissance study. *Miner. Deposita* **49(6)**, 655-665.

Pagé P. and Barnes S-J. (2009) Using trace elements in chromites to constrain the origin of podiform chromitites in the Thetford Mines ophiolite, Québec, Canada. *Econ. Geol.* **104(7),** 997-1018.

Patten C., Barnes S-J., Mathez E.A. and Jenner F.E. (2013) Partition coefficients of chalcophile elements between sulfide and silicate melts and the early crystallization history of sulfide liquid: LA-ICP-MS analysis of MORB sulfide droplets. *Chem. Geol.* **358**, 170-188.

Patten C.G., Pitcairn I.K., Teagle D.A. and Harris M. (2016) Mobility of Au and related elements during the hydrothermal alteration of the oceanic crust: implications for the sources of metals in VMS deposits. *Miner. Deposita* **51**, 179-200.

Patten C.G., Pitcairn I.K. and Teagle D.A.H. (2017) Hydrothermal mobilisation of Au and other metals in supra-subduction oceanic crust: Insights from the Troodos ophiolite. *Ore Geol. Rev.* **86**, 487-508.

Paton C., Hellstrom J., Paul B., Woodhead J. and Hergt J. (2011) Iolite: Freeware for the visualisation and processing of mass spectrometric data. *J. Anal. Atom. Spec.* **26**, 2508-2518.

Peregoedova A., Barnes S.J. and Baker D.R. (2004) The formation of Pt–Ir alloys and Cu–Pd-rich sulfide melts by partial desulfurization of Fe–Ni–Cu sulfides: results of experiments and implications for natural systems. *Chem. Geol.* **208(1-4),** 247-264.

Piña R., Gervilla F., Barnes S-J., Ortega L. and Lunar R. (2012) Distribution of platinum-group and chalcophile elements in the aguablanca Ni-Cu sulfide deposit (SW spain): Evidence from a LA-ICP-MS study. *Chem. Geol.* **302**, 61-75.

Piña R., Gervilla F., Barnes S-J., Ortega L. and Lunar R. (2015) Liquid immiscibility between arsenide and sulfide melts: Evidence from a LA-ICP-MS study in magmatic deposits at Serranía de Ronda (Spain). *Miner. Deposita* **50**, 265-279.

Prichard H., Hutchinson D. and Fisher P. (2004) Petrology and crystallization history of multiphase sulfide droplets in a mafic dike from Uruguay: Implications for the origin of Cu-Ni-PGE sulfide deposits. *Econ. Geol.* **99**, 365-376.

Ripley E.M. and Li C. (2013) Sulfide saturation in mafic magmas: Is external sulfur required for magmatic Ni-Cu-(PGE) ore genesis?. *Econ. Geol.* **108(1),** 45-58.

Samalens N., Barnes S-J. and Sawyer E.W. (2017) The role of black shales as a source of sulfur and semimetals in magmatic nickel-copper deposits: Example from the Partridge River Intrusion, Duluth Complex, Minnesota, USA. *Ore Geol. Rev.* **81(1)**, 173-187.

Scholten L., Watenphul A., Beermann O., Testemale D., Ames D. and Schmidt C. (2018) Nickel and platinum in high-temperature H2O+ HCl fluids: Implications for hydrothermal mobilization. *Geochim. Cosmochim. Acta* **224**, 187-199.

Sullivan N.A., Zajacz Z. and Brenan J.M. (2018) The solubility of Pd and Au in hydrous intermediate silicate melts: the effect of oxygen fugacity and the addition of Cl and S. *Geochim. Cosmochim. Acta* **231**, 15-29.

Tredoux M., Lindsay N.M., Davies G. and McDonald I. (1995) The fractionation of platinum-group elements in magmatic systems, with the suggestion of a novel causal mechanism. *S. Afr. J. Geol.* **98**, 157-167.

Von Gruenewaldt G. (1986) Platinum-group element chromitite associations in the Bushveld Complex. *Econ. Geol.* **81**, 1067-1079.

Von Gruenewaldt G. (1989) Contrasting platinum-group element concentration patterns in cumulates of the Bushveld Complex. *Miner. Deposita*. **24(3**), 219-229.

Wang Z. and Becker H. (2013) Ratios of S, Se and Te in the silicate Earth require a volatile-rich late veneer. *Nature* **499**, 328-331.

Wirth R., Reid D. and Schreiber A. (2013) Nanometer-sized platinum-group minerals (PGM) in base metal sulfides: new evidence for an orthomagmatic origin of the Merensky Reef PGE ore deposit, Bushveld Complex, South Africa. *Can. Mineral.* **51**, 143–155.

Wood S.A. (2002) The aqueous geochemistry of the platinum group elements with applications to ore deposits. In *Geology, Geochemistry, Mineralogy and Mineral Benefication of Platinum Group Element* (ed. L.J. Cabri). Canadian Institute of Mining, Metallurgy and Petroleum, Special volume 54, pp. 211-249.

Yudovskaya M.A., Kinnaird J.A., Grobler D.F., Costin G., Abramova V.D., Dunnett T. and Barnes S-J. (2017) Zonation of Merensky-style platinum-group element mineralization in Turfspruit thick reef facies (Northern Limb of the Bushveld Complex). *Econ. Geol.* **112(6)**, 1333-1365.

Zientek M.L., Cooper R.W., Corson S.R. and Geraghty E.P. (2002) Platinum-group element mineralization in the Stillwater Complex, Montana. In *Geology, Geochemistry, Mineralogy and Mineral Benefication of Platinum Group Element* (ed. L.J. Cabri). Canadian Institute of Mining, Metallurgy and Petroleum, Special volume 54, pp. 459-481.

Chapitre 7 – Synthèse et remarques finales

7. 1 – Introduction

Ce chapitre résume les principales conclusions de ce projet de doctorat et est divisé en trois parties principales. La première partie fournit une synthèse globale des résultats, en se concentrant sur les améliorations de la méthodologie et l'hypothèse qui devaient être testées. La deuxième partie a indiqué le contexte général dans lequel la thèse a été insérée. Enfin, la troisième partie fournit quelques questions soulevées par les résultats du projet et quelques suggestions pour des études futures.

7. 2 – Synthèse des résultats

7.2.1 – Améliorations analytiques pour déterminer TABS dans les matériaux géologiques

La première partie de ce projet de doctorat s'est concentrée sur la mise en œuvre d'une routine d'analyse au LabMaTer (UQAC) qui permet de mesurer de faibles concentrations de TABS dans les matériaux géologiques. Comme présenté au chapitre 2, la méthode de la spectroscopie de fluorescence atomique couplée à un générateur d'hydrure (HG-AFS) a été mise en œuvre et a permis la plupart des analyses du projet. Plusieurs matériaux géologiques internationaux ont été analysés afin de vérifier l'exactitude et la précision de la méthode. Les résultats confirment son utilisation pour la quantification de TABS à de faibles niveaux (quelques ppb).

La mise en œuvre de cette routine a non seulement permis le développement de ce projet, mais peut également soutenir de futures enquêtes. Cela est principalement dû au fait que le nombre d'études basées sur de TABS dans différents contextes a considérablement augmenté au cours des dernières années (Pitcairn, 2004; Lorand et Alard, 2010; König, et al., 2012, 2014; Jenner et O'Neill , 2012; Wang et Becker, 2013; Lissner et al., 2014; Yierpan et al., 2019; Maciag

et Brenan, 2020), et devrait continuer d'augmenter. Cependant, le nombre de laboratoires dans le monde qui sont capables de mesurer les TABS à de faibles niveaux dans les matériaux géologiques est toujours limité. Par conséquent, le projet contribue à de futures études et, de plus, permet à LabMaTer (UQAC) de consolider une position dans l'analyse de ce groupe d'éléments.

7.2.2 – L'histoire de cristallisation d'un liquide sulfuré immiscible

La formation de gisements de sulfures magmatiques a fait l'objet de recherches au cours des dernières décennies, à l'aide de divers outils (Naldrett, 2004; Barnes et Lightfoot, 2005). Cependant, pour comprendre la formation de ces gisements, il faut d'abord considérer comment cristallise un liquide sulfuré. Ce projet contribue à la compréhension globale de la formation de dépôts magmatiques en fournissant des preuves textuelles et de composition pour la formation de pentlandite à des températures élevées, via une réaction péritectique entre le MSS et le liquide sulfuré, comme détaillé dans le chapitre 4. Les résultats soutiennent ce futur les investigations devraient considérer cette étape supplémentaire lors de la formation des dépôts de sulfures magmatiques.

Bien que l'amélioration de la compréhension de la cristallisation d'un liquide sulfuré n'ait pas été l'objectif principal de ce projet, il s'agit d'un produit secondaire de nos recherches. De plus, la compréhension du comportement des TABS lors du fractionnement du liquide sulfuré, et par conséquent de leur rôle lors de la formation des gisements de sulfures magmatiques, repose sur la compréhension du fractionnement du liquide sulfuré lui-même. En effet, l'une des hypothèses étudiées est l'exsolution des MGP à partir des SMB, qui dépend finalement de la façon dont les EGP et TABS peuvent être incorporés dans les SMB pendant la cristallisation. Par conséquent, les résultats présentés au chapitre 4 soutiennent la formation de pentlandite via une réaction péritectique, et l'incorporation de Pd et potentiellement de TABS dans son réseau cristallin.

7.2.3 – Rôle des TABS lors de la cristallisation fractionnée du liquide sulfuré

Cette partie de la thèse répond au problème initial d'un liquide immiscible riche en TABS pouvant se séparer du liquide sulfuré (Hanley 2007; Helmy et al.2007, 2013; Cafagna et Jugo, 2016; Sinyakova et al., 2017), ou les MGP pourraient cristalliser directement à partir du liquide sulfuré (Dare et al., 2014; Duran et al., 2017). Les résultats des variations cryptiques des SMB du district minier de Noril'sk-Talnakh confirment que les concentrations de TABS dans le liquide sulfuré augmentent progressivement pendant la cristallisation fractionnée. Cette augmentation progressive confirme également qu'aucune baisse majeure des concentrations de TABS dans le liquide sulfuré ne s'est produite, comme cela serait attendu lors de la ségrégation de liquide immiscible riche en TABS. De plus, les données expérimentales actuelles et les résultats de modélisation (Li et Audétat, 2015; Liu et Brenan, 2015) soutiennent que même après 99,9% de cristallisation fractionnée du liquide sulfuré, les concentrations en TABS ne sont pas suffisamment élevées pour qu'un liquide immiscible se forme. Au contraire, après un fractionnement étendu, les concentraitons de Pt, Pd et TABS dans le liquide sulfuré atteignent des niveaux qui permettent la cristallisation directe des MGP à partir du liquide sulfuré.

Dans l'ensemble, les résultats confirment le comportement incompatible des TABS pendant la cristallisation fractionnée du liquide sulfuré et la cristallisation directe des MGP, au lieu de la formation d'un liquide immiscible riche en TABS. Dans ce modèle, Pt, Pd et TABS resteront dans les dernières portions fractionnées du liquide sulfuré et cristalliseront des MGP. Cela peut avoir des implications importantes pour la distribution de Pt, Pd et TABS pendant l'altération des gisements de sulfures magmatiques. En effet, la température de cristallisation de ces MGP est faible (<600 ° C; Cabri et Laflamme, 1976; Hoffman et MacLean, 1976; Dare et al., 2014; Duran et al., 2017), et ils peuvent être plus facilement remobilisés (Tomkins et al., 2007). Par conséquent, il est possible que certaines des zones à faible S-haut-Pt-Pd trouvées autour des intrusions soient le résultat de la remobilisation de ces portions les plus fractionnées du liquide sulfuré (Péntek et al., 2008; Tuba et al. , 2014). Dans ces cas, les TABS ne joueraient pas

nécessairement un rôle actif lors du fractionnement du liquide sulfuré, mais pourrait être des éléments importants lors de l'altération des gisements magmatiques de sulfure.

7.2.4 – Rôle des TABS pendant l'exsolution des MGP

Le contexte adéquat pour étudier le rôle de TABS pendant l'exsolution des MGP est en considérant les gisements de sulfure magmatique qui ont subi une cristallisation à l'équilibre. En effet, les variations des teneurs en TABS causées par la cristallisation fractionnée peuvent être ignorées dans ces cas, et ainsi les effets des processus post-cumulus peuvent être plus facilement évalués. Par conséquent, l'étude des *Reefs* à EGP des complexes du Bushveld et Stillwater nous a permis d'évaluer l'hypothèse si les TABS jouent un rôle lors de l'exoslution des MGP, ou même si la concentration des TABS dans les SMB pourraient être un facteur limitant contrôlant l'extension qui les exsolution des MGP peuvent avoir lieu (Makovicky et al., 1990; Makovicky, 2002; Prichard et al., 2004; Godel et al., 2007; Holwell et McDonald, 2007; Godel et Barnes, 2008; Wirth et al., 2013; Junge et al., 2015).

Les résultats présentés dans les chapitres 5 et 6 ont permis de comprendre comment l'exsolution des MGP affecte le contenu des TABS dans les SMB. Les résultats confirment que les EGP créent un potentiel chimique pour l'exsolution des MGP à partir des SMB. Par conséquent, une fois que les EGP ont besoin d'un partenaire ligant pour exsolver à partir des SMB, ils séquestrent les TABS du réseau des SMB. En conséquence, les SMB des échantillons riches en EGP sont épuisé dans TABS, et le budget de roche totale pour ces éléments est expliqué par la présence des MGP. Cependant, il n'y a aucune preuve claire que la concentration initiale de TABS dans les SMB est un facteur important limitant l'exsolution des MGP. Cela est probablement dû au fait que, bien que les TABS soient les ligants les plus fréquents pour les MGP, les EGP peuvent également s’exsolver sous la forme de sulfures ou des alloys.

7.2.5 – La concentration des TABS dans les magmas initiaux qui forment des gisements de EGP

Cette partie du projet s'est concentrée sur l'évaluation de la concentration des TABS dans les liquides initiaux qui cristallisent les gisements de EGP. Ainsi, l'étude du contenu des TABS dans des échantillons de la *Marginal Zone* du complexe du Bushveld a permis de comprendre quels processus affectent la distribution de TABS dans les magmas qui ont cristallisé certains des plus grands gisements de PGE au monde. Les résultats confirment que la distribution des TABS repose en grande partie sur leur comportement chalcophile (Li et Audétat, 2015; Liu et Brenan, 2015; Barnes, 2016). Le Te et le Se sont des éléments fortement chalcophiles, et leur distribution est principalement contrôlée par les sulfures. Par contre, As et Sb ne sont que des éléments légèrement chalcophiles, et leur distribution est principalement contrôlée par le degré d'assimilation crustale des magmas. Le Bi est modérément chalcophile et sa distribution résulte d'une combinaison des processus susmentionnés.

7.3 – Contribution au débat actuel

La thèse est insérée dans l'effort de recherche actuel pour mieux comprendre les différents aspects de la formation des gisements de sulfures magmatiques. Bien que ces gisements aient été largement étudiés au cours des dernières décennies, les récentes améliorations des techniques analytiques ont permis d'étudier la distribution d'un groupe plus large de métaux, comme le TABS, qui était l'objectif principal de ce projet. Nos modèles proposés pour le comportement de TABS pendant la cristallisation fractionnée et à l'équilibre du liquide sulfuré contribuent à cet effort continu pour comprendre la distribution des semi-métaux dans les gisements de sulfure magmatique. De plus, les résultats de la concentration de TABS dans la *Marginal Zone* du complexe du Bushveld contribuent à l'effort actuel de quantification de la concentration de ces éléments dans les magmas ultramafiques et mafiques initiaux. Les résultats

pourraient soutenir de futures recherches visant non seulement à comprendre la distribution de TABS dans les gisements de sulfures magmatiques, mais également des études fondamentales visant à mieux contraindre le cycle géochimique des TABS.

Cette contribution est également alignée sur les efforts actuels pour comprendre la distribution des métaux critiques dans divers réservoirs géologiques (Hattori et al., 2002; Lissner et al., 2014; Patten et al., 2017, 2019; Samalens et al., 2017; Edmonds et al., 2018; Yierpan et al., 2019; Wiesener et al., 2020). Comme indiqué au chapitre 1, il existe une demande croissante pour ces métaux, en particulier pour le développement de technologies énergétiques sans émission de carbone (Commission européenne, 2010 et 2014; Zweibel, 2010; Moss et al., 2013). Par conséquent, les gisements de sulfures magmatiques pourraient éventuellement être considérés à l'avenir comme une source potentielle de semi-métaux (USGS, 2020). Cependant, cette possibilité est encore entravée par les informations limitées sur la concentration de semi-métaux dans les gisements de sulfures magmatiques. Par conséquent, cette thèse fournit des informations sur ce sujet et vise à contribuer à cet effort mondial actuel de recherche de métaux importants pour le développement de sources d'énergie renouvelables.

7.4 – Future investigations

Suite aux études réalisées, plusieurs questions peuvent être posées et des investigations futures proposées:

- Il existe encore un manque de matériaux de référence géologiques bien caractérisés pour les TABS à de faibles niveaux (inférieurs à 1 ppm). De futures investigations sont nécessaires pour améliorer les connaissances sur les matériaux de référence, et ainsi soutenir de meilleures routines analytiques pour TABS.

- Il manque encore des études expérimentales sur les rôles potentiels des TABS (à l'exception de As) dans la saturation des MGP à partir d'un magma silicaté.
- Il y a un effort pour comprendre le cycle géochimique des TABS. Cependant, on sait encore peu de choses sur les concentrations de ces éléments dans les magmas ultramafiques et mafiques initiaux.
- Le rôle de TABS lors de l'altération post-magmatique des gisements de sulfures magmatiques n'est pas encore complètement compris et pourrait sûrement être amélioré par de futures contributions.

7.5 – Références

Barnes, S-J. (2016) Chalcophile elements. In: White WM (Ed.) Encyclopedia of Geochemistry: A Comprehensive Reference Source on the Chemistry of the Earth, Part of the series Encylopedia of Earth Sciences Series pp 1–5

Barnes, S-J., Lightfoot, P.C. (2005) Formation of magmatic nickel sulfide ore deposits and processes affecting their copper and platinum group element contents. Economic Geology 100th Anniversary, 179–213

Cabri, L.J., Laflamme, J.H.G. (1976) The mineralogy of the platinum- group elements from some copper-nickel deposits of the Sudbury area, Ontario. Economic Geology, 71: 1159-195.

Cafagna, F., Jugo, P.J. (2016) An experimental study on the geochemical behavior of highly siderophile elements (HSE) and metalloids (As, Se, Sb, Te, Bi) in a mss-iss-pyrite system at 650° c: A possible magmatic origin for Co-HSE-bearing pyrite and the role of metalloid-rich phases in the fractionation of HSE. Geochimica et Cosmochimica Acta, 178: 233-258

Dare, S.A.S., Barnes, S-J., Prichard, H.M., Fisher, P.C. (2014) Mineralogy and geochemistry of Cu-rich ores from the McCreedy East Ni-Cu-PGE deposit (Sudbury, Canada): Implications for the behavior of platinum group and chalcophile elements at the end of crystallization of a sulfide liquid. Economic Geology, 109: 343-366.

Duran, C.J., Barnes S-J., Plešem P., Prašekm M.K., Zientekm M.L., Pagé P. (2017) Fractional crystallization-induced variations in sulfides from the Noril'sk-Talnakh mining district (polar Siberia, Russia). Ore Geology Reviews, 90: 326-351.

Edmonds, M., Mather, T.A., Liu, E.J. (2018) A distinct metal fingerprint in arc volcanic emissions. Nature Geoscience, 11(10): 790-794.

European Commission (2010) Critical Raw Materials for the EU. Report of the Ad-hoc Working Group on Defining Critical Raw Materials. European Commission, Enterprise and Industry.

European Commission (2014) Report on critical raw materials for the EU. Report of the Ad-hoc Working Group on Defining Critical Raw Materials. European Commission, Enterprise and Industry.

Godel, B., Barnes, S-J., Maier, W.D. (2007) Platinum-group elements in sulphide minerals, platinum-group minerals, and whole-rocks of the Merensky Reef (Bushveld Complex, South Africa): Implications for the formation of the reef. Journal of Petrology, 48: 1569-1604.

Godel, B., Barnes, S-J. (2008) Platinum-group elements in sulfide minerals and the whole rocks of the JM Reef (Stillwater Complex): Implication for the formation of the reef. Chemical Geology, 248: 272-294.

Hanley, J.J. (2007) The role of arsenic-rich melts and mineral phases in the development of high-grade Pt-Pd mineralization within komatiite-associated magmatic Ni-Cu sulfide horizons at Dundonald Beach South, Abitibi subprovince, Ontario, Canada. Economic Geology, 102: 305-317.

Hattori, K.H., Arai, S., Clarke, D.B. (2002) Selenium, tellurium, arsenic and antimony contents of primary mantle sulfides. The Canadian Mineralogist, 40(2): 637-650.

Helmy, H.M., Ballhaus, C., Berndt, J., Bockrath, C., Wohlgemuth-Ueberwasser, C. (2007) Formation of Pt, Pd and Ni tellurides: Experiments in sulfide–telluride systems. Contributions to Mineralogy and Petrology, 153: 577-591.

Helmy, H.M., Ballhaus, C., Fonseca, R., Nagel, T. (2013) Fractionation of platinum, palladium, nickel, and copper in sulfide–arsenide systems at magmatic temperature. Contributions to Mineralogy and Petrology, 166: 1725-1737.

Hoffman, E., MacLean, W.H. (1976) Phase relations of michenerite and merenskyite in the Pd-Bi-Te system. Economic Geology, 71: 1461–1468.

Holwell, D., McDonald, I. (2007) Distribution of platinum-group elements in the Platreef at Overysel, northern Bushveld Complex: A combined PGM and LA-ICP-MS study. Contributions to Mineralogy and Petrology, 154: 171-190.

Jenner, F.E., O'Neill, H.S.C. (2012) Analysis of 60 elements in 616 ocean floor basaltic glasses. Geochemistry, Geophysics, Geosystems, 13(2).

Junge, M., Wirth, R., Oberthür, T., Melcher, F., Schreiber, A. (2015) Mineralogical siting of platinum-group elements in pentlandite from the Bushveld Complex, South Africa. Mineralim Deposita, 50: 41-54.

König, S., Luguet, A., Lorand, J-P., Wombacher, F., Lissner, M. (2012) Selenium and tellurium systematics of the Earth's mantle from high precision analyses of ultra-depleted orogenic peridotites. Geochimica et Cosmochimica Acta, 86: 354-366.

König, S., Lorand, J-P., Luguet, A., Pearson, D.G. (2014) A non-primitive origin of near-chondritic S–Se–Te ratios in mantle peridotites; implications for the Earth's late accretionary history. Earth and Planetary Science Letters, 385: 110-121.

Li, Y., Audétat, A. (2015) Effects of temperature, silicate melt composition, and oxygen fugacity on the partitioning of V, Mn, Co, Ni, Cu, Zn, As, Mo, Ag, Sn, Sb, W, Au, Pb, and Bi between sulfide phases and silicate melt. Geochimica et Cosmochimica Acta, 162: 25-45.

Lissner, M., König, S., Luguet, A., Le Roux, P., Schuth, S., Heuser, A., le Roex, A.P. (2014) Selenium and tellurium systematics in MORBs from the southern Mid-Atlantic Ridge (47–50 S). Geochimica et Cosmochimica Acta, 144: 379-402.

Liu, Y., Brenan, J. (2015) Partitioning of platinum-group elements (PGE) and chalcogens (Se, Te, As, Sb, Bi) between monosulfide-solid solution (MSS), intermediate solid solution (ISS) and sulfide liquid at controlled fO2–fS2 conditions. Geochimica et Cosmochimica Acta, 159: 139-161.

Lorand, J-P., Alard, O. (2010) Determination of selenium and tellurium concentrations in Pyrenean peridotites (Ariege, France): new insight into S/Se/Te systematics of the upper in mantle samples. Chemical Geology, 278(1-2): 120-130.

Maciag, B.J., Brenan, J.M. (2020) Speciation of Arsenic and Antimony in Basaltic Magmas. Geochimica et Cosmochimica Acta, 276: 198-218.

Makovicky, E., Karup-Møller, S., Makovicky, M., Rose-Hansen, J. (1990) Experimental studies on the phase systems Fe-Ni-Pd-S and Fe-Pt-Pd-As-S applied to PGE deposits. Mineralogy and Petrology, 42(1-4): 307-319.

Makovicky, E. (2002) Ternary and quaternary phase systems in PGE: Canadian Institute of Mining, Metallurgy and Petroleum, Special Volume 54: 131–175.

Moss, R.L., Tzimas, E., Kara, H., Willis, P., Kooroshy, J. (2013) The potential risks from metals bottlenecks to the deployment of strategic energy technologies. Energy Policy, 55: 556-564.

Naldrett, A.J. (2004) Magmatic sulphide deposits: Geology, geochemistry and exploration. Springer-Verlag, Berlin: 728 p.

Patten, C.G., Pitcairn, I.K., Teagle, D.A.H. (2017) Hydrothermal mobilisation of Au and other metals in supra-subduction oceanic crust: Insights from the Troodos ophiolite. Ore Geology Reviews, 86: 487-508.

Patten, C.G.C., Pitcairn, I.K., Alt, J.C., Zack, T., Lahaye, Y., Teagle, D.A.H., Markdahl, K. (2019) Metal fluxes during magmatic degassing in the oceanic crust: sulfide mineralisation at ODP site 786B, Izu-Bonin forearc. Mineralium Deposita, 1-21.

Péntek, A., Molnár, F., Watkinson, D.H., Jones, P.C. (2008) Footwall-type Cu-Ni-PGE Mineralization in the Broken Hammer Area, Wisner Township, North Range, Sudbury Structure. Economic Geology, 103: 1005-1028.

Pitcairn, I.K. (2004) Sources of fluids and metals in orogenic gold deposits: the Otago Schists, New Zealand. University of Southampton.

Prichard, H., Hutchinson, D., Fisher, P. (2004) Petrology and crystallization history of multiphase sulfide droplets in a mafic dike from Uruguay: Implications for the origin of Cu-Ni-PGE sulfide deposits. Economic Geology, 99: 365-376.

Samalens, N., Barnes, S-J., Sawyer, E.W. (2017) The role of black shales as a source of sulfur and semimetals in magmatic nickel-copper deposits: Example from the Partridge River Intrusion, Duluth Complex, Minnesota, USA. Ore Geology Reviews, 81(1): 173-187.

Sinyakova, E.F., Kosyakov, V.I., Borisenko, A.S. (2017) Effect of the presence of As, Bi, and Te on the behavior of Pt metals during fractionation crystallization of sulfide magma. Doklady Earth Sciences, 477(2): 1422-1425.

Tuba, G., Molnár, F., Ames, D.E., Péntek, A., Watkinson, D.H., Jones, P.C. (2014) Multi-stage hydrothermal processes involved in "low-sulfide" Cu (–Ni)–PGE mineralization in the footwall of the Sudbury Igneous Complex (Canada): Amy Lake PGE zone, East Range. Mineralium Deposita, 49: 7-47.

U.S. Geological Survey (2020) MineralCommodity Summaries. Accessed at <<https://www.usgs.gov/media/images/mineral-commodities-february-2020>>

Wang, Z., Becker, H. (2013) Ratios of S, Se and Te in the silicate Earth require a volatile-rich late veneer. Nature, 499: 328-331.

Wieser, P., Jenner, F., Edmonds, M., Maclennan, J., Kunz, B. (2020) Chalcophile elements track the fate of sulfur at Kīlauea Volcano, Hawai'i. Geochimica et Cosmochimica Acta.

Wirth, R., Reid, D., Schreiber, A. (2013) Nanometer-sized platinum-group minerals (PGM) in base metal sulfides: new evidence for an orthomagmatic origin of the Merensky Reef PGE ore deposit, Bushveld Complex, South Africa. The Canadian Mineralogist, 51: 143-155.

Yierpan, A., König, S., Labidi, J., Schoenberg, R. (2019) Selenium isotope and S-Se-Te elemental systematics along the Pacific-Antarctic ridge: Role of mantle processes. Geochimica et Cosmochimica Acta, 249: 199-224.

Zweibel, K. (2010) The Impact of Tellurium Supply on Cadmium Telluride Photovoltaics. Science, 328: 699-701.

ANNEXE 1 - Complete dataset for Te, As, Bi, Sb and Se results for international reference materials, and GeoPt proficiency test samples, obtained by HG-AFS.

ANNEXE 1

ID	Geo*PT* #	Rock type	**Results (values in µg g^{-1})**				
			Te	As	Bi	Sb	Se
LoD (3σ)		Blank	0.010	0.019	0.016	0.026	0.002
LoQ (10σ)		Blank	0.032	0.064	0.055	0.088	0.008
CH-4		Gold ore (meta-anorthosite)	0.481	8.693	0.653	0.819	1.914
CH-4		Gold ore (meta-anorthosite)	0.508	7.975	0.831	0.769	2.001
CH-4		Gold ore (meta-anorthosite)	0.417	8.697	0.759	0.783	1.892
CH-4		Gold ore (meta-anorthosite)	0.386	8.057	0.658	0.912	1.952
CH-4		Gold ore (meta-anorthosite)	0.314	8.96	0.57	0.80	1.99
CH-4		Gold ore (meta-anorthosite)	0.316	8.86	0.55	0.91	1.96
CH-4		Gold ore (meta-anorthosite)	0.477	8.497	0.715	0.919	1.879
TDB-1		Diabase	0.045	1.972	0.043	0.853	0.373
TDB-1		Diabase	0.042	2.154	0.097	0.833	0.327
TDB-1		Diabase	0.055	2.503	0.045	0.884	0.330
TDB-1		Diabase	0.037	1.903	0.045	1.140	0.319
TDB-1		Diabase	0.038	2.28	0.09	1.24	0.376
TDB-1		Diabase	0.039	2.18	0.04	1.29	0.34
TDB-1		Diabase	0.034	1.891	0.089	0.998	0.303
KPT-1		Quartz diorite	0.605	1.975	0.919	11.372	2.975
KPT-1		Quartz diorite	0.528	1.931	0.841	10.900	3.182
KPT-1		Quartz diorite	0.465	1.729	0.782	11.067	2.931
KPT-1		Quartz diorite	0.471	2.424	0.840	11.466	2.982
KPT-1		Quartz diorite	0.426	2.32	0.93	11.02	2.86
KPT-1		Quartz diorite	0.442	2.58	1.01	10.69	2.79
KPT-1		Quartz diorite	0.546	2.091	1.028	11.026	2.992
OKUM		Komatiite	0.061	0.29	0.09	0.10	0.09
OKUM		Komatiite	0.051	0.23	0.07	0.13	0.10
OKUM		Komatiite	0.048	0.20	0.06	0.10	0.11
WPR-1		Peridotite	0.510	1.02	0.21	1.02	3.96
WPR-1		Peridotite	0.463	1.25	0.19	0.86	3.86
WPR-1		Peridotite	0.448	0.94	0.18	0.75	3.75
WMG-1		Gabbro	1.324	7.37	0.42	1.88	13.61
WMG-1		Gabbro	1.522	7.01	0.54	2.03	14.30
WMG-1		Gabbro	1.411	6.88	0.50	1.85	12.99
ANG		Anorthosite	0.010	0.020	0.050	0.118	0.029
ANG		Anorthosite	<0.01	0.025	0.083	0.108	0.021
ANG		Anorthosite	<0.01	0.027	0.075	0.126	0.033
BEN		Basalt	<0.01	1.852	<0.016	0.290	0.075
BEN		Basalt	<0.01	1.747	<0.016	0.301	0.061
BEN		Basalt	<0.01	1.824	<0.016	0.289	0.072
BIR-1		Basalt	<0.01	0.049	0.021	0.576	0.015
BIR-1		Basalt	<0.01	0.054	0.016	0.520	0.020
BIR-1		Basalt	<0.01	0.060	0.016	0.532	0.015
W-2		Diabase	0.012	0.789	0.095	0.778	0.085
W-2		Diabase	0.011	0.811	0.063	0.834	0.092
W-2		Diabase	0.011	0.700	0.060	0.746	0.082
WGB-1		Gabbro	0.017	1.542	0.055	1.755	0.098
WGB-1		Gabbro	0.011	1.656	0.040	1.829	0.081
WGB-1		Gabbro	0.012	1.588	0.063	1.846	0.097

ANNEXE 1 – *Cont.*

ID	Geo*PT* #	Rock type	Results (values in µg g^{-1})				
			Te	As	Bi	Sb	Se
OU-3	6	Nanhoron microgranite	<0.01	0.963	0.126	0.204	0.045
OU-3	6	Nanhoron microgranite	0.021	0.839	0.293	0.251	0.017
OU-3	6	Nanhoron microgranite	0.028	0.901	0.161	0.217	0.030
OU-3	6	Nanhoron microgranite	0.023	0.965	0.328	0.213	0.020
OU-4	8	Penmaenmawr microdiorite	0.036	1.365	0.107	0.346	0.022
OU-4	8	Penmaenmawr microdiorite	0.014	1.239	0.099	0.263	0.021
OU-4	8	Penmaenmawr microdiorite	0.016	1.255	0.091	0.302	0.020
OU-4	8	Penmaenmawr microdiorite	<0.01	1.407	0.062	0.246	0.012
CH-1	10	Marine sediment	0.094	3.796	0.256	0.961	0.554
CH-1	10	Marine sediment	0.080	3.822	0.346	0.941	0.560
CH-1	10	Marine sediment	0.078	3.613	0.319	0.942	0.549
CH-1	10	Marine sediment	0.069	3.361	0.317	0.995	0.510
OU-5	11	Leiton dolerite	0.042	2.448	0.085	0.511	0.019
OU-5	11	Leiton dolerite	0.038	2.391	0.061	0.462	0.020
OU-5	11	Leiton dolerite	0.033	2.348	0.102	0.481	0.022
OU-5	11	Leiton dolerite	<0.01	2.464	0.042	0.426	0.022
GAS	12	Serpentine	0.015	113.805	0.112	12.184	0.032
GAS	12	Serpentine	0.024	111.095	0.177	12.399	0.026
GAS	12	Serpentine	0.032	117.172	0.081	12.785	0.025
GAS	12	Serpentine	0.037	120.439	0.195	11.847	0.033
UoK Loess	13	Köln loess	0.023	6.314	0.134	0.385	0.030
UoK Loess	13	Köln loess	0.022	6.391	0.160	0.369	0.028
UoK Loess	13	Köln loess	0.018	6.864	0.153	0.391	0.027
UoK Loess	13	Köln loess	<0.01	6.311	0.190	0.254	0.029
MSAN	15	Ocean Floor sediment	0.082	7.022	0.046	0.372	0.507
MSAN	15	Ocean Floor sediment	0.068	6.839	0.119	0.467	0.527
MSAN	15	Ocean Floor sediment	0.082	7.133	0.124	0.433	0.485
MSAN	15	Ocean Floor sediment	0.080	7.649	0.158	0.555	0.613
BNV-1	16	Nevada basalt	0.015	2.383	0.060	0.192	0.031
BNV-1	16	Nevada basalt	0.046	2.185	0.065	0.154	0.021
BNV-1	16	Nevada basalt	0.013	2.496	0.062	0.168	0.025
BNV-1	16	Nevada basalt	0.017	2.368	0.064	0.141	0.022
OU-8	17	Calcareous sandstone	<0.01	0.888	0.036	0.137	0.008
OU-8	17	Calcareous sandstone	0.025	1.090	0.051	0.173	0.007
OU-8	17	Calcareous sandstone	<0.01	0.924	0.077	0.154	0.004
OU-8	17	Calcareous sandstone	<0.01	0.948	0.070	0.196	0.008
KPT-1	18	Quartz diorite	0.532	2.308	0.987	10.898	2.916
KPT-1	18	Quartz diorite	0.502	2.261	0.814	11.077	3.086
KPT-1	18	Quartz diorite	0.489	2.300	0.824	10.140	3.059
KPT-1	18	Quartz diorite	0.477	1.928	0.792	10.765	2.892
MGR-N	19	Gabbro	0.097	1.857	0.179	0.140	0.449
MGR-N	19	Gabbro	0.074	1.668	0.158	0.154	0.592
MGR-N	19	Gabbro	0.082	1.736	0.144	0.161	0.467
MGR-N	19	Gabbro	0.075	1.793	0.169	0.147	0.493

ANNEXE *1 - Cont.*

ID	Geo*PT* #	Rock type	**Results (values in µg g^{-1})**				
			Te	As	Bi	Sb	Se
OPY-1	20	Ultramafic rock	0.043	0.345	0.033	0.183	0.117
OPY-1	20	Ultramafic rock	0.032	0.342	<0.016	0.221	0.093
OPY-1	20	Ultramafic rock	0.039	0.365	0.016	0.203	0.101
OPY-1	20	Ultramafic rock	0.033	0.245	<0.016	0.146	0.110
MGT-1	21	Granite	<0.01	1.901	1.038	0.297	<0.002
MGT-1	21	Granite	0.061	2.165	1.125	0.216	0.015
MGT-1	21	Granite	0.047	2.061	1.148	0.248	0.007
MGT-1	21	Granite	0.055	2.194	1.098	0.216	0.012
MBL-1	22	Basalt	0.202	1.595	0.081	0.219	0.026
MBL-1	22	Basalt	0.177	1.497	0.107	0.205	0.019
MBL-1	22	Basalt	0.185	1.734	0.091	0.261	0.042
MBL-1	22	Basalt	0.269	1.672	0.090	0.210	0.025
OU-9	23	Separation Lake pegmatite	0.235	2.588	0.023	6.024	<0.002
OU-9	23	Separation Lake pegmatite	0.210	2.756	0.061	7.171	0.006
OU-9	23	Separation Lake pegmatite	0.187	2.726	0.071	6.363	<0.002
OU-9	23	Separation Lake pegmatite	0.211	2.609	0.101	6.213	0.006
OU-10	24	Longmyndian greywacke	0.146	1.771	0.163	0.248	0.013
OU-10	24	Longmyndian greywacke	0.163	1.792	0.119	0.280	0.007
OU-10	24	Longmyndian greywacke	0.195	1.749	0.149	0.238	0.010
OU-10	24	Longmyndian greywacke	0.239	1.764	0.142	0.204	0.010
HTB-1	25	Basalt	0.272	0.218	0.022	0.208	0.159
HTB-1	25	Basalt	0.161	0.215	0.048	0.247	0.219
HTB-1	25	Basalt	0.229	0.192	0.051	0.217	0.134
HTB-1	25	Basalt	0.240	0.186	0.097	0.260	0.181
MGL-AND	27	Andesite	0.178	2.108	0.068	0.213	0.003
MGL-AND	27	Andesite	0.170	1.943	0.088	0.238	0.003
MGL-AND	27	Andesite	0.211	2.064	0.047	0.227	0.004
MGL-AND	27	Andesite	0.233	1.901	0.092	0.243	<0.002
NKT-1	29	Nephelinite	<0.01	1.858	0.053	0.389	0.036
NKT-1	29	Nephelinite	<0.01	1.744	0.026	0.351	0.036
NKT-1	29	Nephelinite	<0.01	1.822	0.061	0.337	0.032
NKT-1	29	Nephelinite	<0.01	1.920	0.070	0.352	0.035
CG-2	30	Syenite	<0.01	4.326	0.159	0.740	0.012
CG-2	30	Syenite	<0.01	4.399	0.179	0.856	0.011
CG-2	30	Syenite	0.024	4.219	0.196	0.843	0.012
CG-2	30	Syenite	<0.01	4.033	0.140	0.840	0.010
SdAR-1	31	Modified River Sediment	0.348	35.270	1.798	5.362	0.321
SdAR-1	31	Modified River Sediment	0.433	35.611	1.682	6.429	0.311
SdAR-1	31	Modified River Sediment	0.404	35.444	1.758	5.861	0.300
SdAR-1	31	Modified River Sediment	0.410	34.231	1.864	6.039	0.268
WG-1	32	Woodstock basalt	<0.01	0.676	0.077	0.074	0.020
WG-1	32	Woodstock basalt	<0.01	0.584	0.063	0.078	0.020
WG-1	32	Woodstock basalt	0.032	0.536	0.038	0.048	0.022
WG-1	32	Woodstock basalt	0.011	0.503	0.031	0.085	0.021

ANNEXE 1 - *Cont.*

ID	Geo*PT* #	Rock type	**Results (values in µg g^{-1})**				
			Te	As	Bi	Sb	Se
DBC-1	33	Ball Clay	0.307	3.250	1.599	1.586	2.471
DBC-1	33	Ball Clay	0.278	3.222	1.660	1.559	2.376
DBC-1	33	Ball Clay	0.241	3.223	1.540	1.530	2.346
DBC-1	33	Ball Clay	0.209	3.445	1.931	1.674	2.578
GRI-1	34	Granite	<0.01	0.941	0.073	0.225	0.048
GRI-1	34	Granite	<0.01	1.015	0.050	0.208	0.046
GRI-1	34	Granite	<0.01	1.036	0.056	0.197	0.049
GRI-1	34	Granite	<0.01	1.185	0.048	0.184	0.055
TLM-1	35	Tonalite	<0.01	2.319	0.104	1.471	0.010
TLM-1	35	Tonalite	<0.01	2.383	0.127	1.645	0.009
TLM-1	35	Tonalite	<0.01	2.353	0.060	1.546	0.010
TLM-1	35	Tonalite	<0.01	2.126	0.078	1.561	0.011
GSM-1	36	Gabbro	0.045	2.833	0.096	1.915	0.187
GSM-1	36	Gabbro	0.029	2.415	0.127	1.957	0.219
GSM-1	36	Gabbro	0.027	2.301	0.133	1.982	0.224
GSM-1	36	Gabbro	0.028	2.331	0.107	1.884	0.220
SdAR-M2	36A	Metal-rich sediment	1.136	76.240	1.151	111.257	3.775
SdAR-M2	36A	Metal-rich sediment	1.015	74.442	0.929	115.430	3.141
SdAR-M2	36A	Metal-rich sediment	1.215	70.763	0.957	112.124	3.110
SdAR-M2	36A	Metal-rich sediment	1.019	70.442	1.167	108.362	3.257
ORPT-1	37	Rhyolite	<0.01	0.384	0.031	0.307	0.003
ORPT-1	37	Rhyolite	<0.01	0.438	0.063	0.280	0.003
ORPT-1	37	Rhyolite	<0.01	0.450	0.071	0.203	0.010
ORPT-1	37	Rhyolite	<0.01	0.420	0.089	0.222	0.004
OU-7	38	Ardnamurchan gabbro	<0.01	0.143	0.024	0.080	0.077
OU-7	38	Ardnamurchan gabbro	<0.01	0.165	0.025	0.041	0.083
OU-7	38	Ardnamurchan gabbro	<0.01	0.153	0.042	0.061	0.084
OU-7	38	Ardnamurchan gabbro	<0.01	0.147	0.037	0.052	0.082
			Te	As	Bi	Sb	Se
HARZ01	38A	Modified harzgurgite	0.017	0.302	0.048	1.092	0.025
HARZ01	38A	Modified harzgurgite	<0.01	0.254	0.075	1.196	0.031
HARZ01	38A	Modified harzgurgite	<0.01	0.252	0.094	1.186	0.032
HARZ01	38A	Modified harzgurgite	0.017	0.319	0.090	1.227	0.038
SyMP-1	39	Syenite	0.132	3.722	0.809	0.238	0.179
SyMP-1	39	Syenite	0.155	3.793	0.805	0.245	0.177
SyMP-1	39	Syenite	0.137	3.672	0.831	0.228	0.183
SyMP-1	39	Syenite	0.127	3.476	0.755	0.213	0.187
MNS-1	39A	Nepheline syenite	0.015	23.082	1.163	2.887	0.037
MNS-1	39A	Nepheline syenite	0.023	21.687	0.949	3.153	0.030
MNS-1	39A	Nepheline syenite	0.023	23.036	1.107	3.225	0.040
MNS-1	39A	Nepheline syenite	0.018	20.771	1.030	3.436	0.034
ShWYO-1	40	Silty marine shale	0.086	10.520	0.343	0.985	0.555
ShWYO-1	40	Silty marine shale	0.074	11.196	0.338	0.836	0.603
ShWYO-1	40	Silty marine shale	0.068	10.191	0.323	0.877	0.548
ShWYO-1	40	Silty marine shale	0.058	9.195	0.329	0.930	0.554
ORA-1	41	Andesite	<0.01	0.263	0.058	0.901	0.005
ORA-1	41	Andesite	<0.01	0.244	0.038	0.976	<0.002
ORA-1	41	Andesite	<0.01	0.238	0.064	0.983	0.005
ORA-1	41	Andesite	<0.01	0.289	0.041	1.042	0.003

ANNEXE 2 - Whole-rock compositions of the samples from the Noril'sk-Talnakh mining district. Data from Duran et al. (2017). n.d. = not detected

ANNEXE 2

Sample ID	Ore type	Intrusion	Ag	As	Au	Bi	Cd	Co	Cu	Fe	In	Ir	Mo	Ni	Os
			ppm	ppm	ppm	ppm	ppm	ppm	%	%	ppm	ppm	ppm	%	ppm
90OMZS2-3	Cu-poor	Kharaelakh	3.93	3.40	0.05	0.25	1.22	1265	4.05	54.70	0.23	0.020	0.27	3.48	0.013
NR6	Cu-poor	Noril'sk I	2.65	3.20	0.13	0.55	0.67	2840	1.76	49.32	0.03	0.020	0.22	3.68	0.012
90KMZ5	Cu-poor	Talnakh	3.79	4.20	0.15	0.28	0.44	1382	3.94	46.40	0.08	0.370	0.94	4.97	0.180
90OMZS2-2	Cu-poor	Kharaelakh	13.43	5.00	0.40	0.86	5.52	1364	10.98	48.90	0.70	0.049	0.26	3.62	0.036
NR-13	Cu-poor	Kharaelakh	2.63	2.90	0.16	0.16	1.31	1900	6.13	43.54	0.23	0.049	0.38	3.92	0.022
NR-14	Cu-poor	Kharaelakh	2.82	3.50	0.11	0.19	1.52	1760	6.66	46.94	0.28	0.049	0.48	3.68	0.027
NR11	Cu-poor	Noril'sk I	10.86	6.00	2.29	2.83	1.25	1060	5.73	31.60	0.50	0.295	1.80	5.48	0.076
90OC13	Cu-rich	Kharaelakh	21.48	4.30	1.10	6.12	16.17	954	20.80	41.10	2.38	0.004	0.14	1.80	0.009
90OMZ67-5-1	Cu-rich	Kharaelakh	22.99	3.30	0.28	0.87	10.54	623	29.10	30.60	2.88	0.001	0.16	2.56	n.d.
90OMZS1-3	Cu-rich	Kharaelakh	21.41	4.50	1.40	2.50	10.91	908	22.75	39.80	1.84	0.044	0.12	2.13	0.043
NR15	Cu-rich	Kharaelakh	49.04	2.70	1.93	4.21	15.62	560	12.39	23.10	1.12	0.002	0.18	1.19	0.003
NR17	Cu-rich	Kharaelakh	73.08	7.50	3.13	11.30	29.45	1200	20.64	34.52	2.72	0.001	0.05	2.18	0.003
NR18	Cu-rich	Kharaelakh	31.05	2.50	2.35	2.12	17.61	430	13.25	21.71	2.00	0.000	0.16	1.11	0.001
90MC15	Cu-rich	Noril'sk I	47.96	11.60	8.00	6.85	11.46	923	24.45	33.30	1.94	0.013	0.32	7.14	0.004
90MC5	Cu-rich	Noril'sk I	17.63	13.70	0.78	9.83	16.53	651	25.15	31.10	2.21	0.002	0.25	5.94	0.001
NR8	Cu-rich	Noril'sk I	27.03	4.00	4.98	2.06	6.19	1130	19.30	30.08	1.60	0.095	0.37	4.08	0.052
NR10	Disseminated	Noril'sk I	0.39	1.70	0.15	0.02	0.10	111	0.41	11.15	0.04	0.022	0.19	0.24	0.006
NR9	Disseminated	Noril'sk I	0.64	2.40	0.16	0.23	0.10	71	0.43	9.03	0.05	0.017	0.46	0.17	0.003

ANNEXE 2 – Cont.

Sample ID	Pb	Pd	Pt	Re	Rh	Ru	S	Sb	Se	Sn	Te	Tl	Zn	(Pt+Pd)/(Rh+Ru+Ir+Os)
	ppm	ppm	ppm	ppm	ppm	ppm	%	ppm	ppm	ppm	ppm	ppm	ppm	
90OMZS2-3	6.9	10.77	1.60	n.d.	0.240	0.057	30.50	< 0.06	50.2	2.32	0.87	0.337	130	37.5
NR6	25.0	8.29	1.52	n.d.	0.249	0.045	33.63	< 0.06	47.5	0.08	0.38	0.107	27	30.2
90KMZ5	2.5	26.00	5.20	0.00	3.500	1.000	32.00	0.06	57.0	0.57	1.56	1.597	42	6.2
90OMZS2-2	33.1	18.00	3.10	n.d.	0.430	0.158	33.80	0.12	63.1	2.11	2.02	0.260	217	31.4
NR-13	7.8	7.49	1.46	n.d.	0.556	0.126	31.34	< 0.06	37.9	0.82	0.64	0.115	134	11.9
NR-14	7.6	8.45	1.54	n.d.	0.542	0.126	33.46	< 0.06	54.6	0.78	1.03	0.098	130	13.4
NR11	33.2	111.79	43.67	n.d.	3.412	0.577	23.24	0.19	92.1	6.43	14.28	1.094	91	35.7
90OC13	210.0	37.00	2.60	n.d.	0.033	0.015	32.88	0.52	87.4	15.74	16.05	0.800	581	647.1
90OMZ67-5-1	185.0	28.00	1.90	n.d.	0.004	0.005	33.08	< 0.06	89.5	24.70	13.63	0.392	203	3250.0
90OMZS1-3	88.4	29.15	7.50	n.d.	0.287	0.096	32.95	0.42	74.5	7.64	7.71	0.581	346	78.1
NR15	83.3	20.04	0.89	n.d.	0.005	0.005	19.58	0.12	47.4	8.05	7.26	0.462	303	1414.7
NR17	135.1	52.60	6.76	n.d.	0.400	0.009	32.60	0.54	128.6	12.62	22.31	1.226	389	143.6
NR18	5.8	15.28	1.33	n.d.	0.057	0.002	20.49	< 0.06	58.9	4.90	6.59	1.619	324	278.8
90MC15	3.1	270.00	74.00	0.014	0.450	0.037	33.25	0.85	166.0	17.67	50.81	1.088	328	683.2
90MC5	1.1	360.00	63.00	0.006	0.089	0.005	33.13	0.33	199.2	7.96	74.22	1.209	313	4368.0
NR8	17.8	148.79	76.56	n.d.	1.410	0.134	31.37	0.26	63.2	4.14	2.35	1.479	442	133.2
NR10	5.3	3.36	1.45	n.d.	0.219	0.052	1.62	< 0.06	3.7	0.62	0.54	0.140	93	16.1
NR9	2.0	5.15	1.63	n.d.	0.179	0.032	1.00	< 0.06	3.8	0.87	0.95	0.087	66	29.3

ANNEXE 3 – Analyses of reference materials used in the calibration of the LA-ICP-MS and in-house reference materials used to monitor the data quality for results from the Noril'sk-Talnakh mining district. Stdev= standard deviation; n= number of analyses; RSD= relative standard deviation; n.d.= not determined.

ANNEXE 3

	Isotope used	^{109}Ag	^{75}As	^{197}Au	^{209}Bi	^{111}Cd	^{59}Co	^{65}Cu	^{115}In	^{193}Ir	^{95}Mo	^{61}Ni	^{189}Os
	Detection limit	0.007	0.065	0.008	0.004	0.037	0.007	0.187	0.005	0.004	0.020	0.643	0.017
	RM used for calibration	GSE-1g	GSE-1g	Po-727	GSE-1g	GSE-1g	GSE-1g	MASS-1	GSE-1g	Po-727	GSE-1g	GSE-1g	Po-727
	Concentrations used	200	260	45.8	320	160	380	13.4	370	48	390	440	46.7
	Stdev	20	90	2.4	30	50	20	0.05	60	1.2	30	30	2.6
		Values obtained for reference materials used as monitors											
JB-MSS-5	Working value (UQAC)	60.9	79	35.9	76.1	<0.26	<1	0.021		40.21	<1	10675	42.58
FeS	Stdev	3.7	11	4.8	2.9			0.007		0.53		1130	0.93
in house	This study (average)	58.8	57.78	37.57	84.19	0.2	0.14	0.023		39.75	0.52	10742	44.38
monitor	Stdev (n= 22)	3.6	5.05	3.71	3.86	0.1	0.09	0.001		2.88	0.06	360	3.85
	RSD (%)	6.2	8.74	9.87	4.58	50.00	64.29	4.35		7.25	11.54	3.35	8.68
	Difference %	-3.43	26.86	4.65	10.63			12.20		-1.14		0.63	4.23
GSE-1g	Working values (Georem, Te UQAC)			7				0.038					
dopped basalt	Stdev			n.d.				0.004					
USGS	This study (average)			8.26				0.037					
	Stdev (n= 13)			0.67				0.001					
	RSD (%)			8.07				2.620					
	Difference %			18.00				-2.63					
MASS-1	Working value (certificate)	50	65	47	60	60	60		50	46.2	59	97	<dl
ZnCuS pressed	Stdev	5	3	n.d.	n.d.	7	10		n.d	n.d	9	15	
power pellet	This study (average)	67.06	56.84	54.6	68.96	52.84	74.5		62.01	58.49	63.95	108	<dl
USGS	Stdev (n= 22)	2.24	2.67	5.18	1.57	3.62	2.47		1.67	8.06	1.56	23	
	RSD (%)	3.33	4.7	9.49	2.28	6.84	3.31		2.69	13.77	2.43	21	
	Difference %	34.12	12.55	16.17	14.93	11.93	24.17		24.02	26.60	8.39	11.63	

ANNEXE 3 – Cont.

	Isotope used	^{208}Pb	^{108}Pd	^{195}Pt	^{185}Re	^{103}Rh	^{101}Ru	^{121}Sb	^{82}Se	^{118}Sn	^{130}Te	^{205}Tl	^{66}Zn
	Detection limit	0.007	0.008	0.013	0.010	0.002	0.015	0.047	1.824	0.050	0.257	0.004	0.174
	RM used for calibration	GSE-1g	Po-727	Po-727	GSE-1g	Po-727	Po-727	GSE-1g	MASS-1	GSE-1g	MASS-1	MASS-1	MASS-1
	Concentrations used	378	43.4	35.5	78.9	41.6	36.5	450	51	280	*15*	*50*	210000
	Stdev	12	0.3	0.8	n.d.	0.3	0.3	110	4	50	n.d	n.d.	500
		Values obtained for reference materials used as monitors											
JB-MSS-5	Working value (UQAC)	71.5	54.04	40.3	20.7	61.4	21.72	59	59.7	<0.5	36.8	<dl	<10
FeS	Stdev	4.5	4.4	4.8	n.d.	4.5	1.7	7.3	10.9		6.6		100.0
in house	This study (average)	77.9	63.65	38.99	21.7	59.97	19.96	75.32	58.41	0.87	39.36	<dl	<36
monitor	Stdev (n= 22)	5.39	4.75	2.9	1.78	4.43	1.79	7.68	4.36	0.32	2.67		
	RSD (%)	6.92	7.46	7.44	8.20	7.39	8.97	10.20	7.46	36.78	6.78		
	Difference %	8.95	17.78	-3.25	4.83	-2.33	-8.10	27.66	-2.16		6.96		
GSE-1g	Working values (Georem, Te UQAC)			30					20		n.d.	1.95	460
dopped basalt	Stdev			n.d.					16		n.d.	0.4	10
USGS	This study (average)			21.21					45.71		180.92	1.39	398.7
	Stdev (n= 13)			3.45					6.7		14.83	0.06	29.1
	RSD (%)			16.25					14.66		8.20	4.54	7.3
	Difference %			-29.30					128.55			-28.72	-13.34
MASS-1	Working value (certificate)	68	<dl	51.9	<dl	<dl	<dl	60		59			
ZnCuS pressed	Stdev	7		n.d.				9		6			
power pellet	This study (average)	79.02	<dl	58.96	<dl	<dl	<dl	72.91		58.81			
USGS	Stdev (n= 22)	2.8		2.5				4.04		2.08			
	RSD (%)	3.54		4.26				5.55		3.54			
	Difference %	16.21		13.60				21.52		-0.32			

ANNEXE 4 - Complete data set of SEM-EDS and LA-ICP-MS analyses of pyrrhotite obtained for the Noril'sk-Talnakh mining district and median values for each sample. Abbreviations: N= number of individual analyses

ANNEXE 4

Sample	Ore type	Intrusion	S	Fe	^{59}Co	^{61}Ni	^{65}Cu	^{66}Zn	^{75}As	^{82}Se	^{95}Mo	^{101}Ru	^{103}Rh	^{108}Pd
			%	%	ppm	ppm	ppm	ppm	ppm	ppm	ppm	ppm	ppm	ppm
Limit of detection			**0.5**	**0.5**	**0.007**	**0.643**	**0.187**	**0.174**	**0.065**	**1.824**	**0.020**	**0.015**	**0.002**	**0.008**
90OMZS2-3	Cu-poor	Kharaelakh	39.02	60.37	27.1	2986	2.3	143.4	0.065	57.6	0.28	0.015	0.174	0.008
90OMZS2-3	Cu-poor	Kharaelakh			52.4	3808	17.5	0.17	0.065	57.7	0.34	0.015	0.238	0.017
90OMZS2-3	Cu-poor	Kharaelakh			34.3	3659	3.2	0.17	0.065	54.2	0.34	0.015	0.201	0.008
90OMZS2-3	Cu-poor	Kharaelakh			36.3	3303	935.0	1.43	0.065	54.7	0.39	0.080	0.162	0.023
90OMZS2-3	Cu-poor	Kharaelakh			28.9	2936	317.9	0.17	0.065	55.3	0.52	0.054	0.272	0.008
90OMZS2-3	Cu-poor	Kharaelakh			24.0	2749	5.5	0.17	0.443	64.3	0.27	0.015	0.165	0.008
Median 90OMZS2-3 (N=6)			**39.0**	**60.4**	**31.6**	**3145**	**11.5**	**0.17**	**0.065**	**56.4**	**0.34**	**0.015**	**0.188**	**0.008**
90KMZ5	Cu-poor	Talnakh	38.6	59.8	158.9	9412	0.6	0.17	0.065	70.4	1.20	0.384	3.571	0.294
90KMZ5	Cu-poor	Talnakh			299.2	11531	1.6	0.17	0.065	71.1	1.38	0.520	3.733	0.543
90KMZ5	Cu-poor	Talnakh			149.6	8851	0.5	0.17	0.065	68.7	1.50	0.480	3.621	0.008
90KMZ5	Cu-poor	Talnakh			498.6	22813	1.7	0.17	0.065	67.3	1.17	0.531	3.827	3.116
90KMZ5	Cu-poor	Talnakh			662.6	24371	0.6	0.17	0.065	68.8	1.99	1.036	4.668	4.806
90KMZ5	Cu-poor	Talnakh			1340	47994	2.4	0.17	0.065	72.5	1.38	1.096	4.525	16.327
Median 90KMZ5 (N=6)			**38.6**	**59.8**	**398.9**	**17172**	**1.1**	**0.17**	**0.065**	**69.6**	**1.38**	**0.525**	**3.780**	**1.829**
NR-6	Cu-poor	Noril'sk I	39.5	58.4	208.8	8570	1.1	0.17	0.065	37.4	0.25	0.161	0.742	0.008
NR-6	Cu-poor	Noril'sk I			243.7	9125	9.3	0.17	0.065	34.0	0.42	0.199	0.529	0.124
NR-6	Cu-poor	Noril'sk I			542.3	16143	2.4	0.17	0.065	32.5	0.15	0.093	0.331	1.994
NR-6	Cu-poor	Noril'sk I			1109	22750	1.3	0.17	0.065	34.3	0.19	0.030	0.263	4.226
Median NR-6 (N=4)			**39.5**	**58.4**	**393.0**	**12634**	**1.9**	**0.17**	**0.065**	**34.2**	**0.22**	**0.127**	**0.430**	**1.059**

ANNEXE 4 – Cont.

Sample	Ore type	^{109}Ag	^{111}Cd	^{115}In	^{118}Sn	^{121}Sb	^{130}Te	^{185}Re	^{189}Os	^{193}Ir	^{195}Pt	^{197}Au	^{205}Tl	^{208}Pb	^{209}Bi
		ppm	ppm	ppm	ppm	ppm	ppm	ppm	ppm	ppm	ppm	ppm	ppm	ppm	ppm
Limit of detection		**0.007**	**0.037**	**0.005**	**0.050**	**0.047**	**0.257**	**0.010**	**0.017**	**0.004**	**0.013**	**0.008**	**0.004**	**0.007**	**0.004**
90OMZS2-3	Cu-poor	0.54	0.037	0.005	0.050	0.047	0.966	0.083	0.017	0.012	0.050	0.008	0.00	0.67	0.03
90OMZS2-3	Cu-poor	1.78	0.037	0.005	0.312	0.047	1.047	0.063	0.017	0.017	0.033	0.008	0.00	1.32	0.09
90OMZS2-3	Cu-poor	0.46	0.093	0.005	0.050	0.047	1.166	0.119	0.017	0.019	0.112	0.008	0.00	1.21	0.12
90OMZS2-3	Cu-poor	2.96	0.087	0.008	0.072	0.047	0.735	0.164	0.017	0.020	0.030	0.008	0.00	1.10	0.06
90OMZS2-3	Cu-poor	0.51	0.087	0.016	0.155	0.047	0.854	0.118	0.017	0.020	0.064	0.008	0.00	1.20	0.14
90OMZS2-3	Cu-poor	0.45	0.087	0.005	0.810	0.047	0.929	0.077	0.017	0.011	0.044	0.008	0.00	1.34	0.14
90OMZS2-3 (N=6)		**0.52**	**0.087**	**0.005**	**0.113**	**0.047**	**0.947**	**0.100**	**0.017**	**0.018**	**0.047**	**0.008**	**0.00**	**1.20**	**0.11**
90KMZ5	Cu-poor	0.86	0.037	0.005	0.050	0.073	1.627	0.287	0.166	0.385	0.268	0.008	0.00	0.15	0.16
90KMZ5	Cu-poor	0.58	0.037	0.005	0.050	0.047	1.646	0.381	0.209	0.418	0.069	0.008	0.00	0.12	0.15
90KMZ5	Cu-poor	0.21	0.037	0.005	0.050	0.047	1.546	0.302	0.182	0.362	0.088	0.008	0.00	0.09	0.16
90KMZ5	Cu-poor	2.64	0.037	0.005	0.050	0.047	1.571	0.344	0.201	0.433	0.264	0.008	0.02	0.80	0.41
90KMZ5	Cu-poor	1.83	0.037	0.005	0.050	0.047	1.496	0.385	0.332	0.611	0.286	0.008	0.00	0.19	0.16
90KMZ5	Cu-poor	5.09	0.089	0.005	0.050	0.047	1.907	0.344	0.252	0.544	0.679	0.008	0.00	0.20	0.20
90KMZ5 (N=6)		**1.34**	**0.037**	**0.005**	**0.050**	**0.047**	**1.599**	**0.344**	**0.205**	**0.426**	**0.266**	**0.008**	**0.00**	**0.17**	**0.16**
NR-6	Cu-poor	0.34	0.037	0.005	0.050	0.047	0.257	0.131	0.017	0.035	0.038	0.008	0.00	1.80	0.25
NR-6	Cu-poor	0.47	0.037	0.005	0.050	0.047	0.257	0.118	0.017	0.032	0.187	0.008	0.00	1.84	0.38
NR-6	Cu-poor	0.88	0.037	0.005	0.050	0.047	0.305	0.099	0.035	0.026	0.226	0.008	0.00	3.24	0.46
NR-6	Cu-poor	1.03	0.037	0.005	0.050	0.047	0.257	0.108	0.021	0.017	0.642	0.008	0.00	4.45	0.23
NR-6 (N=4)		**0.67**	**0.037**	**0.005**	**0.050**	**0.047**	**0.257**	**0.113**	**0.019**	**0.029**	**0.206**	**0.008**	**0.00**	**2.54**	**0.31**

ANNEXE 4 – Cont.

Sample	Ore type	Intrusion	S	Fe	^{59}Co	^{61}Ni	^{65}Cu	^{66}Zn	^{75}As	^{82}Se	^{95}Mo	^{101}Ru	^{103}Rh	^{108}Pd
			%	%	ppm	ppm	ppm	ppm	ppm	ppm	ppm	ppm	ppm	ppm
Limit of detection			**0.5**	**0.5**	**0.007**	**0.643**	**0.187**	**0.174**	**0.065**	**1.824**	**0.020**	**0.015**	**0.002**	**0.008**
90OMZS2-2	Cu-poor	Kharaelakh			23.2	1969	5.5	0.45	0.065	50.2	0.34	0.176	0.834	0.008
90OMZS2-2	Cu-poor	Kharaelakh			21.0	1823	5.2	4.99	0.065	53.5	0.40	0.327	1.084	0.056
90OMZS2-2	Cu-poor	Kharaelakh			22.4	1775	4.9	0.35	0.065	51.9	0.37	0.211	0.836	0.008
90OMZS2-2	Cu-poor	Kharaelakh	38.6	60.0	20.2	1814	4.7	0.57	0.065	54.9	0.34	0.271	0.827	0.044
90OMZS2-2	Cu-poor	Kharaelakh			23.1	1876	3.3	0.57	0.065	54.6	0.29	0.246	1.134	0.008
90OMZS2-2	Cu-poor	Kharaelakh			22.3	1814	5.6	0.63	0.081	56.8	0.42	0.271	0.972	0.021
90OMZS2-2	Cu-poor	Kharaelakh			20.1	1703	3.4	0.80	0.070	59.8	0.44	0.297	1.091	0.033
Median 90OMZS2-2 (N=7)			**38.6**	**60.0**	**22.3**	**1814**	**4.9**	**0.57**	**0.065**	**54.6**	**0.37**	**0.271**	**0.972**	**0.021**
NR-13	Cu-poor	Kharaelakh			67.6	6289	0.7	0.22	0.065	32.4	0.44	0.186	0.818	0.008
NR-13	Cu-poor	Kharaelakh			83.6	5504	1.3	0.29	0.065	33.3	0.47	0.228	0.879	0.008
NR-13	Cu-poor	Kharaelakh	38.5	58.7	108.4	4743	0.5	0.36	0.065	35.7	0.44	0.165	0.832	0.008
NR-13	Cu-poor	Kharaelakh			73.9	4812	1.0	0.28	0.065	36.2	0.61	0.300	0.935	0.008
NR-13	Cu-poor	Kharaelakh			117.8	4145	0.2	0.22	0.065	33.3	0.56	0.202	1.159	0.008
NR-13	Cu-poor	Kharaelakh			62.0	6358	0.8	0.23	0.065	30.4	0.36	0.210	0.749	0.008
Median NR-13 (N=6)			**38.5**	**58.7**	**78.8**	**5158**	**0.8**	**0.26**	**0.065**	**33.3**	**0.46**	**0.206**	**0.855**	**0.008**
NR-14	Cu-poor	Kharaelakh			56.0	7000	1.6	0.34	0.065	43.3	0.66	0.395	2.244	0.008
NR-14	Cu-poor	Kharaelakh			70.2	6863	1.3	0.35	0.082	42.6	0.45	0.177	1.095	0.008
NR-14	Cu-poor	Kharaelakh			62.0	6445	1.5	0.24	0.065	41.5	0.39	0.224	1.035	0.008
NR-14	Cu-poor	Kharaelakh	38.3	58.3	85.3	6944	1.4	0.39	0.065	43.4	0.44	0.137	0.672	0.008
NR-14	Cu-poor	Kharaelakh			74.3	5398	0.9	0.31	0.065	43.6	0.37	0.193	0.625	0.023
NR-14	Cu-poor	Kharaelakh			87.7	5024	0.9	0.17	0.065	43.4	0.36	0.200	0.786	0.008
NR-14	Cu-poor	Kharaelakh			61.9	5940	20.6	0.21	0.065	43.4	0.37	0.186	1.129	0.008
Median NR-14 (N=7)			**38.3**	**58.3**	**70.2**	**6445**	**1.4**	**0.31**	**0.065**	**43.4**	**0.39**	**0.193**	**1.035**	**0.008**

ANNEXE 4 – Cont.

Sample	Ore type	^{109}Ag	^{111}Cd	^{115}In	^{118}Sn	^{121}Sb	^{130}Te	^{185}Re	^{189}Os	^{193}Ir	^{195}Pt	^{197}Au	^{205}Tl	^{208}Pb	^{209}Bi
		ppm	ppm	ppm	ppm	ppm	ppm	ppm	ppm	ppm	ppm	ppm	ppm	ppm	ppm
Limit of detection		**0.007**	**0.037**	**0.005**	**0.050**	**0.047**	**0.257**	**0.010**	**0.017**	**0.004**	**0.013**	**0.008**	**0.004**	**0.007**	**0.004**
90OMZS2-2	Cu-poor	0.30	0.049	0.005	0.050	0.047	1.022	0.165	0.066	0.095	0.013	0.008	0.00	1.88	0.05
90OMZS2-2	Cu-poor	0.35	0.037	0.005	0.050	0.047	1.247	0.177	0.079	0.110	0.141	0.008	0.01	2.57	0.06
90OMZS2-2	Cu-poor	0.62	0.061	0.005	0.050	0.047	1.060	0.168	0.082	0.061	0.030	0.008	0.00	3.24	0.07
90OMZS2-2	Cu-poor	0.40	0.037	0.005	0.055	0.047	1.284	0.126	0.069	0.089	0.096	0.008	0.00	3.20	0.15
90OMZS2-2	Cu-poor	0.90	0.037	0.005	0.050	0.047	1.028	0.184	0.080	0.106	0.106	0.010	0.01	2.83	0.14
90OMZS2-2	Cu-poor	0.38	0.037	0.005	0.050	0.047	0.997	0.156	0.058	0.084	0.066	0.008	0.00	2.08	0.03
90OMZS2-2	Cu-poor	0.36	0.037	0.007	0.064	0.047	0.879	0.193	0.057	0.099	0.107	0.008	0.01	2.32	0.17
90OMZS2-2 (N=7)		**0.38**	**0.037**	**0.005**	**0.050**	**0.047**	**1.028**	**0.168**	**0.069**	**0.095**	**0.096**	**0.008**	**0.00**	**2.57**	**0.07**
NR-13	Cu-poor	0.30	0.037	0.005	0.050	0.047	0.679	0.233	0.027	0.082	0.092	0.008	0.00	1.17	0.10
NR-13	Cu-poor	0.33	0.037	0.003	0.050	0.047	0.829	0.211	0.050	0.094	0.034	0.008	0.00	0.87	0.07
NR-13	Cu-poor	0.47	0.037	0.005	0.050	0.047	1.028	0.217	0.072	0.075	0.054	0.008	0.00	0.92	0.08
NR-13	Cu-poor	0.24	0.037	0.005	0.050	0.047	0.760	0.254	0.089	0.102	0.041	0.008	0.00	0.64	0.08
NR-13	Cu-poor	0.95	0.037	0.006	0.050	0.047	0.891	0.180	0.059	0.093	0.171	0.008	0.01	3.80	0.10
NR-13	Cu-poor	0.21	0.037	0.005	0.050	0.047	0.779	0.181	0.055	0.089	0.050	0.008	0.00	1.18	0.08
NR-13 (N=6)		**0.31**	**0.037**	**0.005**	**0.050**	**0.047**	**0.804**	**0.214**	**0.057**	**0.091**	**0.052**	**0.008**	**0.00**	**1.04**	**0.08**
NR-14	Cu-poor	0.38	0.037	0.005	0.050	0.047	0.717	0.189	0.059	0.099	0.134	0.008	0.00	0.90	0.17
NR-14	Cu-poor	0.17	0.037	0.005	0.137	0.047	0.810	0.166	0.046	0.089	0.074	0.008	0.00	0.44	0.09
NR-14	Cu-poor	0.23	0.037	0.005	0.050	0.047	1.010	0.158	0.066	0.070	0.072	0.008	0.00	0.53	0.12
NR-14	Cu-poor	0.62	0.037	0.005	0.050	0.047	0.773	0.151	0.064	0.072	0.099	0.008	0.00	0.64	0.08
NR-14	Cu-poor	0.83	0.037	0.005	0.050	0.047	1.097	0.147	0.057	0.079	0.156	0.008	0.00	1.16	0.12
NR-14	Cu-poor	0.17	0.037	0.005	0.050	0.047	0.966	0.163	0.052	0.069	0.110	0.008	0.00	0.47	0.14
NR-14	Cu-poor	0.31	0.037	0.005	0.050	0.047	0.841	0.145	0.054	0.059	0.067	0.008	0.00	0.73	0.12
NR-14 (N=7)		**0.31**	**0.037**	**0.005**	**0.050**	**0.047**	**0.841**	**0.155**	**0.057**	**0.072**	**0.099**	**0.008**	**0.00**	**0.64**	**0.12**

ANNEXE 4 – Cont.

Sample	Ore type	Intrusion	S	Fe	^{59}Co	^{61}Ni	^{65}Cu	^{66}Zn	^{75}As	^{82}Se	^{95}Mo	^{101}Ru	^{103}Rh	^{108}Pd
			%	%	ppm	ppm	ppm	ppm	ppm	ppm	ppm	ppm	ppm	ppm
Limit of detection			**0.5**	**0.5**	**0.007**	**0.643**	**0.187**	**0.174**	**0.065**	**1.824**	**0.020**	**0.015**	**0.002**	**0.008**
NR-11	Cu-poor	Noril'sk I			509.9	50487	96.6	0.48	1.434	88.5	3.42	1.253	7.014	8.352
NR-11	Cu-poor	Noril'sk I			389.6	31601	0.5	0.17	0.785	94.7	3.98	1.279	7.268	2.392
NR-11	Cu-poor	Noril'sk I	38.4	59.0	297.3	34032	0.8	0.44	1.434	95.1	3.45	1.192	6.576	0.437
NR-11	Cu-poor	Noril'sk I			323.5	28547	0.7	0.20	0.898	102.2	3.37	1.386	6.775	2.405
NR-11	Cu-poor	Noril'sk I			363.4	32599	1.0	0.19	0.256	89.8	3.73	1.252	6.183	0.691
NR-11	Cu-poor	Noril'sk I			322.9	25431	1.0	0.17	0.108	95.7	3.85	1.237	6.289	0.960
Median NR-11 (N=6)			**38.4**	**59.0**	**343.4**	**32100**	**0.9**	**0.20**	**0.841**	**94.9**	**3.59**	**1.252**	**6.676**	**1.676**
NR-8	Cu-rich	Noril'sk I			99.7	8913	10.1	1.43	1.060	33.5	0.06	0.015	0.002	0.373
NR-8	Cu-rich	Noril'sk I	39.0	58.3	124.7	9262	22.4	1.00	0.065	38.0	0.12	0.048	0.002	0.298
NR-8	Cu-rich	Noril'sk I			96.0	8701	330.3	21.82	0.605	54.8	5.30	0.015	0.002	0.819
Median NR-8 (N=3)			**39.0**	**58.3**	**99.7**	**8913**	**22.4**	**1.43**	**0.605**	**38.0**	**0.12**	**0.015**	**0.002**	**0.373**
NR-18	Cu-rich	Kharaelakh	**38.9**	**57.9**	67.9	8228	548.5	274.3	0.065	92.2	0.02	0.015	0.002	6.313
NR-17	Cu-rich	Kharaelakh			104.1	2543	1.4	0.80	0.150	97.9	0.02	0.015	0.002	1.743
NR-17	Cu-rich	Kharaelakh			84.1	2711	84.1	1247	0.118	97.2	0.04	0.015	0.002	5.242
NR-17	Cu-rich	Kharaelakh			103.2	2749	1.1	81.65	0.156	95.4	0.31	0.015	0.002	2.440
NR-17	Cu-rich	Kharaelakh			73.7	2992	8.7	261.8	0.112	118.4	0.02	0.015	0.002	3.010
Median NR-17 (N=4)			**38.7**	**58.3**	**103.2**	**2749**	**5.7**	**84.77**	**0.150**	**97.9**	**0.02**	**0.015**	**0.002**	**2.440**

ANNEXE 4 – Cont.

Sample	Ore type	^{109}Ag	^{111}Cd	^{115}In	^{118}Sn	^{121}Sb	^{130}Te	^{185}Re	^{189}Os	^{193}Ir	^{195}Pt	^{197}Au	^{205}Tl	^{208}Pb	^{209}Bi
		ppm	ppm	ppm	ppm	ppm	ppm	ppm	ppm	ppm	ppm	ppm	ppm	ppm	ppm
Limit of detection		**0.007**	**0.037**	**0.005**	**0.050**	**0.047**	**0.257**	**0.010**	**0.017**	**0.004**	**0.013**	**0.008**	**0.004**	**0.007**	**0.004**
NR-11	Cu-poor	4.97	0.037	0.005	0.050	0.047	3.303	0.233	0.430	0.698	0.075	0.048	0.01	17.51	1.79
NR-11	Cu-poor	2.68	0.037	0.005	0.087	0.047	4.176	0.188	0.324	0.654	1.589	0.032	0.02	19.20	3.43
NR-11	Cu-poor	2.48	0.037	0.005	0.050	0.047	4.463	0.213	0.299	0.630	2.743	0.008	0.05	10.85	1.32
NR-11	Cu-poor	1.74	0.037	0.005	0.100	0.047	4.887	0.164	0.368	0.642	0.043	0.028	0.02	16.21	0.89
NR-11	Cu-poor	2.95	0.037	0.005	0.050	0.047	3.758	0.147	0.305	0.679	0.673	0.017	0.03	28.67	1.34
NR-11	Cu-poor	1.86	0.037	0.005	0.050	0.047	3.341	0.184	0.337	0.673	0.077	0.007	0.02	8.23	0.82
NR-11 (N=6)		**2.58**	**0.037**	**0.005**	**0.050**	**0.047**	**3.967**	**0.186**	**0.330**	**0.664**	**0.375**	**0.022**	**0.02**	**16.86**	**1.33**
NR-8	Cu-rich	0.72	0.037	0.005	0.050	0.047	0.393	0.010	0.017	0.004	0.013	0.041	0.17	1.12	0.21
NR-8	Cu-rich	1.18	0.087	0.005	0.050	0.047	0.257	0.010	0.017	0.004	0.013	0.008	0.00	3.74	0.34
NR-8	Cu-rich	0.90	0.305	0.091	0.067	0.047	0.729	0.010	0.017	0.004	0.187	0.008	0.00	2.72	0.69
NR-8 (N=3)		**0.90**	**0.087**	**0.005**	**0.050**	**0.047**	**0.393**	**0.010**	**0.017**	**0.004**	**0.013**	**0.008**	**0.00**	**2.72**	**0.34**
NR-18	Cu-rich	16.21	12.466	0.230	0.050	0.047	8.726	0.010	0.017	0.004	0.312	0.021	0.60	3.80	6.11
NR-17	Cu-rich	4.49	0.081	0.005	0.262	0.047	3.179	0.010	0.017	0.004	0.040	0.008	0.05	68.56	2.56
NR-17	Cu-rich	14.59	55.474	0.286	0.193	0.047	10.970	0.010	0.017	0.004	0.026	0.031	0.05	199.5	2.80
NR-17	Cu-rich	5.17	3.615	0.044	0.050	0.047	4.363	0.010	0.017	0.004	0.013	0.008	0.03	51.73	1.02
NR-17	Cu-rich	21.75	10.596	0.125	0.636	0.069	12.092	0.010	0.017	0.004	0.118	0.023	0.02	29.36	0.79
NR-17 (N=4)		**5.17**	**3.802**	**0.050**	**0.262**	**0.047**	**4.363**	**0.010**	**0.017**	**0.004**	**0.026**	**0.010**	**0.03**	**68.56**	**1.37**

ANNEXE 4 – Cont.

Sample	Ore type	Intrusion	S	Fe	^{59}Co	^{61}Ni	^{65}Cu	^{66}Zn	^{75}As	^{82}Se	^{95}Mo	^{101}Ru	^{103}Rh	^{108}Pd
			%	%	ppm	ppm	ppm	ppm	ppm	ppm	ppm	ppm	ppm	ppm
Limit of detection			**0.5**	**0.5**	**0.007**	**0.643**	**0.187**	**0.174**	**0.065**	**1.824**	**0.020**	**0.015**	**0.002**	**0.008**
90OC13	Cu-rich	Kharaelakh			55.5	2431	529.8	137.1	0.065	50.4	0.02	0.015	0.002	0.633
90OC13	Cu-rich	Kharaelakh			21.1	1789	13401.0	617.1	0.065	48.2	0.03	0.015	0.002	2.075
90OC13	Cu-rich	Kharaelakh			28.2	1811	6295.3	286.7	0.065	65.9	0.02	0.015	0.002	2.639
90OC13	Cu-rich	Kharaelakh	37.9	62.0	32.2	2137	5.4	0.21	0.093	53.4	1.27	0.713	3.752	0.035
90OC13	Cu-rich	Kharaelakh			29.3	1988	3.3	0.32	0.065	55.2	2.18	1.112	3.839	0.230
90OC13	Cu-rich	Kharaelakh			27.4	1857	2.5	0.19	0.065	58.4	3.22	4.123	2.649	0.008
90OC13	Cu-rich	Kharaelakh			213.8	4201	2730.1	561.0	0.065	69.7	0.02	0.015	0.002	0.561
Median 90OC13 (N=7)			**37.9**	**62.0**	**29.3**	**1988**	**529.8**	**137.1**	**0.065**	**55.2**	**0.03**	**0.015**	**0.002**	**0.561**
90OMZS1-3	Cu-rich	Kharaelakh			25.1	691	230.6	0.51	0.065	46.0	0.02	0.016	0.002	0.146
90OMZS1-3	Cu-rich	Kharaelakh			12.6	649	2.6	0.22	0.065	60.5	1.66	1.993	3.815	0.019
90OMZS1-3	Cu-rich	Kharaelakh	38.4	61.0	139.0	2998	6482.3	3.43	0.065	49.4	0.02	0.015	0.002	1.309
90OMZS1-3	Cu-rich	Kharaelakh			10.8	431	9.6	0.34	0.065	49.2	0.72	1.196	2.630	0.010
90OMZS1-3	Cu-rich	Kharaelakh			9.2	287	1.8	0.24	0.065	53.5	0.87	1.034	3.241	0.013
90OMZS1-3	Cu-rich	Kharaelakh			15.0	514	6.2	0.34	0.065	110.7	0.02	0.015	0.002	0.008
Median 90OMZS1-3 (N=6)			**38.4**	**61.0**	**13.8**	**581**	**7.9**	**0.34**	**0.065**	**51.5**	**0.37**	**0.525**	**1.316**	**0.016**
NR-10	Disseminated	Noril'sk I			546.6	24433	1.0	0.21	0.141	105.7	0.66	4.771	17.321	0.610
NR-10	Disseminated	Noril'sk I	38.96	58.35	533.5	25181	1.1	0.24	0.181	104.7	0.48	4.726	16.692	0.785
NR-10	Disseminated	Noril'sk I			246.2	12279	0.5	0.19	0.181	107.8	0.55	2.164	10.584	0.474
Median NR-10 (N=6)			**38.96**	**58.35**	**533.5**	**24433**	**1.0**	**0.21**	**0.181**	**105.7**	**0.55**	**4.726**	**16.692**	**0.610**

ANNEXE 4 – Cont.

Sample	Ore type	^{109}Ag	^{111}Cd	^{115}In	^{118}Sn	^{121}Sb	^{130}Te	^{185}Re	^{189}Os	^{193}Ir	^{195}Pt	^{197}Au	^{205}Tl	^{208}Pb	^{209}Bi
		ppm	ppm	ppm	ppm	ppm	ppm	ppm	ppm	ppm	ppm	ppm	ppm	ppm	ppm
Limit of detection		**0.007**	**0.037**	**0.005**	**0.050**	**0.047**	**0.257**	**0.010**	**0.017**	**0.004**	**0.013**	**0.008**	**0.004**	**0.007**	**0.004**
90OC13	Cu-rich	1.15	2.119	0.044	0.436	0.047	1.184	0.010	0.017	0.004	0.079	0.008	0.04	211.9	0.06
90OC13	Cu-rich	3.55	10.596	0.617	1.621	0.047	9.973	0.010	0.017	0.004	0.050	0.015	0.39	405.1	0.19
90OC13	Cu-rich	2.99	4.924	0.147	1.583	0.047	3.117	0.010	0.017	0.004	0.081	0.008	1.08	120.9	0.14
90OC13	Cu-rich	0.37	0.037	0.005	0.050	0.047	2.767	0.311	0.072	0.175	0.070	0.008	0.03	2.18	0.68
90OC13	Cu-rich	0.48	0.037	0.005	0.050	0.047	2.954	0.457	0.082	0.266	0.039	0.008	0.02	2.99	0.73
90OC13	Cu-rich	0.64	0.049	0.005	0.050	0.047	0.536	1.642	1.328	1.446	0.013	0.008	0.02	4.48	0.15
90OC13	Cu-rich	1.90	9.287	0.157	0.330	0.047	5.111	0.010	0.017	0.004	0.068	0.075	0.15	208.2	0.12
90OC13 (N=7)		**1.15**	**2.119**	**0.044**	**0.330**	**0.047**	**2.954**	**0.311**	**0.017**	**0.004**	**0.068**	**0.008**	**0.04**	**120.9**	**0.15**
90OMZS1-3	Cu-rich	1.38	0.037	0.005	0.074	0.047	0.312	0.010	0.017	0.007	0.124	0.008	0.03	5.73	0.10
90OMZS1-3	Cu-rich	0.60	0.053	0.005	0.047	0.047	1.421	1.229	0.636	0.577	0.013	0.008	0.02	3.43	0.26
90OMZS1-3	Cu-rich	4.74	0.181	0.032	0.066	0.047	1.016	0.010	0.017	0.004	0.125	0.059	0.14	27.43	0.06
90OMZS1-3	Cu-rich	1.18	0.064	0.005	0.050	0.047	1.377	0.532	0.287	0.390	0.013	0.008	0.00	2.10	0.12
90OMZS1-3	Cu-rich	0.98	0.088	0.005	0.050	0.047	1.315	0.651	0.324	0.392	0.013	0.008	0.01	2.93	0.14
90OMZS1-3	Cu-rich	1.93	0.037	0.005	0.050	0.047	0.257	0.010	0.017	0.004	0.013	0.008	0.00	4.29	0.00
90OMZS1-3 (N=6)		**1.28**	**0.059**	**0.005**	**0.050**	**0.047**	**1.166**	**0.271**	**0.152**	**0.198**	**0.013**	**0.008**	**0.01**	**3.86**	**0.11**
NR-10	Disseminated	2.85	0.037	0.005	0.050	0.047	11.699	0.167	0.947	1.920	0.586	0.008	0.00	0.06	0.09
NR-10	Disseminated	3.62	0.037	0.005	0.050	0.047	11.082	0.160	0.885	1.889	0.891	0.008	0.00	0.04	0.09
NR-10	Disseminated	0.89	0.037	0.005	0.050	0.047	12.341	0.128	0.474	0.829	0.399	0.019	0.00	0.11	0.07
NR-10 (N=6)		**2.85**	**0.037**	**0.005**	**0.050**	**0.047**	**11.699**	**0.160**	**0.885**	**1.889**	**0.586**	**0.008**	**0.00**	**0.06**	**0.09**

ANNEXE 5 - Complete data set of SEM-EDS and LA-ICP-MS analyses of pentlandite obtained for the Noril'sk-Talnakh mining district and median values for each sample. Abbreviations: N= number of individual analyses

ANNEXE 5

Sample	Ore type	Intrusion	S	Fe	Ni	^{59}Co	^{65}Cu	^{66}Zn	^{75}As	^{82}Se	^{95}Mo	^{101}Ru	^{103}Rh	^{108}Pd
			%	%	%	ppm	ppm	ppm	ppm	ppm	ppm	ppm	ppm	ppm
Limit of detection			**0.5**	**0.5**	**0.5**	**0.007**	**0.187**	**0.174**	**0.065**	**1.824**	**0.020**	**0.015**	**0.002**	**0.008**
90OMZS2-3	Cu-poor	Kharaelakh				14457	198.6	4.27	1.140	56.7	0.322	0.015	0.118	22.8
90OMZS2-3	Cu-poor	Kharaelakh				14554	32.6	2.83	0.065	52.7	0.212	0.015	0.166	6.2
90OMZS2-3	Cu-poor	Kharaelakh	33.5	34.2	31.1	14652	15.6	3.22	0.482	53.1	0.264	0.015	0.154	39.4
90OMZS2-3	Cu-poor	Kharaelakh				14619	9.5	4.53	1.302	51.8	1.042	0.015	0.002	38.3
90OMZS2-3	Cu-poor	Kharaelakh				13350	91.2	20.84	6.479	72.3	0.072	0.015	0.002	26.2
90OMZS2-3	Cu-poor	Kharaelakh				11917	114.0	2.44	0.065	51.8	0.260	0.015	0.002	30.7
Median 90OMZS2-3 (N=6)			**33.5**	**34.2**	**31.1**	**14505**	**61.9**	**3.74**	**0.811**	**52.9**	**0.262**	**0.015**	**0.060**	**28.5**
NR-6	Cu-poor	Noril'sk I				18364	35.8	0.17	0.065	29.2	0.208	0.296	0.209	33.8
NR-6	Cu-poor	Noril'sk I	33.6	29.0	37.5	12764	8.0	520.96	0.065	30.2	0.081	0.137	0.007	45.9
NR-6	Cu-poor	Noril'sk I				14978	25.1	126.98	0.684	29.6	0.101	0.173	0.049	48.4
Median NR-6 (N=3)			**33.6**	**33.0**	**31.5**	**14978**	**25.1**	**126.98**	**0.065**	**29.6**	**0.101**	**0.173**	**0.049**	**45.9**
90OMZS2-2	Cu-poor	Kharaelakh				11363	17.9	1.39	0.508	46.9	0.097	0.177	0.015	111.4
90OMZS2-2	Cu-poor	Kharaelakh	34.0	27.0	38.5	11266	8.1	0.29	0.267	41.4	2.051	0.205	0.034	105.2
90OMZS2-2	Cu-poor	Kharaelakh				11331	6.2	0.36	0.160	45.6	0.020	0.164	0.009	108.1
Median 90OMZS2-2 (N=3)			**34.0**	**32.0**	**31.5**	**11331**	**8.1**	**0.36**	**0.267**	**45.6**	**0.097**	**0.177**	**0.015**	**108.1**
NR-13	Cu-poor	Kharaelakh				11722	112006	1693.12	0.133	31.0	0.028	0.241	0.002	41.3
NR-13	Cu-poor	Kharaelakh				11461	8.8	0.68	0.137	26.9	0.345	0.296	0.579	41.7
NR-13	Cu-poor	Kharaelakh	33.4	30.3	35.9	13578	8987	371.18	0.146	27.2	0.244	0.257	0.321	51.0
NR-13	Cu-poor	Kharaelakh				5858	34188.0	201.87	0.065	25.1	0.319	0.245	0.002	30.9
NR-13	Cu-poor	Kharaelakh				13350	4.2	0.25	0.104	25.4	0.215	0.244	0.661	51.8
NR-13	Cu-poor	Kharaelakh				15661	110.7	1064.71	0.140	28.0	0.020	0.238	0.002	55.2
Median NR-13 (N=6)			**33.4**	**33.3**	**29.9**	**12536**	**4549**	**286.53**	**0.135**	**27.1**	**0.230**	**0.244**	**0.162**	**46.4**

ANNEXE 5 – Cont.

Sample	Ore type	^{109}Ag	^{111}Cd	^{115}In	^{118}Sn	^{121}Sb	^{130}Te	^{185}Re	^{189}Os	^{193}Ir	^{195}Pt	^{197}Au	^{205}Tl	^{208}Pb	^{209}Bi
		ppm	ppm	ppm	ppm	ppm	ppm	ppm	ppm	ppm	ppm	ppm	ppm	ppm	ppm
Limit of detection		**0.007**	**0.037**	**0.005**	**0.050**	**0.047**	**0.257**	**0.010**	**0.017**	**0.004**	**0.013**	**0.008**	**0.004**	**0.007**	**0.004**
90OMZS2-3	Cu-poor	17.45	0.037	0.005	1.69	0.072	1.30	0.049	0.017	0.020	0.716	0.008	0.485	10.29	0.50
90OMZS2-3	Cu-poor	6.84	0.037	0.008	0.42	0.047	0.91	0.068	0.017	0.013	0.111	0.008	0.446	10.13	0.33
90OMZS2-3	Cu-poor	19.80	0.143	0.158	0.40	0.078	1.17	0.079	0.017	0.007	0.319	0.008	1.019	40.37	0.47
90OMZS2-3	Cu-poor	5.86	0.037	0.034	0.72	0.072	0.52	0.079	0.037	0.014	0.368	0.008	0.238	10.74	0.85
90OMZS2-3	Cu-poor	6.09	0.247	0.099	0.52	0.107	3.97	0.010	0.017	0.004	0.225	0.008	1.661	175.82	0.28
90OMZS2-3	Cu-poor	3.13	8.466	0.005	0.42	0.047	1.96	0.010	0.017	0.004	0.212	0.008	0.612	34.51	0.28
90OMZS2-3 (N=6)		**6.46**	**0.090**	**0.021**	**0.47**	**0.072**	**1.24**	**0.059**	**0.017**	**0.010**	**0.272**	**0.008**	**0.549**	**22.63**	**0.40**
NR-6	Cu-poor	4.10	0.037	0.005	0.05	0.047	0.27	0.079	0.017	0.023	0.527	0.008	0.072	1.58	0.20
NR-6	Cu-poor	1.69	0.037	0.009	0.05	0.047	0.78	0.010	0.017	0.004	3.158	0.166	0.654	89.21	2.64
NR-6	Cu-poor	3.32	1.465	0.020	0.05	0.047	0.26	0.061	0.017	0.004	1.205	0.024	0.961	98.01	0.90
NR-6 (N=3)		**3.32**	**0.037**	**0.009**	**0.05**	**0.047**	**0.27**	**0.061**	**0.017**	**0.004**	**1.205**	**0.024**	**0.654**	**89.21**	**0.90**
90OMZS2-2	Cu-poor	5.18	0.078	0.005	0.22	0.047	1.70	0.010	0.017	0.014	0.109	0.008	0.175	42.33	0.63
90OMZS2-2	Cu-poor	2.64	0.032	0.005	0.05	0.047	0.35	0.599	0.104	0.004	0.032	0.008	0.163	7.13	0.01
90OMZS2-2	Cu-poor	2.18	0.037	0.006	0.05	0.059	1.47	0.010	0.017	0.004	0.062	0.008	0.036	2.75	0.04
90OMZS2-2 (N=3)		**2.64**	**0.037**	**0.005**	**0.05**	**0.047**	**1.47**	**0.010**	**0.017**	**0.004**	**0.062**	**0.008**	**0.163**	**7.13**	**0.04**
NR-13	Cu-poor	30.93	11.494	0.927	0.36	0.047	0.83	0.010	0.017	0.004	2.702	0.008	1.902	41.38	0.29
NR-13	Cu-poor	11.23	0.037	0.005	0.05	0.047	0.56	0.173	0.043	0.046	1.527	0.012	0.032	15.37	0.24
NR-13	Cu-poor	14.39	2.409	0.139	0.29	0.047	1.16	0.089	0.017	0.027	3.523	0.008	0.508	46.24	0.39
NR-13	Cu-poor	13.12	2.149	0.152	0.23	0.047	0.71	0.492	0.173	0.107	1.459	0.008	0.136	27.29	0.43
NR-13	Cu-poor	9.87	0.037	0.005	0.05	0.047	0.50	0.156	0.017	0.054	3.093	0.024	0.140	16.61	0.18
NR-13	Cu-poor	4.27	4.884	0.169	0.16	0.047	0.93	0.010	0.017	0.004	2.579	0.019	0.104	22.69	0.27
NR-13 (N=6)		**12.18**	**2.279**	**0.146**	**0.20**	**0.047**	**0.77**	**0.122**	**0.017**	**0.037**	**2.641**	**0.010**	**0.138**	**24.99**	**0.28**

ANNEXE 5 – Cont.

Sample	Ore type	Intrusion	S	Fe	Ni	^{59}Co	^{65}Cu	^{66}Zn	^{75}As	^{82}Se	^{95}Mo	^{101}Ru	^{103}Rh	^{108}Pd
			%	%	%	ppm	ppm	ppm	ppm	ppm	ppm	ppm	ppm	ppm
Limit of detection			**0.5**	**0.5**	**0.5**	**0.007**	**0.187**	**0.174**	**0.065**	**1.824**	**0.020**	**0.015**	**0.002**	**0.008**
NR-14	Cu-poor	Kharaelakh				16378	537.2	478.63	0.212	39.4	0.781	0.054	0.002	63.4
NR-14	Cu-poor	Kharaelakh				21652	3.6	0.12	0.156	41.6	0.316	0.289	0.508	69.2
NR-14	Cu-poor	Kharaelakh	33.2	30.3	35.3	19829	328.9	30.93	0.326	38.9	0.345	0.369	0.288	108.1
NR-14	Cu-poor	Kharaelakh				15987	4363.0	117.22	0.156	41.8	0.277	0.376	0.789	53.5
NR-14	Cu-poor	Kharaelakh				17029	41.7	0.62	0.179	39.4	0.306	0.309	0.620	59.1
Median NR-14 (N=5)			**33.2**	**32.3**	**32.3**	**17029**	**328.9**	**30.93**	**0.179**	**39.4**	**0.316**	**0.309**	**0.508**	**63.4**
NR-11	Cu-poor	Noril'sk I				6037	0.7	0.22	0.316	82.1	2.800	1.219	8.563	993.1
NR-11	Cu-poor	Noril'sk I				6642	5.4	130.24	0.550	80.7	1.888	1.158	4.734	475.4
NR-11	Cu-poor	Noril'sk I	33.4	30.6	37.4	5802	1.9	0.33	0.081	79.8	7.163	0.804	11.982	1439
NR-11	Cu-poor	Noril'sk I				6453	1.6	0.57	0.456	86.0	2.507	1.218	6.925	470.5
NR-11	Cu-poor	Noril'sk I				6125	5.9	0.39	0.612	74.9	15.303	1.116	12.080	1696
NR-11	Cu-poor	Noril'sk I				6707	1.2	0.39	0.160	83.4	2.090	1.487	6.219	471.8
Median NR-11 (N=6)			**33.4**	**30.6**	**37.4**	**6289**	**1.7**	**0.39**	**0.386**	**81.4**	**2.654**	**1.188**	**7.744**	**734.2**
NR-8	Cu-rich	Noril'sk I				5688	6.0	0.17	0.498	56.7	0.020	3.211	17.322	2478
NR-8	Cu-rich	Noril'sk I	32.4	30.2	37.6	5802	1.7	0.17	0.648	52.7	0.020	2.819	20.252	1967
NR-8	Cu-rich	Noril'sk I				7717	104.2	19.21	0.065	65.4	0.912	2.869	15.463	833.5
NR-8	Cu-rich	Noril'sk I				5926	6.8	0.17	0.671	56.3	0.020	1.587	16.605	1801
Median NR-8 (N=4)			**32.4**	**30.2**	**39.6**	**5864**	**6.4**	**0.17**	**0.573**	**56.5**	**0.020**	**2.844**	**16.963**	**1884**
90MC15	Cu-rich	Noril'sk I				4203	11103	3.22	1.156	120.8	0.550	0.149	0.777	760.9
90MC15	Cu-rich	Noril'sk I				4370	16085	4.85	0.257	122.8	0.316	0.126	0.011	769.7
90MC15	Cu-rich	Noril'sk I	31.2	31.2	35.4	4412	15.6	0.44	2.400	125.4	1.455	1.086	5.333	641.4
90MC15	Cu-rich	Noril'sk I				3943	14229	78.14	2.116	123.4	1.605	0.401	4.830	683.0
90MC15	Cu-rich	Noril'sk I				4894	21.2	0.34	0.485	132.2	1.400	0.215	1.797	732.6
Median 90MC15 (N=5)			**31.2**	**31.2**	**35.4**	**4370**	**11103**	**3.22**	**1.156**	**123.4**	**1.400**	**0.215**	**1.797**	**732.6**

ANNEXE 5 – Cont.

Sample	Ore type	^{109}Ag	^{111}Cd	^{115}In	^{118}Sn	^{121}Sb	^{130}Te	^{185}Re	^{189}Os	^{193}Ir	^{195}Pt	^{197}Au	^{205}Tl	^{208}Pb	^{209}Bi
		ppm	ppm	ppm	ppm	ppm	ppm	ppm	ppm	ppm	ppm	ppm	ppm	ppm	ppm
Limit of detection		**0.007**	**0.037**	**0.005**	**0.050**	**0.047**	**0.257**	**0.010**	**0.017**	**0.004**	**0.013**	**0.008**	**0.004**	**0.007**	**0.004**
NR-14	Cu-poor	2.18	2.963	0.198	0.07	0.085	0.44	0.642	0.072	0.004	1.735	0.008	0.257	15.99	0.21
NR-14	Cu-poor	1.14	0.037	0.005	0.11	0.047	0.68	0.175	0.065	0.075	3.523	0.011	0.009	0.73	0.03
NR-14	Cu-poor	3.26	0.189	0.025	0.40	0.179	0.97	0.113	0.036	0.045	6.772	0.014	0.119	8.76	0.62
NR-14	Cu-poor	4.59	0.814	0.101	0.05	0.047	0.26	0.141	0.055	0.052	0.902	0.042	0.241	16.21	0.21
NR-14	Cu-poor	1.64	0.037	0.005	0.05	0.047	0.62	0.118	0.050	0.054	0.710	0.033	0.049	5.76	0.10
NR-14 (N=5)		**2.18**	**0.189**	**0.025**	**0.07**	**0.047**	**0.62**	**0.141**	**0.055**	**0.052**	**1.735**	**0.014**	**0.119**	**8.76**	**0.21**
NR-11	Cu-poor	2.28	0.055	0.005	0.05	0.047	3.97	0.156	0.225	0.547	0.433	0.008	0.189	1.97	0.28
NR-11	Cu-poor	4.82	0.037	0.005	0.07	0.047	3.91	0.133	0.221	0.453	0.977	0.041	3.451	16.28	0.58
NR-11	Cu-poor	1.66	0.037	0.029	0.88	0.059	1.37	0.160	0.088	0.456	0.843	0.035	1.449	1.21	0.03
NR-11	Cu-poor	3.00	0.037	0.005	0.06	0.047	2.51	0.154	0.316	0.537	0.013	0.015	0.606	3.26	0.15
NR-11	Cu-poor	3.22	0.037	0.005	0.07	0.047	4.82	0.208	0.221	0.554	0.446	0.046	1.335	2.04	0.29
NR-11	Cu-poor	2.12	0.078	0.005	0.08	0.047	3.09	0.175	0.274	0.583	2.116	0.019	1.368	25.07	0.91
NR-11 (N=6)		**2.64**	**0.037**	**0.005**	**0.07**	**0.047**	**3.50**	**0.158**	**0.223**	**0.542**	**0.645**	**0.027**	**1.351**	**2.65**	**0.29**
NR-8	Cu-rich	0.64	0.037	0.005	0.05	0.047	2.18	0.543	0.697	1.602	37.021	0.030	0.099	57.31	1.43
NR-8	Cu-rich	0.54	0.037	0.005	0.13	0.047	2.16	0.419	0.537	1.742	31.713	0.008	0.091	51.12	0.35
NR-8	Cu-rich	6.22	0.469	0.005	0.22	0.047	2.57	0.582	0.755	1.934	11.754	0.518	2.702	13.51	1.99
NR-8	Cu-rich	0.92	0.087	0.005	0.05	0.047	0.81	0.282	0.280	0.889	22.955	0.056	0.899	1.50	0.05
NR-8 (N=4)		**0.78**	**0.062**	**0.005**	**0.09**	**0.047**	**2.17**	**0.481**	**0.617**	**1.672**	**27.334**	**0.043**	**0.499**	**32.32**	**0.89**
90MC15	Cu-rich	17.61	0.446	0.005	0.09	0.047	35.88	0.093	0.017	0.004	4.558	0.008	0.335	7.75	1.60
90MC15	Cu-rich	33.54	0.599	0.009	0.07	0.047	34.42	0.010	0.017	0.004	1.986	0.008	1.726	11.56	0.23
90MC15	Cu-rich	8.14	0.075	0.037	0.05	0.047	33.41	0.560	0.017	0.016	0.837	0.008	0.270	2.51	0.79
90MC15	Cu-rich	53.72	2.605	0.426	0.08	0.047	36.50	0.541	0.017	0.009	2.930	0.019	0.648	14.62	1.07
90MC15	Cu-rich	59.58	0.055	0.005	0.05	0.047	39.56	0.165	0.017	0.004	0.133	0.008	0.130	0.48	1.58
90MC15 (N=5)		**33.54**	**0.446**	**0.009**	**0.07**	**0.047**	**35.88**	**0.165**	**0.017**	**0.004**	**1.986**	**0.008**	**0.335**	**7.75**	**1.07**

ANNEXE 5 – Cont.

Sample	Ore type	Intrusion	S	Fe	Ni	^{59}Co	^{65}Cu	^{66}Zn	^{75}As	^{82}Se	^{95}Mo	^{101}Ru	^{103}Rh	^{108}Pd
			%	%	%	ppm	ppm	ppm	ppm	ppm	ppm	ppm	ppm	ppm
Limit of detection			**0.5**	**0.5**	**0.5**	**0.007**	**0.187**	**0.174**	**0.065**	**1.824**	**0.020**	**0.015**	**0.002**	**0.008**
90MC5	Cu-rich	Noril'sk I				3487	11363	1.08	0.524	170.6	0.365	0.247	0.725	996.3
90MC5	Cu-rich	Noril'sk I				4106	24094	1.89	0.101	168.7	0.031	0.051	0.002	1016
90MC5	Cu-rich	Noril'sk I	31.2	30.6	35.6	3787	17257	9.12	0.176	170.0	0.208	0.196	0.026	961.1
90MC5	Cu-rich	Noril'sk I				3256	19471	3.87	0.081	166.4	0.020	0.119	0.002	1035
90MC5	Cu-rich	Noril'sk I				3399	9931	1.05	0.514	171.9	0.238	0.153	0.345	1369
90MC5	Cu-rich	Noril'sk I				3725	12308	1.73	0.071	168.3	0.020	0.067	0.002	998.9
Median 90MC5 (N=6)			**31.2**	**30.6**	**35.6**	**3606**	**14782**	**1.81**	**0.138**	**169.3**	**0.120**	**0.136**	**0.014**	**1007**
NR-18	Cu-rich	Kharaelakh				5333	2377	23.77	0.065	71.3	0.020	0.423	0.002	270.2
NR-18	Cu-rich	Kharaelakh	33.1	29.8	37.0	5525	60.9	3.74	0.065	72.9	0.020	0.360	0.002	296.0
NR-18	Cu-rich	Kharaelakh				7098	81.4	0.98	0.065	65.8	0.020	0.344	0.002	386.8
NR-18	Cu-rich	Kharaelakh				6512	13.3	390.72	0.065	72.9	0.042	0.167	0.055	2683
Median NR-18 (N=4)			**33.1**	**29.8**	**37.0**	**6019**	**71.1**	**13.76**	**0.065**	**72.1**	**0.020**	**0.352**	**0.002**	**341.4**
NR-17	Cu-rich	Kharaelakh				9996	2.9	0.52	0.397	77.5	0.020	0.198	0.007	521.9
NR-17	Cu-rich	Kharaelakh				10208	5.2	0.48	0.254	82.4	0.025	0.138	0.002	394.0
NR-17	Cu-rich	Kharaelakh				9778	250.7	0.93	0.234	81.7	0.020	0.095	0.002	391.0
NR-17	Cu-rich	Kharaelakh	33.2	31.4	35.1	10719	18.9	0.36	0.459	89.5	0.020	0.133	0.002	369.6
NR-17	Cu-rich	Kharaelakh				10777	2.9	0.61	0.160	82.7	0.020	0.142	0.093	627.4
NR-17	Cu-rich	Kharaelakh				10341	1.4	0.30	0.241	89.5	0.020	0.096	0.002	502.1
NR-17	Cu-rich	Kharaelakh				9843	31.6	1.27	0.202	91.8	0.021	0.115	0.013	502.7
NR-17	Cu-rich	Kharaelakh				9690	1.2	0.43	0.195	88.6	0.020	0.197	0.084	710.5
Median NR-17 (N=8)			**33.2**	**31.4**	**35.1**	**10102**	**4.1**	**0.50**	**0.238**	**85.6**	**0.020**	**0.135**	**0.005**	**502.4**

ANNEXE 5 – Cont.

Sample	Ore type	^{109}Ag	^{111}Cd	^{115}In	^{118}Sn	^{121}Sb	^{130}Te	^{185}Re	^{189}Os	^{193}Ir	^{195}Pt	^{197}Au	^{205}Tl	^{208}Pb	^{209}Bi
		ppm	ppm	ppm	ppm	ppm	ppm	ppm	ppm	ppm	ppm	ppm	ppm	ppm	ppm
Limit of detection		**0.007**	**0.037**	**0.005**	**0.050**	**0.047**	**0.257**	**0.010**	**0.017**	**0.004**	**0.013**	**0.008**	**0.004**	**0.007**	**0.004**
90MC5	Cu-rich	35.30	0.847	0.005	0.05	0.047	66.29	0.089	0.059	0.024	3.842	0.008	0.290	8.53	1.33
90MC5	Cu-rich	26.34	1.169	0.005	0.06	0.047	63.69	0.010	0.017	0.004	4.135	0.008	0.384	8.17	0.08
90MC5	Cu-rich	21.07	1.302	0.005	0.06	0.047	67.86	0.016	0.017	0.004	6.838	0.008	0.378	16.70	0.37
90MC5	Cu-rich	57.31	1.325	0.031	0.07	0.047	65.71	0.010	0.017	0.004	2.670	0.008	0.886	13.25	0.02
90MC5	Cu-rich	33.21	0.606	0.005	0.05	0.047	60.33	0.041	0.017	0.004	6.219	0.008	0.205	4.95	1.62
90MC5	Cu-rich	40.70	0.931	0.012	0.06	0.047	52.10	0.010	0.017	0.004	2.475	0.008	0.355	6.45	0.03
90MC5 (N=6)		**34.25**	**1.050**	**0.005**	**0.06**	**0.047**	**64.70**	**0.013**	**0.017**	**0.004**	**3.989**	**0.008**	**0.366**	**8.35**	**0.22**
NR-18	Cu-rich	2.74	0.707	0.640	0.32	0.047	8.37	0.010	0.017	0.004	0.150	0.008	2.637	21.49	1.76
NR-18	Cu-rich	1.19	0.173	0.113	0.16	0.047	8.50	0.010	0.017	0.004	0.189	0.017	1.250	7.85	1.19
NR-18	Cu-rich	0.62	0.140	0.015	0.07	0.047	8.82	0.010	0.017	0.004	0.013	0.008	0.521	3.74	0.04
NR-18	Cu-rich	0.81	0.037	0.005	0.05	0.047	5.89	0.010	0.017	0.004	0.251	0.008	0.606	0.46	0.10
NR-18 (N=4)		**1.00**	**0.156**	**0.064**	**0.11**	**0.047**	**8.43**	**0.010**	**0.017**	**0.004**	**0.169**	**0.008**	**0.928**	**5.80**	**0.65**
NR-17	Cu-rich	1.99	0.037	0.008	0.08	0.047	8.24	0.010	0.017	0.004	0.221	0.104	0.485	12.47	0.10
NR-17	Cu-rich	2.51	0.062	0.009	0.52	0.047	2.68	0.010	0.017	0.004	0.013	0.410	1.403	70.00	0.12
NR-17	Cu-rich	6.55	0.049	0.034	0.13	0.047	8.76	0.010	0.017	0.004	0.137	0.703	0.291	7.49	0.06
NR-17	Cu-rich	4.20	0.037	0.021	0.32	0.047	4.40	0.556	0.017	0.004	0.462	0.892	1.657	99.96	0.20
NR-17	Cu-rich	4.72	0.037	0.005	0.05	0.047	5.96	0.010	0.017	0.004	0.044	1.823	0.726	32.89	0.05
NR-17	Cu-rich	3.85	0.037	0.005	0.05	0.047	2.56	0.010	0.017	0.004	0.106	0.619	0.775	31.26	0.05
NR-17	Cu-rich	4.46	0.130	0.021	0.08	0.047	6.06	0.010	0.017	0.004	0.124	0.847	1.374	19.89	0.05
NR-17	Cu-rich	2.93	0.037	0.005	2.28	0.072	3.16	0.010	0.017	0.004	0.035	0.501	0.110	1.63	0.03
NR-17 (N=8)		**4.02**	**0.037**	**0.008**	**0.10**	**0.047**	**5.18**	**0.010**	**0.017**	**0.004**	**0.115**	**0.661**	**0.751**	**25.58**	**0.06**

ANNEXE 5 – Cont.

Sample	Ore type	Intrusion	S	Fe	Ni	^{59}Co	^{65}Cu	^{66}Zn	^{75}As	^{82}Se	^{95}Mo	^{101}Ru	^{103}Rh	^{108}Pd
			%	%	%	ppm	ppm	ppm	ppm	ppm	ppm	ppm	ppm	ppm
Limit of detection			**0.5**	**0.5**	**0.5**	**0.007**	**0.187**	**0.174**	**0.065**	**1.824**	**0.020**	**0.015**	**0.002**	**0.008**
90OMZ67-5-1	Cu-rich	Kharaelakh				9442	657.7	4.07	0.586	114.0	0.423	0.077	0.038	227.9
90OMZ67-5-1	Cu-rich	Kharaelakh	34.0	33.4	32.0	11103	299.6	7.03	5.731	112.7	0.091	0.127	0.002	180.2
90OMZ67-5-1	Cu-rich	Kharaelakh				10256	46.6	1.32	1.237	116.9	0.127	0.033	0.002	40.4
Median 90OMZ67-5-1 (N=3)			**33.0**	**28.4**	**39.0**	**10256**	**299.6**	**4.07**	**1.237**	**114.0**	**0.127**	**0.077**	**0.002**	**180.2**
90OC13	Cu-rich	Kharaelakh				17192	5.3	6.84	0.150	57.3	0.020	0.134	0.005	50.3
90OC13	Cu-rich	Kharaelakh				17810	3.0	1.27	0.085	62.5	0.020	0.088	0.002	96.4
90OC13	Cu-rich	Kharaelakh				16899	60.6	3.42	0.143	100.9	0.020	0.171	0.007	67.1
90OC13	Cu-rich	Kharaelakh	32.9	33.5	32.6	17941	3.6	0.19	0.130	46.6	0.020	0.042	0.004	51.2
90OC13	Cu-rich	Kharaelakh				17615	14.0	0.28	0.065	52.7	0.020	0.015	0.002	55.5
90OC13	Cu-rich	Kharaelakh				17778	8.7	0.36	0.137	48.5	0.022	0.137	0.002	54.8
90OC13	Cu-rich	Kharaelakh				19145	42.3	3.09	0.199	59.3	0.020	0.382	0.003	52.5
Median 90OC13 (N=7)			**32.9**	**33.5**	**32.6**	**17778**	**8.7**	**1.27**	**0.137**	**57.3**	**0.020**	**0.134**	**0.003**	**54.8**
90OMZS1-3	Cu-rich	Kharaelakh	33.6	35.4	30.1	11500	102.2	0.90	0.133	52.8	0.020	0.033	0.003	140.3
90OMZS1-3	Cu-rich	Kharaelakh				11461	188.8	0.98	0.212	46.2	0.029	0.057	0.006	123.1
Median 90OMZS1-3 (N=2)			**33.6**	**35.4**	**30.1**	**11481**	**145.5**	**0.94**	**0.173**	**49.5**	**0.024**	**0.045**	**0.005**	**131.7**
NR-10	Disseminated	Noril'sk I				9257	0.8	0.19	0.065	94.1	1.986	5.730	17.029	680.8
NR-10	Disseminated	Noril'sk I	33.2	29.9	36.9	8931	1.4	1.04	0.140	91.8	0.902	6.476	14.815	260.5
NR-10	Disseminated	Noril'sk I				9801	3.1	0.39	0.215	98.3	2.833	3.420	10.614	625.2
Median NR-10 (N=3)			**33.2**	**29.9**	**36.9**	**9257**	**1.4**	**0.39**	**0.140**	**94.1**	**1.986**	**5.730**	**14.815**	**625.2**

ANNEXE 5 – Cont.

Sample	Ore type	^{109}Ag	^{111}Cd	^{115}In	^{118}Sn	^{121}Sb	^{130}Te	^{185}Re	^{189}Os	^{193}Ir	^{195}Pt	^{197}Au	^{205}Tl	^{208}Pb	^{209}Bi
		ppm	ppm	ppm	ppm	ppm	ppm	ppm	ppm	ppm	ppm	ppm	ppm	ppm	ppm
Limit of detection		**0.007**	**0.037**	**0.005**	**0.050**	**0.047**	**0.257**	**0.010**	**0.017**	**0.004**	**0.013**	**0.008**	**0.004**	**0.007**	**0.004**
90OMZ67-5-1	Cu-rich	22.79	0.150	0.005	4.75	0.068	16.35	0.010	0.017	0.004	0.013	0.035	8.205	32.56	0.06
90OMZ67-5-1	Cu-rich	14.65	0.104	0.018	0.60	0.267	17.22	0.010	0.017	0.004	0.166	0.008	0.892	74.24	1.34
90OMZ67-5-1	Cu-rich	3.29	0.037	0.005	1.92	0.047	16.83	0.010	0.017	0.004	0.013	0.008	0.247	25.72	1.43
90OMZ67-5-1 (N=3)		**14.65**	**0.104**	**0.005**	**1.92**	**0.068**	**16.83**	**0.010**	**0.017**	**0.004**	**0.013**	**0.008**	**0.892**	**32.56**	**1.34**
90OC13	Cu-rich	4.20	0.104	0.019	0.18	0.047	8.82	0.010	0.017	0.004	0.111	0.008	0.580	58.28	0.68
90OC13	Cu-rich	13.32	0.046	0.036	0.29	0.047	11.53	0.010	0.017	0.004	0.104	0.008	0.078	27.68	0.63
90OC13	Cu-rich	7.36	0.137	0.145	15.66	1.107	4.23	0.010	0.017	0.004	0.023	0.065	11.917	145.87	0.79
90OC13	Cu-rich	1.93	0.037	0.005	0.64	0.047	4.69	0.010	0.017	0.004	0.014	0.008	0.628	21.95	0.11
90OC13	Cu-rich	4.00	0.037	0.007	0.05	0.047	3.74	0.010	0.017	0.004	0.013	0.008	0.518	7.20	0.08
90OC13	Cu-rich	3.83	0.037	0.016	0.05	0.047	5.18	0.010	0.017	0.004	0.013	0.008	0.171	17.84	0.17
90OC13	Cu-rich	7.07	0.104	0.035	0.25	0.047	7.42	0.010	0.017	0.004	0.013	0.010	2.022	13.28	0.16
90OC13 (N=7)		**4.20**	**0.046**	**0.019**	**0.25**	**0.047**	**5.18**	**0.010**	**0.017**	**0.004**	**0.014**	**0.008**	**0.580**	**21.95**	**0.17**
90OMZS1-3	Cu-rich	21.78	0.085	0.005	0.15	0.047	6.09	0.010	0.017	0.004	0.287	0.008	4.558	167.03	0.31
90OMZS1-3	Cu-rich	9.61	0.059	0.005	0.31	0.055	3.97	0.010	0.017	0.004	0.075	0.010	4.428	332.11	1.02
90OMZS1-3 (N=2)		**15.69**	**0.072**	**0.005**	**0.23**	**0.051**	**5.03**	**0.010**	**0.017**	**0.004**	**0.181**	**0.009**	**4.493**	**249.57**	**0.67**
NR-10	Disseminated	0.76	0.037	0.005	0.05	0.047	7.13	0.156	1.381	2.247	15.596	0.008	0.078	2.12	0.10
NR-10	Disseminated	1.06	0.037	0.005	0.22	0.047	9.93	0.225	1.149	2.227	2.442	0.075	1.068	21.03	0.06
NR-10	Disseminated	0.34	0.037	0.005	0.05	0.047	10.00	0.197	0.609	1.241	28.392	0.008	0.342	6.87	0.01
NR-10 (N=3)		**0.76**	**0.037**	**0.005**	**0.05**	**0.047**	**9.93**	**0.197**	**1.149**	**2.227**	**15.596**	**0.008**	**0.342**	**6.87**	**0.06**

ANNEXE 6 - Complete data set of SEM-EDS and LA-ICP-MS analyses of chalcopyrite obtained for the Noril'sk-Talnakh mining district and median values for each sample. Abbreviations: N= number of individual analyses; n.r.= not reported.

ANNEXE 6

Sample	Ore type	Intrusion	S	Fe	Cu	^{59}Co	^{61}Ni	^{66}Zn	^{75}As	^{82}Se	^{95}Mo	^{101}Ru	^{103}Rh	^{108}Pd
			%	%	%	ppm	ppm	ppm	ppm	ppm	ppm	ppm	ppm	ppm
Limit of detection			**0.5**	**0.5**	**0.5**	**0.007**	**0.643**	**0.174**	**0.065**	**1.824**	**0.020**	**0.015**	**n.r.**	**0.008**
90OMZS2-3	Cu-poor	Kharaelakh				0.822	26.2	569	5.42	52.3	0.040	0.198	n.r.	0.074
90OMZS2-3	Cu-poor	Kharaelakh				0.843	38.6	351	4.56	53.3	0.029	0.231	n.r.	0.028
90OMZS2-3	Cu-poor	Kharaelakh				0.426	76.1	223	0.07	57.2	0.020	0.061	n.r.	0.008
90OMZS2-3	Cu-poor	Kharaelakh	35.0	32.3	32.5	6.695	37.4	733	0.07	54.5	0.020	0.039	n.r.	0.008
90OMZS2-3	Cu-poor	Kharaelakh				1.187	79.1	438	0.47	51.6	0.020	0.095	n.r.	0.008
90OMZS2-3	Cu-poor	Kharaelakh				4.565	133.9	642	0.07	50.8	0.029	0.058	n.r.	0.008
90OMZS2-3	Cu-poor	Kharaelakh				0.453	32.3	288	3.62	57.5	0.020	0.042	n.r.	0.008
Median 90OMZS2-3 (N=7)			**35.0**	**32.3**	**32.5**	**0.843**	**38.6**	**438**	**0.47**	**53.3**	**0.020**	**0.061**	n.r.	**0.008**
90KMZ5	Cu-poor	Talnakh				0.216	10.7	400	0.07	61.8	0.020	0.048	n.r.	0.008
90KMZ5	Cu-poor	Talnakh				0.545	51.7	306	0.07	63.0	1.801	0.103	n.r.	0.008
90KMZ5	Cu-poor	Talnakh	33.3	31.2	34.1	10.955	270.8	295	0.67	59.9	2.069	0.133	n.r.	0.014
90KMZ5	Cu-poor	Talnakh				0.234	12.2	405	0.07	60.9	0.020	0.092	n.r.	0.008
90KMZ5	Cu-poor	Talnakh				18.562	654.2	466	0.07	60.5	0.061	0.118	n.r.	1.021
Median 90OKMZ5 (N=5)			**33.3**	**31.2**	**34.1**	**0.545**	**51.7**	**400**	**0.07**	**60.9**	**0.061**	**0.103**	n.r.	**0.008**
NR-6	Cu-poor	Noril'sk I				10.651	639.0	587	0.07	28.9	0.020	0.156	n.r.	0.304
NR-6	Cu-poor	Noril'sk I	35.1	30.3	34.0	7.303	699.9	411	0.07	28.5	0.020	0.204	n.r.	0.171
NR-6	Cu-poor	Noril'sk I				0.432	52.9	563	0.07	27.4	0.020	0.204	n.r.	0.008
NR-6	Cu-poor	Noril'sk I				0.913	47.2	432	0.07	26.0	0.020	0.143	n.r.	0.045
Median NR-6 (N=4)			**35.1**	**30.3**	**34.0**	**4.108**	**346.0**	**498**	**0.07**	**27.9**	**0.020**	**0.180**	n.r.	**0.108**

ANNEXE 6 – Cont.

Sample	Ore type	^{109}Ag	^{111}Cd	^{115}In	^{118}Sn	^{121}Sb	^{130}Te	^{185}Re	^{189}Os	^{193}Ir	^{195}Pt	^{197}Au	^{205}Tl	^{208}Pb	^{209}Bi
		ppm	ppm	ppm	ppm	ppm	ppm	ppm	ppm	ppm	ppm	ppm	ppm	ppm	ppm
Limit of detection		**0.007**	**0.037**	**0.005**	**0.050**	**0.047**	**0.257**	**0.010**	**0.017**	**0.004**	**0.013**	**0.008**	**0.004**	**0.007**	**0.004**
90OMZS2-3	Cu-poor	2.62	7.21	1.62	2.62	0.143	1.64	0.010	0.017	0.004	0.639	0.008	0.011	44.73	0.064
90OMZS2-3	Cu-poor	5.90	6.97	1.58	2.43	0.107	1.13	0.010	0.017	0.004	0.013	0.008	0.019	10.59	0.062
90OMZS2-3	Cu-poor	2.76	4.90	1.71	1.53	0.047	2.29	0.010	0.017	0.004	0.013	0.008	0.028	15.28	0.064
90OMZS2-3	Cu-poor	1.79	8.79	2.31	2.88	0.047	2.77	0.010	0.017	0.004	0.073	0.008	0.045	52.64	0.155
90OMZS2-3	Cu-poor	4.56	6.36	1.38	1.94	0.047	1.70	0.010	0.017	0.004	0.013	0.008	0.004	42.72	0.118
90OMZS2-3	Cu-poor	4.02	6.66	1.50	2.80	0.047	1.16	0.010	0.017	0.004	0.013	0.008	0.040	8.98	0.052
90OMZS2-3	Cu-poor	3.37	5.33	1.88	1.97	0.075	3.22	0.010	0.017	0.004	0.295	0.008	0.044	19.87	0.079
90OMZS2-3 (N=7)		**3.37**	**6.66**	**1.62**	**2.43**	**0.047**	**1.70**	**0.010**	**0.017**	**0.004**	**0.013**	**0.008**	**0.028**	**19.87**	**0.064**
90KMZ5	Cu-poor	12.81	3.62	0.80	3.85	0.047	2.25	0.010	0.017	0.004	0.210	0.008	0.004	1.99	0.219
90KMZ5	Cu-poor	13.94	3.65	0.38	1.17	0.113	1.36	0.334	0.228	0.268	0.487	0.008	0.087	2.23	0.175
90KMZ5	Cu-poor	12.51	3.47	0.15	0.26	0.076	1.13	0.410	0.180	0.149	0.882	0.008	1.022	6.97	0.609
90KMZ5	Cu-poor	11.62	3.77	0.49	2.16	0.047	2.46	0.010	0.017	0.004	0.456	0.008	0.008	1.72	0.170
90KMZ5	Cu-poor	13.48	4.93	0.52	1.54	0.047	2.01	0.164	0.017	0.004	0.277	0.008	2.130	3.69	0.110
90OKMZ5 (N=5)		**12.81**	**3.65**	**0.49**	**1.54**	**0.047**	**2.01**	**0.164**	**0.017**	**0.004**	**0.456**	**0.008**	**0.087**	**2.23**	**0.175**
NR-6	Cu-poor	2.74	11.69	0.75	0.16	0.047	0.39	0.010	0.017	0.004	0.051	0.008	0.019	18.26	0.197
NR-6	Cu-poor	2.01	9.04	0.53	0.09	0.047	0.33	0.010	0.017	0.004	0.085	0.008	0.004	11.78	0.096
NR-6	Cu-poor	4.08	13.54	0.50	0.05	0.047	0.51	0.010	0.017	0.004	0.030	0.008	0.009	14.15	0.086
NR-6	Cu-poor	2.14	9.62	0.73	0.10	0.047	0.50	0.010	0.017	0.004	0.119	0.008	0.009	11.02	0.108
NR-6 (N=4)		**2.44**	**10.65**	**0.63**	**0.10**	**0.047**	**0.44**	**0.010**	**0.017**	**0.004**	**0.068**	**0.008**	**0.009**	**12.96**	**0.102**

ANNEXE 6 – Cont.

Sample	Ore type	Intrusion	S	Fe	Cu	^{59}Co	^{61}Ni	^{66}Zn	^{75}As	^{82}Se	^{95}Mo	^{101}Ru	^{103}Rh	^{108}Pd
			%	%	%	ppm	ppm	ppm	ppm	ppm	ppm	ppm	ppm	ppm
Limit of detection			**0.5**	**0.5**	**0.5**	**0.007**	**0.643**	**0.174**	**0.065**	**1.824**	**0.020**	**0.015**	**n.r.**	**0.008**
90OMZS2-2	Cu-poor	Kharaelakh				0.034	7.4	301	0.07	49.9	0.020	0.085	n.r.	0.008
90OMZS2-2	Cu-poor	Kharaelakh				0.186	9.4	453	0.07	55.4	0.020	0.063	n.r.	0.008
90OMZS2-2	Cu-poor	Kharaelakh				0.061	5.8	260	0.07	48.4	0.020	0.085	n.r.	0.008
90OMZS2-2	Cu-poor	Kharaelakh	35.7	30.3	34.3	0.107	7.2	353	0.07	51.6	0.020	0.070	n.r.	0.008
90OMZS2-2	Cu-poor	Kharaelakh				0.070	9.0	453	0.07	54.7	0.020	0.097	n.r.	0.008
90OMZS2-2	Cu-poor	Kharaelakh				2.008	14.0	374	0.05	56.1	0.020	0.100	n.r.	0.008
90OMZS2-2	Cu-poor	Kharaelakh				0.100	7.5	459	0.07	58.1	0.020	0.119	n.r.	0.008
Median 90OMZS2-2 (N=7)			**35.7**	**30.3**	**34.3**	**0.100**	**7.5**	**374**	**0.07**	**54.7**	**0.020**	**0.085**	n.r.	**0.008**
NR-13	Cu-poor	Kharaelakh				0.721	57.8	782	0.07	29.0	0.020	0.134	n.r.	0.008
NR-13	Cu-poor	Kharaelakh				0.569	52.3	694	0.07	29.4	0.020	0.122	n.r.	0.008
NR-13	Cu-poor	Kharaelakh				1.126	130.8	779	0.07	30.8	0.020	0.132	n.r.	0.008
NR-13	Cu-poor	Kharaelakh	34.9	30.2	33.7	0.557	54.2	642	0.07	29.5	0.020	0.109	n.r.	0.008
NR-13	Cu-poor	Kharaelakh				0.943	65.7	1095	0.07	29.5	0.020	0.091	n.r.	0.008
NR-13	Cu-poor	Kharaelakh				0.383	51.4	520	0.07	29.1	0.020	0.137	n.r.	0.008
Median NR-13 (N=7)			**34.9**	**30.2**	**33.7**	**0.645**	**56.0**	**736**	**0.07**	**29.4**	**0.020**	**0.127**	n.r.	**0.008**
NR-14	Cu-poor	Kharaelakh				0.353	53.3	566	0.07	38.7	0.020	0.119	n.r.	0.008
NR-14	Cu-poor	Kharaelakh				0.218	59.0	444	0.07	38.3	0.020	0.122	n.r.	0.017
NR-14	Cu-poor	Kharaelakh				0.529	58.7	764	0.07	37.3	0.020	0.112	n.r.	0.008
NR-14	Cu-poor	Kharaelakh	34.8	30.2	33.9	0.919	79.4	405	0.07	37.6	0.020	0.116	n.r.	0.008
NR-14	Cu-poor	Kharaelakh				0.505	69.1	666	0.07	37.1	0.020	0.131	n.r.	0.008
NR-14	Cu-poor	Kharaelakh				0.240	58.4	466	0.07	39.7	0.020	0.115	n.r.	0.008
Median NR-14 (N=6)			**34.8**	**30.2**	**33.9**	**0.429**	**58.9**	**516**	**0.07**	**38.0**	**0.020**	**0.117**	n.r.	**0.008**

ANNEXE 6 – Cont.

Sample	Ore type	^{109}Ag	^{111}Cd	^{115}In	^{118}Sn	^{121}Sb	^{130}Te	^{185}Re	^{189}Os	^{193}Ir	^{195}Pt	^{197}Au	^{205}Tl	^{208}Pb	^{209}Bi
		ppm	ppm	ppm	ppm	ppm	ppm	ppm	ppm	ppm	ppm	ppm	ppm	ppm	ppm
Limit of detection		**0.007**	**0.037**	**0.005**	**0.050**	**0.047**	**0.257**	**0.010**	**0.017**	**0.004**	**0.013**	**0.008**	**0.004**	**0.007**	**0.004**
90OMZS2-2	Cu-poor	2.67	10.25	2.25	0.67	0.047	2.16	0.010	0.017	0.004	0.044	0.008	0.059	44.43	0.015
90OMZS2-2	Cu-poor	2.64	13.05	2.60	1.05	0.047	2.28	0.010	0.017	0.004	0.020	0.008	0.011	94.33	0.019
90OMZS2-2	Cu-poor	2.31	9.77	2.46	0.91	0.047	2.31	0.010	0.017	0.004	0.038	0.008	0.004	71.21	0.020
90OMZS2-2	Cu-poor	2.28	12.93	2.31	0.91	0.047	2.58	0.010	0.017	0.004	0.023	0.008	0.008	79.09	0.014
90OMZS2-2	Cu-poor	2.40	13.30	2.02	1.30	0.047	2.65	0.010	0.017	0.004	0.047	0.008	0.008	56.48	0.017
90OMZS2-2	Cu-poor	2.30	11.50	2.50	0.79	0.047	2.89	0.010	0.017	0.004	0.019	0.008	0.019	45.04	0.030
90OMZS2-2	Cu-poor	1.91	12.39	2.14	1.38	0.047	2.80	0.010	0.017	0.004	0.033	0.008	0.004	74.71	0.017
90OMZS2-2 (N=7)		**2.31**	**12.39**	**2.31**	**0.91**	**0.047**	**2.58**	**0.010**	**0.017**	**0.004**	**0.033**	**0.008**	**0.008**	**71.21**	**0.017**
NR-13	Cu-poor	0.53	6.54	1.27	2.43	0.047	0.87	0.010	0.017	0.004	0.097	0.008	0.004	25.84	0.073
NR-13	Cu-poor	0.77	5.93	1.48	2.38	0.047	0.77	0.010	0.017	0.004	0.176	0.008	0.096	19.69	0.116
NR-13	Cu-poor	1.34	7.18	1.43	1.70	0.047	1.24	0.010	0.017	0.004	0.175	0.008	0.011	30.55	0.081
NR-13	Cu-poor	0.70	6.03	1.23	2.35	0.047	1.29	0.010	0.017	0.004	0.138	0.008	0.004	24.59	0.060
NR-13	Cu-poor	1.83	11.29	1.35	1.67	0.047	0.82	0.010	0.017	0.004	0.114	0.008	0.049	31.04	0.074
NR-13	Cu-poor	0.63	4.84	1.15	2.35	0.047	1.00	0.010	0.017	0.004	0.086	0.008	0.004	44.00	0.059
NR-13 (N=7)		**0.73**	**6.28**	**1.31**	**2.35**	**0.047**	**0.94**	**0.010**	**0.017**	**0.004**	**0.126**	**0.008**	**0.008**	**28.19**	**0.073**
NR-14	Cu-poor	0.65	6.88	1.42	1.47	0.047	0.97	0.010	0.017	0.004	0.074	0.008	0.095	23.43	0.093
NR-14	Cu-poor	0.63	5.48	1.49	1.83	0.047	0.86	0.010	0.017	0.004	0.062	0.008	0.058	45.16	0.090
NR-14	Cu-poor	1.07	8.46	1.46	2.18	0.047	1.55	0.010	0.017	0.004	0.240	0.008	0.012	21.73	0.079
NR-14	Cu-poor	1.20	5.90	1.73	2.68	0.047	1.79	0.010	0.017	0.004	0.396	0.008	0.009	12.35	0.098
NR-14	Cu-poor	1.30	8.37	1.33	1.73	0.047	1.18	0.010	0.017	0.004	0.140	0.008	0.426	33.20	0.199
NR-14	Cu-poor	1.54	7.88	1.72	1.63	0.047	0.81	0.010	0.017	0.004	0.097	0.008	0.158	42.39	0.127
NR-14 (N=6)		**1.14**	**7.38**	**1.48**	**1.78**	**0.047**	**1.08**	**0.010**	**0.017**	**0.004**	**0.119**	**0.008**	**0.076**	**28.32**	**0.096**

ANNEXE 6 – Cont.

Sample	Ore type	Intrusion	S	Fe	Cu	^{59}Co	^{61}Ni	^{66}Zn	^{75}As	^{82}Se	^{95}Mo	^{101}Ru	^{103}Rh	^{108}Pd
			%	%	%	ppm	ppm	ppm	ppm	ppm	ppm	ppm	ppm	ppm
Limit of detection			**0.5**	**0.5**	**0.5**	**0.007**	**0.643**	**0.174**	**0.065**	**1.824**	**0.020**	**0.015**	**n.r.**	**0.008**
NR-11	Cu-poor	Noril'sk I	33.3	30.7	34.8	0.146	24.6	505	0.07	87.9	0.158	0.103	n.r.	0.089
NR-11	Cu-poor	Noril'sk I				30.734	2221	414	0.07	81.8	0.020	0.122	n.r.	11.893
NR-11	Cu-poor	Noril'sk I				0.131	15.8	272	0.07	72.7	0.020	0.103	n.r.	0.027
NR-11	Cu-poor	Noril'sk I				0.035	10.8	341	0.07	85.0	0.020	0.106	n.r.	0.021
Median NR-11 (N=4)			**33.3**	**30.7**	**34.8**	**0.138**	**20.2**	**377**	**0.07**	**83.4**	**0.020**	**0.104**	n.r.	**0.058**
NR-8	Cu-rich	Noril'sk I	34.7	30.2	33.6	0.639	37.7	627	0.07	42.6	0.020	0.164	n.r.	0.008
NR-8	Cu-rich	Noril'sk I				0.292	25.9	730	0.61	41.5	0.020	0.201	n.r.	0.038
NR-8	Cu-rich	Noril'sk I				6.086	210.0	673	0.07	39.2	0.020	0.179	n.r.	1.010
NR-8	Cu-rich	Noril'sk I				0.338	22.8	563	0.07	45.0	0.020	0.182	n.r.	0.071
NR-8	Cu-rich	Noril'sk I				2.130	203.9	569	0.07	39.7	0.020	0.130	n.r.	1.071
Median NR-8 (N=5)			**34.7**	**30.2**	**33.6**	**0.639**	**37.7**	**627**	**0.07**	**41.5**	**0.020**	**0.179**	n.r.	**0.071**
90MC15	Cu-rich	Noril'sk I	33.5	30.5	34.6	0.009	49.3	83	0.22	135.7	0.058	0.080	n.r.	0.911
90MC15	Cu-rich	Noril'sk I				0.007	48.4	83	0.16	138.5	0.085	0.045	n.r.	0.384
90MC15	Cu-rich	Noril'sk I				0.015	44.4	76	0.14	133.6	0.079	0.090	n.r.	0.626
90MC15	Cu-rich	Noril'sk I				0.761	410.8	72	0.16	130.5	0.055	0.066	n.r.	0.730
90MC15	Cu-rich	Noril'sk I				0.074	56.6	213	0.13	133.6	0.097	0.092	n.r.	0.756
90MC15	Cu-rich	Noril'sk I				0.008	42.6	73	0.20	132.7	0.082	0.094	n.r.	1.017
Median 90MC15 (N=6)			**33.5**	**30.5**	**34.6**	**0.012**	**48.8**	**79**	**0.16**	**133.6**	**0.081**	**0.085**	n.r.	**0.743**

ANNEXE 6 – Cont.

Sample	Ore type	^{109}Ag	^{111}Cd	^{115}In	^{118}Sn	^{121}Sb	^{130}Te	^{185}Re	^{189}Os	^{193}Ir	^{195}Pt	^{197}Au	^{205}Tl	^{208}Pb	^{209}Bi
		ppm	ppm	ppm	ppm	ppm	ppm	ppm	ppm	ppm	ppm	ppm	ppm	ppm	ppm
Limit of detection		**0.007**	**0.037**	**0.005**	**0.050**	**0.047**	**0.257**	**0.010**	**0.017**	**0.004**	**0.013**	**0.008**	**0.004**	**0.007**	**0.004**
NR-11	Cu-poor	28.30	4.50	1.58	0.40	0.047	11.53	0.010	0.017	0.007	0.195	0.008	0.100	6.66	1.102
NR-11	Cu-poor	35.60	4.69	1.72	0.09	0.047	12.66	0.010	0.017	0.004	0.350	0.012	0.274	33.59	0.057
NR-11	Cu-poor	27.48	2.83	1.19	0.48	0.047	4.90	0.010	0.017	0.004	0.347	0.008	0.061	17.53	0.161
NR-11	Cu-poor	29.06	3.41	1.40	0.28	0.047	7.18	0.010	0.017	0.004	0.323	0.008	0.137	18.23	0.124
NR-11 (N=4)		**28.68**	**3.96**	**1.49**	**0.34**	**0.047**	**9.36**	**0.010**	**0.017**	**0.004**	**0.335**	**0.008**	**0.119**	**17.88**	**0.143**
NR-8	Cu-rich	14.76	8.37	1.61	2.37	0.047	1.80	0.010	0.017	0.004	0.044	0.008	0.167	2.96	0.108
NR-8	Cu-rich	18.71	8.64	1.68	1.95	0.047	1.95	0.010	0.017	0.004	0.107	0.008	0.082	8.70	0.138
NR-8	Cu-rich	14.64	7.97	1.94	7.42	0.047	1.90	0.010	0.017	0.004	0.155	0.008	0.155	10.68	0.188
NR-8	Cu-rich	17.56	7.30	2.14	2.62	0.047	2.00	0.010	0.017	0.004	0.043	0.008	0.444	13.27	0.487
NR-8	Cu-rich	46.56	7.06	1.33	1.80	0.047	1.75	0.010	0.017	0.004	0.063	0.008	0.144	4.75	0.142
NR-8 (N=5)		**17.56**	**7.97**	**1.68**	**2.37**	**0.047**	**1.90**	**0.010**	**0.017**	**0.004**	**0.063**	**0.008**	**0.155**	**8.70**	**0.142**
90MC15	Cu-rich	11.75	3.86	1.31	0.05	0.047	39.47	0.010	0.017	0.004	0.037	0.008	0.828	1.44	0.017
90MC15	Cu-rich	12.14	3.77	1.77	0.05	0.047	39.19	0.010	0.017	0.004	0.029	0.008	1.019	1.16	0.004
90MC15	Cu-rich	7.77	3.56	1.41	0.05	0.047	39.29	0.010	0.017	0.004	0.033	0.008	1.056	1.19	0.004
90MC15	Cu-rich	10.16	4.17	0.76	0.05	0.047	39.44	0.010	0.017	0.004	0.025	0.008	1.083	0.87	0.008
90MC15	Cu-rich	14.73	5.84	1.71	0.05	0.047	40.14	0.010	0.017	0.004	0.042	0.008	1.086	1.47	0.004
90MC15	Cu-rich	9.13	3.16	1.12	0.05	0.047	39.99	0.010	0.017	0.004	0.023	0.008	0.989	1.13	0.005
90MC15 (N=6)		**10.95**	**3.82**	**1.36**	**0.05**	**0.047**	**39.45**	**0.010**	**0.017**	**0.004**	**0.031**	**0.008**	**1.038**	**1.17**	**0.004**

ANNEXE 6 – Cont.

Sample	Ore type	Intrusion	S	Fe	Cu	^{59}Co	^{61}Ni	^{66}Zn	^{75}As	^{82}Se	^{95}Mo	^{101}Ru	^{103}Rh	^{108}Pd
			%	%	%	ppm	ppm	ppm	ppm	ppm	ppm	ppm	ppm	ppm
Limit of detection			**0.5**	**0.5**	**0.5**	**0.007**	**0.643**	**0.174**	**0.065**	**1.824**	**0.020**	**0.015**	**n.r.**	**0.008**
90MC5	Cu-rich	Noril'sk I	32.4	30.7	33.3	0.116	41.4	121	0.07	172.5	0.041	0.078	n.r.	5.701
90MC5	Cu-rich	Noril'sk I				0.077	41.1	66	0.07	179.2	0.076	0.116	n.r.	2.720
90MC5	Cu-rich	Noril'sk I				0.057	29.6	152	0.07	172.2	0.020	0.099	n.r.	4.402
90MC5	Cu-rich	Noril'sk I				0.102	35.9	107	0.07	174.7	0.022	0.073	n.r.	5.266
90MC5	Cu-rich	Noril'sk I				0.049	41.1	68	0.07	172.2	0.067	0.116	n.r.	4.198
90MC5	Cu-rich	Noril'sk I				0.042	36.7	75	0.07	168.3	0.113	0.106	n.r.	2.602
Median 90MC5 (N=6)			**32.4**	**30.7**	**33.3**	**0.067**	**38.9**	**91**	**0.07**	**172.4**	**0.054**	**0.103**	n.r.	**4.300**
NR-18	Cu-rich	Kharaelakh	34.7	30.1	33.9	0.170	36.2	364	0.07	74.2	0.020	0.134	n.r.	3.122
NR-18	Cu-rich	Kharaelakh				60.860	486.9	405	0.07	72.7	0.020	0.166	n.r.	1.306
NR-18	Cu-rich	Kharaelakh				0.149	32.9	584	0.07	76.7	0.020	0.143	n.r.	3.442
NR-18	Cu-rich	Kharaelakh				0.085	36.5	311	0.07	69.1	0.020	0.131	n.r.	0.287
Median NR-18 (N=4)			**34.7**	**30.1**	**33.9**	**0.160**	**36.4**	**384**	**0.07**	**73.5**	**0.020**	**0.138**	n.r.	**2.214**
NR-17	Cu-rich	Kharaelakh	34.5	30.1	33.7	0.563	75.2	426	0.07	88.9	0.020	0.097	n.r.	0.538
NR-17	Cu-rich	Kharaelakh				0.730	61.2	417	0.07	88.9	0.020	0.125	n.r.	0.700
NR-17	Cu-rich	Kharaelakh				1.035	67.6	1126	0.11	88.9	0.020	0.097	n.r.	0.008
NR-17	Cu-rich	Kharaelakh				0.234	50.8	459	0.07	90.7	0.020	0.112	n.r.	0.008
NR-17	Cu-rich	Kharaelakh				6.725	270.8	581	0.09	87.9	0.020	0.097	n.r.	1.392
NR-17	Cu-rich	Kharaelakh				0.186	38.3	393	0.07	92.2	0.020	0.100	n.r.	0.473
NR-17	Cu-rich	Kharaelakh				0.329	43.2	584	0.08	111.1	0.020	0.116	n.r.	0.731
Median NR-17 (N=7)			**34.5**	**30.1**	**33.7**	**0.563**	**61.2**	**459**	**0.07**	**88.9**	**0.020**	**0.100**	n.r.	**0.538**

ANNEXE 6 – Cont.

Sample	Ore type	^{109}Ag	^{111}Cd	^{115}In	^{118}Sn	^{121}Sb	^{130}Te	^{185}Re	^{189}Os	^{193}Ir	^{195}Pt	^{197}Au	^{205}Tl	^{208}Pb	^{209}Bi
		ppm	ppm	ppm	ppm	ppm	ppm	ppm	ppm	ppm	ppm	ppm	ppm	ppm	ppm
Limit of detection		**0.007**	**0.037**	**0.005**	**0.050**	**0.047**	**0.257**	**0.010**	**0.017**	**0.004**	**0.013**	**0.008**	**0.004**	**0.007**	**0.004**
90MC5	Cu-rich	9.94	6.03	1.10	0.07	0.047	64.42	0.010	0.017	0.004	0.033	0.008	0.319	0.46	0.006
90MC5	Cu-rich	12.57	5.08	0.14	0.05	0.047	69.44	0.010	0.017	0.004	0.016	0.008	0.374	0.23	0.004
90MC5	Cu-rich	11.49	6.03	0.53	0.05	0.047	61.04	0.010	0.017	0.004	0.085	0.008	0.708	0.58	0.004
90MC5	Cu-rich	10.38	6.30	1.22	0.05	0.047	69.99	0.010	0.017	0.004	0.032	0.008	0.858	0.32	0.004
90MC5	Cu-rich	11.29	5.57	0.41	0.09	0.047	63.36	0.010	0.017	0.004	0.079	0.008	1.041	0.14	0.004
90MC5	Cu-rich	10.27	5.69	0.51	0.05	0.047	52.34	0.010	0.017	0.004	0.046	0.008	0.968	0.13	0.004
90MC5 (N=6)		**10.83**	**5.86**	**0.52**	**0.05**	**0.047**	**63.89**	**0.010**	**0.017**	**0.004**	**0.040**	**0.008**	**0.783**	**0.28**	**0.004**
NR-18	Cu-rich	8.31	21.21	2.06	1.97	0.047	9.62	0.010	0.017	0.004	0.420	0.012	0.539	0.32	0.895
NR-18	Cu-rich	8.19	21.82	3.90	2.30	0.047	7.21	0.010	0.017	0.004	0.076	0.010	0.050	0.48	0.609
NR-18	Cu-rich	5.10	26.17	2.49	1.64	0.047	9.25	0.010	0.017	0.004	0.246	0.016	0.155	0.22	1.643
NR-18	Cu-rich	2.86	14.27	3.86	1.56	0.047	5.66	0.010	0.017	0.004	0.030	0.010	0.134	0.42	0.578
NR-18 (N=4)		**6.64**	**21.51**	**3.17**	**1.80**	**0.047**	**8.23**	**0.010**	**0.017**	**0.004**	**0.161**	**0.011**	**0.145**	**0.37**	**0.752**
NR-17	Cu-rich	21.61	34.69	3.78	6.57	0.047	12.45	0.010	0.017	0.004	0.265	1.278	0.128	23.92	0.913
NR-17	Cu-rich	10.47	37.12	3.44	4.92	0.047	13.57	0.010	0.017	0.004	0.456	0.056	0.110	12.72	0.353
NR-17	Cu-rich	8.79	69.68	4.70	3.20	0.047	14.36	0.010	0.017	0.004	0.822	0.055	0.085	16.25	0.609
NR-17	Cu-rich	2.68	36.91	3.32	6.85	0.047	6.33	0.010	0.017	0.004	0.113	0.027	0.071	24.10	0.148
NR-17	Cu-rich	8.92	44.43	2.80	4.19	0.047	11.93	0.010	0.017	0.004	0.484	0.053	0.105	27.23	0.639
NR-17	Cu-rich	6.94	37.73	3.66	4.63	0.047	11.84	0.010	0.017	0.004	0.170	0.075	0.154	16.89	0.197
NR-17	Cu-rich	8.67	46.25	5.09	3.97	0.047	17.07	0.010	0.017	0.004	0.316	0.075	0.133	22.40	0.262
NR-17 (N=7)		**8.79**	**37.73**	**3.66**	**4.63**	**0.047**	**12.45**	**0.010**	**0.017**	**0.004**	**0.316**	**0.056**	**0.110**	**22.40**	**0.353**

ANNEXE 6 – Cont.

Sample	Ore type	Intrusion	S	Fe	Cu	^{59}Co	^{61}Ni	^{66}Zn	^{75}As	^{82}Se	^{95}Mo	^{101}Ru	^{103}Rh	^{108}Pd
			%	%	%	ppm	ppm	ppm	ppm	ppm	ppm	ppm	ppm	ppm
Limit of detection			**0.5**	**0.5**	**0.5**	**0.007**	**0.643**	**0.174**	**0.065**	**1.824**	**0.020**	**0.015**	**n.r.**	**0.008**
90OMZ67-5-1	Cu-rich	Kharaelakh	35.5	30.7	34.5	0.186	73.0	371	0.17	93.4	0.051	0.087	n.r.	0.008
90OMZ67-5-1	Cu-rich	Kharaelakh				0.186	82.8	596	0.08	85.8	0.058	0.091	n.r.	0.008
90OMZ67-5-1	Cu-rich	Kharaelakh				0.195	67.3	320	0.19	91.6	0.055	0.082	n.r.	0.008
90OMZ67-5-1	Cu-rich	Kharaelakh				0.219	73.3	116	0.11	86.9	0.086	0.111	n.r.	0.008
Median 90OMZ67-5-1 (N=4)			**35.5**	**30.7**	**34.5**	**0.190**	**73.2**	**345**	**0.14**	**89.3**	**0.056**	**0.089**	n.r.	**0.008**
90OC13	Cu-rich	Kharaelakh	33.9	30.6	34.4	0.761	25.3	633	0.07	58.4	0.020	0.122	n.r.	0.113
90OC13	Cu-rich	Kharaelakh				0.170	14.9	298	0.07	65.7	0.020	0.079	n.r.	0.069
90OC13	Cu-rich	Kharaelakh				0.216	15.5	490	0.07	65.7	0.020	0.100	n.r.	0.008
90OC13	Cu-rich	Kharaelakh				0.176	14.0	533	0.07	57.8	0.020	0.060	n.r.	0.008
90OC13	Cu-rich	Kharaelakh				1.339	42.9	2130	0.07	61.5	0.020	0.088	n.r.	0.008
90OC13	Cu-rich	Kharaelakh				0.204	15.5	332	0.07	59.2	0.020	0.091	n.r.	0.007
90OC13	Cu-rich	Kharaelakh				0.316	15.9	432	0.07	60.7	0.020	0.089	n.r.	0.008
Median 90OC13 (N=7)			**33.9**	**30.6**	**34.4**	**0.216**	**15.5**	**490**	**0.07**	**60.7**	**0.020**	**0.089**	n.r.	**0.008**
90OMZS1-3	Cu-rich	Kharaelakh	35.0	31.0	33.6	0.082	3.4	161	0.07	66.0	0.020	0.091	n.r.	0.008
90OMZS1-3	Cu-rich	Kharaelakh				0.092	5.4	253	0.07	64.8	0.020	0.046	n.r.	0.008
90OMZS1-3	Cu-rich	Kharaelakh				18.258	9.1	202	0.07	72.1	0.020	0.075	n.r.	1.402
90OMZS1-3	Cu-rich	Kharaelakh				0.093	5.3	181	0.07	62.0	0.020	0.069	n.r.	0.070
90OMZS1-3	Cu-rich	Kharaelakh				0.882	4.0	178	0.07	67.0	0.020	0.089	n.r.	0.028
90OMZS1-3	Cu-rich	Kharaelakh				0.096	5.5	180	0.07	70.6	0.020	0.082	n.r.	0.008
90OMZS1-3	Cu-rich	Kharaelakh				0.228	8.8	201	0.07	72.4	0.183	0.065	n.r.	0.008
Median 90OMZS1-3 (N=7)			**35.0**	**31.0**	**33.6**	**0.096**	**5.4**	**181**	**0.07**	**67.0**	**0.020**	**0.075**	n.r.	**0.008**

ANNEXE 6 – Cont.

Sample	Ore type	^{109}Ag	^{111}Cd	^{115}In	^{118}Sn	^{121}Sb	^{130}Te	^{185}Re	^{189}Os	^{193}Ir	^{195}Pt	^{197}Au	^{205}Tl	^{208}Pb	^{209}Bi
		ppm	ppm	ppm	ppm	ppm	ppm	ppm	ppm	ppm	ppm	ppm	ppm	ppm	ppm
Limit of detection		**0.007**	**0.037**	**0.005**	**0.050**	**0.047**	**0.257**	**0.010**	**0.017**	**0.004**	**0.013**	**0.008**	**0.004**	**0.007**	**0.004**
90OMZ67-5-1	Cu-rich	15.18	24.47	4.43	19.14	0.047	14.24	0.010	0.017	0.004	0.013	0.012	0.113	163.1	0.012
90OMZ67-5-1	Cu-rich	13.09	29.52	3.88	25.35	0.047	12.87	0.010	0.017	0.004	0.013	0.008	0.121	57.76	0.041
90OMZ67-5-1	Cu-rich	21.33	23.13	4.15	12.29	0.047	14.27	0.010	0.017	0.004	0.013	0.015	0.119	220.0	0.025
90OMZ67-5-1	Cu-rich	31.83	14.85	3.70	22.55	0.047	13.82	0.010	0.017	0.004	0.013	0.008	0.109	185.0	0.019
90OMZ67-5-1 (N=4)		**18.26**	**23.80**	**4.01**	**20.84**	**0.047**	**14.03**	**0.010**	**0.017**	**0.004**	**0.013**	**0.010**	**0.116**	**174.1**	**0.022**
90OC13	Cu-rich	7.30	16.46	4.26	2.29	0.047	11.93	0.010	0.017	0.004	0.417	0.008	0.069	90.38	0.417
90OC13	Cu-rich	8.92	10.25	4.62	2.01	0.047	13.69	0.010	0.017	0.004	0.110	0.008	0.085	175.6	0.087
90OC13	Cu-rich	5.75	15.70	4.58	1.38	0.047	11.69	0.010	0.017	0.004	0.320	0.008	0.088	60.10	0.347
90OC13	Cu-rich	6.79	16.13	4.18	3.18	0.047	11.78	0.010	0.017	0.004	0.073	0.008	0.064	75.10	0.143
90OC13	Cu-rich	7.55	43.21	4.49	1.28	0.047	11.96	0.010	0.017	0.004	0.080	0.008	0.195	79.42	0.091
90OC13	Cu-rich	5.42	11.69	4.27	1.54	0.047	10.16	0.010	0.017	0.004	0.079	0.008	0.191	115.0	0.081
90OC13	Cu-rich	5.07	13.94	4.77	2.56	0.047	9.65	0.010	0.017	0.004	0.077	0.008	0.138	145.2	0.237
90OC13 (N=7)		**6.79**	**15.70**	**4.49**	**2.01**	**0.047**	**11.78**	**0.010**	**0.017**	**0.004**	**0.080**	**0.008**	**0.088**	**90.38**	**0.143**
90OMZS1-3	Cu-rich	4.25	8.12	3.21	0.05	0.047	7.91	0.010	0.017	0.004	0.032	0.035	0.027	246.5	0.013
90OMZS1-3	Cu-rich	3.76	10.13	3.07	0.06	0.047	7.79	0.010	0.017	0.004	0.018	0.050	0.033	195.1	0.006
90OMZS1-3	Cu-rich	5.82	9.89	2.98	0.85	0.047	8.65	0.010	0.017	0.004	0.560	0.067	0.051	83.07	0.496
90OMZS1-3	Cu-rich	4.09	7.15	2.95	0.05	0.047	6.93	0.010	0.017	0.004	0.103	0.063	0.017	107.1	0.176
90OMZS1-3	Cu-rich	4.31	8.95	2.99	0.05	0.047	8.03	0.010	0.017	0.004	0.158	0.077	0.029	139.7	0.092
90OMZS1-3	Cu-rich	3.68	8.46	2.86	0.05	0.047	8.58	0.010	0.017	0.004	0.122	0.051	0.046	195.7	0.049
90OMZS1-3	Cu-rich	4.56	9.71	2.89	0.05	0.047	9.04	0.010	0.017	0.004	0.152	0.058	0.320	203.6	0.054
90OMZS1-3 (N=7)		**4.25**	**8.95**	**2.98**	**0.05**	**0.047**	**8.03**	**0.010**	**0.017**	**0.004**	**0.122**	**0.058**	**0.033**	**195.1**	**0.054**

ANNEXE 6 – Cont.

Sample	Ore type	Intrusion	S	Fe	Cu	^{59}Co	^{61}Ni	^{66}Zn	^{75}As	^{82}Se	^{95}Mo	^{101}Ru	^{103}Rh	^{108}Pd
			%	%	%	ppm	ppm	ppm	ppm	ppm	ppm	ppm	ppm	ppm
Limit of detection			**0.5**	**0.5**	**0.5**	**0.007**	**0.643**	**0.174**	**0.065**	**1.824**	**0.020**	**0.015**	**n.r.**	**0.008**
NR-15	Cu-rich	Kharaelakh	33.7	31.5	33.9	0.201	50.8	399	0.07	62.7	0.020	0.073	n.r.	0.182
NR-15	Cu-rich	Kharaelakh				13.998	477.8	307	0.10	56.9	0.020	0.093	n.r.	3.985
NR-15	Cu-rich	Kharaelakh				3.043	127.8	545	0.07	58.1	0.020	0.058	n.r.	0.662
NR-15	Cu-rich	Kharaelakh				4.565	255.6	612	0.07	60.4	0.020	0.100	n.r.	0.570
Median NR-15 (N=4)			**33.7**	**31.5**	**33.9**	**3.804**	**191.7**	**472**	**0.07**	**59.3**	**0.020**	**0.083**	n.r.	**0.616**
NR-10	Disseminated	Noril'sk I	34.5	30.3	33.9	0.825	53.3	3317	0.07	78.4	0.020	0.091	n.r.	0.008
NR-10	Disseminated	Noril'sk I				1.430	72.7	3895	0.07	84.3	0.020	0.131	n.r.	0.075
NR-10	Disseminated	Noril'sk I				0.694	66.0	1935	0.07	82.5	0.020	0.109	n.r.	0.008
Median NR-10 (N=3)			**34.5**	**30.3**	**33.9**	**0.825**	**66.0**	**3317**	**0.07**	**82.5**	**0.020**	**0.109**	n.r.	**0.008**
NR-9	Disseminated	Noril'sk I	33.6	31.6	34.0	882.470	2221	444	0.07	136.3	0.020	0.096	n.r.	14.056
NR-9	Disseminated	Noril'sk I				760.750	1735	882	0.07	147.6	0.020	0.109	n.r.	12.975
NR-9	Disseminated	Noril'sk I				3256.010	6968	1613	0.12	128.7	0.029	0.099	n.r.	16.622
NR-9	Disseminated	Noril'sk I				432.106	1339	493	0.13	120.5	0.033	0.049	n.r.	17.310
NR-9	Disseminated	Noril'sk I				1825.800	3469	505	0.07	145.5	0.020	0.066	n.r.	8.462
Median NR-9 (N=5)			**33.6**	**31.6**	**34.0**	**882.470**	**2221**	**505**	**0.07**	**136.3**	**0.020**	**0.096**	n.r.	**14.056**

ANNEXE 6 – Cont.

Sample	Ore type	^{109}Ag	^{111}Cd	^{115}In	^{118}Sn	^{121}Sb	^{130}Te	^{185}Re	^{189}Os	^{193}Ir	^{195}Pt	^{197}Au	^{205}Tl	^{208}Pb	^{209}Bi
		ppm	ppm	ppm	ppm	ppm	ppm	ppm	ppm	ppm	ppm	ppm	ppm	ppm	ppm
Limit of detection		**0.007**	**0.037**	**0.005**	**0.050**	**0.047**	**0.257**	**0.010**	**0.017**	**0.004**	**0.013**	**0.008**	**0.004**	**0.007**	**0.004**
NR-15	Cu-rich	1.70	20.39	2.02	0.05	0.047	5.26	0.010	0.017	0.004	0.013	0.008	0.043	11.23	0.286
NR-15	Cu-rich	3.44	17.25	2.11	0.15	0.047	8.31	0.010	0.017	0.004	0.030	0.008	0.047	63.90	2.769
NR-15	Cu-rich	3.13	27.39	2.28	0.20	0.047	8.76	0.010	0.017	0.004	0.013	0.027	0.029	16.71	0.320
NR-15	Cu-rich	3.13	26.05	1.99	0.12	0.047	6.91	0.010	0.017	0.004	0.024	0.012	0.031	19.35	0.499
NR-15 (N=4)		**3.13**	**23.22**	**2.07**	**0.14**	**0.047**	**7.61**	**0.010**	**0.017**	**0.004**	**0.018**	**0.010**	**0.037**	**18.03**	**0.409**
NR-10	Disseminated	2.83	3.01	1.46	0.14	0.047	16.43	0.010	0.017	0.007	0.682	0.015	0.004	1.61	0.034
NR-10	Disseminated	1.96	5.20	1.38	0.10	0.047	14.39	0.010	0.017	0.008	1.263	0.026	0.004	40.75	0.063
NR-10	Disseminated	2.50	2.77	1.53	0.05	0.047	17.62	0.010	0.017	0.004	0.192	0.026	0.037	7.82	0.022
NR-10 (N=3)		**2.50**	**3.01**	**1.46**	**0.10**	**0.047**	**16.43**	**0.010**	**0.017**	**0.007**	**0.682**	**0.026**	**0.004**	**7.82**	**0.034**
NR-9	Disseminated	11.53	0.97	2.11	1.37	0.047	40.38	0.010	0.018	0.004	0.013	0.008	0.110	24.22	1.357
NR-9	Disseminated	9.68	1.46	2.06	1.28	0.047	47.74	0.010	0.017	0.004	0.013	0.008	0.064	24.65	1.226
NR-9	Disseminated	10.86	2.50	1.89	2.59	0.047	45.16	0.010	0.017	0.004	0.013	0.008	0.066	20.72	1.418
NR-9	Disseminated	14.91	1.03	1.77	0.96	0.085	36.82	0.010	0.017	0.004	0.014	0.019	0.374	20.75	1.552
NR-9	Disseminated	10.86	0.83	2.34	1.86	0.047	45.13	0.010	0.017	0.004	0.013	0.008	0.262	16.68	0.657
NR-9 (N=5)		**10.86**	**1.03**	**2.06**	**1.37**	**0.047**	**45.13**	**0.010**	**0.017**	**0.004**	**0.013**	**0.008**	**0.110**	**20.75**	**1.357**

ANNEXE 7 - Complete data set of SEM-EDS and LA-ICP-MS analyses of cubanite obtained for the Noril'sk-Talnakh mining district and median values for each sample. Abbreviations: N= number of individual analyses; n.r.= not reported.

ANNEXE 7

Sample	Ore type	Intrusion	S	Fe	Cu	^{59}Co	^{61}Ni	^{66}Zn	^{75}As	^{82}Se	^{95}Mo	^{101}Ru	^{103}Rh	^{108}Pd
			%	%	%	ppm	ppm	ppm	ppm	ppm	ppm	ppm	ppm	ppm
Limit of detection			**0.5**	**0.5**	**0.5**	**0.007**	**0.643**	**0.174**	**0.065**	**1.824**	**0.020**	**0.015**	**n.r.**	**0.008**
90MC15	Cu-rich	Noril'sk I				0.05	18.9	103.3	0.20	143.2	0.09	0.041	n.r.	0.981
90MC15	Cu-rich	Noril'sk I				0.16	33.3	156.4	0.17	142.0	0.04	0.078	n.r.	0.910
90MC15	Cu-rich	Noril'sk I	34.0	41.0	23.2	0.07	29.2	189.3	0.26	144.8	0.13	0.090	n.r.	0.670
90MC15	Cu-rich	Noril'sk I				0.23	444	502.0	0.32	141.6	0.11	0.070	n.r.	0.958
90MC15	Cu-rich	Noril'sk I				0.14	85.2	452.7	0.23	139.1	0.10	0.059	n.r.	0.843
90MC15	Cu-rich	Noril'sk I				0.18	30.0	307.8	0.16	146.1	0.07	0.049	n.r.	1.063
Median 90MC15 (N=6)			**34.0**	**41.0**	**23.2**	**0.15**	**31.7**	**248.5**	**0.21**	**142.6**	**0.10**	**0.064**	n.r.	**0.934**
90OMZS1-3	Cu-rich	Kharaelakh				13.99	235	13.6	0.07	69.3	0.02	0.054	n.r.	0.038
90OMZS1-3	Cu-rich	Kharaelakh				76.95	1646	91.8	0.07	64.2	0.02	0.044	n.r.	0.671
90OMZS1-3	Cu-rich	Kharaelakh				10.29	230	21.4	0.07	78.6	0.02	0.045	n.r.	0.054
90OMZS1-3	Cu-rich	Kharaelakh	34.8	41.4	22.3	1.36	32.9	4.2	0.07	73.6	0.02	0.054	n.r.	0.080
90OMZS1-3	Cu-rich	Kharaelakh				0.38	16.5	18.1	0.07	67.1	0.02	0.082	n.r.	0.008
90OMZS1-3	Cu-rich	Kharaelakh				5.56	104	197.5	0.07	21.3	0.02	0.078	n.r.	0.017
90OMZS1-3	Cu-rich	Kharaelakh				1.31	43.2	56.4	0.07	74.2	0.02	0.053	n.r.	0.008
90OMZS1-3	Cu-rich	Kharaelakh				156.37	2922	42.4	0.07	71.6	0.02	0.068	n.r.	0.844
Median 90OMZS1-3 (N=8)			**34.8**	**41.4**	**22.3**	**7.92**	**167**	**31.9**	**0.07**	**70.5**	**0.02**	**0.054**	n.r.	**0.046**
90OMZS2-2	Cu-poor	Kharaelakh	34.5	41.7	22.8	5.35	198	366.2	0.07	52.6	0.02	0.098	n.r.	0.008

ANNEXE 7 – Cont.

Sample	Ore type	^{109}Ag	^{111}Cd	^{115}In	^{118}Sn	^{121}Sb	^{130}Te	^{185}Re	^{189}Os	^{193}Ir	^{195}Pt	^{197}Au	^{205}Tl	^{208}Pb	^{209}Bi
		ppm	ppm	ppm	ppm	ppm	ppm	ppm	ppm	ppm	ppm	ppm	ppm	ppm	ppm
Limit of detection		**0.007**	**0.037**	**0.005**	**0.050**	**0.047**	**0.257**	**0.010**	**0.017**	**0.004**	**0.013**	**0.008**	**0.004**	**0.007**	**0.004**
90MC15	Cu-rich	29.18	5.97	1.55	0.050	0.047	41.68	0.010	0.017	0.004	0.055	0.008	1.066	1.19	0.004
90MC15	Cu-rich	34.98	8.56	1.50	0.070	0.047	39.67	0.010	0.017	0.004	0.041	0.008	1.053	0.90	0.004
90MC15	Cu-rich	35.97	8.72	1.02	0.050	0.047	40.16	0.010	0.017	0.004	0.026	0.008	1.037	1.29	0.009
90MC15	Cu-rich	40.90	24.65	1.76	0.050	0.047	40.90	0.010	0.017	0.004	0.030	0.014	1.181	1.50	0.004
90MC15	Cu-rich	37.41	22.80	1.13	0.050	0.047	41.31	0.010	0.017	0.004	0.041	0.008	1.074	1.82	0.005
90MC15	Cu-rich	55.06	15.39	2.37	0.050	0.047	39.71	0.010	0.017	0.004	0.016	0.008	1.090	1.41	0.004
90MC15 (N=6)		**36.69**	**12.06**	**1.52**	**0.050**	**0.047**	**40.53**	**0.010**	**0.017**	**0.004**	**0.036**	**0.008**	**1.070**	**1.35**	**0.004**
90OMZS1-3	Cu-rich	14.90	0.67	0.84	0.050	0.047	8.52	0.010	0.017	0.004	0.251	0.026	0.058	34.98	0.140
90OMZS1-3	Cu-rich	11.32	2.55	0.33	0.050	0.047	5.09	0.010	0.017	0.004	0.030	0.026	0.071	9.59	0.019
90OMZS1-3	Cu-rich	7.70	1.08	0.08	0.050	0.047	4.61	0.010	0.017	0.004	0.144	0.015	0.032	7.90	0.095
90OMZS1-3	Cu-rich	9.75	0.45	0.04	0.060	0.047	5.60	0.010	0.017	0.004	0.477	0.136	0.015	4.49	0.391
90OMZS1-3	Cu-rich	5.64	1.07	0.84	0.050	0.047	7.16	0.010	0.017	0.004	0.024	0.058	0.027	14.16	0.023
90OMZS1-3	Cu-rich	4.50	7.08	0.70	0.119	0.049	0.38	0.010	0.017	0.004	0.013	0.015	0.807	44.85	0.009
90OMZS1-3	Cu-rich	10.66	1.93	0.12	0.050	0.047	7.78	0.010	0.017	0.004	0.128	0.020	0.118	26.62	0.067
90OMZS1-3	Cu-rich	10.90	1.69	0.39	0.050	0.047	3.95	0.010	0.017	0.004	0.039	0.072	0.154	18.06	0.029
90OMZS1-3 (N=8)		**10.21**	**1.38**	**0.36**	**0.050**	**0.047**	**5.34**	**0.010**	**0.017**	**0.004**	**0.083**	**0.026**	**0.065**	**16.11**	**0.048**
90OMZS2-2	Cu-poor	21.11	25.68	2.23	0.737	0.047	2.34	0.010	0.017	0.004	0.013	0.008	0.028	87.20	0.021

ANNEXE 8 - Partition coefficients of elements between pentlandite (Pn) and pyrrhotite (Po), Pn and chalcopyrite (Ccp), Ccp and Po, and Ccp and cubanite (Cbn) calculated for each sample from the Noril'sk-Talnakh mining district. The median partition coefficients are the median values of individual partition coefficients calculated for all samples. Results in red are below detection limits and were not used for calculation. Abbreviations: N= number of individual analyses; n.r.= not reported.

ANNEXE 8

Pentlandite and Pyrrhotite (DPn/Po)	Co	Cu	Zn	As	Se	Mo	Ru	Rh	Pd	Ag	Cd	In
	ppm	ppm	ppm	ppm	ppm	ppm	ppm	ppm	ppm	ppm	ppm	ppm
Pentlandite median values - 90OMZS2-3 (N=6)	14505	61.9	3.7	0.81	52.9	0.26	0.01	0.06	28.5	6.46	0.09	0.02
Pyrrhotite median values - 90OMZS2-3 (N=6)	32	11.5	0.2	0.07	56.4	0.34	0.01	0.19	0.01	0.52	0.09	0.01
DPn/Po - 90OMZS2-3	**459**	**5.4**			**0.9**	**0.76**		**0.32**		**12.33**	**1.03**	
Pentlandite median values - NR-6 (N=3)	14978	25.1	127.0	0.07	29.6	0.10	0.17	0.05	45.9	3.32	0.04	0.01
Pyrrhotite median values - NR-6 (N=4)	393	1.9	0.2	0.07	34.2	0.22	0.13	0.43	1.1	0.67	0.04	0.01
DPn/Po - NR-6	**38**	**13.4**	**730.3**		**0.9**	**0.46**	**1.37**	**0.11**	**43.3**	**4.94**		
Pentlandite median values - NR-8 (N=4)	5864	6.4	0.2	0.57	56.5	0.02	2.84	16.96	1883.6	0.78	0.06	0.01
Pyrrhotite median values - NR-8 (N=3)	100	22.4	1.4	0.60	38.0	0.12	0.01	0.00	0.4	0.90	0.09	0.01
DPn/Po - NR-8	**59**	**0.3**	**0.1**	**0.95**	**1.5**				**5056.4**	**0.86**	**0.71**	
Pentlandite median values - NR-18 (N=4)	6019	71.1	13.8	0.07	72.1	0.02	0.35	0.00	341.4	1.00	0.16	0.06
Pyrrhotite median values -NR-18 (N=1)	68	548.5	274.3	0.07	92.2	0.02	0.01	0.00	6.3	16.21	12.47	0.23
DPn/Po - NR-18	**89**	**0.1**	**0.1**		**0.8**				**54.1**	**0.06**	**0.01**	**0.28**
Pentlandite median values - NR-17 (N=8)	10102	4.1	0.5	0.24	85.6	0.02	0.14	0.00	502.4	4.02	0.04	0.01
Pyrrhotite median values - NR-17 (N=5)	103	5.7	84.8	0.15	97.9	0.02	0.01	0.00	2.4	5.17	3.80	0.05
DPn/Po - NR-17	**98**	**0.7**	**0.0**	**1.59**	**0.9**				**205.9**	**0.78**		**0.16**
Pentlandite median values - 90OC13 (N=7)	17778	8.7	1.3	0.14	57.3	0.02	0.13	0.00	54.8	4.20	0.05	0.02
Pyrrhotite median values - 90OC13 (N=7)	29	529.8	137.1	0.07	55.2	0.03	0.01	0.00	0.6	1.15	2.12	0.04
DPn/Po - 90OC13	**607**	**0.0**	**0.0**		**1.0**				**97.8**	**3.64**	**0.02**	**0.44**
Pentlandite median values - 90OMZS1-3 (N=2)	11481	145.5	0.9	0.17	49.5	0.02	0.04	0.00	131.7	15.69	0.07	0.01
Pyrrhotite median values - 90OMZS1-3 (N=6)	14	7.9	0.3	0.07	51.5	0.37	0.53	1.32	0.02	1.28	0.06	0.01
DPn/Po - 90OMZS1-3	**830**	**18.5**	**2.8**		**1.0**	**0.07**	**0.08**	**0.00**	**8383.8**	**12.28**	**1.22**	

ANNEXE 8 – Cont.

Pentlandite and Pyrrhotite (DPn/Po)	Sn	Sb	Te	Re	Os	Ir	Pt	Au	Tl	Pb	Bi
	ppm	ppm	ppm	ppm	ppm	ppm	ppm	ppm	ppm	ppm	ppm
Pentlandite median values - 90OMZS2-3 (N=6)	0.47	0.07	1.24	0.06	0.02	0.01	0.27	0.01	0.55	22.63	0.40
Pyrrhotite median values - 90OMZS2-3 (N=6)	0.11	0.05	0.95	0.10	0.02	0.02	0.05	0.01	0.00	1.20	0.11
DPn/Po - 90OMZS2-3	**4.18**		**1.31**	**0.58**		**0.54**	**5.78**			**18.81**	**3.77**
Pentlandite median values - NR-6 (N=3)	0.05	0.05	0.27	0.06	0.02	0.00	1.20	0.02	0.65	89.21	0.90
Pyrrhotite median values - NR-6 (N=4)	0.05	0.05	0.26	0.11	0.02	0.03	0.21	0.01	0.00	2.54	0.31
DPn/Po - NR-6				**0.54**			**5.84**			**35.08**	**2.85**
Pentlandite median values - NR-8 (N=4)	0.09	0.05	2.17	0.48	0.62	1.67	27.33	0.04	0.50	32.32	0.89
Pyrrhotite median values - NR-8 (N=3)	0.05	0.05	0.39	0.01	0.02	0.00	0.01	0.01	0.00	2.72	0.34
DPn/Po - NR-8			**5.53**							**11.89**	**2.65**
Pentlandite median values - NR-18 (N=4)	0.11	0.05	8.43	0.01	0.02	0.00	0.17	0.01	0.93	5.80	0.65
Pyrrhotite median values -NR-18 (N=1)	0.05	0.05	8.73	0.01	0.02	0.00	0.31	0.02	0.60	3.80	6.11
DPn/Po - NR-18			**0.97**				**0.54**		**1.53**	**1.52**	**0.11**
Pentlandite median values - NR-17 (N=8)	0.10	0.05	5.18	0.01	0.02	0.00	0.11	0.66	0.75	25.58	0.06
Pyrrhotite median values - NR-17 (N=5)	0.26	0.05	4.36	0.01	0.02	0.00	0.03	0.01	0.03	68.56	1.37
DPn/Po - NR-17	**0.40**		**1.19**				**4.39**	**66.28**	**21.50**	**0.37**	**0.04**
Pentlandite median values - 90OC13 (N=7)	0.25	0.05	5.18	0.01	0.02	0.00	0.01	0.01	0.58	21.95	0.17
Pyrrhotite median values - 90OC13 (N=7)	0.33	0.05	2.95	0.01	0.02	0.00	0.07	0.01	0.04	120.92	0.15
DPn/Po - 90OC13	**0.76**		**1.75**				**0.21**		**12.91**	**0.18**	**1.18**
Pentlandite median values - 90OMZS1-3 (N=2)	0.23	0.05	5.03	0.01	0.02	0.00	0.18	0.01	4.49	249.57	0.67
Pyrrhotite median values - 90OMZS1-3 (N=6)	0.05	0.05	1.17	0.27	0.15	0.20	0.01	0.01	0.01	3.86	0.11
DPn/Po - 90OMZS1-3			**4.32**		**0.11**				**300.37**	**64.69**	**6.27**

ANNEXE 8 – Cont.

Pentlandite and Pyrrhotite (DPn/Po)	Co	Cu	Zn	As	Se	Mo	Ru	Rh	Pd	Ag	Cd	In
	ppm	ppm	ppm	ppm	ppm	ppm	ppm	ppm	ppm	ppm	ppm	ppm
Pentlandite median values - NR-10 (N=3)	9257	1.4	0.4	0.14	94.1	1.99	5.73	14.81	625.2	0.76	0.04	0.01
Pyrrhotite median values - NR-10 (N=6)	534	1.0	0.2	0.18	105.7	0.55	4.73	16.69	0.6	2.85	0.04	0.01
DPn/Po - NR-10	**17**	**1.4**	**1.9**	**0.77**	**0.9**	**3.62**	**1.21**	**0.89**	**1024.4**	**0.26**		
Pentlandite median values - 90OMZS2-2 (N=3)	11331	8.1	0.4	0.27	45.6	0.10	0.18	0.02	108.1	2.64	0.04	0.01
Pyrrhotite median values - 90OMZS2-2 (N=7)	22	4.9	0.6	0.07	54.6	0.37	0.27	0.97	0.02	0.38	0.04	0.01
DPn/Po - 90OMZS2-2	**508**	**1.7**	**0.6**		**0.8**	**0.26**	**0.65**	**0.02**	**5069.0**	**6.95**		
Pentlandite median values - NR-13 (N=6)	12536	4548.6	286.5	0.14	27.1	0.23	0.24	0.16	46.4	12.18	2.28	0.15
Pyrrhotite median values - NR-13 (N=6)	79	0.8	0.3	0.07	33.3	0.46	0.21	0.86	0.01	0.31	0.04	0.01
DPn/Po - NR-13	**159**	**6031.1**	**1121**		**0.8**	**0.50**	**1.19**	**0.19**		**39.07**		
Pentlandite median values - NR-14 (N=5)	17029	328.9	30.9	0.18	39.4	0.32	0.31	0.51	63.4	2.18	0.19	0.03
Pyrrhotite median values - NR-14 (N=7)	70	1.4	0.3	0.07	43.4	0.39	0.19	1.04	0.01	0.31	0.04	0.01
DPn/Po - NR-14	**242**	**236.6**	**99.3**		**0.9**	**0.80**	**1.60**	**0.49**		**7.01**		
Pentlandite median values - NR-11 (N=6)	6289	1.7	0.4	0.39	81.4	2.65	1.19	7.74	734.2	2.64	0.04	0.01
Pyrrhotite median values - NR-11 (N=6)	343	0.9	0.2	0.84	94.9	3.59	1.25	6.68	1.7	2.58	0.04	0.01
DPn/Po - NR-11	**18**	**1.9**	**2.0**	**0.46**	**0.9**	**0.74**	**0.95**	**1.16**	**438.1**	**1.02**		
DPn/Po median values	**129**	**1.8**	**1.9**	**0.86**	**0.9**	**0.62**	**1.19**	**0.26**	**438.1**	**4.29**	**0.71**	**0.28**
DPn/Po min	**17**	**0.0**	**0.0**	**0.46**	**0.8**	**0.07**	**0.08**	**0.00**	**43.3**	**0.06**	**0.01**	**0.16**
DPn/Po max	**830**	**6031.1**	**1121**	**1.59**	**1.5**	**3.62**	**1.60**	**1.16**	**8383.8**	**39.07**	**1.22**	**0.44**

ANNEXE 8 – Cont.

Pentlandite and Pyrrhotite (DPn/Po)	Sn	Sb	Te	Re	Os	Ir	Pt	Au	Tl	Pb	Bi
	ppm	ppm	ppm	ppm	ppm	ppm	ppm	ppm	ppm	ppm	ppm
Pentlandite median values - NR-10 (N=3)	0.05	0.05	9.93	0.20	1.15	2.23	15.60	0.01	0.34	6.87	0.06
Pyrrhotite median values - NR-10 (N=6)	0.05	0.05	11.70	0.16	0.89	1.89	0.59	0.01	0.00	0.06	0.09
DPn/Po - NR-10			**0.85**	**1.23**	**1.30**	**1.18**	**26.62**			**119.81**	**0.61**
Pentlandite median values - 90OMZS2-2 (N=3)	0.05	0.05	1.47	0.01	0.02	0.00	0.06	0.01	0.16	7.13	0.04
Pyrrhotite median values - 90OMZS2-2 (N=7)	0.05	0.05	1.03	0.17	0.07	0.10	0.10	0.01	0.00	2.57	0.07
DPn/Po - 90OMZS2-2			**1.43**				**0.65**		**32.65**	**2.77**	**0.56**
Pentlandite median values - NR-13 (N=6)	0.20	0.05	0.77	0.12	0.02	0.04	2.64	0.01	0.14	24.99	0.28
Pyrrhotite median values - NR-13 (N=6)	0.05	0.05	0.80	0.21	0.06	0.09	0.05	0.01	0.00	1.04	0.08
DPn/Po - NR-13			**0.96**	**0.57**		**0.40**	**50.74**			**24.01**	**3.60**
Pentlandite median values - NR-14 (N=5)	0.07	0.05	0.62	0.14	0.06	0.05	1.74	0.01	0.12	8.76	0.21
Pyrrhotite median values - NR-14 (N=7)	0.05	0.05	0.84	0.16	0.06	0.07	0.10	0.01	0.00	0.64	0.12
DPn/Po - NR-14			**0.74**	**0.89**	**0.98**	**0.73**	**17.51**			**13.78**	**1.81**
Pentlandite median values - NR-11 (N=6)	0.07	0.05	3.50	0.16	0.22	0.54	0.64	0.03	1.35	2.65	0.29
Pyrrhotite median values - NR-11 (N=6)	0.05	0.05	3.97	0.19	0.33	0.66	0.37	0.02	0.02	16.86	1.33
DPn/Po - NR-11	**1.41**		**0.88**	**0.85**	**0.68**	**0.82**	**1.72**	**1.20**	**69.93**	**0.16**	**0.22**
DPn/Po median values	**1.08**		**1.19**	**0.47**	**0.83**	**0.73**	**5.08**	**33.74**	**27.08**	**12.83**	**1.50**
DPn/Po min	**0.40**		**0.74**	**0.35**	**0.11**	**0.40**	**0.21**	**1.20**	**1.53**	**0.16**	**0.04**
DPn/Po max	**4.18**		**5.53**	**1.23**	**1.30**	**1.18**	**50.74**	**66.28**	**300.37**	**119.81**	**6.27**

ANNEXE 8 – Cont.

Pentlandite and Chalcopyrite (DPn/Ccp)	Co	Cu	Zn	As	Se	Mo	Ru	Rh	Pd	Ag	Cd	In
	ppm	ppm	ppm	ppm	ppm	ppm	ppm	ppm	ppm	ppm	ppm	ppm
Pentlandite median values - 90OMZS2-3 (N=6)	14505	3.7	0.81	52.9	0.26	0.01	0.06	28.5	6.46	0.09	0.02	0.47
Chalcopyrite median values - 90OMZS2-3 (N=7)	0.8	438.2	0.47	53.3	0.02	0.06	n.r.	0.01	3.37	6.66	1.62	2.43
DPn/Ccp - 90OMZS2-3	**17209**	**0.01**	**1.73**	**0.99**					**1.92**	**0.01**	**0.01**	**0.19**
Pentlandite median values - NR-6 (N=3)	14978	127.0	0.07	29.6	0.10	0.17	0.05	45.9	3.32	0.04	0.01	0.05
Chalcopyrite median values - NR-6 (N=4)	4.1	497.5	0.07	27.9	0.02	0.18	n.r.	0.11	2.44	10.65	0.63	0.10
DPn/Ccp - NR-6	**3646**	**0.26**		**1.06**		**0.96**		**424.8**	**1.36**		**0.01**	
Pentlandite median values - NR-8 (N=4)	5864	0.2	0.57	56.5	0.02	2.84	16.96	1883.6	0.78	0.06	0.01	0.09
Chalcopyrite median values - NR-8 (N=5)	0.6	626.9	0.07	41.5	0.02	0.18	n.r.	0.07	17.56	7.97	1.68	2.37
DPn/Ccp - NR-8	**9176**		**8.78**	**1.36**		**15.91**		**26498.0**	**0.04**	**0.01**		**0.04**
Pentlandite median values - 90MC15 (N=5)	4370	3.2	1.16	123.4	1.40	0.21	1.80	732.6	33.54	0.45	0.01	0.07
Chalcopyrite median values - 90MC15 (N=6)	0.0	79.1	0.16	133.6	0.08	0.08	n.r.	0.74	10.95	3.82	1.36	0.05
DPn/Ccp - 90MC15	**358984**	**0.04**	**7.30**	**0.92**	**17.36**	**2.54**		**985.8**	**3.06**	**0.12**	**0.01**	
Pentlandite median values - 90MC5 (N=6)	3606	1.8	0.14	169.3	0.12	0.14	0.01	1007.4	34.25	1.05	0.01	0.06
Chalcopyrite median values - 90MC5 (N=6)	0.1	91.0	0.07	172.4	0.05	0.10	n.r.	4.30	10.83	5.86	0.52	0.05
DPn/Ccp - 90MC5	**53865**	**0.02**		**0.98**	**2.21**	**1.32**		**234.3**	**3.16**	**0.18**		
Pentlandite median values - NR-18 (N=4)	6019	13.8	0.07	72.1	0.02	0.35	0.00	341.4	1.00	0.16	0.06	0.11
Chalcopyrite median values - NR-18 (N=4)	0.2	384.5	0.07	73.5	0.02	0.14	n.r.	2.21	6.64	21.51	3.17	1.80
DPn/Ccp - NR-18	**37674**	**0.04**	**1.00**	**0.98**		**2.54**		**154.2**	**0.15**	**0.01**	**0.02**	**0.06**
Pentlandite median values - NR-17 (N=8)	10102	0.5	0.24	85.6	0.02	0.14	0.00	502.4	4.02	0.04	0.01	0.10
Chalcopyrite median values - NR-17 (N=7)	0.6	459.2	0.07	88.9	0.02	0.10	n.r.	0.54	8.79	37.73	3.66	4.63
DPn/Ccp - NR-17	**17944**	**0.00**		**0.96**		**1.35**		**933.0**	**0.46**		**0.00**	**0.02**
Pentlandite median values - 90OMZ67-5-1 (N=3)	10256	4.1	1.24	114.0	0.13	0.08	0.00	3.2	14.65	0.10	0.01	1.92
Chalcopyrite median values - 90OMZ67-5-1 (N=4)	0.2	345.4	0.14	89.3	0.06	0.09	n.r.	0.01	18.26	23.80	4.01	20.84
DPn/Ccp - 90OMZ67-5-1	**53842**	**0.01**	**8.74**	**1.28**	**2.26**	**0.86**			**0.80**	**0.00**		**0.09**

ANNEXE 8 – Cont.

Pentlandite and Chalcopyrite (DPn/Ccp)	Sn	Sb	Te	Re	Os	Ir	Pt	Au	Tl	Pb	Bi
	ppm	ppm	ppm	ppm	ppm	ppm	ppm	ppm	ppm	ppm	ppm
Pentlandite median values - 90OMZS2-3 (N=6)	0.07	1.24	0.09	0.02	0.01	0.27	0.01	0.55	22.63	0.40	
Chalcopyrite median values - 90OMZS2-3 (N=7)	0.05	1.70	0.01	0.02	0.00	0.01	0.01	0.03	19.87	0.06	
DPn/Ccp - 90OMZS2-3		**0.73**				**20.31**		**19.39**	**1.14**	**6.22**	
Pentlandite median values - NR-6 (N=3)	0.05	0.27	0.09	0.02	0.00	1.20	0.02	0.65	89.21	0.90	
Chalcopyrite median values - NR-6 (N=4)	0.05	0.44	0.01	0.02	0.00	0.07	0.01	0.01	12.96	0.10	
DPn/Ccp - NR-6		**0.60**				**17.75**		**72.90**	**6.88**	**8.79**	
Pentlandite median values - NR-8 (N=4)	0.05	2.17	0.73	0.41	1.7	27.33	0.04	0.50	32.32	0.89	
Chalcopyrite median values - NR-8 (N=5)	0.05	1.90	0.01	0.02	0.00	0.06	0.01	0.16	8.70	0.14	
DPn/Ccp - NR-8		**1.15**				**433.94**		**3.21**	**3.71**	**6.27**	
Pentlandite median values - 90MC15 (N=5)	0.05	35.88	0.25	0.02	0.00	1.99	0.01	0.34	7.75	1.07	
Chalcopyrite median values - 90MC15 (N=6)	0.05	39.45	0.01	0.02	0.00	0.03	0.01	1.04	1.17	0.00	
DPn/Ccp - 90MC15		**0.91**				**63.99**		**0.32**	**6.61**	**242.31**	
Pentlandite median values - 90MC5 (N=6)	0.05	64.70	0.02	0.02	0.00	3.99	0.01	0.37	8.35	0.22	
Chalcopyrite median values - 90MC5 (N=6)	0.05	63.89	0.01	0.02	0.00	0.04	0.01	0.78	0.28	0.00	
DPn/Ccp - 90MC5		**1.01**				**100.44**		**0.47**	**29.99**		
Pentlandite median values - NR-18 (N=4)	0.05	8.43	0.01	0.02	0.00	0.17	0.01	0.93	5.80	0.65	
Chalcopyrite median values - NR-18 (N=4)	0.05	8.23	0.01	0.02	0.00	0.16	0.01	0.14	0.37	0.75	
DPn/Ccp - NR-18		**1.02**				**1.05**		**6.42**	**15.68**	**0.86**	
Pentlandite median values - NR-17 (N=8)	0.05	5.18	0.01	0.02	0.00	0.11	0.66	0.75	25.58	0.06	
Chalcopyrite median values - NR-17 (N=7)	0.05	12.45	0.01	0.02	0.00	0.32	0.06	0.11	22.40	0.35	
DPn/Ccp - NR-17		**0.42**				**0.36**	**11.74**	**6.83**	**1.14**	**0.16**	
Pentlandite median values - 90OMZ67-5-1 (N=3)	0.07	16.83	0.01	0.02	0.00	0.01	0.01	0.89	32.56	1.34	
Chalcopyrite median values - 90OMZ67-5-1 (N=4)	0.05	14.03	0.01	0.02	0.00	0.01	0.01	0.12	174.06	0.02	
DPn/Ccp - 90OMZ67-5-1		**1.20**						**7.72**	**0.19**	**61.66**	

ANNEXE 8 – Cont.

Pentlandite and Chalcopyrite (DPn/Ccp)	Co	Cu	Zn	As	Se	Mo	Ru	Rh	Pd	Ag	Cd	In
	ppm	ppm	ppm	ppm	ppm	ppm	ppm	ppm	ppm	ppm	ppm	ppm
Pentlandite median values - 90OC13 (N=7)	17778	1.3	0.14	57.3	0.02	0.13	0.00	54.8	4.20	0.05	0.02	0.25
Chalcopyrite median values - 90OC13 (N=7)	0.2	489.9	0.07	60.7	0.02	0.09	n.r.	0.01	6.79	15.70	4.49	2.01
DPn/Ccp - 90OC13	**82284**	**0.00**		**0.94**		**1.50**			**0.62**	**0.00**	**0.00**	**0.12**
Pentlandite median values - 90OMZS1-3 (N=2)	11481	0.9	0.17	49.5	0.02	0.04	0.00	131.7	15.69	0.07	0.01	0.23
Chalcopyrite median values - 90OMZS1-3 (N=7)	0.1	181.4	0.07	67.0	0.02	0.07	n.r.	0.01	4.25	8.95	2.98	0.05
DPn/Ccp - 90OMZS1-3	**119016**	**0.01**		**0.74**		**0.60**			**3.69**	**0.01**		
Pentlandite median values - NR-10 (N=3)	9257	0.4	0.14	94.1	1.99	5.73	14.81	625.2	0.76	0.04	0.01	0.05
Chalcopyrite median values - NR-10 (N=3)	0.8	3316.9	0.07	82.5	0.02	0.11	n.r.	0.01	2.50	3.01	1.46	0.10
DPn/Ccp - NR-10	**11225**	**0.00**		**1.14**		**52.37**			**0.30**			
Pentlandite median values - 90OMZS2-2 (N=3)	11331	0.4	0.27	45.6	0.10	0.18	0.02	108.1	2.64	0.04	0.01	0.05
Chalcopyrite median values - 90OMZS2-2 (N=7)	0.1	374.3	0.07	54.7	0.02	0.09	n.r.	0.01	2.31	12.39	2.31	0.91
DPn/Ccp - 90OMZS2-2	**112836**	**0.00**		**0.83**		**2.08**			**1.14**			
Pentlandite median values - NR-13 (N=6)	12536	286.5	0.14	27.1	0.23	0.24	0.16	46.4	12.18	2.28	0.15	0.20
Chalcopyrite median values - NR-13 (N=7)	0.6	736.4	0.07	29.4	0.02	0.13	n.r.	0.01	0.73	6.28	1.31	2.35
DPn/Ccp - NR-13	**19432**	**0.39**		**0.92**		**1.93**			**16.57**	**0.36**	**0.11**	**0.08**
Pentlandite median values - NR-14 (N=5)	17029	30.9	0.18	39.4	0.32	0.31	0.51	63.4	2.18	0.19	0.03	0.07
Chalcopyrite median values - NR-14 (N=6)	0.4	515.8	0.07	38.0	0.02	0.12	n.r.	0.01	1.14	7.38	1.48	1.78
DPn/Ccp - NR-14	**39689**	**0.06**		**1.04**		**2.63**			**1.92**	**0.03**	**0.02**	**0.04**
Pentlandite median values - NR-11 (N=6)	6289	0.4	0.39	81.4	2.65	1.19	7.74	734.2	2.64	0.04	0.01	0.07
Chalcopyrite median values - NR-11 (N=4)	0.1	377.3	0.07	83.4	0.02	0.10	n.r.	0.06	28.68	3.96	1.49	0.34
DPn/Ccp - NR-11	**45422**	**0.00**		**0.98**		**11.37**		**12691**	**0.09**			**0.21**
DPn/Ccp median values	**39689**	**0.01**	**7.30**	**0.98**	**2.26**	**2.00**		**933**	**1.14**	**0.01**	**0.01**	**0.08**
DPn/Ccp min	**3646**	**0.00**	**1.00**	**0.74**	**2.21**	**0.60**		**154.2**	**0.04**	**0.00**	**0.00**	**0.02**
DPn/Ccp max	**358984**	**0.39**	**8.78**	**1.36**	**17.36**	**52.37**		**26498**	**16.57**	**0.36**	**0.11**	**0.21**

ANNEXE 8 – Cont.

Pentlandite and Chalcopyrite (DPn/Ccp)	Sn	Sb	Te	Re	Os	Ir	Pt	Au	Tl	Pb	Bi
	ppm	ppm	ppm	ppm	ppm	ppm	ppm	ppm	ppm	ppm	ppm
Pentlandite median values - 90OC13 (N=7)	0.05	5.18	0.01	0.02	0.00	0.01	0.01	0.58	21.95	0.17	
Chalcopyrite median values - 90OC13 (N=7)	0.05	11.78	0.01	0.02	0.00	0.08	0.01	0.09	90.38	0.14	
DPn/Ccp - 90OC13		**0.44**				**0.17**		**6.57**	**0.24**	**1.21**	
Pentlandite median values - 90OMZS1-3 (N=2)	0.05	5.03	0.01	0.02	0.00	0.18	0.01	4.49	249.57	0.67	
Chalcopyrite median values - 90OMZS1-3 (N=7)	0.05	8.03	0.01	0.02	0.00	0.12	0.06	0.03	195.06	0.05	
DPn/Ccp - 90OMZS1-3		**0.63**				**1.48**		**135.47**	**1.28**	**12.43**	
Pentlandite median values - NR-10 (N=3)	0.05	9.93	0.30	0.76	2.2	15.60	0.01	0.34	6.87	0.06	
Chalcopyrite median values - NR-10 (N=3)	0.05	16.43	0.01	0.02	0.01	0.68	0.03	0.00	7.82	0.03	
DPn/Ccp - NR-10		**0.60**			**332.7**	**22.88**			**0.88**	**1.72**	
Pentlandite median values - 90OMZS2-2 (N=3)	0.05	1.47	0.01	0.02	0.00	0.06	0.01	0.16	7.13	0.04	
Chalcopyrite median values - 90OMZS2-2 (N=7)	0.05	2.58	0.01	0.02	0.00	0.03	0.01	0.01	71.21	0.02	
DPn/Ccp - 90OMZS2-2		**0.57**				**1.91**		**21.40**	**0.10**	**2.39**	
Pentlandite median values - NR-13 (N=6)	0.05	0.77	0.19	0.02	0.04	2.64	0.01	0.14	24.99	0.28	
Chalcopyrite median values - NR-13 (N=7)	0.05	0.94	0.01	0.02	0.00	0.13	0.01	0.01	28.19	0.07	
DPn/Ccp - NR-13		**0.82**				**20.91**		**18.05**	**0.89**	**3.82**	
Pentlandite median values - NR-14 (N=5)	0.05	0.62	0.21	0.04	0.05	1.74	0.01	0.12	8.76	0.21	
Chalcopyrite median values - NR-14 (N=6)	0.05	1.08	0.01	0.02	0.00	0.12	0.01	0.08	28.32	0.10	
DPn/Ccp - NR-14		**0.58**				**14.62**		**1.56**	**0.31**	**2.22**	
Pentlandite median values - NR-11 (N=6)	0.05	3.50	0.24	0.15	0.54	0.64	0.03	1.35	2.65	0.29	
Chalcopyrite median values - NR-11 (N=4)	0.05	9.36	0.01	0.02	0.00	0.33	0.01	0.12	17.88	0.14	
DPn/Ccp - NR-11		**0.37**				**1.93**		**11.39**	**0.15**	**2.01**	
DPn/Ccp median values		**0.63**			**332.67**	**16.19**	**11.74**	**7.27**	**1.14**	**3.11**	
DPn/Ccp min		**0.37**			**332.67**	**0.17**	**11.74**	**0.32**	**0.10**	**0.16**	
DPn/Ccp max		**1.20**			**332.67**	**433.94**	**11.74**	**135.47**	**29.99**	**242.31**	

ANNEXE 8 – Cont.

Chalcopyrite and Pyrrhotite (DCcp/Po)	Co	Cu	Zn	As	Se	Mo	Ru	Rh	Pd	Ag	Cd	In
	ppm	ppm	ppm	ppm	ppm	ppm	ppm	ppm	ppm	ppm	ppm	ppm
Chalcopyrite median values - 90OMZS2-3 (N=7)	0.8	39	438.2	0.47	53.3	0.02	0.06	n.r.	0.01	3.37	6.66	1.62
Pyrrhotite median values - 90OMZS2-3 (N=6)	31.6	3145	0.2	0.07	56.4	0.34	0.01	0.19	0.01	0.52	0.09	0.01
DCcp/Po - 90OMZS2-3	**0.03**	**0.01**			**0.94**					**6.44**	**76.60**	
Chalcopyrite median values - 90OKMZ5 (N=5)	0.5	52	399.9	0.07	60.9	0.06	0.10	n.r.	0.01	12.81	3.65	0.49
Pyrrhotite median values - 90KMZ5 (N=6)	398.9	17172	0.2	0.07	69.6	1.38	0.53	3.78	1.83	1.34	0.04	0.01
DCcp/Po - 90OKMZ5	**0.00**	**0.00**			**0.87**	**0.04**	**0.20**			**9.54**		
Chalcopyrite median values - NR-6 (N=4)	4.1	346	497.5	0.07	27.9	0.02	0.18	n.r.	0.11	2.44	10.65	0.63
Pyrrhotite median values - NR-6 (N=4)	393.0	12634	0.2	0.07	34.2	0.22	0.13	0.43	1.06	0.67	0.04	0.01
DCcp/Po - NR-6	**0.01**	**0.03**			**0.82**		**1.42**		**0.10**	**3.63**		
Chalcopyrite median values - NR-8 (N=5)	0.6	38	626.9	0.07	41.5	0.02	0.18	n.r.	0.07	17.56	7.97	1.68
Pyrrhotite median values - NR-8 (N=3)	99.7	8913	1.4	0.60	38.0	0.12	0.01	0.00	0.37	0.90	0.09	0.01
DCcp/Po - NR-8	**0.01**	**0.00**	**437.26**		**1.09**				**0.19**	**19.43**	**91.64**	
Chalcopyrite median values - NR-18 (N=4)	0.2	36	384.5	0.07	73.5	0.02	0.14	n.r.	2.21	6.64	21.51	3.17
Pyrrhotite median values - NR-18 (N=1)	67.9	8228	274.3	0.07	92.2	0.02	0.01	0.00	6.31	16.21	12.47	0.23
DCcp/Po - NR-18	**0.00**	**0.00**	**1.40**		**0.80**				**0.35**	**0.41**	**1.73**	**13.77**
Chalcopyrite median values - NR-17 (N=7)	0.6	61	459.2	0.07	88.9	0.02	0.10	n.r.	0.54	8.79	37.73	3.66
Pyrrhotite median values - NR-17 (N=5)	103.2	2749	84.8	0.15	97.9	0.02	0.01	0.00	2.44	5.17	3.80	0.05
DCcp/Po - NR-17	**0.01**	**0.02**	**5.42**		**0.91**				**0.22**	**1.70**	**9.92**	**73.00**
Chalcopyrite median values - 90OC13 (N=7)	0.2	16	489.9	0.07	60.7	0.02	0.09	n.r.	0.01	6.79	15.70	4.49
Pyrrhotite median values - 90OC13 (N=7)	29.3	1988	137.1	0.07	55.2	0.03	0.01	0.00	0.56	1.15	2.12	0.04
DCcp/Po - 90OC13	**0.01**	**0.01**	**3.57**		**1.10**					**5.88**	**7.41**	**102.27**
Chalcopyrite median values - 90OMZS1-3 (N=7)	0.1	5	181.4	0.07	67.0	0.02	0.07	n.r.	0.01	4.25	8.95	2.98
Pyrrhotite median values - 90OMZS1-3 (N=6)	13.8	581	0.3	0.07	51.5	0.37	0.53	1.32	0.02	1.28	0.06	0.01
DCcp/Po - 90OMZS1-3	**0.01**	**0.01**	**533.89**		**1.30**		**0.14**			**3.33**	**152.69**	

ANNEXE 8 – Cont.

Chalcopyrite and Pyrrhotite (DCcp/Po)	Sn	Sb	Te	Re	Os	Ir	Pt	Au	Tl	Pb	Bi
	ppm	ppm	ppm	ppm	ppm	ppm	ppm	ppm	ppm	ppm	ppm
Chalcopyrite median values - 90OMZS2-3 (N=7)	2.43	0.05	1.70	0.01	0.02	0.00	0.01	0.01	0.03	19.87	0.06
Pyrrhotite median values - 90OMZS2-3 (N=6)	0.11	0.05	0.95	0.10	0.02	0.02	0.05	0.01	0.00	1.20	0.11
DCcp/Po - 90OMZS2-3	**21.43**		**1.80**				**0.28**			**16.52**	**0.61**
Chalcopyrite median values - 90OKMZ5 (N=5)	1.54	0.05	2.01	0.16	0.02	0.00	0.46	0.01	0.09	2.23	0.18
Pyrrhotite median values - 90KMZ5 (N=6)	0.05	0.05	1.60	0.34	0.21	0.43	0.27	0.01	0.00	0.17	0.16
DCcp/Po - 90OKMZ5			**1.25**	**0.48**			**1.72**			**13.24**	**1.07**
Chalcopyrite median values - NR-6 (N=4)	0.10	0.05	0.44	0.01	0.02	0.00	0.07	0.01	0.01	12.96	0.10
Pyrrhotite median values - NR-6 (N=4)	0.05	0.05	0.26	0.11	0.02	0.03	0.21	0.01	0.00	2.54	0.31
DCcp/Po - NR-6							**0.33**			**5.10**	**0.32**
Chalcopyrite median values - NR-8 (N=5)	2.37	0.05	1.90	0.01	0.02	0.00	0.06	0.01	0.16	8.70	0.14
Pyrrhotite median values - NR-8 (N=3)	0.05	0.05	0.39	0.01	0.02	0.00	0.01	0.01	0.00	2.72	0.34
DCcp/Po - NR-8			**4.83**							**3.20**	**0.42**
Chalcopyrite median values - NR-18 (N=4)	1.80	0.05	8.23	0.01	0.02	0.00	0.16	0.01	0.14	0.37	0.75
Pyrrhotite median values - NR-18 (N=1)	0.05	0.05	8.73	0.01	0.02	0.00	0.31	0.02	0.60	3.80	6.11
DCcp/Po - NR-18			**0.94**				**0.52**	**0.54**	**0.24**	**0.10**	**0.12**
Chalcopyrite median values - NR-17 (N=7)	4.63	0.05	12.45	0.01	0.02	0.00	0.32	0.06	0.11	22.40	0.35
Pyrrhotite median values - NR-17 (N=5)	0.26	0.05	4.36	0.01	0.02	0.00	0.03	0.01	0.03	68.56	1.37
DCcp/Po - NR-17	**17.68**		**2.85**				**12.09**	**5.64**	**3.15**	**0.33**	**0.26**
Chalcopyrite median values - 90OC13 (N=7)	2.01	0.05	11.78	0.01	0.02	0.00	0.08	0.01	0.09	90.38	0.14
Pyrrhotite median values - 90OC13 (N=7)	0.33	0.05	2.95	0.01	0.02	0.00	0.07	0.01	0.04	120.92	0.15
DCcp/Po - 90OC13	**6.09**		**3.99**				**1.18**		**1.97**	**0.75**	**0.98**
Chalcopyrite median values - 90OMZS1-3 (N=7)	0.05	0.05	8.03	0.01	0.02	0.00	0.12	0.06	0.03	195.06	0.05
Pyrrhotite median values - 90OMZS1-3 (N=6)	0.05	0.05	1.17	0.27	0.15	0.20	0.01	0.01	0.01	3.86	0.11
DCcp/Po - 90OMZS1-3			**6.89**						**2.22**	**50.56**	**0.50**

ANNEXE 8 – Cont.

Chalcopyrite and Pyrrhotite (DCcp/Po)	Co	Cu	Zn	As	Se	Mo	Ru	Rh	Pd	Ag	Cd	In
	ppm	ppm	ppm	ppm	ppm	ppm	ppm	ppm	ppm	ppm	ppm	ppm
Chalcopyrite median values - NR-10 (N=3)	0.8	66	3316.9	0.07	82.5	0.02	0.11	n.r.	0.01	2.50	3.01	1.46
Pyrrhotite median values - NR-10 (N=6)	533.5	24433	0.2	0.18	105.7	0.55	4.73	16.69	0.61	2.85	0.04	0.01
DCcp/Po - NR-10	**0.00**	**0.00**	**16125.66**		**0.78**		**0.02**			**0.88**		
Chalcopyrite median values - 90OMZS2-2 (N=7)	0.1	8	374.3	0.07	54.7	0.02	0.09	n.r.	0.01	2.31	12.39	2.31
Pyrrhotite median values - 90OMZS2-2 (N=7)	22.3	1814	0.6	0.07	54.6	0.37	0.27	0.97	0.02	0.38	0.04	0.01
DCcp/Po - 90OMZS2-2	**0.00**	**0.00**	**652.71**		**1.00**		**0.31**			**6.07**		
Chalcopyrite median values - NR-13 (N=7)	0.6	56	736.4	0.07	29.4	0.02	0.13	n.r.	0.01	0.73	6.28	1.31
Pyrrhotite median values - NR-13 (N=6)	78.8	5158	0.3	0.07	33.3	0.46	0.21	0.86	0.01	0.31	0.04	0.01
DCcp/Po - NR-13	**0.01**	**0.01**	**2881.62**		**0.88**		**0.62**			**2.36**		
Chalcopyrite median values - NR-14 (N=6)	0.4	59	515.8	0.07	38.0	0.02	0.12	n.r.	0.01	1.14	7.38	1.48
Pyrrhotite median values - NR-14 (N=7)	70.2	6445	0.3	0.07	43.4	0.39	0.19	1.04	0.01	0.31	0.04	0.01
DCcp/Po - NR-14	**0.01**	**0.01**	**1655.02**		**0.88**		**0.61**			**3.65**		
Chalcopyrite median values - NR-11 (N=4)	0.1	20	377.3	0.07	83.4	0.02	0.10	n.r.	0.06	28.68	3.96	1.49
Pyrrhotite median values - NR-11 (N=6)	343.4	32100	0.2	0.84	94.9	3.59	1.25	6.68	1.68	2.58	0.04	0.01
DCcp/Po - NR-11	**0.00**	**0.00**	**1921.83**		**0.88**		**0.08**		**0.03**	**11.11**		
DCcp/Po median values	**0.01**	**0.01**	**593.3**		**0.88**	**0.04**	**0.26**		**0.19**	**3.65**	**43.26**	**73.00**
DCcp/Po min	**0.00**	**0.00**	**1.4**		**0.78**	**0.04**	**0.02**		**0.03**	**0.41**	**1.73**	**13.77**
DCcp/Po max	**0.03**	**0.03**	**16125.7**		**1.30**	**0.04**	**1.42**		**0.35**	**19.43**	**152.69**	**102.27**

ANNEXE 8 – Cont.

Chalcopyrite and Pyrrhotite (DCcp/Po)	Sn	Sb	Te	Re	Os	Ir	Pt	Au	Tl	Pb	Bi
	ppm	ppm	ppm	ppm	ppm	ppm	ppm	ppm	ppm	ppm	ppm
Chalcopyrite median values - NR-10 (N=3)	0.10	0.05	16.43	0.01	0.02	0.01	0.68	0.03	0.00	7.82	0.03
Pyrrhotite median values - NR-10 (N=6)	0.05	0.05	11.70	0.16	0.89	1.89	0.59	0.01	0.00	0.06	0.09
DCcp/Po - NR-10			**1.40**			**0.00**	**1.16**	**3.18**		**136.38**	**0.36**
Chalcopyrite median values - 90OMZS2-2 (N=7)	0.91	0.05	2.58	0.01	0.02	0.00	0.03	0.01	0.01	71.21	0.02
Pyrrhotite median values - 90OMZS2-2 (N=7)	0.05	0.05	1.03	0.17	0.07	0.10	0.10	0.01	0.00	2.57	0.07
DCcp/Po - 90OMZS2-2			**2.51**				**0.34**		**1.53**	**27.66**	**0.24**
Chalcopyrite median values - NR-13 (N=7)	2.35	0.05	0.94	0.01	0.02	0.00	0.13	0.01	0.01	28.19	0.07
Pyrrhotite median values - NR-13 (N=6)	0.05	0.05	0.80	0.21	0.06	0.09	0.05	0.01	0.00	1.04	0.08
DCcp/Po - NR-13			**1.16**				**2.43**			**27.09**	**0.94**
Chalcopyrite median values - NR-14 (N=6)	1.78	0.05	1.08	0.01	0.02	0.00	0.12	0.01	0.08	28.32	0.10
Pyrrhotite median values - NR-14 (N=7)	0.05	0.05	0.84	0.16	0.06	0.07	0.10	0.01	0.00	0.64	0.12
DCcp/Po - NR-14			**1.28**				**1.20**			**44.54**	**0.81**
Chalcopyrite median values - NR-11 (N=4)	0.34	0.05	9.36	0.01	0.02	0.00	0.33	0.01	0.12	17.88	0.14
Pyrrhotite median values - NR-11 (N=6)	0.05	0.05	3.97	0.19	0.33	0.66	0.37	0.02	0.02	16.86	1.33
DCcp/Po - NR-11	**6.82**		**2.36**				**0.89**		**6.14**	**1.06**	**0.11**
DCcp/Po median values	**12.25**		**2.08**	**0.31**		**0.00**	**1.16**	**3.18**	**2.09**	**13.24**	**0.42**
DCcp/Po min	**6.09**		**0.94**	**0.31**		**0.00**	**0.28**	**0.54**	**0.24**	**0.10**	**0.11**
DCcp/Po max	**21.43**		**6.89**	**0.48**		**0.00**	**12.09**	**5.64**	**6.14**	**136.38**	**1.07**

ANNEXE 8 – Cont.

Chalcopyrite and Cubanite (DCcp/Cbn)	Co	Cu	Zn	As	Se	Mo	Ru	Rh	Pd	Ag	Cd	In
	ppm	ppm	ppm	ppm	ppm	ppm	ppm	ppm	ppm	ppm	ppm	ppm
Chalcopyrite median values - 90MC15 (N=6)	0.01	49	79.1	0.16	133.6	0.08	0.08	n.r.	0.74	10.95	3.82	1.36
Cubanite median values - 90MC15 (N=6)	0.15	32	248.5	0.21	142.6	0.10	0.06	n.r.	0.93	36.69	12.06	1.52
DCcp/Cbn - 90MC15	**0.08**	**1.5**	**0.32**	**0.74**	**0.94**	**0.83**	**1.32**		**0.80**	**0.30**	**0.32**	**0.89**
Chalcopyrite median values - 90OMZS1-3 (N=7)	0.10	5	181.4	0.07	67.0	0.02	0.07	n.r.	0.01	4.25	8.95	2.98
Cubanite median values - 90OMZS1-3 (N=8)	7.92	167	31.9	0.07	70.5	0.02	0.05	n.r.	0.05	10.21	1.38	0.36
DCcp/Cbn - 90OMZS1-3	**0.01**	**0.03**	**5.69**		**0.95**		**1.38**			**0.42**	**6.46**	**8.27**
Chalcopyrite median values - 90OMZS2-2 (N=7)	0.10	8	374.3	0.07	54.7	0.02	0.09	n.r.	0.01	2.31	12.39	2.31
Cubanite median values - 90OMZS2-2 (N=1)	5.35	198	366.2	0.07	52.6	0.02	0.10	n.r.	0.01	21.11	25.68	2.23
DCcp/Cbn - 90OMZS2-2	**0.02**	**0.04**	**1.02**		**1.04**		**0.87**			**0.11**	**0.48**	**1.04**
DCcp/Cbn median values	**0.02**	**0.04**	**1.02**	**0.74**	**0.95**	**0.83**	**1.32**		**0.80**	**0.30**	**0.48**	**1.04**
DCcp/Cbn min	**0.01**	**0.03**	**0.32**	**0.74**	**0.94**	**0.83**	**0.87**		**0.80**	**0.11**	**0.32**	**0.89**
DCcp/Cbn max	**0.08**	**1.54**	**5.69**	**0.74**	**1.04**	**0.83**	**1.38**		**0.80**	**0.42**	**6.46**	**8.27**

ANNEXE 8 – Cont.

Chalcopyrite and Cubanite (DCcp/Cbn)	Sn	Sb	Te	Re	Os	Ir	Pt	Au	Tl	Pb	Bi
	ppm	ppm	ppm	ppm	ppm	ppm	ppm	ppm	ppm	ppm	ppm
Chalcopyrite median values - 90MC15 (N=6)	0.05	0.05	39.45	0.01	0.02	0.00	0.03	0.01	1.04	1.17	0.00
Cubanite median values - 90MC15 (N=6)	0.05	0.05	40.53	0.01	0.02	0.00	0.04	0.01	1.07	1.35	0.00
DCcp/Cbn - 90MC15			**0.97**				**0.87**		**0.97**	**0.87**	
Chalcopyrite median values - 90OMZS1-3 (N=7)	0.05	0.05	8.03	0.01	0.02	0.00	0.12	0.06	0.03	195.06	0.05
Cubanite median values - 90OMZS1-3 (N=8)	0.05	0.05	5.34	0.01	0.02	0.00	0.08	0.03	0.06	16.11	0.05
DCcp/Cbn - 90OMZS1-3			**1.50**				**1.46**	**2.25**	**0.51**	**12.11**	**1.12**
Chalcopyrite median values - 90OMZS2-2 (N=7)	0.91	0.05	2.58	0.01	0.02	0.00	0.03	0.01	0.01	71.21	0.02
Cubanite median values - 90OMZS2-2 (N=1)	0.74	0.05	2.34	0.01	0.02	0.00	0.01	0.01	0.03	87.20	0.02
DCcp/Cbn - 90OMZS2-2	**1.24**		**1.10**						**0.27**	**0.82**	**0.78**
DCcp/Cbn median values	**1.24**		**1.10**				**1.17**	**2.25**	**0.51**	**0.87**	**0.95**
DCcp/Cbn min	**1.24**		**0.97**				**0.87**	**2.25**	**0.27**	**0.82**	**0.78**
DCcp/Cbn max	**1.24**		**1.50**				**1.46**	**2.25**	**0.97**	**12.11**	**1.12**

ANNEXE 9 - Average proportion (%) of each element hosted in pyrrhotite (Po), pentlandite (Pn), chalcopyrite (Ccp), cubanite (Cbn) and sum, from the Cu-poor and Transitional, Cu-rich and Cu-rich (with cubanite) ores of the Noril'sk-Talnakh mining district. The whole-rock data used for the mass balance calculations is reported by Duran et al. (2017) (ANNEXE 2). Abbreviations: BMS= base-metal sulfides; n.r.= not reported; N= number of samples

ANNEXE 9

Ore Type/BMS	Ag	As	Au	Bi	Cd	Co	In	Ir	Mo	Os	Pb	Pd	Pt	Rh	Ru	Sb	Se	Sn	Te	Tl	Zn
Cu-poor and transitional massive sulfides (N= 7)																					
Po	7%	0%	0%	26%	0%	2%	0%	85%	70%	108%	8%	0%	2%	79%	80%	0%	50%	0%	51%	0%	0%
Pn	9%	1%	0%	12%	0%	86%	1%	7%	7%	0%	19%	68%	4%	3%	23%	0%	8%	1%	7%	15%	1%
Ccp	8%	0%	0%	3%	82%	0%	104%	0%	0%	0%	36%	0%	0%	n.r.	17%	0%	14%	14%	21%	1%	78%
Sum	***24%***	***1%***	***0%***	***41%***	***83%***	***89%***	***105%***	***92%***	***76%***	***108%***	***63%***	***68%***	***6%***	***82%***	***120%***	***0%***	***71%***	***14%***	***78%***	***16%***	***80%***
Cu-rich massive sulfide (N= 7)																					
Po	2%	0%	0%	3%	3%	2%	0%	n.r.	2%	n.r.	11%	1%	0%	n.r.	n.r.	0%	18%	0%	5%	1%	6%
Pn	1%	0%	0%	1%	0%	69%	0%	n.r.	1%	n.r.	2%	49%	0%	n.r.	n.r.	0%	5%	0%	5%	3%	0%
Ccp	19%	0%	0%	2%	59%	0%	68%	n.r.	0%	n.r.	19%	1%	1%	n.r.	n.r.	0%	46%	14%	46%	5%	57%
Sum	***21%***	***0%***	***0%***	***6%***	***62%***	***71%***	***68%***	**n.r.**	***3%***	**n.r.**	***33%***	***51%***	***1%***	**n.r.**	**n.r.**	***0%***	***70%***	***15%***	***57%***	***10%***	***63%***
Cu-rich massive sulfide with cubanite (N= 2)																					
Po	1%	0%	0%	1%	0%	0%	0%	n.r.	48%	n.r.	1%	0%	0%	n.r.	n.r.	0%	11%	0%	2%	0%	0%
Pn	10%	1%	0%	3%	0%	91%	0%	n.r.	45%	n.r.	35%	43%	0%	n.r.	n.r.	0%	10%	0%	9%	30%	0%
Ccp	13%	0%	1%	1%	33%	0%	67%	n.r.	3%	n.r.	74%	0%	0%	n.r.	n.r.	0%	50%	0%	53%	30%	22%
Cbn	9%	0%	0%	0%	9%	0%	7%	n.r.	3%	n.r.	5%	0%	0%	n.r.	n.r.	1%	13%	0%	11%	8%	6%
Sum	***32%***	***1%***	***1%***	***4%***	***43%***	***92%***	***74%***	**n.r.**	***99%***	**n.r.**	***114%***	***43%***	***1%***	**n.r.**	**n.r.**	***1%***	***83%***	***1%***	***75%***	***69%***	***29%***

ANNEXE 10 - Detailed methodology for LA-ICP-MS analyses.

Analyses by laser ablation-inductively coupled plasma-mass spectrometry (LA-ICP-MS) were performed at LabMaTer, Université du Québec à Chicoutimi (UQAC), using an Excimer 193 nm RESOlution M-50 laser ablation system (Australian Scientific Instrument) equipped with a double volume cell S-155 (Laurin Technic) and coupled with an Agilent 7900 mass spectrometer. The LA-ICP-MS tuning parameters were a laser frequency of 10 Hz, a power of 3 to 5 mJ/pulse, a dwell time of 7.5 ms, a rastering speed of 5 to 10 μm/s, and a fluence of 3 J/cm^2. Line scans across the surface of sulfides grains were made with beam sizes of 44, 33, and 25 μm, depending on grain size. The gas blank was measured for 30s before switching on the laser for at least 60s (Fig. A1a). The ablated material was then carried into the ICP-MS by an Ar–He gas mix at a rate of 0.8–1 L/min for Ar and 350 mL/min for He, and 2mL/min of nitrogen was also added to the mixture. Data reduction was carried out using the Iolite package for Igor Pro software (Paton et al., 2011).

Maps of element distribution were made on different sulfide minerals using a laser frequency of 15 Hz and a power of 5 mJ/pulse. The beam size (15 to 58 μm) and the stage movement speed (10 to 15 μm/s) were adapted to optimize spatial resolution and analysis time for grains of different sizes. The maps were generated using the Iolite software package on the basis of the time-resolved composition of each element. The maps indicate the relative concentration of the elements and are semi-quantitative.

The following isotopes were monitored: ^{29}Si, ^{33}S, ^{34}S, ^{57}Fe, ^{59}Co, ^{61}Ni, ^{63}Cu, ^{65}Cu, ^{66}Zn, ^{75}As, ^{77}Se, ^{82}Se, ^{95}Mo, ^{99}Ru, ^{101}Ru, ^{103}Rh, ^{105}Pd, ^{108}Pd, ^{109}Ag, ^{111}Cd, ^{113}In, ^{115}In, ^{118}Sn, ^{121}Sb, ^{128}Te, ^{130}Te, ^{185}Re, ^{189}Os, ^{193}Ir, ^{194}Pt, ^{195}Pt, ^{197}Au, ^{203}Tl, ^{205}Tl, ^{208}Pb and ^{209}Bi. Inclusions of accessory minerals such as platinum-group minerals (Fig. 1B) were commonly encountered during analysis and they were excluded from the signal to obtain the true sulfide composition. Analyses of pentlandite grains showing zonation of trace elements were performed in a perpendicular line from pyrrhotite to chalcopyrite (Fig. 1C; see manuscript for further explanation on the origin of zonation), and the signal was completely integrated to obtain the average composition (Fig. 1D and 1E).

Polyatomic interference of ^{61}Ni^{40}Ar on ^{101}Ru was corrected using ^{101}Ru measured in a NiS blank which does not contain Ru. Polyatomic interference of ^{63}Cu^{40}Ar on ^{103}Rh was corrected using ^{103}Rh measured in MASS-1, which contains 13.4% ^{63}Cu but no ^{103}Rh. The ^{103}Rh values in chalcopyrite are not reported as the interference is too important to be corrected. Direct interferences of ^{108}Cd on ^{108}Pd and ^{115}Sn on ^{115}In were corrected manually by monitoring ^{111}Cd and ^{118}Sn, respectively.

Internal standardization was based on ^{57}Fe using stoichiometric iron values of pentlandite (i.e. 32.56 %). Three certified reference materials were used for external calibration: Laflamme Po727,which is a synthetic FeS doped with ~40 ppm PGE and Au supplied by Memorial University of Newfoundland, was used to calibrate for PGE and Au; MASS-1 (Wilson et al., 2002), which is a ZnCuFeS pressed powder pellet doped with 50–70 ppm of most chalcophile

elements, supplied by the United States Geological Survey (USGS), was used to calibrate for Cu, Se, Te, Tl and Zn; GSE-1g, which is a natural basaltic glass fused and doped with most elements at 300-500 ppm, supplied by the USGS, was used to calibrate for Ag, As, Bi, Cd, Co, In, Mo, Ni, Pb, Re, Sb and Sn using preferred values from the GeoReM database (Jochum et al., 2005). MASS-1, GSE-1g and JB-MSS5 (an FeS sulfide containing 50-70 ppm of most chalcophile elements, supplied by James Brenan) were also used for intra-standard quality control.

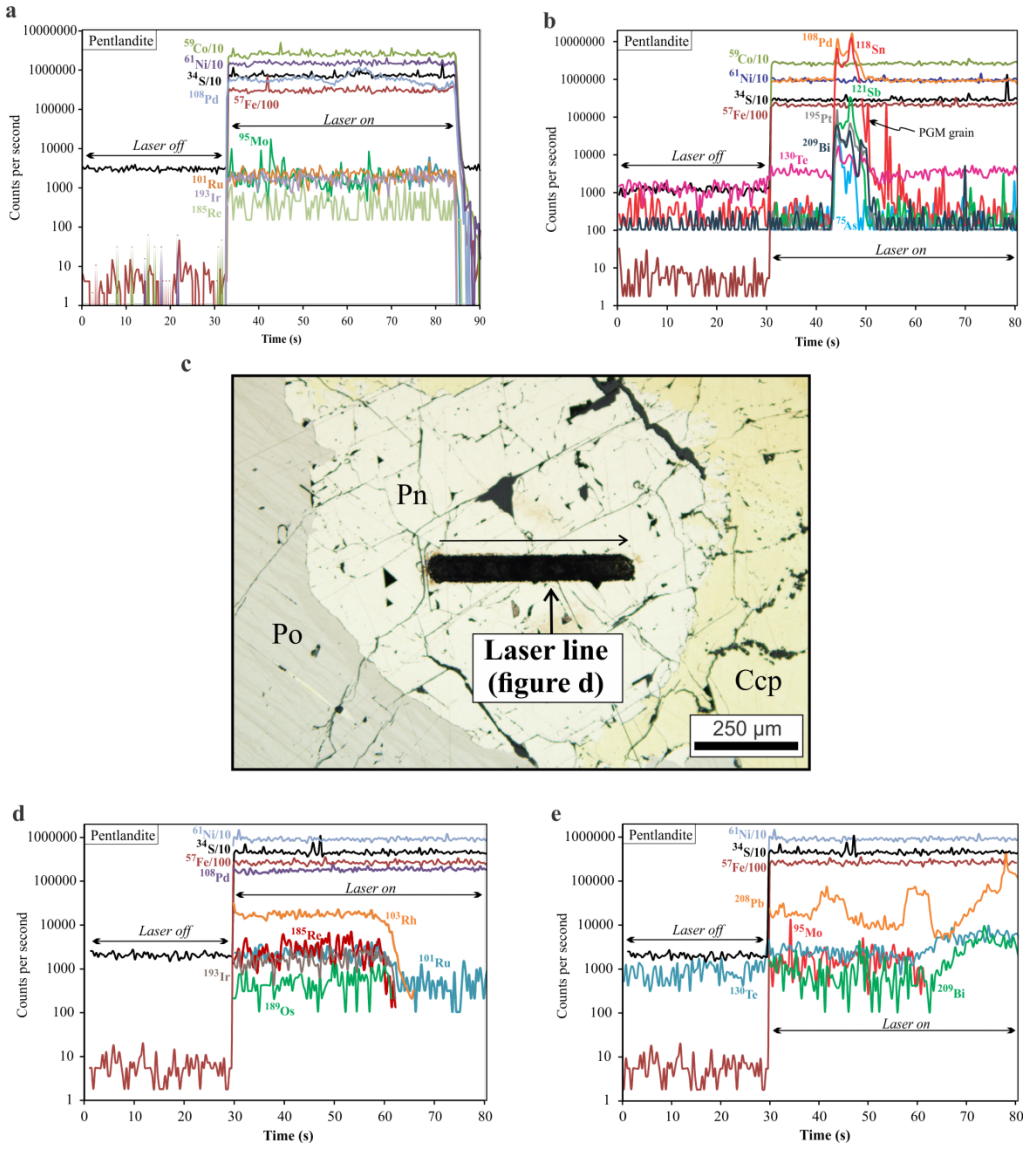
a
Pentlandite
^{59}Co/10
^{61}Ni/10
^{34}S/10
^{108}Pd
^{57}Fe/100
Laser off
Laser on
^{95}Mo
^{101}Ru
^{193}Ir
^{185}Re
Counts per second
Time (s)
b
Pentlandite
^{108}Pd
^{118}Sn
^{59}Co/10
^{61}Ni/10
^{34}S/10
^{57}Fe/100
^{121}Sb
^{195}Pt
PGM grain
^{209}Bi
^{130}Te
^{75}As
Laser off
Laser on
Counts per second
Time (s)
c
Pn
Po
Ccp
Laser line
(figure d)
250 µm
d
Pentlandite
^{61}Ni/10
^{34}S/10
^{57}Fe/100
^{108}Pd
Laser on
Laser off
^{103}Rh
^{185}Re
^{193}Ir
^{101}Ru
^{189}Os
Counts per second
Time (s)
e
Pentlandite
^{61}Ni/10
^{34}S/10
^{57}Fe/100
^{208}Pb
Laser off
^{95}Mo
^{130}Te
^{209}Bi
Laser on
Counts per second
Time (s)

Figure 1 - Time (seconds) versus counts spectra for LA-ICP-MS analyses of pentlandite. A) Granular pentlandite containing Co, Mo, Re, Pd, Ru and Ir in solid solution. Note that the concentration of trace elements is constant through all the line scan. B) Granular pentlandite hosting an inclusion of PGM grain with Pd-Pt-As-Bi-Sb-Sn-Te, intersected by the laser at 45-50s. C) Reflected light photomicrography of contact pentlandite in between pyrrhotite and chalcopyrite showing the laser ablation line scan. Note that the laser line was positioned perpendicular from pyrrhotite towards chalcopyrite (arrow indicating the direction of the line scan). D)/E) Contact pentlandite obtained from laser line scan in figure "c". Note the zonation of Re, Rh, Ru and Os, with higher counts near the contact with pyrrhotite, decreasing towards the contact with chalcopyrite, and increasing counts of Te, Bi and Pb towards the same contact. Ccp – chalcopyrite; Pn – pentlandite; Po – pyrrhotite.

References:

Jochum, K. P., Nohl, U., Herwig, K., Lammel, E., Stoll, B., and Hofmann, A.W., 2005, GeoReM: a new geochemical database for reference materials and isotopic standards: Geostandards and Geoanalytical Research, v. 29, p. 333-338.

Paton, C., Hellstrom, J., Paul, B., Woodhead, J., and Hergt, J., 2011, Iolite: Freeware for the visualisation and processing of mass spectrometric data: Journal of Analytical Atomic Spectrometry, v. 26, no. 12, p. 2508-2518.

Wilson, S. A., Ridley, W. I., and Koenig, A. E., 2002, Development of sulfide calibration standards for the laser ablation inductively-coupled plasma mass spectrometry technique: Journal of Analytical Atomic Spectrometry, v. 17, p. 406-409.

ANNEXE 11 - Analyses of reference materials used to monitor the data quality for whole-rock TABS and Se results from the Marginal Zone of the Bushveld Complex. Normal font certificate or assigned value, italics average of literature values and Mansur et al. (2019) (Chapter 2) for CH-4 amd TDB-1, median of GeoPt18 round for KPT-1. Detection limit = 3*sigma of the blank; Stdev = standard deviation; RSD= relative standard deviation; n= number of individual analyses

ANNEXE 11

		As	Bi	Sb	Se	Te
		ppm	ppm	ppm	ppm	ppm
Reference material	Detection limit	*0.003*	*0.005*	*0.005*	*0.002*	*0.006*
CH-4 Anorthosite CANMET	Certificate value	8.80	0.6	0.77	2.1	*0.36*
	Stdev	0.60	0.2	0.4	0.2	*0.072*
	This study	8.34	0.73	0.861	1.942	0.438
	Stdev (n= 4)	0.21	0.14	0.076	0.042	0.032
	Relative stdev	2.55	18.67	8.86	2.15	7.31
TDB-1 Diabase CANMET	Certificate value	2.50	*0.063*	1	*0.38*	*0.036*
	Stdev	0.50	*0.0189*	0.4	*0.032*	*0.007*
	This study	2.01	0.088	0.938	0.372	0.032
	Stdev (n= 4)	0.19	0.008	0.057	0.073	0.005
	Relative stdev	9.44	9.04	6.03	19.55	16.07
GeoPT-18/ KPT-1 Sulfide-bearing dolerite IAG	Assigned value	*2.20*	0.94	10.10	2.90	*0.35*
	Stdev	*0.26*	0.19	1.27	0.46	*0.08*
	This study	2.28	0.902	11.08	2.93	0.47
	Stdev (n= 4)	0.11	0.095	0.156	0.047	0.046
	Relative stdev	4.85	10.58	1.40	1.62	9.81

ANNEXE 12 - Complete dataset of whole-rock TABS and Se analyses of samples from the Marginal Zone of the Bushveld Complex obtained in this study, and results previously reported by Barnes and Maier (2002) and Barnes et al. (2009; 2010) used for comparison. The TABS and Se values for upper (Hu and Gao 2008) and lower (Rudnick and Gao 2003) continental crust , komatiite and MORB (Arevalo and McDonough 2010) used for comparison are also reported. The geological reference material OKUM is used as a proxy for a komatiite composition (IAGEO). Values in bold are below the detection limit and were replaced by half of the detection limit values. All values in ppm. DL - Detection limit; n.r. - not reported

ANNEXE 12

			This study				
Sample	Unit	Texture	As	Bi	Sb	Se	Te
DL			*0.003*	*0.005*	*0.005*	*0.002*	*0.006*
DI-225	B-1	Quenched	1.702	0.043	0.148	0.104	0.020
CD-001		Quenched	2.765	0.058	0.164	0.128	0.013
CD-017		Quenched	3.079	0.097	0.383	0.157	0.033
DI-204		Quenched	0.824	0.026	0.064	0.116	0.016
ECBV-018		Granular	1.720	0.068	0.174	0.111	0.016
ECBV-019		Quenched	1.716	0.051	0.200	0.157	0.024
ECBV-021		Quenched	1.663	0.044	0.157	0.104	0.018
ECBV-049A		Granular	0.127	0.014	0.019	0.122	0.016
ECBV-105		Granular	2.927	0.082	0.222	0.121	0.022
ECBV-106		Quenched	2.490	0.035	0.157	0.103	0.008
ECBV-111		Granular	1.395	0.022	0.322	0.020	0.004
Average B-1			1.855	0.049	0.183	0.113	0.017
Bc-6	B-2	Fine-grained	0.124	0.006	**0.003**	0.060	**0.003**
Bc-25		Fine-grained	0.176	0.010	0.008	0.051	**0.003**
CO-066		Granular	0.070	0.017	0.018	0.051	0.006
CO-253		Granular	0.069	0.017	0.015	0.267	0.018
ECBV-025		Granular	0.032	0.015	0.012	0.102	0.007
ECBV-026		Granular	0.060	**0.003**	0.032	0.158	0.012
ECBV-058		Granular	0.178	0.017	0.014	0.033	0.010
ECBV-064		Granular	0.354	0.006	0.056	0.035	**0.003**
Average B-2			0.133	0.011	0.020	0.095	0.008

ANNEXE 12 – Cont.

			This study				
Sample	Unit	Texture	As	Bi	Sb	Se	Te
DL			*0.003*	*0.005*	*0.005*	*0.002*	*0.006*
CO-048	B-3	Fine-grained	0.077	0.006	0.032	0.019	**0.003**
CO-252		Fine-grained	0.030	0.013	0.008	0.011	**0.003**
ECBV-013		Fine-grained	0.093	**0.003**	0.028	0.022	**0.003**
ECBV-063		Fine-grained	0.152	0.013	0.006	0.121	0.008
Average B-3			0.088	0.009	0.019	0.043	0.004
60:40 mixture of B1:B2			1.166	0.034	0.117	0.106	0.013
Upper Continental Crust (UC)			5.700	0.230	0.750	0.083	0.027
Lower Continental Crust (LC)			0.200	0.200	0.100	0.170	0.005
Komatiite (OKUM)			0.450	0.010	0.020	0.210	0.020
MORB			0.18	0.07	0.07	0.11	0.02
Bulk 60% komatiite + 40% Upper Crust			2.388	0.134	0.342	0.099	0.023
AFC 30% UC with komatiite + 27% fractation crystallization			2.483	0.161	0.371	0.140	0.030
AFC 30% LC with komatiite + 27% fractation crystallization			0.255	0.149	0.108	0.175	0.021

ANNEXE 12 – Cont.

		Data from Barnes and Maier (2002) and Barnes et al (2009; 2010)												
Sample	Unit	S	Ni	Cu	Os	Ir	Ru	Rh	Pt	Pd	Hf	La	Sm	Th
DI-225	B-1	619	n.r.	58	n.r.	n.r.	n.r.	n.r.	n.r.	n.r.	n.r.	n.r.	n.r.	n.r.
CD-001		466	241	46	0.00033	0.00049	0.00329	0.0017	0.02165	0.01516	1.91	19.36	2.79	3.38
CD-017		491	408	67	0.00043	0.00074	0.00257	0.00191	0.02502	0.01682	1.29	15.17	2.5	2.5
DI-204		465	300	47	<0.1	0.0002	0.00096	0.00186	0.01458	0.01129	1.34	12.88	2.02	2.59
ECBV-018		360	336	44	0.0011	0.00052	<2	0.002	0.025	0.015	1.76	16.74	2.35	3.68
ECBV-019		439	288	45	0.00123	0.00106	0.00227	0.00195	0.0193	0.01249	1.84	17.44	2.4	4.02
ECBV-021		619	190	58	0.00034	0.00053	0.00313	0.00182	0.01935	0.02193	2.36	20.7	3.14	3.93
ECBV-049A		400	324	54	n.r.	n.r.	n.r.	n.r.	n.r.	n.r.	1.96	17.24	3.08	1.76
ECBV-105		426	165	53	0.00016	0.00044	<2	0.0013	0.015	0.0117	2.78	22.82	3.65	4.96
ECBV-106		280	220	55	0.00035	0.00031	<2	0.0017	0.015	0.0075	1.93	20.85	3.22	4.25
ECBV-111		n.r.	368	39	n.r.	n.r.	n.r.	n.r.	n.r.	n.r.	1.92	16.78	2.84	3.58
Average B-1		457	284	51.5	0.001	0.001	0.002	0.002	0.019	0.014	1.91	18.00	2.80	3.47
Bc-6	B-2	168	121	77.8	<0.15	0.00023	0.00125	0.00108	0.01099	0.00957	1.5	15.3	3.85	0.65
Bc-25		56	125	77.8	<0.15	0.0002	0.0006	0.00071	0.01238	0.0072	1.5	15.26	3.89	0.59
CO-066		165	86	51	<0.15	0.00016	0.0004	0.00037	0.00453	0.00155	n.r.	n.r.	n.r.	
CO-253		299	104	110	<0.15	0.0001	0.00016	0.00021	0.00217	0.00135	1.1	15.56	4.26	0.52
ECBV-025		n.r.	122	84.4	<0.1	0.00002	<2	<0.3	0.002	<2	1.38	14	3.75	0.417
ECBV-026		160	148	111.1	0.00012	0.00024	<2	<0.3	0.008	0.0046	1.11	12.89	3.34	0.632
ECBV-058		79	173	42.5	<0.1	0.00038	<2	0.0005	0.021	0.0117	0.87	11.71	2.84	0.381
ECBV-064		111	125	66.9	<0.1	0.00023	<2	0.0012	0.014	0.0108	1.47	16.17	4.09	1.146
Average B-2		148	126	77.7	0.000	0.000	0.001	0.001	0.009	0.007	1.28	14.41	3.72	0.62
CO-048	B-3	44	163	75	0.00023	0.00036	0.0018	0.00112	0.0184	0.00765	0.4	3.42	1.17	0.27
CO-252		53	123	3	0.00019	0.00047	0.00182	0.00122	0.01998	0.00589	0.2	1.78	0.72	0.03
ECBV-013		81	151	9.9	<0.1	0.00027	<2	0.0008	0.015	0.0054	0.74	5.14	1.36	0.564
ECBV-063		520	151	278.8	n.r.	n.r.	n.r.	n.r.	n.r.	n.r.	0.78	6.98	2.39	0.457
Average B-3		175	147	91.7	0.0002	0.0004	0.002	0.001	0.018	0.006	0.53	4.33	1.41	0.33025
60:40 mixture of B1:B2		333.214	220.600	61.948	0.000	0.000	0.002	0.001	0.015	0.011	1.80	14.10	2.97	2.56

ANNEXE 13 - Modelling of the distribution of TABS, Se and Pd in the Merensky Reef at the Impala and Rustenburg sections. Observed values for TABS and Se are from Chapter 6 (ANNEXE 16). All values in ppm.

ANNEXE 13

Intrusion	Locality	Sample	Rock	Height (cm)	Melt	S	wt frac cum sul	Cumulate sil and oxide	As melt	As sul	As sum	As observed	As model/obs
		IM-1	Norite	108	0.166	1560	0.004	0.830	0.192	0.009	0.201	0.065	3.080
		IM-3	Norite	98	0.194	1880	0.005	0.802	0.224	0.011	0.236	0.086	2.743
		IM-5	Norite	88	0.206	2560	0.007	0.788	0.238	0.016	0.254	0.117	2.179
		IM-7	Melanorite	78	0.274	4480	0.012	0.714	0.318	0.028	0.346	0.184	1.884
		IM-9	Melanorite	68	0.343	7320	0.020	0.637	0.398	0.046	0.444	0.228	1.945
		IM-11	Melanorite	58	0.276	4560	0.012	0.712	0.320	0.028	0.348	0.198	1.760
		IM-13	Melanorite	48	0.509	680	0.000	0.491	0.590	0.001	0.591	0.444	1.330
		IM-15	Melanorite	38	0.526	880	0.001	0.473	0.611	0.002	0.613	0.413	1.486
		IM-17	Melanorite	28	0.522	680	0.000	0.477	0.606	0.001	0.607	0.225	2.695
		IM-18	Melanorite	23	0.345	1360	0.003	0.652	0.400	0.007	0.407	0.216	1.886
		IM-19	Melanorite	18	0.341	4680	0.012	0.647	0.395	0.029	0.424	0.227	1.869
Bushveld Complex	Impala mine	IM-20	Melanorite	13	0.198	12120	0.034	0.768	0.230	0.079	0.309	0.178	1.741
		IM-21	Melanorite	8	0.236	20480	0.058	0.706	0.273	0.134	0.408	0.115	3.530
		IM-22	Upper Chromitite	6	0.055	3400	0.010	0.936	0.064	0.022	0.086	0.109	0.788
		IM-23	Mela-norite	3	0.086	5960	0.017	0.897	0.100	0.039	0.139	0.081	1.720
		IM-24	Lower Chromitite	0	0.103	4080	0.011	0.885	0.120	0.026	0.146	0.069	2.111
		IM-25	Anorthosite	-3	0.101	4080	0.011	0.888	0.117	0.026	0.143	0.082	1.755
		IM-26	Leuconorite	-8	0.068	18320	0.052	0.880	0.079	0.121	0.200	0.096	2.088
		IM-27	Leuconorite	-17	0.068	4480	0.013	0.920	0.078	0.029	0.108	0.052	2.085
		IM-28	Leuconorite	-23	0.085	9720	0.028	0.887	0.099	0.064	0.163	0.060	2.708
		IM-30	Leuconorite	-33	0.086	440	0.001	0.913	0.100	0.002	0.102	0.035	2.915
		IM-32	Leuconorite	-48	0.104	196	0.000	0.896	0.120	0.001	0.121	*0.003*	
		IM-34	Leuconorite	-58	0.091	173	0.000	0.909	0.106	0.001	0.106	*0.003*	
		IM-36	Leuconorite	-68	0.077	178	0.000	0.922	0.090	0.001	0.090	0.036	2.503

ANNEXE 13 – Cont.

Intrusion	Locality	Sample	Bi melt	Bi sul	Bi sum	Bi observed	Bi model/obs	Sb melt	Sb sul	Sb sum	Sb obs	Sb model/obs	Te melt	Te sul	Te sum	Te obs	Te model/obs
Bushveld Complex	Impala mine	IM-1	0.006	0.035	0.040	0.008	4.808	0.020	0.002	0.022	0.040	0.549	0.002	0.019	0.022	0.065	0.331
		IM-3	0.007	0.042	0.049	0.022	2.184	0.023	0.003	0.026	0.022	1.190	0.003	0.023	0.026	0.124	0.210
		IM-5	0.007	0.059	0.066	0.029	2.269	0.024	0.004	0.028	0.006	4.968	0.003	0.032	0.035	0.098	0.360
		IM-7	0.009	0.105	0.114	0.157	0.727	0.032	0.007	0.040	0.011	3.464	0.004	0.058	0.062	0.316	0.195
		IM-9	0.012	0.174	0.185	0.166	1.114	0.041	0.012	0.052	0.033	1.582	0.005	0.096	0.101	0.303	0.333
		IM-11	0.010	0.107	0.116	0.060	1.940	0.033	0.007	0.040	0.021	1.880	0.004	0.059	0.063	0.186	0.337
		IM-13	0.018	0.004	0.022	0.014	1.510	0.060	0.000	0.061	0.031	1.939	0.007	0.002	0.010	0.022	0.433
		IM-15	0.018	0.009	0.027	0.005	5.344	0.062	0.001	0.063	0.026	2.427	0.008	0.005	0.012	0.049	0.256
		IM-17	0.018	0.004	0.022	0.008	2.838	0.062	0.000	0.062	0.015	4.042	0.008	0.002	0.010	0.020	0.481
		IM-18	0.012	0.025	0.037	0.110	0.338	0.041	0.002	0.043	0.024	1.743	0.005	0.014	0.019	0.129	0.147
		IM-19	0.012	0.214	0.226	0.543	0.416	0.040	0.007	0.048	0.048	0.997	0.005	0.539	0.544	0.679	0.801
		IM-20	0.007	0.588	0.595	0.846	0.703	0.023	0.020	0.044	0.036	1.198	0.003	1.481	1.483	1.555	0.954
		IM-21	0.008	0.998	1.006	0.938	1.073	0.028	0.034	0.062	0.039	1.610	0.003	2.514	2.518	2.390	1.053
		IM-22	0.002	0.165	0.167	0.285	0.585	0.006	0.006	0.012	0.025	0.482	0.001	0.415	0.416	0.322	1.291
		IM-23	0.003	0.290	0.293	0.210	1.391	0.010	0.010	0.020	0.043	0.470	0.001	0.729	0.731	0.408	1.791
		IM-24	0.004	0.196	0.200	0.172	1.161	0.012	0.007	0.019	0.017	1.114	0.002	0.494	0.495	0.399	1.242
		IM-25	0.003	0.196	0.200	0.160	1.252	0.012	0.007	0.019	0.060	0.312	0.001	0.494	0.496	0.511	0.969
		IM-26	0.002	0.900	0.902	0.733	1.231	0.008	0.031	0.039	0.054	0.717	0.001	2.267	2.268	2.599	0.873
		IM-27	0.002	0.218	0.220	0.313	0.703	0.008	0.007	0.015	0.022	0.700	0.001	0.548	0.549	0.855	0.642
		IM-28	0.003	0.475	0.478	0.399	1.199	0.010	0.016	0.026	0.029	0.917	0.001	1.197	1.198	1.198	1.000
		IM-30	0.003	0.009	0.012	*0.005*	2.180	0.010	0.001	0.011	*0.005*	2.079	0.001	0.005	0.006	0.009	0.650
		IM-32	0.004	0.002	0.006	0.013	0.467	0.012	0.000	0.012	0.009	1.386	0.002	0.001	0.003	0.011	0.253
		IM-34	0.003	0.002	0.005	*0.005*	0.959	0.011	0.000	0.011	0.009	1.150	0.001	0.001	0.002	*0.006*	0.387
		IM-36	0.003	0.003	0.005	*0.005*	0.958	0.009	0.000	0.009	0.010	0.903	0.001	0.001	0.003	*0.006*	0.396

ANNEXE 13 – Cont.

Intrusion	Locality	Sample	Rock	Height (cm)	Melt	S	wt frac cum sul	Cumulate sil and oxide	As melt	As sul	As sum	As observed	As model/obs
Bushveld Complex	Rustenburg mine	M4	Melanorite	27	0.124	9800	0.028	0.848	0.144	0.064	0.208	0.123	1.686
		M3	Melanorite	23	0.077	8900	0.025	0.898	0.089	0.058	0.147	0.143	1.029
		M2	Melanorite	18	0.116	7400	0.021	0.863	0.135	0.048	0.183	0.076	2.405
		M1	Melanorite	13.5	0.133	32100	0.091	0.775	0.155	0.212	0.366	0.143	2.559
		UC	Upper Chromitite	10	0.134	5300	0.015	0.852	0.155	0.034	0.189	0.070	2.688
		CGM-2	Coarse-grained melanorite	6	0.113	13900	0.039	0.847	0.132	0.091	0.223	0.203	1.101
		CGM-1	Coarse-grained melanorite	2	0.135	30700	0.087	0.778	0.156	0.203	0.359	0.126	2.842
		LC	Lower Chromitite	0	0.168	4700	0.013	0.819	0.195	0.030	0.225	0.046	4.903
		AN	Anorthosite	-2	0.114	3700	0.010	0.875	0.133	0.024	0.156	0.071	2.214

Intrusion	Locality	Sample	Bi melt	Bi sul	Bi sum	Bi observed	Bi model/obs	Sb melt	Sb sul	Sb sum	Sb obs	Sb model/obs	Te melt	Te sul	Te sum	Te obs	Te model/obs
Bushveld Complex	Rustenburg mine	M4	0.004	0.477	0.481	0.378	1.272	0.015	0.016	0.031	0.034	0.923	0.002	1.202	1.203	0.857	1.404
		M3	0.003	0.435	0.438	0.369	1.186	0.009	0.015	0.024	0.060	0.402	0.001	1.096	1.097	0.832	1.318
		M2	0.004	0.359	0.363	0.400	0.909	0.014	0.012	0.026	0.033	0.782	0.002	0.905	0.906	0.760	1.192
		M1	0.005	1.576	1.581	1.404	1.126	0.016	0.054	0.070	0.062	1.124	0.002	3.970	3.972	4.453	0.892
		UC	0.005	0.255	0.259	0.329	0.788	0.016	0.009	0.025	0.037	0.656	0.002	0.642	0.644	0.748	0.861
		CGM-2	0.004	0.680	0.684	0.605	1.130	0.013	0.023	0.037	0.028	1.302	0.002	1.712	1.714	1.763	0.972
		CGM-1	0.005	1.507	1.512	1.561	0.968	0.016	0.052	0.068	0.040	1.706	0.002	3.796	3.798	4.389	0.865
		LC	0.006	0.223	0.229	0.353	0.650	0.020	0.008	0.028	0.048	0.573	0.002	0.563	0.565	0.573	0.986
		AN	0.004	0.177	0.181	0.220	0.820	0.014	0.006	0.020	0.011	1.773	0.002	0.445	0.447	0.666	0.672

ANNEXE 13 – Cont.

Intrusion	Locality	Se melt	Se sul	Se sum	Se obs	Se model/obs	Pd melt	Pd sul	Pd sum	Pd observed	Pd model/obs
Bushveld Complex	Rustenburg mine	0.013	3.505	3.518	4.143	0.849	0.001	4.559	4.560	2.16	2.111
		0.008	3.196	3.204	3.860	0.830	0.001	4.158	4.158	2.36	1.762
		0.012	2.639	2.651	2.843	0.932	0.001	3.432	3.433	2.22	1.547
		0.014	11.580	11.594	14.646	0.792	0.001	15.062	15.064	11.9	1.266
		0.014	1.872	1.886	1.994	0.945	0.001	2.434	2.436	4.27	0.570
		0.012	4.994	5.006	5.656	0.885	0.001	6.496	6.497	5.94	1.094
		0.014	11.072	11.087	14.323	0.774	0.001	14.402	14.403	16.29	0.884
		0.018	1.642	1.659	1.630	1.018	0.002	2.135	2.137	4.4	0.486
		0.012	1.299	1.311	1.567	0.836	0.001	1.690	1.691	4.03	0.420

Composition of the cumulate sulfides using zone refining equation		Cs=cl*(D-(D-1)*@EXP(-(1/D*N)))					
	N	As	Bi	Sb	Te	Se	Pd
Composition of the cumulate sulfide inside reef Csul	20000	2.32	17.26	0.59	43.47	126.79	164.92
Composition of the cumulate sulfide outside reef	350	2.32	8.71	0.59	4.81	32.15	3.66
Ci = 60:40 mixture B1+B2		1.160	0.035	0.118	0.015	0.106	0.0105
D sul/sil		2	500	5	3000	1200	40000

ANNEXE 14 - Analyses of reference materials used to monitor the data quality for whole-rock TABS and Se results from the Merensky Reef and J-M Reef of the Bushveld and Stillwater Complexes. Normal font certificate or assigned value, italics average of literature values and Mansur et al. (2019) (Chapter 2) for CH-4 amd TDB-1, median of GeoPt18 round for KPT-1. Detection limit = 3*sigma of the blank; Stdev = standard deviation; RSD= relative standard deviation; n= number of individual analyses

ANNEXE 14

		As	Bi	Sb	Se	Te
		ppm	ppm	ppm	ppm	ppm
Reference material	Detection limit ppm	*0.003*	*0.005*	*0.005*	*0.002*	*0.006*
CH-4 Anorthosite CANMET	Certificate value	8.80	0.6	0.77	2.1	*0.36*
	Stdev	0.60	0.2	0.4	0.2	0.072
	RDS%	6.82	33.33	51.95	9.52	20.00
	This study	8.34	0.73	0.861	1.942	0.438
	Stdev (n= 4)	0.21	0.14	0.076	0.042	0.032
	Relative difference %	5.18	21.69	11.83	7.52	21.70
TDB-1 Diabase CANMET	Certificate value	2.50	*0.063*	1	*0.38*	*0.036*
	Stdev	0.50	*0.0189*	0.4	*0.032*	*0.007*
	RDS%	20.00	30.00	40.00	8.42	20.00
	This study	2.01	0.088	0.938	0.372	0.032
	Stdev (n= 4)	0.19	0.008	0.057	0.073	0.005
	Relative difference %	19.42	39.08	6.20	2.21	10.99
GeoPT-18/ KPT-1 Sulfide-bearing dolerite IAG	Certificate value	2.20	0.94	10.10	2.71	0.35
	Stdev	0.53	0.19	1.27	0.46	0.09
	RDS%	24.09	20.21	12.57	16.97	25.71
	This study	2.28	0.902	11.08	2.93	0.47
	Stdev (n= 4)	0.11	0.095	0.156	0.047	0.046
	Relative difference %	3.56	4.04	9.69	8.12	34.95

ANNEXE 15 - Analyses of reference materials used in the calibration of the LA-ICP-MS and in-house reference materials used to monitor the data quality for analyses of sulfide minerals and phlogopite from the Bushveld and Stillwater Complexes. Stdev= standard deviation; n= number of analyses; RSD= relative standard deviation; n.d.= not determined.

ANNEXE 15

Reference materials and results for base sulfide minerals													
Element	^{34}S	^{57}Fe	^{59}Co	^{61}Ni	^{65}Cu	^{66}Zn	^{75}As	^{82}Se	^{95}Mo	^{101}Ru	^{103}Rh	^{108}Pd	^{109}Ag
Detection limits	58.364		0.008	0.306	0.182	0.079	0.044	0.617	0.008	0.008	0.001	0.027	0.003
Reference materials	Po-727	Po-727	MASS-1	GSE-1g	MASS-1	MASS-1	MASS-1	MASS-1	MASS-1	Po-727	Po-727	Po-727	MASS-1
Concentrations used	390900	610700	60	440	134000	210000	65	51	59	36.5	41.6	43.4	50
Stdev	1600	2100	10	30	500	5000	3	4	9	0.3	0.3	0.3	5
JB-MSS-5 Working value	404700	570000	0.28	10487	208	n.d.	79.0	47.3	0.23	21.7	61.4	65.2	53
Stdev	n.d.	9000	0.02	n.d.	24	n.d.	11.0	13.4	0.02	2.3	7.2	5.1	4.9
AVE JB-MSS-5	388912		0.623	10799	216	8	63.3	61.5	0.45	19.8	57.8	50.3	46.3
Stdev (n= 25)	26000.17		0.36	390	25	3	5.2	5.1	0.10	1.5	4.1	3.2	2.2
RSD (%)	7%		57%	4%	11%	34%	8%	8%	23%	7%	7%	6%	5%
GSE-1 g Working value	n.d.	98717	380		380	460	260	20	390	n.d.	n.d.	n.d.	200
Stdev	n.d.	2332	20		40	10	90	16	30	n.d.	n.d.	n.d.	20
AVE GSE-1g	2502.16		335.76		382	407	342	51	384	0.05	34.9	105	152
Stdev (n= 25)	1344.73		14.20		33	29	12	10	16	0.02	9.4	27	11
RSD (%)	54%		4%		9%	7%	4%	20%	4%	31%	27%	26%	7%
MASS-1 Working value	276000	156000		97						n.d.	n.d.	n.d.	
Stdev	1000	1000		15						n.d.	n.d.	n.d.	
AVE MASS-1	265472	IS		105						0.01	0.7	0.98	
Stdev (n= 25)	14339.86			10						0.00	0.2	0.14	
RSD (%)	5%			9%						31%	23%	14%	
UQAC FeS-1 Working value	400000	450000	637	25000	23000	275	1050	310	66	65	64	60	155
Stdev	12000	n.d.	47	1500	1300	28	105	42	4	6.5	5.6	6	16
AVE UQAC-FeS-1	376848		614.5188	24687	21614	254	1141	304	69	71.1	59.8	43.7	134
Stdev (n= 25)	24153.25		26.33	871	690	22	53	13	1	2.3	2.0	5.7	10
RSD (%)	6%		4%	4%	3%	9%	5%	4%	2%	3%	3%	13%	7%

ANNEXE 15 – Cont.

Reference materials and results for base sulfide minerals													
Element	^{111}Cd	^{115}In	^{118}Sn	^{121}Sb	^{128}Te	^{185}Re	^{189}Os	^{193}Ir	^{195}Pt	^{197}Au	^{205}Tl	^{208}Pb	^{209}Bi
Detection limits	0.025	0.014	0.018	0.012	0.079	0.004	0.008	0.002	0.004	0.007	0.002	0.005	0.002
Reference materials	MASS-1	GSE-1g	MASS-1	MASS-1	MASS-1	GSE-1g	Po-727	Po-727	Po-727	Po-727	MASS-1	MASS-1	MASS-1
Concentrations used	60	370	59	60	15	78.9	46.7	48	35.5	45.8	50	68	60
Stdev	7	60	6	9	n.d.	n.d.	2.6	1.2	0.8	2.4	n.d.	7	n.d.
JB-MSS-5 Working value	0.13	n.d.	n.d.	61	44	21	42.6	40.2	39.9	35.9	n.d.	72	76
Stdev	0.04	n.d.	n.d.	7	3	n.d.	0.9	0.5	1	4.8	n.d.	5	3
AVE JB-MSS-5	0.08	0.05	1.0	54	32	24	53.8	38.6	35.3	33.0	0.02	65	73
Stdev (n= 25)	0.06	0.09	0.5	4	4	3	2.6	2.3	1.8	4.9	0.04	3	6
RSD (%)	71%	173%	52%	7%	13%	8%	5%	6%	5%	15%	221%	5%	9%
GSE-1 g Working value	160		280	450	n.d.		n.d.	n.d.	30	7	2	378	320
Stdev	50		50	110	n.d.		n.d.	n.d.	n.d.	n.d.	n.d.	12	30
AVE GSE-1g	227		319	337	208		0.02	23.6	18.5	6.8	1.4	328	297
Stdev (n= 25)	24		12	13	12		0.01	9.5	6.2	1.2	0.1	24	15
RSD (%)	11%		4%	4%	6%		51%	40%	33%	18%	5%	7%	5%
MASS-1 Working value		50				n.d.	n.d.	46.3	51.9	47			
Stdev		n.d.				n.d.	n.d.	n.d.	n.d.	n.d.			
AVE MASS-1		61.6				0.01	0.01	59.9	49.9	47.3			
Stdev (n= 25)		2.2				0.02	0.00	1.5	2.3	3.2			
RSD (%)		4%				126%	83%	3%	5%	7%			
UQAC FeS-1 Working value	n.d.	9.4	180	88	170	70	75	60	50	65	n.d.	90	120
Stdev	n.d.	1.1	18	9	17	7	15	6	10	6.5	n.d.	9	20
AVE UQAC-FeS-1	2.2	10.1	182	81	141	85	90	55.8	41.5	64.1	0.3	83	108
Stdev (n= 25)	0.3	0.5	12	9	7	4	5	3.4	5.4	6.0	0.1	5	4
RSD (%)	13%	5%	7%	11%	5%	4%	5%	6%	13%	9%	22%	6%	4%

ANNEXE 15 – Cont.

Correction for interferences	
Ru^{101} corrected for Ni^{61}	1% Ni produced approximately 0.007 ppm Ru
Pd^{108} corrected for Cd^{108}	1ppm Cd produced approximately 0.034 ppm Pd
Rh^{103} corrected for Cu^{63}	1% Cu produced approximately 0.1 ppm Rh
In^{115} corrected for Sn^{115}	1ppm Sn produced approximately 0.004 ppm In

ANNEXE 15 – Cont.

Reference materials and results for K-phlogopite													
Element	^{29}Si	^{24}Mg	^{27}Al	^{57}Fe	^{39}K	^{47}Ti	^{52}Cr	^{61}Ni	^{51}V	^{55}Mn	^{44}Ca	^{23}Na	^{7}Li
Detection limits	167.94	0.32893	0.68745	2.14068	1.35378	0.33845	0.75978	0.15372	508.446	0.68034	16.41300	0.59071	0.196
Reference materials	GSE-1g	GSE-1g	GSE-1g	GSE-1g	GSE-1g	GSE-1g	GSE-1g	GSE-1g	GSE-1g	GSE-1g	GSE-1g	GSE-1g	GSE-1g
Concentrations	250994	21106	68804	98717	21800	450	400	440	440	590	52858	28934	430
Stdev	7011	181	2117	2332	200	42	80	30	20	20	2143	1484	60
Working value	224259	51318	92145	72598	1577	7012	300.2	145.7	238	1255	86787	15506	6
Stdev	9418	6935	12438	13310	166	1319	21.5	18.9	27	93	4643	1335	1.4
AVE G-Prob6	226067	51230	76670	74333	1475	7200	340	152	264	1307	88467	14413	5.8
Stdev (n=4)	4629	637	5929	3591	169	199	12	10	17	75	2023	743	0.2
RSD (%)	2%	1%	8%	5%	11%	3%	3%	7%	6%	6%	2%	5%	4%
Working value	248657	21709	70922	103381	25300	7432	42	58	44	220	51429	26709	43
Stdev	3739	241	1588	777	300	360	3	4	2	20	714	1484	6
AVE GSD-1g	244700	21300	67000	100933	24083	7817	44.2	60.4	43.8	221	51940	25120	42.6
Stdev (n=4)	2030	349	4371	4050	600	59	2.2	2.0	1.9	9	367	687	1.9
RSD (%)	1%	2%	7%	4%	2%	1%	5%	3%	4%	4%	1%	3%	4%
Working value	327180	465	10797	458	486	434	405	458.7	442	485	82144	99415	485
Stdev	-	54	-	9	92	30	64	4	86	10	-	-	44
AVE NIST SRM 610	339267	604	13043	517	702	609	474	562	492	496	94167	103433	466
Stdev (n=4)	5498	44	1951	55	116	16	17	28	20	15	1002	3402	15
RSD (%)	2%	7%	15%	11%	17%	3%	4%	5%	4%	3%	1%	3%	3%
Working value	336061	77	11167	51	66.3	44	36	38.8	39	38	85002	103858	42
Stdev	-	60	-	2	0.8	10	6	0.2	8	2	-	-	6
AVE NIST SRM 612	359167	107	14373	58	68	62	45	54	42.9	42	94067	106333	49
Stdev (n=4)	4252	5	1350	5	5.6	11	2	8.9	2	4	231	2914	2
RSD (%)	1%	5%	9%	9%	8%	17%	4%	16%	4%	10%	0%	3%	5%

ANNEXE 15 – Cont.

Reference materials and results for K-phlogopite													
Element	^{9}Be	^{11}B	^{45}Sc	^{59}Co	^{65}Cu	^{66}Zn	^{69}Ga	^{72}Ge	^{75}As	^{85}Rb	^{88}Sr	^{90}Zr	^{93}Nb
Detection limits	0.092	0.243	0.047	0.015	0.085	0.183	0.050	0.252	0.112	0.055	0.011	0.014	0.009
Reference materials	GSE-1g	GSE-1g	GSE-1g	GSE-1g	GSE-1g	GSE-1g	GSE-1g	GSE-1g	GSE-1g	GSE-1g	GSE-1g	GSE-1g	GSE-1g
Concentrations	490	330	530	380	380	460	490	320	260	356	447	410	420
Stdev	80	120	20	20	40	10	70	80	90	4	5	30	40
Working value	0.4	-	36.8	46.9	89.5	70.8	16.0	1.26	-	-	166.6	55.1	4.16
Stdev	0.14	-	2.6	3.5	20.3	16.6	2.0	0.41	-	-	26.1	2.4	0.41
AVE G-Prob6	0.42	2.8	39.4	48.5	76.7	75.3	24.7	1.21	1.88	1.76	166.4	54.5	3.96
Stdev (n=4)	0.02	0.5	0.3	2.8	6.6	6.3	0.9	0.08	0.16	0.07	3.5	0.9	0.06
RSD (%)	4%	16%	1%	6%	9%	8%	3%	7%	8%	4%	2%	2%	2%
Working value	46	50	52	40	42	54	54	32	27	37.3	69.4	42	42
Stdev	5	20	2	2	2	2	7	8	8	0.4	0.7	2	3
AVE GSD-1g	49.7	49.1	54	39.3	44.5	52.5	51.7	30.6	24.8	34.8	68.9	43.4	41.7
Stdev (n=4)	0.5	1.0	0.7	1.6	6.6	2.5	1.0	0.7	1.7	0.8	1.1	1.7	1.0
RSD (%)	1%	2%	1%	4%	15%	5%	2%	2%	7%	2%	2%	4%	2%
Working value	466	356	441	405	430	456	438	426	317	425.7	515.5	440	419
Stdev	38	14	20	46	48	38	22	20	24	0.8	0.5	16	116
AVE NIST SRM 610	553	310	511	430	502	490	432	357	288	434.4	522.3	486	482
Stdev (n=4)	10	14	23	17	20	21	14	18	6	19.5	5.1	16	6
RSD (%)	2%	4%	5%	4%	4%	4%	3%	5%	2%	4%	1%	3%	1%
Working value	38	35	41	35	37	38	36	35	37	31.4	78.4	38	40
Stdev	6	6	8	4	6	8	4	6	14	0.4	0.2	4	6
AVE NIST SRM 612	47	44	46	39	43	124	38	32	33	34.6	81.4	44	42
Stdev (n=4)	1	1	1	1	7	61	1	1	2	0.6	0.7	2.5	1.6
RSD (%)	1%	3%	3%	2%	16%	49%	1%	3%	6%	2%	1%	6%	4%

ANNEXE 15 – Cont.

Reference materials and results for K-phlogopite												
Element	^{95}Mo	^{107}Ag	^{115}In	^{118}Sn	^{121}Sb	^{133}Cs	^{137}Ba	^{178}Hf	^{181}Ta	^{205}Tl	^{208}Pb	^{209}Bi
Detection limits	0.047	0.032	0.007	0.073	0.024	0.040	0.053	0.014	0.003	0.006	0.006	0.005
Reference materials	GSE-1g	GSE-1g	GSE-1g	GSE-1g	GSE-1g	GSE-1g	GSE-1g	GSE-1g	GSE-1g	GSE-1g	GSE-1g	GSE-1g
Concentrations	390	200	370	280	450	310	427	395	390	2	378	320
Stdev	30	20	60	50	110	20	5	7	40		12	30
Working value	-	-	-	1.33	0.13	0.04	173	1.52	0.28	-	3.28	-
Stdev	-	-	-	0.71	0.01	0.01	26	0.15	0.03	-	0.78	-
AVE G-Prob6	0.426	0.96	0.06	1.60	0.17	0.13	165	1.44	0.24	0.02	3.48	0.02
Stdev (n=4)	0.037	0.03	0.01	0.16	0.06	0.09	7	0.02	0.00	0.00	0.19	0.01
RSD (%)	9%	3%	15%	10%	36%	65%	4%	1%	2%	20%	5%	41%
Working value	39	23	38	29	43	32	67	39	40	0.9	50	35
Stdev	3	3	5	6	7	2	1	2	4	0.1	2	4
AVE GSD-1g	37.4	21.0	36.4	27.2	42.1	31.3	67.1	40.0	40.0	0.82	45.9	30.7
Stdev (n=4)	0.7	0.4	0.5	0.4	0.9	0.1	0.7	1.6	0.9	0.05	1.0	1.2
RSD (%)	2%	2%	1%	2%	2%	0%	1%	4%	2%	6%	2%	4%
Working value	410	239	441	396	369	361	435	432	452	61	426	358
Stdev	58	38	64	36	56	136	46	30	78	4	1	98
AVE NIST SRM 610	447	256	420	395	427	401	475	455	456	67	442	373
Stdev (n=4)	11	10	12	16	13	6	9	12	2	2	13	14
RSD (%)	3%	4%	3%	4%	3%	1%	2%	3%	1%	3%	3%	4%
Working value	38	22	43	38	38	42	39.7	35	40	15.1	38.57	30
Stdev	4	0.3	8	4	4	6	0.8	8	4	1.4	0.2	12
AVE NIST SRM 612	41	22	39	48	42	49	42.4	37	40	15	39.0	35
Stdev (n=4)	0.3	0.2	0.7	2.8	0.2	2.8	2.1	0.9	1.6	1.0	1.3	0.3
RSD (%)	1%	1%	2%	6%	0%	6%	5%	2%	4%	7%	3%	1%

ANNEXE 16 - Complete dataset of whole-rock TABS and Se analyses of samples from the Bushveld and Stillwater Complexes obtained in this study, and results previously reported by Barnes and Maier (2002), Godel et al. (2007), Godel and Barnes (2008) and Barnes et al. (2020) used for comparison. Values in bold are below the detection limit and were replaced by half of the detection limit values. All values in ppm. DL - Detection limit; bdl – below detection limit.

ANNEXE 16

						This study				
Intrusion	Locality	Sample	Rock	Sulfide texture	Height (cm)	As (ppm)	Bi (ppm)	Sb (ppm)	Se (ppm)	Te (ppm)
Detection limit						*0.003*	*0.005*	*0.005*	*0.002*	*0.006*
Bushveld Complex	Impala mine	IM-1	Norite	Minor disseminated	108	0.065	0.008	0.040	0.446	0.065
		IM-3	Norite	Minor disseminated	98	0.086	0.022	0.022	0.557	0.124
		IM-5	Norite	Minor disseminated	88	0.117	0.029	0.006	0.737	0.098
		IM-7	Melanorite	Disseminated interstitial	78	0.184	0.157	0.011	1.396	0.316
		IM-9	Melanorite	Disseminated interstitial	68	0.228	0.166	0.033	1.438	0.303
		IM-11	Melanorite	Minor disseminated	58	0.198	0.060	0.021	1.255	0.186
		IM-13	Melanorite	Minor disseminated	48	0.444	0.014	0.031	0.229	0.022
		IM-15	Melanorite	Disseminated interstitial	38	0.413	0.005	0.026	0.314	0.049
		IM-17	Melanorite	Disseminated interstitial	28	0.225	0.008	0.015	0.178	0.020
		IM-18	Melanorite	Disseminated interstitial	23	0.216	0.110	0.024	0.540	0.129
		IM-19	Melanorite	Disseminated interstitial	18	0.227	0.543	0.048	2.804	0.679
		IM-20	Melanorite	Disseminated interstitial	13	0.178	0.846	0.036	5.103	1.555
		IM-21	Melanorite	Disseminated interstitial	8	0.115	0.938	0.039	7.098	2.390
		IM-22	Upper Chromitite	Disseminated interstitial	6	0.109	0.285	0.025	1.067	0.322
		IM-23	Mela-norite	Disseminated interstitial	3	0.081	0.210	0.043	2.033	0.408
		IM-24	Lower Chromitite	Disseminated interstitial	0	0.069	0.172	0.017	1.356	0.399
		IM-25	Anorthosite	Disseminated interstitial	-3	0.082	0.160	0.060	1.629	0.511
		IM-26	Leuconorite	Disseminated interstitial	-8	0.096	0.733	0.054	5.921	2.599
		IM-27	Leuconorite	Disseminated interstitial	-17	0.052	0.313	0.022	1.477	0.855
		IM-28	Leuconorite	Disseminated interstitial	-23	0.060	0.399	0.029	2.930	1.198
		IM-30	Leuconorite	Minor disseminated	-33	0.035	*0.005*	*0.005*	0.096	0.009
		IM-32	Leuconorite	Minor disseminated	-48	*0.003*	0.013	0.009	0.026	0.011
		IM-34	Leuconorite	Minor disseminated	-58	*0.003*	*0.005*	0.009	0.022	*0.006*
		IM-36	Leuconorite	Minor disseminated	-68	0.036	*0.005*	0.010	0.025	*0.006*

ANNEXE 16 – Cont.

	Barnes and Maier (2002)												
Sample	S (ppm)	Cu (ppm)	Ni (ppm)	Os (ppb)	Ir (ppb)	Ru (ppb)	Rh (ppb)	Pt (ppb)	Pd (ppb)	Au (ppb)	Se/Te	Hf (ppm)	(TABS)/(Pd+Pt)
IM-1	1560	303	905	<1	1.08	5	2.7	35	21	51	6.85	0.350	11.16
IM-3	1880	359	1105	<1	1.07	8	1.8	50	20	75	4.50	0.340	11.58
IM-5	2560	437	1354	1.6	1.50	5	2	53	17	93	7.52	0.320	14.09
IM-7	4480	793	2300	2.5	3.9	27	4.6	169	42	235	4.42	0.600	9.78
IM-9	7320	941	2736	4	5.5	18	7	213	44	266	4.75	0.720	8.44
IM-11	4560	649	1858	4.5	5.3	35	11	144	30	165	6.73	0.710	9.88
IM-13	680	164	789	2.9	2.1	9	3.8	39	8	23	10.19	1.330	15.78
IM-15	880	208	875	<1	2.0	11	2.9	41	27	35	6.42	1.030	11.85
IM-17	680	169	765	1.4	2.8	17	6.1	68	53	36	8.77	0.820	3.69
IM-18	1360	315	834	4.7	4.7	27	15	136	147	44	4.18	0.490	3.60
IM-19	4680	1412	2468	23	27	144	68	1062	1381	366	4.13	0.640	1.76
IM-20	12120	2231	5424	82	31	116	89	6418	3064	1250	3.28	0.090	0.81
IM-21	20480	2452	8143	267	322	1628	682	18987	6330	1268	2.97	0.380	0.42
IM-22	3400	1215	2130	413	552	2708	1141	22827	2056	315	3.31	*0.05*	0.07
IM-23	5960	936	3060	254	308	1692	830	13369	2807	1076	4.98	0.160	0.17
IM-24	4080	887	3400	715	1264	6140	2665	37320	4173	339	3.40	0.310	0.05
IM-25	4080	691	1411	97	105	600	286	5126	3025	389	3.18	0.070	0.30
IM-26	18320	2442	6448	262	307	1752	770	18276	9871	2000	2.28	*0.05*	0.33
IM-27	4480	836	2117	105	94	704	263	5660	3699	754	1.73	0.050	0.29
IM-28	9720	1318	3680	166	79	1051	394	4302	3032	1153	2.45	0.110	0.63
IM-30	440	105	298	<1	2.4	<5	6.4	91	52	21	10.19	0.100	1.05
IM-32	196	69	223	0.9	0.42	<5	1.9	8	<4	2	2.39	0.200	
IM-34	173	46	205	<0.6	0.37	<5	1.2	<4	<2	2	3.47	0.130	
IM-36	178	46	203	<1	0.57	7	1.1	6	<3	1	3.98	*0.05*	

ANNEXE 16 – Cont.

						This study				
Intrusion	Locality	Sample	Rock	Sulfide texture	Height (cm)	As (ppm)	Bi (ppm)	Sb (ppm)	Se (ppm)	Te (ppm)
Bushveld Complex	Rustenburg mine	M4	Melanorite	Disseminated interstitial	27	0.123	0.378	0.034	4.143	0.857
		M3	Melanorite	Disseminated interstitial	23	0.143	0.369	0.060	3.860	0.832
		M2	Melanorite	Disseminated interstitial	18	0.076	0.400	0.033	2.843	0.760
		M1	Melanorite	Disseminated interstitial	13.5	0.143	1.404	0.062	14.646	4.453
		UC	Upper Chromitite	Disseminated interstitial	10	0.070	0.329	0.037	1.994	0.748
		CGM-2	Coarse-grained melanorite	Disseminated interstitial	6	0.203	0.605	0.028	5.656	1.763
		CGM-1	Coarse-grained melanorite	Disseminated interstitial	2	0.126	1.561	0.040	14.323	4.389
		LC	Lower Chromitite	Disseminated interstitial	0	0.046	0.353	0.048	1.630	0.573
		AN	Anorthosite	Minor disseminated	-2	0.071	0.220	0.011	1.567	0.666
Stillwater Complex	East Boulder mine	ST-12	Melatroctolite	Disseminated interstitial		0.385	0.437	0.022	5.609	3.075
		ST-14	Anorthosite	Disseminated interstitial		0.064	0.164	*0.005*	1.883	0.771
		ST-16	Leuconorite	Disseminated interstitial		0.080	0.266	*0.005*	6.922	1.848
		ST-17	Olivine melagabbronorite	Disseminated interstitial		0.017	0.155	0.018	1.654	0.739
	Stillwater mine	P-3	Leucogabbronorite	Disseminated interstitial		0.045	0.338	*0.005*	7.043	4.477
		P-4	Anorthosite	Disseminated interstitial		0.017	0.399	*0.005*	6.668	3.381
	Lower Banded Series (GNII)	BS-18	Leucogabbronorite	Disseminated interstitial		0.026	0.050	0.016	2.060	0.303

ANNEXE 16 – Cont.

	Godel et al. (2007)												
Sample	S (ppm)	Cu (ppm)	Ni (ppm)	Os (ppb)	Ir (ppb)	Ru (ppb)	Rh (ppb)	Pt (ppb)	Pd (ppb)	Au (ppb)	Se/Te	Hf (ppm)	(TABS)/(Pd+Pt)
M4	9800	1400	4200	70	70	320	170	5210	2160	220	4.83	0.180	0.75
M3	8900	1100	4100	90	100	640	200	2480	2360	420	4.64	0.140	1.09
M2	7400	1000	2900	90	100	360	210	3140	2220	340	3.74	0.210	0.77
M1	32100	2800	13700	490	630	2780	1690	16550	11900	1270	3.29	0.140	0.73
UC	5300	1400	2300	260	350	1700	1000	13450	4270	310	2.67	0.360	0.18
CGM-2	13900	4300	4400	140	140	600	400	8840	5940	4640	3.21	0.210	0.56
CGM-1	30700	3500	13100	580	580	2530	1340	42080	16290	2560	3.26	0.370	0.35
LC	4700	1300	2200	730	1110	5410	3800	33100	4400	340	2.84	0.420	0.07
AN	3700	900	1300	100	120	500	420	5340	4030	330	2.35	0.080	0.27
	Godel and Barnes (2008)												
	S (ppm)	Cu (ppm)	Ni (ppm)	Os (ppb)	Ir (ppb)	Ru (ppb)	Rh (ppb)	Pt (ppb)	Pd (ppb)	Au (ppb)	Se/Te	Hf (ppm)	
ST-12	7520	1768.15	3787.1	1155	383	785	2400	166355	248678	3489	1.82	0.220	0.02
ST-14	3320	689.03	919.44	68	36	113	313	7811	40757	669	2.44	0.110	0.06
ST-16	10090	1835.13	3120.93	156	30	132	201	23007	45007	727	3.75	0.110	0.13
ST-17	2690	443.77	1917.85	91	32	68	281	11391	37134	498	2.24	0.170	0.05
	Barnes et al. (2020)												
P-3	8024	1703	2543	227.7	97.99	297.4	890.6	28260	118400	2481	1.57	0.140	0.08
P-4	9804	2865	4212	68.52	30.86	95.12	222	9479	39330	826.5	1.97	0.090	0.21
BS-18	3043	1192	941	bdl	bdl	bdl	bdl	0.695	1.926	54.85	6.80	*0.045*	936.77

ANNEXE 17 - Complete data set of LA-ICP-MS analyses of K-Phlogopite obtained in this study for the Merensky Reef at the Impala mine. Values in wt% for major and minor elements, and in ppm for trace elements. The SiO2 values are from Li et al. (2005). LOD – limit of detection.

ANNEXE 17

Sample	SiO_2	Na_2O	MgO	Al_2O_3	K_2O	CaO	TiO_2	V_2O_5	Cr_2O_3	MnO_2	FeO	NiO
LOD		0.00006	0.00003	0.00007	0.00014	0.00164	0.00003	0.05084	0.00008	0.00007	0.00021	0.00002
IM-13	40.23	0.18	19.99	14.04	8.92	0.01	2.72	0.238	0.45	0.04	8.99	0.18
IM-13	40.23	0.18	19.52	13.74	8.99	0.02	3.53	0.311	0.57	0.04	9.09	0.19
IM-13	40.23	0.18	18.50	14.15	8.88	0.00	5.41	0.218	0.95	0.04	8.49	0.21
IM-13	40.23	0.15	19.40	14.10	9.06	0.02	4.09	0.192	0.72	0.04	8.50	0.21
IM-13	40.23	0.15	18.60	14.13	8.99	0.00	4.84	0.227	0.84	0.04	8.67	0.22
IM-13	40.23	0.16	18.28	14.16	9.04	0.01	5.08	0.228	0.94	0.04	8.81	0.22
IM-13	40.23	0.19	18.18	13.64	8.74	0.15	4.92	0.556	1.20	0.03	9.02	0.20
IM-13	40.23	0.20	18.02	13.74	8.82	0.00	5.13	0.445	0.97	0.04	9.20	0.20
IM-13	40.23	0.19	17.92	13.63	8.87	0.10	5.32	0.532	1.16	0.04	9.16	0.20
IM-13	40.23	0.16	17.95	13.61	8.89	0.05	5.17	0.534	1.41	0.03	9.10	0.20
IM-13	40.23	0.20	17.64	13.61	8.92	0.15	5.34	0.531	1.34	0.03	9.26	0.21
IM-13	40.23	0.16	17.95	13.59	8.69	0.27	5.27	0.520	1.08	0.03	9.07	0.20
IM-13	40.23	0.17	18.39	14.12	8.65	0.15	4.76	0.511	0.87	0.04	9.02	0.19
IM-13	40.23	0.15	20.15	14.10	9.10	0.00	2.52	0.129	0.68	0.04	8.68	0.17
IM-13	40.23	0.10	21.26	14.49	9.41	0.49	0.73	0.083	0.24	0.04	8.41	0.17
IM-15	40.23	0.14	19.04	14.12	9.13	0.67	4.05	0.193	0.80	0.04	8.53	0.22
IM-15	40.23	0.15	18.40	13.70	9.14	0.05	5.06	0.201	1.04	0.04	8.64	0.22
IM-15	40.23	0.19	19.43	13.98	9.10	0.00	3.98	0.206	0.70	0.04	8.45	0.22
IM-15	40.23	0.21	18.32	13.74	9.02	0.05	5.54	0.217	0.96	0.04	8.70	0.22
IM-15	40.23	0.17	20.55	13.93	9.26	0.02	2.10	0.122	0.47	0.04	8.33	0.18
IM-15	40.23	0.20	19.16	13.79	8.97	0.00	4.54	0.221	0.82	0.04	8.39	0.21
IM-15	40.23	0.17	20.08	13.91	9.02	0.09	3.33	0.167	0.61	0.03	8.15	0.19
IM-15	40.23	0.16	20.70	14.04	8.95	0.43	2.17	0.140	0.49	0.03	8.13	0.18
IM-15	40.23	0.16	21.19	14.19	9.12	0.00	1.32	0.077	0.39	0.03	8.31	0.16
IM-15	40.23	0.17	20.64	14.14	8.90	0.00	2.21	0.138	0.47	0.04	8.13	0.21

ANNEXE 17 – Cont.

Sample	^{7}Li	^{9}Be	^{11}B	^{45}Sc	^{59}Co	^{65}Cu	^{66}Zn	^{69}Ga	^{72}Ge	^{75}As	^{85}Rb	^{88}Sr	^{90}Zr
LOD	0.196	0.092	0.243	0.047	0.015	0.085	0.183	0.050	0.252	0.112	0.055	0.011	0.014
IM-13	10.08	0.25	25.96	35.39	114.8	1.76	59.84	49.1	0.99	4.11	559	1.69	9.30
IM-13	9.20	0.19	18.57	44.71	114.9	1.90	64.80	92.9	0.86	1.88	508	1.99	8.26
IM-13	7.19	0.32	4.13	24.38	112.8	2.56	56.02	331.9	0.59	0.28	462	2.86	9.44
IM-13	7.45	0.16	6.16	22.79	110.6	1.77	60.59	179.4	0.83	0.38	532	1.83	6.92
IM-13	6.65	0.11	2.65	22.75	113.4	4.36	58.98	310.8	0.62	0.25	508	2.92	15.95
IM-13	6.75	0.24	2.88	23.29	112.4	5.41	59.12	445.1	0.82	0.20	461	3.97	15.89
IM-13	7.45	0.25	5.82	53.65	108.7	2.01	47.99	219.5	0.63	0.15	456	4.30	5.02
IM-13	8.22	0.26	5.60	75.83	116.3	2.30	51.30	274.2	0.66	0.18	455	3.41	6.38
IM-13	7.84	0.28	5.82	64.09	115.7	2.37	48.68	254.1	0.68	0.11	452	3.92	4.87
IM-13	6.75	0.27	5.95	57.28	113.8	3.93	44.48	222.3	0.74	0.11	461	3.47	4.93
IM-13	8.17	0.27	5.59	55.97	117.4	3.77	47.81	252.3	0.71	0.14	449	4.04	5.09
IM-13	6.54	0.21	6.12	49.03	116.1	1.65	44.06	176.9	0.67	0.11	510	4.06	4.74
IM-13	7.41	0.21	5.48	30.76	113.1	1.52	49.94	155.2	0.54	0.15	491	4.50	7.39
IM-13	12.07	0.24	16.82	18.65	110.0	1.59	62.12	39.1	0.90	0.93	606	1.18	4.54
IM-13	10.25	0.11	18.93	18.63	104.2	2.08	64.17	23.0	1.09	1.05	632	2.33	18.86
IM-15	7.29	0.12	2.29	21.86	111.7	2.11	58.19	215.2	0.60	0.15	552	2.84	9.79
IM-15	6.20	0.25	2.38	22.66	114.7	2.45	57.57	268.6	0.79	0.13	475	3.52	12.12
IM-15	9.35	0.26	6.27	21.76	112.6	3.74	59.64	202.0	0.67	0.51	499	2.38	11.20
IM-15	7.18	0.39	6.97	22.37	114.0	2.97	56.41	313.3	0.63	0.32	501	3.71	7.97
IM-15	11.58	0.24	31.16	23.37	106.4	1.04	60.54	32.6	0.85	1.78	600	1.62	9.25
IM-15	7.68	0.47	7.20	24.03	115.0	6.66	58.59	219.2	0.77	0.34	482	2.32	11.53
IM-15	9.60	0.35	12.51	18.95	110.1	1.41	55.36	58.1	0.73	0.72	552	1.63	8.78
IM-15	10.77	0.25	15.95	18.00	110.3	1.69	60.13	35.5	0.80	1.31	609	2.84	9.73
IM-15	10.86	0.14	26.60	20.81	106.7	0.95	59.52	27.3	0.93	2.95	618	1.18	12.42
IM-15	12.14	0.24	15.47	20.10	110.3	17.71	53.94	39.4	0.77	0.97	579	0.97	11.85

ANNEXE 17 – Cont.

Sample	^{93}Nb	^{95}Mo	^{107}Ag	^{115}In	^{118}Sn	^{121}Sb	^{133}Cs	^{137}Ba	^{178}Hf	^{181}Ta	^{205}Tl	^{208}Pb	^{209}Bi
LOD	0.009	0.047	0.032	0.007	0.073	0.024	0.040	0.053	0.014	0.003	0.006	0.006	0.005
IM-13	37.71	0.19	0.03	0.04	2.97	0.25	7.78	506	0.52	2.15	3.89	1.87	0.589
IM-13	33.68	0.10	0.03	0.04	3.30	0.17	5.48	1196	0.47	1.63	3.62	1.78	0.009
IM-13	45.16	0.16	0.03	0.05	4.40	0.06	3.84	4900	0.42	1.39	3.30	1.44	0.005
IM-13	52.89	0.18	0.03	0.04	4.58	0.04	4.85	2588	0.37	1.55	3.93	1.04	0.005
IM-13	33.06	0.26	0.06	0.05	5.10	0.08	4.88	4566	0.65	1.18	3.51	1.66	0.010
IM-13	35.84	0.15	0.07	0.05	4.73	0.06	3.61	6497	0.58	1.30	3.39	1.90	0.013
IM-13	5.43	0.05	0.03	0.03	2.53	0.02	4.63	3239	0.21	0.20	3.28	1.29	0.005
IM-13	10.93	0.07	0.03	0.04	2.25	0.03	3.93	4075	0.28	0.47	3.11	1.49	0.005
IM-13	4.62	0.05	0.03	0.03	2.15	0.03	3.99	3808	0.18	0.23	3.12	1.18	0.005
IM-13	2.59	0.05	0.06	0.03	2.32	0.02	4.03	3268	0.18	0.12	3.45	1.45	0.005
IM-13	4.88	0.05	0.05	0.03	2.51	0.03	3.74	3842	0.21	0.21	3.24	1.38	0.005
IM-13	3.77	0.05	0.03	0.03	2.21	0.04	4.32	2622	0.19	0.25	3.54	1.06	0.005
IM-13	2.67	0.05	0.03	0.03	3.42	0.02	4.68	2251	0.33	0.23	3.54	1.38	0.005
IM-13	51.99	0.18	0.03	0.04	4.05	0.11	7.02	380	0.36	2.28	4.35	0.98	0.005
IM-13	51.60	0.35	0.04	0.06	4.95	0.17	20.99	115	1.48	5.82	4.55	0.83	0.005
IM-15	44.66	0.21	0.20	0.06	5.57	0.04	4.37	3368	0.45	1.28	4.20	1.25	0.005
IM-15	46.15	0.16	0.17	0.05	4.88	0.04	3.87	4335	0.51	1.34	3.49	1.70	0.005
IM-15	57.03	0.19	0.12	0.05	6.03	0.10	4.17	3106	0.54	1.71	3.60	2.61	0.011
IM-15	45.43	0.14	0.12	0.04	4.29	0.07	4.41	4937	0.39	1.46	3.48	3.13	0.007
IM-15	83.46	0.41	0.12	0.06	6.18	0.23	10.92	268	0.58	3.57	4.37	1.43	0.007
IM-15	55.62	0.23	0.23	0.06	5.50	0.08	4.05	3370	0.54	1.47	3.63	2.65	0.009
IM-15	71.88	0.30	0.29	0.06	5.39	0.12	5.52	688	0.44	2.29	4.16	1.97	0.005
IM-15	81.40	0.47	0.26	0.06	6.04	0.19	8.94	310	0.55	3.42	4.28	1.85	0.008
IM-15	76.99	0.64	0.17	0.06	5.28	0.29	9.98	214	0.89	3.80	4.38	4.30	0.009
IM-15	80.34	0.26	0.05	0.07	6.21	0.11	7.94	381	0.65	3.36	4.24	0.86	0.005

ANNEXE 18 - Complete data set of LA-ICP-MS analyses of pyrrhotite obtained in this study and median values for each sample from the Bushveld and Stillwater Complexes. The Fe values used for internal standardization are from Godel et al. (2008a) for samples from the Stillwater Complex, Godel et al. (2007) for samples from the Rustenburg mine, and stoichiometric values (i.e., 62.3%) for samples from the Impala mine. LOD - limit of detection.

ANNEXE 18

Intrusion	Locality	Sample	Rock	Height (cm)	^{34}S	^{59}Co	^{61}Ni	^{65}Cu	^{66}Zn	^{75}As	^{82}Se	^{95}Mo	^{101}Ru	^{103}Rh	^{108}Pd	^{109}Ag
LOD					58	0.008	0.306	0.276	0.079	0.044	0.6	0.008	0.008	0.001	0.027	0.003
Bushveld Complex	Impala mine	IM-1	Norite	108	364631	111.57	4363	0.75	0.079	2.244	195.8	0.090	0.751	0.066	0.090	0.058
					426961	143.98	5373	0.65	0.187	2.680	175.0	0.008	1.025	0.099	0.122	0.077
					370240	157.29	3335	5.33	0.079	1.496	163.3	0.056	1.266	0.121	0.122	0.164
					378343	169.54	5074	1.25	0.436	2.493	159.4	0.212	0.915	0.061	0.085	0.224
Median IM-1					**374292**	**150.64**	**4718**	**1.00**	**0.133**	**2.369**	**169.2**	**0.073**	**0.970**	**0.082**	**0.106**	**0.121**
Bushveld Complex	Impala mine	IM-3	Norite	98	330349	84.77	4114	1.99	0.079	2.243	98.5	0.008	0.641	0.063	0.090	0.139
					354658	86.64	4525	0.85	0.625	1.434	183.9	0.044	0.109	0.001	0.102	0.089
					330972	90.38	4488	1.75	0.079	22.439	94.2	0.008	1.618	2.867	0.079	0.165
					362137	87.89	4893	0.85	1.434	5.496	184.4	0.046	0.265	0.090	0.027	0.128
					365254	87.26	4581	0.64	0.079	1.371	165.0	0.053	1.265	0.123	0.134	0.125
Median IM-3					**354658**	**87.26**	**4525**	**0.85**	**0.079**	**2.243**	**165.0**	**0.044**	**0.641**	**0.090**	**0.090**	**0.128**
Bushveld Complex	Impala mine	IM-5	Norite	88	319184	128.86	7854	1.05	0.079	0.997	150.8	0.014	0.157	0.003	0.051	0.127
					329726	42.38	4930	2.43	0.243	0.990	159.4	0.142	0.365	0.004	0.356	0.232
					349671	67.32	7168	1.41	0.079	1.336	160.0	0.022	0.433	0.001	0.155	0.355
					330972	64.82	6669	0.95	0.748	1.932	181.9	0.062	0.241	0.053	0.027	0.218
					361514	41.14	4675	1.50	0.313	1.309	177.6	0.049	0.265	0.074	0.099	0.212
					359644	41.76	4170	1.23	0.079	2.119	155.8	0.021	0.465	0.014	0.656	0.318
Median IM-5					**340322**	**53.60**	**5800**	**1.32**	**0.161**	**1.322**	**159.7**	**0.035**	**0.315**	**0.009**	**0.127**	**0.225**
Bushveld Complex	Impala mine	IM-7	Melanorite	78	361514	7.48	4743	3.24	0.935	0.810	166.9	1.496	2.272	0.211	2.355	0.175
					355281	13.84	5797	2.51	0.561	1.448	188.8	0.636	2.359	0.077	1.200	0.319
					342815	18.14	5298	2.87	0.123	0.935	196.3	0.193	1.972	0.055	4.556	0.169
					390077	8.04	5080	1.19	19.946	2.306	199.2	0.106	0.259	0.069	3.666	0.343
Median IM-7					**358398**	**10.94**	**5189**	**2.69**	**0.748**	**1.191**	**192.6**	**0.414**	**2.122**	**0.073**	**3.010**	**0.247**

ANNEXE 18 – Cont.

Intrusion	Locality	Sample	^{111}Cd	^{115}In	^{118}Sn	^{121}Sb	^{128}Te	^{185}Re	^{189}Os	^{193}Ir	^{195}Pt	^{197}Au	^{205}Tl	^{208}Pb	^{209}Bi
LOD			0.025	0.014	0.018	0.012	0.079	0.004	0.008	0.002	0.004	0.007	0.002	0.005	0.002
Bushveld Complex	Impala mine	IM-1	0.224	0.014	0.099	0.012	0.505	0.367	0.287	0.175	0.016	0.007	0.002	0.168	0.699
			0.143	0.014	0.059	0.012	1.079	0.150	0.201	0.137	0.032	0.014	0.002	0.467	0.455
			0.060	0.014	0.107	0.012	0.455	0.130	0.131	0.092	0.004	0.017	0.002	0.493	0.517
			0.081	0.014	0.124	0.012	1.184	0.561	0.642	0.118	0.256	0.007	0.017	0.302	0.580
Median IM-1			**0.112**	**0.014**	**0.103**	**0.012**	**0.792**	**0.258**	**0.244**	**0.128**	**0.024**	**0.010**	**0.002**	**0.385**	**0.549**
Bushveld Complex	Impala mine	IM-3	0.075	0.014	0.110	0.012	0.686	0.004	0.422	0.122	0.019	0.007	0.002	0.380	0.461
			0.156	0.014	0.133	0.012	1.256	0.082	0.369	0.075	0.004	0.007	0.002	0.530	1.436
			0.076	0.014	0.122	0.012	0.935	0.102	0.310	0.648	0.380	0.007	0.002	0.150	1.247
			0.050	0.014	0.086	0.012	2.320	0.055	0.206	0.086	0.004	0.007	0.002	0.365	0.942
			0.181	0.014	0.059	0.012	0.943	0.099	0.193	0.207	0.004	0.007	0.002	0.268	1.842
Median IM-3			**0.076**	**0.014**	**0.110**	**0.012**	**0.943**	**0.082**	**0.310**	**0.122**	**0.004**	**0.007**	**0.002**	**0.365**	**1.247**
Bushveld Complex	Impala mine	IM-5	0.025	0.014	0.123	0.012	0.180	0.057	0.146	0.039	0.004	0.007	0.002	0.275	1.524
			0.131	0.014	0.102	0.012	0.386	0.137	0.156	0.056	0.016	0.009	0.002	0.178	1.530
			0.125	0.014	0.150	0.012	1.274	0.139	0.355	0.084	0.004	0.007	0.002	0.704	0.948
			0.206	0.014	0.087	0.012	0.563	0.199	0.217	0.097	0.004	0.007	0.002	0.318	0.701
			0.086	0.014	0.200	0.012	0.517	0.181	0.150	0.076	0.004	0.007	0.002	0.330	0.654
			0.293	0.014	0.033	0.012	0.879	0.200	0.233	0.037	0.009	0.007	0.002	0.133	1.787
Median IM-5			**0.128**	**0.014**	**0.113**	**0.012**	**0.540**	**0.160**	**0.187**	**0.066**	**0.004**	**0.007**	**0.002**	**0.297**	**1.236**
Bushveld Complex	Impala mine	IM-7	0.243	0.014	0.203	0.012	0.230	0.530	3.114	1.063	2.680	0.007	0.002	1.683	0.002
			0.135	0.014	0.097	0.012	0.307	0.543	2.672	0.606	1.371	0.012	0.002	1.240	0.017
			0.136	0.014	0.076	0.012	0.449	0.139	3.176	0.588	0.760	0.112	0.009	1.434	0.031
			0.249	0.014	0.102	0.012	0.102	0.211	2.026	0.773	0.480	0.007	0.029	4.924	0.018
Median IM-7			**0.190**	**0.014**	**0.099**	**0.012**	**0.268**	**0.371**	**2.893**	**0.690**	**1.066**	**0.009**	**0.006**	**1.558**	**0.018**

ANNEXE 18 – Cont.

Intrusion	Locality	Sample	Rock	Height (cm)	^{34}S	^{59}Co	^{61}Ni	^{65}Cu	^{66}Zn	^{75}As	^{82}Se	^{95}Mo	^{101}Ru	^{103}Rh	^{108}Pd	^{109}Ag
LOD					58	0.008	0.306	0.276	0.079	0.044	0.6	0.008	0.008	0.001	0.027	0.003
Bushveld Complex	Impala mine	IM-9	Melanorite	68	332328	9.72	1456	1.09	0.079	0.686	160.1	0.268	0.480	0.090	0.632	0.263
					312897	10.85	193	5.80	1.435	0.249	178.2	0.030	0.947	0.038	0.212	0.605
					354034	44.88	7230	2.68	0.123	1.808	183.0	0.187	0.743	0.145	0.100	0.087
					377720	22.38	6856	3.55	0.566	1.310	180.5	0.149	1.242	0.074	2.665	0.168
					361514	55.47	4164	43.01	2.255	1.122	168.3	0.313	0.484	0.096	1.003	0.187
					324116	31.17	4619	153.90	13.089	1.377	174.4	0.150	0.091	0.157	0.233	0.287
Median IM-9					**343181**	**26.77**	**4391**	**4.67**	**1.001**	**1.216**	**176.3**	**0.168**	**0.613**	**0.093**	**0.433**	**0.225**
Bushveld Complex	Impala mine	IM-11	Melanorite	58	335959	44.50	6096	4.05	0.659	1.123	256.8	0.093	0.968	0.052	0.090	0.268
					343438	40.23	5971	4.11	0.323	1.873	198.2	0.015	0.020	0.142	0.102	0.642
					344685	42.37	6420	3.18	0.312	1.683	243.7	0.008	0.195	0.001	0.256	0.397
					330972	27.24	5859	5.22	0.079	1.748	218.2	0.058	0.108	0.063	0.099	0.384
					348425	76.67	4612	4.86	0.250	0.873	237.0	0.087	0.016	0.110	0.122	0.243
					359184	53.60	4301	1.40	0.499	1.934	199.5	0.075	0.008	0.088	0.099	0.240
					364007	44.00	7716	5.67	0.448	0.856	250.6	0.100	0.793	0.098	0.066	0.176
Median IM-11					**344685**	**44.00**	**5971**	**4.11**	**0.323**	**1.683**	**237.0**	**0.075**	**0.108**	**0.088**	**0.099**	**0.268**
Bushveld Complex	Impala mine	IM-13	Melanorite	48	403844	43.01	9038	2.10	1.122	0.686	180.6	0.008	0.281	0.001	0.076	0.431
					330349	43.56	4488	3.62	0.376	7.978	187.0	0.008	0.539	0.355	0.053	0.114
					314143	37.90	4425	4.80	0.811	0.561	129.6	0.008	0.359	0.155	0.027	0.997
					396310	39.27	4189	152.91	3.366	0.044	187.6	0.031	0.060	0.012	0.090	0.265
					374603	36.15	5984	1.37	1.456	0.044	158.2	0.037	0.027	0.096	0.122	0.132
					362137	124.04	6981	2.31	0.256	0.937	160.8	0.022	0.009	0.002	0.102	0.289
					347178	40.51	6669	2.56	0.495	1.488	186.9	0.102	0.008	0.122	0.023	0.158
Median IM-13					**362137**	**40.51**	**5984**	**2.56**	**0.811**	**0.686**	**180.6**	**0.022**	**0.060**	**0.096**	**0.076**	**0.265**

ANNEXE 18 – Cont.

Intrusion	Locality	Sample	^{111}Cd	^{115}In	^{118}Sn	^{121}Sb	^{128}Te	^{185}Re	^{189}Os	^{193}Ir	^{195}Pt	^{197}Au	^{205}Tl	^{208}Pb	^{209}Bi
LOD			0.025	0.014	0.018	0.012	0.079	0.004	0.008	0.002	0.004	0.007	0.002	0.005	0.002
Bushveld Complex	Impala mine	IM-9	0.156	0.014	0.206	0.012	0.873	1.247	0.199	0.256	0.004	0.007	0.002	0.598	1.364
			0.225	0.014	0.145	0.012	1.060	0.081	0.311	0.150	0.004	0.013	0.002	0.480	0.866
			0.605	0.014	0.143	0.012	0.810	0.212	0.249	0.224	0.032	0.007	0.002	0.517	0.923
			0.139	0.014	0.211	0.012	0.586	0.182	0.223	0.449	0.031	0.035	0.002	0.393	1.348
			1.234	0.014	0.106	0.012	0.413	0.154	0.175	0.323	0.004	0.050	0.002	0.320	0.773
			0.025	0.014	0.100	0.012	0.967	0.393	0.322	0.345	0.004	0.007	0.010	0.368	1.910
Median IM-9			**0.191**	**0.014**	**0.144**	**0.012**	**0.841**	**0.197**	**0.236**	**0.290**	**0.004**	**0.010**	**0.002**	**0.436**	**1.136**
Bushveld Complex	Impala mine	IM-11	0.132	0.014	0.118	0.012	0.393	0.122	0.299	0.104	0.037	0.007	0.002	0.379	1.486
			0.856	0.014	0.367	0.069	0.652	0.004	0.221	0.002	0.004	0.026	0.002	1.159	1.035
			0.182	0.014	0.134	0.012	0.324	0.303	0.143	0.090	0.004	0.021	0.002	0.474	0.605
			1.033	0.014	1.033	0.012	0.287	0.249	0.190	0.124	0.004	0.010	0.002	0.654	0.798
			0.193	0.014	0.402	0.012	0.767	0.053	0.193	0.002	0.004	0.020	0.002	0.376	1.947
			0.362	0.014	0.303	0.012	0.436	0.087	0.211	0.066	0.034	0.007	0.002	0.735	1.128
			0.145	0.014	0.083	0.012	0.233	0.156	0.287	0.218	0.023	0.007	0.002	0.156	1.752
Median IM-11			**0.193**	**0.014**	**0.303**	**0.012**	**0.393**	**0.122**	**0.211**	**0.090**	**0.004**	**0.010**	**0.002**	**0.474**	**1.128**
Bushveld Complex	Impala mine	IM-13	0.212	0.014	0.018	0.065	0.623	0.004	0.093	0.002	0.004	0.022	0.051	1.808	1.977
			0.287	0.014	0.251	0.168	1.197	0.255	0.148	0.032	0.162	0.007	0.002	1.122	0.986
			0.089	0.014	1.032	0.075	1.130	0.299	0.027	0.002	0.004	0.007	0.002	3.931	5.111
			0.897	0.014	0.187	0.012	1.234	0.200	0.121	0.051	0.004	0.011	0.008	0.274	1.467
			0.231	0.014	0.299	0.012	0.760	0.069	0.234	0.002	0.004	0.028	0.015	0.792	2.362
			0.455	0.014	0.478	0.012	0.900	0.105	0.013	0.042	0.004	0.032	0.024	0.605	0.841
			0.405	0.014	0.106	0.012	0.717	0.093	0.076	0.036	0.004	0.037	0.019	0.218	3.467
Median IM-13			**0.287**	**0.014**	**0.251**	**0.012**	**0.900**	**0.105**	**0.093**	**0.032**	**0.004**	**0.022**	**0.015**	**0.792**	**1.977**

ANNEXE 18 – Cont.

Intrusion	Locality	Sample	Rock	Height (cm)	^{34}S	^{59}Co	^{61}Ni	^{65}Cu	^{66}Zn	^{75}As	^{82}Se	^{95}Mo	^{101}Ru	^{103}Rh	^{108}Pd	^{109}Ag
LOD					58	0.008	0.306	0.276	0.079	0.044	0.6	0.008	0.008	0.001	0.027	0.003
Bushveld Complex	Impala mine	IM-15	Melanorite	38	335335	19.70	4033	5.18	0.190	0.632	170.8	0.008	0.008	0.001	0.099	0.405
					335335	34.28	4351	9.66	0.326	0.561	154.4	0.008	0.060	0.124	0.069	1.683
Median IM-15					**335335**	**26.99**	**4192**	**7.42**	**0.258**	**0.597**	**162.6**	**0.008**	**0.034**	**0.063**	**0.084**	**1.044**
Bushveld Complex	Impala mine	IM-17	Melanorite	28	355281	19.01	3422	3.43	0.256	1.247	255.7	0.054	0.008	0.001	0.027	0.272
					339699	20.82	4550	4.43	1.522	0.125	211.9	0.105	0.209	0.063	0.070	0.135
					350918	41.20	5236	8.12	1.122	0.189	293.0	0.099	0.146	0.024	0.079	0.116
					373980	26.55	4139	2.37	0.079	0.571	245.7	0.022	0.032	0.079	0.123	0.115
Median IM-17					**353099**	**23.69**	**4344**	**3.93**	**0.689**	**0.380**	**250.7**	**0.076**	**0.089**	**0.044**	**0.074**	**0.125**
Bushveld Complex	Impala mine	IM-18	Melanorite	23	379590	27.92	3709	14.34	0.079	2.496	248.7	0.069	0.008	0.088	0.212	0.087
					348425	24.56	3453	6.23	0.364	1.676	286.7	0.101	0.072	0.076	0.086	0.049
					361514	47.99	6432	2.18	0.254	3.054	238.7	0.029	3.783	0.241	0.322	0.118
Median IM-18					**361514**	**27.92**	**3709**	**6.23**	**0.254**	**2.496**	**248.7**	**0.069**	**0.072**	**0.088**	**0.212**	**0.087**
Bushveld Complex	Impala mine	IM-19	Melanorite	18	398858	66.69	5859	2.12	0.079	1.621	183.3	0.043	0.589	0.088	6.333	0.050
					355281	21.94	5205	1.76	0.079	4.488	212.5	0.461	7.738	0.099	2.666	0.095
					377720	21.88	5535	1.98	0.251	3.241	268.0	0.337	5.736	0.055	0.989	0.090
					368994	23.12	4986	2.30	0.567	4.477	203.2	0.271	4.191	0.145	1.022	0.065
					327233	61.71	6358	154.25	0.689	4.986	199.0	0.280	5.655	0.179	0.369	0.143
					362761	28.86	5946	112.19	0.350	5.236	205.7	0.318	8.220	0.091	2.337	0.067
					398912	19.63	4799	71.26	1.367	6.108	224.1	0.467	0.480	0.233	0.478	0.188
					398912	8.35	3241	5.80	0.079	2.182	172.0	0.255	4.122	0.184	3.670	0.148
					362543	17.33	4862	1.56	11.843	1.745	218.6	0.149	1.120	0.216	4.002	0.062
Median IM-19					**368994**	**21.94**	**5205**	**2.30**	**0.350**	**4.477**	**205.7**	**0.280**	**4.191**	**0.145**	**2.337**	**0.090**

ANNEXE 18 – Cont.

Intrusion	Locality	Sample	^{111}Cd	^{115}In	^{118}Sn	^{121}Sb	^{128}Te	^{185}Re	^{189}Os	^{193}Ir	^{195}Pt	^{197}Au	^{205}Tl	^{208}Pb	^{209}Bi
LOD			0.025	0.014	0.018	0.012	0.079	0.004	0.008	0.002	0.004	0.007	0.002	0.005	0.002
Bushveld Complex	Impala mine	IM-15	0.585	0.014	0.106	0.012	2.309	0.099	0.020	0.002	0.004	0.007	0.012	0.555	0.767
			0.162	0.014	0.087	0.012	1.230	0.143	0.047	0.002	0.004	0.007	0.002	4.365	2.680
Median IM-15			**0.374**	**0.014**	**0.096**	**0.012**	**1.770**	**0.121**	**0.033**	**0.002**	**0.004**	**0.007**	**0.007**	**2.460**	**1.723**
Bushveld Complex	Impala mine	IM-17	0.436	0.014	0.070	0.012	0.478	0.099	0.231	0.043	0.004	0.007	0.013	2.082	1.393
			0.160	0.014	0.099	0.012	0.580	0.355	0.687	0.063	0.007	0.019	0.002	0.929	1.194
			0.129	0.014	0.077	0.012	0.118	0.106	0.386	0.079	0.004	0.029	0.002	1.066	0.330
			2.032	0.014	0.102	0.012	0.966	0.064	0.512	0.009	0.004	0.016	0.002	0.879	2.654
Median IM-17			**0.298**	**0.014**	**0.088**	**0.012**	**0.529**	**0.102**	**0.449**	**0.053**	**0.004**	**0.017**	**0.002**	**0.997**	**1.293**
Bushveld Complex	Impala mine	IM-18	0.118	0.014	0.224	0.012	1.109	0.206	0.592	0.055	0.029	0.022	0.199	3.054	0.126
			0.195	0.014	0.102	0.012	0.537	0.099	0.689	0.244	0.004	0.007	0.043	1.776	0.522
			0.587	0.014	0.302	0.012	0.399	0.120	0.841	0.879	0.021	0.007	0.039	0.337	0.418
Median IM-18			**0.195**	**0.014**	**0.224**	**0.012**	**0.537**	**0.120**	**0.689**	**0.244**	**0.021**	**0.007**	**0.043**	**1.776**	**0.418**
Bushveld Complex	Impala mine	IM-19	0.025	0.016	0.199	0.012	0.524	0.386	0.755	1.200	0.004	0.030	0.156	51.111	0.199
			0.255	0.014	0.302	0.012	0.330	0.424	1.483	2.637	0.081	0.007	0.002	0.330	0.206
			0.025	0.014	0.193	0.012	0.090	0.648	1.764	2.051	0.131	0.007	0.002	0.802	0.212
			0.025	0.014	0.092	0.012	0.081	0.549	1.215	2.238	0.033	0.007	0.002	0.302	0.143
			0.164	0.014	0.203	0.082	0.212	0.324	1.284	1.321	0.007	0.007	0.002	0.661	0.125
			0.367	0.014	0.040	0.034	0.231	0.368	1.627	2.593	0.004	0.007	0.028	0.237	0.445
			0.380	0.014	0.233	0.012	0.156	0.455	1.870	0.067	0.004	0.007	0.062	1.816	0.115
			0.442	0.018	0.181	0.065	0.989	0.854	2.202	0.002	0.004	0.007	0.069	0.767	0.580
			0.025	0.014	0.111	0.012	0.367	0.154	1.546	0.368	0.059	0.007	0.019	0.717	0.181
Median IM-19			**0.164**	**0.014**	**0.193**	**0.012**	**0.231**	**0.424**	**1.546**	**1.321**	**0.007**	**0.007**	**0.019**	**0.717**	**0.199**

ANNEXE 18 – Cont.

Intrusion	Locality	Sample	Rock	Height (cm)	^{34}S	^{59}Co	^{61}Ni	^{65}Cu	^{66}Zn	^{75}As	^{82}Se	^{95}Mo	^{101}Ru	^{103}Rh	^{108}Pd	^{109}Ag
LOD					58	0.008	0.306	0.276	0.079	0.044	0.6	0.008	0.008	0.001	0.027	0.003
Bushveld Complex	Impala mine	IM-20	Melanorite	13	386446	15.46	5535	3.80	0.079	4.799	192.4	0.374	3.480	0.073	0.900	0.045
					384576	13.77	5448	3.94	0.365	4.486	238.0	0.363	6.234	0.121	1.200	0.132
					358398	16.21	5797	2.70	0.079	6.233	211.8	0.430	5.669	0.059	0.745	0.120
					367747	15.58	4986	5.36	2.930	2.122	248.1	0.120	1.461	0.135	0.967	0.003
					351541	13.34	1976	3.38	1.234	1.763	156.9	0.024	2.566	0.246	2.337	0.070
					386174	23.87	6856	4.30	0.241	0.879	256.2	0.266	4.026	0.106	5.023	0.138
					390009	18.45	5360	3.86	1.240	0.044	277.7	0.105	3.684	0.079	0.234	0.164
Median IM-20					**384576**	**15.58**	**5448**	**3.86**	**0.365**	**2.122**	**238.0**	**0.266**	**3.684**	**0.106**	**0.967**	**0.120**
Bushveld Complex	Impala mine	IM-21	Melanorite	8	330349	186.99	3889	7.42	0.079	2.867	167.0	0.281	15.146	0.293	0.255	1.203
					377097	9.16	3684	8.41	0.079	3.740	177.3	0.126	2.201	0.345	0.323	0.436
					373980	14.40	5173	5.55	1.830	3.927	212.0	0.117	10.893	0.125	1.233	0.102
					365796	14.83	3416	201.25	0.878	2.930	201.3	0.175	2.226	0.134	0.423	0.100
					373357	14.96	4139	3.30	0.257	3.677	210.2	0.099	6.234	0.099	5.332	0.088
					357693	10.22	4482	2.48	0.785	2.057	214.7	0.144	4.234	0.345	4.200	0.055
Median IM-21					**369576**	**14.62**	**4014**	**6.48**	**0.521**	**3.303**	**205.8**	**0.135**	**5.234**	**0.214**	**0.828**	**0.101**
Bushveld Complex	Impala mine	IM-22	Upper Chromitite	6	398912	11.22	4488	2.01	0.079	4.987	189.4	0.075	5.211	0.131	0.212	1.371
					342815	10.10	3802	1.68	0.897	2.431	162.7	0.210	2.106	0.545	0.900	0.474
					386446	18.14	5672	3.20	2.022	3.303	189.5	0.125	6.283	0.386	2.022	1.060
					415118	17.58	6108	2.80	11.345	3.615	239.3	0.218	6.964	0.474	0.897	0.661
					375227	16.39	5298	2.08	0.079	4.494	215.4	0.168	4.587	1.244	4.033	1.434
					395172	15.15	4637	3.26	1.255	0.533	233.1	0.355	3.801	0.233	0.246	0.386
					416988	16.14	4893	1.28	0.567	0.165	243.1	0.268	4.054	0.210	0.746	1.069
Median IM-22					**395172**	**16.14**	**4893**	**2.08**	**0.897**	**3.303**	**215.4**	**0.210**	**4.587**	**0.386**	**0.897**	**1.060**

ANNEXE 18 – Cont.

Intrusion	Locality	Sample	^{111}Cd	^{115}In	^{118}Sn	^{121}Sb	^{128}Te	^{185}Re	^{189}Os	^{193}Ir	^{195}Pt	^{197}Au	^{205}Tl	^{208}Pb	^{209}Bi
LOD			0.025	0.014	0.018	0.012	0.079	0.004	0.008	0.002	0.004	0.007	0.002	0.005	0.002
Bushveld Complex	Impala mine	IM-20	0.633	0.014	0.037	0.012	0.357	0.866	0.857	1.184	0.150	0.026	0.002	0.899	0.129
			0.254	0.014	0.110	0.012	0.224	0.337	0.879	2.553	0.355	0.014	0.002	0.943	0.118
			0.025	0.014	0.204	0.012	2.032	0.168	1.228	1.278	0.305	0.035	0.002	0.854	1.224
			0.106	0.014	0.200	0.143	0.387	0.142	0.499	0.569	0.004	0.007	0.002	0.237	0.205
			0.122	0.014	0.201	0.100	1.256	0.479	0.008	2.056	0.014	0.007	0.002	0.537	0.168
			0.117	0.014	0.072	0.044	0.397	0.511	0.823	1.047	0.187	0.007	0.002	0.262	0.268
			0.175	0.030	0.230	0.012	0.617	0.573	1.022	0.792	0.039	0.031	0.002	0.642	0.374
Median IM-20			**0.122**	**0.014**	**0.200**	**0.012**	**0.397**	**0.479**	**0.857**	**1.184**	**0.150**	**0.014**	**0.002**	**0.642**	**0.205**
Bushveld Complex	Impala mine	IM-21	0.025	0.014	0.072	0.012	0.367	0.405	2.680	2.930	1.621	0.007	0.002	34.905	3.615
			0.037	0.014	0.095	0.069	0.422	0.233	0.051	0.867	0.060	0.007	0.125	14.398	0.138
			0.025	0.014	0.087	0.012	0.145	0.318	3.696	3.241	0.115	0.007	0.002	0.518	0.556
			0.237	0.014	0.230	0.012	0.356	0.327	1.951	0.972	0.499	0.007	0.002	0.581	2.233
			0.025	0.014	0.122	0.012	0.268	0.456	1.066	0.349	0.004	0.007	0.002	0.511	0.056
			0.025	0.014	0.087	0.012	0.079	0.319	1.172	0.480	0.156	0.007	0.002	0.885	0.2233.
Median IM-21			**0.025**	**0.014**	**0.091**	**0.012**	**0.312**	**0.323**	**1.561**	**0.920**	**0.135**	**0.007**	**0.002**	**0.733**	**0.556**
Bushveld Complex	Impala mine	IM-22	0.099	0.014	0.096	0.012	0.655	0.236	1.265	0.787	0.308	0.007	0.040	2.256	2.221
			0.088	0.014	0.109	0.012	0.262	0.423	2.038	1.639	0.004	0.007	0.002	1.072	0.075
			1.234	0.014	0.402	0.012	0.079	0.295	6.700	5.572	0.586	0.007	0.002	0.549	0.062
			1.022	0.014	0.140	0.032	0.542	0.399	6.233	8.652	0.792	0.007	0.002	0.740	0.123
			0.255	0.014	0.256	0.012	1.233	0.374	6.358	5.261	0.598	0.007	0.002	0.754	0.031
			0.182	0.014	0.018	0.060	0.688	0.357	6.108	4.048	0.262	0.018	0.002	0.779	0.133
			0.049	0.014	0.330	0.012	0.079	0.338	5.610	3.572	0.143	0.007	0.002	1.060	0.061
Median IM-22			**0.182**	**0.014**	**0.140**	**0.012**	**0.542**	**0.357**	**6.108**	**4.048**	**0.308**	**0.007**	**0.002**	**0.779**	**0.075**

ANNEXE 18 – Cont.

Intrusion	Locality	Sample	Rock	Height (cm)	^{34}S	^{59}Co	^{61}Ni	^{65}Cu	^{66}Zn	^{75}As	^{82}Se	^{95}Mo	^{101}Ru	^{103}Rh	^{108}Pd	^{109}Ag
LOD					58	0.008	0.306	0.276	0.079	0.044	0.6	0.008	0.008	0.001	0.027	0.003
Bushveld Complex	Impala mine	IM-24	Lower Chromitite	0	387693	13.15	4238	137.63	0.589	0.044	200.7	0.102	1.233	0.560	0.805	0.106
					393302	13.59	4176	1.43	0.566	1.184	230.0	0.077	1.624	1.233	0.215	1.653
					394549	15.40	4301	0.54	1.230	1.022	223.8	0.059	2.055	3.566	1.233	0.125
					360891	27.43	3303	13.09	0.079	0.945	249.2	0.122	5.201	0.474	2.022	1.745
					372733	13.70	9350	3.68	0.079	0.748	179.5	0.154	3.829	0.393	0.892	0.193
					415118	21.19	5423	5.58	0.079	1.811	211.3	0.075	2.886	2.122	0.498	0.437
					414495	13.28	4494	94.23	0.259	2.475	214.3	0.163	3.014	0.978	0.588	0.183
Median IM-24					**393302**	**13.70**	**4301**	**5.58**	**0.259**	**1.022**	**214.3**	**0.102**	**2.886**	**0.978**	**0.805**	**0.193**
Bushveld Complex	Impala mine	IM-26	Leuconorite	-8	429454	17.33	8228	1.87	0.079	1.060	167.1	0.474	1.781	1.452	2.122	0.119
					370240	13.20	5859	2.93	2.805	1.253	158.9	0.362	1.439	0.119	0.989	0.107
					379590	17.14	7667	2.39	1.099	2.677	188.3	0.126	1.648	1.346	0.755	0.150
					363384	17.02	6283	0.96	0.422	2.063	197.5	0.162	5.622	0.162	3.205	0.640
					395172	19.14	6108	1.12	0.522	2.992	200.1	0.460	2.566	3.234	5.022	0.086
					387069	25.06	4519	2.81	0.358	1.738	188.9	0.561	1.870	0.405	2.012	0.231
Median IM-26					**383330**	**17.23**	**6196**	**2.13**	**0.472**	**1.901**	**188.6**	**0.411**	**1.826**	**0.876**	**2.067**	**0.134**
Bushveld Complex	Impala mine	IM-28	Leuconorite	-23	365145	18.01	4986	8.11	8.539	1.529	145.2	0.046	1.203	0.423	2.666	0.220
					339699	19.88	3254	7.29	0.498	0.633	183.9	0.059	4.567	0.090	0.789	0.352
					358398	18.26	5485	5.81	1.234	2.478	168.3	0.149	0.838	0.125	0.588	0.152
					371487	24.68	4612	5.71	0.258	2.970	242.8	0.062	6.225	0.119	2.188	0.241
Median IM-28					**361771**	**19.07**	**4799**	**6.55**	**0.866**	**2.003**	**176.1**	**0.061**	**2.885**	**0.122**	**1.488**	**0.231**

ANNEXE 18 – Cont.

Intrusion	Locality	Sample	^{111}Cd	^{115}In	^{118}Sn	^{121}Sb	^{128}Te	^{185}Re	^{189}Os	^{193}Ir	^{195}Pt	^{197}Au	^{205}Tl	^{208}Pb	^{209}Bi
LOD			0.025	0.014	0.018	0.012	0.079	0.004	0.008	0.002	0.004	0.007	0.002	0.005	0.002
Bushveld Complex	Impala mine	IM-24	0.149	0.014	0.136	0.090	0.566	0.243	0.666	5.428	0.308	0.007	0.002	0.854	0.144
			0.489	0.014	0.097	0.075	1.202	0.131	2.032	3.060	0.039	0.007	0.002	0.887	0.002
			0.655	0.014	0.206	0.055	0.804	0.079	0.299	1.646	0.087	0.007	0.002	0.777	0.024
			0.423	0.014	0.137	0.012	0.157	0.311	0.106	0.530	0.004	0.007	0.002	1.812	0.552
			0.545	0.014	0.018	0.097	0.202	0.170	5.423	4.079	0.310	0.007	0.016	1.689	0.037
			0.234	0.014	0.123	0.052	0.106	0.214	4.027	3.556	0.343	0.007	0.075	2.326	0.002
			0.305	0.014	0.087	0.026	0.967	0.145	4.675	2.989	0.362	0.007	0.002	0.960	0.112
Median IM-24			**0.423**	**0.014**	**0.123**	**0.055**	**0.566**	**0.170**	**2.032**	**3.060**	**0.308**	**0.007**	**0.002**	**0.960**	**0.037**
Bushveld Complex	Impala mine	IM-26	0.179	0.014	0.162	0.012	0.661	0.090	5.049	2.549	0.010	0.007	0.002	1.116	0.042
			0.168	0.014	0.130	0.031	3.111	0.810	3.864	1.745	0.249	0.007	0.055	2.619	0.124
			0.099	0.014	0.121	0.012	0.904	0.154	2.468	1.527	0.004	0.007	0.002	1.022	0.090
			0.145	0.014	0.150	0.012	0.579	0.218	3.117	3.664	0.044	0.007	0.002	1.180	0.068
			0.274	0.014	0.189	0.056	2.115	0.138	3.677	1.945	0.092	0.007	0.002	1.309	0.123
			0.212	0.014	0.323	0.081	0.985	0.312	2.842	3.702	0.069	0.007	0.026	2.182	0.062
Median IM-26			**0.174**	**0.014**	**0.156**	**0.021**	**0.944**	**0.186**	**3.397**	**2.247**	**0.056**	**0.007**	**0.002**	**1.244**	**0.079**
Bushveld Complex	Impala mine	IM-28	0.123	0.014	0.210	0.042	0.414	0.120	0.530	0.874	0.011	0.007	0.023	2.057	0.170
			0.097	0.014	0.124	0.012	0.989	0.090	0.922	0.357	0.037	0.007	0.181	1.684	0.255
			0.256	0.014	0.256	0.012	0.698	0.200	2.244	0.835	0.405	0.007	0.087	2.119	0.047
			0.123	0.014	0.115	0.012	2.322	0.004	2.836	0.474	0.004	0.007	0.002	0.891	0.170
Median IM-28			**0.123**	**0.014**	**0.167**	**0.012**	**0.843**	**0.105**	**1.583**	**0.654**	**0.024**	**0.007**	**0.055**	**1.870**	**0.170**

ANNEXE 18 – Cont.

Intrusion	Locality	Sample	Rock	Height (cm)	^{34}S	^{59}Co	^{61}Ni	^{65}Cu	^{66}Zn	^{75}As	^{82}Se	^{95}Mo	^{101}Ru	^{103}Rh
LOD					58	0.008	0.306	0.276	0.079	0.044	0.6	0.008	0.008	0.001
Bushveld Complex	Rustemburg mine	AN	Anorthosite	-2	393194	20.32	3110	1.31	0.234	0.044	246.9	0.123	2.057	0.922
					399427	15.08	4949	7.60	0.562	0.044	224.4	0.673	6.669	0.323
					415118	12.34	4868	6.61	1.234	0.820	237.5	0.670	3.490	0.199
					407638	26.80	4157	5.24	0.436	0.436	213.8	0.480	10.122	1.522
Median AN					**403532**	**17.70**	**4513**	**5.92**	**0.499**	**0.240**	**230.9**	**0.575**	**5.080**	**0.623**
Bushveld Complex	Rustemburg mine	LC	Lower chromitite	0	416364	10.80	3815	2.99	3.022	0.172	172.0	0.455	3.553	1.069
					381460	8.41	3441	6.98	0.997	0.487	153.3	0.224	1.566	0.256
					407015	10.66	4232	6.11	1.127	0.250	168.9	0.256	6.255	0.522
					406174	11.28	4843	2.12	0.251	0.476	213.7	0.221	2.512	0.123
Median LC					**406594**	**10.73**	**4023**	**4.55**	**1.062**	**0.363**	**170.5**	**0.240**	**3.032**	**0.389**
Bushveld Complex	Rustemburg mine	CGM-1	Coarse-grained melanorite	2	376310	16.14	3297	2.71	3.054	0.224	210.4	0.054	4.232	0.261
					394549	19.63	3428	11.84	6.856	0.156	200.1	0.143	8.720	0.456
					373871	15.21	3279	2.26	0.268	0.280	198.3	0.187	4.718	0.312
					402652	7.15	1215	4.55	0.586	0.405	195.1	0.240	6.239	0.367
					404522	11.53	3272	4.74	0.087	0.172	193.8	0.312	8.352	0.654
					393302	12.65	3734	5.49	0.293	0.511	203.8	0.524	33.658	1.452
					387015	10.54	3709	4.36	0.236	0.479	197.4	0.333	12.092	0.524
Median CGM-1					**393302**	**12.65**	**3297**	**4.55**	**0.293**	**0.280**	**198.3**	**0.240**	**8.352**	**0.456**

ANNEXE 18 – Cont.

Locality	Sample	^{108}Pd	^{109}Ag	^{111}Cd	^{115}In	^{118}Sn	^{121}Sb	^{128}Te	^{185}Re	^{189}Os	^{193}Ir	^{195}Pt	^{197}Au	^{205}Tl	^{208}Pb	^{209}Bi
LOD		0.027	0.003	0.025	0.014	0.018	0.012	0.079	0.004	0.008	0.002	0.004	0.007	0.002	0.005	0.002
Rustemburg mine	AN	0.211	0.757	0.322	0.024	0.150	0.012	1.200	0.123	0.522	2.113	5.367	0.033	0.007	5.634	0.323
		2.034	0.122	0.989	0.090	0.249	0.012	2.123	0.435	4.924	5.553	1.384	0.007	0.002	0.960	1.123
		1.032	0.399	1.367	0.014	0.125	0.012	0.567	0.368	3.690	2.518	0.997	0.007	0.002	3.615	0.175
		0.455	0.108	0.262	0.019	0.456	0.026	0.337	0.318	1.272	1.922	0.549	0.010	0.006	1.932	0.134
Median AN		**0.744**	**0.261**	**0.655**	**0.021**	**0.199**	**0.012**	**0.883**	**0.343**	**2.481**	**2.316**	**1.191**	**0.008**	**0.004**	**2.774**	**0.249**
Rustemburg mine	LC	0.203	0.082	0.211	0.014	0.093	0.027	0.293	0.119	1.596	6.869	0.623	0.007	0.002	0.760	0.255
		0.234	0.153	0.323	0.030	0.117	0.012	0.412	0.187	0.754	2.424	0.218	0.007	0.007	1.521	0.046
		0.123	0.145	1.234	0.023	0.018	0.087	0.100	0.349	1.991	0.636	0.193	0.007	0.002	1.496	0.302
		0.099	0.523	0.025	0.099	0.322	0.069	0.155	0.158	5.291	1.795	0.871	0.009	0.002	2.194	0.167
Median LC		**0.163**	**0.149**	**0.267**	**0.026**	**0.105**	**0.048**	**0.224**	**0.172**	**1.793**	**2.110**	**0.421**	**0.007**	**0.002**	**1.508**	**0.211**
Rustemburg mine	CGM-1	0.456	0.150	0.025	0.014	0.268	0.012	0.079	0.236	5.934	3.914	0.115	0.007	0.002	0.866	0.039
		0.233	0.451	0.025	0.014	0.060	0.012	0.399	0.160	8.564	7.168	0.617	0.007	0.002	0.657	0.153
		0.644	0.113	0.224	0.097	0.041	0.020	0.280	0.141	6.644	4.506	0.486	0.007	0.002	0.524	0.566
		1.120	0.374	0.155	0.014	0.038	0.012	0.755	0.018	5.460	2.618	0.287	0.007	0.002	0.729	0.065
		0.311	1.233	0.025	0.079	0.566	0.012	0.249	0.611	6.171	5.590	0.358	0.007	0.002	0.718	0.060
		0.122	0.194	0.655	0.014	0.449	0.012	0.280	0.580	8.228	8.913	0.742	0.007	0.002	1.377	0.243
		0.234	0.978	1.234	0.014	0.156	2.805	0.234	0.461	5.485	5.292	0.293	0.007	0.002	0.526	0.745
Median CGM-1		**0.311**	**0.374**	**0.155**	**0.014**	**0.156**	**0.012**	**0.280**	**0.236**	**6.171**	**5.292**	**0.358**	**0.007**	**0.002**	**0.718**	**0.153**

ANNEXE 18 – Cont.

Intrusion	Locality	Sample	Rock	Height (cm)	^{34}S	^{59}Co	^{61}Ni	^{65}Cu	^{66}Zn	^{75}As	^{82}Se	^{95}Mo	^{101}Ru	^{103}Rh
LOD					58	0.008	0.306	0.276	0.079	0.044	0.6	0.008	0.008	0.001
Bushveld Complex	Rustemburg mine	CGM-2	Coarse-grained melanorite	6	375850	7.35	1109	3.43	0.303	0.044	173.9	0.290	10.347	0.140
					390809	7.79	1346	5.25	0.866	0.337	165.8	0.405	25.244	0.291
					410131	9.47	1415	5.73	1.047	0.443	178.3	0.263	19.946	0.209
					367124	14.86	1795	3.65	7.255	0.181	190.1	0.187	38.520	5.111
					372110	4.92	1729	2.57	1.233	0.044	177.4	0.008	0.181	0.405
					391432	11.30	1664	5.50	0.356	0.619	185.7	0.271	20.320	0.188
					419481	10.25	1377	5.38	0.518	0.287	204.1	0.160	10.970	1.103
					395796	9.60	1222	6.30	0.517	0.418	196.4	0.162	14.772	0.323
Median CGM-2					**391121**	**9.54**	**1396**	**5.31**	**0.692**	**0.312**	**182.0**	**0.225**	**17.359**	**0.307**
Bushveld Complex	Rustemburg mine	UC	Upper chromitite	10	408885	11.66	3060	6.73	1.450	0.253	215.2	0.190	2.618	0.123
					423844	11.14	2680	2.93	0.193	0.570	244.3	0.124	8.352	0.090
					406310	125.22	2817	3.67	0.079	0.774	215.0	0.157	1.870	0.567
					388316	86.96	2188	8.14	0.564	0.869	166.4	0.370	1.278	1.200
					413248	14.74	4450	2.66	0.989	0.234	198.8	0.523	4.438	0.099
					422597	11.91	3858	2.62	3.254	0.169	202.6	0.499	1.172	0.422
Median UC					**408885**	**14.74**	**3060**	**2.93**	**0.880**	**0.467**	**215.0**	**0.237**	**2.618**	**0.322**
Bushveld Complex	Rustemburg mine	M-1	Melanorite	13.5	406392	7.23	1421	6.54	0.320	0.461	154.0	0.343	4.550	0.126
					391432	9.66	1527	3.62	0.522	0.424	158.6	0.479	17.203	0.323
					403275	7.30	1652	4.11	0.132	0.256	169.5	0.206	5.610	0.211
					403275	8.52	1602	2.74	0.079	0.522	194.3	0.181	2.830	0.367
					381920	9.04	1502	7.73	0.751	0.123	204.4	0.181	1.085	1.256
					411378	4.80	711	7.98	0.079	0.426	185.1	0.009	2.531	0.989
					390194	6.36	798	6.98	0.266	0.312	233.3	0.240	4.924	0.122
Median M-1					**397042**	**8.60**	**1527**	**4.36**	**0.320**	**0.256**	**185.1**	**0.206**	**4.550**	**0.267**

ANNEXE 18 – Cont.

Locality	Sample	^{108}Pd	^{109}Ag	^{111}Cd	^{115}In	^{118}Sn	^{121}Sb	^{128}Te	^{185}Re	^{189}Os	^{193}Ir	^{195}Pt	^{197}Au	^{205}Tl	^{208}Pb	^{209}Bi
LOD		0.027	0.003	0.025	0.014	0.018	0.012	0.079	0.004	0.008	0.002	0.004	0.007	0.002	0.005	0.002
Rustemburg mine	CGM-2	0.233	0.234	0.025	0.014	0.789	0.012	0.386	0.478	4.737	4.675	0.199	0.007	0.002	0.611	0.323
		0.456	0.349	0.255	0.090	0.224	0.012	0.545	0.474	6.856	6.563	0.208	0.007	0.002	1.103	0.040
		1.098	0.293	0.076	0.014	0.018	0.012	0.789	0.430	5.248	5.684	0.231	0.007	0.006	1.172	0.074
		1.124	0.667	0.233	0.037	0.327	0.012	0.243	0.054	9.474	6.545	0.411	0.436	0.002	2.168	0.505
		0.212	0.786	0.025	0.014	1.322	0.012	0.176	0.004	0.008	0.567	1.245	0.118	0.002	1.172	0.026
		0.345	0.206	0.145	0.014	0.168	0.012	0.256	0.062	6.607	5.984	0.212	0.007	0.002	1.028	0.072
		0.445	0.425	0.589	0.016	0.018	0.012	0.171	0.052	3.802	5.049	0.107	0.007	0.002	1.134	1.233
		0.523	0.779	0.025	0.014	0.355	0.012	1.234	0.124	6.117	5.859	0.112	0.007	0.003	2.019	0.900
Median CGM-2		**0.450**	**0.387**	**0.110**	**0.014**	**0.276**	**0.012**	**0.321**	**0.093**	**5.682**	**5.772**	**0.210**	**0.007**	**0.002**	**1.153**	**0.198**
Rustemburg mine	UC	0.989	0.659	0.227	0.014	1.109	0.012	0.401	0.231	0.258	17.826	5.547	0.007	0.002	2.001	0.062
		2.356	0.078	0.856	0.014	1.033	0.012	0.303	0.362	2.294	4.749	0.758	0.017	0.002	0.767	0.323
		0.122	0.162	0.099	0.014	0.130	0.013	0.079	0.355	1.608	1.864	0.390	0.007	0.007	1.508	1.300
		0.367	0.341	1.323	0.014	0.566	0.012	0.423	0.573	0.868	2.132	0.573	0.007	0.002	2.759	0.048
		0.136	0.455	0.031	0.014	0.107	0.012	1.022	0.443	4.974	3.677	0.137	0.012	0.002	0.804	0.522
		0.367	0.562	0.122	0.016	0.789	0.020	0.174	0.580	4.351	2.493	1.197	0.007	0.003	0.785	0.100
Median UC		**0.367**	**0.341**	**0.122**	**0.014**	**0.566**	**0.012**	**0.317**	**0.443**	**2.294**	**3.677**	**0.573**	**0.007**	**0.002**	**0.804**	**0.123**
Rustemburg mine	M-1	2.255	0.169	0.025	0.014	0.018	0.012	0.079	0.598	3.615	3.727	0.062	0.007	0.002	0.698	0.123
		0.989	0.249	0.255	0.014	0.237	0.016	0.079	0.723	7.978	5.797	0.350	0.007	0.002	1.091	0.032
		0.789	0.128	0.029	0.070	0.257	0.012	1.200	0.280	3.989	3.671	0.240	0.007	0.002	1.234	0.323
		0.367	0.237	0.855	0.014	0.136	0.012	0.104	0.330	2.562	0.735	0.055	0.016	0.002	2.199	0.256
		0.756	1.200	0.755	0.233	0.150	0.012	0.566	0.246	1.540	0.467	0.081	0.007	0.002	2.231	0.044
		2.365	0.362	0.090	0.014	0.633	0.012	0.878	0.358	2.811	1.116	0.066	0.007	0.002	1.147	0.020
		1.563	0.503	0.025	0.014	0.855	0.012	0.237	0.704	4.301	2.774	0.337	0.007	0.004	1.828	0.045
Median M-1		**0.989**	**0.237**	**0.178**	**0.014**	**0.150**	**0.012**	**0.237**	**0.358**	**3.397**	**2.774**	**0.118**	**0.007**	**0.002**	**1.234**	**0.045**

ANNEXE 18 – Cont.

Intrusion	Locality	Sample	Rock	Height (cm)	^{34}S	^{59}Co	^{61}Ni	^{65}Cu	^{66}Zn	^{75}As	^{82}Se	^{95}Mo	^{101}Ru	^{103}Rh
LOD					58	0.008	0.306	0.276	0.079	0.044	0.6	0.008	0.008	0.001
Bushveld Complex	Rustemburg mine	M-2	Melanorite	18	406364	8.04	1577	2.24	0.180	0.320	214.6	0.136	5.092	0.234
					413248	9.47	1708	3.43	0.079	0.044	226.9	0.125	4.369	0.136
					407584	11.84	2182	2.97	1.337	0.131	202.0	0.095	5.379	0.786
					387693	12.03	1957	4.36	0.079	0.269	203.7	0.322	5.815	0.122
					380836	12.72	2231	4.60	0.399	0.580	184.4	0.197	10.845	2.367
					371947	23.56	1302	15.15	4.200	0.430	201.9	7.417	25.056	0.717
Median M-2					**397029**	**11.94**	**1833**	**3.90**	**0.290**	**0.295**	**202.9**	**0.166**	**5.597**	**0.475**
Bushveld Complex	Rustemburg mine	M-3	Melanorite	23	402652	25.18	5485	4.32	0.218	0.233	179.3	0.423	3.771	0.233
					392029	21.57	6065	3.68	12.256	0.566	207.6	3.802	5.223	0.099
					387069	29.17	6090	3.66	2.200	0.274	179.0	0.312	5.173	0.322
					401871	22.31	6221	4.36	0.343	0.305	213.6	0.178	5.547	0.989
					390186	22.94	6152	4.74	0.590	0.143	194.5	0.436	4.263	0.123
					387693	19.88	5610	3.20	0.381	0.044	225.0	0.490	5.260	0.087
Median M-3					**391107**	**22.63**	**6077**	**4.00**	**0.486**	**0.254**	**201.0**	**0.430**	**5.198**	**0.178**
Bushveld Complex	Rustemburg mine	M-4	Melanorite	27	372733	18.14	4656	1.93	0.411	0.146	181.5	0.169	11.593	5.622
					380836	10.85	3572	3.82	3.567	0.633	216.5	0.255	0.605	0.877
					375850	12.22	3815	4.11	0.516	0.310	191.7	0.167	4.575	0.256
					431947	8.15	3272	1.02	0.328	0.900	162.1	0.122	0.343	0.367
					413248	20.26	4438	2.99	0.545	0.044	203.7	0.119	8.539	0.790
					389563	14.90	3858	2.63	0.430	0.206	191.4	0.147	4.799	0.256
Median M-4					**385199**	**13.56**	**3836**	**2.81**	**0.473**	**0.258**	**191.5**	**0.157**	**4.687**	**0.578**

ANNEXE 18 – Cont.

Locality	Sample	^{108}Pd	^{109}Ag	^{111}Cd	^{115}In	^{118}Sn	^{121}Sb	^{128}Te	^{185}Re	^{189}Os	^{193}Ir	^{195}Pt	^{197}Au	^{205}Tl	^{208}Pb	^{209}Bi
LOD		0.027	0.003	0.025	0.014	0.018	0.012	0.079	0.004	0.008	0.002	0.004	0.007	0.002	0.005	0.002
Rustemburg mine	M-2	0.890	0.900	0.025	0.022	0.088	0.012	0.305	0.240	4.020	2.026	0.136	0.007	0.002	0.667	0.099
		0.545	0.255	0.211	0.014	0.049	0.012	2.002	0.268	5.069	1.758	0.188	0.007	0.002	1.024	0.212
		2.333	0.112	0.122	0.086	0.256	0.012	1.522	0.242	4.949	2.562	0.171	0.007	0.002	1.180	0.036
		4.226	0.236	0.025	0.014	0.034	0.035	0.079	0.274	3.017	1.938	0.064	0.007	0.002	1.183	0.655
		3.225	0.074	0.138	0.045	0.421	0.018	1.367	0.278	3.902	2.848	0.103	0.007	0.002	1.258	0.032
		0.989	0.103	0.025	0.014	0.123	1.122	0.900	4.176	8.602	10.035	17.889	0.007	0.004	0.948	0.522
Median M-2		**1.661**	**0.174**	**0.074**	**0.018**	**0.106**	**0.015**	**1.133**	**0.271**	**4.485**	**2.294**	**0.154**	**0.007**	**0.002**	**1.102**	**0.155**
Rustemburg mine	M-3	7.559	0.196	0.126	0.014	0.099	0.012	0.367	0.232	0.898	0.717	0.073	0.007	0.002	1.098	0.203
		0.900	1.323	0.025	0.123	0.084	0.012	0.215	0.891	1.159	0.935	0.073	0.007	0.004	1.109	0.119
		0.248	0.102	0.323	0.014	0.122	0.016	0.079	0.425	1.147	0.960	0.035	0.007	0.002	0.644	0.522
		0.789	0.133	0.025	0.023	0.018	0.012	0.558	0.287	0.979	0.935	0.151	0.007	0.002	0.947	0.118
		0.566	0.855	0.099	0.014	0.367	0.012	0.699	0.154	0.891	0.748	0.004	0.007	0.002	0.904	0.095
		0.478	0.789	0.076	0.014	0.755	0.012	2.226	0.224	1.377	0.979	0.010	0.007	0.436	0.668	0.123
Median M-3		**0.677**	**0.492**	**0.087**	**0.014**	**0.111**	**0.012**	**0.462**	**0.260**	**1.063**	**0.935**	**0.054**	**0.007**	**0.002**	**0.926**	**0.121**
Rustemburg mine	M-4	0.989	1.022	0.063	0.014	0.234	0.012	1.323	0.014	2.101	1.658	0.055	0.007	0.002	0.810	0.022
		0.633	0.199	2.221	0.033	0.422	0.012	0.255	0.157	0.479	0.142	0.004	0.007	0.002	1.558	0.123
		5.633	0.149	0.025	0.099	0.127	0.012	0.190	0.006	1.614	0.742	0.083	0.007	0.002	0.689	0.096
		1.200	0.146	0.029	0.014	0.018	0.012	0.223	0.004	0.505	0.068	0.004	0.007	0.002	0.972	0.102
		0.300	0.175	0.090	0.122	0.086	0.012	0.986	0.526	2.612	2.412	0.271	0.007	0.002	1.343	0.211
		0.256	0.396	0.153	0.014	0.234	0.012	0.310	0.413	2.480	1.247	0.190	0.007	0.011	2.674	0.027
Median M-4		**0.811**	**0.187**	**0.077**	**0.024**	**0.180**	**0.012**	**0.283**	**0.086**	**1.857**	**0.994**	**0.069**	**0.007**	**0.002**	**1.158**	**0.099**

ANNEXE 18 – Cont.

Intrusion	Locality	Sample	Rock	^{34}S	^{59}Co	^{61}Ni	^{65}Cu	^{66}Zn	^{75}As	^{82}Se	^{95}Mo	^{101}Ru	^{103}Rh	^{108}Pd
LOD				58	0.008	0.306	0.276	0.079	0.044	0.6	0.008	0.008	0.001	0.027
Stillwater Complex	East Boulder mine	ST-12	Mela troctolite	378343	42.57	947	5.61	0.079	0.174	255.6	0.056	0.249	1.023	27.200
				442543	17.70	89	19.32	1.371	0.236	157.7	0.008	0.106	1.322	2.022
				375850	23.75	430	517.34	0.349	0.044	176.4	0.062	1.003	0.263	21.023
				406392	50.49	464	218.16	0.623	0.206	196.3	0.044	0.845	0.122	1.185
				386446	25.37	315	11.22	0.168	0.135	236.2	0.008	1.321	0.345	32.022
				418858	14.52	221	8.35	0.524	0.166	134.6	0.014	0.599	0.099	4.337
Median ST-12				**396419**	**24.56**	**373**	**15.27**	**0.436**	**0.170**	**186.4**	**0.029**	**0.722**	**0.304**	**12.680**
Stillwater Complex	East Boulder mine	ST-14	Anorthosite	413871	47.93	3790	0.37	0.079	0.044	245.6	0.008	1.988	0.504	5.022
				417611	101.60	5373	1.06	0.249	0.145	221.3	0.098	2.132	1.102	2.102
				437557	94.87	4226	0.28	0.125	0.044	229.4	0.276	0.318	0.202	9.225
				394549	73.55	5678	8.73	0.393	0.162	253.7	0.008	0.143	0.262	14.021
				405063	61.71	4525	0.93	0.598	0.044	274.3	0.145	3.235	0.458	15.234
				420104	51.98	4257	2.06	0.461	0.168	246.8	0.008	2.973	0.425	10.322
				404440	76.04	4774	2.49	0.243	0.354	245.6	0.008	3.771	1.097	6.545
Median ST-14				**413871**	**73.55**	**4525**	**1.06**	**0.249**	**0.145**	**245.6**	**0.008**	**2.132**	**0.458**	**9.225**
Stillwater Complex	East Boulder mine	ST-16	Leuconorite	394549	50.67	7018	3.37	0.810	0.044	240.6	0.087	1.489	0.878	3.022
				417584	76.15	8041	2.62	0.380	0.199	273.6	0.293	2.100	0.083	37.394
				399535	71.06	7293	1.62	0.767	0.044	259.9	0.349	2.611	0.201	2.018
				422597	74.48	8602	1.18	0.175	0.099	263.7	0.039	0.879	0.123	0.989
				412625	89.76	8041	1.87	0.079	0.314	254.3	0.137	0.885	0.001	4.211
				388939	44.07	7897	2.49	0.079	0.056	263.2	0.452	1.994	0.922	4.040
Median ST-16				**406080**	**72.77**	**7969**	**2.18**	**0.277**	**0.077**	**261.6**	**0.215**	**1.741**	**0.162**	**3.531**

ANNEXE 18 – Cont.

Locality	Sample	^{109}Ag	^{111}Cd	^{115}In	^{118}Sn	^{121}Sb	^{128}Te	^{185}Re	^{189}Os	^{193}Ir	^{195}Pt	^{197}Au	^{205}Tl	^{208}Pb	^{209}Bi
LOD		0.003	0.025	0.014	0.018	0.012	0.079	0.004	0.008	0.002	0.004	0.007	0.002	0.005	0.002
East Boulder mine	ST-12	3.255	0.211	0.014	0.125	0.014	0.079	0.004	0.168	0.823	0.004	0.007	0.002	0.343	0.024
		0.879	0.655	0.014	0.018	0.012	0.187	0.032	0.231	0.411	0.004	0.007	0.002	0.935	0.489
		0.262	0.088	0.014	0.018	0.012	0.079	0.004	0.118	0.386	0.008	0.009	0.002	0.580	0.011
		2.979	0.025	0.014	0.214	0.012	0.322	0.025	0.042	0.318	0.004	0.012	0.002	1.878	4.363
		0.137	0.126	0.014	0.025	0.012	0.199	0.048	0.037	0.330	0.088	0.007	0.002	0.430	0.002
		0.891	0.037	0.014	0.086	0.012	0.079	0.004	0.026	0.189	0.022	0.007	0.034	1.646	0.032
Median ST-12		**0.885**	**0.107**	**0.014**	**0.055**	**0.012**	**0.133**	**0.015**	**0.080**	**0.358**	**0.006**	**0.007**	**0.002**	**0.757**	**0.028**
East Boulder mine	ST-14	0.455	0.025	0.014	0.037	0.014	0.120	0.007	0.052	4.450	0.024	0.007	0.002	1.621	0.002
		1.355	0.069	0.018	0.337	0.012	0.274	0.022	0.318	2.780	0.015	0.007	0.090	3.927	0.097
		0.898	0.025	0.014	0.237	0.012	0.352	0.096	0.436	1.134	0.004	0.007	0.002	2.743	0.005
		0.399	1.023	0.014	0.018	0.012	0.115	0.010	0.031	0.328	0.230	0.007	0.006	5.797	0.989
		0.799	1.632	0.014	0.112	0.026	0.218	0.008	0.355	2.898	0.013	0.007	0.099	1.533	0.003
		0.259	0.025	0.120	0.452	0.012	0.099	0.088	0.256	2.711	0.004	0.007	0.002	1.215	2.022
		0.312	0.976	0.014	0.044	0.012	0.079	0.004	0.260	3.758	0.004	0.007	0.002	1.315	0.542
Median ST-14		**0.455**	**0.069**	**0.014**	**0.112**	**0.012**	**0.120**	**0.010**	**0.260**	**2.780**	**0.013**	**0.007**	**0.002**	**1.621**	**0.097**
East Boulder mine	ST-16	0.443	0.099	0.014	0.234	0.048	0.499	0.623	0.305	0.170	0.027	0.007	0.006	2.306	0.002
		0.735	0.112	0.014	0.323	0.012	0.197	0.632	0.972	1.178	0.123	0.007	0.003	0.443	1.234
		0.150	0.025	0.014	0.056	0.012	0.337	0.561	1.184	1.234	0.019	0.007	0.002	5.700	0.976
		0.212	0.212	0.014	0.099	0.012	0.137	0.118	0.916	0.779	0.198	0.008	0.002	0.573	0.097
		0.648	1.323	0.014	0.018	0.012	0.756	0.499	1.004	0.611	0.099	0.007	0.004	1.751	0.004
		1.255	0.025	0.014	0.037	0.012	0.112	0.062	1.191	1.010	0.034	0.007	0.002	0.424	0.005
Median ST-16		**0.545**	**0.106**	**0.014**	**0.077**	**0.012**	**0.267**	**0.530**	**0.988**	**0.894**	**0.067**	**0.007**	**0.002**	**1.162**	**0.051**

ANNEXE 18 – Cont.

Intrusion	Locality	Sample	Rock	^{34}S	^{59}Co	^{61}Ni	^{65}Cu	^{66}Zn	^{75}As	^{82}Se	^{95}Mo	^{101}Ru	^{103}Rh	^{108}Pd
LOD				58	0.008	0.306	0.276	0.079	0.044	0.6	0.008	0.008	0.001	0.027
Stillwater Complex	East Boulder mine	ST-17	Olivine gabbronorite	344685	1.84	152	8.10	0.187	0.187	144.0	0.008	1.367	0.001	1.234
				359021	2.62	24	20.57	0.079	0.499	119.1	0.008	2.589	0.098	5.366
				339699	1.70	268	2.93	0.374	0.044	249.3	0.008	0.106	0.123	0.978
				393926	2.71	354	13.71	0.630	0.605	251.2	0.008	0.979	0.086	2.656
				357151	2.56	256	23.69	0.249	0.125	177.6	0.050	0.156	0.001	5.689
Median ST-17				**357151**	**2.56**	**256**	**13.71**	**0.249**	**0.187**	**177.6**	**0.008**	**0.979**	**0.086**	**2.656**
Stillwater Complex	Stillwater mine	P-4	Anorthosite	454386	16.83	6270	0.93	1.234	0.623	383.1	0.076	1.190	0.013	0.063
				397665	15.43	6831	0.42	0.256	0.586	428.1	0.099	1.782	0.605	0.855
				404522	21.32	5747	0.28	0.456	0.823	409.9	0.123	1.795	0.524	1.022
				404522	21.44	7480	0.28	0.224	0.530	413.7	0.008	1.895	1.646	0.122
Median P-4				**404522**	**19.07**	**6551**	**0.35**	**0.356**	**0.605**	**411.8**	**0.087**	**1.789**	**0.564**	**0.489**
Stillwater Complex	Stillwater mine	P-3	Leuco gabbronorite	421974	24.06	3054	0.69	0.567	0.044	344.7	0.059	3.054	0.021	0.098
				420728	24.37	2568	1.43	0.190	0.044	327.2	0.098	2.973	0.544	1.022
				424467	24.31	4182	0.28	2.655	0.106	336.0	0.126	4.145	0.307	2.033
				445036	22.50	4351	1.12	0.633	0.159	304.2	0.019	4.700	0.068	0.027
				402652	23.93	2774	0.28	0.368	0.243	294.2	0.041	2.823	0.100	0.522
				410755	25.49	3802	0.28	0.255	0.126	310.4	0.031	3.939	0.174	0.052
Median P-3				**421351**	**24.18**	**3428**	**0.48**	**0.467**	**0.116**	**318.8**	**0.050**	**3.497**	**0.137**	**0.310**

ANNEXE 18 – Cont.

Locality	Sample	^{109}Ag	^{111}Cd	^{115}In	^{118}Sn	^{121}Sb	^{128}Te	^{185}Re	^{189}Os	^{193}Ir	^{195}Pt	^{197}Au	^{205}Tl	^{208}Pb	^{209}Bi
LOD		0.003	0.025	0.014	0.018	0.012	0.079	0.004	0.008	0.002	0.004	0.007	0.002	0.005	0.002
East Boulder mine	ST-17	0.024	0.044	0.014	0.156	0.017	0.125	0.004	0.032	0.131	0.004	0.007	0.088	0.324	0.002
		1.234	3.256	0.014	0.120	0.012	0.097	0.004	0.099	0.100	0.004	0.007	0.002	0.299	0.009
		0.175	0.755	0.014	0.255	0.012	0.123	0.017	0.008	1.720	0.004	0.007	0.014	0.486	0.234
		0.046	1.656	0.014	0.057	0.012	0.233	0.020	0.053	1.359	0.014	0.007	0.057	0.355	0.125
		0.978	0.978	0.014	0.018	0.025	0.079	0.016	0.059	0.698	0.004	0.007	0.004	0.330	0.002
Median ST-17		**0.175**	**0.978**	**0.014**	**0.120**	**0.012**	**0.123**	**0.016**	**0.053**	**0.698**	**0.004**	**0.007**	**0.014**	**0.330**	**0.009**
Stillwater mine	P-4	0.131	0.025	0.014	0.018	0.019	0.423	0.017	0.480	0.760	0.075	0.007	0.002	2.618	0.589
		0.157	1.233	0.014	0.120	0.012	0.146	0.059	0.461	1.022	0.545	0.007	0.003	0.436	0.098
		0.146	0.589	0.014	0.093	0.012	0.150	0.013	0.069	0.424	0.014	0.007	0.090	0.386	0.007
		0.131	0.025	0.014	0.123	0.012	0.234	0.123	0.237	0.505	0.006	0.007	0.100	0.499	0.102
Median P-4		**0.139**	**0.307**	**0.014**	**0.107**	**0.012**	**0.192**	**0.038**	**0.349**	**0.633**	**0.044**	**0.007**	**0.046**	**0.467**	**0.100**
Stillwater mine	P-3	0.841	0.025	0.014	0.036	0.012	0.123	0.007	0.231	3.889	0.022	0.007	0.002	4.862	0.200
		0.657	0.031	0.014	0.018	0.029	0.323	0.057	0.342	3.447	0.004	0.007	0.037	4.363	0.123
		0.430	1.033	0.014	0.211	0.032	0.561	0.037	0.337	4.737	0.004	0.007	0.002	2.556	0.355
		0.611	0.026	0.014	0.099	0.019	0.274	0.123	0.232	4.363	0.323	0.011	0.002	3.802	0.005
		0.792	0.123	0.014	0.075	0.062	0.175	0.005	0.224	3.709	0.256	0.007	0.002	12.466	0.099
		0.380	0.025	0.014	0.048	0.012	0.326	0.004	0.181	5.130	0.004	0.007	0.002	1.166	0.099
Median P-3		**0.634**	**0.029**	**0.014**	**0.061**	**0.024**	**0.298**	**0.022**	**0.232**	**4.126**	**0.013**	**0.007**	**0.002**	**4.083**	**0.111**

ANNEXE 18 – Cont.

Intrusion	Locality	Sample	Rock	^{34}S	^{59}Co	^{61}Ni	^{65}Cu	^{66}Zn	^{75}As	^{82}Se	^{95}Mo	^{101}Ru	^{103}Rh	^{108}Pd
LOD				58	0.008	0.306	0.276	0.079	0.044	0.6	0.008	0.008	0.001	0.027
Stillwater Complex	Banded Series	BS-18	Leuco gabbronorite	456256	116.06	15645	0.28	0.131	0.212	233.7	0.305	0.008	0.001	0.027
				444413	111.26	12703	0.28	1.033	0.700	216.3	0.118	0.008	0.001	0.079
				441296	126.28	12852	0.28	3.256	0.143	215.7	0.203	0.097	0.001	0.027
				458126	155.70	13021	0.28	0.299	0.137	197.0	0.237	0.008	0.001	0.088
				446283	119.67	13052	0.28	0.266	0.566	215.0	0.356	0.090	0.001	0.027
				446906	112.51	13326	0.28	0.642	0.348	181.4	0.368	0.122	0.001	0.027
				471215	133.64	12491	0.28	0.461	0.150	198.2	0.199	0.008	0.001	0.027
				459995	136.25	11537	0.28	0.873	0.259	239.3	0.143	0.008	0.001	0.027
				439427	118.61	11357	0.28	2.356	0.355	167.7	0.199	0.008	0.001	0.099
				436933	142.92	11874	0.28	0.242	1.322	210.7	0.567	0.008	0.001	0.027
				421351	137.75	15526	0.62	0.118	0.789	229.4	0.008	0.008	0.001	0.027
Median BS-18				**446906**	**133.64**	**12703**	**0.28**	**0.370**	**0.231**	**210.7**	**0.203**	**0.008**	**0.001**	**0.027**
Stillwater Complex	Picket Pin	PP-AN	Anorthosite	445036	88.57	6825	0.28	0.212	0.044	195.1	0.131	2.435	0.979	0.989
				414495	124.04	8726	0.28	2.369	1.566	195.7	0.162	1.269	0.866	0.200
				420104	93.00	7673	1.37	0.405	0.088	188.2	0.411	1.631	4.625	0.689
				422597	137.13	9412	0.60	0.966	0.219	128.4	0.008	0.989	0.989	0.545
				413871	84.15	7068	0.28	0.231	0.044	192.6	0.107	1.519	1.907	1.023
				392679	85.21	6289	0.28	2.522	0.367	184.5	1.002	1.207	2.007	0.456
				422597	99.48	8489	0.28	0.588	0.099	189.5	0.137	1.306	0.954	0.878
				400782	86.83	7230	0.28	1.367	0.162	184.4	0.935	1.369	3.235	2.655
				415118	84.39	6619	0.28	0.112	0.175	171.4	0.873	1.637	2.954	4.367
				390186	92.87	6700	0.28	0.079	0.189	171.3	0.323	0.802	1.215	0.589
Median PP-AN				**415118**	**92.87**	**7068**	**0.28**	**0.405**	**0.162**	**184.5**	**0.243**	**1.369**	**1.907**	**0.689**

ANNEXE 18 – Cont.

Locality	Sample	^{109}Ag	^{111}Cd	^{115}In	^{118}Sn	^{121}Sb	^{128}Te	^{185}Re	^{189}Os	^{193}Ir	^{195}Pt	^{197}Au	^{205}Tl	^{208}Pb	^{209}Bi
LOD		0.003	0.025	0.014	0.018	0.012	0.079	0.004	0.008	0.002	0.004	0.007	0.002	0.005	0.002
Banded Series	BS-18	0.673	0.025	0.014	0.094	0.012	0.079	2.119	0.008	0.002	0.004	0.007	0.022	2.605	0.592
		0.176	0.025	0.014	0.071	0.012	0.380	0.679	0.008	0.002	0.004	0.007	0.002	1.901	0.367
		0.517	0.025	0.014	0.099	0.012	0.079	0.004	0.008	0.002	0.004	0.007	0.002	2.263	0.492
		0.147	0.025	0.014	0.123	0.012	0.079	1.496	0.008	0.002	0.004	0.007	0.002	1.702	0.133
		0.105	0.099	0.014	0.099	0.012	0.079	0.004	0.008	0.002	0.004	0.007	0.002	2.119	0.892
		0.536	0.523	0.014	0.323	0.012	0.598	1.621	0.008	0.002	0.004	0.007	0.002	5.547	1.362
		0.241	0.025	0.014	0.018	0.012	0.362	0.004	0.008	0.002	0.004	0.007	0.002	2.269	0.123
		0.219	0.025	0.014	0.255	0.012	0.312	1.122	0.008	0.002	0.004	0.007	0.002	1.589	0.115
		0.319	0.025	0.014	0.089	0.012	0.511	1.309	0.008	0.002	0.004	0.007	0.002	2.625	1.536
		0.371	0.025	0.014	0.067	0.012	0.779	4.051	0.008	0.002	0.004	0.007	0.002	1.982	0.229
		0.280	0.025	0.014	0.122	0.012	0.079	0.004	0.008	0.014	0.004	0.007	0.002	1.178	0.137
Median BS-18		**0.241**	**0.025**	**0.014**	**0.098**	**0.012**	**0.079**	**0.679**	**0.008**	**0.002**	**0.004**	**0.007**	**0.002**	**1.982**	**0.367**
Picket Pin	PP-AN	0.656	0.122	0.014	0.108	0.012	0.079	0.617	1.103	0.511	0.057	0.007	0.002	0.206	0.002
		0.423	1.932	0.014	0.018	0.012	0.079	0.467	0.555	0.642	0.059	0.007	0.016	0.399	0.002
		0.567	0.087	0.014	0.233	0.012	0.900	1.303	0.673	0.398	0.079	0.007	0.002	0.280	0.012
		0.330	2.369	0.014	0.103	0.012	0.079	0.455	0.008	0.002	0.004	0.007	0.002	0.492	0.090
		0.120	0.025	0.014	0.078	0.012	0.455	0.152	0.954	0.542	0.025	0.007	0.002	0.242	0.012
		0.156	2.333	0.014	0.065	0.012	0.656	0.122	0.467	0.045	0.004	0.007	0.002	0.505	0.023
		0.164	0.099	0.014	0.099	0.012	0.079	0.514	0.561	0.475	0.042	0.007	0.002	0.499	0.014
		0.176	0.234	0.014	0.367	0.012	0.456	0.542	0.623	0.510	0.050	0.007	0.002	0.249	0.013
		0.123	0.523	0.014	0.200	0.012	0.079	0.841	0.735	0.623	0.106	0.007	0.002	0.124	0.099
		0.168	0.025	0.014	0.018	0.012	0.099	0.099	0.085	0.158	0.004	0.007	0.002	0.748	0.089
Median PP-AN		**0.168**	**0.122**	**0.014**	**0.103**	**0.012**	**0.099**	**0.514**	**0.623**	**0.510**	**0.050**	**0.007**	**0.002**	**0.399**	**0.014**

ANNEXE 19 - Complete data set of LA-ICP-MS analyses of pentlandite obtained in this study and median values for each sample from the Bushveld and Stillwater Complexes. The Fe values used for internal standardization are from Godel et al. (2008a) for samples from the Stillwater Complex, Godel et al. (2007) for samples from the Rustenburg mine, and stoichiometric values (i.e., 32.6%) for samples from the Impala mine. LOD - limit of detection.

ANNEXE 19

Intrusion	Locality	Sample	Rock	Height (cm)	^{34}S	^{59}Co	^{61}Ni	^{65}Cu	^{66}Zn	^{75}As	^{82}Se	^{95}Mo	^{101}Ru	^{103}Rh	^{108}Pd	^{109}Ag
LOD					58	0.004	0.3	0.28	0.079	0.044	0.6	0.008	0.01	0.00	0.03	0.003
Bushveld Complex	Impala mine	IM-1	Norite	108	347928	12438	342816	58.32	5.633	15.373	149.3	0.008	0.24	0.22	2.86	2.833
					336715	12256	390720	1.63	0.079	15.210	134.4	0.119	0.35	0.38	2.31	1.205
Median IM-1					**342322**	**12347**	**366768**	**29.97**	**2.856**	**15.291**	**141.9**	**0.063**	**0.29**	**0.30**	**2.58**	**2.019**
Bushveld Complex	Impala mine	IM-3	Norite	98	355968	8882	340912	0.66	0.311	25.920	166.5	0.031	0.70	0.35	2.04	0.318
					391160	10917	407388	0.32	0.079	10.823	187.8	0.098	0.18	0.11	2.42	1.529
					372912	10566	385064	0.69	0.585	12.430	182.3	0.008	1.22	0.38	3.72	1.206
					322575	8563	376768	0.28	0.814	10.419	128.6	0.234	1.27	0.78	2.14	0.324
					341880	8759	363048	10.09	0.079	25.397	159.5	0.020	0.81	0.18	3.35	0.814
					332112	10712	379560	2.47	0.537	9.712	123.5	0.008	0.01	1.12	1.79	0.147
Median IM-3					**348924**	**9724**	**378164**	**0.68**	**0.424**	**11.627**	**163.0**	**0.025**	**0.75**	**0.36**	**2.28**	**0.569**
Bushveld Complex	Impala mine	IM-5	Norite	88	314249	10173	364672	0.52	0.456	1.791	154.5	0.035	0.38	0.18	2.89	0.378
					281970	9052	390256	0.68	0.554	2.116	163.1	0.122	0.18	0.21	2.90	0.414
					344806	10368	364753	3.26	0.179	2.898	157.8	0.270	0.01	0.79	2.96	0.687
					299574	10452	353512	1.92	1.074	0.358	159.1	0.008	1.16	0.86	3.87	0.505
Median IM-5					**306911**	**10270**	**364713**	**1.30**	**0.505**	**1.954**	**158.4**	**0.078**	**0.28**	**0.50**	**2.93**	**0.459**
Bushveld Complex	Impala mine	IM-7	Melanorite	78	319088	7131	380952	45.58	2.735	2.344	167.9	0.053	4.52	19.15	86.24	8.140
					315464	6645	366144	18.12	4.531	2.483	157.9	0.027	3.74	11.24	78.75	6.376
Median IM-7					**317276**	**6888**	**373548**	**31.85**	**3.633**	**2.414**	**162.9**	**0.040**	**4.13**	**15.20**	**82.49**	**7.258**
Bushveld Complex	Impala mine	IM-9	Melanorite	68	346528	8763	349615	216.59	2.266	0.249	165.4	0.088	1.93	0.09	1.79	0.690
					321225	8489	367928	3.06	0.079	16.931	146.8	0.130	0.41	0.34	4.02	0.356
					282946	7896	374482	4.23	1.888	1.088	166.7	0.111	0.23	0.23	14.32	1.104
					292063	8393	320730	47.86	1.237	7.489	98.7	0.039	0.52	0.19	1.40	6.838
					329714	8177	380954	7.81	4.070	6.610	155.8	0.098	0.41	0.04	3.22	1.498
Median IM-9					**321225**	**8393**	**367928**	**7.81**	**1.888**	**6.610**	**155.8**	**0.098**	**0.41**	**0.19**	**3.22**	**1.104**

ANNEXE 19 – Cont.

Intrusion	Locality	Sample	^{111}Cd	^{115}In	^{118}Sn	^{121}Sb	^{128}Te	^{185}Re	^{189}Os	^{193}Ir	^{195}Pt	^{197}Au	^{205}Tl	^{208}Pb	^{209}Bi
LOD			0.025	0.014	0.018	0.012	0.079	0.004	0.008	0.002	0.004	0.007	0.002	0.005	0.002
Bushveld Complex	Impala mine	IM-1	0.267	0.014	0.147	0.137	43.211	0.123	0.13	0.09	0.00	0.007	5.079	15.759	2.758
			0.085	0.088	0.072	0.012	45.258	0.225	0.56	0.17	0.00	0.107	0.142	1.726	2.568
Median IM-1			**0.176**	**0.051**	**0.109**	**0.074**	**44.235**	**0.174**	**0.35**	**0.13**	**0.00**	**0.057**	**2.611**	**8.742**	**2.663**
Bushveld Complex	Impala mine	IM-3	0.025	0.014	0.018	0.012	33.214	0.339	0.24	0.04	0.01	0.009	1.071	5.530	1.577
			0.075	0.211	0.100	0.012	34.836	0.071	0.01	0.03	0.00	0.030	0.033	0.068	0.655
			0.252	0.566	0.084	0.012	50.453	0.395	0.11	0.05	0.03	0.007	0.019	2.925	2.011
			0.136	0.014	0.067	0.012	11.168	0.113	0.03	0.04	0.00	0.009	0.039	0.324	2.215
			0.140	0.014	0.018	0.117	24.094	0.236	0.11	0.03	0.00	0.037	0.189	1.074	1.187
			0.137	0.032	0.018	0.012	39.377	0.083	0.04	0.02	0.00	0.036	0.479	2.572	2.826
Median IM-3			**0.136**	**0.023**	**0.043**	**0.012**	**34.025**	**0.174**	**0.07**	**0.04**	**0.00**	**0.019**	**0.114**	**1.823**	**1.794**
Bushveld Complex	Impala mine	IM-5	0.117	0.014	0.018	0.012	8.005	0.189	0.08	0.04	0.00	0.007	0.114	0.365	0.122
			0.026	0.014	0.018	0.012	10.777	0.169	0.10	0.07	0.01	0.018	0.038	0.150	0.817
			0.025	0.014	0.018	0.012	6.940	0.004	0.02	0.29	0.02	0.016	2.572	4.396	1.335
			0.218	0.014	0.018	0.098	10.628	0.004	0.20	0.00	0.00	0.037	1.205	7.163	2.684
Median IM-5			**0.072**	**0.014**	**0.018**	**0.012**	**9.316**	**0.086**	**0.09**	**0.06**	**0.01**	**0.017**	**0.659**	**2.380**	**1.076**
Bushveld Complex	Impala mine	IM-7	0.130	0.014	0.018	0.161	0.241	0.153	4.30	2.55	2.67	0.007	3.321	7.814	0.018
			0.154	0.123	0.050	0.137	0.134	0.319	3.81	1.07	4.43	0.011	0.638	2.987	0.025
Median IM-7			**0.142**	**0.068**	**0.034**	**0.149**	**0.188**	**0.236**	**4.06**	**1.81**	**3.55**	**0.009**	**1.979**	**5.401**	**0.021**
Bushveld Complex	Impala mine	IM-9	0.114	0.014	0.124	0.068	28.107	0.149	0.58	0.39	0.00	0.007	0.117	0.957	4.661
			2.024	0.756	0.018	0.065	27.192	0.303	0.58	0.35	0.01	0.014	0.104	0.863	2.247
			1.022	0.014	0.146	0.110	19.182	0.505	0.11	0.26	0.00	0.007	11.070	35.490	1.791
			0.208	0.067	0.088	0.114	30.932	0.199	0.11	0.10	0.00	0.027	0.160	2.120	3.028
			0.025	0.014	0.018	0.091	19.862	0.081	0.09	0.12	0.00	0.012	2.019	11.950	5.275
Median IM-9			**0.208**	**0.014**	**0.088**	**0.091**	**27.192**	**0.199**	**0.11**	**0.26**	**0.00**	**0.012**	**0.160**	**2.120**	**3.028**

ANNEXE 19 – Cont.

Intrusion	Locality	Sample	Rock	Height (cm)	^{34}S	^{59}Co	^{61}Ni	^{65}Cu	^{66}Zn	^{75}As	^{82}Se	^{95}Mo	^{101}Ru	^{103}Rh	^{108}Pd	^{109}Ag
LOD					58	0.004	0.3	0.28	0.079	0.044	0.6	0.008	0.01	0.00	0.03	0.003
Bushveld Complex	Impala mine	IM-11	Melanorite	58	309320	9921	365144	52.10	2.051	4.233	154.9	0.069	5.55	0.18	2.11	1.628
					330621	8896	393962	1.24	0.079	1.502	158.8	0.008	0.28	0.57	2.89	0.228
					324432	10047	323504	4.92	0.079	3.614	151.0	0.008	2.36	0.14	2.14	0.879
					349784	10094	371203	2.83	1.097	8.400	168.6	0.097	0.77	0.28	2.05	1.220
					296296	9238	350263	6.25	0.079	3.321	133.5	0.008	0.46	0.18	1.57	0.280
					335368	10489	364685	19.54	0.789	4.624	147.8	0.008	0.58	0.68	2.28	2.179
Median IM-11					**327526**	**9984**	**364915**	**5.58**	**0.434**	**3.923**	**152.9**	**0.008**	**0.67**	**0.23**	**2.13**	**1.050**
Bushveld Complex	Impala mine	IM-13	Melanorite	48	306447	12472	371022	0.81	1.335	20.187	260.5	0.070	0.95	1.76	5.20	0.283
					367678	16606	363513	0.85	1.172	17.257	237.7	0.008	1.59	0.31	6.48	0.508
					328856	10363	358160	0.86	0.391	24.094	150.8	0.122	0.39	0.32	3.29	0.427
					302808	1366	387464	2.60	0.586	38.746	198.6	0.008	1.10	1.59	3.19	0.424
Median IM-13					**317652**	**11418**	**367268**	**0.85**	**0.879**	**22.141**	**218.2**	**0.039**	**1.03**	**0.95**	**4.24**	**0.426**
Bushveld Complex	Impala mine	IM-15	Melanorite	38	330248	12405	328856	15.30	3.972	30.932	152.7	0.008	3.18	5.77	1.81	12.698
Median IM-15					**330248**	**12405**	**328856**	**15.30**	**3.972**	**30.932**	**152.7**	**0.008**	**3.18**	**5.77**	**1.81**	**12.698**
Bushveld Complex	Impala mine	IM-17	Melanorite	28	326992	10387	328902	26.55	2.116	9.768	127.8	0.008	0.99	2.36	13.20	0.716
					296257	12275	346103	7.49	0.716	9.931	155.1	0.026	0.72	0.28	35.11	0.912
					309378	12177	361416	6.84	0.896	2.182	145.4	0.157	0.10	0.47	8.22	0.501
Median IM-17					**309378**	**12177**	**346103**	**7.49**	**0.896**	**9.768**	**145.4**	**0.026**	**0.72**	**0.47**	**13.20**	**0.716**
Bushveld Complex	Impala mine	IM-18	Melanorite	23	328758	9866	380261	387	6.186	5.958	151.9	0.008	0.14	18.62	49.48	1.081
					297598	18559	354904	866	0.079	9.866	137.4	0.021	1.21	8.23	14.34	0.803
Median IM-18					**313178**	**14212**	**367583**	**627**	**3.133**	**7.912**	**144.6**	**0.015**	**0.68**	**13.42**	**31.91**	**0.942**

ANNEXE 19 – Cont.

Intrusion	Locality	Sample	^{111}Cd	^{115}In	^{118}Sn	^{121}Sb	^{128}Te	^{185}Re	^{189}Os	^{193}Ir	^{195}Pt	^{197}Au	^{205}Tl	^{208}Pb	^{209}Bi
LOD			0.025	0.014	0.018	0.012	0.079	0.004	0.008	0.002	0.004	0.007	0.002	0.005	0.002
Bushveld Complex	Impala mine	IM-11	0.025	0.014	0.303	0.012	17.521	0.316	1.17	0.22	0.00	0.017	0.143	2.019	1.332
			0.179	0.014	0.018	0.012	12.465	0.174	0.02	0.00	0.00	0.007	0.021	0.215	0.163
			0.293	0.088	0.153	0.012	9.442	0.094	0.01	0.10	0.00	0.022	0.716	2.051	2.609
			0.173	1.002	0.052	0.101	14.001	0.137	0.19	0.16	0.00	0.007	0.407	5.893	0.879
			2.878	0.014	0.018	0.012	9.679	0.352	0.03	0.06	0.00	0.020	0.010	0.163	2.255
			0.025	0.645	0.211	0.012	21.164	0.095	0.16	0.11	0.00	0.023	0.293	1.302	1.531
Median IM-11			**0.176**	**0.051**	**0.103**	**0.012**	**13.233**	**0.155**	**0.10**	**0.10**	**0.00**	**0.018**	**0.218**	**1.661**	**1.431**
Bushveld Complex	Impala mine	IM-13	0.423	0.014	0.148	0.111	22.466	0.081	0.21	0.08	0.03	0.024	0.127	0.381	1.205
			0.878	0.014	0.119	0.012	14.558	0.228	0.22	0.01	0.00	0.007	0.137	0.912	1.742
			0.025	1.033	0.116	0.091	16.280	0.163	0.23	0.06	0.00	0.022	0.002	0.169	0.120
			0.025	0.014	0.358	0.012	23.350	0.004	0.01	0.12	0.00	0.007	0.089	0.757	1.407
Median IM-13			**0.224**	**0.014**	**0.133**	**0.051**	**19.373**	**0.122**	**0.22**	**0.07**	**0.00**	**0.014**	**0.108**	**0.569**	**1.306**
Bushveld Complex	Impala mine	IM-15	0.326	0.069	0.328	0.012	33.769	0.267	0.33	0.03	0.00	0.033	24.094	76.842	2.768
Median IM-15			**0.326**	**0.069**	**0.328**	**0.012**	**33.769**	**0.267**	**0.33**	**0.03**	**0.00**	**0.033**	**24.094**	**76.842**	**2.768**
Bushveld Complex	Impala mine	IM-17	0.391	0.014	0.124	0.012	21.815	0.065	0.60	0.01	0.00	0.007	0.456	38.095	0.891
			0.989	1.224	0.125	0.279	12.940	0.004	0.36	0.11	0.04	0.009	0.672	18.234	0.671
			0.025	0.014	0.166	0.012	18.466	0.133	0.21	0.02	0.00	0.007	0.254	3.191	2.391
Median IM-17			**0.391**	**0.014**	**0.125**	**0.012**	**18.466**	**0.065**	**0.36**	**0.02**	**0.00**	**0.007**	**0.456**	**18.234**	**0.891**
Bushveld Complex	Impala mine	IM-18	0.475	0.014	0.257	0.146	15.075	0.186	0.57	0.19	0.03	0.013	0.391	6.024	0.176
			2.554	0.088	0.018	0.012	5.112	0.004	0.01	0.10	0.00	0.007	4.233	13.024	0.353
Median IM-18			**1.515**	**0.051**	**0.138**	**0.079**	**10.094**	**0.095**	**0.29**	**0.14**	**0.02**	**0.010**	**2.312**	**9.524**	**0.265**

ANNEXE 19 – Cont.

Intrusion	Locality	Sample	Rock	Height (cm)	^{34}S	^{59}Co	^{61}Ni	^{65}Cu	^{66}Zn	^{75}As	^{82}Se	^{95}Mo	^{101}Ru	^{103}Rh	^{108}Pd	^{109}Ag
LOD					58	0.004	0.3	0.28	0.079	0.044	0.6	0.008	0.01	0.00	0.03	0.003
Bushveld Complex	Impala mine	IM-19	Melanorite	18	351648	9638	403753	0.63	2.963	2.930	169.3	0.008	1.02	5.26	133.20	0.840
					313553	7000	375023	765.20	2.475	1.465	72.9	0.008	0.37	15.99	216.85	0.648
					324298	9657	401203	1.50	0.079	1.302	215.9	0.008	9.47	21.07	242.57	0.658
					309247	7163	420154	1.36	0.079	0.716	185.6	0.094	15.11	15.03	230.20	0.479
					328714	6772	358176	87.91	0.079	1.140	201.9	0.008	5.53	22.00	302.21	0.332
					309281	8010	364096	2.34	0.521	2.051	273.5	0.110	3.15	16.15	247.34	0.274
					348134	11103	357183	4.25	0.079	1.009	129.9	0.026	17.23	39.02	135.78	0.570
					354873	6317	322344	129.44	0.079	1.100	195.4	0.008	4.03	16.97	201.34	0.628
Median IM-19					**326506**	**7586**	**369560**	**3.30**	**0.079**	**1.221**	**190.5**	**0.008**	**4.78**	**16.56**	**223.52**	**0.599**
Bushveld Complex	Impala mine	IM-20	Melanorite	13	319075	4200	364724	30.61	4.786	0.195	162.8	0.052	0.01	16.54	81.18	0.583
					337411	6838	338624	126.27	0.079	0.535	115.9	0.008	6.12	0.18	26.04	0.401
					320016	10233	315226	11.40	0.079	1.335	93.1	0.123	0.23	52.24	128.90	0.736
					351626	5177	423280	24.42	0.079	0.474	179.3	0.302	1.26	11.01	142.94	0.456
					348475	9754	335368	19.02	0.079	2.214	180.1	0.008	3.11	4.23	117.91	0.736
					319124	5698	324949	1.49	0.124	1.146	197.6	0.008	0.66	4.92	102.89	0.664
					315832	9654	345136	18.56	0.079	0.684	156.3	1.004	0.01	8.22	102.66	0.563
					312685	6479	377696	17.58	0.079	1.530	117.9	0.008	0.88	21.98	144.25	1.335
					283314	7033	328902	5.08	0.079	0.357	218.2	0.008	0.79	15.60	51.12	0.459
					319127	7684	328844	13.35	0.079	0.548	203.6	0.078	0.01	4.59	56.32	1.400
Median IM-20					**319126**	**6935**	**336996**	**18.07**	**0.079**	**0.616**	**171.0**	**0.030**	**0.72**	**9.61**	**102.78**	**0.624**

ANNEXE 19 – Cont.

Intrusion	Locality	Sample	^{111}Cd	^{115}In	^{118}Sn	^{121}Sb	^{128}Te	^{185}Re	^{189}Os	^{193}Ir	^{195}Pt	^{197}Au	^{205}Tl	^{208}Pb	^{209}Bi
LOD			0.025	0.014	0.018	0.012	0.079	0.004	0.008	0.002	0.004	0.007	0.002	0.005	0.002
Bushveld Complex	Impala mine	IM-19	0.260	0.014	0.018	0.012	3.502	0.114	0.05	0.21	0.00	0.007	1.856	5.861	0.703
			0.025	0.014	0.131	0.012	0.625	0.251	1.05	2.47	0.00	0.011	5.210	28.653	0.177
			0.182	0.027	0.018	0.012	1.823	0.166	2.64	3.45	0.00	0.010	1.888	3.614	0.040
			0.025	0.014	0.098	0.012	0.781	0.599	5.80	2.07	0.04	0.007	0.021	0.651	0.072
			2.013	0.022	0.102	0.042	0.790	0.293	2.21	1.57	0.00	0.007	0.348	1.042	0.121
			0.039	0.069	0.060	0.012	2.833	0.144	0.72	0.80	0.00	0.007	2.149	4.982	0.234
			0.025	0.014	0.018	0.012	0.699	0.004	0.04	3.23	0.00	0.007	2.312	9.768	0.789
			2.441	0.014	0.091	0.012	0.753	0.257	2.02	0.82	0.00	0.007	0.444	7.825	0.055
Median IM-19			**0.111**	**0.014**	**0.076**	**0.012**	**0.786**	**0.208**	**1.54**	**1.82**	**0.00**	**0.007**	**1.872**	**5.421**	**0.149**
Bushveld Complex	Impala mine	IM-20	0.025	0.122	0.086	0.012	0.237	0.254	1.47	1.36	0.00	0.007	0.041	2.344	0.117
			0.091	0.056	0.018	0.012	0.757	0.004	0.01	2.02	0.00	0.024	0.046	1.433	0.352
			0.025	0.014	0.057	0.012	3.647	1.006	1.12	0.04	0.00	0.007	0.127	3.223	0.124
			1.079	0.014	0.018	0.012	0.315	0.720	1.27	1.27	0.01	0.007	0.002	0.565	0.045
			0.231	2.001	0.127	0.012	1.140	0.287	0.76	0.41	0.00	0.007	2.150	6.512	0.202
			0.025	0.014	0.062	0.012	0.959	0.475	0.49	0.05	0.00	0.026	1.477	2.590	0.358
			0.989	0.062	0.208	0.081	0.079	0.238	0.42	4.66	0.00	0.007	0.059	1.368	1.848
			0.878	0.014	0.018	0.012	0.098	0.004	1.24	0.02	0.00	0.007	0.062	0.394	0.878
			0.025	0.014	0.099	0.069	0.079	0.326	1.37	1.58	0.02	0.007	0.107	0.804	0.757
			0.184	0.014	0.097	0.012	0.228	0.110	0.31	0.39	0.02	0.007	8.791	21.815	0.869
Median IM-20			**0.138**	**0.014**	**0.074**	**0.012**	**0.276**	**0.270**	**0.94**	**0.84**	**0.00**	**0.007**	**0.085**	**1.888**	**0.355**

ANNEXE 19 – Cont.

Intrusion	Locality	Sample	Rock	Height (cm)	^{34}S	^{59}Co	^{61}Ni	^{65}Cu	^{66}Zn	^{75}As	^{82}Se	^{95}Mo	^{101}Ru	^{103}Rh	^{108}Pd	^{109}Ag
LOD					58	0.004	0.3	0.28	0.079	0.044	0.6	0.008	0.01	0.00	0.03	0.003
Bushveld Complex	Impala mine	IM-21	Melanorite	8	338624	4396	328953	5.14	0.362	0.637	120.3	0.008	2.99	14.65	160.85	0.723
					338577	4527	340578	72.15	0.079	0.393	144.2	0.075	5.00	1.54	162.80	1.090
					343301	8956	361566	541.20	1.921	0.781	123.3	0.008	0.01	6.26	301.21	1.397
					338601	5340	384208	20.51	0.079	1.089	166.1	0.510	6.70	3.55	256.48	1.357
					328768	4949	257224	15.63	0.079	0.205	159.9	0.098	22.54	20.19	72.61	1.029
					315468	6284	338656	3.45	0.079	0.488	160.9	0.045	20.26	15.24	36.15	0.892
					351702	6349	371254	4.69	2.898	0.456	154.0	0.065	14.62	35.88	56.97	0.700
Median IM-21					**338601**	**5340**	**340578**	**15.63**	**0.079**	**0.488**	**154.0**	**0.065**	**6.70**	**14.65**	**160.85**	**1.029**
Bushveld Complex	Impala mine	IM-22	Upper Chromitite	6	317786	4754	372698	14.65	0.079	1.823	132.8	0.008	2.17	47.54	143.58	1.563
					270135	2368	361423	8.14	0.985	2.442	109.7	0.310	0.20	58.23	89.22	4.558
					393976	5503	348392	2.41	2.423	0.297	136.5	0.008	1.21	3.55	149.77	4.884
					325600	2670	398616	16.28	4.884	0.670	143.3	0.159	0.01	9.22	105.50	32.560
					323972	4591	366987	4.56	2.344	0.391	124.8	0.008	4.36	11.85	284.26	3.907
Median IM-22					**323972**	**4591**	**366987**	**8.14**	**2.344**	**0.670**	**132.8**	**0.008**	**1.21**	**11.85**	**143.58**	**4.558**
Bushveld Complex	Impala mine	IM-24	Lower Chromitite	0	335368	4689	375236	1.02	0.079	0.044	188.8	0.357	9.70	244.20	285.22	1.368
					312576	4624	337955	140.82	0.658	0.725	170.6	0.008	7.00	137.08	325.20	4.742
					302808	5000	339243	87.31	0.387	1.661	186.9	0.008	5.27	94.42	175.18	1.357
					397232	4917	385398	1.89	0.079	2.670	274.3	0.008	16.23	62.52	199.59	0.612
					374440	5861	428973	1.94	0.127	1.563	262.6	0.872	28.02	615.38	92.15	1.370
					354785	5144	376755	1.73	1.254	0.700	164.9	0.008	2.86	729.34	387.23	7.814
					329711	5613	336132	8.47	0.079	0.044	224.7	1.023	31.96	413.51	172.57	1.237
					312523	4587	374658	0.43	1.875	1.628	151.7	0.008	14.38	145.22	200.25	1.446
Median IM-24					**332540**	**4958**	**374947**	**1.91**	**0.257**	**1.144**	**187.9**	**0.008**	**12.04**	**194.71**	**199.92**	**1.369**

ANNEXE 19 – Cont.

Intrusion	Locality	Sample	^{111}Cd	^{115}In	^{118}Sn	^{121}Sb	^{128}Te	^{185}Re	^{189}Os	^{193}Ir	^{195}Pt	^{197}Au	^{205}Tl	^{208}Pb	^{209}Bi
LOD			0.025	0.014	0.018	0.012	0.079	0.004	0.008	0.002	0.004	0.007	0.002	0.005	0.002
Bushveld Complex	Impala mine	IM-21	0.025	0.014	0.020	0.012	0.300	0.221	0.81	2.79	0.85	0.007	0.002	100.936	1.023
			1.033	2.666	0.075	0.046	0.326	0.068	0.25	3.23	0.60	0.007	1.758	9.776	0.062
			0.112	0.014	0.076	0.078	0.079	0.056	0.01	0.86	1.17	0.015	1.498	13.147	1.552
			0.412	3.001	0.104	0.012	0.358	0.274	2.57	1.01	0.92	0.007	2.279	9.123	0.068
			0.025	0.989	0.018	0.012	0.130	0.273	5.89	12.37	8.56	0.021	10.680	53.073	6.089
			0.025	0.014	0.122	0.012	0.197	0.241	5.57	4.36	0.13	0.015	2.051	21.164	0.107
			0.228	0.014	0.879	0.086	0.652	0.116	5.24	3.32	0.16	0.007	1.890	39.144	0.030
Median IM-21			**0.112**	**0.014**	**0.076**	**0.012**	**0.300**	**0.221**	**2.57**	**3.23**	**0.85**	**0.007**	**1.890**	**21.164**	**0.107**
Bushveld Complex	Impala mine	IM-22	0.143	0.014	0.037	0.012	0.723	0.345	7.00	4.66	5.70	0.007	0.879	9.125	0.039
			2.112	0.689	0.076	0.012	0.783	0.004	1.04	11.23	0.85	0.007	0.958	24.746	0.381
			0.877	0.014	0.018	0.012	0.230	0.245	0.11	0.22	1.82	0.007	0.697	7.897	0.422
			0.025	0.723	2.605	0.123	0.079	0.004	2.03	0.98	0.94	0.007	4.558	59.585	0.125
			0.202	0.014	0.124	0.079	0.356	0.300	5.08	3.19	2.34	0.007	2.702	19.862	0.101
Median IM-22			**0.202**	**0.014**	**0.076**	**0.012**	**0.356**	**0.245**	**2.03**	**3.19**	**1.82**	**0.007**	**0.958**	**19.862**	**0.125**
Bushveld Complex	Impala mine	IM-24	0.025	0.015	0.070	0.012	0.130	0.088	3.97	22.23	3.65	0.007	1.009	3.940	0.021
			0.025	0.088	0.018	0.012	0.488	0.240	2.18	7.10	3.26	0.007	0.065	2.182	0.026
			0.756	0.014	0.018	0.012	1.042	0.189	2.18	4.72	4.07	0.007	0.890	4.367	0.046
			0.088	0.122	0.211	0.040	0.210	0.092	1.40	11.75	4.40	0.007	0.042	0.628	0.002
			0.211	0.014	0.098	0.012	0.240	0.057	1.09	26.05	5.54	0.007	0.018	1.563	1.689
			0.025	0.233	0.018	0.012	0.244	0.004	4.03	23.12	4.20	0.007	0.221	1.878	0.002
			0.025	0.033	0.018	0.099	1.237	0.319	18.88	10.09	2.18	0.007	0.002	0.540	0.002
			0.025	0.014	0.087	0.012	0.386	0.423	15.01	7.20	4.04	0.021	0.052	2.214	2.211
Median IM-24			**0.025**	**0.024**	**0.044**	**0.012**	**0.315**	**0.141**	**3.08**	**10.92**	**4.05**	**0.007**	**0.059**	**2.030**	**0.024**

ANNEXE 19 – Cont.

Intrusion	Locality	Sample	Rock	Height (cm)	^{34}S	^{59}Co	^{61}Ni	^{65}Cu	^{66}Zn	^{75}As	^{82}Se	^{95}Mo	^{101}Ru	^{103}Rh	^{108}Pd	^{109}Ag
LOD					58	0.004	0.3	0.28	0.079	0.044	0.6	0.008	0.01	0.00	0.03	0.003
Bushveld Complex	Impala mine	IM-26	Leuconorite	-8	329102	4103	315923	192.74	25.071	1.237	170.0	0.033	0.10	5.26	208.38	3.821
					309411	4037	387542	6.02	2.996	1.777	185.4	0.008	0.54	2.22	354.91	2.817
					351724	3223	325600	8.47	8.767	1.831	175.4	2.605	0.01	8.92	236.38	0.635
					304110	4435	347456	5.44	11.233	1.368	155.6	0.008	0.72	43.63	175.82	0.899
					319073	3028	399792	29.96	10.419	0.707	169.6	0.008	0.01	52.10	257.23	0.433
Median IM-26					**319073**	**4037**	**347456**	**8.47**	**10.419**	**1.368**	**170.0**	**0.008**	**0.10**	**8.92**	**236.38**	**0.899**
Bushveld Complex	Impala mine	IM-28	Leuconorite	-23	302825	6642	351648	4.04	6.838	0.433	142.9	0.038	1.50	25.07	402.82	1.270
					319133	3972	383498	13.97	0.079	0.301	137.5	0.008	0.01	16.25	319.09	3.557
Median IM-28					**310979**	**5307**	**367573**	**9.00**	**3.458**	**0.367**	**140.2**	**0.023**	**0.75**	**20.66**	**360.95**	**2.413**

ANNEXE 19 – Cont.

Intrusion	Locality	Sample	^{111}Cd	^{115}In	^{118}Sn	^{121}Sb	^{128}Te	^{185}Re	^{189}Os	^{193}Ir	^{195}Pt	^{197}Au	^{205}Tl	^{208}Pb	^{209}Bi
LOD			0.025	0.014	0.018	0.012	0.079	0.004	0.008	0.002	0.004	0.007	0.002	0.005	0.002
Bushveld Complex	Impala mine	IM-26	0.237	0.039	0.511	0.078	0.456	0.086	2.42	1.80	1.11	0.016	17.582	34.839	3.061
			0.025	0.023	0.179	0.012	1.864	0.010	1.18	8.99	0.06	0.007	3.451	12.698	0.781
			0.088	0.014	0.109	0.036	0.410	0.035	1.75	0.42	1.40	0.007	1.865	9.125	1.107
			0.634	0.054	0.173	0.012	0.267	0.028	2.77	18.88	4.64	0.023	4.265	33.537	6.121
			0.025	0.014	0.231	0.012	0.491	0.195	4.33	0.72	0.92	0.062	1.954	10.094	0.199
Median IM-26			**0.088**	**0.023**	**0.179**	**0.012**	**0.456**	**0.035**	**2.42**	**1.80**	**1.11**	**0.016**	**3.451**	**12.698**	**1.107**
Bushveld Complex	Impala mine	IM-28	0.025	0.014	0.195	0.036	0.164	0.280	3.19	1.53	3.39	0.012	0.218	7.684	0.205
			0.566	0.014	0.070	0.012	0.489	0.004	1.28	1.97	3.35	0.007	4.037	13.675	0.515
Median IM-28			**0.296**	**0.014**	**0.133**	**0.024**	**0.327**	**0.142**	**2.24**	**1.75**	**3.37**	**0.009**	**2.128**	**10.680**	**0.360**

ANNEXE 19 – Cont.

Intrusion	Locality	Sample	Rock	Height (cm)	^{34}S	^{59}Co	^{61}Ni	^{65}Cu	^{66}Zn	^{75}As	^{82}Se	^{95}Mo	^{101}Ru	^{103}Rh
LOD					58	0.004	0.3	0.28	0.079	0.044	0.6	0.008	0.01	0.00
Bushveld Complex	Rustenburg mine	AN	Anorthosite	-2	360439	4461	328205	0.91	0.079	0.044	198.0	0.037	8.42	321.02
					357464	8965	356858	58.61	0.079	1.069	260.3	0.008	4.16	53.56
Median AN					**358952**	**6713**	**342531**	**29.76**	**0.079**	**0.557**	**229.1**	**0.022**	**6.29**	**187.29**
Bushveld Complex	Rustenburg mine	LC	Lower chromitite	0	359462	5503	339926	2.08	2.605	0.044	183.5	0.008	7.20	5.76
					344402	4819	319088	12.05	1.693	0.698	240.0	0.058	4.68	31.58
					354733	5756	358224	2.67	0.539	1.270	231.4	0.368	1.59	44.84
Median LC					**354733**	**5503**	**339926**	**2.67**	**1.693**	**0.698**	**231.4**	**0.058**	**4.68**	**31.58**
Bushveld Complex	Rustenburg mine	CGM-1	Coarse-grained melanorite	2	347223	4734	336019	7.78	0.684	0.079	258.5	0.062	18.16	51.84
					365974	4702	332324	14.00	0.912	0.720	262.1	0.091	4.09	29.34
					330158	6414	291738	10.81	0.300	0.749	259.2	0.008	12.01	19.01
					354742	4298	324298	1.15	0.402	0.586	117.2	0.042	5.72	62.74
					331135	4302	308994	1.37	0.303	0.514	169.3	0.012	17.83	15.21
Median CGM-1					**347223**	**4702**	**324298**	**7.78**	**0.402**	**0.586**	**258.5**	**0.042**	**12.01**	**29.34**
Bushveld Complex	Rustenburg mine	CGM-2	Coarse-grained melanorite	6	335374	5379	302808	5.40	0.139	0.044	156.9	0.218	19.79	7.81
					301506	5275	269271	6.81	0.079	0.044	184.6	0.814	9.53	14.72
					322995	4838	285265	6.56	0.402	0.044	111.4	0.124	3.77	29.63
					332438	5405	319739	4.75	0.156	0.046	128.9	0.008	6.44	8.79
					334066	5210	309320	9.44	0.199	0.078	121.4	0.008	2.26	23.08
					328766	4689	283272	7.72	0.358	0.091	161.8	0.293	18.94	17.68
					322670	5665	287830	3.65	0.079	0.044	250.7	0.008	25.06	54.38
Median CGM-2					**328766**	**5275**	**287830**	**6.56**	**0.156**	**0.044**	**156.9**	**0.124**	**9.53**	**17.68**

ANNEXE 19 – Cont.

Locality	Sample	^{108}Pd	^{109}Ag	^{111}Cd	^{115}In	^{118}Sn	^{121}Sb	^{128}Te	^{185}Re	^{189}Os	^{193}Ir	^{195}Pt	^{197}Au	^{205}Tl	^{208}Pb	^{209}Bi
LOD		0.03	0.003	0.025	0.014	0.018	0.012	0.079	0.004	0.008	0.002	0.004	0.007	0.002	0.005	0.002
Rustemburg mine	AN	114.61	0.762	1.022	0.014	0.142	0.012	0.122	0.201	0.90	13.00	3.81	0.020	0.028	2.377	0.002
		369.23	0.446	0.877	0.014	0.088	0.012	0.211	0.029	1.02	17.39	8.56	0.007	0.781	3.878	0.009
Median AN		**241.92**	**0.604**	**0.950**	**0.014**	**0.115**	**0.012**	**0.167**	**0.115**	**0.96**	**15.19**	**6.18**	**0.013**	**0.405**	**3.127**	**0.005**
Rustemburg mine	LC	133.17	6.488	0.072	0.014	0.135	0.069	0.211	0.004	0.13	1.66	9.86	0.007	0.033	0.847	0.090
		309.08	0.651	0.025	0.014	0.023	0.199	0.586	0.136	4.20	5.54	7.20	0.007	1.302	10.014	0.020
		199.27	1.595	0.025	0.014	0.018	0.012	0.147	0.667	5.73	4.40	6.84	0.007	0.163	6.610	0.056
Median LC		**199.27**	**1.595**	**0.025**	**0.014**	**0.023**	**0.069**	**0.211**	**0.136**	**4.20**	**4.40**	**7.20**	**0.007**	**0.163**	**6.610**	**0.056**
Rustemburg mine	CGM-1	162.80	1.648	0.140	0.014	0.018	0.080	0.274	0.179	7.20	8.89	0.73	0.019	2.312	15.954	0.038
		169.31	5.112	0.025	0.014	0.057	0.102	0.879	0.293	4.92	4.49	0.86	0.007	2.158	19.536	0.117
		228.25	5.689	2.004	0.014	0.018	0.068	0.079	1.032	6.71	3.97	3.00	0.007	1.172	19.679	0.075
		137.07	2.409	0.078	0.014	0.018	0.012	0.079	0.381	3.39	10.32	1.17	0.008	0.231	42.328	0.005
		170.61	2.699	0.025	0.014	0.018	0.012	0.111	0.127	4.56	5.19	2.80	0.007	0.306	0.374	0.143
Median CGM-1		**169.31**	**2.699**	**0.078**	**0.014**	**0.018**	**0.068**	**0.111**	**0.293**	**4.92**	**5.19**	**1.17**	**0.007**	**1.172**	**19.536**	**0.075**
Rustemburg mine	CGM-2	186.24	1.511	0.025	0.014	0.018	0.012	2.051	0.374	3.84	4.98	0.44	0.007	0.002	0.302	0.038
		177.45	2.507	0.025	0.014	0.047	0.012	1.628	0.580	2.64	5.89	0.54	0.012	0.723	9.801	0.042
		132.19	5.210	1.333	0.014	0.091	0.012	0.251	0.099	3.88	5.44	0.88	0.007	0.050	2.605	0.326
		283.27	3.354	0.025	0.014	0.077	0.030	0.697	0.140	7.42	6.28	0.36	0.007	0.008	0.124	0.002
		297.60	3.126	0.025	0.014	0.039	0.012	0.274	0.195	2.30	6.12	0.48	0.007	0.035	0.951	0.002
		257.22	2.865	0.900	0.014	0.018	0.071	0.212	0.111	5.94	6.84	0.40	0.007	0.417	5.698	0.013
		311.27	2.963	0.025	0.014	0.018	0.012	0.457	0.091	12.89	9.74	0.24	0.007	0.033	1.613	0.011
Median CGM-2		**257.22**	**2.963**	**0.025**	**0.014**	**0.039**	**0.012**	**0.457**	**0.140**	**3.88**	**6.12**	**0.44**	**0.007**	**0.035**	**1.613**	**0.013**

ANNEXE 19 – Cont.

Intrusion	Locality	Sample	Rock	Height (cm)	^{34}S	^{59}Co	^{61}Ni	^{65}Cu	^{66}Zn	^{75}As	^{82}Se	^{95}Mo	^{101}Ru	^{103}Rh
LOD					58	0.004	0.3	0.28	0.079	0.044	0.6	0.008	0.01	0.00
Bushveld Complex	Rustemburg mine	UC	Upper chromitite	10	343198	5789	328530	0.42	0.197	0.847	94.4	0.008	0.32	25.66
					343212	6377	320521	1.79	0.079	0.044	186.2	0.008	7.51	41.03
					359882	5763	356844	3.00	1.042	0.044	184.3	0.211	1.55	135.33
					356206	5747	352625	3.26	0.726	0.814	226.9	0.087	1.88	13.74
Median UC					**349709**	**5776**	**340578**	**2.39**	**0.462**	**0.429**	**185.3**	**0.047**	**1.72**	**33.34**
Bushveld Complex	Rustemburg mine	M-1	Melanorite	13.5	334256	5011	310297	3.81	0.555	0.267	147.2	0.008	7.19	22.34
					387474	4959	293691	7.59	1.056	0.466	233.5	0.076	19.53	57.11
					328836	5646	301506	8.27	0.587	0.238	206.1	0.008	6.21	23.93
					334717	4793	280342	2.38	0.079	0.569	241.6	0.574	5.14	30.83
					310297	4896	276760	3.35	2.986	1.205	106.8	0.078	23.11	119.82
					331461	6412	299878	3.29	0.781	0.163	82.4	0.069	0.10	13.02
					313623	6219	276434	2.68	0.079	0.088	118.8	0.008	2.34	12.70
					332125	13350	315931	4.37	0.079	0.044	138.7	0.008	7.28	13.02
					330484	5697	283598	7.20	5.303	1.107	173.5	0.027	7.29	16.64
					310948	5893	253317	8.82	0.079	0.346	184.0	0.064	4.00	0.54
					312585	6675	322561	2.57	0.079	0.098	175.8	0.036	24.02	23.22
Median M-1					**330484**	**5697**	**293691**	**3.81**	**0.555**	**0.267**	**173.5**	**0.036**	**7.19**	**22.34**
Bushveld Complex	Rustemburg mine	M-2	Melanorite	18	333089	5734	344810	2.80	0.977	0.247	177.5	1.302	24.08	25.92
					333740	6286	366626	10.74	0.752	0.169	186.5	0.072	0.68	4.59
					329507	7066	338950	1.43	0.260	0.044	199.9	0.030	2.37	2.49
					319077	4363	310622	172.57	1.184	0.075	155.3	0.038	24.22	21.98
					323321	5207	338146	0.41	0.079	0.044	145.5	0.008	36.13	44.28
Median M-2					**329507**	**5734**	**338950**	**2.80**	**0.752**	**0.075**	**177.5**	**0.038**	**24.08**	**21.98**

ANNEXE 19 – Cont.

Locality	Sample	^{108}Pd	^{109}Ag	^{111}Cd	^{115}In	^{118}Sn	^{121}Sb	^{128}Te	^{185}Re	^{189}Os	^{193}Ir	^{195}Pt	^{197}Au	^{205}Tl	^{208}Pb	^{209}Bi
LOD		0.03	0.003	0.025	0.014	0.018	0.012	0.079	0.004	0.008	0.002	0.004	0.007	0.002	0.005	0.002
Rustemburg mine	UC	472.12	0.878	0.069	0.014	0.156	0.020	0.236	0.137	0.49	1.31	7.39	0.007	0.005	2.507	0.003
		446.07	1.354	0.025	0.014	0.171	0.012	0.246	0.554	7.16	6.97	8.69	0.007	0.145	4.037	0.019
		90.52	0.469	1.355	0.014	0.300	0.061	0.436	0.143	3.45	1.86	9.08	0.007	0.010	0.720	0.123
		91.16	1.097	0.288	0.014	0.018	0.012	0.079	0.259	3.52	3.56	9.02	0.007	1.693	11.476	0.038
Median UC		**268.62**	**0.987**	**0.178**	**0.014**	**0.164**	**0.016**	**0.241**	**0.201**	**3.48**	**2.71**	**8.86**	**0.007**	**0.077**	**3.272**	**0.028**
Rustemburg mine	M-1	180.06	3.484	0.025	0.014	0.052	0.012	0.609	0.449	3.87	3.29	1.27	0.007	0.094	2.833	0.002
		163.45	3.601	0.060	0.014	0.018	0.012	1.270	0.430	9.57	13.76	0.59	0.007	0.319	8.075	0.002
		169.31	2.618	0.025	0.014	0.018	0.049	2.019	0.400	6.28	10.39	1.71	0.007	1.114	8.270	0.051
		155.96	5.633	0.025	0.356	0.077	0.012	0.287	0.479	2.77	4.00	1.65	0.007	0.025	1.237	0.088
		161.82	3.940	0.145	0.014	0.090	0.012	0.176	0.716	5.50	8.60	2.98	0.007	0.169	5.177	0.348
		174.20	1.693	0.025	0.014	0.018	0.012	0.599	0.105	0.01	1.38	4.00	0.007	0.013	1.335	0.002
		184.29	2.051	0.025	0.021	0.018	0.012	0.468	0.215	1.89	1.77	2.70	0.007	0.002	0.436	0.002
		153.35	2.247	0.189	0.014	0.018	0.012	0.869	0.348	5.05	2.47	3.03	0.018	0.002	3.302	0.002
		130.57	2.605	0.025	0.822	0.179	0.012	0.521	0.212	5.34	3.54	1.70	0.007	0.055	2.125	0.016
		89.22	2.214	0.025	0.014	0.069	0.012	0.079	0.089	1.17	0.26	1.28	0.007	0.277	13.102	0.065
		234.43	1.804	0.025	0.222	0.018	0.012	0.079	0.313	4.95	4.23	3.87	0.007	0.009	1.954	0.002
Median M-1		**163.45**	**2.605**	**0.025**	**0.014**	**0.018**	**0.012**	**0.521**	**0.348**	**4.95**	**3.54**	**1.71**	**0.007**	**0.055**	**2.833**	**0.002**
Rustemburg mine	M-2	156.94	1.456	0.025	0.014	0.018	0.182	0.322	14.978	5.70	5.25	6.67	0.007	1.188	11.298	0.488
		905.17	1.032	0.742	0.588	0.111	0.018	0.169	0.335	0.97	0.91	11.14	0.007	0.267	10.322	0.014
		167.68	0.749	1.022	0.014	0.018	0.012	0.079	0.410	5.76	3.71	4.17	0.007	1.595	5.275	0.002
		94.74	1.211	0.176	0.122	0.018	0.024	0.313	0.332	4.66	4.06	0.01	0.007	0.088	2.784	0.103
		179.73	0.208	0.025	0.014	0.066	0.012	0.079	0.017	7.23	7.49	6.90	0.007	0.023	0.724	0.137
Median M-2		**167.68**	**1.032**	**0.176**	**0.014**	**0.018**	**0.018**	**0.169**	**0.335**	**5.70**	**4.06**	**6.67**	**0.007**	**0.267**	**5.275**	**0.103**

ANNEXE 19 – Cont.

Intrusion	Locality	Sample	Rock	Height (cm)	^{34}S	^{59}Co	^{61}Ni	^{65}Cu	^{66}Zn	^{75}As	^{82}Se	^{95}Mo	^{101}Ru	^{103}Rh
LOD					58	0.004	0.3	0.28	0.079	0.044	0.6	0.008	0.01	0.00
Bushveld Complex	Rustemburg mine	M-3	Melanorite	23	329182	5057	353927	0.99	0.218	0.469	181.7	0.034	4.52	4.59
					335368	6154	368234	0.47	0.079	0.717	189.8	0.578	6.73	4.66
					331786	5307	371066	2.18	0.079	0.333	133.8	0.133	4.61	4.86
					322344	11201	352315	1.76	0.079	0.374	195.0	0.008	5.82	4.10
					348392	5372	375623	0.95	0.340	0.287	172.2	0.026	4.52	35.12
					333803	8544	349369	1.68	0.270	0.371	178.8	0.008	6.80	4.53
Median M-3					**332795**	**5763**	**361081**	**1.33**	**0.149**	**0.373**	**180.2**	**0.030**	**5.21**	**4.62**
Bushveld Complex	Rustemburg mine	M-4	Melanorite	27	323726	5330	366348	59.21	1.241	0.216	167.6	0.008	28.51	7.62
					357834	5988	325417	5.96	293.040	0.466	191.5	0.316	17.18	8.76
					348383	7522	354551	8.57	2.121	0.264	170.9	0.008	10.08	38.02
					319414	6512	333414	0.79	0.079	0.044	148.2	0.008	5.85	26.21
					308018	8974	319266	814.26	0.259	0.159	85.3	0.008	0.13	0.00
Median M-4					**323726**	**6512**	**333414**	**8.57**	**1.241**	**0.216**	**167.6**	**0.008**	**10.08**	**8.76**

ANNEXE 19 – Cont.

Locality	Sample	^{108}Pd	^{109}Ag	^{111}Cd	^{115}In	^{118}Sn	^{121}Sb	^{128}Te	^{185}Re	^{189}Os	^{193}Ir	^{195}Pt	^{197}Au	^{205}Tl	^{208}Pb	^{209}Bi
LOD		0.03	0.003	0.025	0.014	0.018	0.012	0.079	0.004	0.008	0.002	0.004	0.007	0.002	0.005	0.002
Rustemburg mine	M-3	41.61	1.074	0.878	0.123	0.018	0.012	2.475	0.041	0.31	1.03	0.00	0.007	0.182	3.061	0.125
		39.39	0.846	0.080	0.014	0.098	0.012	6.512	1.595	1.34	1.58	0.04	0.027	0.081	1.465	0.065
		40.05	0.768	0.656	0.700	0.018	0.012	2.865	0.092	0.78	9.67	0.00	0.007	0.124	2.786	0.098
		128.21	0.473	0.025	1.556	0.093	0.012	4.558	0.321	1.38	1.29	0.00	0.007	0.074	2.247	0.094
		39.27	0.876	0.050	0.014	0.018	0.127	1.473	0.391	0.74	0.84	0.01	0.007	0.384	1.959	0.046
		75.22	8.791	0.097	0.014	0.067	0.012	2.898	0.135	1.13	0.82	0.00	0.007	1.610	9.302	0.135
Median M-3		**40.83**	**0.861**	**0.088**	**0.068**	**0.043**	**0.012**	**2.882**	**0.228**	**0.95**	**1.16**	**0.00**	**0.007**	**0.153**	**2.516**	**0.096**
Rustemburg mine	M-4	67.40	1.426	0.025	0.014	0.068	0.052	0.079	0.093	3.55	2.45	3.19	0.007	0.147	3.647	0.014
		39.66	6.512	0.966	0.120	0.070	0.296	2.930	1.726	2.25	2.15	2.74	7.814	0.977	29.304	0.195
		49.32	1.003	0.147	0.212	0.029	0.100	2.990	0.141	1.95	1.75	0.02	0.007	0.661	8.694	0.189
		179.41	1.553	0.145	0.014	0.067	0.026	0.079	0.384	3.35	3.19	5.18	0.007	0.011	2.339	0.002
		148.15	2.352	0.025	0.014	0.094	0.012	0.079	0.004	0.01	0.00	3.74	0.007	0.016	0.462	0.011
Median M-4		**67.40**	**1.553**	**0.145**	**0.014**	**0.068**	**0.052**	**0.079**	**0.141**	**2.25**	**2.15**	**3.19**	**0.007**	**0.147**	**3.647**	**0.014**

ANNEXE 19 – Cont.

Intrusion	Locality	Sample	Rock	^{34}S	^{59}Co	^{61}Ni	^{65}Cu	^{66}Zn	^{75}As	^{82}Se	^{95}Mo	^{101}Ru	^{103}Rh	^{108}Pd
LOD				58	0.004	0.3	0.28	0.079	0.044	0.6	0.008	0.01	0.00	0.03
Stillwater Complex	East Boulder mine	ST-12	Mela troctolite	283272	10908	251038	7945	7.489	0.065	240.9	0.008	122.30	273.04	19847.36
				324949	11526	265690	83	0.228	0.254	527.5	0.008	147.16	287.18	20521.76
				308994	10647	280016	6838	2.442	0.423	511.2	0.008	179.72	239.93	19894.14
				299552	11917	270248	218	0.749	0.521	547.0	0.008	218.47	288.15	14945.03
				303785	10354	250061	1698	8.791	0.044	320.4	0.008	107.86	258.83	18982.48
				303785	10191	280993	90	0.256	0.249	505.7	0.010	90.03	239.64	15270.63
				294994	9052	262759	3024	6.219	0.121	472.1	0.008	88.67	314.18	16214.87
				315506	12308	259503	9214	1.433	0.044	386.9	0.012	70.49	312.28	18819.68
				306064	9768	243549	4759	3.907	0.044	221.4	0.008	81.81	197.91	17094.00
Median ST-12				**303785**	**10647**	**262759**	**3024**	**2.442**	**0.121**	**472.1**	**0.008**	**107.86**	**273.04**	**18819.68**
Stillwater Complex	East Boulder mine	ST-14	Anorthosite	379324	7521	374440	2.96	2.548	0.044	436.3	0.008	2.17	61.84	2428.98
				377696	6694	351184	7.16	0.488	1.074	423.3	0.008	5.00	43.54	11363.44
				356858	6707	347415	1.04	0.623	1.172	410.3	0.008	3.63	53.75	5158.72
				373789	7424	373463	15.95	0.458	0.228	407.0	0.008	4.24	41.92	4544.15
				330256	6382	315832	0.46	0.326	0.260	351.6	0.008	3.53	31.91	3256.00
Median ST-14				**373789**	**6707**	**351184**	**2.96**	**0.488**	**0.260**	**410.3**	**0.008**	**3.63**	**43.54**	**4544.15**
Stillwater Complex	East Boulder mine	ST-16	Leuconorite	382580	5600	393976	1.47	1.442	0.651	239.6	0.323	1.08	17.49	3187.22
				349369	4689	344680	1.14	3.254	0.044	267.0	0.488	3.54	9.51	4460.72
				364672	4982	361416	0.72	4.255	0.044	309.3	0.008	1.91	16.51	3913.71
				343182	4786	363370	1.69	5.670	0.054	286.9	0.332	4.68	16.67	3943.01
				384208	4884	394912	17.91	8.113	0.341	293.0	0.042	0.87	12.28	3428.16
				330720	3810	462352	1.66	3.332	0.554	384.2	0.107	7.02	14.71	2428.98
Median ST-16				**357020**	**4835**	**378673**	**1.56**	**3.794**	**0.198**	**289.9**	**0.215**	**2.72**	**15.61**	**3670.93**

ANNEXE 19 – Cont.

Locality	Sample	^{109}Ag	^{111}Cd	^{115}In	^{118}Sn	^{121}Sb	^{128}Te	^{185}Re	^{189}Os	^{193}Ir	^{195}Pt	^{197}Au	^{205}Tl	^{208}Pb	^{209}Bi
LOD		0.003	0.025	0.014	0.018	0.012	0.079	0.004	0.008	0.002	0.004	0.007	0.002	0.005	0.002
East Boulder mine	ST-12	6.740	0.858	0.014	0.018	0.012	0.079	0.107	19.18	17.91	0.45	0.007	0.013	0.554	0.002
		10.256	0.622	0.014	0.029	0.039	0.684	0.315	42.98	40.93	0.52	0.007	0.006	0.322	0.009
		22.011	0.456	0.014	0.033	0.055	0.912	0.150	60.83	36.04	0.09	0.007	0.002	0.264	0.002
		11.787	0.270	0.014	0.124	0.012	0.195	0.347	61.21	43.63	0.31	0.013	0.031	0.387	0.002
		8.075	0.120	0.014	0.036	0.012	0.716	0.415	9.34	17.00	0.15	0.007	0.060	0.065	0.002
		6.024	0.186	0.014	0.065	0.012	0.163	0.120	20.64	25.95	0.27	0.011	0.002	0.034	0.002
		7.945	0.274	0.014	0.042	0.012	0.423	0.124	12.93	23.57	0.46	0.007	0.030	0.781	0.002
		2.813	1.250	0.014	0.137	0.035	0.698	0.386	15.91	33.22	0.20	0.007	0.007	0.251	0.008
		5.503	1.165	0.014	0.081	0.059	0.554	0.425	16.22	21.68	0.28	0.007	0.022	3.810	0.003
Median ST-12		**7.945**	**0.456**	**0.014**	**0.042**	**0.012**	**0.554**	**0.315**	**19.18**	**25.95**	**0.28**	**0.007**	**0.013**	**0.322**	**0.002**
East Boulder mine	ST-14	0.540	0.025	0.014	0.046	0.033	0.201	0.004	0.65	13.74	5.27	0.007	0.944	6.772	0.002
		2.898	0.994	0.019	0.018	0.085	0.260	0.098	0.41	2.20	0.67	0.008	1.465	9.442	0.004
		1.328	0.072	0.014	0.100	0.072	0.944	0.130	0.20	2.48	0.08	0.007	1.107	4.200	0.008
		3.875	1.346	0.019	0.130	0.052	2.084	0.004	0.36	3.42	7.36	0.029	0.423	1.791	0.012
		2.116	0.163	0.014	0.018	0.013	1.220	0.201	0.49	6.02	4.23	0.007	0.619	6.838	0.021
Median ST-14		**2.116**	**0.163**	**0.014**	**0.046**	**0.052**	**0.944**	**0.098**	**0.41**	**3.42**	**4.23**	**0.007**	**0.944**	**6.772**	**0.008**
East Boulder mine	ST-16	0.713	0.100	0.014	0.085	0.012	0.651	0.004	0.48	0.61	1.22	0.008	0.003	0.254	0.002
		0.987	0.101	0.014	0.059	0.012	1.465	0.582	1.79	0.55	4.22	0.007	0.002	0.208	0.098
		1.433	1.554	0.014	0.049	0.012	0.977	0.098	1.30	1.13	3.53	0.007	0.014	0.749	0.076
		0.537	0.335	0.014	0.018	0.012	1.856	0.218	1.76	1.21	7.29	0.007	0.002	0.091	0.004
		1.172	1.332	0.014	0.018	0.012	1.433	0.123	1.07	0.20	3.47	0.011	0.012	1.107	0.012
		1.042	0.211	0.014	0.018	0.012	0.293	0.358	1.91	1.98	5.76	0.007	0.002	0.323	0.002
Median ST-16		**1.014**	**0.273**	**0.014**	**0.034**	**0.012**	**1.205**	**0.170**	**1.53**	**0.87**	**3.88**	**0.007**	**0.002**	**0.289**	**0.008**

ANNEXE 19 – Cont.

Intrusion	Locality	Sample	Rock	^{34}S	^{59}Co	^{61}Ni	^{65}Cu	^{66}Zn	^{75}As	^{82}Se	^{95}Mo	^{101}Ru	^{103}Rh	^{108}Pd
LOD				58	0.004	0.3	0.28	0.079	0.044	0.6	0.008	0.01	0.00	0.03
Stillwater Complex	East Boulder mine	ST-17	Olivine melagabbronorite	294713	4978	211034	2702	358.160	0.232	367.9	0.008	21.78	83.01	3679.26
				313736	4777	269638	12536	302.400	0.912	302.8	0.008	18.20	75.15	14000.67
				278201	2716	249918	19536	10.745	0.619	433.0	0.008	25.72	173.11	2682.94
				289133	6317	221127	12796	344.240	0.293	312.6	0.036	20.41	329.11	4265.33
				312576	5438	203638	1628	52.221	0.044	302.8	0.072	34.28	342.85	6207.53
Median ST-17				**294713**	**4978**	**221127**	**12536**	**302.400**	**0.293**	**312.6**	**0.008**	**21.78**	**173.11**	**4265.33**
Stillwater Complex	Stillwater mine	P-4	Anorthosite	361416	1527	363695	2.05	2.247	0.488	284.5	0.008	2.51	5.87	1826.61
				403744	1475	416768	1.04	0.079	0.185	253.3	0.023	2.19	6.04	1800.57
				364346	1635	397232	1.95	0.163	0.044	279.3	0.014	3.01	6.35	1667.48
				352625	1651	370858	0.28	0.079	0.044	354.9	0.010	6.47	6.72	1976.39
				349369	1817	373789	0.34	0.293	0.044	306.1	0.013	7.51	4.01	1934.06
				357183	1719	379324	0.28	0.079	0.406	308.5	0.008	2.92	3.38	2031.74
Median P-4				**359300**	**1643**	**376556**	**0.69**	**0.121**	**0.115**	**295.3**	**0.012**	**2.97**	**5.96**	**1880.34**
Stillwater Complex	Stillwater mine	P-3	Leuco gabbronorite	348392	3643	338298	6.19	2.312	0.508	390.7	0.036	7.87	32.01	4142.45
				322018	3744	332112	7.07	1.001	0.150	174.5	0.008	6.86	11.31	7684.16
				340252	4233	315181	3.09	3.225	0.044	219.1	0.008	8.00	31.68	7651.60
				354904	4581	344485	5.54	0.182	0.288	332.1	0.008	6.41	14.47	8302.80
				323646	4428	324623	28.98	2.037	0.456	259.2	0.029	4.16	30.74	6153.84
Median P-3				**340252**	**4233**	**332112**	**6.19**	**2.037**	**0.288**	**259.2**	**0.008**	**6.86**	**30.74**	**7651.60**

ANNEXE 19 – Cont.

Locality	Sample	^{109}Ag	^{111}Cd	^{115}In	^{118}Sn	^{121}Sb	^{128}Te	^{185}Re	^{189}Os	^{193}Ir	^{195}Pt	^{197}Au	^{205}Tl	^{208}Pb	^{209}Bi
LOD		0.003	0.025	0.014	0.018	0.012	0.079	0.004	0.008	0.002	0.004	0.007	0.002	0.005	0.002
East Boulder mine	ST-17	2.670	0.554	0.014	0.274	0.012	1.009	0.059	9.25	8.79	3.87	0.007	0.228	0.326	0.010
		6.772	3.972	0.014	0.140	0.075	1.107	0.060	8.07	8.53	3.42	0.007	0.085	2.116	0.002
		9.377	0.130	0.014	0.055	0.023	0.170	0.014	5.30	2.26	1.81	0.007	0.004	0.563	0.007
		7.758	1.009	0.014	0.056	0.018	0.847	0.027	3.74	4.18	5.31	0.007	0.040	2.084	0.012
		6.675	0.025	0.014	0.114	0.012	0.699	0.004	4.17	11.20	5.11	0.007	0.002	0.791	0.002
Median ST-17		**6.772**	**0.554**	**0.014**	**0.114**	**0.018**	**0.847**	**0.027**	**5.30**	**8.53**	**3.87**	**0.007**	**0.040**	**0.791**	**0.007**
Stillwater mine	P-4	0.365	0.046	0.014	0.192	0.012	0.749	0.004	0.26	2.58	5.99	0.007	1.003	4.428	0.006
		1.133	0.025	0.014	0.348	0.016	0.079	0.023	0.50	0.18	6.74	0.009	1.042	4.103	0.085
		1.569	0.025	0.014	0.169	0.012	0.122	0.004	1.55	0.33	0.03	0.007	1.791	2.670	0.002
		1.071	0.025	0.228	0.068	0.012	4.037	0.031	0.73	0.46	0.02	0.007	0.466	1.400	0.002
		1.534	0.025	0.014	0.018	0.029	3.419	0.030	0.78	0.02	0.01	0.007	0.153	2.671	0.009
		0.423	0.036	0.014	0.13556425.	0.027	3.842	0.062	0.46	1.54	0.04	0.007	0.042	0.182	0.005
Median P-4		**1.102**	**0.025**	**0.014**	**0.169**	**0.014**	**2.084**	**0.027**	**0.62**	**0.39**	**0.04**	**0.007**	**0.734**	**2.670**	**0.006**
Stillwater mine	P-3	10.973	0.025	0.014	0.107	0.057	6.675	0.019	0.23	4.21	0.04	0.007	1.661	52.096	0.029
		7.293	0.025	0.014	0.018	0.012	2.409	0.005	0.19	5.37	5.73	0.007	0.342	1.595	0.002
		3.777	0.025	0.014	0.182	0.104	0.619	0.008	0.45	4.53	6.64	0.007	1.058	8.140	0.002
		7.228	0.033	0.014	0.201	0.107	0.908	0.028	0.45	5.47	6.81	0.007	0.684	9.117	0.008
		12.373	0.025	0.014	0.018	0.062	0.624	0.055	0.33	5.18	4.59	0.007	0.008	1.661	0.002
Median P-3		**7.293**	**0.025**	**0.014**	**0.107**	**0.062**	**0.908**	**0.019**	**0.33**	**5.18**	**5.73**	**0.007**	**0.684**	**8.140**	**0.002**

ANNEXE 19 – Cont.

Intrusion	Locality	Sample	Rock	^{34}S	^{59}Co	^{61}Ni	^{65}Cu	^{66}Zn	^{75}As	^{82}Se	^{95}Mo	^{101}Ru	^{103}Rh	^{108}Pd
LOD				58	0.004	0.3	0.28	0.079	0.044	0.6	0.008	0.01	0.00	0.03
Stillwater Complex	Banded Series	BS-18	Leuco gabbronorite	354912	9377	363744	1.11	0.521	1.042	214.9	0.358	0.01	0.01	0.04
				394627	9465	374766	0.84	0.117	5.372	303.1	0.008	0.01	0.00	0.15
				357977	9605	404395	0.28	0.384	4.982	226.6	0.008	0.07	0.00	0.09
				403744	5926	386536	0.75	0.079	0.347	192.1	0.008	0.14	0.00	0.13
				416768	6740	373789	31.86	0.336	4.265	325.3	0.068	0.01	0.03	0.13
				433048	8303	392022	1.27	0.427	0.628	163.1	0.008	0.07	0.00	0.20
				410582	8107	400488	1.33	35.816	0.326	175.5	0.008	0.08	0.00	0.16
				351233	8283	349279	2.70	0.619	0.430	182.3	0.067	0.04	0.00	0.16
				406349	8694	354676	2.28	0.079	5.796	254.0	0.008	0.01	0.03	0.11
				415140	8436	356072	520.96	5.210	3.744	285.2	0.049	0.01	0.02	0.10
				361416	7717	407000	0.28	0.188	1.595	341.9	0.008	0.18	0.00	0.04
				376072	7316	361326	1.40	2.084	1.758	282.9	0.081	0.24	0.00	0.17
				396581	7433	420024	0.73	3.223	5.470	297.3	0.169	0.04	0.01	0.19
Median BS-18				**396581**	**8283**	**374766**	**1.27**	**0.427**	**1.758**	**254.0**	**0.008**	**0.04**	**0.00**	**0.13**
Stillwater Complex	Picket Pin	PP-AN	Anorthosite	410256	8726	291412	6.71	49.784	0.257	218.2	0.008	0.14	15.63	81.35
				399377	12015	372161	34.19	29.304	0.218	227.3	0.099	1.06	0.66	67.02
				403146	12698	356442	1.70	45.258	0.306	342.9	0.008	0.08	1.05	28.76
				407749	12210	376068	1.30	11.526	0.249	231.2	0.391	1.35	6.25	19.72
				395612	12470	356817	976.80	20.187	0.215	377.4	0.008	0.05	1.04	205.99
				437281	11168	329226	0.72	58.282	0.044	284.6	0.147	0.15	5.11	11.29
				414489	9823	297924	1.20	3.191	0.475	232.5	0.313	0.23	11.33	2.70
				388351	9967	354249	2.33	34.286	0.231	302.5	1.498	1.09	2.60	13.47
Median PP-AN				**405447**	**11591**	**355346**	**2.01**	**31.795**	**0.240**	**258.5**	**0.123**	**0.19**	**3.86**	**24.24**

ANNEXE 19 – Cont.

Locality	Sample	^{109}Ag	^{111}Cd	^{115}In	^{118}Sn	^{121}Sb	^{128}Te	^{185}Re	^{189}Os	^{193}Ir	^{195}Pt	^{197}Au	^{205}Tl	^{208}Pb	^{209}Bi
LOD		0.003	0.025	0.014	0.018	0.012	0.079	0.004	0.008	0.002	0.004	0.007	0.002	0.005	0.002
Banded Series	BS-18	1.986	0.025	0.039	0.018	0.012	89.536	0.033	0.01	0.00	0.00	0.007	1.368	9.135	1.198
		0.996	0.025	0.014	0.018	0.012	66.422	0.004	0.01	0.00	0.00	0.007	0.002	1.986	1.728
		0.306	0.025	0.014	0.018	0.012	91.168	0.004	0.01	0.02	0.00	0.007	0.002	0.531	0.416
		1.954	0.025	0.014	0.018	0.012	29.019	0.004	0.01	0.00	0.00	0.007	0.140	11.396	0.749
		2.572	0.025	0.014	0.108	0.012	41.677	0.004	0.01	0.01	0.00	0.007	0.046	0.716	1.254
		2.396	0.025	0.014	0.078	0.012	46.345	0.004	0.01	0.00	0.00	0.007	0.101	7.847	0.619
		0.599	0.199	0.014	0.117	0.012	35.568	0.004	0.01	0.00	0.00	0.007	0.057	1.188	0.493
		1.009	0.025	0.014	0.293	0.814	16.671	0.004	0.01	0.00	0.00	0.007	0.434	140.008	2.311
		0.342	0.025	0.014	0.101	0.012	166.707	1.377	0.01	0.04	0.00	0.007	0.002	0.619	0.908
		1.107	0.505	0.014	0.102	0.423	55.873	0.075	0.01	0.00	0.00	0.007	2.898	39.072	1.511
		0.785	0.025	0.014	0.018	0.287	119.821	0.104	0.01	0.00	0.00	0.007	0.036	18.885	0.440
		0.801	0.025	0.014	0.150	1.140	89.214	0.078	0.01	0.00	0.00	0.007	0.739	64.794	0.695
		6.121	0.025	0.014	0.018	0.106	151.078	0.027	0.01	0.00	0.00	0.088	3.093	22.141	1.563
Median BS-18		**1.009**	**0.025**	**0.014**	**0.078**	**0.012**	**66.422**	**0.004**	**0.01**	**0.00**	**0.00**	**0.007**	**0.101**	**9.135**	**0.908**
Picket Pin	PP-AN	1.164	1.465	0.037	0.018	0.012	0.079	0.004	0.10	0.38	0.20	0.007	0.140	7.261	0.029
		0.518	1.563	0.014	0.018	0.012	0.456	0.004	0.52	0.29	0.10	0.007	0.576	13.057	0.041
		2.201	2.735	0.014	0.018	0.012	0.079	0.004	0.05	0.05	5.05	0.007	0.876	15.368	0.007
		0.863	2.344	0.014	0.018	0.012	0.088	0.651	0.88	0.29	3.32	0.007	0.540	10.452	0.002
		4.265	3.484	0.014	0.018	0.012	0.079	0.039	0.01	0.03	0.78	0.007	0.654	24.453	0.008
		0.150	1.335	0.014	0.018	0.012	0.079	0.749	0.38	0.98	0.52	0.007	0.098	1.801	0.020
		0.684	0.492	0.014	0.018	0.012	0.079	1.237	0.51	1.55	5.14	0.007	0.060	0.944	0.002
		1.439	1.381	0.014	0.018	0.012	0.079	1.693	0.35	0.41	0.79	0.007	0.215	12.210	0.004
Median PP-AN		**1.014**	**1.514**	**0.014**	**0.018**	**0.012**	**0.079**	**0.345**	**0.36**	**0.34**	**0.79**	**0.007**	**0.378**	**11.331**	**0.008**

ANNEXE 20 - Complete data set of LA-ICP-MS analyses of chalcopyrite obtained in this study and median values for each sample from the Bushveld and Stillwater Complexes. The Fe values used for internal standardization are from Godel et al. (2008a) for samples from the Stillwater Complex, Godel et al. (2007) for samples from the Rustenburg mine, and stoichiometric values (i.e., 30.4%) for samples from the Impala mine. LOD - limit of detection; n.r. – not reported.

ANNEXE 20

Intrusion	Locality	Sample	Rock	Height (cm)	^{34}S	^{59}Co	^{61}Ni	^{65}Cu	^{66}Zn	^{75}As	^{82}Se	^{95}Mo	^{101}Ru	^{103}Rh	^{108}Pd	^{109}Ag
LOD					58	0.008	0.31	0.2	0.1	0.044	0.6	0.008	0.008	0.001	0.027	0.003
Bushveld Complex	Impala mine	IM-1	Norite	108	324909	1.035	82.77	326514	240.4	1.704	94.6	0.008	0.008	n.r.	0.064	13.085
					328340	7.912	94.33	404719	356.0	0.852	95.6	0.023	0.030	n.r.	0.123	1.369
Median IM-1					**326624**	**4.473**	**88.55**	**365616**	**298.2**	**1.278**	**95.1**	**0.016**	**0.019**	n.r.	**0.093**	**7.227**
Bushveld Complex	Impala mine	IM-3	Norite	98	329431	10.133	60.86	325297	243.4	0.641	95.9	0.054	0.008	n.r.	0.027	0.855
					290911	17.649	1004.51	317689	225.2	1.430	68.5	0.008	0.008	n.r.	0.234	1.278
					310260	0.149	41.69	362117	187.1	0.700	67.6	0.008	0.027	n.r.	0.084	1.735
Median IM-3					**310260**	**10.133**	**60.86**	**325297**	**225.2**	**0.700**	**68.5**	**0.008**	**0.008**	n.r.	**0.084**	**1.278**
Bushveld Complex	Impala mine	IM-5	Norite	88	330042	0.307	46.25	334730	224.0	1.461	66.9	0.063	0.015	n.r.	0.122	0.968
					297217	3.236	39.86	346984	245.3	0.192	71.8	0.008	0.061	n.r.	0.257	1.461
					313828	0.256	35.30	321103	241.3	0.312	74.2	0.030	0.055	n.r.	0.027	1.339
					298214	9.129	89.77	334562	244.8	1.674	81.6	0.008	0.030	n.r.	0.066	0.992
Median IM-5					**306021**	**1.771**	**43.06**	**334646**	**243.0**	**0.886**	**73.0**	**0.019**	**0.043**	n.r.	**0.094**	**1.165**
Bushveld Complex	Impala mine	IM-7	Melanorite	78	296388	0.228	63.29	318298	268.1	1.369	85.5	0.064	0.058	n.r.	0.255	10.529
					322558	0.067	58.73	335339	252.0	1.065	95.7	0.008	0.156	n.r.	2.527	1.674
					334783	1.023	35.60	318906	288.2	1.126	112.9	0.026	0.024	n.r.	1.067	1.704
					300648	0.008	68.47	329861	294.6	0.943	108.0	0.008	0.012	n.r.	0.099	1.876
					312737	2.130	109.55	356031	331.7	1.075	82.5	0.008	0.043	n.r.	0.566	1.765
Median IM-7					**312737**	**0.228**	**63.29**	**329861**	**288.2**	**1.075**	**95.7**	**0.008**	**0.043**	n.r.	**0.566**	**1.765**
Bushveld Complex	Impala mine	IM-9	Melanorite	68	285129	0.052	51.77	318865	244.7	0.712	90.4	0.021	0.040	n.r.	0.443	0.952
					336346	0.097	57.82	328340	161.0	0.669	80.6	0.015	0.014	n.r.	0.129	0.551
					317554	0.113	50.21	352075	234.3	0.044	92.5	0.098	0.015	n.r.	0.027	1.083
					280869	3.465	64.21	380375	274.5	0.761	105.9	0.008	0.063	n.r.	0.357	0.782
					280565	0.061	47.17	341729	235.2	0.556	62.1	0.085	0.024	n.r.	0.099	1.400
					322390	0.128	52.34	341685	359.1	0.243	59.9	0.008	0.008	n.r.	0.145	1.019
Median IM-9					**301342**	**0.105**	**52.05**	**341707**	**240.0**	**0.613**	**85.5**	**0.018**	**0.020**	n.r.	**0.137**	**0.986**

ANNEXE 20 – Cont.

Intrusion	Locality	Sample	^{111}Cd	^{115}In	^{118}Sn	^{121}Sb	^{128}Te	^{185}Re	^{189}Os	^{193}Ir	^{195}Pt	^{197}Au	^{205}Tl	^{208}Pb	^{209}Bi
LOD			0.025	0.014	0.018	0.012	0.079	0.004	0.008	0.002	0.004	0.007	0.002	0.005	0.002
Bushveld Complex	Impala mine	IM-1	1.187	0.346	0.134	0.131	0.822	0.004	0.008	0.036	0.004	0.103	0.131	28.300	1.987
			2.130	0.397	0.335	0.052	1.704	0.051	0.024	0.002	0.004	0.007	0.024	20.084	2.518
Median IM-1			**1.658**	**0.372**	**0.234**	**0.091**	**1.263**	**0.027**	**0.016**	**0.019**	**0.004**	**0.055**	**0.077**	**24.192**	**2.253**
Bushveld Complex	Impala mine	IM-3	1.248	0.733	0.234	0.012	1.826	0.023	0.008	0.002	0.067	0.007	0.002	5.417	2.050
			1.156	0.918	0.219	0.012	1.461	0.004	0.008	0.113	0.004	0.041	0.026	9.433	2.080
			1.238	1.542	0.423	0.012	2.822	0.004	0.008	0.002	0.004	0.007	0.002	11.868	1.829
Median IM-3			**1.238**	**0.918**	**0.234**	**0.012**	**1.826**	**0.004**	**0.008**	**0.002**	**0.004**	**0.007**	**0.002**	**9.433**	**2.050**
Bushveld Complex	Impala mine	IM-5	0.943	1.147	0.018	0.012	2.069	0.055	0.008	0.002	0.004	0.007	0.002	4.686	2.651
			1.095	1.679	0.102	0.012	2.248	0.004	0.045	0.002	0.004	0.007	0.009	5.690	0.685
			1.035	1.518	0.094	0.012	1.095	0.004	0.008	0.002	0.004	0.015	0.002	7.577	1.812
			0.913	0.608	0.323	0.012	3.217	0.128	0.064	0.082	0.004	0.011	0.002	9.129	1.613
Median IM-5			**0.989**	**1.333**	**0.098**	**0.012**	**2.158**	**0.029**	**0.026**	**0.002**	**0.004**	**0.009**	**0.002**	**6.634**	**1.713**
Bushveld Complex	Impala mine	IM-7	2.259	1.497	2.465	0.499	0.079	0.098	0.008	0.004	0.007	0.007	0.030	13.815	0.084
			3.195	1.574	1.448	0.012	0.426	0.004	0.201	0.103	0.004	0.027	0.002	11.046	0.061
			2.434	3.155	2.678	0.012	0.368	0.102	0.008	0.002	0.064	0.007	0.030	152.150	0.231
			3.165	1.451	1.795	0.012	0.107	0.004	0.082	0.002	0.017	0.015	0.029	51.427	0.039
			2.982	0.862	0.511	0.012	0.225	0.004	0.008	0.023	0.004	0.007	0.070	31.343	0.030
Median IM-7			**2.982**	**1.497**	**1.795**	**0.012**	**0.225**	**0.004**	**0.008**	**0.004**	**0.007**	**0.007**	**0.030**	**31.343**	**0.061**
Bushveld Complex	Impala mine	IM-9	5.688	0.218	0.228	0.012	3.104	0.004	0.008	0.002	0.023	0.009	0.002	6.056	3.956
			3.682	2.122	0.073	0.012	2.282	0.004	0.012	0.128	0.019	0.026	0.002	3.925	1.804
			1.430	0.851	0.155	0.012	2.826	0.054	0.122	0.002	0.004	0.007	0.009	8.186	2.479
			1.720	1.076	0.365	0.012	1.643	0.004	0.008	0.002	0.006	0.007	0.033	8.764	3.402
			1.735	0.860	0.192	0.012	3.913	0.004	0.013	0.003	0.005	0.010	0.002	7.851	1.369
			2.465	0.872	0.408	0.012	1.339	0.023	0.008	0.002	0.004	0.007	0.002	8.794	4.895
Median IM-9			**2.100**	**0.866**	**0.210**	**0.012**	**2.554**	**0.004**	**0.010**	**0.002**	**0.006**	**0.008**	**0.002**	**8.018**	**2.940**

ANNEXE 20 – Cont.

Intrusion	Locality	Sample	Rock	Height (cm)	^{34}S	^{59}Co	^{61}Ni	^{65}Cu	^{66}Zn	^{75}As	^{82}Se	^{95}Mo	^{101}Ru	^{103}Rh	^{108}Pd	^{109}Ag
LOD					58	0.008	0.31	0.2	0.1	0.044	0.6	0.008	0.008	0.001	0.027	0.003
Bushveld Complex	Impala mine	IM-11	Melanorite	58	331478	0.008	55.69	344772	383.4	1.400	89.5	0.008	0.015	n.r.	0.069	1.406
					298346	0.057	52.04	360805	273.6	1.371	79.7	0.008	0.122	n.r.	0.027	0.971
					327868	0.175	52.35	338074	323.5	0.335	87.3	0.066	0.025	n.r.	0.234	0.934
					316472	5.476	62.38	331781	287.0	0.340	84.3	0.008	0.099	n.r.	0.145	1.433
					286358	0.134	51.80	328955	261.7	0.044	93.4	0.102	0.008	n.r.	0.099	1.318
Median IM-11					**316472**	**0.134**	**52.35**	**338074**	**287.0**	**0.340**	**87.3**	**0.008**	**0.025**	n.r.	**0.099**	**1.318**
Bushveld Complex	Impala mine	IM-13	Melanorite	48	297605	0.180	41.71	365160	199.0	0.456	94.3	0.008	0.008	n.r.	2.066	1.948
					322128	0.721	59.34	323471	238.0	0.431	97.0	0.107	0.102	n.r.	0.066	0.977
					295171	0.198	53.25	315863	197.5	0.730	72.1	0.008	0.021	n.r.	0.048	1.522
					272957	4.613	70.90	365452	205.7	0.044	67.9	0.056	0.036	n.r.	0.027	1.217
Median IM-13					**296388**	**0.459**	**56.30**	**344315**	**202.4**	**0.443**	**83.2**	**0.032**	**0.029**	n.r.	**0.057**	**1.369**
Bushveld Complex	Impala mine	IM-15	Melanorite	38	320320	3.422	54.77	332601	293.6	0.822	84.0	0.012	0.020	n.r.	0.343	1.059
Median IM-15					**320320**	**3.422**	**54.77**	**332601**	**293.6**	**0.822**	**84.0**	**0.012**	**0.020**	n.r.	**0.343**	**1.059**
Bushveld Complex	Impala mine	IM-17	Melanorite	28	313733	0.099	46.86	349945	328.6	2.617	109.5	0.008	0.052	n.r.	0.124	1.165
					321037	0.131	41.99	351467	309.5	0.044	98.6	0.018	0.076	n.r.	0.244	1.293
Median IM-17					**317385**	**0.115**	**44.43**	**350706**	**319.1**	**1.331**	**104.1**	**0.013**	**0.064**	n.r.	**0.184**	**1.229**
Bushveld Complex	Impala mine	IM-18	Melanorite	23	313429	0.843	124.76	318910	289.7	0.609	100.7	0.008	0.008	n.r.	0.027	0.998
					324688	0.219	40.47	336860	357.6	1.709	106.1	0.100	0.036	n.r.	0.987	1.159
					319819	18.867	401.88	352923	307.6	1.278	102.2	0.066	0.011	n.r.	0.050	1.071
Median IM-18					**319819**	**0.843**	**124.76**	**336860**	**307.6**	**1.278**	**102.2**	**0.066**	**0.011**	n.r.	**0.050**	**1.071**

ANNEXE 20 – Cont.

Intrusion	Locality	Sample	^{111}Cd	^{115}In	^{118}Sn	^{121}Sb	^{128}Te	^{185}Re	^{189}Os	^{193}Ir	^{195}Pt	^{197}Au	^{205}Tl	^{208}Pb	^{209}Bi
LOD			0.025	0.014	0.018	0.012	0.079	0.004	0.008	0.002	0.004	0.007	0.002	0.005	0.002
Bushveld Complex	Impala mine	IM-11	1.674	0.908	0.648	0.061	2.769	0.004	0.008	0.003	0.040	0.043	0.002	11.633	2.161
			1.400	0.914	0.435	0.012	1.917	0.004	0.008	0.002	0.004	0.019	0.002	11.959	3.886
			1.928	0.930	0.230	0.012	1.430	0.104	0.009	0.075	0.004	0.029	0.014	10.498	2.129
			2.158	2.986	0.210	0.012	1.217	0.004	0.008	0.002	0.004	0.030	0.002	12.355	1.348
			1.704	0.915	0.180	0.012	3.522	0.054	0.055	0.009	0.004	0.007	0.009	11.229	2.491
Median IM-11			**1.704**	**0.915**	**0.230**	**0.012**	**1.917**	**0.004**	**0.008**	**0.003**	**0.004**	**0.029**	**0.002**	**11.633**	**2.161**
Bushveld Complex	Impala mine	IM-13	0.822	1.204	0.170	0.012	1.187	0.013	0.012	0.002	0.004	0.013	0.002	7.925	2.475
			1.004	1.789	0.104	0.012	2.552	0.004	0.008	0.002	0.004	0.007	0.002	8.003	1.083
			0.774	0.766	0.113	0.012	2.339	0.066	0.023	0.002	0.004	0.026	0.002	6.664	2.313
			0.609	2.321	0.207	0.012	1.244	0.004	0.008	0.002	0.004	0.031	0.032	7.912	0.149
Median IM-13			**0.798**	**1.497**	**0.141**	**0.012**	**1.791**	**0.008**	**0.010**	**0.002**	**0.004**	**0.019**	**0.002**	**7.919**	**1.698**
Bushveld Complex	Impala mine	IM-15	1.675	1.506	0.167	0.012	2.765	0.021	0.008	0.002	0.004	0.007	0.011	16.858	1.659
Median IM-15			**1.675**	**1.506**	**0.167**	**0.012**	**2.765**	**0.021**	**0.008**	**0.002**	**0.004**	**0.007**	**0.011**	**16.858**	**1.659**
Bushveld Complex	Impala mine	IM-17	1.856	1.237	0.368	0.012	1.669	0.004	0.054	0.002	0.004	0.007	0.002	8.338	1.663
			2.587	4.563	0.140	0.012	2.308	0.103	0.008	0.002	0.004	0.014	0.002	13.102	0.537
Median IM-17			**2.221**	**2.900**	**0.254**	**0.012**	**1.989**	**0.053**	**0.031**	**0.002**	**0.004**	**0.010**	**0.002**	**10.720**	**1.100**
Bushveld Complex	Impala mine	IM-18	1.522	0.836	0.105	0.037	0.852	0.047	0.008	0.002	0.004	0.007	0.024	14.302	0.060
			2.802	1.691	0.237	0.012	0.447	0.004	0.021	0.002	0.004	0.007	0.034	14.211	0.505
			2.039	1.807	0.055	0.012	0.344	0.004	0.123	0.099	0.004	0.007	0.046	8.277	0.286
Median IM-18			**2.039**	**1.691**	**0.105**	**0.012**	**0.447**	**0.004**	**0.021**	**0.002**	**0.004**	**0.007**	**0.034**	**14.211**	**0.286**

ANNEXE 20 – Cont.

Intrusion	Locality	Sample	Rock	Height (cm)	^{34}S	^{59}Co	^{61}Ni	^{65}Cu	^{66}Zn	^{75}As	^{82}Se	^{95}Mo	^{101}Ru	^{103}Rh	^{108}Pd	^{109}Ag
LOD					58	0.008	0.31	0.2	0.1	0.044	0.6	0.008	0.008	0.001	0.027	0.003
Bushveld Complex	Impala mine	IM-19	Melanorite	18	340607	0.654	94.03	345953	347.2	2.800	79.1	0.010	0.053	n.r.	0.031	0.676
					309473	0.258	64.82	338386	284.8	2.161	72.4	0.008	0.031	n.r.	0.027	0.627
					323345	0.103	28.60	330720	244.4	1.217	84.1	0.008	0.027	n.r.	0.233	1.506
					322410	0.161	33.17	328964	252.6	1.680	83.4	0.100	0.021	n.r.	0.562	1.321
					315863	0.129	32.56	335643	289.1	2.008	73.0	0.008	0.018	n.r.	0.755	1.269
					329253	0.286	35.32	344468	288.7	1.735	75.1	0.008	0.024	n.r.	1.213	1.382
					301257	0.338	39.93	331886	262.0	1.102	75.8	0.048	0.232	n.r.	0.233	0.879
					343859	0.079	31.95	338686	301.3	2.708	83.7	0.008	0.060	n.r.	0.027	2.130
					309579	0.131	14.61	318567	241.0	1.248	76.4	0.036	0.008	n.r.	0.027	2.800
Median IM-19					**322410**	**0.161**	**33.17**	**335643**	**284.8**	**1.735**	**76.4**	**0.008**	**0.027**	n.r.	**0.233**	**1.321**
Bushveld Complex	Impala mine	IM-20	Melanorite	13	300344	0.085	32.86	377332	245.6	1.682	65.1	0.046	0.051	n.r.	0.027	0.897
					339998	0.082	35.91	336556	253.8	2.313	70.0	0.012	0.024	n.r.	0.257	0.849
					305213	0.137	28.62	353522	324.6	1.582	78.2	0.008	0.048	n.r.	0.244	2.556
					328476	4.747	123.74	337403	233.7	0.250	57.5	0.020	0.313	n.r.	0.531	0.888
					296378	0.114	33.78	343859	264.7	0.044	55.4	0.017	0.027	n.r.	0.034	0.946
					314646	0.008	28.91	352707	257.4	0.365	65.6	0.008	0.072	n.r.	0.312	0.864
					322254	0.008	39.56	343555	236.0	2.800	81.2	0.008	0.051	n.r.	1.012	0.822
					334867	1.652	34.60	339295	218.5	1.071	80.3	0.062	0.017	n.r.	0.090	0.803
					307647	0.008	24.69	377382	221.2	1.643	75.2	0.008	0.045	n.r.	0.066	2.617
					315847	2.336	31.34	336520	273.9	2.465	87.9	0.155	0.099	n.r.	0.122	1.099
					303996	0.008	32.69	341425	358.2	2.282	92.5	0.008	0.039	n.r.	0.422	2.465
Median IM-20					**314646**	**0.085**	**32.86**	**343555**	**253.8**	**1.643**	**75.2**	**0.012**	**0.048**	n.r.	**0.244**	**0.897**

ANNEXE 20 – Cont.

Intrusion	Locality	Sample	^{111}Cd	^{115}In	^{118}Sn	^{121}Sb	^{128}Te	^{185}Re	^{189}Os	^{193}Ir	^{195}Pt	^{197}Au	^{205}Tl	^{208}Pb	^{209}Bi
LOD			0.025	0.014	0.018	0.012	0.079	0.004	0.008	0.002	0.004	0.007	0.002	0.005	0.002
Bushveld Complex	Impala mine	IM-19	1.984	0.993	1.400	0.012	0.094	0.004	0.020	0.004	0.004	0.007	0.002	14.728	0.119
			2.179	1.108	1.494	0.012	0.079	0.022	0.008	0.002	0.004	0.007	0.002	8.425	0.119
			1.702	1.105	1.482	0.012	0.244	0.004	0.008	0.002	0.004	0.018	0.002	10.011	0.059
			1.765	1.227	1.491	0.012	0.079	0.004	0.008	0.026	0.004	0.007	0.002	11.022	0.054
			2.234	0.989	0.867	0.012	0.158	0.004	0.024	0.034	0.004	0.007	0.002	96.159	0.101
			2.708	1.180	1.083	0.012	0.099	0.004	0.008	0.002	0.004	0.016	0.002	39.863	0.137
			2.526	1.079	0.475	0.046	0.359	0.056	0.055	0.045	0.004	0.007	0.002	8.399	0.487
			2.739	1.076	1.978	0.012	0.079	0.042	0.008	0.002	0.004	0.007	0.002	7.422	0.131
			3.986	5.263	1.193	0.012	0.423	0.004	0.008	0.002	0.018	0.007	0.002	5.295	0.103
Median IM-19			**2.234**	**1.105**	**1.400**	**0.012**	**0.099**	**0.004**	**0.008**	**0.002**	**0.004**	**0.007**	**0.002**	**10.011**	**0.119**
Bushveld Complex	Impala mine	IM-20	3.226	1.242	1.531	0.012	0.455	0.004	0.008	0.002	0.004	0.029	0.002	11.898	0.341
			3.176	0.894	1.976	0.012	0.079	0.004	0.233	0.122	0.004	0.025	0.002	13.998	0.192
			3.591	1.158	1.339	0.030	0.216	0.062	0.008	0.006	0.004	0.007	0.002	18.867	0.752
			3.224	0.884	1.190	0.012	0.128	0.102	0.008	0.002	0.012	0.007	0.019	8.366	0.313
			3.773	0.911	1.330	0.012	0.277	0.004	0.008	0.002	0.008	0.007	0.002	11.320	0.277
			2.579	1.220	0.995	0.012	0.365	0.004	0.034	0.033	0.010	0.016	0.002	7.821	0.216
			2.800	1.142	2.200	0.012	0.189	0.004	0.008	0.002	0.004	0.007	0.002	72.423	0.180
			2.642	1.093	1.518	0.012	0.079	0.062	0.008	0.022	0.004	0.007	0.002	9.555	0.219
			2.574	3.561	1.378	0.012	0.210	0.004	0.027	0.002	0.004	0.007	0.002	8.520	0.228
			2.837	1.079	2.069	0.012	0.122	0.004	0.008	0.002	0.004	0.007	0.002	7.790	0.201
			3.185	1.111	1.585	0.012	0.079	0.004	0.008	0.002	0.004	0.007	0.002	37.429	0.338
Median IM-20			**3.176**	**1.111**	**1.518**	**0.012**	**0.189**	**0.004**	**0.008**	**0.002**	**0.004**	**0.007**	**0.002**	**11.320**	**0.228**

ANNEXE 20 – Cont.

Intrusion	Locality	Sample	Rock	Height (cm)	^{34}S	^{59}Co	^{61}Ni	^{65}Cu	^{66}Zn	^{75}As	^{82}Se	^{95}Mo	^{101}Ru	^{103}Rh	^{108}Pd	^{109}Ag
LOD					58	0.008	0.31	0.2	0.1	0.044	0.6	0.008	0.008	0.001	0.027	0.003
Bushveld Complex	Impala mine	IM-21	Melanorite	8	318602	0.101	34.39	345076	249.8	1.286	74.9	0.008	0.039	n.r.	2.033	0.910
					351467	2.127	41.74	339639	258.7	1.978	85.9	0.032	0.013	n.r.	0.211	0.855
					318602	6.655	40.78	333503	228.2	0.553	66.0	0.008	0.124	n.r.	0.086	1.126
					304979	0.562	41.08	336252	276.9	1.765	65.7	0.008	0.072	n.r.	0.095	0.901
					316436	0.099	41.38	332602	413.8	1.004	68.0	0.065	0.036	n.r.	1.236	0.910
					348518	0.231	51.97	332771	242.5	1.887	73.6	0.008	0.060	n.r.	0.562	1.528
Median IM-21					**318602**	**0.397**	**41.23**	**334877**	**254.2**	**1.525**	**70.8**	**0.008**	**0.050**	n.r.	**0.387**	**0.910**
Bushveld Complex	Impala mine	IM-22	Upper Chromitite	6	333209	2.300	37.73	347511	328.6	1.795	74.8	0.011	0.091	n.r.	1.365	1.266
					328948	0.088	46.27	347206	303.1	2.739	75.1	0.048	0.036	n.r.	0.755	1.254
					326514	0.566	51.43	356979	410.8	1.688	77.2	0.057	0.054	n.r.	1.455	1.287
					345685	0.090	47.78	345381	319.5	2.039	87.2	0.016	0.011	n.r.	0.158	1.310
					359758	0.263	62.08	355422	250.7	1.136	85.2	0.008	1.024	n.r.	0.234	1.539
					353333	0.008	45.07	347815	398.6	2.678	92.2	0.008	0.008	n.r.	0.085	0.986
Median IM-22					**339447**	**0.177**	**47.02**	**347663**	**324.1**	**1.917**	**81.2**	**0.013**	**0.045**	n.r.	**0.494**	**1.277**
Bushveld Complex	Impala mine	IM-24	Lower Chromitite	0	324758	1.233	26.17	342642	268.7	0.740	76.7	0.008	0.012	n.r.	1.022	5.903
					325297	0.233	24.34	327731	256.5	0.253	66.6	0.008	0.015	n.r.	0.788	10.864
					332904	4.266	30.73	358161	281.2	0.822	67.0	0.018	0.014	n.r.	2.215	1.564
					326425	0.008	28.86	357016	244.0	0.655	77.9	0.008	0.039	n.r.	0.845	1.701
					339599	2.769	65.14	386461	189.0	0.367	85.8	0.023	0.008	n.r.	0.027	7.364
					340512	0.087	66.95	350554	157.6	0.310	76.1	0.090	0.039	n.r.	0.522	1.439
					334730	0.008	43.21	341537	237.4	1.124	73.0	0.008	0.082	n.r.	0.267	1.199
Median IM-24					**332904**	**0.233**	**30.73**	**350554**	**244.0**	**0.655**	**76.1**	**0.008**	**0.015**	n.r.	**0.788**	**1.701**

ANNEXE 20 – Cont.

Intrusion	Locality	Sample	^{111}Cd	^{115}In	^{118}Sn	^{121}Sb	^{128}Te	^{185}Re	^{189}Os	^{193}Ir	^{195}Pt	^{197}Au	^{205}Tl	^{208}Pb	^{209}Bi
LOD			0.025	0.014	0.018	0.012	0.079	0.004	0.008	0.002	0.004	0.007	0.002	0.005	0.002
Bushveld Complex	Impala mine	IM-21	2.820	1.660	1.272	0.012	0.079	0.004	0.065	0.002	0.004	0.007	0.002	2.860	0.016
			3.720	2.066	0.764	0.012	0.423	0.004	0.008	0.054	0.043	0.007	0.002	5.508	0.079
			3.239	1.533	1.147	0.012	0.079	0.124	0.008	0.002	0.012	0.007	0.018	5.934	0.033
			3.804	0.698	0.660	0.012	0.327	0.004	0.008	0.122	0.004	0.013	0.002	14.363	0.095
			4.747	0.627	0.673	0.012	0.079	0.053	0.244	0.002	0.017	0.007	0.002	8.642	0.118
			4.260	4.562	0.426	0.012	0.222	0.004	0.008	0.002	0.033	0.014	0.020	12.872	0.463
Median IM-21			**3.762**	**1.596**	**0.718**	**0.012**	**0.151**	**0.004**	**0.008**	**0.002**	**0.014**	**0.007**	**0.002**	**7.288**	**0.087**
Bushveld Complex	Impala mine	IM-22	4.382	1.105	0.769	0.012	0.079	0.004	0.010	0.002	0.034	0.007	0.002	16.037	0.058
			4.595	1.510	1.522	0.012	0.567	0.004	0.008	0.002	0.005	0.007	0.002	12.202	0.002
			6.025	1.820	1.728	0.012	0.207	0.004	0.008	0.123	0.004	0.007	0.002	15.763	0.018
			4.712	1.664	1.719	0.033	0.099	0.004	0.008	0.002	0.004	0.007	0.002	13.922	0.023
			2.678	1.185	0.444	0.012	0.149	0.004	0.008	0.002	0.004	0.007	0.037	7.181	0.002
			7.242	1.002	1.561	0.012	0.143	0.004	0.008	0.002	0.018	0.007	0.002	5.721	0.021
Median IM-22			**4.654**	**1.348**	**1.541**	**0.012**	**0.146**	**0.004**	**0.008**	**0.002**	**0.004**	**0.007**	**0.002**	**13.062**	**0.019**
Bushveld Complex	Impala mine	IM-24	2.612	2.309	0.289	0.012	0.079	0.004	0.008	0.002	0.025	0.014	0.002	3.073	0.014
			7.455	2.160	0.157	0.012	0.079	0.004	0.008	0.002	0.024	0.007	0.016	12.598	0.014
			3.624	1.566	0.296	0.012	0.139	0.004	0.008	0.002	0.015	0.007	0.002	10.820	0.041
			2.860	3.266	0.173	0.012	0.103	0.004	0.101	0.002	0.046	0.007	0.040	9.370	0.060
			4.656	2.072	0.156	0.012	0.211	0.004	0.008	0.201	0.004	0.007	0.002	3.834	0.002
			3.784	1.384	0.462	0.012	0.451	0.004	0.008	0.002	0.070	0.013	0.107	10.924	0.133
			3.712	1.266	0.076	0.040	0.525	0.004	0.008	0.002	0.006	0.007	0.002	4.991	0.017
Median IM-24			**3.712**	**2.072**	**0.173**	**0.012**	**0.139**	**0.004**	**0.008**	**0.002**	**0.024**	**0.007**	**0.002**	**9.370**	**0.017**

ANNEXE 20 – Cont.

Intrusion	Locality	Sample	Rock	Height (cm)	^{34}S	^{59}Co	^{61}Ni	^{65}Cu	^{66}Zn	^{75}As	^{82}Se	^{95}Mo	^{101}Ru	^{103}Rh	^{108}Pd	^{109}Ag
LOD					58	0.008	0.31	0.2	0.1	0.044	0.6	0.008	0.008	0.001	0.027	0.003
Bushveld Complex	Impala mine	IM-26	Leuconorite	-8	314038	0.119	56.60	334539	324.7	0.913	88.2	0.015	0.039	n.r.	0.323	1.413
					327427	0.092	59.03	365160	328.3	1.339	88.6	0.123	0.033	n.r.	2.311	1.190
					334870	0.526	53.56	345569	339.3	0.548	78.5	0.008	0.012	n.r.	0.655	1.431
					316168	15.023	45.69	339026	297.9	2.168	86.7	0.099	0.027	n.r.	0.566	1.479
					316558	2.433	36.50	343513	313.4	0.860	70.6	0.008	0.020	n.r.	1.036	1.473
Median IM-26					**316558**	**0.526**	**53.56**	**343513**	**324.7**	**0.913**	**86.7**	**0.015**	**0.027**	n.r.	**0.655**	**1.431**
Bushveld Complex	Impala mine	IM-28	Leuconorite	-23	316476	0.350	55.08	322862	253.7	1.445	60.3	0.231	0.032	n.r.	0.551	0.931
					317689	1.327	51.12	349758	234.6	1.095	83.1	0.082	0.008	n.r.	0.123	0.886
					335947	0.274	65.12	326686	264.0	1.343	86.1	0.426	0.032	n.r.	2.033	1.007
					343992	0.132	77.90	332579	353.0	0.325	72.3	0.082	0.014	n.r.	0.098	1.187
Median IM-28					**326818**	**0.312**	**60.10**	**329632**	**258.8**	**1.219**	**77.7**	**0.157**	**0.023**	n.r.	**0.337**	**0.969**

ANNEXE 20 – Cont.

Intrusion	Locality	Sample	^{111}Cd	^{115}In	^{118}Sn	^{121}Sb	^{128}Te	^{185}Re	^{189}Os	^{193}Ir	^{195}Pt	^{197}Au	^{205}Tl	^{208}Pb	^{209}Bi
LOD			0.025	0.014	0.018	0.012	0.079	0.004	0.008	0.002	0.004	0.007	0.002	0.005	0.002
Bushveld Complex	Impala mine	IM-26	5.538	3.616	6.451	0.012	0.235	0.004	0.008	0.002	0.012	0.008	0.025	410.805	0.064
			4.321	1.387	6.908	0.012	0.228	0.004	0.008	0.002	0.013	0.007	0.022	164.322	0.074
			3.073	1.461	5.903	0.012	0.201	0.004	0.058	0.120	0.004	0.007	0.016	213.010	0.048
			2.891	2.624	5.112	0.012	0.079	0.004	0.008	0.002	0.010	0.007	0.002	7.394	0.076
			8.923	1.698	4.138	0.012	0.362	0.004	0.008	0.002	0.007	0.007	0.002	368.203	0.045
Median IM-26			**4.321**	**1.698**	**5.903**	**0.012**	**0.228**	**0.004**	**0.008**	**0.002**	**0.010**	**0.007**	**0.016**	**213.010**	**0.064**
Bushveld Complex	Impala mine	IM-28	1.887	1.147	0.977	0.012	0.079	0.004	0.008	0.002	0.004	0.007	0.040	17.345	0.111
			5.636	3.457	2.404	0.012	0.412	0.004	0.126	0.002	0.004	0.007	0.002	5.234	0.030
			2.350	1.247	3.439	0.012	0.232	0.004	0.008	0.107	0.004	0.007	0.066	5.632	0.076
			1.552	1.659	3.986	0.012	0.356	0.004	0.100	0.002	0.110	0.007	0.058	4.412	0.167
Median IM-28			**2.118**	**1.453**	**2.921**	**0.012**	**0.294**	**0.004**	**0.054**	**0.002**	**0.004**	**0.007**	**0.049**	**5.433**	**0.094**

ANNEXE 20 – Cont.

Intrusion	Locality	Sample	Rock	Height (cm)	^{34}S	^{59}Co	^{61}Ni	^{65}Cu	^{66}Zn	^{75}As	^{82}Se	^{95}Mo	^{101}Ru	^{103}Rh
LOD					58	0.008	0.31	0.2	0.1	0.044	0.6	0.008	0.008	0.001
Bushveld Complex	Rustemburg mine	AN	Anorthosite	-2	376723	0.110	55.99	329994	329.9	0.044	82.2	0.014	0.008	n.r.
					362243	0.121	59.95	323167	374.3	0.524	86.4	0.008	0.008	n.r.
					381592	0.091	65.73	328786	363.9	1.308	85.9	0.066	0.024	n.r.
Median AN					**376723**	**0.110**	**59.95**	**328786**	**363.9**	**0.524**	**85.9**	**0.014**	**0.008**	n.r.
Bushveld Complex	Rustemburg mine	LC	Lower chromitite	0	360679	0.099	27.39	323775	249.7	0.344	79.0	0.008	0.040	n.r.
					386765	0.071	22.84	343853	244.7	0.044	91.9	0.037	0.008	n.r.
					379766	0.050	26.47	341334	260.5	0.044	88.0	0.008	0.008	n.r.
					356157	2.034	27.97	312212	268.4	0.044	79.4	0.052	0.008	n.r.
					358770	0.114	31.04	335822	266.9	0.044	99.5	0.008	0.008	n.r.
					381288	0.120	26.20	328786	280.6	0.044	79.0	0.024	0.018	n.r.
Median LC					**370223**	**0.107**	**26.93**	**332304**	**263.7**	**0.044**	**83.7**	**0.016**	**0.008**	n.r.
Bushveld Complex	Rustemburg mine	CGM-1	Coarse-grained melanorite	2	346598	0.107	20.40	308560	347.5	0.292	77.0	0.008	0.009	n.r.
					344373	4.200	21.91	329125	246.5	0.641	92.2	0.179	0.021	n.r.
					392456	0.487	55.94	324688	298.2	0.044	81.6	0.066	0.143	n.r.
Median CGM-1					**346598**	**0.487**	**21.91**	**324688**	**298.2**	**0.292**	**81.6**	**0.066**	**0.021**	n.r.
Bushveld Complex	Rustemburg mine	CGM-2	Coarse-grained melanorite	6	346902	0.017	15.52	313733	411.2	0.210	101.9	0.009	0.016	n.r.
					362669	2.022	21.62	325601	316.5	0.432	164.9	0.097	0.023	n.r.
					349945	0.143	13.08	308865	176.2	0.137	185.0	0.142	4.017	n.r.
					351457	0.055	19.48	309169	243.1	0.371	82.6	0.008	0.019	n.r.
					346689	5.622	80.03	318257	189.6	0.412	79.2	0.268	4.595	n.r.
Median CGM-2					**349945**	**0.143**	**19.48**	**313733**	**243.1**	**0.371**	**101.9**	**0.097**	**0.023**	n.r.

ANNEXE 20 – Cont.

Locality	Sample	^{108}Pd	^{109}Ag	^{111}Cd	^{115}In	^{118}Sn	^{121}Sb	^{128}Te	^{185}Re	^{189}Os	^{193}Ir	^{195}Pt	^{197}Au	^{205}Tl	^{208}Pb	^{209}Bi
LOD		0.027	0.003	0.025	0.014	0.018	0.012	0.079	0.004	0.008	0.002	0.004	0.007	0.002	0.005	0.002
Rustemburg mine	AN	1.057	1.546	19.232	1.885	3.013	0.012	0.079	0.004	0.008	0.002	0.021	0.007	0.011	1.448	0.002
		0.988	8.757	19.901	3.094	3.165	0.012	0.314	0.004	0.027	0.002	0.049	0.007	0.028	1.826	0.004
		2.122	3.347	20.266	2.010	3.712	0.012	0.120	0.004	0.008	0.002	0.004	0.013	0.090	2.130	0.057
Median AN		**1.057**	**3.347**	**19.901**	**2.010**	**3.165**	**0.012**	**0.120**	**0.004**	**0.008**	**0.002**	**0.021**	**0.007**	**0.028**	**1.826**	**0.004**
Rustemburg mine	LC	0.755	1.129	10.864	2.147	0.286	0.012	0.365	0.004	0.008	0.087	0.004	0.007	0.002	6.147	0.002
		0.212	6.844	10.224	2.248	0.240	0.012	0.167	0.004	0.008	0.002	0.004	0.007	0.002	3.043	0.020
		0.027	1.369	10.498	1.781	0.587	0.015	0.289	0.013	0.008	0.002	0.011	0.007	0.003	1.619	0.002
		1.210	1.302	13.663	2.433	0.332	0.012	0.079	0.004	0.008	0.002	0.004	0.007	0.006	2.294	0.002
		0.567	7.881	18.045	4.697	0.499	0.058	0.356	0.004	0.008	0.002	0.004	0.011	0.002	1.692	0.011
		0.233	1.263	11.685	3.463	0.018	0.012	0.102	0.004	0.008	0.002	0.004	0.007	0.002	5.325	0.056
Median LC		**0.400**	**1.336**	**11.274**	**2.341**	**0.309**	**0.012**	**0.228**	**0.004**	**0.008**	**0.002**	**0.004**	**0.007**	**0.002**	**2.669**	**0.007**
Rustemburg mine	CGM-1	3.125	1.044	4.138	1.120	0.018	0.012	0.204	0.004	0.008	0.002	0.004	0.007	0.013	4.668	0.015
		1.240	1.707	4.346	3.326	0.077	0.082	0.079	0.004	0.008	0.005	0.004	0.023	0.016	4.838	0.008
		0.786	3.499	12.111	2.473	0.179	0.207	0.079	0.004	0.008	0.002	0.004	0.021	0.017	3.712	0.012
Median CGM-1		**1.240**	**1.707**	**4.346**	**2.473**	**0.077**	**0.082**	**0.079**	**0.004**	**0.008**	**0.002**	**0.004**	**0.021**	**0.016**	**4.668**	**0.012**
Rustemburg mine	CGM-2	0.589	1.954	3.987	0.681	0.061	0.012	0.125	0.004	0.008	0.002	0.004	0.007	0.002	2.404	0.002
		0.475	2.042	3.350	0.691	0.018	0.012	0.098	0.004	0.008	0.006	0.004	0.007	0.006	2.221	0.006
		4.589	2.039	3.013	0.651	0.103	0.012	0.146	0.016	1.095	1.619	0.037	0.007	0.002	2.291	0.152
		3.256	1.327	2.647	1.089	0.018	0.012	0.190	0.004	0.008	0.002	0.011	0.007	0.008	5.266	0.002
		0.878	1.823	2.574	1.360	0.107	0.012	0.262	0.493	5.569	2.891	0.170	0.007	0.026	11.630	0.131
Median CGM-2		**0.878**	**1.954**	**3.013**	**0.691**	**0.061**	**0.012**	**0.146**	**0.004**	**0.008**	**0.006**	**0.011**	**0.007**	**0.006**	**2.404**	**0.006**

ANNEXE 20 – Cont.

Intrusion	Locality	Sample	Rock	Height (cm)	^{34}S	^{59}Co	^{61}Ni	^{65}Cu	^{66}Zn	^{75}As	^{82}Se	^{95}Mo	^{101}Ru	^{103}Rh
LOD					58	0.008	0.31	0.2	0.1	0.044	0.6	0.008	0.008	0.001
Bushveld Complex	Rustemburg mine	UC	Upper chromitite	10	393156	0.124	23.74	319515	362.1	0.044	80.9	0.008	0.011	n.r.
					377941	0.856	87.37	324271	343.9	0.513	68.8	0.086	0.018	n.r.
					389504	0.083	25.26	322558	357.2	0.487	75.2	0.008	0.024	n.r.
					371889	0.229	17.69	332418	185.0	0.321	105.0	0.155	0.008	n.r.
					380376	7.567	124.57	319985	377.6	0.254	65.4	0.008	0.008	n.r.
					366682	0.199	43.51	322148	371.2	0.323	71.5	0.008	0.013	n.r.
Median UC					**379158**	**0.214**	**34.39**	**322353**	**359.7**	**0.322**	**73.4**	**0.008**	**0.012**	n.r.
Bushveld Complex	Rustemburg mine	M-1	Melanorite	13.5	349336	0.040	16.13	320428	295.2	0.044	128.7	0.061	0.046	n.r.
					370158	1.308	279.96	313429	392.5	0.552	137.5	0.213	2.008	n.r.
					369725	0.008	16.79	324080	224.3	0.307	80.6	0.008	0.008	n.r.
					345381	0.018	7.00	319926	188.7	0.494	75.3	0.126	0.008	n.r.
					352579	0.057	9.87	321949	544.7	0.274	75.7	0.008	0.008	n.r.
					347112	0.104	29.52	333374	323.7	0.791	107.7	0.025	0.064	n.r.
Median M-1					**350957**	**0.049**	**16.46**	**321189**	**309.4**	**0.400**	**94.2**	**0.043**	**0.027**	n.r.
Bushveld Complex	Rustemburg mine	M-2	Melanorite	18	331383	0.234	35.91	316525	447.3	0.044	63.0	0.008	0.049	n.r.
					345685	0.058	51.73	318298	426.0	0.044	67.0	0.145	0.008	n.r.
					327587	0.060	39.81	312516	333.7	0.246	77.2	0.008	0.009	n.r.
					331991	0.097	22.52	310690	325.3	0.067	95.2	0.099	0.033	n.r.
					336860	0.094	37.75	318602	365.2	0.562	84.7	0.008	0.013	n.r.
					342033	3.067	38.34	314342	285.1	0.044	129.3	0.008	0.021	n.r.
Median M-2					**334426**	**0.096**	**38.04**	**315433**	**349.4**	**0.056**	**81.0**	**0.008**	**0.017**	n.r.

ANNEXE 20 – Cont.

Locality	Sample	^{108}Pd	^{109}Ag	^{111}Cd	^{115}In	^{118}Sn	^{121}Sb	^{128}Te	^{185}Re	^{189}Os	^{193}Ir	^{195}Pt	^{197}Au	^{205}Tl	^{208}Pb	^{209}Bi
LOD		0.027	0.003	0.025	0.014	0.018	0.012	0.079	0.004	0.008	0.002	0.004	0.007	0.002	0.005	0.002
Rustemburg mine	UC	0.266	16.219	43.515	1.683	0.018	0.012	0.079	0.004	0.008	0.003	0.219	0.007	0.019	10.772	0.002
		0.456	1.768	14.546	1.582	0.141	0.012	0.535	0.004	0.008	0.097	0.055	0.007	0.002	5.356	0.016
		1.036	1.887	20.327	1.865	0.064	0.012	0.168	0.007	0.008	0.002	0.004	0.007	0.002	7.340	0.018
		0.099	1.310	19.475	1.671	0.123	0.012	0.217	0.004	0.008	0.002	0.004	0.007	0.002	3.865	0.002
		2.011	1.935	16.463	1.351	0.018	0.012	0.079	0.024	0.008	0.084	0.004	0.007	0.002	6.158	0.029
		0.102	1.485	17.071	1.108	0.097	0.012	0.312	0.004	0.008	0.002	0.058	0.007	0.008	6.482	0.023
Median UC		**0.361**	**1.827**	**18.273**	**1.626**	**0.080**	**0.012**	**0.192**	**0.004**	**0.008**	**0.002**	**0.029**	**0.007**	**0.002**	**6.320**	**0.017**
Rustemburg mine	M-1	0.027	2.982	6.755	3.544	0.110	0.012	0.187	0.061	0.008	0.055	0.125	0.007	0.023	16.432	0.016
		0.027	2.297	10.285	0.337	0.161	0.024	0.259	0.356	2.313	0.721	0.228	0.007	0.020	8.689	0.100
		0.027	0.636	3.925	1.500	0.522	0.012	0.079	0.004	0.008	0.002	0.011	0.007	0.013	8.969	0.002
		0.027	0.666	3.269	1.089	0.231	0.012	0.321	0.066	0.008	0.002	0.004	0.037	0.002	4.899	0.012
		0.027	1.032	4.869	1.129	0.018	0.012	0.123	0.021	0.008	0.002	0.013	0.009	0.002	6.451	0.005
		0.027	1.990	9.403	1.281	0.146	0.012	0.456	0.021	0.008	0.233	0.088	0.007	0.016	16.889	0.058
Median M-1		**0.027**	**1.511**	**5.812**	**1.205**	**0.154**	**0.012**	**0.223**	**0.041**	**0.008**	**0.028**	**0.051**	**0.007**	**0.015**	**8.829**	**0.014**
Rustemburg mine	M-2	0.027	2.097	13.328	1.475	0.180	0.012	0.079	0.120	0.008	0.002	0.081	0.007	0.004	6.573	0.002
		0.027	1.346	13.237	3.655	0.176	0.012	0.174	0.004	0.008	0.522	0.039	0.029	0.009	5.538	0.008
		0.027	1.062	8.825	1.491	0.455	0.016	0.079	0.004	0.008	0.002	0.004	0.007	0.005	7.060	0.015
		0.027	4.729	15.580	2.458	0.295	0.012	0.116	0.004	0.008	0.090	0.079	0.007	0.002	1.701	0.025
		0.027	1.297	10.620	1.066	0.146	0.012	0.566	0.046	0.008	0.002	0.004	0.007	0.002	4.595	0.022
		0.027	0.904	10.681	1.104	0.157	0.012	0.735	0.004	0.008	0.002	0.599	0.007	0.012	11.411	0.320
Median M-2		**0.027**	**1.321**	**11.959**	**1.483**	**0.178**	**0.012**	**0.145**	**0.004**	**0.008**	**0.002**	**0.059**	**0.007**	**0.005**	**6.056**	**0.019**

ANNEXE 20 – Cont.

Intrusion	Locality	Sample	Rock	Height (cm)	^{34}S	^{59}Co	^{61}Ni	^{65}Cu	^{66}Zn	^{75}As	^{82}Se	^{95}Mo	^{101}Ru	^{103}Rh
LOD					58	0.008	0.31	0.2	0.1	0.044	0.6	0.008	0.008	0.001
Bushveld Complex	Rustemburg mine	M-3	Melanorite	23	329861	0.201	61.77	314951	763.8	0.121	80.0	0.256	0.012	n.r.
					324992	12.449	48.69	313125	310.7	0.240	78.0	0.008	0.042	n.r.
					338990	0.132	43.82	315559	343.3	0.402	74.6	0.107	0.008	n.r.
					359076	4.523	52.95	336688	364.0	0.044	79.2	0.008	0.014	n.r.
					334121	0.055	40.17	321341	397.2	0.099	72.7	0.076	0.014	n.r.
Median M-3					**334121**	**0.201**	**48.69**	**315559**	**364.0**	**0.121**	**78.0**	**0.076**	**0.014**	n.r.
Bushveld Complex	Rustemburg mine	M-4	Melanorite	27	341778	0.086	46.56	326215	419.9	0.044	79.0	0.008	0.008	n.r.
					337530	2.034	58.12	323428	372.4	0.170	77.4	0.010	0.024	n.r.
					347511	0.110	50.26	327839	287.6	0.112	81.9	0.008	0.008	n.r.
					330470	13.466	69.99	319979	302.8	0.044	98.6	0.008	0.008	n.r.
					349976	0.943	45.34	338976	232.2	0.044	88.9	0.057	0.012	n.r.
					359089	1.023	23.44	316776	329.3	0.236	82.6	0.066	0.024	n.r.
Median M-4					**344644**	**0.983**	**48.41**	**324821**	**316.0**	**0.078**	**82.2**	**0.009**	**0.010**	n.r.

ANNEXE 20 – Cont.

Locality	Sample	^{108}Pd	^{109}Ag	^{111}Cd	^{115}In	^{118}Sn	^{121}Sb	^{128}Te	^{185}Re	^{189}Os	^{193}Ir	^{195}Pt	^{197}Au	^{205}Tl	^{208}Pb	^{209}Bi
LOD		0.027	0.003	0.025	0.014	0.018	0.012	0.079	0.004	0.008	0.002	0.004	0.007	0.002	0.005	0.002
Rustemburg mine	M-3	0.027	0.937	22.214	4.203	3.585	0.012	0.271	0.004	0.008	0.745	0.004	0.007	0.007	2.161	0.042
		0.027	1.157	14.120	1.469	3.533	0.012	0.134	0.088	0.008	0.002	0.004	0.007	0.002	1.409	0.040
		0.027	1.004	12.142	1.395	2.145	0.012	0.117	0.004	0.008	0.002	0.004	0.007	0.009	6.299	0.225
		0.027	0.973	14.424	3.227	3.076	0.012	0.250	0.004	0.008	0.002	0.004	0.007	0.002	1.680	0.056
		0.027	1.083	13.176	1.526	2.927	0.012	1.022	0.066	0.008	0.066	0.004	0.007	0.002	3.256	0.098
Median M-3		**0.027**	**1.004**	**14.120**	**1.526**	**3.076**	**0.012**	**0.250**	**0.004**	**0.008**	**0.002**	**0.004**	**0.007**	**0.002**	**2.161**	**0.056**
Rustemburg mine	M-4	0.027	1.175	12.872	2.211	0.977	0.012	1.211	0.122	0.008	0.002	0.012	0.007	0.002	3.867	0.026
		0.027	0.870	12.263	1.411	0.368	0.012	0.079	0.004	0.008	0.002	0.029	0.007	0.010	8.673	0.051
		0.027	0.837	9.616	2.082	1.233	0.012	0.562	0.004	0.008	0.002	0.091	0.007	0.002	9.586	0.050
		0.027	3.280	12.385	1.282	0.651	0.012	0.436	0.004	0.008	1.023	0.004	0.007	0.004	2.663	0.098
		0.027	0.870	8.946	1.430	0.116	0.012	0.429	0.099	0.008	0.002	0.004	0.007	0.002	6.177	0.770
		0.027	3.712	10.803	0.943	0.158	0.012	0.079	0.004	0.018	0.232	0.018	0.052	0.019	4.230	0.027
Median M-4		**0.027**	**1.022**	**11.533**	**1.420**	**0.510**	**0.012**	**0.432**	**0.004**	**0.008**	**0.002**	**0.015**	**0.007**	**0.003**	**5.204**	**0.050**

ANNEXE 20 – Cont.

Intrusion	Locality	Sample	Rock	^{34}S	^{59}Co	^{61}Ni	^{65}Cu	^{66}Zn	^{75}As	^{82}Se	^{95}Mo	^{101}Ru	^{103}Rh	^{108}Pd
LOD				58	0.008	0.31	0.2	0.1	0.044	0.6	0.008	0.008	0.001	0.027
Stillwater Complex	East Boulder mine	ST-12	Mela troctolite	330774	2.830	33.47	340816	184.8	0.248	227.6	0.008	0.216	n.r.	1.146
				385548	4.601	34.62	317290	144.7	0.156	189.9	0.037	0.110	n.r.	1.858
Median ST-12				**358161**	**3.715**	**34.05**	**329053**	**164.7**	**0.202**	**208.7**	**0.022**	**0.163**	n.r.	**1.502**
Stillwater Complex	East Boulder mine	ST-14	Anorthosite	361204	0.210	44.73	348119	234.9	0.044	174.7	0.008	0.015	n.r.	0.027
				349641	0.301	72.42	339295	284.5	0.122	157.9	0.015	0.033	n.r.	0.212
				363943	0.207	36.52	337773	260.8	0.365	146.1	0.008	0.046	n.r.	0.521
				362726	0.298	40.17	322988	263.8	0.183	161.6	0.024	0.120	n.r.	0.027
				353292	0.316	28.91	348424	256.8	0.426	153.4	0.008	0.008	n.r.	3.245
				356031	0.417	45.04	339903	332.8	0.213	143.3	0.008	0.088	n.r.	0.321
Median ST-14				**358618**	**0.300**	**42.45**	**339599**	**262.3**	**0.198**	**155.6**	**0.008**	**0.040**	n.r.	**0.266**
Stillwater Complex	East Boulder mine	ST-16	Leuconorite	362421	4.869	21.61	362726	598.8	0.044	183.2	0.335	0.099	n.r.	0.027
				363639	0.450	5.17	340207	489.9	0.091	188.4	0.009	0.123	n.r.	0.027
				357553	0.435	5.78	330596	569.0	0.396	211.8	0.008	0.013	n.r.	0.126
				357575	0.320	7.91	359378	368.2	0.548	174.4	0.256	0.030	n.r.	0.027
				356335	1.826	133.89	346902	337.8	0.639	186.8	0.186	0.096	n.r.	3.365
				330375	0.073	24.65	350554	529.5	0.044	197.8	0.199	0.008	n.r.	0.324
Median ST-16				**357564**	**0.443**	**14.76**	**348728**	**509.7**	**0.243**	**187.6**	**0.192**	**0.063**	n.r.	**0.076**
Stillwater Complex	East Boulder mine	ST-17	Olivine mela gabbronorite	341425	267.784	286.04	274783	1551.3	0.390	234.3	0.076	0.008	n.r.	0.027
				361698	197.795	221.39	322139	161.3	0.255	162.8	0.008	0.098	n.r.	0.268
				348424	37.733	139.45	309473	549.1	0.517	185.6	0.124	0.008	n.r.	0.161
				352379	52.100	51.73	317994	489.3	0.304	198.4	0.008	0.061	n.r.	0.544
Median ST-17				**350401**	**124.947**	**180.42**	**313733**	**519.2**	**0.347**	**192.0**	**0.042**	**0.034**	n.r.	**0.214**

ANNEXE 20 – Cont.

Locality	Sample	^{109}Ag	^{111}Cd	^{115}In	^{118}Sn	^{121}Sb	^{128}Te	^{185}Re	^{189}Os	^{193}Ir	^{195}Pt	^{197}Au	^{205}Tl	^{208}Pb	^{209}Bi
LOD		0.003	0.025	0.014	0.018	0.012	0.079	0.004	0.008	0.002	0.004	0.007	0.002	0.005	0.002
East Boulder mine	ST-12	0.943	0.904	0.036	0.143	0.024	0.079	0.004	0.090	0.002	0.004	0.024	0.352	1.156	0.090
		1.917	0.339	0.136	0.204	0.012	0.169	0.004	0.120	0.076	0.030	0.007	0.256	2.383	0.105
Median ST-12		**1.430**	**0.622**	**0.086**	**0.174**	**0.018**	**0.124**	**0.004**	**0.105**	**0.039**	**0.017**	**0.016**	**0.304**	**1.769**	**0.097**
East Boulder mine	ST-14	3.286	1.156	0.218	0.201	0.012	0.304	0.004	0.008	0.002	0.004	0.007	0.002	20.297	0.002
		2.821	1.278	0.456	0.018	0.012	0.091	0.004	0.015	0.042	0.004	0.007	0.076	11.716	0.015
		13.267	1.856	0.267	0.103	0.012	0.517	0.004	0.008	0.002	0.016	0.007	0.010	13.602	0.002
		8.094	0.761	0.231	0.521	0.012	0.396	0.004	0.085	0.066	0.008	0.007	0.002	8.064	0.003
		14.211	1.795	0.270	0.119	0.012	0.211	0.004	0.012	0.002	0.007	0.007	0.012	11.594	0.006
		10.194	1.126	0.246	0.354	0.012	1.233	0.004	0.008	0.063	0.004	0.007	0.036	7.364	0.057
Median ST-14		**9.144**	**1.217**	**0.257**	**0.160**	**0.012**	**0.350**	**0.004**	**0.010**	**0.022**	**0.005**	**0.007**	**0.011**	**11.655**	**0.005**
East Boulder mine	ST-16	41.324	5.690	0.751	0.183	0.012	0.099	1.522	0.207	0.005	0.140	0.007	0.007	11.837	0.014
		33.656	8.886	0.772	0.243	0.012	0.232	0.004	0.008	0.002	0.243	0.007	0.002	3.895	0.010
		32.895	8.916	1.523	0.216	0.012	0.079	0.004	0.008	0.002	0.026	0.007	0.002	1.001	0.003
		33.138	8.338	0.732	0.563	0.016	0.082	0.004	0.008	0.002	0.076	0.007	0.003	5.264	0.015
		33.321	8.520	0.766	0.262	0.012	0.079	0.004	0.010	0.002	0.097	0.007	0.002	4.504	0.010
		34.508	8.307	0.863	0.386	0.012	0.152	0.004	0.008	0.002	0.004	0.037	0.027	6.116	0.013
Median ST-16		**33.488**	**8.429**	**0.769**	**0.253**	**0.012**	**0.090**	**0.004**	**0.008**	**0.002**	**0.087**	**0.007**	**0.003**	**4.884**	**0.012**
East Boulder mine	ST-17	0.660	13.998	0.317	0.018	0.079	0.310	0.004	0.030	0.049	0.004	0.007	0.271	3.704	0.024
		0.934	0.669	0.123	0.018	0.012	0.079	0.004	0.008	0.002	0.015	0.007	0.210	4.291	0.002
		0.954	1.613	0.655	0.052	0.057	0.609	0.004	0.057	0.057	0.004	0.033	0.222	10.285	0.103
		3.588	0.974	0.374	0.037	0.064	0.422	0.004	0.008	0.023	0.004	0.007	0.455	10.985	0.086
Median ST-17		**0.944**	**1.293**	**0.346**	**0.027**	**0.061**	**0.366**	**0.004**	**0.019**	**0.036**	**0.004**	**0.007**	**0.246**	**7.288**	**0.055**

ANNEXE 20 – Cont.

Intrusion	Locality	Sample	Rock	^{34}S	^{59}Co	^{61}Ni	^{65}Cu	^{66}Zn	^{75}As	^{82}Se	^{95}Mo	^{101}Ru	^{103}Rh	^{108}Pd
LOD				58	0.008	0.31	0.2	0.1	0.044	0.6	0.008	0.008	0.001	0.027
Stillwater Complex	Stillwater mine	P-4	Anorthosite	353901	0.043	13.69	331991	206.9	0.044	127.5	0.008	0.008	n.r.	0.027
				365464	0.055	18.87	341120	282.7	0.061	142.1	0.062	0.027	n.r.	0.467
				378245	0.100	31.65	353597	317.7	0.546	144.9	0.040	0.008	n.r.	0.122
				363983	0.008	22.82	348125	256.2	0.044	141.2	0.008	0.030	n.r.	1.323
				359683	0.094	23.43	345989	260.2	0.267	161.4	0.086	0.066	n.r.	0.255
				383722	4.022	34.69	349641	280.0	0.044	156.8	0.008	0.052	n.r.	0.027
Median P-4				**364724**	**0.075**	**23.13**	**347057**	**270.1**	**0.053**	**143.5**	**0.024**	**0.029**	n.r.	**0.189**
Stillwater Complex	Stillwater mine	P-3	Leuco gabbronorite	360596	6.086	1308.49	342946	499.1	0.347	197.9	0.008	0.014	n.r.	24.154
				351771	0.271	7.76	337469	483.8	0.044	188.6	0.063	0.102	n.r.	0.423
				355727	0.578	14.30	338382	727.3	0.044	209.7	0.077	0.037	n.r.	2.662
				351467	0.371	6.48	331383	184.1	0.044	197.2	0.010	0.030	n.r.	6.478
				358465	0.152	14.31	344163	213.0	0.044	218.5	0.052	0.017	n.r.	0.544
				352988	1.478	23.48	332600	538.6	0.253	218.8	0.008	0.043	n.r.	0.636
Median P-3				**354357**	**0.475**	**14.31**	**337925**	**491.4**	**0.044**	**203.8**	**0.031**	**0.033**	n.r.	**1.649**

ANNEXE 20 – Cont.

Locality	Sample	^{109}Ag	^{111}Cd	^{115}In	^{118}Sn	^{121}Sb	^{128}Te	^{185}Re	^{189}Os	^{193}Ir	^{195}Pt	^{197}Au	^{205}Tl	^{208}Pb	^{209}Bi
LOD		0.003	0.025	0.014	0.018	0.012	0.079	0.004	0.008	0.002	0.004	0.007	0.002	0.005	0.002
Stillwater mine	P-4	2.587	5.508	0.222	0.070	0.027	0.761	0.004	0.008	0.002	0.274	0.007	0.002	2.952	0.017
		2.666	4.625	0.177	0.057	0.021	0.122	0.004	0.059	0.048	0.004	0.008	0.002	0.949	0.002
		0.545	4.291	0.152	0.018	0.012	0.274	0.004	0.008	0.002	0.004	0.008	0.002	0.761	0.023
		1.537	2.708	0.204	0.122	0.012	0.168	0.004	0.063	0.036	0.009	0.007	0.003	1.716	0.024
		0.742	4.199	0.164	0.018	0.012	0.131	0.004	0.008	0.002	0.017	0.009	0.002	1.865	0.002
		0.761	3.925	0.137	0.018	0.012	0.079	0.004	0.076	0.103	0.004	0.010	0.005	2.069	0.002
Median P-4		**1.149**	**4.245**	**0.171**	**0.038**	**0.012**	**0.149**	**0.004**	**0.033**	**0.019**	**0.007**	**0.008**	**0.002**	**1.791**	**0.009**
Stillwater mine	P-3	8.338	5.660	1.519	0.645	0.023	0.173	0.004	0.008	0.007	0.051	0.010	0.016	7.394	0.002
		8.155	5.812	1.547	0.581	0.012	0.079	0.004	0.008	0.002	0.004	0.007	0.005	11.563	0.109
		7.090	7.912	0.974	0.326	0.021	0.079	0.004	0.096	0.057	0.032	0.012	0.019	24.587	0.002
		12.476	3.256	0.949	0.322	0.019	0.099	0.004	0.008	0.002	0.137	0.007	0.023	11.320	0.002
		9.646	4.351	0.459	0.088	0.012	0.118	0.004	0.086	0.103	0.004	0.007	0.002	6.269	0.057
		8.124	7.760	0.523	0.131	0.012	0.210	0.004	0.008	0.002	0.004	0.007	0.002	5.599	0.002
Median P-3		**8.247**	**5.736**	**0.962**	**0.324**	**0.015**	**0.108**	**0.004**	**0.008**	**0.004**	**0.018**	**0.007**	**0.010**	**9.357**	**0.002**

ANNEXE 20 – Cont.

Intrusion	Locality	Sample	Rock	^{34}S	^{59}Co	^{61}Ni	^{65}Cu	^{66}Zn	^{75}As	^{82}Se	^{95}Mo	^{101}Ru	^{103}Rh	^{108}Pd
LOD				58	0.008	0.31	0.2	0.1	0.044	0.6	0.008	0.008	0.001	0.027
Stillwater Complex	Banded Series	BS-18	Leuco gabbronorite	371550	0.173	20.39	332904	401.7	0.044	186.2	0.008	0.008	n.r.	0.027
				375506	0.383	7.30	329253	480.8	0.044	171.3	0.008	0.008	n.r.	0.027
				371855	0.472	17.35	321037	245.9	0.116	159.1	0.008	0.008	n.r.	0.027
				366986	0.402	14.52	332296	380.4	0.044	145.5	0.008	0.008	n.r.	0.027
				370333	0.453	19.17	334730	443.1	0.302	140.9	0.008	0.008	n.r.	0.027
				361508	11.563	213.01	330774	442.5	0.044	149.1	0.008	0.008	n.r.	0.027
				359987	1.461	79.12	327427	463.4	0.044	150.0	0.008	0.008	n.r.	0.027
				365769	0.241	7.55	335034	459.5	0.044	144.5	0.008	0.008	n.r.	0.027
				359789	0.140	0.31	333209	380.7	0.326	130.5	0.008	0.008	n.r.	0.027
				359074	2.434	6.42	331078	505.1	0.044	143.6	0.008	0.008	n.r.	0.027
				353287	0.138	2.89	335454	493.0	0.290	131.5	0.008	0.008	n.r.	0.027
				353215	0.161	3.59	338077	417.3	0.044	151.8	0.008	0.008	n.r.	0.027
				348119	0.167	12.48	337796	317.1	0.113	151.5	0.008	0.008	n.r.	0.027
Median BS-18				**363639**	**0.353**	**13.50**	**332600**	**429.9**	**0.074**	**150.8**	**0.008**	**0.008**	n.r.	**0.027**
Stillwater Complex	Picket Pin	PP-AN	Anorthosite	351459	0.341	15.52	317254	191.4	0.044	124.2	0.008	0.090	n.r.	0.216
				368785	0.186	0.31	331368	271.7	0.192	96.2	0.008	0.008	n.r.	0.090
				346293	0.210	0.31	333909	270.8	0.119	124.5	0.008	0.008	n.r.	0.027
				339903	0.283	2.98	319819	248.6	0.124	126.6	0.008	0.047	n.r.	1.022
				354814	0.514	44.51	328948	223.7	0.044	135.1	0.008	0.015	n.r.	0.027
				341479	0.313	8.54	320732	327.4	0.044	121.4	0.008	0.057	n.r.	0.027
				341729	0.396	17.95	331254	318.9	0.044	125.7	0.008	0.021	n.r.	0.063
				342338	0.289	8.03	324992	307.3	0.143	125.4	0.008	0.008	n.r.	0.076
				350249	0.718	176.49	324384	346.9	0.044	123.9	0.008	0.008	n.r.	0.855
				353276	0.359	48.69	324384	322.6	0.044	131.8	0.008	0.008	n.r.	0.345
Median PP-AN				**350249**	**0.341**	**9.74**	**324992**	**271.7**	**0.044**	**124.5**	**0.008**	**0.015**	n.r.	**0.076**

ANNEXE 20 – Cont.

Locality	Sample	^{109}Ag	^{111}Cd	^{115}In	^{118}Sn	^{121}Sb	^{128}Te	^{185}Re	^{189}Os	^{193}Ir	^{195}Pt	^{197}Au	^{205}Tl	^{208}Pb	^{209}Bi
LOD		0.003	0.025	0.014	0.018	0.012	0.079	0.004	0.008	0.002	0.004	0.007	0.002	0.005	0.002
Banded Series	BS-18	15.915	2.830	0.744	0.533	0.012	10.955	0.004	0.008	0.002	0.004	0.007	0.012	10.437	1.126
		3.128	3.499	0.337	0.231	0.012	0.487	0.004	0.008	0.002	0.004	0.007	0.155	12.750	1.993
		5.264	1.826	0.191	0.097	0.055	0.487	0.004	0.008	0.002	0.004	0.007	0.010	8.916	1.268
		10.468	2.769	0.327	0.341	0.012	2.252	0.004	0.008	0.002	0.004	0.007	0.002	6.786	1.505
		10.766	2.760	0.306	0.338	0.012	5.082	0.004	0.008	0.002	0.004	0.007	0.002	6.857	0.529
		14.546	3.317	0.537	0.347	0.012	7.699	0.004	0.008	0.002	0.004	0.007	0.002	11.168	0.612
		15.458	3.560	0.519	0.344	0.012	11.229	0.004	0.008	0.002	0.004	0.007	0.002	5.964	1.822
		9.424	2.952	1.136	0.566	0.012	3.104	0.004	0.008	0.002	0.004	0.007	0.011	9.007	0.569
		11.259	1.978	0.385	1.187	0.012	1.445	0.004	0.008	0.002	0.004	0.007	0.012	8.155	1.657
		7.577	4.169	1.145	0.752	0.012	13.054	0.004	0.008	0.002	0.004	0.007	0.011	10.072	1.257
		6.594	3.895	1.096	0.679	0.012	0.715	0.004	0.008	0.002	0.004	0.007	0.014	10.529	1.310
		7.358	2.374	0.618	1.695	0.012	4.960	0.004	0.008	0.002	0.004	0.007	0.002	4.625	0.975
		3.064	2.221	0.661	0.597	0.012	11.411	0.004	0.008	0.002	0.004	0.007	0.002	7.121	1.771
Median BS-18		**9.946**	**2.891**	**0.528**	**0.379**	**0.012**	**2.678**	**0.004**	**0.008**	**0.002**	**0.004**	**0.007**	**0.006**	**8.962**	**1.191**
Picket Pin	PP-AN	1.184	6.634	0.620	0.085	0.012	0.079	0.004	0.008	0.002	0.103	0.007	0.017	8.460	0.088
		0.514	9.007	0.554	0.067	0.012	0.142	0.004	0.054	0.042	0.004	0.007	0.002	0.499	0.007
		0.697	7.925	0.699	0.158	0.012	0.099	0.004	0.087	0.034	0.004	0.007	0.002	2.100	0.036
		1.147	8.794	0.623	0.091	0.012	0.079	0.004	0.100	0.002	0.004	0.007	0.002	3.086	0.027
		37.733	8.216	0.709	0.100	0.012	0.102	0.004	0.037	0.068	0.058	0.007	0.008	2.343	0.095
		0.326	8.673	0.623	0.168	0.012	0.079	0.004	0.008	0.002	0.004	0.007	0.002	1.205	0.002
		0.274	8.399	0.669	0.128	0.012	0.098	0.004	0.062	0.095	0.004	0.007	0.002	1.102	0.046
		0.329	8.884	0.633	0.018	0.012	0.455	0.004	0.022	0.002	0.004	0.007	0.002	1.439	0.014
		1.022	9.920	0.678	0.149	0.012	0.212	0.004	0.008	0.002	0.004	0.007	0.002	2.252	0.091
		2.921	9.798	0.703	0.776	0.012	0.079	0.004	0.008	0.002	0.004	0.007	0.002	2.282	0.023
Median PP-NA		**1.022**	**8.673**	**0.669**	**0.103**	**0.012**	**0.098**	**0.004**	**0.022**	**0.002**	**0.004**	**0.007**	**0.002**	**2.252**	**0.036**

ANNEXE 21 - Average proportion (%) of each element hosted in pyrrhotite (Po), pentlandite (Pn), chalcopyrite (Ccp), phlogopite (phlog) and sum, from different localities of the Bushveld and Stillwater Complexes. Abbreviations: BMS= base-metal sulfides; n.r.= not reported; n.d.= not determined; N= number of samples.

ANNEXE 21

Intrusion	Locality	BMS	Co	Pd	Ir	Pt	Rh	Os	Ru	Au	Sb
Bushveld Complex	Impala Mine - samples above the Merensky Reef interval (N= 8)	Po	0.2%	1.1%	15.3%	0.0%	4.0%	41.3%	11.2%	0.0%	0.1%
		Pn	21.7%	27.3%	7.1%	0.0%	21.8%	16.4%	13.3%	0.0%	0.2%
		Ccp	0.0%	0.5%	0.1%	0.0%	n.r.	0.7%	0.2%	0.0%	0.1%
		phlog									6.5%
		Sum	**22.0%**	**29.0%**	**22.4%**	**0.0%**	**25.8%**	**58.4%**	**24.7%**	**0.1%**	**6.9%**
Bushveld Complex	Impala Mine, Merensky Reef - Silicate rocks only (N= 6)	Po	0.2%	0.5%	16.1%	0.0%	1.0%	21.9%	6.6%	0.0%	0.5%
		Pn	58.3%	53.9%	21.8%	0.1%	77.7%	16.9%	6.1%	0.0%	0.4%
		Ccp	0.0%	0.0%	0.0%	0.0%	n.r.	0.1%	0.0%	0.0%	0.2%
		Sum	**58.5%**	**54.4%**	**38.0%**	**0.1%**	**78.7%**	**38.9%**	**12.8%**	**0.0%**	**1.1%**
Bushveld Complex	Impala Mine, Merensky Reef - Chromitites only (N= 2)	Po	0.0%	0.0%	0.6%	0.0%	0.0%	1.1%	0.1%	0.0%	0.2%
		Pn	17.0%	38.8%	5.2%	0.1%	33.9%	3.1%	1.0%	0.0%	0.4%
		Ccp	0.0%	0.1%	0.0%	0.0%	n.r.	0.0%	0.0%	0.0%	0.2%
		Sum	**17.0%**	**38.9%**	**5.8%**	**0.1%**	**33.9%**	**4.2%**	**1.1%**	**0.0%**	**0.8%**
Bushveld Complex	Rustenburg Mine, Merensky Reef - Silicate rocks only (N= 7)	Po	0.1%	0.3%	26.1%	0.0%	1.0%	33.4%	13.2%	0.0%	0.4%
		Pn	54.2%	50.7%	40.0%	0.4%	61.4%	16.0%	15.5%	0.0%	0.6%
		Ccp	0.0%	0.0%	0.0%	0.0%	n.r.	0.0%	0.0%	0.0%	0.2%
		Sum	**54.3%**	**51.0%**	**66.0%**	**0.5%**	**62.4%**	**49.5%**	**28.7%**	**0.0%**	**1.2%**
Bushveld Complex	Rustenburg Mine, Merensky Reef - Chromitites only (N= 2)	Po	0.0%	0.0%	1.9%	0.0%	0.1%	3.7%	0.8%	0.0%	0.2%
		Pn	20.1%	35.9%	3.9%	0.3%	13.9%	19.6%	2.7%	0.0%	0.6%
		Ccp	0.0%	0.0%	0.0%	0.0%	n.r.	0.0%	0.0%	0.0%	0.1%
		Sum	**20.1%**	**36.0%**	**5.8%**	**0.3%**	**14.0%**	**23.4%**	**3.5%**	**0.0%**	**0.9%**

ANNEXE 21 – Cont.

Intrusion	Locality	BMS	Bi	As	Te	Se	Cd	Pb	Sn	Zn
Bushveld Complex	Impala Mine - samples above the Merensky Reef interval (N= 8)	Po	14.14%	5.53%	2.19%	61.54%	n.d.	n.d.	n.d.	n.d.
		Pn	11.85%	9.38%	74.14%	52.53%	n.d.	n.d.	n.d.	n.d.
		Ccp	7.33%	0.53%	2.60%	16.56%	n.d.	n.d.	n.d.	n.d.
		phlog	<1.5	3.00%						
		Sum	**33.32%**	**18.44%**	**78.93%**	**130.64%**	**n.d.**	**n.d.**	**n.d.**	**n.d.**
Bushveld Complex	Impala Mine, Merensky Reef - Silicate rocks only (N= 6)	Po	0.49%	33.47%	0.58%	73.90%	n.d.	n.d.	n.d.	n.d.
		Pn	0.45%	5.47%	0.30%	39.30%	n.d.	n.d.	n.d.	n.d.
		Ccp	0.09%	6.39%	0.07%	10.51%	n.d.	n.d.	n.d.	n.d.
		Sum	**1.04%**	**45.33%**	**0.95%**	**123.71%**	**n.d.**	**n.d.**	**n.d.**	**n.d.**
Bushveld Complex	Impala Mine, Merensky Reef - Chromitites only (N= 2)	Po	0.03%	2.71%	0.18%	21.05%	n.d.	n.d.	n.d.	n.d.
		Pn	0.17%	8.66%	0.63%	79.84%	n.d.	n.d.	n.d.	n.d.
		Ccp	0.02%	4.27%	0.12%	20.39%	n.d.	n.d.	n.d.	n.d.
		Sum	**0.23%**	**15.64%**	**0.93%**	**121.28%**	**n.d.**	**n.d.**	**n.d.**	**n.d.**
Bushveld Complex	Rustenburg Mine, Merensky Reef - Silicate rocks only (N= 7)	Po	0.36%	2.51%	0.40%	47.70%	n.d.	n.d.	n.d.	n.d.
		Pn	0.04%	2.67%	0.16%	47.84%	n.d.	n.d.	n.d.	n.d.
		Ccp	0.01%	2.03%	0.06%	8.55%	n.d.	n.d.	n.d.	n.d.
		Sum	**0.42%**	**7.21%**	**0.62%**	**104.10%**	**n.d.**	**n.d.**	**n.d.**	**n.d.**
Bushveld Complex	Rustenburg Mine, Merensky Reef - Chromitites only (N= 2)	Po	0.13%	1.98%	0.11%	29.32%	n.d.	n.d.	n.d.	n.d.
		Pn	0.08%	6.98%	0.23%	73.30%	n.d.	n.d.	n.d.	n.d.
		Ccp	0.02%	1.18%	0.13%	18.03%	n.d.	n.d.	n.d.	n.d.
		Sum	**0.23%**	**10.14%**	**0.47%**	**120.66%**	**n.d.**	**n.d.**	**n.d.**	**n.d.**

ANNEXE 21 – Cont.

Intrusion	Locality	BMS	Co	Pd	Ir	Pt	Rh	Os	Ru	Au	Sb
Stillwater Complex	East Boulder Mine - J-M Reef (N= 4)	Po	0.5%	0.1%	17.2%	0.0%	0.9%	0.8%	2.7%	0.0%	0.7%
		Pn	49.1%	62.6%	45.8%	0.1%	88.0%	12.2%	76.1%	0.0%	1.3%
		Ccp	0.0%	0.0%	0.1%	0.0%	n.r.	0.0%	0.1%	0.0%	0.5%
		Sum	**49.7%**	**62.7%**	**63.1%**	**0.1%**	**88.9%**	**13.1%**	**78.9%**	**0.0%**	**2.5%**
Stillwater Complex	Stillwater Mine - J-M Reef (N= 2)	Po	0.3%	0.0%	25.2%	0.0%	2.2%	2.2%	4.5%	0.0%	7.5%
		Pn	42.1%	51.5%	27.3%	0.1%	28.2%	5.6%	26.3%	0.0%	17.1%
		Ccp	0.0%	0.0%	0.3%	0.0%	n.r.	0.2%	0.1%	0.0%	3.6%
		Sum	**42.3%**	**51.5%**	**52.8%**	**0.1%**	**30.5%**	**8.0%**	**30.8%**	**0.0%**	**28.2%**
Stillwater Complex	Banded Series - Gabbronorite II (N= 1)	Po	0.5%	2.3%	n.d.	1.0%	n.d.	n.d.	n.d.	0.0%	0.1%
		Pn	45.6%	17.1%	n.d.	1.5%	n.d.	n.d.	n.d.	0.0%	0.2%
		Ccp	0.0%	5.0%	n.d.	2.1%	n.d.	n.d.	n.d.	0.0%	0.3%
		Sum	**46.1%**	**24.4%**	**n.d.**	**4.6%**	**n.d.**	**n.d.**	**n.d.**	**0.1%**	**0.6%**

ANNEXE 21 – Cont.

Intrusion	Locality	BMS	Bi	As	Te	Se	Cd	Pb	Sn	Zn
Stillwater Complex	East Boulder Mine - J-M Reef (N= 4)	Po	0.14%	1.07%	0.05%	35.41%	0.36%	0.12%	0.22%	0.00%
		Pn	0.02%	1.55%	0.43%	69.95%	0.82%	0.29%	0.15%	0.05%
		Ccp	0.04%	1.11%	0.05%	16.59%	1.97%	0.83%	0.32%	1.65%
		Sum	**0.19%**	**3.72%**	**0.52%**	**121.96%**	**3.15%**	**1.25%**	**0.69%**	**1.70%**
Stillwater Complex	Stillwater Mine - J-M Reef (N= 2)	Po	0.23%	13.21%	0.05%	40.69%	3.75%	0.83%	0.40%	0.03%
		Pn	0.01%	6.19%	0.42%	38.86%	0.66%	2.23%	0.94%	0.05%
		Ccp	0.01%	1.52%	0.02%	16.17%	87.31%	1.44%	0.43%	21.22%
		Sum	**0.25%**	**20.92%**	**0.49%**	**95.73%**	**91.72%**	**4.51%**	**1.78%**	**21.30%**
Stillwater Complex	Banded Series - Gabbronorite II (N= 1)	Po	1.22%	1.48%	0.04%	17.02%	0.10%	0.30%	0.15%	0.00%
		Pn	4.55%	16.99%	55.07%	30.95%	0.16%	2.09%	0.18%	0.00%
		Ccp	8.52%	1.02%	3.17%	26.23%	25.90%	2.92%	1.23%	5.31%
		Sum	**14.29%**	**19.49%**	**58.28%**	**74.21%**	**26.16%**	**5.30%**	**1.56%**	**5.32%**